

# Advances in sea state modeling and climate change impacts

**Edited by**

Adem Akpinar, Giovanni Besio and Bahareh Kamranzad

**Published in**

Frontiers in Marine Science



#### FRONTIERS EBOOK COPYRIGHT STATEMENT

The copyright in the text of individual articles in this ebook is the property of their respective authors or their respective institutions or funders. The copyright in graphics and images within each article may be subject to copyright of other parties. In both cases this is subject to a license granted to Frontiers.

The compilation of articles constituting this ebook is the property of Frontiers.

Each article within this ebook, and the ebook itself, are published under the most recent version of the Creative Commons CC-BY licence. The version current at the date of publication of this ebook is CC-BY 4.0. If the CC-BY licence is updated, the licence granted by Frontiers is automatically updated to the new version.

When exercising any right under the CC-BY licence, Frontiers must be attributed as the original publisher of the article or ebook, as applicable.

Authors have the responsibility of ensuring that any graphics or other materials which are the property of others may be included in the CC-BY licence, but this should be checked before relying on the CC-BY licence to reproduce those materials. Any copyright notices relating to those materials must be complied with.

Copyright and source acknowledgement notices may not be removed and must be displayed in any copy, derivative work or partial copy which includes the elements in question.

All copyright, and all rights therein, are protected by national and international copyright laws. The above represents a summary only. For further information please read Frontiers' Conditions for Website Use and Copyright Statement, and the applicable CC-BY licence.

ISSN 1664-8714  
ISBN 978-2-83251-948-6  
DOI 10.3389/978-2-83251-948-6

## About Frontiers

Frontiers is more than just an open access publisher of scholarly articles: it is a pioneering approach to the world of academia, radically improving the way scholarly research is managed. The grand vision of Frontiers is a world where all people have an equal opportunity to seek, share and generate knowledge. Frontiers provides immediate and permanent online open access to all its publications, but this alone is not enough to realize our grand goals.

## Frontiers journal series

The Frontiers journal series is a multi-tier and interdisciplinary set of open-access, online journals, promising a paradigm shift from the current review, selection and dissemination processes in academic publishing. All Frontiers journals are driven by researchers for researchers; therefore, they constitute a service to the scholarly community. At the same time, the *Frontiers journal series* operates on a revolutionary invention, the tiered publishing system, initially addressing specific communities of scholars, and gradually climbing up to broader public understanding, thus serving the interests of the lay society, too.

## Dedication to quality

Each Frontiers article is a landmark of the highest quality, thanks to genuinely collaborative interactions between authors and review editors, who include some of the world's best academicians. Research must be certified by peers before entering a stream of knowledge that may eventually reach the public - and shape society; therefore, Frontiers only applies the most rigorous and unbiased reviews. Frontiers revolutionizes research publishing by freely delivering the most outstanding research, evaluated with no bias from both the academic and social point of view. By applying the most advanced information technologies, Frontiers is catapulting scholarly publishing into a new generation.

## What are Frontiers Research Topics?

Frontiers Research Topics are very popular trademarks of the *Frontiers journals series*: they are collections of at least ten articles, all centered on a particular subject. With their unique mix of varied contributions from Original Research to Review Articles, Frontiers Research Topics unify the most influential researchers, the latest key findings and historical advances in a hot research area.

Find out more on how to host your own Frontiers Research Topic or contribute to one as an author by contacting the Frontiers editorial office: [frontiersin.org/about/contact](https://frontiersin.org/about/contact)

# Advances in sea state modeling and climate change impacts

## Topic editors

Adem Akpınar — Bursa Uludağ University, Türkiye

Giovanni Besio — University of Genoa, Italy

Bahareh Kamranzad — University of Strathclyde, United Kingdom

## Citation

Akpınar, A., Besio, G., Kamranzad, B., eds. (2023). *Advances in sea state modeling and climate change impacts*. Lausanne: Frontiers Media SA.  
doi: 10.3389/978-2-83251-948-6

## Table of contents

- 05 **Editorial: Advances in sea state modeling and climate change impacts**  
Adem Akpınar, Giovanni Besio and Bahareh Kamranzad
- 08 **Wave Climate Variability and Occurrence of Mudbanks Along the Southwest Coast of India**  
Yana V. Saprykina, S. V. Samiksha and Sergey Yu. Kuznetsov
- 22 **Projections of Directional Spectra Help to Unravel the Future Behavior of Wind Waves**  
Hector Lobeto, Melisa Menendez and Iñigo J. Losada
- 32 **Characterizing the Non-linear Interactions Between Tide, Storm Surge, and River Flow in the Delaware Bay Estuary, United States**  
Ziyu Xiao, Zhaoqing Yang, Taiping Wang, Ning Sun, Mark Wigmosta and David Judi
- 49 **Evaluation of Wave-Ice Parameterization Models in WAVEWATCH III® Along the Coastal Area of the Sea of Okhotsk During Winter**  
Shinsuke Iwasaki and Junichi Otsuka
- 61 **Numerical Analysis of the Effect of Binary Typhoons on Ocean Surface Waves in Waters Surrounding Taiwan**  
Tzu-Yin Chang, Hongey Chen, Shih-Chun Hsiao, Han-Lun Wu and Wei-Bo Chen
- 80 **Wind Waves in the Mediterranean Sea: An ERA5 Reanalysis Wind-Based Climatology**  
Francesco Barbariol, Silvio Davison, Francesco Marcello Falcieri, Rossella Ferretti, Antonio Ricchi, Mauro Sclavo and Alvis Benetazzo
- 103 **Dynamical Projections of the Mean and Extreme Wave Climate in the Bohai Sea, Yellow Sea and East China Sea**  
Delei Li, Jianlong Feng, Yuchao Zhu, Joanna Staneva, Jifeng Qi, Arno Behrens, Donghyun Lee, Seung-Ki Min and Baoshu Yin
- 119 **Atmosphere-Ocean Coupled Variability in the Arabian/Persian Gulf**  
Fahad Al Senafi
- 131 **The Skill Assessment of Weather and Research Forecasting and WAVEWATCH-III Models During Recent Meteotsunami Event in the Persian Gulf**  
Mohsen Rahimian, Mostafa Beyramzadeh and Seyed Mostafa Siadatmousavi
- 150 **Sea Levels Dynamical Downscaling and Climate Change Projections at the Uruguayan Coast**  
Michelle Jackson, Monica Fossati and Sebastian Solari

- 165 **Long-Term and Seasonal Variability of Wind and Wave Extremes in the Arctic Ocean**  
Isabela S. Cabral, Ian R. Young and Alessandro Toffoli
- 178 **A Generalized Two-Scale Approximation for Ocean Wave Models**  
William Perrie, Bechara Toulany and Michael Casey
- 195 **Long-Term Variability of the East Sea Intermediate Water Thickness: Regime Shift of Intermediate Layer in the Mid-1990s**  
JongJin Park
- 215 **Effects of Internal Climate Variability on Historical Ocean Wave Height Trend Assessment**  
Mercè Casas-Prat, Xiaolan L. Wang, Nobuhito Mori, Yang Feng, Rodney Chan and Tomoya Shimura
- 226 **Trend detection by innovative polygon trend analysis for winds and waves**  
Fatma Akçay, Bilal Bingölbali, Adem Akpınar and Murat Kankal
- 241 **Spatiotemporal variability and climate teleconnections of global ocean wave power**  
Chuanchuan Cao, Ge Chen, Chengcheng Qian and Jie Shang
- 253 **Regional wave model climate projections for coastal impact assessments under a high greenhouse gas emission scenario**  
Jian Su, Jens Murawski, Jacob W. Nielsen and Kristine S. Madsen
- 266 **Model simulated freshwater transport along the Labrador current east of the Grand Banks of Newfoundland**  
Yongxing Ma, Youyu Lu, Xianmin Hu, Denis Gilbert, Scott A. Socolofsky and Michel Boufadel



## OPEN ACCESS

## EDITED AND REVIEWED BY

Ming Li,  
University of Maryland, College Park,  
United States

## \*CORRESPONDENCE

Adem Akpinar  
✉ [ademakpinar@uludag.edu.tr](mailto:ademakpinar@uludag.edu.tr)

## SPECIALTY SECTION

This article was submitted to  
Physical Oceanography,  
a section of the journal  
Frontiers in Marine Science

RECEIVED 25 January 2023

ACCEPTED 27 February 2023

PUBLISHED 03 March 2023

## CITATION

Akpinar A, Besio G and Kamranzad B (2023)  
Editorial: Advances in sea state modeling  
and climate change impacts.  
*Front. Mar. Sci.* 10:1151020.  
doi: 10.3389/fmars.2023.1151020

## COPYRIGHT

© 2023 Akpinar, Besio and Kamranzad. This  
is an open-access article distributed under  
the terms of the [Creative Commons  
Attribution License \(CC BY\)](https://creativecommons.org/licenses/by/4.0/). The use,  
distribution or reproduction in other  
forums is permitted, provided the original  
author(s) and the copyright owner(s) are  
credited and that the original publication in  
this journal is cited, in accordance with  
accepted academic practice. No use,  
distribution or reproduction is permitted  
which does not comply with these terms.

# Editorial: Advances in sea state modeling and climate change impacts

Adem Akpinar<sup>1\*</sup>, Giovanni Besio<sup>2</sup> and Bahareh Kamranzad<sup>3</sup>

<sup>1</sup>Department of Civil Engineering, Bursa Uludağ University, Bursa, Türkiye, <sup>2</sup>Department of Civil, Chemical, and Environmental Engineering, University of Genoa, Genoa, Italy, <sup>3</sup>Department of Civil and Environmental Engineering, University of Strathclyde, Glasgow, United Kingdom

## KEYWORDS

waves, winds, sea state modeling, climate, and climate change

## Editorial on the Research Topic

[Advances in sea state modeling and climate change impacts](#)

## 1 Introduction

Research on generating accurate wind and wave hindcasts and investigating climate change effects on marine environments and conditions have become popular in recent decades. The wind and wave modeling communities have made significant developments in physical and numerical parameterizations and model performance in sea state modeling. Knowledge of the marine environment has been understood better with modeled wind and wave datasets, supplemented by *in-situ* and remotely sensed data. The quality of wind data is being improved, which leads to generating the wave climate with higher accuracy. Therefore, improvements in wind predictions are of prime interest. This Editorial on Frontiers in Marine Science aims to bring together a diverse group of experts to discuss the latest advancements in wind and wave hindcasts and climate models. The focus is on understanding the most recent developments in wave hindcasts in various marine environments, as well as identifying the potential impacts of climate change on ocean climate. The research articles included in this collection showcase the most recent findings on topics such as sea state modeling, wind and wave climate, wave and sea level projections, and more.

## 2 Sea state modeling

This thematic section focuses on some papers about sea state modeling in different sea areas. This summary covers the impact of various wave-ice parameterization models on wave model hindcast performance, the role of non-linear tide-surge-river interactions in exacerbating flooding, the effects of binary typhoons on ocean surface waves, the evaluation of WRF and WAVEWATCH-III<sup>®</sup> (WWIII) models during a meteotsunami event, and introduces a two-scale approximation as a new method for estimating transfer rates in wind-wave spectra.

Iwasaki and Otsuka conducted an evaluation of the wave-ice parameterization models in WWIII along the coastal region of the Sea of Okhotsk during winter. They discovered that the accuracy was lower in ice-covered areas compared to open-water areas, with a noticeable discrepancy between the six sea ice models. The simulations that incorporated sea ice greatly improved the wave field bias in coastal areas as compared to the simulations without sea ice. Xiao et al. characterized the non-linear interactions between tide, storm surge, and river flow using the unstructured-grid Finite Volume Community Ocean Model in the Delaware Bay Estuary, United States. The authors indicated that the tide-surge interactions mainly influenced diurnal tides, and semidiurnal tides were damped due to tide-river interactions. The effect of binary typhoons on ocean surface waves was numerically analyzed by Chang et al. in waters surrounding Taiwan. These effects were elucidated near the tracks of the three super typhoons. The results of the analysis indicate that binary typhoons not only lead to an increase in significant wave height ( $H_s$ ), but also result in an enhancement of one-dimensional wave energy and two-dimensional directional wave spectra. Rahimian et al. conducted a reliability assessment of the WRF and WWIII models during a recent meteotsunami event in the Persian Gulf. They determined that the Mellor-Yamada-Nakanishi-Niino (the Mellor-Yamada-Janjic) scheme produced the best performance for stations over the water (land) for planetary boundary and surface layer (Eta similarity). Additionally, the results of the study revealed that the calibrated ST6 formulation with the Gaussian Quadrature Method produced a more accurate prediction of the wave spectrum. Perrie et al. proposed a generalized two-scale approximation for estimating transfer rates in wind-wave spectra. They introduced a generalized formulation of the two-scale approximation into the WAVEWATCHIII™ model, which can handle multiple peaked spectra, sheared spectra, and sea-swell combinations. The new methodology has been shown to significantly improve the accuracy of the results and was validated through application to real test cases.

### 3 Wind and wave climates

This thematic section presents six studies on the examination of wind and wave climates in various regions. These studies explore into the topics of wave climate variability and mudbank formation, a comprehensive analysis of wave climatology, the long-term and seasonal variations of wind and wave extremes, the impact of internal climate variability on historical ocean wave height trends, the spatial and temporal variability and climate teleconnections of global ocean wave power, and the use of innovative polygon trend analysis for detecting trends in winds and waves. Saprykina et al. analyzed the relationship between wave climate variability and the formation of mudbanks along the southwestern coast of India. They employed the wavelet correlation method to find significant correlations between the height of wind waves and swell and various climatic indices, including both positive and negative phases, on different time scales. The study also identified the time lags between these fluctuations. Barbariol et al. conducted a study of the wind waves in the Mediterranean Sea and presented their

findings in the form of a 40-year wave hindcast. The authors investigated the relationship between the wind waves and atmospheric parameter anomalies, as well as with teleconnection patterns. They discovered that the Scandinavian index variability had the strongest correlation with the variability of the Mediterranean Sea wind waves, particularly in the case of typical winter sea states. Additionally, the authors found that the typical and extreme significant and maximum individual wave heights in the Mediterranean Sea tend to decrease in the summer and increase in the winter. Cabral et al. conducted a study of the historical trends of extreme waves in the Arctic Ocean using a 28-year wave hindcast and a non-stationary approach to analyze the time-varying statistical properties. They found substantial seasonal differences and robust positive trends in extreme wave height, particularly in the East Siberian seas and Beaufort, with increasing rates of up to 60% for the 100-year return period, despite a marginal increase in wind speed of up to 5%. Casas-Prat et al. evaluated the trends in the annual mean and maximum  $H_s$  using a 100-member ensemble with a single model initial-condition for the period 1951 to 2010. They discovered that relying on a single member was insufficient in identifying the statistically significant positive trend present in the ensemble in some regions of the Southern Ocean. Cao et al. analyzed the ERA5 reanalysis data from 1979 to 2020 and quantified the global distribution and variability of wave power. According to their findings, the regions with the highest potential for wave energy were located in the westerlies of both hemispheres. Furthermore, they observed a trend of increasing wave power in the Southern Ocean, which dominated the overall pattern of global wave power. Akçay et al. compared the effectiveness of innovative trend methods and traditional methods in identifying the trends of monthly mean and maximum wind speed and  $H_s$  in the Black Sea coast using 42 years of SWAN wave simulations forced by CFSR winds. The results of the Mann-Kendall test indicated a low occurrence of trends for both parameters, while the IPTA method identified stronger trends.

### 4 Wave and sea level projections

In this thematic section, sea level and wave climate projections are studied, in the context of the mean and extreme wave climate, directional spectra, and regional wave climate.

Li et al. examined the projected changes in the average and extreme wave climate in the East China Sea, Yellow Sea, and Bohai Sea for two future time frames (2021-2050 and 2071-2100) under the RCP2.6 and RCP8.5 scenarios. They discovered that the average annual and seasonal  $H_s$  is expected to decline during both future periods and under both scenarios. However, in contrast, the annual and summer/winter 99<sup>th</sup> percentile  $H_s$  is likely to increase in a significant portion of the study area. Lobeto et al. analyzed the projections of directional wave spectra to understand how wind waves will behave in the future using a seven-member wave climate projection ensemble under a high-emissions scenario. They pointed out that relying solely on integrated wave parameters such as  $H_s$  and mean wave period can conceal important information about the direction, magnitude, and reliability of wave climate changes. This

is because positive and negative variations within the spectrum can cancel each other out, leading to an underestimated change for certain wave systems. [Su et al.](#) analyzed the impact of climate change on the water level caused by storm surges and wind waves in Køge Bay, near the entrance of the Baltic Sea, which has a low tidal range. The authors found that the change in wave height and period during stormy conditions is negligible. However, when taking into account sea level rise, the simulation showed that under storm surge conditions, the wave height is expected to double in the near future (mid-century), and the wave period may also increase by around 1.5 seconds. [Jackson et al.](#) used a dynamical downscaling approach, consisting of a series of nested two-dimensional hydrodynamic models, to calculate the anticipated changes in the total sea level climate and its components along the Uruguayan coast. The authors found that the primary contributor to the projected changes in the area is the rising regional mean sea level, followed by the impact of increased water depth on the tidal component amplitudes.

## 5 Other topics

Finally, the Research Topic includes three papers aiming to investigate inter-annual to multi-decadal sea surface temperature (SST) variability, freshwater transport by the Labrador Current, and the long-term variability of intermediate water thickness.

[Al Senafi](#) utilized an empirical orthogonal function (EOF) decomposition analysis to study the interannual to multi-decadal variability of sea surface temperatures (SST) in the Persian Gulf from 1982 to 2020. The author found that the warming rate from 1982 to 2020 was as high as 0.59°C per decade and concluded that despite the overall warming trend of SST, there was a cooling period, which then shifted back to warming and has been increasing since 2003. [Ma et al.](#) analyzed the freshwater transport by the Labrador Current around the Grand Banks of Newfoundland using 26 years of data from the Global Ocean Physical Reanalysis (GLORYS12v1). The study found that the seasonal and inter-annual variations of the freshwater transport in the eastern area of the Grand Banks of Newfoundland are primarily driven by variations in the horizontal velocity of the Labrador Current, while changes in salinity play a significant role in the variation of the

freshwater transport north of 45°N. [Park](#) studied the fluctuations of the East Sea intermediate water (ESIW) thickness over a long period and the change in the intermediate layer that took place in the mid-1990s. The author proposed that the shift in the regime of the East Sea meridional overturning circulation was behind this change. Before the mid-1990s, the variability of the ESIW layer was largely influenced by active deep-water formation, but after the mid-1990s, the formation rate of the ESIW became the primary factor in determining its thickness variability.

## Author contributions

All authors listed have made a substantial, direct, and intellectual contribution to the work and approved it for publication.

## Acknowledgments

We deeply thank all the reviewers who have participated in this Research Topic.

## Conflict of interest

The authors declare that the research was conducted in the absence of any commercial or financial relationships that could be construed as a potential conflict of interest.

## Publisher's note

All claims expressed in this article are solely those of the authors and do not necessarily represent those of their affiliated organizations, or those of the publisher, the editors and the reviewers. Any product that may be evaluated in this article, or claim that may be made by its manufacturer, is not guaranteed or endorsed by the publisher.





# Wave Climate Variability and Occurrence of Mudbanks Along the Southwest Coast of India

Yana V. Saprykina<sup>1\*</sup>, S. V. Samiksha<sup>2</sup> and Sergey Yu. Kuznetsov<sup>1</sup>

<sup>1</sup> Shirshov Institute of Oceanology, Russian Academy of Sciences, Moscow, Russia, <sup>2</sup> Council of Scientific and Industrial Research-National Institute of Oceanography, Dona Paula, India

## OPEN ACCESS

### Edited by:

Adem Akpinar,  
Uludağ University, Turkey

### Reviewed by:

Prasad Bhaskaran,  
Indian Institute of Technology  
Kharagpur, India  
Thomas Mortlock,  
Risk Frontiers, Australia

### \*Correspondence:

Yana V. Saprykina  
saprykina@ocean.ru

### Specialty section:

This article was submitted to  
Physical Oceanography,  
a section of the journal  
Frontiers in Marine Science

**Received:** 23 February 2021

**Accepted:** 22 March 2021

**Published:** 22 April 2021

### Citation:

Saprykina YV, Samiksha SV and  
Kuznetsov SY (2021) Wave Climate  
Variability and Occurrence  
of Mudbanks Along the Southwest  
Coast of India.  
*Front. Mar. Sci.* 8:671379.  
doi: 10.3389/fmars.2021.671379

Mudbanks (MBs) are a natural phenomenon, forming along the southwest coast of India during southwest monsoon (SWM), almost every year. High waves initiate these formations. The temporal variability (both intra-annual and multi-decadal) of wave climate of the southeastern Arabian Sea (AS) is related to main climate indices which determine climate fluctuations in this region, and based on that, occurrence of MBs is illustrated. Voluntary Observing Ships data and climate indices such as El Niño phenomenon index for the site 5N-5S and 170W-120W (NINO3.4), El Niño/Southern Oscillation (ENSO), Southern Oscillation Index (SOI), Pacific Decadal Oscillation (PDO), AAO, Atlantic Multi-decadal Oscillation (AMO), and IO Dipole (IOD) have been analyzed. Using wavelet correlation method, high correlations with positive and negative phase of climatic indices (IOD, SOI, NINO3.4, ENSO, AMO, PDO, and AAO) fluctuations in heights of wind waves and swell and time lags between them on monthly, yearly, decadal, and multi-decadal time scales are identified. For the first time, high correlation between the annual fluctuations of AMO and monthly average wave heights is shown. It has been found that the El Niño phenomenon plays a major role in the variability of wave climate of the southeastern AS for all time scales. A strong variability in wave climate at short time scales, such as 0.5, 1, 3.0–3.5, 4–5, and 7–8 years, is evident from the analyses. Decadal changes correspond to 10, 12–13, and 16 years. The influence of El Niño is manifested with a delay of several months (3–6) on annual time scales and about 1–2 years on a decadal and multi-decadal time scales. Possible connection between the occurrence of MBs and variability in wave climate in the southeastern AS is shown for the periods 7, 10–12, 18–20, and about 40 years correlating with fluctuation in the climate indices—IOD, ENSO, NINO3.4, and SOI. It is shown that intra-annual fluctuations in occurrence and duration of existence of MBs depend on the distribution of highest monthly averaged significant wave heights (SWHs) in the summer monsoon cycle.

**Keywords:** mudbanks, wind climate, climate indices, Arabian Sea, Voluntary Observing Ships data, wavelet correlation analysis, wind wave and swell

## INTRODUCTION

Mudbank (MB) is the natural phenomenon occurring along the southwest coast of India (Kerala coast) during southwest monsoon (SWM) season. It is a calm and turbid region with very high suspended sediment concentration, and attenuates the high energy monsoon waves due to wave–mud interaction. The main criterion for the formation of MB is the existence of high energy waves,

which are capable of bringing clay and mud and keeping them in suspension for weeks/months together. Previous studies state that the appearance and lifetime of MBs depend on waves in a particular monsoon period, and vary from year to year (Mathew et al., 1995). Locally known as “Chakara,” these MBs act as boon for fishermen as they dampen the high waves of SWM and provide a kind of “temporary harbors” with calm water, thereby allowing fishing activities in the nearshore region. Biological productivity is also enhanced in this region, which in turn plays a major role for good fish catch. Damodaran and Kurian (1972); Gopinathan and Qasim (1974), Nair et al. (1984); Rao et al. (1984), and Martin Thompson (1986) studied the socio-economic impacts of MB due to high biological productivity. Despite the predominance of the economic effect from the appearance of MBs in this region, it is also necessary to take into account the dynamics of MBs when designing ports, marinas, offshore platforms, etc., in the vicinity of MBs formation regions in order to avoid, for example, possible siltation around coastal structures and changes in loads on them. Over the years, different aspects of MB have been studied by several researchers, viz., hydrography (Kurup and Varadachari, 1975; Nair, 1985), physical oceanography (Mathew et al., 1995; Jiang and Mehta, 1996; Tatavarti and Narayana, 2006; Samiksha et al., 2017; Muraleedharan et al., 2018), water quality characteristics (Rao et al., 1984; Balachandran, 2004), ecology (Nair et al., 1984; Martin Thompson, 1986), sedimentological (Ramachandran and Mallik, 1985; Mallik et al., 1988; Narayana et al., 2008), mineralogical (Nair and Murty, 1968; Rao et al., 1984), geochemical (Jacob and Qasim, 1974; Ramachandran, 1989; Badesab et al., 2018), hydrochemical (Nair and Balchand, 1992), and rheological (Faas, 1995; Jiang and Mehta, 1996; Shynu et al., 2017). Mathew et al. (1995) stated that MB usually forms at 12 locations along the Kerala coast (Alleppy coastal zone) (**Figure 1**) during the SWM. The Alleppy coastal zone is a prograding coastline with wide sandy beaches to the north and narrow sandy beaches to the south. The hinterland is marshland underlain by fine sediments. The shelf is narrow, and beach ridges exist at 20 m water depth. The shelf gradient is gentle, and 10 and 20 m isobaths are at about 5 and 10 km distance from the shore (Narayana et al., 2008). This coast is a micro-tidal region having semidiurnal tidal ranges < 1 m. The tidal currents are not significant except at river mouths and estuaries (Kurup, 1977). The average annual rainfall exceeds 3000 mm, and more than 70% occurs during the SWM (June–September). The tropical storms form comparatively less in the Arabian Sea (AS) than the Bay of Bengal (BoB), and that also in general, during the NE monsoon season. However, high waves are generated during the SWM. Here MBs play an important role in dampening this high waves, and thereby controlling erosion along this part of the coast.

Mudbanks prevail in semi-circular shape and extend up to 8–10 km offshore in water depth up to 15 m and 3–4 km alongshore. As was shown mud dominated bottom can damp the waves (Rajesh Kumar et al., 2008; Parvathy and Bhaskaran, 2019) and this effect comparable with wave attenuation due to the vegetation (Samiksha et al., 2019). Samiksha et al. (2017) studied the wave attenuation due to the MBs using measurements and modeling and found that 65–70% of waves dampened in the MBs

area. Philip et al. (2013) found that the formation is associated with increased upwelling along the coast. Jacob et al. (2015) and Loveson et al. (2016) argued over the validity of subterranean conduit flow of mud/water from the Vembanad Lagoon. Shynu et al. (2017) carried out seasonal time series measurements of suspended particulate matter in the MBs region and postulated that the dissipated wave energy might have probably eroded the bottom sediment and formed the near-bed fluid mud. As was recently shown in Saprykina et al. (2020), wave dissipation leads to frequency downshifting process in wave spectra due to difference of wave attenuation coefficients at the beginning and the end of this process will lead to formation first erosive and then accumulative profile, i.e., MB. Though different hypotheses were proposed for explaining the formation of MB, none of them is conclusive due to lack of convincing scientific/field supports holistically.

When we compare earlier study of Mathew et al. (1995) with recent studies, we can show that the frequency of MB occurrence has reduced in the recent years (Noujas et al., 2013; Parvathy et al., 2015). Therefore, in the present study, we made an attempt to investigate the possible connection between the frequency of occurrence of MBs and variability in wave climate of the eastern AS.

The North Indian Ocean (NIO) comprises of two basins, namely, the AS and the BoB. The wave climatology in the NIO changes primarily due to wind reversal during two seasons—SWM and northeast monsoon (NEM). Wave characteristics in both the basins are different during the two seasons. The wave climate of eastern AS is described by many researchers (Prasada Rao and Baba, 1996; Kumar et al., 2000; Amrutha et al., 2016; Nair and Kumar, 2016; SanilKumar and Jesbin, 2016; Naseef and Kumar, 2017) based on various datasets. The wave climate of the eastern AS shows seasonal variability with maximum wave height during SWM (Sanjiv et al., 2012; Glejin et al., 2013b; Anoop et al., 2014; Kumar et al., 2014). Johnson et al. (2012) studied wave parameters at three locations in the eastern AS during SWM, and found increase in significant wave height (SWH) as we move from south to north. Shanas and SanilKumar (2014) and Glejin et al. (2013b) studied the changes in wind speed and SWH in the eastern AS by analyzing 34 years of ERA data and concluded that the average SWH in the eastern AS during pre-monsoon (February–May), SWM (June–September), and post-monsoon (October–January) are about 1.0, 2.7, and 0.7 m, respectively, with an annual average value of approximately 1.1 m. Few studies (Neetu et al., 2006; Glejin et al., 2013b; Amrutha et al., 2016) also proved that the wind waves of the eastern AS are also strongly affected by the diurnal variations of sea/land breeze activity during the non-monsoon period. Wave climate along the west coast of India (WCI) is dominated by swells during SWM and NEM and by wind seas during pre-monsoon season (Prasada Rao and Baba, 1996; Kumar et al., 2000; Aboobacker et al., 2011; Vethamony et al., 2011). In the eastern AS, SWHs are generally low during NEM and pre-monsoon, and higher during SWM (Kumar and Kumar, 2008; Vethamony et al., 2009; Aboobacker et al., 2011). Long period Southern Ocean swells are also observed in the eastern AS, except during SWM (Glejin et al., 2013a,b). Recently,

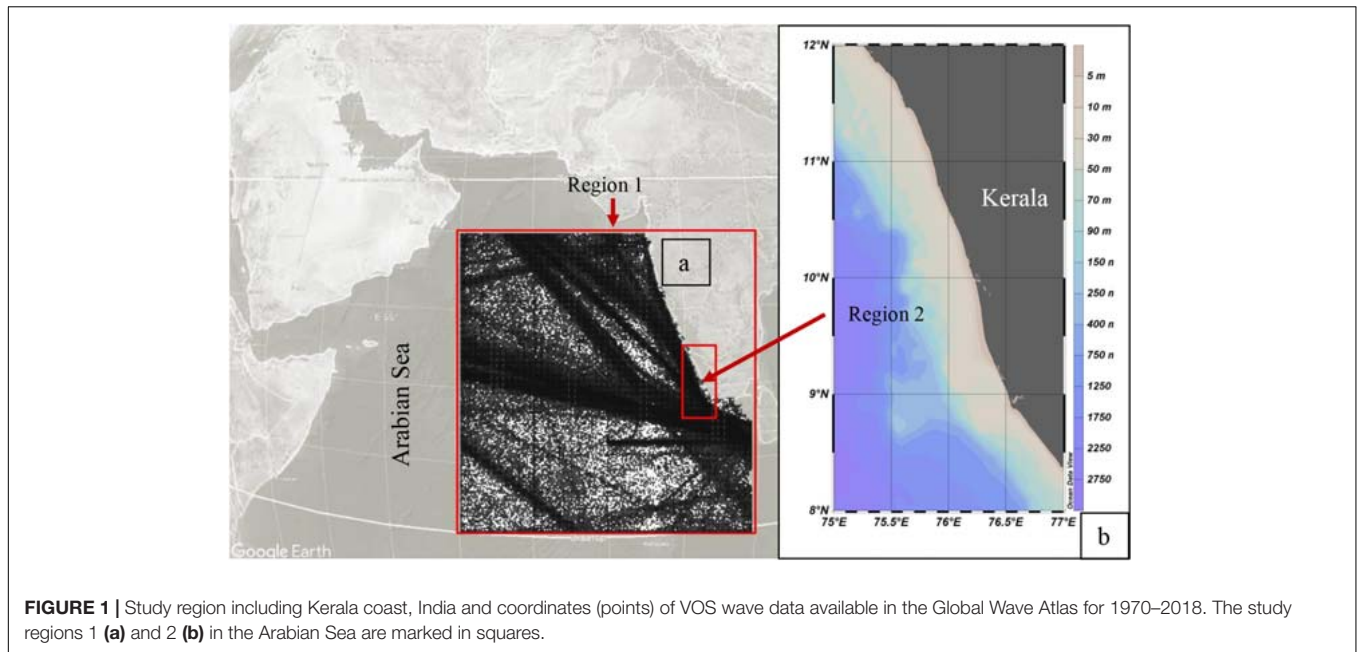


**FIGURE 1** | Study region including Kerala coast, India and coordinates (points) of VOS wave data available in the Global Wave Atlas for 1970–2018. The study regions 1 (a) and 2 (b) in the Arabian Sea are marked in squares.

Sreelakshmi and Bhaskaran (2020a; 2020b; 2020c) carried out detailed studies on the wind and wave climatology in the IO, using global datasets such as ERA-Interim, ERA40, and ERA5. They divided IO into different sectors based on diversified wave characteristics and discussed the trends in wind and wave climate, sector wise in the whole IO.

Stopa and Cheung (2014) studied the periodicity and patterns of global ocean wind and wave climate and revealed that wave climate of IO and Pacific Ocean depends on the El Niño/Southern Oscillation (ENSO) and Antarctic Oscillation (AAO). Anoop et al. (2016) examined the impact of IO Dipole (IOD) on the surface wind field of the AS and its impact on the wave climate during October, when the winds are weak and the IOD is the strongest. Their study concluded that the IOD impact depends on variations in the wind fields during different phases of IOD event. Decrease in SWHs was observed in the central and southwest coast of India during positive phase of IOD, whereas SWHs increase during the negative phase of IOD. They also observed that in the eastern AS, IOD impact is stronger than ENSO with more effect in the central eastern AS. A study carried out by Chowdhury and Behera (2017) made an attempt to investigate the effects of a changing wave climate on longshore sediment transport (LST) along the central WCI. They tried to link the variability in wind waves and swells with the changes in the LST over the period of time. Their study concluded that the decay in LST is directly linked to the decrease in the wave activity. As of now, there are numerous study on various aspects related to MB of Kerala, but the impact of wave variability on the occurrences of MB is still unexplored.

Therefore, in the present paper, we studied the variation of wave climate through climate indices, and explored the possible connections of these fluctuations with appearance of MBs and their evolution in different years. For the analysis of wave climate of the eastern AS, visual observations made from the voluntary

ships (VOSs) were used. The temporal variability (both intra-annual and multi-decadal) in wave climate of the eastern AS is related with the main climate indices, and based on that, occurrence of MBs over the years is discussed.

## DATA AND METHODS

### Wave Data

The available field wave data are not sufficient and suitable for this type of analysis to investigate the relationship between wave climate and main climate indices describing the dynamics in the Indian Ocean (IO) because of their temporal and spatial limitations. The reanalysis wave data could not be used for this analysis, due to the main disadvantage of poor reproduction of wave conditions in the nearshore and on long time scales (decadal periods) because they are based on wind reanalysis. This is determined by the errors in the reanalysis of wind data for long periods back to time and the discrepancy between the reanalysis of wind data and observations in the coastal zone. When analyzing climatic changes, this can lead to the detection of spurious trends (Bloomfield et al., 2018) or, conversely, not to detect changes on multi-decade periods (Saprykina et al., 2019). In Samiksha et al. (2017), discrepancies in the buoy and model wave heights were attributed to the possible formation of MBs (model could not accurately reproduce nearshore wave heights). Wave measurements available for this region are very rare and limited to a few months only. In this situation, visual observations are the only source of data available in the coastal zone of Kerala. Therefore, for the analysis of wave climate, visual observations made from VOSs have been used. The successful use of these data for the analysis of climate change is shown in many scientific papers (Barnett, 1983; Gulev et al., 2003). Validation of these data is available with full-scale field measurements by buoys and

radars, and a good similarity is observed (Soares, 1986; Grigorieva and Badulin, 2016; Grigorieva et al., 2017). In the past, along the coast of India, Chandramohan et al. (1991) visually observed wave and current data were used to estimate LST along the north Karnataka coast. The quality of visual observation data in relation to measured and model data is discussed in detail in Soares (1986); Gulev et al. (2003), and Grigorieva et al. (2017). The discrepancies between VOS data and measurements are mainly found while comparing non-averaging observations. Otherwise, when comparing with monthly mean or annual data, the accuracy has significantly increased, and as noted in Gulev et al. (2003) for many locations, observational uncertainties are within 20% of mean values, which is acceptable for climatological studies. The accuracy also depends on the number of observations. From this point of view, the IO has very large number of wave observations, as the ship traffic is huge. In general, the accuracy for VOS data is 0.5 m for wave heights, 1 s for periods, and  $10^\circ$  for directions (Gulev et al., 2003; Grigorieva et al., 2017). It is very well comparable with altimetry data (0.4 m for wave heights, no wave period,  $17\text{--}20^\circ$  for directions) and buoys data (0.2 m for wave heights, 1 s for periods,  $10^\circ$  for directions) (Grigorieva and Badulin, 2016; Saprykina and Kuznetsov, 2018a).

Voluntary ship data were extracted from the Global Wave Atlas, which was created at the Shirshov Institute of Oceanology of Russian Academy of Sciences. The details of VOS data included in the Atlas, methods of preprocessing (artificial errors correction or elimination, correction of small wave heights, checking extreme wave heights and inconsistency of wave parameters, checking the accuracy of wind sea and swell separation, applying the steepness and wave age control using combined criteria, etc.), and validation are described in Gulev et al. (2003); Freeman et al. (2017), and Grigorieva et al. (2017). Quality checked data of Wave Atlas include about 30% of all available VOS data. In the observation scheme of VOS, wave parameters (SWH and mean wave period) of wind waves and swells are recorded separately, first on the basis of expert visual assessments of observers (seafarers and ocean scientists), and second, in accordance with the unified methodology adopted for such observations in recent decades. Waves propagating in the absence of wind, long waves with a direction different from wind and any other genesis of which cannot be associated with the effect of wind, can be classified as swell waves. Most of the observations in the Wave Atlas additionally provide information such as wind speed and direction, data, time, coordinate (longitude, latitude), wave period, etc. For the IO, such records are available since 1888; however, the most complete data (in particular, wave height and period of wind waves and swell, wind speed, direction of propagation, and coordinates) and verified database are available from 1970 only. Thus, from the IO dataset, we have extracted data for the period 1970–2018 in the domain extending from  $0^\circ$  to  $20^\circ\text{N}$  and  $60^\circ$  to  $85^\circ\text{E}$  (Region 1) (Figure 1). A separate sub-region including Alleppy coastal zone was also extracted along the coast of Kerala extending between  $8^\circ\text{--}12^\circ\text{N}$  and  $75^\circ\text{--}77^\circ\text{E}$  (Region 2).

Figure 2 shows the number of observations extracted from January 1970 to December 2018 by month, dependences of available wave height on the number of observations, and wave

parameters (height and period) for a site near the coast (region 2) and region 1, without region 2. Figure 2 clearly shows that the number of observations near the coast of Kerala is significantly less, but at a qualitative level, the wave parameters are approximately the same. The heights of wind waves and swells near the shore (region 2) are slightly lower. Near the coast, waves with a period of the order of 1 s were recorded, while in region 1, such waves were practically not observed (Figures 2E,F). For both swells and wind waves in the selected regions of IO, there is slightly dependence especially of large wave height on the number of observations (Figures 2B,D). This is quite understandable, since high waves are less common than low ones, and the more observations, the more likely to register higher waves. When comparing the wave heights in the two regions, no significant qualitative difference, for example, possibly caused by the presence of MBs, is observed. The dependence of the wave height on the period has the same character (Figures 2E,F).

To verify the data of VOS observations, we additionally compared the VOS data with available waverider buoy data measured off Kerala coast (near MB region, region 2). Two waverider buoys were installed in Alleppy coastal zone at 15 m water depth (May 21 to July 31, 2014) and 7 m water depth (June 26 to July 31, 2014) at the distances 10 and 6 km from the shore, consequently. More details about the field measurements are given in Samiksha et al. (2017). The comparison of SWHs between available VOS observations nearshore and buoy measurements is shown in Figure 3.

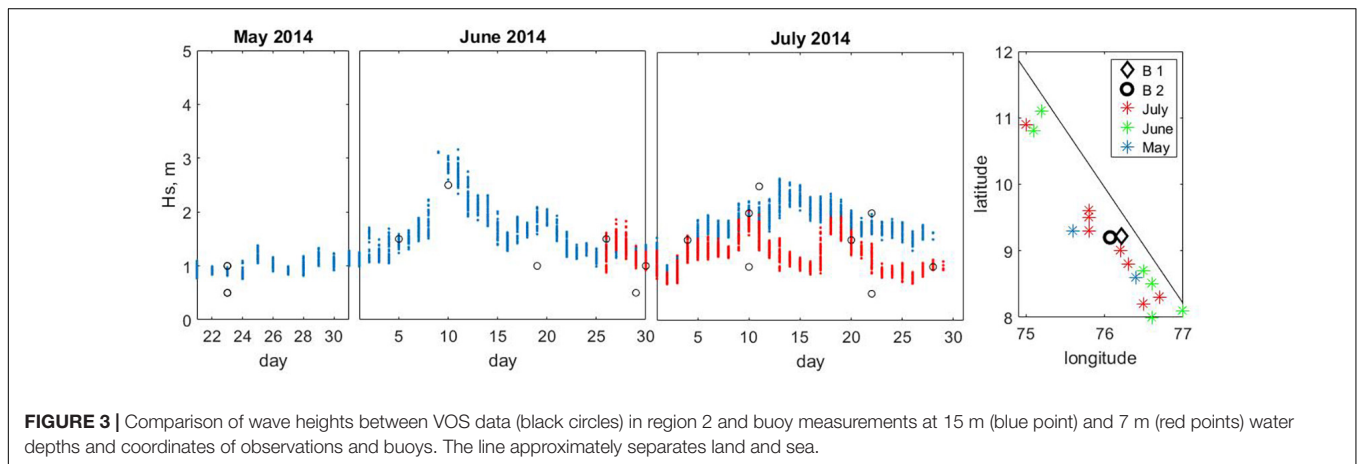
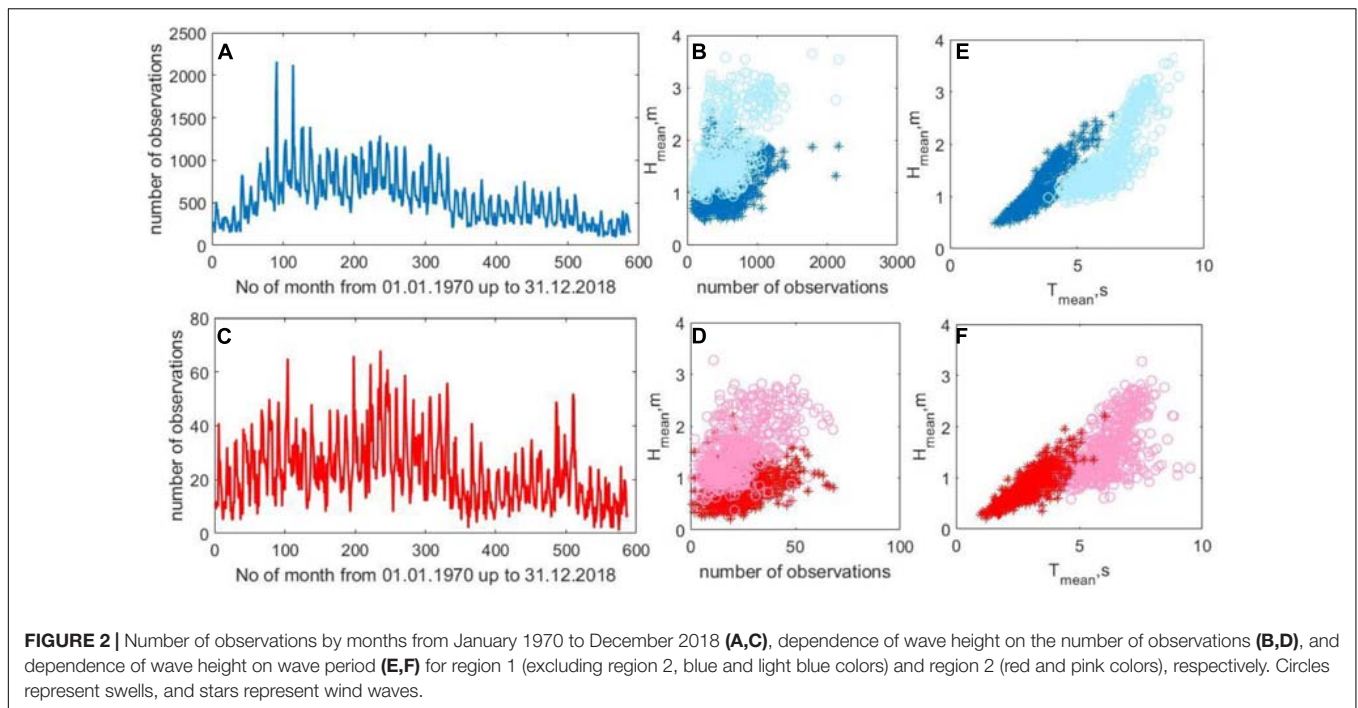
Figure 3 shows the qualitative coincidence change in SWHs. The observed differences in the heights are explained by differences in the averaging methods. The buoy data are obtained as a result of averaging the 20-min time series, and the data of VOS observations are actually given as non-averaged parameters of the observed individual waves. Inconsistencies can also be due to wave shoaling and dissipation in nearshore zone.

## Climatic Indices

The following main climate indices, which traditionally reflect the influence of El Niño phenomenon in the AS in which the monsoon intensity is associated with the dynamics of the IO were considered in the present study: (i) IOD, (ii) Southern Oscillation Index (SOI), (iii) AAO, (iv) ENSO, (v) El Niño phenomenon index for the site  $5\text{N}\text{--}5\text{S}$  and  $170\text{W}\text{--}120\text{W}$  (NINO3.4), (vi) Pacific Decadal Oscillation (PDO), and (vii) Atlantic Multi-decadal Oscillation (AMO). The time series of these indices and their description are available on websites of the offices of the US National Oceanic-Atmospheric Agency <https://www.cpc.ncep.noaa.gov> and <https://www.esrl.noaa.gov>. The time series of NINO3.4, ENSO, IOD, AMO, and SOI from 1970 to 2018, PDO from 1970 to 2017, and AAO from 1979 to 2018 were analyzed.

## Methods of Analysis

For analysis, the wave heights were monthly averaged. As the time series of monthly averaged VOS data are short (49 years or 588 months), in order to obtain periodicity, especially, the decadal and multi-decadal scales, instead of using the classical spectral analysis based on FFT and DFT methods, we have used the Yule-Walker parametric method and the method of



continuous wavelet transform with the Morlet wavelet function (Torrence and Compo, 1998; Saprykina and Kuznetsov, 2018a,b).

The Yule-Walker parametric method of spectral analysis is based on applying an autoregression model on the data series, in which the variable to be studied will linearly depend on its own previous values and on some stochastic term (Stoica and Moses, 2005). For sinusoidal time series, Yule-Walker method allows us to determine the period even if the length of the series is about half of the period, i.e., for our study, it is possible to detect period about 98 years. For long time series or for short-time periodicity, the results of classical spectral analysis (FFT and DFT methods) and Yule-Walker method will be the same (Stoica and Moses, 2005). So Yule-Walker parametric method of spectral analysis will allow detecting at the same time both multi-decadal (for which length of data is very short) and monthly periods (for which length of data is enough).

Wavelet transform is a kind of scanning of time series by frequencies. Like Yule-Walker method, it allows us to determine the periodicity of processes in short series of half the specified period. In addition, wavelet analysis represents the fluctuation of the spectrum in time, in contrast to the spectral analysis, which averages the spectrum over time. This allows us to assess the structure of the process as a whole and analyze its stationarity/non-stationarity. As shown in Saprykina and Kuznetsov (2018a; 2018b), fluctuations of climatic indices (for example, AMO and PDO) are non-stationary in time and can be non-linear due to modulation of high frequencies by low frequencies. In this case, the use of classical correlation analysis applied to linear stationary processes is impossible. Therefore, to obtain the correlations, we have used the recently developed method of wavelet correlations. Wavelet-correlations method is the construction of a correlation function between the wavelet

transforms of two signals for the same wavelet-frequency bands. It is analog to the classical correlation analysis, when original signals are initially filtered on a set of narrow-banded signals of characteristic frequency bands, and then the correlations between these narrow-banded signals are analyzed. If the number of such narrow-banded signals is sufficiently large, then each narrow-band signal can be considered as a quasi-stationary signal, and makes it possible to analyze the correlations between two non-stationary processes.

## RESULTS AND DISCUSSION

### Homogeneity of Arabian Sea Wave Climate

The changes in the monthly averaged heights (MAH) of the wind waves and swells for regions 2 and 1 are shown in **Figures 4B,E**. The MAH of swells do not have a linear trend; however, the heights of wind waves show a slight increase in the last one decade. MAH of waves have periodic fluctuations. Maximum fluctuations occur during the year and the maximum number of SWH in a year appears in the summer months (June–August) for both the regions (**Figures 4A,D**). However, in some years, in region 2 near the coast, the highest swells were observed in September (**Figures 4A,D**). In general, the long-term average annual cycle of changes in MAH of waves is similar for both the regions (**Figures 4C,F**), except that the maximum MAH of wind waves in the coastal region are observed in June and in the offshore (region1) in July. This may serve as an indirect sign that peak of the MBs formation is observed in the coastal region in July (Samiksha et al., 2017) and attenuate the waves, compared to the rest of the eastern AS.

**Figure 5** shows that qualitatively the fluctuations and trends in monthly averaged wave heights are the same for both the regions. The relationship between them is linear with a coefficient of 1.1, the deviation from 1 is due to the fact that the data of region 2 contain more nearshore data and, in general, their height is 0.2 m less. Taking into account the analysis of the heights of individual waves of the two regions, made above, we can assume that the data of monthly averaged wave heights in the two regions of eastern AS are homogeneous (**Figures 2, 5**). Therefore, it can be expected that changes in wave climate will occur in the same manner for both the coastal and the offshore regions. Hence, in order to analyze the wave climate variability, we have merged the data of both the regions to have more data for reliable analysis. The wave data homogeneity of the two regions also indicate that the AS as a whole can influence the dynamics/formation of MBs.

### Variability of Arabian Sea Wave Climate

**Figure 6** and **Supplementary Figure 1** present the results of spectral parametric analysis performed by the Yule-Walker method and a wavelet analysis for the changes in the MAH of wind waves and swells for region 1. For analysis, mean value and linear trend were removed from the time series of monthly averaged wave heights. It is clearly seen that the characteristic periods observed at small time scales are the annual and semi-annual variability of wave heights (both swells and wind

waves), associated with SWM in the summer period (June–July) (**Figure 4**). The characteristic peaks of this variability are present both on the spectra and on the wavelet diagrams. According to wavelet analysis, fluctuations in this time range for the period 1970–2018 are almost stationary, and have no visible time trends (**Figures 4, 6** and **Supplementary Figure 1**).

As for the decadal and multi-decadal oscillations of average monthly wave heights are concerned, it is clearly seen on the wavelet diagrams (**Figure 6** and **Supplementary Figure 1**) that the periods of these oscillations are non-stationary, and there are linear trends in their periods, both for wind waves and for swells (for example, in the range of periods from 40 to 200 months). The non-stationary nature of the process of changing the monthly averaged wave heights at these time scales does not allow the use of spectral analysis to clearly distinguish periods in this range, especially for wind waves (**Figure 6** and **Supplementary Figure 1**, spectra), although this periodicity is clearly visible on wavelet diagrams. In general, based on the results of spectral and wavelet analysis, it can be stated that changes in average monthly heights of wind waves and swell waves have the same variability on periods of 6 months, 1 year, 3 years, 4–5 years, and 7–8 years, and similar periodicity on longer and multi-decadal scales in range about 10–16 and 20–40 years.

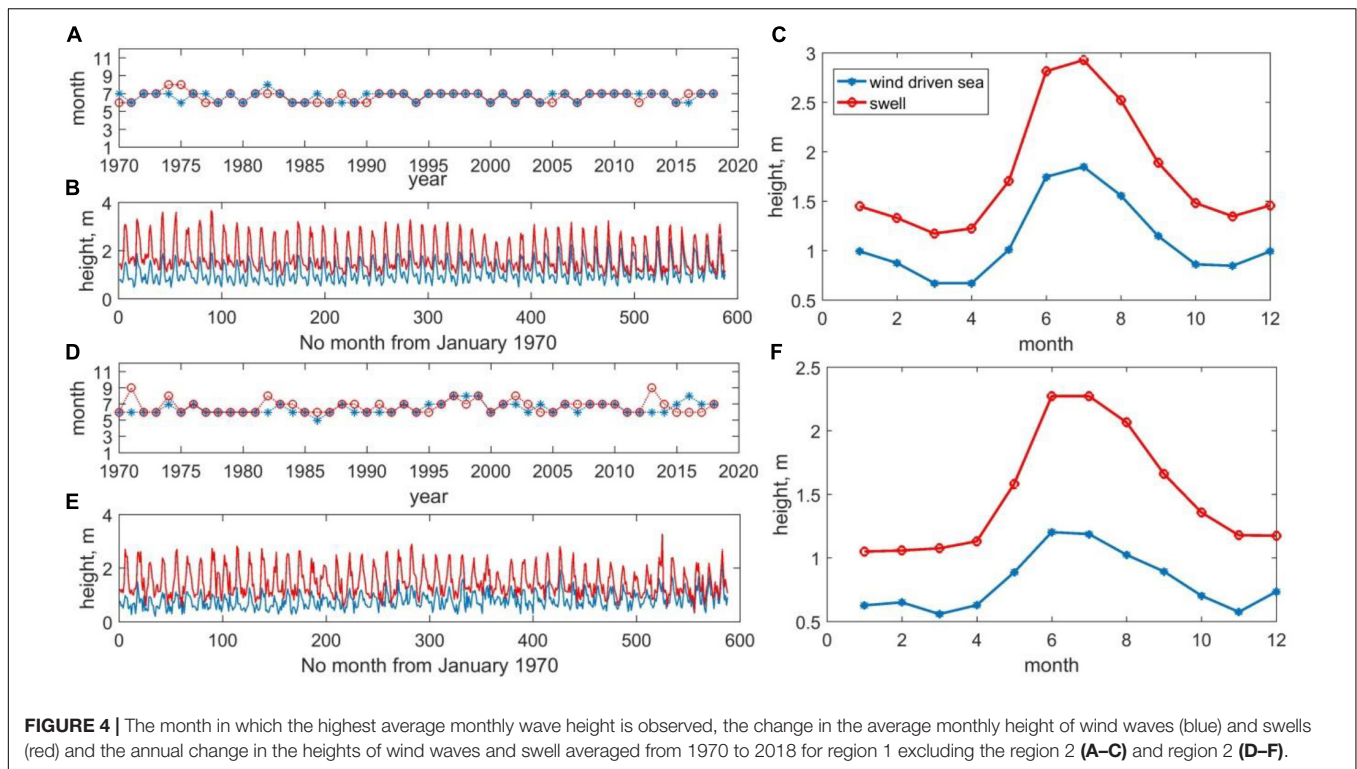
### Variability of Climate Indices

The results of wavelet analysis show that the changes in the selected indices are also non-stationary. To save this article space, we have discussed only two of them—IOD and NINO3.4. For example, changes in IOD index have a pronounced trend on the scales of variability from 50 to 100 months and from 350 to 200 months (**Figure 7A**). Changes in the NINO3.4 index have a visible trend in the period range, 100–200 months (**Figure 7B**). At the same time, the variability of both indices is stationary in the range of 6–12 months. The unsteady nature of PDO and AMO changes has been discussed in detail in Saprykina and Kuznetsov (2018a,b). Thus, the wavelet analysis made it possible to explain the non-stationarity of changes in all indices in a given time range.

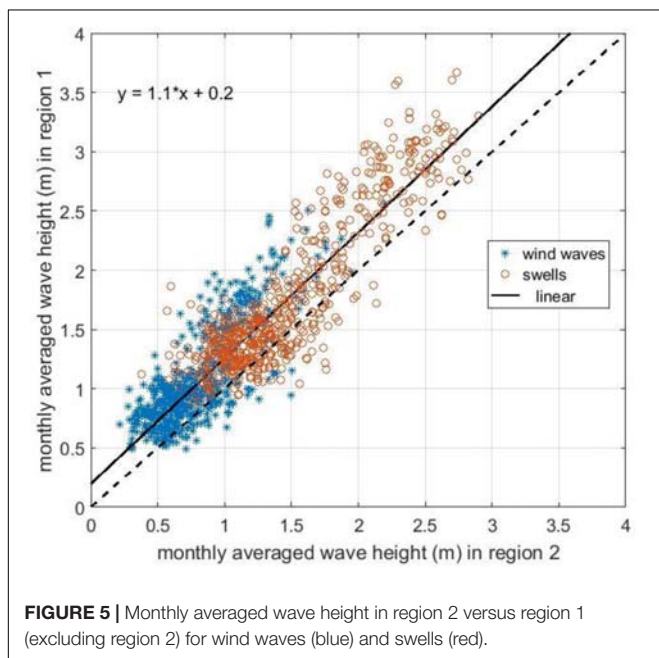
### Analysis of Connection Variability of Monthly Averaged Wave Heights With Climate Indices

As expected the classical correlation analysis showed rather low correlations with the select climate indices (correlation coefficients are less than 0.2), except for correlation with NINO3.4 index—correlation coefficient is 0.39. Such low connections can be explained by the non-stationary changes in both wave heights and indices. To obtain correlations between non-stationary processes, the wavelet correlation method has been used in the present study. The wavelet correlation coefficients at zero time lag for MAH of wind waves and swell waves are shown in **Figure 8**. The corresponding wavelet cross correlation diagrams, for some indices versus time lags, are shown in **Supplementary Figure 2**.

A zero time lag means that two processes occur simultaneously. It can be seen that for periods less than a



decade, changes in the heights of wind waves and swell waves are associated with changes in the same climate indices. Some differences are observed in periods more than 10 years. **Supplementary Table 1** shows the characteristic periods of variability of the monthly averaged wave heights and swells and their correlation (correlation coefficient > 0.4) with the select climate indices.



The correlations between some indices will be significantly higher if we take into account the time lag between climate processes and the change in wave heights (**Supplementary Figure 2**). For example, the positive phase of the annual and semi-annual changes in the NINO3.4 index leads to an increase in wave heights with a lag of 2 months (correlation coefficient is 0.80 for both the periods). There is 1-year lag between the positive phase of NINO3.4 oscillations with a period of about 10 years and the averaged monthly wave heights (correlation coefficients are 0.50 and 0.80, for wind waves and swells, respectively) (**Supplementary Figures 2c,d**). The lag between positive phase of the ENSO change during the year and 6 months and increase in wave height occurs with a lag of 1 month with correlation coefficients of 0.60 and 0.68 for wind waves and swells in both periods, respectively. A negative phase of SOI oscillation with a period of about 10 years will lead to an increase in the height of wind waves and swell waves with a lag of 1 year (correlation coefficients are negative:  $-0.60$  and  $-0.75$ , respectively), and a positive phase of oscillation with a period of 20 years will have a lag of 2 years (correlation coefficient is 0.70) (**Supplementary Figures 2a,b**). The positive phase of ENSO index leads to an increase in wave heights for a period of 10–13 years with a lag of 6 months to 1 year, both for wind waves and for swell waves (correlation coefficients are 0.55 and 0.70, respectively). Also, a positive phase of ENSO oscillation with a period of 16 years correlates with an increase in the height of wind waves with a lag of 2 years (correlation coefficient is 0.50). The negative phase of AMO with 7–8 years period of oscillation will lead to an increase in the height of wind waves after 1 year (correlation coefficient is  $-0.65$ ), and the positive phase of oscillation with a period

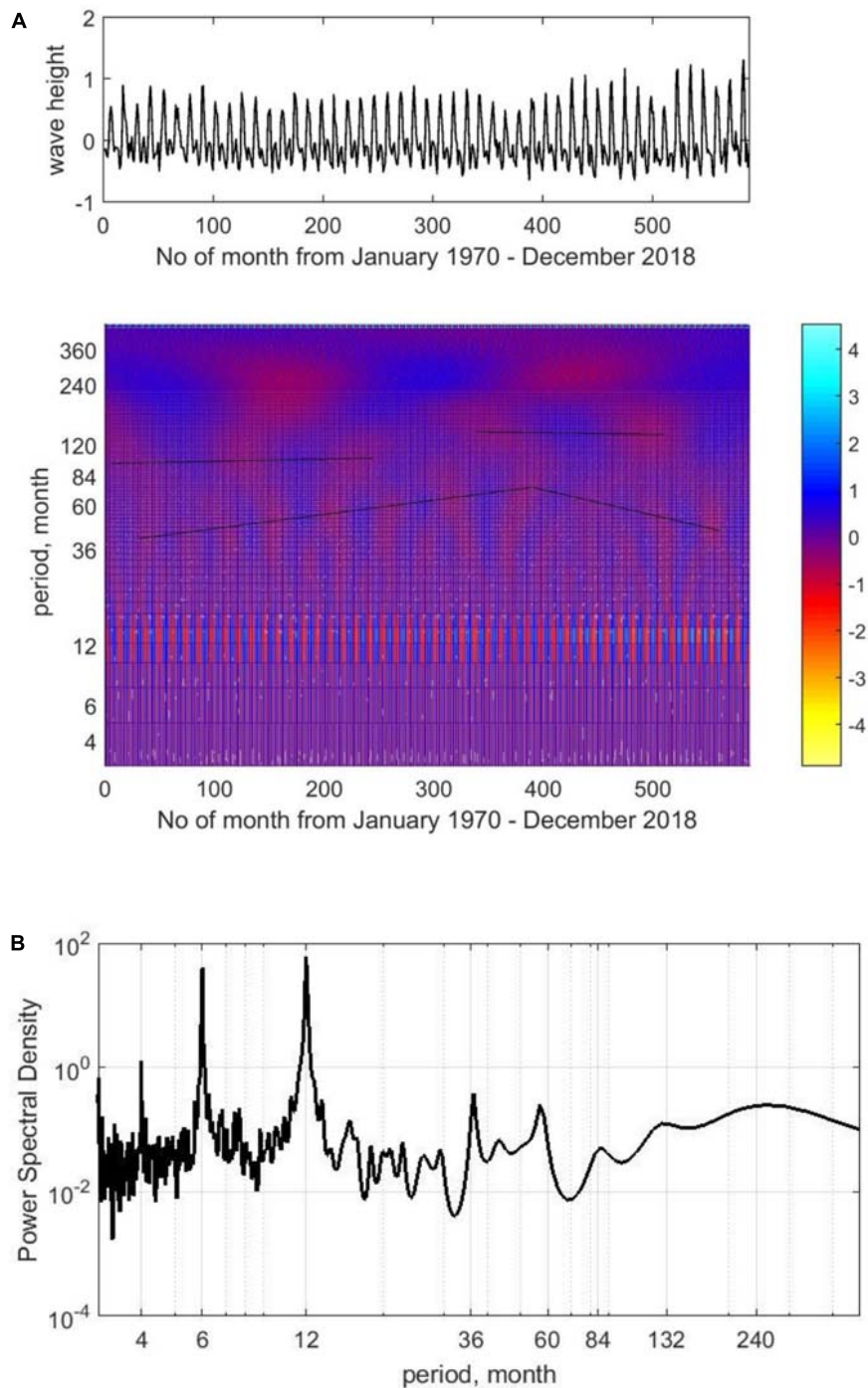


**FIGURE 6** | Change in monthly averaged heights of wind waves. Wavelet transform **(A)** and power spectral density Yule-walker method **(B)** (for wavelet analysis, mean value and linear trend were excluded from height series). The lines show the available trends in coefficient fluctuations.

of 16 years will also increase the height of swells after 1 year (correlation coefficient is 0.80) (**Supplementary Figures 2e,f**).

The negative phase of fluctuations in the PDO index with a period of 16 years leads to an increase in the swell height with a lag of 2 years (correlation coefficient is  $-0.65$ ) (**Supplementary Figures 2g,i**). Also, in the diagrams of wavelet

correlations (**Figure 6** and **Supplementary Figure 2**), one can notice a rather high correlation between changes in wave heights and fluctuations of climate indices occurring with a time lag, which was not detected at zero time lag. So, for a change in the MAH of swells, a variability of 13 years period associated with fluctuations in the IOD index exists, like the monthly



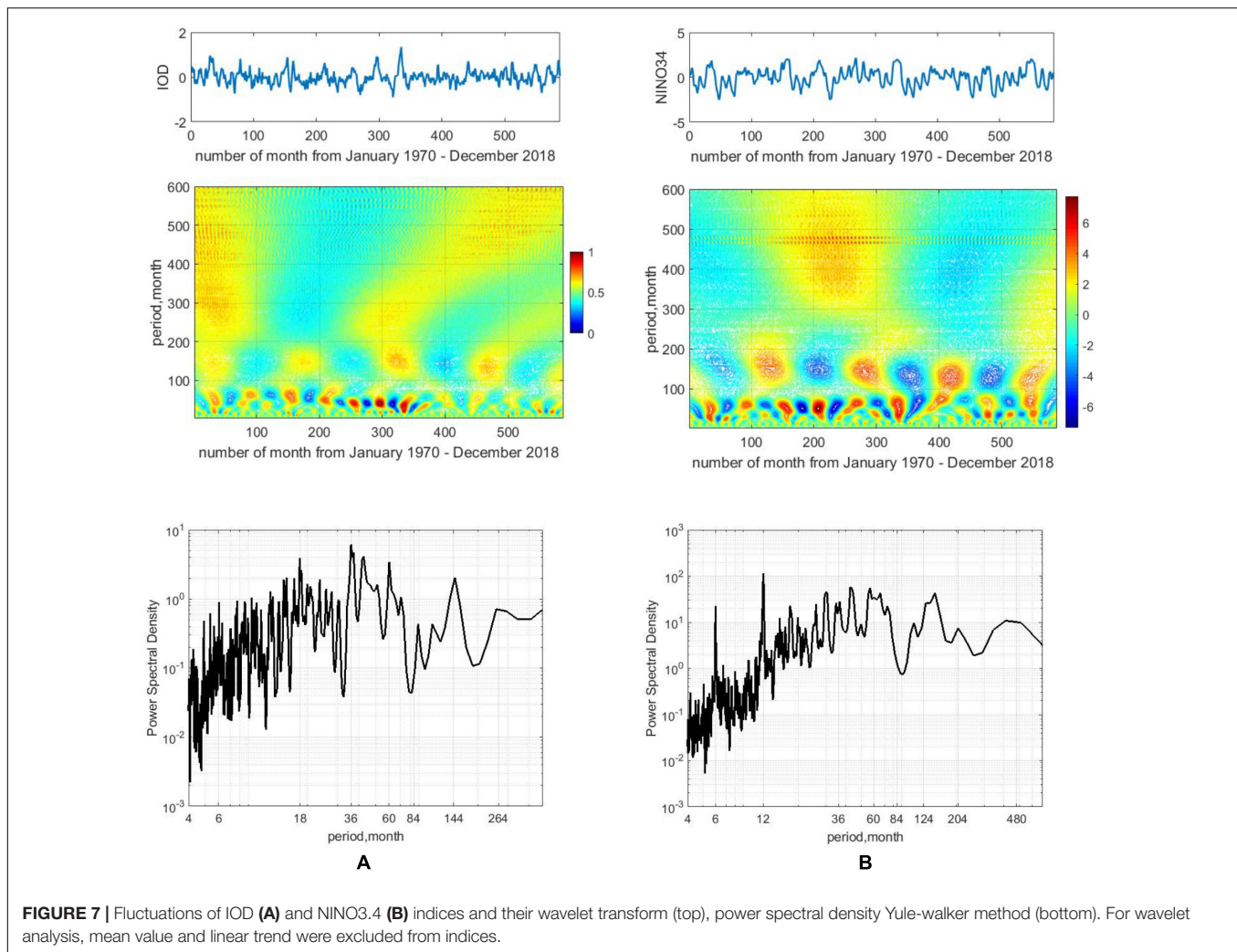


**FIGURE 7 |** Fluctuations of IOD (A) and NINO3.4 (B) indices and their wavelet transform (top), power spectral density Yule-walker method (bottom). For wavelet analysis, mean value and linear trend were excluded from indices.

averaged wind waves, but it is lagged by about 2 years (correlation coefficient is  $-0.65$ ).

For the SOI index, there is a relationship between a period of change of 20 years and fluctuations in the average monthly swell height as well as for wind waves, lagged by 2 years (correlation coefficient is  $0.55$ ). For the NINO3.4 index, there is a high correlation between the increase in the height of wind waves and its positive phase for a period of 16 years with a lag of 2–3 years (correlation coefficient is  $0.65$ ).

An increase in the MAH of wind waves with a period of 3 years can be associated with a positive phase of oscillations of the AMO index over the same period (correlation coefficient is  $0.60$ ) and occurs 6 months later. There is also a relationship between the negative phase of fluctuations in the AMO index with a period of 8 years (correlation coefficient is  $-0.50$ ) and the increase in the height of swells that occurs after a year.

The annual fluctuations in the heights of both wind waves and swells are closely connected to fluctuations in the PDO index, lagged by 3 months. A correlation between the negative phase of AAO fluctuations with periods of 12–13 years and an increase in the height of swells (correlation coefficient is  $-0.80$ ) with a lag

of 1 year has been identified (**Supplementary Figures 2j,k**). It should be especially noted that the averaged monthly height of wind waves varies in phase with fluctuations in the IOD index over the periods 3, 7, 13, and 20 years.

Thus, as a result of the analysis, the following periods of fluctuations in the MAH of wind waves and swells were identified: 0.5 year (associated with NINO3.4 and ENSO), 1.0 year (due to a change in NINO3.4, ENSO, AMO, and PDO), 3.0–3.5 years (associated with a change in NINO3.4, ENSO, SOI, and IOD), 4.0–5.0 years (associated with a change in PDO and AAO), 7.0–8.0 years (associated with a change in IOD and AMO), 10.0 years (associated with a change in SOI, NINO3.4, and ENSO), 12.0–13.0 years (associated with a change in IOD and AAO), 16.0 years (associated with a change in NINO3.4 and PDO), 20.0 years (associated with a change in SOI, NINO3.4, and AAO) and 30.0 years (associated with a change in PDO and AAO). For all indices except PDO, there are high correlations on periods about 40 years. Note that on all time scales, the most significant connection between the wave climate and the El Niño phenomenon changes in which are directly or indirectly taken into account in the indices NINO3.4, ENSO, SOI, and PDO.

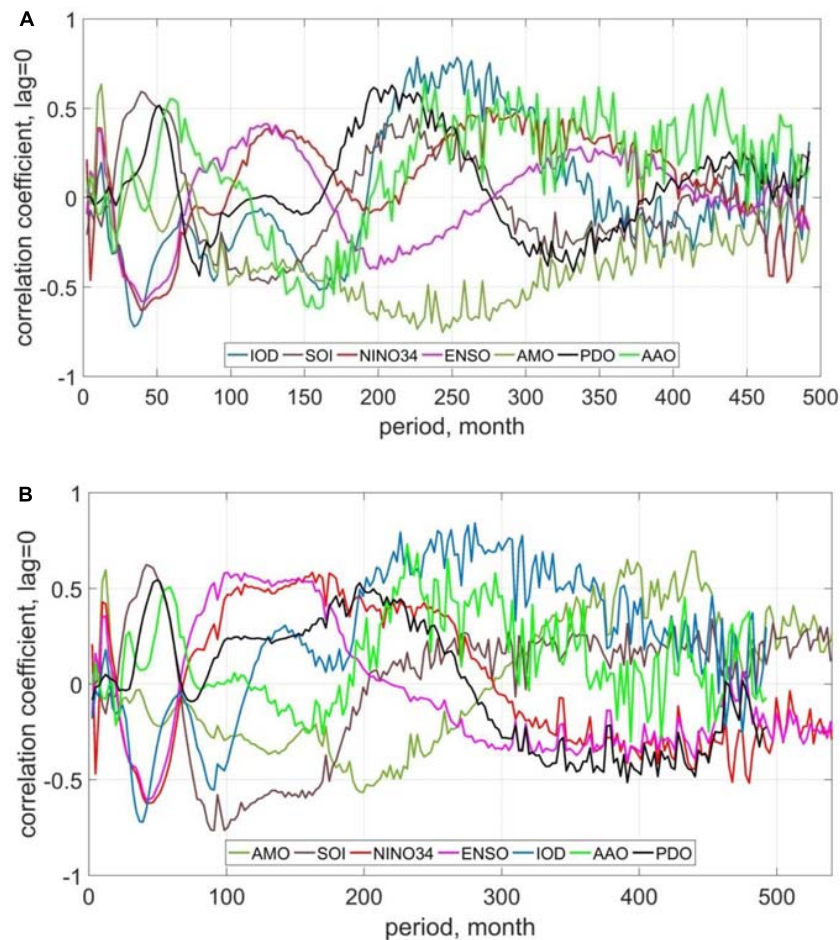


**FIGURE 8** | Wavelet correlation coefficients between changes in climate indices and averaged monthly height of wind waves **(A)** and swell waves **(B)** at zero time lag.

## Possible Connections of Arabian Sea Wave Climate Fluctuations and Occurrence of Mudbanks

As discussed in Section “Introduction,” there have been many studies dealing with various aspects of appearance and disappearance of MBs at various locations along the Kerala coast. Numerous studies confirm the fact that high waves during the monsoon period initiate the appearance of MBs. This gives us a reason to speculate and form a hypothesis about how the identified periods of fluctuations in wave heights could influence the evolution of MBs and how this is confirmed by the available observations.

In Mathew et al. (1995), measured SWH and time of existence of MB off Alleppy in summer monsoon of 1986–1989 are shown in the same figure. It can be seen from this figure that the time of appearance and duration of existence of MB depend on the maximum wave heights in the summer monsoon cycle. So, if the maximum wave heights were in May–early June during 1986–1989, MBs were observed from mid-June to mid-July (in 1989). If the height of maximum waves was observed in mid-June, MB appeared from mid-July to end of August (in 1986). In

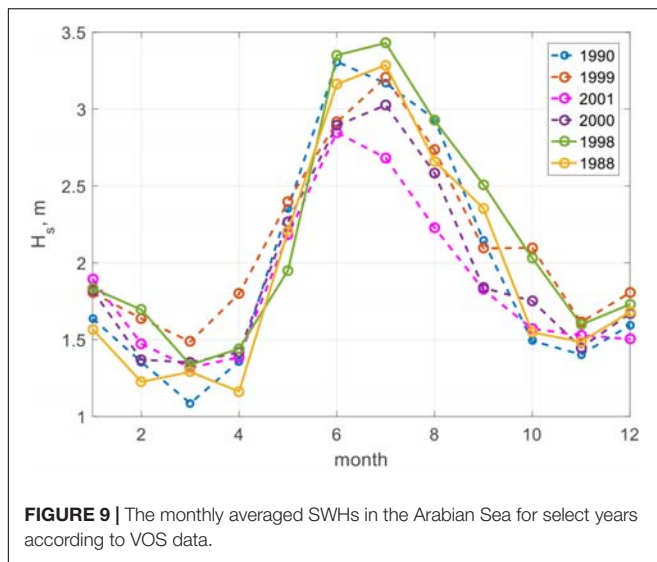
1988, the highest waves were observed in June and July, which corresponded to the existence of MB from mid-June to early August. This indicates that the time of appearance of MB and their “lifetime” are associated with distribution of maximal SWH in the monsoon cycle. Despite the fact that the maximum MAH of wind waves and swells in the monsoon cycle during 1979–2018 have been observed in June, it is clearly seen that there are deviations from this average cycle, when the largest waves are observed in other months (**Figure 4**). In **Figure 9**, changes in the monthly averaged SWH during summer monsoon years in which observations of times of appearance and times of existence of MBs in the Kerala region are available are presented in Philip et al. (2013).

SWH is calculated using the following formula:

$$H_s = \sqrt{H_{wind}^2 + H_{swell}^2} \quad (1)$$

where  $H_{wind}$  = SWH of wind waves and  $H_{swell}$  = SWH of swells.

If we refer to **Figure 9**, we find that in 1990 and 2001, MBs appeared off Kerala in June, which corresponds to the time (month) of maximum monthly averaged SWH. In 1999, they were observed during May–September, which corresponds



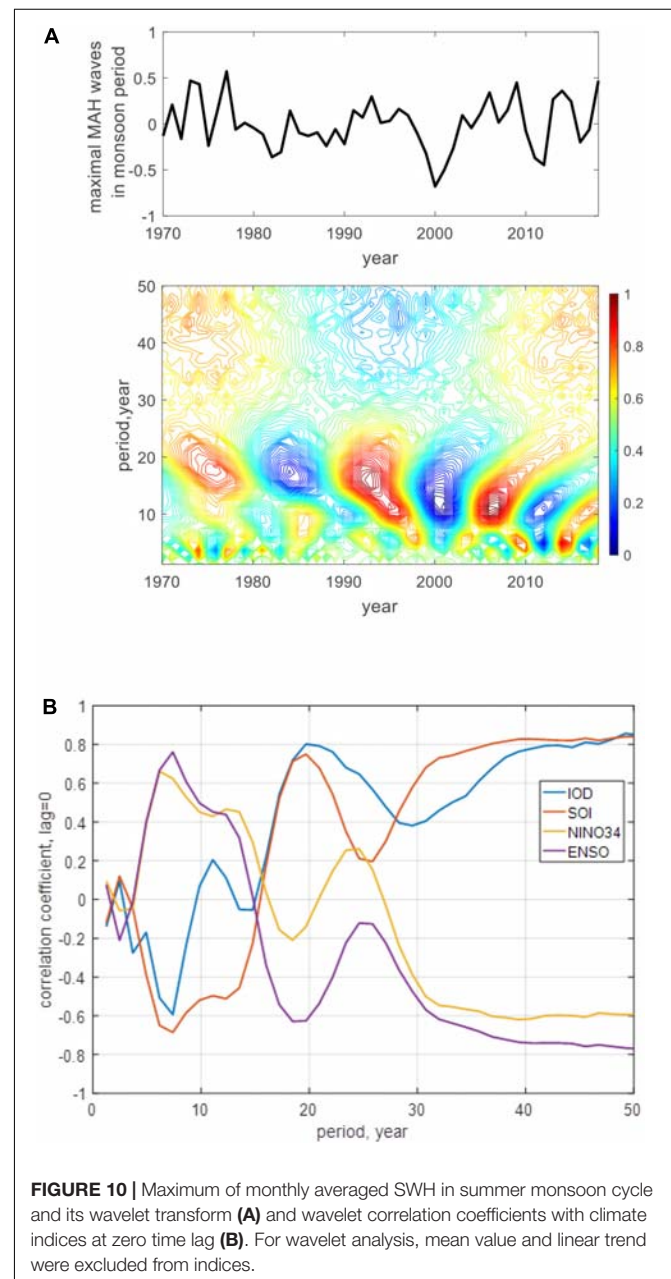
to the time of higher waves already set in May and the peak of monthly averaged SWH in July. In 2000, MB appeared in August, and maximum monthly averaged SWH was observed in July. In 1988 and 1998 (10 years period), MBs were observed from June to August, and, as can be seen in **Figure 9**, this corresponds to approximately the same summer monsoon cycle of monthly averaged SWH, with maximum heights in June and July. According to the results of wave climate analysis carried out in the previous section, the possible 10-year periodicity of such a cycle could be related to the influence of climate indices SOI, NINO3.4, and ENSO (**Supplementary Table 1**).

Because the appearance of MBs depends on the heights of the waves and, as the analysis of **Figure 9** shows, the wave height threshold for their formation is 2 m. As shown in Saprykina et al. (2020), the mechanism of MBs formation due to the wave transformation depends on the rate of dissipation of their energy above the bottom profile. In this case, it is important that must be two characteristic regions: first with a strong dissipation of the wave energy and then with a weak one, which will lead to the formation of an erosive (weighing of particles) and then an accumulative bottom profile due to their transfer, i.e., the formation of an MB. If the wave height is too high, then the length of the erosional area will significantly prevail, the particles will be in a suspended state, and the MBs will not have time to form. Therefore, MBs sometimes form not in the months when the highest waves were observed, but in the following months, when the wave height is lower, for example, in 1988, 1998, 1999, and 2000 years. In general, knowledge of the patterns of annual and long-term changes in wave heights in the monsoon cycle can also make it possible to predict the time of the appearance of MBs on different parts of the Kerala coastline due to the features of wave transformation over the bottom topography of each area.

Let us discuss how does the maximal of the monthly averaged SWH in summer monsoon cycle changes during 1970–2018. **Figure 10A** shows a series of these maximal (mean value is removed) and its wavelet transform. **Figure 10B** shows

the corresponding wavelet correlation coefficients with climate indices SOI, NINO3.4, ENSO, and IOD at zero time lag. Periods of the order of 7, 10–12, 18–20, and about 40 years associated with the fluctuations of these climate indices are clearly visible. It is confirmed by high values of modulus of the wavelet correlation coefficients (**Figure 10B**).

Webster et al. (1999) noted that El Niño events have indirect influence on IO and can force it to coincide with periods of its internal dynamics. Although IOD is considered as the main climate index of IO dynamics, as can be seen from **Figure 10B**, the combined mutual influence of SOI, NINO3.4, and ENSO indices in addition to the influence of IOD determines the main important periods of variability of the maximum



monthly averaged SWH during the monsoon period: 7, 18–20, and about 40 years.

Parvathy et al. (2015) have listed out the occurrences of MBs off southwest coast of India by taking into account all the reported data in the past and also discussed the significance of the recent and past MB in coastal dynamics. They reported that the best known MB of the southwest coast of India is Alleppy. Earlier reported areas of MB formation are the Munambam–Chettuwa sector at Chettuwa, Vadanappally, Nattika, Thalikulam, and Kaipamangalam (Mathew et al., 1995). But, presently these locations do not show any occurrences of MBs, and as reported by Noujas et al. (2013) during monsoons (2009–12), the MB occurrences were observed at Kara to Kaipamangalam sector. As reported in Noujas et al. (2013), based on the literature survey and interaction with the local people in the studied area, the location of occurrence of MBs moved southward from Chettuwa to Thalikkulam to Nattika to Edamuttam to Kaipamangalam to Bhajanandom successively during the last 40 years, and it remained stable in the same sector for 5–10 years. From 2013 onward, the occurrences of MB were reported in the Thykal and Punnapra region, Alleppy. About 10–12 years back, MBs which were seen confined to Purakkad region have moved south toward Punnapra region and since then it is forming at Punnapra region repeatedly (Parvathy et al., 2015).

The movement of MBs southward could be connected to the identified about 40 year period of El Niño events—for example, its influence on Monsoon Current in the IO (Webster et al., 1999). Suppose such possible influence is applied on West India Coastal Current (WICC), it could transport huge volume of water and suspended sediments from the coastal northern AS into the southeastern AS so that MB movement can be associated with simultaneous long-term fluctuations (about 40 years) of IOD, SOI, and El Niño. Unfortunately, the absence of detailed systematic long-term observations at least in a few locations in the study region does not allow us to obtain unambiguous clear connections between fluctuations of the wave climate and MBs occurrence. However, the above reasoning about the relationship between wave climate fluctuations is in a good agreement with the visual long-term observations of MBs evolution on the Kerala coast available in the literature. Thus, we hypothesize possible periods of movement of MB with the main climate indices, which further requires verification of other data.

## CONCLUSION

The analysis of wave data of VOS observations for the period 1970–2018 showed that the annual periodicity of changes in wave climate in the eastern AS, both in the coastal region and in the offshore is associated with the summer monsoon.

It has been found that the El Niño phenomenon plays a major role in the variability of wave climate of the eastern AS in all time scales, and its influence is directly or indirectly taken into account while calculating climate indices such as NINO3.4, ENSO, SOI, and PDO. The influence of El Niño is manifested with a delay of several months (3–6) on annual time scales and about 1–2 years on a decadal to multi-decadal time scales. To analyze the

relationship between the change in the wave climate of this region and the El Niño fluctuation, the NINO3.4 index is recommended since it shows the maximum correlation links on all time scales of the variability.

The strong variability of the wave climate at short time scales has been identified: 0.5 year, 1 year, 3–3.5 years (with a time lag of about 6 months), 4–5 years and 7–8 years (with a time lag of about 1 year). Decadal periods of change correspond to 10, 12–13, and 16 (with time lag of about 1 year) years.

The multi-decadal fluctuations occur with a period of 20 years (correlate with IOD and AAO indices), 30 years (correlate with AAO and PDO indices), and about 40 years (correlate with IOD, ENSO, NINO3.4, and SOI).

It is shown that intra-annual fluctuations in appearance and duration of existence of MBs depend on the distribution of highest monthly averaged SWHs in the summer monsoon cycle. The monthly averaged SWH threshold for their formation is 2 m. Through annual fluctuations of highest waves in monsoon cycle, a possible relationship between the wave climate variability of the AS and the formation of MBs can be shown for the periods 7, 10–12, 18–20, and about 40 years. It correlates with fluctuation of IOD, ENSO, NINO3.4, and SOI climate indices.

## DATA AVAILABILITY STATEMENT

The original contributions presented in the study are included in the article/**Supplementary Material**, further inquiries can be directed to the corresponding author/s.

## AUTHOR CONTRIBUTIONS

YS: main idea, writing the main content of the manuscript, and data analysis. SS: writing the manuscript and archival data collection. SK: data analysis. All authors agreed to be accountable for the content of the manuscript.

## FUNDING

This work was partly supported by RFBR Project No. 20-55-46005.

## ACKNOWLEDGMENTS

This study was performed in the frame of the state assignment theme no. 0128-2021-0004. SS thanks Director, CSIR-National Institute of Oceanography, Goa for his support in the work. The NIO contribution number is 6708.

## SUPPLEMENTARY MATERIAL

The Supplementary Material for this article can be found online at: <https://www.frontiersin.org/articles/10.3389/fmars.2021.671379/full#supplementary-material>

## REFERENCES

- Aboobacker, V. M., Rashmi, R., Vethamony, P., and Menon, H. B. (2011). On the dominance of pre-existing swells over wind seas along the west coast of India. *Cont. Shelf Res.* 31, 1701–1712. doi: 10.1016/j.csr.2011.07.010
- Amrutha, M. M., Kumar, V. S., Sandhya, K. G., Nair, T. B., and Rathod, J. L. (2016). Wave hindcast studies using SWAN nested in WAVEWATCH III-comparison with measured nearshore buoy data off Karwar, eastern Arabian Sea. *Ocean Eng.* 119, 114–124.
- Anoop, T. R., Kumar, V. S., and Shanas, P. R. (2014). Spatial and temporal variation of surface waves in shallow waters along the eastern Arabian Sea. *Ocean Eng.* 81, 150–157. doi: 10.1016/j.oceaneng.2014.02.010
- Anoop, T. R., SanilKumar, V., Shanas, P. R., Glejin, J., and Amrutha, M. M. (2016). Indian ocean dipole modulated wave climate of eastern Arabian Sea. *Ocean Sci. Discuss.* 12, 2473–2496.
- Badesab, F., Gaikwad, V., Gireeshkumar, T. R., Naikgaonkar, O., Deenadayalan, K., Samiksha, S. V., et al. (2018). Magnetic tracing of sediment dynamics of mudbanks off southwest coast of India. *Environ. Earth Sci.* 77:625. doi: 10.1007/s12665-018-7807-6
- Balachandran, K. K. (2004). Does subterranean flow initiate mud banks off the southwest coast of India? *Estuar. Coast. Shelf Sci.* 59, 589–598. doi: 10.1016/j.ecss.2003.11.004
- Barnett, T. P. (1983). Interaction of the monsoon and pacific trade wind system at interannual time scales part I: the equatorial zone. *Mon. Weather Rev.* 111, 756–773. doi: 10.1175/1520-0493(1983)111<0756:iotmap>2.0.co;2
- Bloomfield, H. C., Shaffrey, L. C., Hodges, K. I., and Vidale, P. L. (2018). A critical assessment of the long-term changes in the wintertime surface Arctic Oscillation and Northern Hemisphere storminess in the ERA20C reanalysis. *Environmental Res. Lett.* 13:094904. doi: 10.1088/1748-9326/aad5c5
- Chandramohan, P., Kumar, V. S., and Nayak, B. U. (1991). Wave statistics around the Indian coast based on ship observed data. *Indian J. Mar. Sci.* 20, 87–92.
- Chowdhury, P., and Behera, M. R. (2017). Effect of long-term wave climate variability on longshore sediment transport along regional coastlines. *Prog. Oceanogr.* 156, 145–153. doi: 10.1016/j.pocan.2017.06.001
- Damodaran, R., and Kurian, V. C. (1972). *Studies on the Benthose of the Mud Bank Regions of the Kerala Coast*. Kochi: Cochin University of Science and Technology.
- Faas, R. W. (1995). Mudbanks of the southwest coast of India III: role of non-Newtonian flow properties in the generation and maintenance of mudbanks. *J. Coast. Res.* 11, 911–917.
- Freeman, E., Woodruff, S. D., Worley, S. J., Lubker, S. J., Kent, E. C., Angel, W. E., et al. (2017). ICOADS Release 3.0: a major update to the historical marine climate record. *Int. J. Climatol.* 37, 2211–2232. doi: 10.1002/joc.4775
- Glejin, J., Kumar, V. S., and Nair, T. B. (2013a). Monsoon and cyclone induced wave climate over the near shore waters off Puduchery, south western Bay of Bengal. *Ocean Eng.* 72, 277–286. doi: 10.1016/j.oceaneng.2013.07.013
- Glejin, J., Sanil Kumar, V., Nair, B., and Singh, J. (2013b). Influence of winds on temporally varying short and long period gravity waves in the near shore regions of the eastern Arabian Sea. *Ocean Sci.* 9, 343–353. doi: 10.5194/os-9-343-2013
- Gopinathan, C. K., and Qasim, S. Z. (1974). Mud banks of Kerala-their formation and characteristics. *Indian J. Mar. Sci.* 3, 105–114.
- Grigorieva, V. G., and Badulin, S. I. (2016). Wind wave characteristics based on visual observations and satellite altimetry. *Oceanology* 56, 19–24. doi: 10.1134/S0001437016010045
- Grigorieva, V. G., Gulev, S. K., and Gavrikov, A. V. (2017). Global historical archive of wind waves based on voluntary observing ship data. *Oceanology* 57, 229–231. doi: 10.1134/S0001437017020060
- Gulev, S. K., Grigorieva, V., Sterl, A., and Woolf, D. (2003). Assessment of the reliability of wave observations from voluntary observing ships: Insights from the validation of a global wind wave climatology based on voluntary observing ship data. *J. Geophys. Res. Oceans* 108:3236.
- Jacob, N., Ansari, M. A., and Revichandran, C. (2015). Environmental isotopes to test hypotheses for fluid mud (mud bank) generation mechanisms along the southwest coast of India. *Estuar. Coast. Shelf Sci.* 164, 115–123. doi: 10.1016/j.ecss.2015.07.018
- Jacob, P. G., and Qasim, S. Z. (1974). Mud of a mud bank in Kerala, south-west coast of India. *Indian J. Mar. Sci.* 3, 115–119.
- Jiang, F., and Mehta, A. J. (1996). Mud banks of the Southwest Coast of India. V: wave attenuation. *J. Coast. Res.* 12, 890–897.
- Johnson, G., Kumar, V. S., Chempalayil, S. P., Singh, J., Pednekar, P., Kumar, K. A., et al. (2012). Variations in swells along eastern arabian sea during the summer monsoon. *Open J. Mar. Sci.* 02, 43–50. doi: 10.4236/ojms.2012.22006
- Kumar, V. S., and Kumar, K. A. (2008). Spectral characteristics of high shallow water waves. *Ocean Eng.* 35, 900–911. doi: 10.1016/j.oceaneng.2008.01.016
- Kumar, V. S., Chandramohan, P., Kumar, K. A., Gowthaman, R., and Pednekar, P. (2000). Longshore currents and sediment transport along Kannirajapuram Coast, Tamilnadu, India. *J. Coastal. Res.* 16, 247–254.
- Kumar, V. S., Dubhashi, K. K., and Nair, T. B. (2014). Spectral wave characteristics off Gangavaram, Bay of Bengal. *J. Oceanogr.* 70, 307–321. doi: 10.1007/s10872-014-0223-y
- Kurup, P. G. (1977). *Studies on the Physical Aspects of the Mudbanks Along the Kerala Coast With Special Reference to the Purakkad mud Bank*. Ph.D. Thesis, University of Cochin.
- Kurup, P. G., and Varadachari, V. V. R. (1975). Flocculation of mud in mud bank at Purakkad, Kerala Coast. *Indian J. Mar. Sci.* 4, 21–24.
- Loveson, V. J., Dubey, R., Kumar, D., Nigam, R., and Naqvi, S. W. A. (2016). An insight into subterranean flow proposition around Alleppey mudbank coastal sector, Kerala, India: inferences from the subsurface profiles of Ground Penetrating Radar. *Environ. Earth Sci.* 75, 1361. doi: 10.1007/s12665-016-6172-6
- Mallik, T. K., Mukherji, K. K., and Ramachandran, K. K. (1988). Sedimentology of the Kerala mud banks (fluid muds?). *Mar. Geol.* 80, 99–118. doi: 10.1016/0025-3227(88)90074-6
- Martin Thompson, P. K. (1986). Seasonal distribution of cyclopid copepods of the mud banks off Alleppey, Kerala coast. *J. Mar. Biol. Assoc. India* 28, 48–56.
- Mathew, J., Baba, M., and Kurian, N. P. (1995). Mudbanks of the Southwest Coast of India. I: wave characteristics. *J. Coast. Res.* 11, 168–178.
- Muraleedharan, K. R., Dinesh Kumar, P. K., Prasanna Kumar, S., John, S., Srijith, B., Anil Kumar, K., et al. (2018). Formation mechanism of Mud Bank along the southwest coast of India. *Estuar. Coasts* 41, 1021–1035. doi: 10.1007/s12237-017-0340-0
- Nair, A. S. K. (1985). “Morphological variation of mudbanks and their impact on shoreline stability,” in *Proceedings of the 1985 Australasian Conference on Coastal and Ocean Engineering*, (Newcastle West NSW: Institution of Engineers, Australia), 465.
- Nair, M. A., and Kumar, V. S. (2016). Spectral wave climatology off Ratnagiri, northeast Arabian Sea. *Nat. Hazards* 82, 1565–1588. doi: 10.1007/s11069-016-2257-5
- Nair, P. N., Gopinathan, C. P., Balachandran, V. K., Mathew, K. J., Regunathan, A., Rao, D. S., et al. (1984). Ecology of mudbanks-phytoplankton productivity in Alleppey mudbank. *CMFRI Bull.* 31, 28–35.
- Nair, R. R., and Murty, P. S. N. (1968). Clay mineralogy of the mud banks of Cochin. *Curr. Sci. India* 37, 589–590.
- Nair, S. M., and Balchand, A. N. (1992). Hydrochemical constituents in the Alleppey mudbank area, southwest coast of India. *Indian J. Mar. Sci.* 21, 183–187.
- Narayana, A. C., Jago, C. F., Manojkumar, P., and Tatavarti, R. (2008). Nearshore sediment characteristics and formation of mudbanks along the Kerala coast, southwest India. *Estuar. Coast. Shelf Sci.* 78, 341–352. doi: 10.1016/j.ecss.2007.12.012
- Naseef, T. M., and Kumar, V. S. (2017). Variations in return value estimate of ocean surface waves—a study based on measured buoy data and ERA-Interim reanalysis data. *Nat. Hazards Earth Syst. Sci.* 17, 1763. doi: 10.5194/nhess-17-1763-2017
- Neetu, S., Shetye, S., and Chandramohan, P. (2006). Impact of sea breeze on wind-seas off Goa, west coast of India. *J. Earth Syst. Sci.* 115, 229–234. doi: 10.1007/bf02702036
- Noujas, V., Thomas, K. V., and Badarees, K. O. (2013). Shoreline management plan for a mudbank influenced coast along Munambam-Chettuwa in central Kerala. *Proc. HYDRO 2013 Int.* 118–126.
- Parvathy, K. G., and Bhaskaran, P. K. (2019). Nearshore modelling of wind-waves and its attenuation characteristics over a mud dominated shelf in the Head Bay of Bengal. *Reg. Stud. Mar. Sci.* 29:100665. doi: 10.1016/j.risma.2019.100665

- Parvathy, K. G., Noujas, V., Thomas, K. V., and Ramesh, H. (2015). Impact of mudbanks on coastal dynamics. *Aqua. Proc.* 4, 1514–1521. doi: 10.1016/j.aqpro.2015.02.196
- Philip, A. S., Babu, C. A., and Hareeshkumar, P. V. (2013). Meteorological aspects of mud bank formation along south west coast of India. *Cont. Shelf Res.* 65, 45–51. doi: 10.1016/j.csr.2013.05.016
- Prasada Rao, C. V. K., and Baba, M. (1996). Observed wave characteristics during growth and decay: a case study. *Cont. Shelf Res.* 16, 1509–1520. doi: 10.1016/0278-4343(95)00084-4
- Rajesh Kumar, R., Raturi, A., Prasad Kumar, B., Bhar, A., Bala Subrahmanyam, D., and Jose, F. (2008). Parameterization of wave attenuation in muddy beds and implication on coastal structures. *Coast. Eng. J.* 50, 309–324. doi: 10.1142/s0578563408001843
- Ramachandran, K. K. (1989). Geochemical characteristics of Mudbank environment, a case study from Quilandy, West Coast of India. *J. Geol. Soc. India* 33, 55–63.
- Ramachandran, K. K., and Mallik, T. K. (1985). Sedimentological aspects of Alleppey Mud Bank, west coast of India. *Indian J. Mar. Sci.* 14, 133–135.
- Rao, D. S., Regunathan, A., Mathew, K. J., Gopinathan, C. P., and Murty, A. V. S. (1984). Mud of the mudbank: its distribution and physical and chemical characteristics. *CMFRI Bull.* 31, 21–24.
- Samiksha, S. V., Vethamony, P., Bhaskaran, P. K., Pednekar, P., Jishad, M., and James, R. A. (2019). Attenuation of wave energy due to mangrove vegetation off Mumbai, India. *Energies* 12, 4286. doi: 10.3390/en12224286
- Samiksha, S. V., Vethamony, P., Rogers, W. E., Pednekar, P. S., Babu, M. T., and Dineshkumar, P. K. (2017). Wave energy dissipation due to mudbanks formed off southwest coast of India. *Estuar. Coast. Shelf Sci.* 196, 387–398. doi: 10.1016/j.ecss.2017.07.018
- SanilKumar, V., and Jesbin, G. (2016). Influence of Indian summer monsoon variability on the surface waves in the coastal regions of eastern Arabian Sea. *Ann. Geophys.* 34, 871–885. doi: 10.5194/angeo-34-871-2016
- Sanjiv, P. C., SanilKumar, V., Johnson, G., Dora, G. U., and Vinayaraj, P. (2012). Interannual and seasonal variations in nearshore wave characteristics off Honnavar, west coast of India. *Curr. Sci.* 103, 286–292.
- Saprykina, Y. V., and Kuznetsov, S. Y. (2018a). Analysis of the variability of wave energy due to climate changes on the example of the black sea. *Energies* 11, 2020. doi: 10.3390/en11082020
- Saprykina, Y. V., and Kuznetsov, S. Y. (2018b). Methods of analyzing nonstationary variability of the black sea wave climate. *Phys. Oceanogr.* 25, 317–329. doi: 10.22449/1573-160X-2018-4-317-329
- Saprykina, Y., Kuznetsov, S., and Valchev, N. (2019). Multidecadal fluctuations of storminess of black sea due to teleconnection patterns on the base of modelling and field wave data. *Lect. Notes Civil Eng.* 22, 773–781. doi: 10.1007/978-981-13-3119-0\_51
- Saprykina, Y., Shtremel, M., Volvaiker, S., and Kuznetsov, S. (2020). Frequency downshifting in wave spectra in coastal zone and its influence on mudbank formation. *J. Mar. Sci. Eng.* 8:723. doi: 10.3390/jmse8090723
- Shanas, P. R., and SanilKumar, V. (2014). Temporal variations in the wind and wave climate at a location in the eastern Arabian Sea based on ERA-Interim reanalysis data. *Nat. Hazards Earth Syst. Sci.* 14, 1371–1381. doi: 10.5194/nhess-14-1371-2014
- Shynu, R., Rao, V. P., Samiksha, S. V., Vethamony, P., Naqvi, S. W. A., Kessarkar, P. M., et al. (2017). Suspended matter and fluid mud off Alleppey, southwest coast of India. *Estuar. Coast Shelf Sci.* 185, 31–43. doi: 10.1016/j.ecss.2016.11.023
- Soares, C. G. (1986). Assessment of the uncertainty in visual observations of wave height. *Ocean Eng.* 13, 37–56. doi: 10.1016/0029-8018(86)90003-x
- Sreelakshmi, S., and Bhaskaran, P. K. (2020a). Regional wise characteristic study of significant wave height for the Indian Ocean. *Clim. Dyn.* 54, 3405–3423. doi: 10.1007/s00382020-05186-6
- Sreelakshmi, S., and Bhaskaran, P. K. (2020b). Spatio-temporal distribution and variability of high threshold wind speed and significant wave height for the Indian ocean. *Pure Appl. Geophys.* 177, 4559–4575. doi: 10.1007/s00024-020-02462-8
- Sreelakshmi, S., and Bhaskaran, P. K. (2020c). Wind-generated wave climate variability in the Indian Ocean using ERA-5 dataset. *Ocean Eng.* 209, 107486. doi: 10.1016/j.oceaneng.2020.107486
- Stoica, P., and Moses, R. (2005). *Spectral Analysis of Signals*. Upper Saddle River, NJ: Pearson Prentice Hall, 447.
- Stopa, J. E., and Cheung, K. F. (2014). Intercomparison of wind and wave data from the ECMWF reanalysis interim and the NCEP climate forecast system reanalysis. *Ocean Model.* 75, 65–83. doi: 10.1016/j.ocemod.2013.12.006
- Tatavarti, R., and Narayana, A. C. (2006). Hydrodynamics in a mud bank regime during nonmonsoon and monsoon seasons. *J. Coast. Res.* 22, 1463–1473. doi: 10.2112/05-0461.1
- Torrence, C., and Compo, G. P. (1998). A practical guide to wavelet analysis. *Bull. Am. Meteorol. Soc.* 79, 61–78.
- Vethamony, P., Aboobacker, V. M., Menon, H. B., Kumar, K. A., and Cavaleri, L. (2011). Superimposition of wind seas on pre-existing swells off Goa coast. *J. Mar. Syst.* 87, 47–54. doi: 10.1016/j.jmarsys.2011.02.024
- Vethamony, P., Aboobacker, V. M., Sudheesh, K., Babu, M. T., and Kumar, K. A. (2009). Demarcation of inland vessels' limit off Mormugao port region, India: a pilot study for the safety of inland vessels using wave modelling. *Nat. Hazards* 49, 411–420. doi: 10.1007/s11069-008-9295-6
- Webster, P. J., Moore, A. M., Loschnigg, J. P., and Leben, R. R. (1999). Coupled ocean–atmosphere dynamics in the Indian Ocean during 1997–98. *Nature* 401, 356–360. doi: 10.1038/43848

**Conflict of Interest:** The authors declare that the research was conducted in the absence of any commercial or financial relationships that could be construed as a potential conflict of interest.

Copyright © 2021 Saprykina, Samiksha and Kuznetsov. This is an open-access article distributed under the terms of the Creative Commons Attribution License (CC BY). The use, distribution or reproduction in other forums is permitted, provided the original author(s) and the copyright owner(s) are credited and that the original publication in this journal is cited, in accordance with accepted academic practice. No use, distribution or reproduction is permitted which does not comply with these terms.



# Projections of Directional Spectra Help to Unravel the Future Behavior of Wind Waves

Hector Lobeto\*, Melisa Menendez and Iñigo J. Losada

*IHCantabria - Instituto de Hidráulica Ambiental de la Universidad de Cantabria, Santander, Spain*

Based on a novel approach, present-day and future spectral wind-wave conditions in a high-emission scenario from a seven-member wave climate projection ensemble are compared. The spectral analysis at the selected locations aids in understanding the propagation of swell projected changes from the generation areas across the ocean basins. For example, a projected increase in the energy from Southern Ocean swells can be observed in all ocean basins and both hemispheres, which is especially relevant in the west coast of North America due to the penetration of these swells beyond 30°N. Similarly, a consistent decrease in the energy of large northern Atlantic swells is noted close to the equator. This work provides evidence that assessments based on only integrated wave parameters (e.g., significant wave height and mean wave period) can mask information about the sign, magnitude, and robustness of the actual wave climate changes due to the offset of positive and negative variations within the spectrum, leading to a significant underestimation of the change associated with certain wave systems.

**Keywords:** ocean waves, wave climate projections, wave energy, swell, wind-wave spectrum

## OPEN ACCESS

### Edited by:

Giovanni Besio,  
University of Genoa, Italy

### Reviewed by:

Lorenzo Mentaschi,  
Joint Research Centre (JRC),  
Belgium  
Andrea Lira Loarca,  
University of Genoa, Italy

### \*Correspondence:

Hector Lobeto  
lobetoh@unican.es

### Specialty section:

This article was submitted to  
*Global Change and the Future  
Ocean*,  
a section of the journal  
*Frontiers in Marine Science*

**Received:** 18 January 2021

**Accepted:** 23 April 2021

**Published:** 20 May 2021

### Citation:

Lobeto H, Menendez M and  
Losada IJ (2021) Projections of  
*Directional Spectra Help to Unravel  
the Future Behavior of Wind Waves.*  
*Front. Mar. Sci.* 8:655490.  
doi: 10.3389/fmars.2021.655490

## INTRODUCTION

The sea surface elevation spectrum constitutes the most complete way to describe wind waves as a stochastic process. This spectrum represents the distribution of energy resulting from the contributions of several superimposed waves with different periods and directions that reach a particular location (Holthuijsen, 2007), and it is essential for assessing coastal processes and engineering designs. The distribution and magnitude of the energy within the spectrum provide information about the number of wave systems it contains, as well as their degree of development. Two are the main ways to represent the spectral energy: in terms of the wave frequency (hereinafter known as frequency spectrum) and in terms of wave frequency and wave propagation direction (hereinafter known as directional spectrum). The frequency spectrum has been used extensively by fitting observations to parametric spectral forms (e.g., JONSWAP and Pierson-Moskowitz). Directional spectra provide additional information by characterizing how wave energy is spread along directional sectors, enabling us to undertake a more detailed analysis of the wave climatology in a particular location (Espejo et al., 2014; Shimura and Mori, 2019) and to identify the different wave systems reaching it (Portilla-Yandún et al., 2015). More recently, directional spectra have been utilized to develop studies at global scale, assessing the wave climate seasonality through the identification of wave modes and their variations throughout

the year (Echevarria et al., 2019), as well as their relation with climate teleconnection patterns (Echevarria et al., 2020).

The prominent role of wind-generated waves in ocean sea surface dynamics (Cavaleri et al., 2012) implies that changes in magnitude, direction, and frequency may have a notable impact on offshore related economic activities (e.g., offshore industry and shipping routes) and in coastal areas, affecting processes such as shoreline erosion (Toimil et al., 2020) and flooding (Hemer et al., 2012a; Melet et al., 2018; Kirezci et al., 2020). Projected changes in wind-generated waves induced by climate change have thus been widely studied, especially during the last decade (e.g., Hemer et al., 2013; Mori et al., 2013), to assess both the magnitude of future variations and associated uncertainty (Morim et al., 2019). The numerous studies that have been conducted are usually developed on the outputs of general circulation model (GCM)-based wave climate projection ensembles, covering different greenhouse-gas (GHG) concentrations scenarios and temporal horizons. The GCMs are characterized by systematic biases caused by factors such as the spatial resolution or the simplifications introduced by the parametrization of physical processes (Maraun et al., 2017), hence also inducing biases in projections of wind waves (Hemer et al., 2012b). Despite bias correction (BC) is usual practice in climatic variables such as precipitation or temperature, its application in wave climate ensembles is relatively recent. In this regard, since its need was demonstrated (Lemos et al., 2020a), BC has been applied in various wave climate studies (Lemos et al., 2020b; Meucci et al., 2020; Lobeto et al., 2021). All these researches apply BC to ensembles of integrated wave parameters, not existing, to the best of our knowledge, any study applying BC to wave spectra.

Despite the wave spectrum fully describes the wind wave climate, almost all the studies on changes in wave climate due to climate change assess the projected variations in representative integrated wave parameters. The reasons behind this simplification lie in the huge storage capacity demanded by directional spectra and the extended use of integrated parameters in multiple formulations related to the design of marine structures and coastal processes. In particular, the usual approach relates the expected changes in wave climate with future changes in significant wave height ( $H_s$ ; e.g., Fan et al., 2013; Wang et al., 2014), which have led to a consensus about the expected changes in annual and seasonal mean  $H_s$  in some regions along the global ocean. In this regard, there exist agreement on an increase in  $H_s$  in the Southern Ocean and tropical eastern Pacific and a decrease in the North Atlantic Ocean, northwestern Pacific, and Mediterranean Sea (Morim et al., 2018; Oppenheimer et al., 2019). Nonetheless, a deeper understanding of these future variations needs the study of a wider number of variables, such as period and direction, especially considering the notable role their changes may have in coastal impacts (e.g., van Gent et al., 2008; Harley et al., 2017). The assessment of changes in period and direction through parameters, such as mean wave period ( $T_m$ ) and mean wave direction ( $Dir_m$ ), is now common practice (e.g., Casas-Prat et al., 2018), which offers a closer vision to the expected change in the full wave spectrum. In the same vein, there is

an increasing interest in evaluating the effect of climate change in variables that integrate different parameters and provide more complete information about wave climate. For example, the wave energy flux (e.g., Mentaschi et al., 2017), a variable that integrates wave height and wave period, has been proven to be a valid indicator of global warming (Reguero et al., 2019) and provided robust changes in areas where  $H_s$  changes alone have great uncertainty (Lemos et al., 2019). However, none of the described studies provide any information about the projected changes in the different wave systems reaching a certain location as it can only be derived from directional spectra.

Based on the above information and to gain a broader understanding of how the global wave climate will be affected by climate change, as well as its consequences for impact assessments, this study attempts to explore the future changes in directional spectra under a high-emission scenario across all ocean regions. We aim to show the added value offered by a novel approach that explore simultaneously the effect of climate change on the energy, period, and direction of the waves, unraveling as well the differences with respect to the standard use of projected integrated wave parameters.

## DATA AND METHODS

### Wave Climate Data

Global wave climate projections are generated using the third-generation numerical wave model WaveWatch III v4.18 (Tolman, 2014). Surface-wind fields and ice coverage outputs from CMIP5 GCMs are considered as inputs to develop a seven-member ensemble (further information in **Supplementary Material**). Present-day and future wave conditions are characterized through 20-year time slices (1986–2005 and 2081–2100, respectively). The RCP8.5 greenhouse gas (GHG) emission scenario, one of the representative concentration pathways (RCPs) covered in the Fifth Assessment Report (AR5) from the International Panel on Climate Change (IPCC; Cubasch et al., 2013), is selected to conduct the research. This scenario represents a concentration trajectory characterized by a radiative forcing of  $8.5 \text{ W/m}^2$  by 2100 in the absence of a drastic reduction in GHG emission rates. In addition, GOW2 wave hindcast (Perez et al., 2017) is used as reference data for the present-day wave climate, both to analyze the mean wave climatology and to assess the magnitude of the systematic biases in the projections by comparing the annual mean wave spectrum (**Supplementary Material**).

The projected changes from directional spectra are analyzed at 14 selected locations according to geographical and physical criteria (**Figure 1**). Concerning the former, we choose a representative sample of regional wave conditions along the global coast. Thus, six points are selected in the Pacific basin, three along the east coast ( $P_2$ ,  $P_{11}$ , and  $P_{12}$ ) and another three along the west coast ( $P_1$ ,  $P_9$ , and  $P_{10}$ ). Six points are also analyzed in the Atlantic basin, three in the west coast ( $P_3$ ,  $P_4$ , and  $P_{13}$ ) and three more along the east coast ( $P_5$ ,  $P_6$ , and  $P_7$ ). Finally, two more points are selected in the Indian



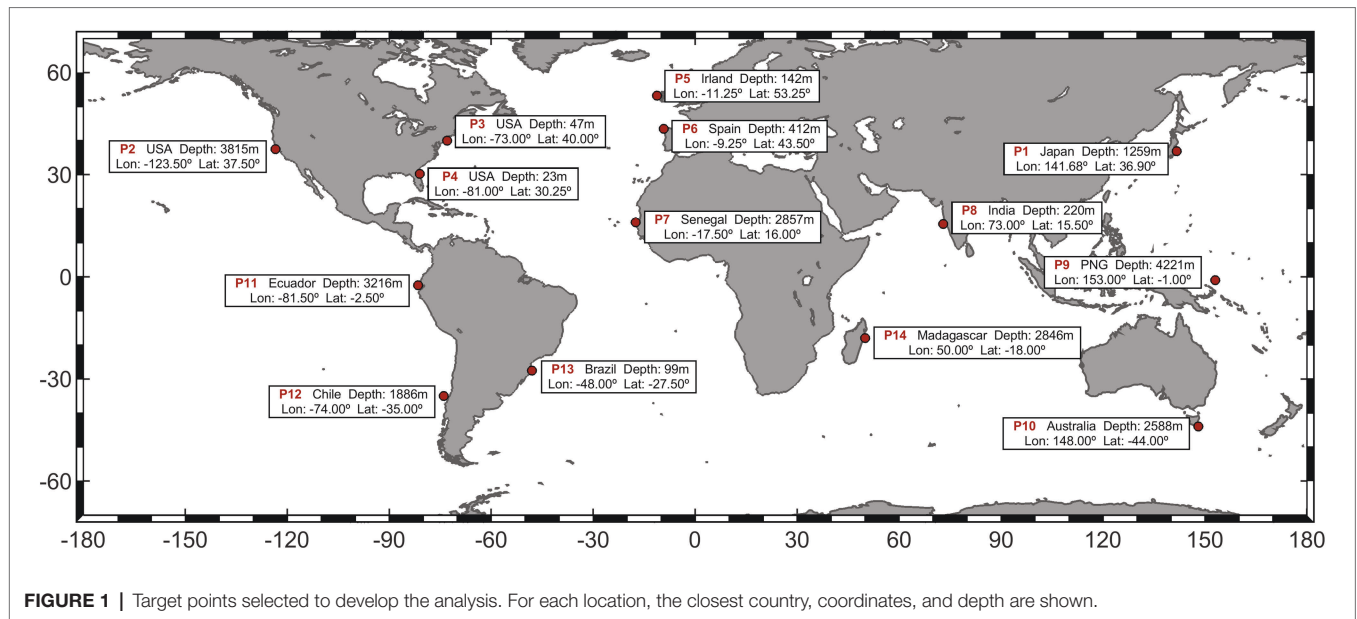


**FIGURE 1** | Target points selected to develop the analysis. For each location, the closest country, coordinates, and depth are shown.

basin (P8 and P14). Physical criteria account, first, for a multimodal wave climate at the target locations (Echevarria et al., 2019), i.e., reached by multiple wave systems. Second, the selected locations should be at a distance to the coast higher than 30 km to avoid local diffraction and/or non-linear processes due to propagation in shallow waters.

As a result of the simulations, hourly time series of directional spectra are stored at the target locations (Figure 1), discretized in 32 frequency bins, exponentially distributed from 0.0373 to 0.7159 Hz (i.e., from 1.4 to 26.8 s) and 24 directional sectors of 15° each, i.e., each spectrum is divided into 768 frequency-direction spectral bins (hereinafter spectral bins).

### Projected Changes and Uncertainty Assessment

The projected change for each GCM is obtained as the difference between the annual mean spectrum of future and present-day wave climate. The ensemble mean change is then calculated as the average of the individual changes for each GCM (Eq. 1), i.e., we assume equal contributions from all the ensemble members.

$$\Delta E_{ens} = \frac{\sum_{i=1}^{i=N} E_{fc}^i - E_{pc}^i}{N} \tag{1}$$

where  $N$  is the number of models,  $\Delta E_{ens}$  is the projected ensemble mean change,  $E_{pc}^i$  is the mean wave spectrum for the present climate (1986–2005), and  $E_{fc}^i$  is the mean wave spectrum for the future climate (2081–2100).

The uncertainty of the projected change is assessed based on a method proposed in the AR5 report (Tebaldi et al., 2011; Collins et al., 2013), which consists in the analysis of its significance first and then considering the agreement in the sign of change between the members of the wave climate projection ensemble. Nevertheless, as the number of selected

models is notably smaller than in the study defining the method (21 vs. 7), we require a stricter agreement between members to consider the changes to be robust. Namely, more than 80% of the models ( $\geq 6$ ) must present a statistically significant change, and at least 80% of them must agree on the sign of change. The statistical significance is calculated by applying a Welch's  $t$ -test to the mean of the reference and future periods at the 95% confidence level. The consideration of an unequal variance  $t$ -test lies in the possible shift of the energy along the frequency and direction axes in the future, hence causing a change in the energy variance at each spectral bin with respect to the present-day climate. Spectral bins in which the change is found to be robust are highlighted. Only changes above 1% of the maximum change within the spectrum are highlighted to ease the understanding of the results.

### RESULTS

The spectral approach enables the detailed study of future changes in wave energy, providing the variations at each spectral bin. Similarly, it is possible to assess how the bulk of the energy moves along the frequency axis. To this end, for each direction, we calculate the range of periods within which the energy interquartile range is concentrated at present and in the future, and then we determine its shift. Nevertheless, an accurate analysis of wave climate spectral changes at each of these locations also requires specific study of local wind conditions and the geometry of the coast to account for reflections. Considering the main purpose of this work, we focus on only the main wave systems that reach the target points, neglecting the small changes related to local wind seas, which represent a very small percentage of the total energy in the spectrum.

Below, we provide a brief description of the present-day wave climate at each location (Figure 2) and the main projected changes by the end of the century under the RCP8.5 scenario (Figure 3).

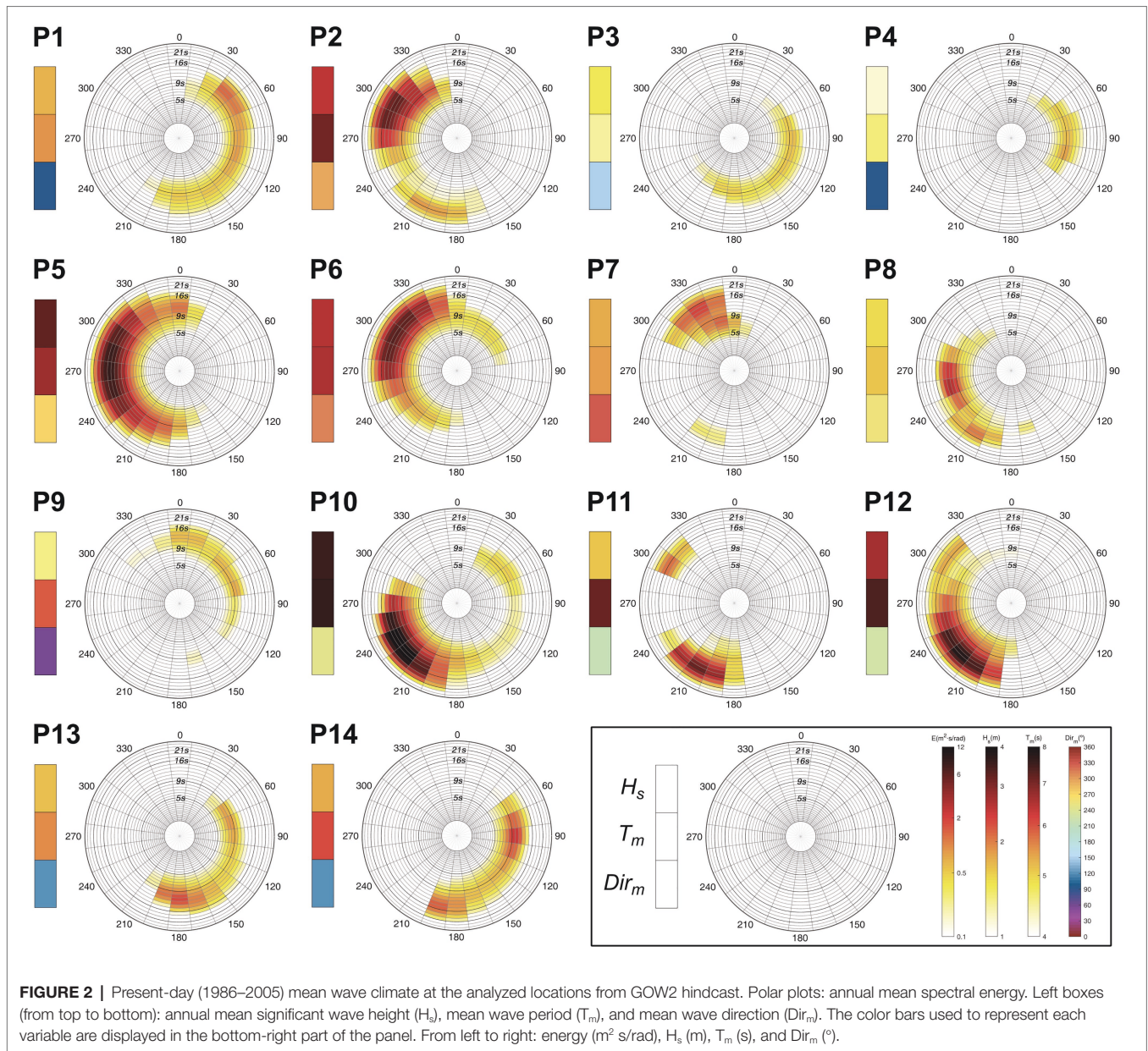


**FIGURE 2 |** Present-day (1986–2005) mean wave climate at the analyzed locations from GOW2 hindcast. Polar plots: annual mean spectral energy. Left boxes (from top to bottom): annual mean significant wave height ( $H_s$ ), mean wave period ( $T_m$ ), and mean wave direction ( $Dir_m$ ). The color bars used to represent each variable are displayed in the bottom-right part of the panel. From left to right: energy ( $m^2 s/rad$ ),  $H_s$  (m),  $T_m$  (s), and  $Dir_m$  ( $^\circ$ ).

For completeness, the shift in the energy interquartile range for each direction is shown (Figure 4). The information provided by the assessment of the directional spectra that cannot be obtained from integrated wave parameters is highlighted.

P5 and P6 are in the northeastern Atlantic on the European coast. Most of the wave energy at these points is carried by swells propagating from the west at P5 and northwest at P6, which are generated under extratropical storms crossing the northernmost Atlantic Ocean (Camus et al., 2014; Pérez et al., 2014). These points show the greatest decrease in energy among all the locations analyzed (Figure 3), as well as a shift to lower periods (Figure 4). A closer look at P5 also highlights an expected robust negative change in the low-energetic swells coming from the north and the wind seas from the south. Analogously, the results at P6 also show a future decrease in

the wind seas coming from the northeast and southwest. This negative pattern at both points agrees with the expected decrease in  $H_s$  and with the results obtained in previous studies regarding projected changes in wave height along the European Atlantic coast (Bricheno and Wolf, 2018). Although P7 is also located in the northeastern Atlantic, its lower latitude ( $16^\circ$  north) causes it to not only be affected by swells generated in the Northern Hemisphere (NH) but also by swells that travel from the Southern Hemisphere (SH) that cross the equator, especially during austral winter (Semedo et al., 2011; Supplementary Figure 1). This point is also reached by the wind seas coming from the northeast and northwest with a mean period of approximately 8 s (Figure 2). Therefore, the robust decreases in  $H_s$  and  $T_m$  integrate the variations in these four wave systems, concealing the nonuniform behavior of the spectral projected changes (i.e., there are spectral

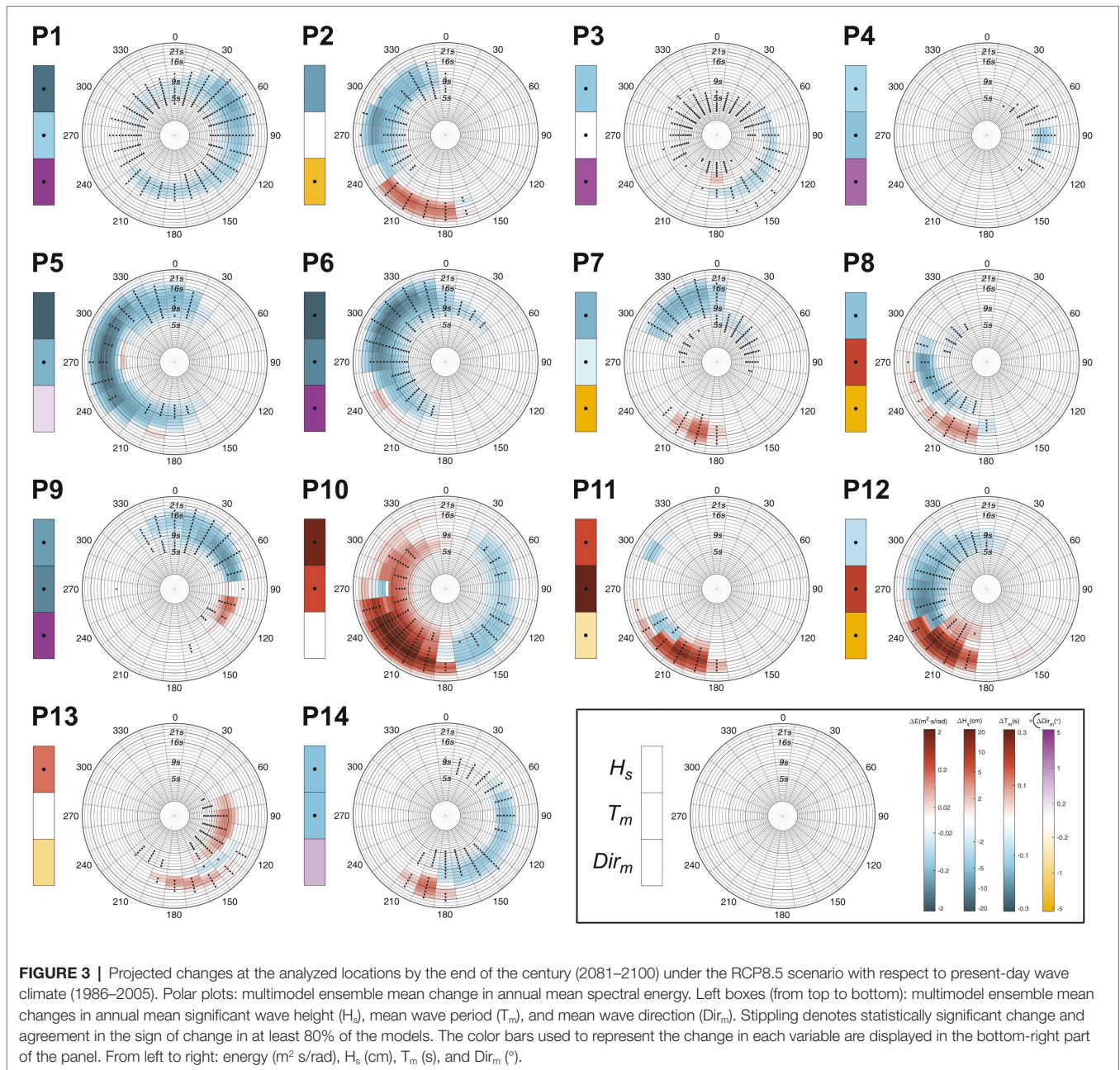
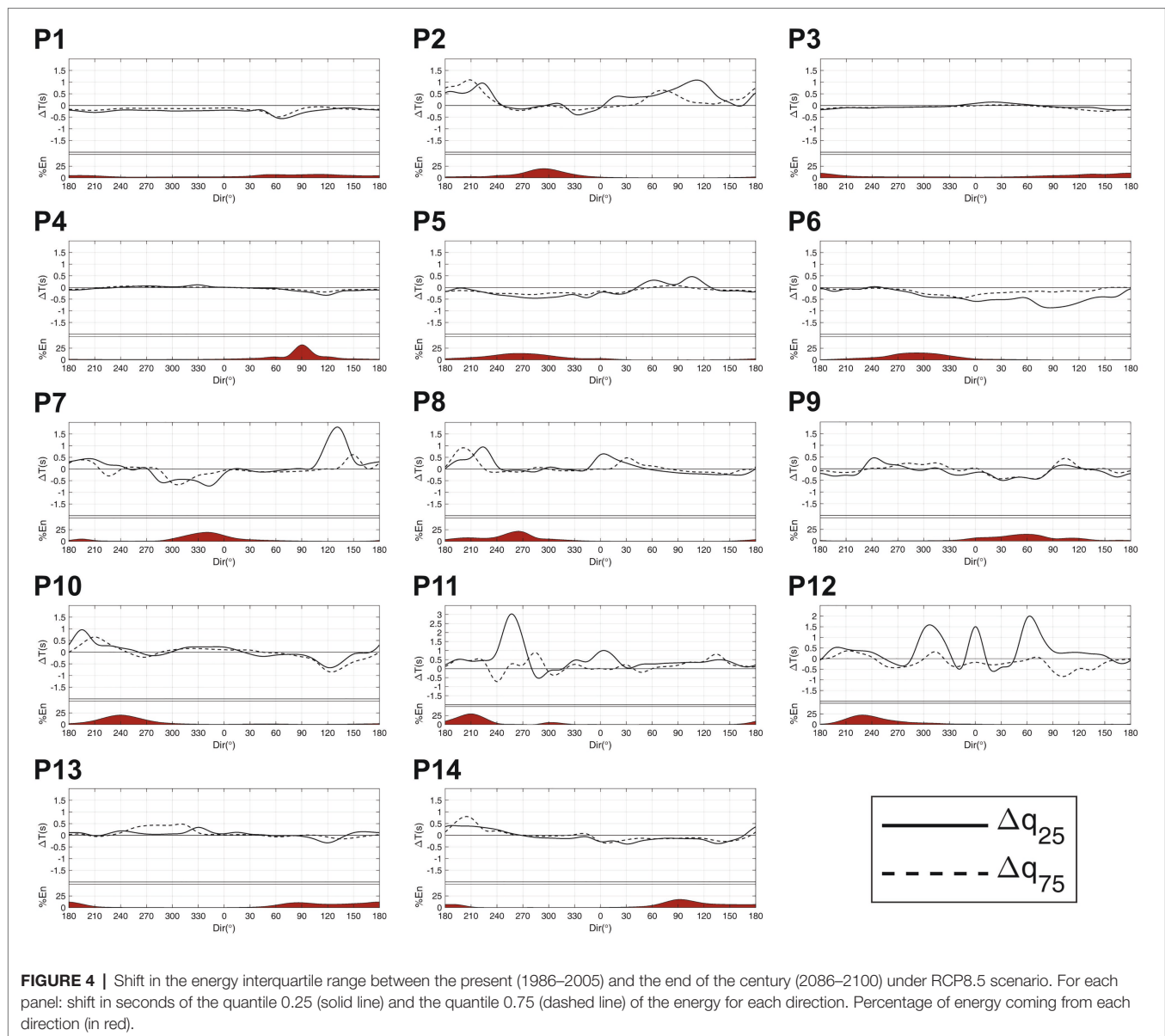


**FIGURE 3 |** Projected changes at the analyzed locations by the end of the century (2081–2100) under the RCP8.5 scenario with respect to present-day wave climate (1986–2005). Polar plots: multimodel ensemble mean change in annual mean spectral energy. Left boxes (from top to bottom): multimodel ensemble mean changes in annual mean significant wave height ( $H_s$ ), mean wave period ( $T_m$ ), and mean wave direction ( $Dir_m$ ). Stippling denotes statistically significant change and agreement in the sign of change in at least 80% of the models. The color bars used to represent the change in each variable are displayed in the bottom-right part of the panel. From left to right: energy ( $m^2 s/rad$ ),  $H_s$  (cm),  $T_m$  (s), and  $Dir_m$  ( $^\circ$ ).

bins with both signs of change). Thus, while an increase and displacement to higher periods are expected for swells generated in the SH, a decrease is projected in the energy carried by swells and wind seas from the North Atlantic Ocean, which agrees with the results at *P5* and *P6*.

The North Atlantic west coast is represented by *P3* and *P4*, which are low energy locations affected by low-period waves. Most of the energy that reaches *P4* comes from waves generated by trade winds in the tropical North Atlantic that propagate from the east with a mean period of approximately 9 s. The results show a robust decrease in this energy and a shift to lower periods, agreeing with the projected decreases in  $H_s$  and  $T_m$ . *P3* is mainly affected by swells generated in

the tropical-north trade wind region coming from the southeast and two local wind-wave systems that propagate from the south and east. Spectral results show a generalized projected decrease and a negligible shift in the energy that is consistent with the decrease expected in  $H_s$  and the almost null decrease in  $T_m$ . *P13* is located on the coast of Brazil in the tropical southwestern Atlantic. The mean wave climate indicates that it is mainly affected by swells generated in the Southern Ocean that propagate from the south, swells generated in the tropical south Atlantic coming from the east and wind waves propagating from a direction of approximately  $200^\circ$ . The projected increase in  $H_s$  agrees with the change expected for the energy carried by southern and eastern swells. However, while a displacement



of the energy to higher periods is expected for swells from the Southern Ocean, the opposite is obtained for eastern waves, which likely causes the very low projected change found in  $T_m$ .

*P2* is located on the west coast of North America, so it is mainly affected by the swells generated by extratropical storms in the North Pacific. This point is also affected by wind seas coming from the northwest and by mature energetic swells generated in the Southern Ocean that penetrate the NH mostly during austral winter (Young, 1999; Semedo et al., 2011; **Supplementary Figure 2**). The results show a robust projected increase in southern swells with periods between 14 and 22 s. Nevertheless, a consistent change is not found for the largest swells generated in the northernmost Pacific, as has been found in the Atlantic (i.e., periods above 14 s). **Figure 4** displays a notable shift in the southern energy to higher periods and an almost null shift in the north Pacific energy. The integration

of all these spectral changes leads to an uncertain decrease in  $H_s$  and a very small increase in  $T_m$  that mask the important increase expected for long southern swells.

The southeastern Pacific wave climate is studied at locations *P11* and *P12*. The main energy contributors to the total energy at these points are swells generated in the Southern Ocean. Despite their southern latitude, both points still receive a low amount of energy during boreal winter carried by very long swells from the NH (**Supplementary Figures 3, 4**); together with *P2*, this provides evidence of the seasonal displacement of the swell front in the eastern Pacific (Young, 1999). Regarding *P11*, a bipolar change pattern in the energy coming from southern mid-latitudes can be observed, showing a robust increase in the swells generated below approximately 40°S and a consistent decrease in waves from higher latitudes. The shift to higher periods and the large changes expected for the energy carried

by the southernmost swells induce a projected increase in  $H_s$  and  $T_m$ . The results at  $P12$  exhibit the same robust bipolar pattern as at  $P11$  and an increase in wind seas propagating from the south. The balance between spectral energy variations with different signs is clearly the cause of the low negative change expected in  $H_s$ , which is not reflecting, as it occurs at  $P2$ , the notable increase expected for very energetic Southern Ocean swells. Finally, a robust decreasing signal is not found for long swells coming from the NH at  $P11$  and  $P12$ , corroborating the results at  $P2$ .

The northwestern Pacific coast is represented by a point located on the east coast of Japan ( $P1$ ). This point is affected by the energetic swells generated in the northernmost Pacific, swells coming from the east, and swells from the south. The projected spectral changes highlight a robust decrease in energy and a remarkable shift to lower periods that is consistent with the projected negative changes in  $H_s$  and  $T_m$ .  $P9$  is close to the equator (latitude  $1^\circ\text{S}$ ) and is sheltered from the Southern Ocean swells due to the presence of Australia and multiple islands. Therefore, most of the energy arriving at this point is carried by the waves originating in the NH, namely swells coming from the north and northeast. However, a swell system generated in the tropical south Pacific propagating from the southeast is still discernible. Regarding the projected changes, an energy increase with a slight shift to higher periods likely related to the found intensification of southeasterly trades (Timmermann et al., 2010), is expected for southern waves, and in line with the results at  $P1$ , a robust decrease with a shift to lower periods can be observed in the wave systems generated in the NH. The preponderant role of northern wave systems induces negative projected changes in  $H_s$  and  $T_m$ , precluding the possibility of reaching any conclusion about future variations in energy from SH waves. Finally, the southwestern Pacific wave climate is studied at  $P10$ , a point located in the Southern Ocean and affected by highly energetic swells generated by southern westerly winds. In addition, it is also reached by swells coming from the southeast and northeast and wind seas coming from the west. Projected spectral changes show a robust bipolar pattern characterized by an increase in wave systems with a western component and a decrease in wave systems coming from the eastern directional sectors. Therefore, the consistent increase obtained in  $H_s$  involves a great loss of information since it cannot account for the important projected decrease in waves coming from the east. Moreover, **Figure 4** shows a shift in energy to higher periods for swells propagating from the southwest and the opposite for waves coming from the east, resulting in a robust projected increase in  $T_m$  that masks the existent energy shift to lower periods.

Changes in the wave conditions in the Indian basin are studied at  $P14$  and  $P8$ . The mean wave climate shows that  $P14$  is mainly reached by three wave systems: the Southern Ocean swells from the south and the southeast and the tropical-north swells from the northeast. While a robust increase is obtained in swells from the south, a consistent decrease is seen for the other two wave systems. In addition, a shift to lower periods is observed for waves coming from the east, and in agreement with previous locations, a shift to higher periods is observed for the Southern Ocean energy. Although robust decreases in  $H_s$  and  $T_m$  are obtained, the consideration of changes from

integrated parameters prevents the derivation of the clear increase found for southern swells. Regarding  $P8$ , although it is located in tropical northern Indian, it is still affected by swells generated in the Southern Ocean that travel beyond the equator. This point also receives waves generated in the tropical Indian Ocean propagating from the west that are especially strong during the summer monsoon season (Portilla-Yandún, 2018) and wind waves from the northwest. A projected uncertain decrease is observed for tropical swells with no clear energy shift. By contrast, a robust increase in the energy carried by swells generated in the Southern Ocean with a shift to higher periods is found. Integrated wave parameters indicate a consistent decrease in  $H_s$ , which conceals the change in southern swells, as seen at  $P14$ .

The assessment of the projected changes at each location independently provides us a global overview of the spectral changes and allows us to draw some conclusions about the future behavior of energetic swells (large-period swells) along the world's coasts. Results evidence a robust increase in the energy carried by swells generated by extratropical cyclone activity in the Southern Ocean below approximately  $40^\circ\text{S}$  that can be observed at points located in the Southern Pacific (e.g.,  $P11$  and  $P12$ ), Atlantic ( $P13$ ), and Indian basins ( $P14$ ). Similarly, the propagation of these swells beyond the equator makes it feasible to note this consistent increase in northern locations, such as on the west coast of North America, Senegal, and India ( $P2$ ,  $P7$ , and  $P8$ , respectively). This positive change may be related to the increase in energy transferred to the ocean surface due to the expected intensification of surface westerly winds in the roaring forties and furious fifties regions (Swart and Fyfe, 2012) and could also be favored by the fetch increase caused by the expected reduction in ice coverage in high latitudes (Thomson and Rogers, 2014). Regarding changes in northern energetic swells, a clear decrease in the energy carried by swells generated by extratropical storms in the northernmost Atlantic can be observed at points located in Europe ( $P5$  and  $P6$ ) and with a lower magnitude along the tropical coast of Africa ( $P7$ ). Nonetheless, a robust change cannot be found in the energetic swells (periods above 14 s) coming from the northernmost Pacific on the coast of North America ( $P2$ ) or at points located in the SH that still receive northern mature swells during boreal winter ( $P11$  and  $P12$ ).

## DISCUSSION

The assessment of projected wave climate changes from directional spectra provides information that cannot be obtained from the commonly used method based on integrated wave parameters. While the spectral approach allows us to separately analyze the sign and magnitude of change from different swells and seas that reach a certain location, the consideration of changes from integrated wave parameters necessarily overlooks the existence of positive and negative variations within the spectrum. Similarly, the analysis of wave climate changes following the standard approach may entail an underestimation of the actual changes due to the integration of variations with opposite sign from different wave systems. The results on the coast of Chile ( $P12$ ; **Figure 3**) are clear evidence for this statement. Notwithstanding that the projected change from

integrated parameters indicates a low decrease in significant wave height, future changes from directional spectra show a clear bipolar change pattern characterized by positive and negative variations with a high magnitude (increase for southwestern swells and decrease for western swells). This issue can also be seen in other locations, such as the west coast of North America (*P2*) and southwestern Indian (*P14*).

Moreover, the uncertainty assessment of the projected changes denotes that the spectral analysis can provide consistent results for some of the wave systems that integrate the spectrum, even when the projected changes from integrated wave parameters exhibit a lack of robustness. This can be observed at points in both the Pacific (*P2*) and Atlantic (*P5*) basins. In this regard, although changes in significant wave height are not robust in the northwestern Pacific coast, spectral changes indicate that the future variations in large swells propagating from the Southern Ocean at *P2* are still robust. Similarly, a strong conclusion about the future behavior of northern swells and southern seas can be derived at *P5* on the British coast from the spectral approach despite the great uncertainty associated with the change in significant wave height.

The spectral analysis also shows a misleading climate change signal from the mean wave period. Again, there can be an offset of variations with opposite sign that can drive a deceptive change, making it unfeasible to observe the existence of negative and positive variations and more importantly, to see the actual magnitude of the projected change associated to each wave system. From the number of locations analyzed, a clear increase in periods in the Southern Ocean energetic swells can be seen. Nevertheless, the assessment from integrated parameters masks this projected increase when these swells are not the main energy contributor at the location of analysis. The points located in the tropical eastern Atlantic (*P7*) and southeastern Pacific (*P12*) are two examples of this issue.

The use of integrated wave parameters can have severe implications in locations where an increase and shift in the energy carried by recurrent wave systems to higher periods are masked. In other words, although a decrease can be projected for integrated parameters, such as the mean period or significant wave height, the spectral approach can show a notable increase in wave systems periodically reaching a certain location. Separately assessing the projected changes in the most severe wave systems that reach the coast, especially at coastal stretches affected by a multimodal wave climate, can help to more accurately determine the impacts derived from changes in wave conditions in view of the significant influence that wave period and direction have on coastal processes.

The present study is developed without correcting the existing systematic bias of the wave climate projections (**Supplementary Figures 5–18**). In this regard, despite BC has recently been shown to be optimal to obtain more accurate projected changes in integrated wave parameters (Lemos et al., 2020a), its application to directional spectra is yet to be addressed. Furthermore, the way of application of BC to integrated wave parameters (e.g., quantile mapping) cannot be directly extrapolated to directional spectra. As previously seen, future changes do not only apply to the energy magnitude within the spectrum, since shifts along

the frequency and direction axes may also occur. The energy in a certain spectral bin at present could move to another one in the future, therefore, introducing an important error if we correct the bias equally in both time periods. In addition, the bias assessment indicates a heterogeneous bias pattern within the spectrum for some locations (e.g., *P7* and *P10*), precluding a proportional correction based on the comparison of an integrated parameter such as the total energy. Despite the lack of BC, since its application do not alter the sign of the projected changes (Lemos et al., 2020a), and we are comparing ensemble changes of integrated parameters and wave directional spectra from the same models (i.e., affected by the same GCM biases), the obtained results can be considered as a reliable evidence of the added value offered by the spectral approach. Nevertheless, further research is needed to raise a BC technique applicable to spectra that accounts for the described issues and helps to provide more accurate changes.

We consider that the results presented in this study offer a clear vision of the potential contribution of directional spectra within the understanding of wave climate projected changes and their implications, which is evidence of a misleading climate change signal in some cases according to the standard approach based on integrated wave parameters. These insights, together with the technological progress that boosts storage in larger databases, encourage the development of deeper studies that are not constrained to a limited number of locations and the annual mean climate, opening the door to a much more advanced comprehension of the future behavior of wind waves in entire regions.

## DATA AVAILABILITY STATEMENT

The raw data supporting the conclusions of this article will be made available by the authors, without undue reservation.

## AUTHOR CONTRIBUTIONS

HL, MM, and IL designed the research, analyzed the results, and wrote the paper. HL performed the research. All authors contributed to the article and approved the submitted version.

## FUNDING

HL and MM acknowledge the support by the Spanish Ministry of Science and Innovation (MICINN, grants FPU17/06203 and RYC-2014-16469, respectively). This work is funded by EXCEED (grant RTI2018-096449-B-I00) from the Spanish State Research Agency.

## SUPPLEMENTARY MATERIAL

The Supplementary Material for this article can be found online at: <https://www.frontiersin.org/article/10.3389/fmars.2021.655490/full#supplementary-material>

## REFERENCES

- Bricheno, L. M., and Wolf, J. (2018). Future wave conditions of Europe, in response to high-end climate change scenarios. *J. Geophys. Res. Oceans* 123, 8762–8791. doi: 10.1029/2018JC013866
- Camus, P., Menéndez, M., Méndez, F. J., Izaguirre, C., Espejo, A., Cánovas, V., et al. (2014). A weather-type statistical downscaling framework for ocean wave climate. *J. Geophys. Res. Oceans* 119, 7389–7405. doi: 10.1002/2014JC010141
- Casas-Prat, M., Wang, X. L., and Swart, N. (2018). CMIP5-based global wave climate projections including the entire Arctic Ocean. *Ocean Model.* 123, 66–85. doi: 10.1016/j.ocemod.2017.12.003
- Cavaleri, L., Fox-Kemper, B., and Hemer, M. (2012). Wind waves in the coupled climate system. *Bull. Am. Meteorol. Soc.* 93, 1651–1661. doi: 10.1175/BAMS-D-11-00170.1
- Collins, M., Knutti, R., Arblaster, J., Dufresne, J.-L., Fichet, T., Friedlingstein, P., et al. (2013). “Long-term climate change: projections, commitments and irreversibility,” in *Climate Change 2013: The Physical Science Basis. Contribution of Working Group I to the Fifth Assessment Report of the Intergovernmental Panel on Climate Change*. eds. T. F. Stocker, D. Qin, G.-K. Plattner, M. Tignor, S. K. Allen, J. Boschung et al. (Cambridge, United Kingdom and New York, NY, USA: Cambridge University Press).
- Cubasch, U., Wuebbles, D., Chen, D., Facchini, M. C., Frame, D., Mahowald, N., et al. (2013). “Introduction,” in *Climate Change 2013: The Physical Science Basis. Contribution of Working Group I to the Fifth Assessment Report of the Intergovernmental Panel on Climate Change*. eds. T. F. Stocker, D. Qin, G.-K. Plattner, M. Tignor, S. K. Allen, J. Boschung et al. (Cambridge, United Kingdom and New York, NY, USA: Cambridge University Press).
- Echevarria, E. R., Hemer, M. A., and Holbrook, N. J. (2019). Seasonal variability of the global spectral wind wave climate. *J. Geophys. Res. Oceans* 124, 2924–2939. doi: 10.1029/2018JC014620
- Echevarria, E. R., Hemer, M. A., Holbrook, N. J., and Marshall, A. G. (2020). Influence of the Pacific-South American modes on the global spectral wind-wave climate. *J. Geophys. Res. Oceans* 125, 1–16. doi: 10.1029/2020JC016354
- Espejo, A., Camus, P., Losada, I. J., and Méndez, F. J. (2014). Spectral Ocean wave climate variability based on atmospheric circulation patterns. *J. Phys. Oceanogr.* 44, 2139–2152. doi: 10.1175/JPO-D-13-0276.1
- Fan, Y., Held, I. M., Lin, S. J., and Wang, X. L. (2013). Ocean warming effect on surface gravity wave climate change for the end of the twenty-first century. *J. Clim.* 26, 6046–6066. doi: 10.1175/JCLI-D-12-00410.1
- Harley, M. D., Turner, I. L., Kinsela, M. A., Middleton, J. H., Mumford, P. J., Splinter, K. D., et al. (2017). Extreme coastal erosion enhanced by anomalous extratropical storm wave direction. *Sci. Rep.* 7:6033. doi: 10.1038/s41598-017-05792-1
- Hemer, M. A., Fan, Y., Mori, N., Semedo, A., and Wang, X. L. (2013). Projected changes in wave climate from a multi-model ensemble. *Nat. Clim. Chang.* 3, 471–476. doi: 10.1038/nclimate1791
- Hemer, M. A., McInnes, K. L., and Ranasinghe, R. (2012a). Climate and variability bias adjustment of climate model-derived winds for a southeast Australian dynamical wave model. *Ocean Dyn.* 62, 87–104. doi: 10.1007/s10236-011-0486-4
- Hemer, M. A., Wang, X. L., Weissse, R., and Swail, V. R. (2012b). Advancing wind-waves climate science: The COWCLIP project. *Bull. Am. Meteorol. Soc.* 93, 791–796. doi: 10.1175/BAMS-D-11-00184.1
- Holthuijsen, L. H. (2007). *Waves in Oceanic and Coastal Waters*. Cambridge: Cambridge University Press.
- Kirezci, E., Young, I. R., Ranasinghe, R., Muis, S., Nicholls, R. J., Lincke, D., et al. (2020). Projections of global-scale extreme sea levels and resulting episodic coastal flooding over the 21st century. *Sci. Rep.* 10:11629. doi: 10.1038/s41598-020-67736-6
- Lemos, G., Menendez, M., Semedo, A., Camus, P., Hemer, M., Dobrynin, M., et al. (2020a). On the need of bias correction methods for wave climate projections. *Glob. Planet. Chang.* 186:103109. doi: 10.1016/j.gloplacha.2019.103109
- Lemos, G., Semedo, A., Dobrynin, M., Behrens, A., Staneva, J., Bidlot, J. R., et al. (2019). Mid-twenty-first century global wave climate projections: results from a dynamic CMIP5 based ensemble. *Glob. Planet. Chang.* 172, 69–87. doi: 10.1016/j.gloplacha.2018.09.011
- Lemos, G., Semedo, A., Dobrynin, M., Menendez, M., and Miranda, P. M. A. (2020b). Bias-corrected cmip5-derived single-forcing future wind-wave climate projections toward the end of the twenty-first century. *J. Appl. Meteorol. Climatol.* 59, 1393–1414. doi: 10.1175/JAMC-D-19-0297.1
- Lobeto, H., Menendez, M., and Losada, I. J. (2021). Future behavior of wind wave extremes due to climate change. *Sci. Rep.* 11:7869. doi: 10.1038/s41598-021-86524-4
- Maraun, D., Shepherd, T. G., Widmann, M., Zappa, G., Walton, D., Gutiérrez, J. M., et al. (2017). Towards process-informed bias correction of climate change simulations. *Nat. Clim. Chang.* 7, 764–773. doi: 10.1038/nclimate3418
- Melet, A., Meyssignac, B., Almar, R., and Le Cozannet, G. (2018). Under-estimated wave contribution to coastal sea-level rise. *Nat. Clim. Chang.* 8, 234–239. doi: 10.1038/s41558-018-0088-y
- Mentaschi, L., Voudoukas, M. I., Voukouvalas, E., Dosio, A., and Feyen, L. (2017). Global changes of extreme coastal wave energy fluxes triggered by intensified teleconnection patterns. *Geophys. Res. Lett.* 44, 2416–2426. doi: 10.1002/2016GL072488
- Meucci, A., Young, I. R., Hemer, M., Kirezci, E., and Ranasinghe, R. (2020). Projected 21st century changes in extreme wind-wave events. *Sci. Adv.* 6, 7295–7305. doi: 10.1126/sciadv.aaz7295
- Mori, N., Shimura, T., Yasuda, T., and Mase, H. (2013). Multi-model climate projections of ocean surface variables under different climate scenarios-future change of waves, sea level and wind. *Ocean Eng.* 71, 122–129. doi: 10.1016/j.oceaneng.2013.02.016
- Morim, J., Hemer, M., Cartwright, N., Strauss, D., and Andutta, F. (2018). On the concordance of 21st century wind-wave climate projections. *Glob. Planet. Chang.* 167, 160–171. doi: 10.1016/j.gloplacha.2018.05.005
- Morim, J., Hemer, M., Wang, X. L., Cartwright, N., Trenham, C., Semedo, A., et al. (2019). Robustness and uncertainties in global multivariate wind-wave climate projections. *Nat. Clim. Chang.* 9, 711–718. doi: 10.1038/s41558-019-0542-5
- Oppenheimer, M., Glavovic, B., Hinkel, J., van de Wal, R., Magnan, A. K., Abd-Elgawad, A., et al. (2019). Sea level rise and implications for low lying islands, coasts and communities. In IPCC Special Report on the Ocean and Cryosphere in a Changing Climate.
- Pérez, J., Méndez, F. J., Menéndez, M., and Losada, I. J. (2014). ESTELA: a method for evaluating the source and travel time of the wave energy reaching a local area. *Ocean Dyn.* 64, 1181–1191. doi: 10.1007/s10236-014-0740-7
- Perez, J., Menendez, M., and Losada, I. J. (2017). GOW2: a global wave hindcast for coastal applications. *Coast. Eng.* 124, 1–11. doi: 10.1016/j.coastaleng.2017.03.005
- Portilla-Yandún, J. (2018). The global signature of ocean wave spectra. *Geophys. Res. Lett.* 45, 267–276. doi: 10.1002/2017GL076431
- Portilla-Yandún, J., Cavaleri, L., and Van Vledder, G. P. (2015). Wave spectra partitioning and long term statistical distribution. *Ocean Model.* 96, 148–160.
- Reguero, B. G., Losada, I. J., and Méndez, F. J. (2019). A recent increase in global wave power as a consequence of oceanic warming. *Nat. Commun.* 10:205. doi: 10.1038/s41467-018-08066-0
- Semedo, A., Sušelj, K., Rutgersson, A., and Sterl, A. (2011). A global view on the wind sea and swell climate and variability from ERA-40. *J. Clim.* 24, 1461–1479. doi: 10.1175/2010JCLI3718.1
- Shimura, T., and Mori, N. (2019). High-resolution wave climate hindcast around Japan and its spectral representation. *Coast. Eng.* 151, 1–9. doi: 10.1016/j.coastaleng.2019.04.013
- Swart, N. C., and Fyfe, J. C. (2012). Observed and simulated changes in the Southern Hemisphere surface westerly wind-stress. *Geophys. Res. Lett.* 39, 6–11. doi: 10.1029/2012GL052810
- Tibaldi, C., Arblaster, J. M., and Knutti, R. (2011). Mapping model agreement on future climate projections. *Geophys. Res. Lett.* 38, 1–5. doi: 10.1029/2011GL049863
- Thomson, J., and Rogers, W. E. (2014). Swell and sea in the emerging Arctic Ocean. *Geophys. Res. Lett.* 41, 3136–3140. doi: 10.1002/2014GL059983
- Timmermann, A., McGregor, S., and Jin, F. F. (2010). Wind effects on past and future regional sea level trends in the southern Indo-Pacific. *J. Clim.* 23, 4429–4437. doi: 10.1175/2010JCLI3519.1
- Toimil, A., Camus, P., Losada, I. J., Le Cozannet, G., Nicholls, R. J., Idier, D., et al. (2020). Climate change-driven coastal erosion modelling in temperate sandy beaches: methods and uncertainty treatment. *Earth Sci. Rev.* 202:103110. doi: 10.1016/j.earscirev.2020.103110
- Tolman, H. L. (2014). Development Group User Manual and System Documentation of WAVEWATCH III<sup>®</sup> version 4.18. Technical Note 316, NOAA/NWS/NCEP/MMAB, 282.

- van Gent, M. R. A., van Thiel de Vries, J. S. M., Coeveld, E. M., de Vroeg, J. H., and van de Graaff, J. (2008). Large-scale dune erosion tests to study the influence of wave periods. *Coast. Eng.* 55, 1041–1051. doi: 10.1016/j.coastaleng.2008.04.003
- Wang, X. L., Feng, Y., and Swail, V. R. (2014). Changes in global ocean wave heights as projected using multimodel CMIP5 simulations. *Geophys. Res. Lett.* 41, 1026–1034. doi: 10.1002/2013GL058650
- Young, I. R. (1999). Seasonal variability of the global ocean wind and wave climate. *Int. J. Climatol.* 19, 931–950. doi: 10.1002/(SICI)1097-0088(199907)19:9<931::AID-JOC412>3.0.CO;2-O

**Conflict of Interest:** The authors declare that the research was conducted in the absence of any commercial or financial relationships that could be construed as a potential conflict of interest.

Copyright © 2021 Lobeto, Menendez and Losada. This is an open-access article distributed under the terms of the Creative Commons Attribution License (CC BY). The use, distribution or reproduction in other forums is permitted, provided the original author(s) and the copyright owner(s) are credited and that the original publication in this journal is cited, in accordance with accepted academic practice. No use, distribution or reproduction is permitted which does not comply with these terms.





# Characterizing the Non-linear Interactions Between Tide, Storm Surge, and River Flow in the Delaware Bay Estuary, United States

Ziyu Xiao<sup>1</sup>, Zhaoqing Yang<sup>1,2\*</sup>, Taiping Wang<sup>1</sup>, Ning Sun<sup>3</sup>, Mark Wigmosta<sup>2,3</sup> and David Judi<sup>3</sup>

<sup>1</sup> Pacific Northwest National Laboratory, Coastal Sciences Division, Seattle, WA, United States, <sup>2</sup> Department of Civil and Environmental Engineering, University of Washington, Seattle, WA, United States, <sup>3</sup> Pacific Northwest National Laboratory, Earth Sciences Division, Richland, WA, United States

## OPEN ACCESS

### Edited by:

Bahareh Kamranzad,  
Kyoto University, Japan

### Reviewed by:

Pascal Matte,  
Environment and Climate Change,  
Canada  
Chen Wei-Bo,  
National Science and Technology  
Center for Disaster Reduction  
(NCDR), Taiwan

### \*Correspondence:

Zhaoqing Yang  
zhaoqing.yang@pnnl.gov

### Specialty section:

This article was submitted to  
Coastal Ocean Processes,  
a section of the journal  
Frontiers in Marine Science

**Received:** 27 May 2021

**Accepted:** 30 June 2021

**Published:** 30 July 2021

### Citation:

Xiao Z, Yang Z, Wang T, Sun N,  
Wigmosta M and Judi D (2021)  
Characterizing the Non-linear  
Interactions Between Tide, Storm  
Surge, and River Flow in the Delaware  
Bay Estuary, United States.  
*Front. Mar. Sci.* 8:715557.  
doi: 10.3389/fmars.2021.715557

Low-lying coastal areas in the mid-Atlantic region are prone to compound flooding resulting from the co-occurrence of river floods and coastal storm surges. To better understand the contribution of non-linear tide-surge-river interactions to compound flooding, the unstructured-grid Finite Volume Community Ocean Model was applied to simulate coastal storm surge and flooding in the Delaware Bay Estuary in the United States. The model was validated with tide gauge data in the estuary for selected hurricane events. Non-linear interactions between tide-surge-river were investigated using a non-stationary tidal analysis method, which decomposes the interactions' components at the frequency domain. Model results indicated that tide-river interactions damped semidiurnal tides, while the tide-surge interactions mainly influenced diurnal tides. Tide-river interactions suppressed the water level upstream while tide-surge interaction increased the water level downstream, which resulted in a transition zone of damping and enhancing effects where the tide-surge-river interaction was prominent. Evident compound flooding was observed as a result of non-linear tide-surge-river interactions. Furthermore, sensitivity analysis was carried out to evaluate the effect of river flooding on the non-linear interactions. The transition zone of damping and enhancing effects shifted downstream as the river flow rate increased.

**Keywords:** storm surge, non-linear interactions, river flood, compound flooding, numerical modeling, Delaware Bay, tropical cyclones, FVCOM

## INTRODUCTION

Coastal flooding hazards caused by tropical cyclones present a severe risk to nearly 40% of the U.S. population living in low-lying coastal areas. The co-occurrence of storm surge and river flooding may cause compound flooding (Bevacqua et al., 2019), which results in extreme water levels caused by non-linear interactions of storm surges, river flood, and astronomical tides (Doodson, 1956; Proudman, 1957; Rossiter, 1961; Johns et al., 1985; Arns et al., 2020). Coastal flood risks associated with compound flooding cannot be simply estimated by superposition of astronomical tides and river-induced and storm-surge-induced water levels. Non-linear interactions are known to exist

between tides, storm surge, and river flow, but understanding of how non-linear interactions exacerbate the compounding effect is limited. The total water levels could be increased or decreased by the non-linear interactions between storm surges, river flow, and tides. Furthermore, such non-linear interaction is sensitive to sea level rise, storm intensity, and river flow as a result of climate change (Yang et al., 2014; Li et al., 2020), which makes the flood hazard risk even more complex and unpredictable.

The characteristics and mechanisms of tide-surge interactions (TSIs) have been widely studied during recent decades (Proudman, 1955; Prandle and Wolf, 1978; Wolf, 1978; Idier et al., 2012; Zhang et al., 2020). In an early study conducted in the North Sea and River Thames, United Kingdom, observed TSI was found to amplify surge height significantly on rising tides, independent of initial surge height or the relative phase difference between tides and surges (Proudman, 1955). Horsburgh and Wilson (2007) gave a first-order explanation of the surge cluster that occurs with rising tide based on the phase shift of the tidal signal (the effect of surge on tides) combined with the modulation of surge production due to the change in water depth (the effect of tides on surge). Olbert et al. (2013) applied a statistical method to the hindcast over 1959–2005 in the Irish Sea and found that surges tend to peak at a particular phase of tide irrespective of the timing of the storm landfall but with site specificity. The degree of total water level modulation due to TSI is also site-specific and varies with surge height and tidal ranges (Keers, 1968; Prandle and Wolf, 1978). Prandle and Wolf (1978) used a one-dimensional model to show that TSI is mainly produced by the quadratic friction effect followed by the shallow water and advective effects, and that the shallow water and advective effects can be dominant on rising tides, while quadratic friction can be prominent on high tides.

Tides that propagate into the upper estuaries are subject to tide-river interactions (TRIs), resulting in the modulation of tidal amplitudes at specific tidal frequencies by bottom friction and river flow (Godin, 1999; Horrevoets et al., 2004). Based on the shallow water equation, TRI can be caused by three non-linear terms: spatial acceleration, friction, and a gradient of river flow (Dronkers, 1964). The TRI between river flow and tides has been demonstrated to attenuate tidal energy in the upstream of an estuary, while it stimulates energy transfer from the principal tides to overtides in the downstream (Guo et al., 2015). However, the variation in TRI corresponding to varying river flow and its damping effect on total water level have not been described in detail.

Tide-surge-river interactions (TSRIs) are the non-linear interactions among tides, storm surge and river flow, which add additional complexity to TSIs due to the presence of storm surge and river flooding. Although TSRIs are rarely studied, they are an important component of storm surges. For example, Dinapoli et al. (2021) found that the current due to river flow (CDR) non-linearly interacts with both the tides and storm surges in the Río de la Plata estuary. Their work further suggests the tide-CDR and surge-CDR interactions both induce asymmetries in the water level and the interactions are mainly caused by the quadratic bottom friction. Spicer et al. (2019) and Spicer et al. (2021) collected observations in Maine estuaries during

“windstorms” and pointed out the TSRI to be the dominant mechanism contributing to upstream surge amplification (which is estimated to be exceeding 1m and more than double than non-tidal forcing induced surges). By testing different combinations of the atmospheric forcing effect on generating the extreme water levels via non-stationary tidal harmonic analysis (Matte et al., 2013), the mechanism to generate TSRI is found to be related to the increased mean flow and frictional energy from wind forcing (Spicer et al., 2021). A comprehensive review on different interaction mechanisms between SLR-tide-surge, tide-surge, tide-river, wave-surge, tide-wave, and SLR-wave was conducted along the coasts and estuaries worldwide (Idier et al., 2019), the values of the interactions vary from a few tens of centimeters to over 1 m.

Many previous studies focused on TSI or TRI independently. However, during compound flooding events when extreme surge levels co-occur with extreme river flooding, both TSI and TRI modulate the total water levels (TWLs) as part of TSRI. To the authors' knowledge, the relative importance of TSI and TRI to the overall TSRI during compound flooding events has not been well documented. Spicer et al. (2019) raised attention to the importance of distinguishing how non-linear TRI varies from TSI by using a non-stationary tidal analysis method to account for non-linear interactions. The methods to analyze tidal constituents of a tidal record have been well summarized by Hoitink and Jay (2016), based on assumptions of either stationary or non-stationary environments. The traditional stationary methods, such as harmonic analysis (Pawlowicz et al., 2002), assume that tidal constituents are fixed and independent from oceanic and atmospheric forcings, thus appropriate for tides in the deep ocean (Dean, 1966; Godin, 1972; Flinchem and Jay, 2000). For tides affected by rivers and coastal processes, the non-stationary method can resolve the time-changing tidal amplitude and phase due to strong non-linear interactions between atmospheric forcing, river flow, and tides (Jay and Flinchem, 1997; Matte et al., 2013, 2014; Sassi and Hoitink, 2013; Guo et al., 2015). Jalón-Rojas et al. (2018) compared the advantages and disadvantages of stationary and non-stationary methods used in tidal analysis and concluded that the stationary method does not reproduce the time-varying properties of the tidal signal and therefore cannot be used to predict the non-linear interactions between tidal constituents and non-tidal forcing variations; however, the non-stationary method can be used to distinguish non-linear components. Lastly, although the effects of wind waves and wave-current interaction could have additional impact on storm surge, we decided not to explicitly include wind waves in this study due to two main reasons. First, in a recent study by Ye et al. (2020) using a comprehensive hydrodynamic model framework that includes wind waves, the authors found that the effect of wave-current interaction on storm surge is very small (i.e., a few centimeters) inside Delaware Bay during Hurricane Irene. Second, we feel it is important to first elucidate the effects of TSRIs on storm surge before further expand the scope to include more processes, which include wind waves and baroclinic processes. On the other hand, studies by Sheng et al. (2010) and Hsiao et al. (2019) also suggested that wave-induced setup could contribute significantly to the storm surge elevation, depending on specific study sites and hurricane/typhoon events. Thus, to

explicitly include wind waves should be considered in the next phase of modeling work.

Numerical model simulations offer good insights to help isolate each interaction process and estimate the uncertainty of flooding risk caused by the complexity of non-linear interactions. This paper presents the results of a modeling study conducted to investigate the variations between TRL, TSI, and TSRI and evaluate their interactions and their contributions to the TWL during compound flooding events in the Delaware Bay Estuary (DBE). By comparing non-linear terms produced during selected historical hurricane events, this study characterized the damping and amplification effects of different non-linear interaction processes on TWL and analyzed the underlying mechanisms. The non-stationary tidal analysis method was applied to quantify the relative contribution by diurnal, semidiurnal, and quarter-diurnal tidal bands to the non-linear interactions. In addition, the sensitivity of non-linear interaction to different return period river flows was explored.

## METHODOLOGY

### Study Site

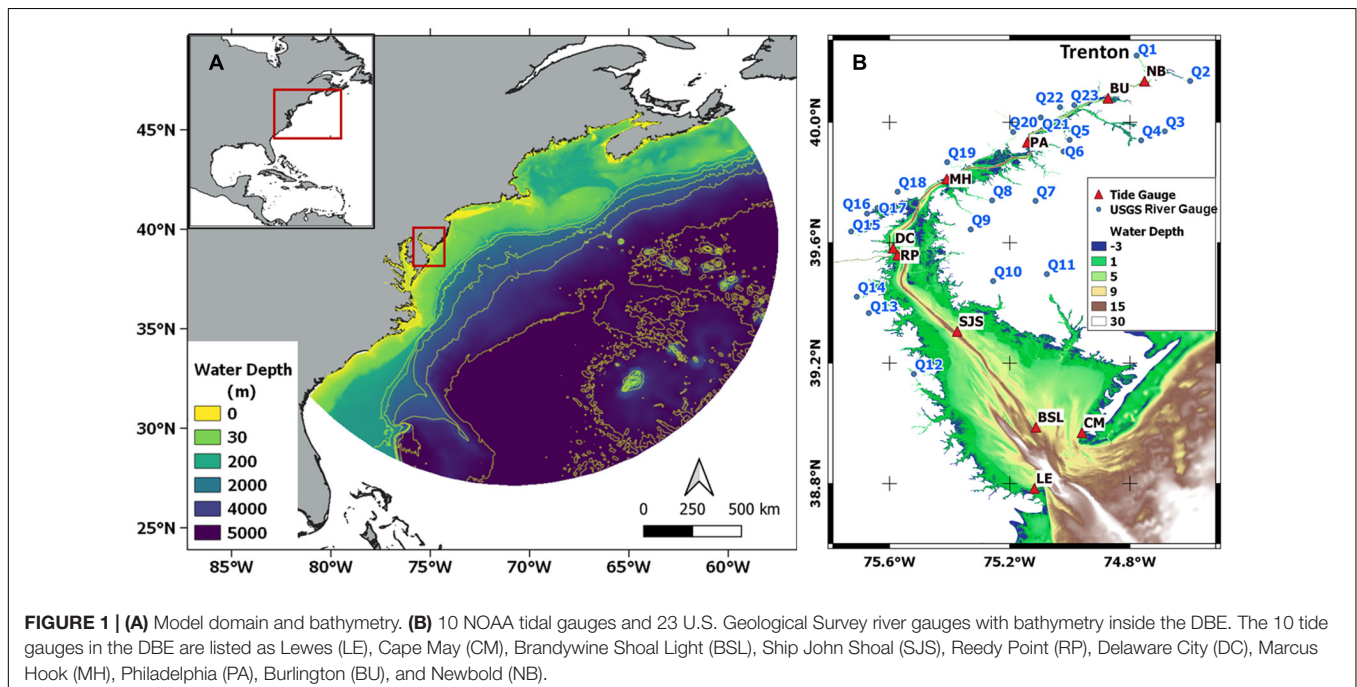
The funnel-shaped DBE is located on the mid-Atlantic coast of the United States (**Figure 1A**). The estuary mouth is about 18 km wide and the bay has a maximum width of 45 km in the lower bay and converges to a width of 0.3 km at Trenton (**Figure 1B**), stretching about 210 km toward the head of a tidal freshwater river (Sharp, 1984). Mean estuary depth is 7 m, the deepest waters exceed 30 m, and a shipping channel has been progressively deepened since the late 1800s by increasing the thalweg of the estuary from roughly 8 to 15 m (Pareja Roman, 2019). The DBE is dominated by semidiurnal tides where M2 and

S2 tides account for up to 96% of the tidal variability (Aristizabal and Chant, 2013), which is strongly convergent and moderately dissipative in terms of tidal energy (Lanzoni and Seminara, 1998). The tidal range is approximately 1.5 m at the estuary mouth and is amplified upstream; the maximum tidal current is approximately 1 m/s (Wong and Sommerfield, 2009). The Delaware River provides more than half of the freshwater discharge to the estuary (Whitney and Garvine, 2006). A hydraulic jump is observed ~2.7 km downstream of the Trenton tidal gauge (**Figure 1B**) due to the abrupt transition in bathymetry and roughly represents the upstream limit of tidal intrusion (Zhang et al., 2020).

Delaware Bay Estuary is undammed along its main stem and has networks of tidal flats that store vegetation, sediment, and nutrients in the lower bay. DBE provides a natural testbed for examining the mechanisms and characteristics of non-linear interactions among different physical processes under extreme storm conditions.

### Numerical Model

The numerical model used in this study is the unstructured-grid, Finite-Volume Community Ocean Model (FVCOM) (Chen et al., 2003). FVCOM has been used extensively for modeling storm surge in many coastal regions worldwide (Song et al., 2013; Chen et al., 2014, 2016; Wang and Yang, 2019; Yang et al., 2021). The unstructured-grid framework allows the flexibility to robustly simulate fine-scale dynamic processes in any complex estuarine and coastal bay system. In this study, an unstructured-grid for the DBE was developed to cover a model domain that extends ~1500 km offshore from the coast and ~240 km upstream from the DBE mouth (**Figure 2**). The model grid consisted of 822,684 triangle elements and 429,847 nodes. The unstructured-grid resolution varies from 40 km at the open



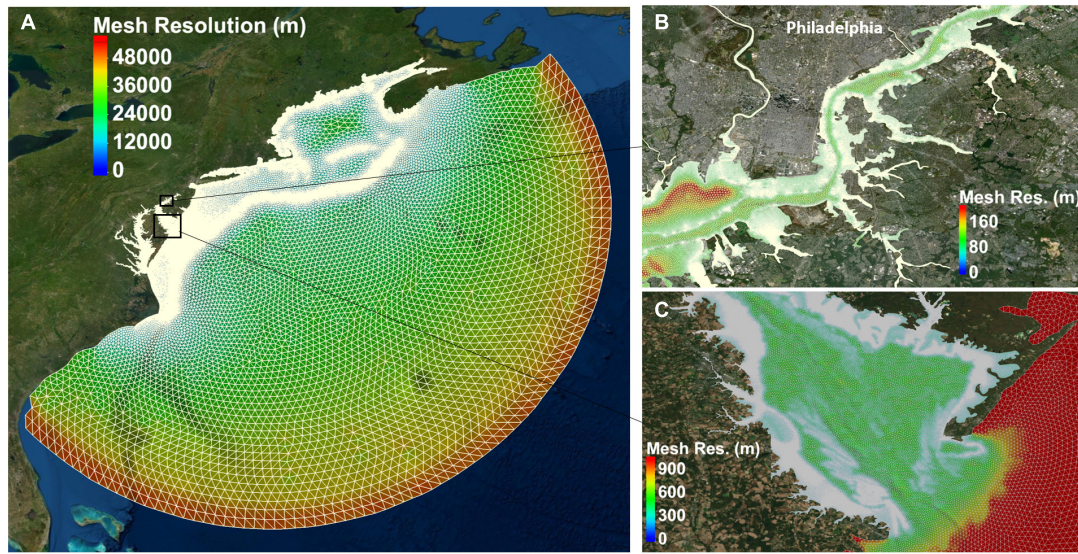


**FIGURE 2 |** FVCOM model grid (white line) with color contours showing the mesh resolution **(A)** the whole model domain **(B)** zoom-in of the upper channel near Philadelphia **(C)** lower bay near estuary mouth.

boundary to approximately 100 m in the estuary, and the highest resolution of 20 m is for tributaries. The average grid resolution for the floodplain is approximately 100 m. The land boundary of floodplain is cut off at 3 m above the mean sea level to allow for simulation of inland inundation. A sigma-stretched vertical coordinate of five layers was used for all the model runs. The wetting and drying algorithm, which incorporates a bottom viscous layer of specified thickness ( $D_{min} = 5$  cm in the present study), was applied to simulate the inundation process in the intertidal zone and floodplain.

Model open-boundary conditions were specified by tidal elevations obtained from the TPXO8.0 global ocean tide model<sup>1</sup>. Sea surface wind field was obtained from the global atmospheric reanalysis model European Centre for Medium-Range Weather Forecasts (ECMWF) Reanalysis v5 (ERA5), which has a spatial resolution of 30 km and temporal resolution of 1 hr. River flows collected at 23 U.S. Geological Survey (USGS) river gauges in the DBE were specified as the river boundary condition (Figure 1). The main rivers discharged into DBE are the Delaware River (Q1) and Schuylkill River (Q2), which, respectively, contribute about 58% and 14% of the total freshwater inflow (Sharp, 1984). Sensitivity tests of bottom roughness conducted by Ye et al. (2020) suggested that a spatially varying bottom roughness is necessary to represent the different bottom characteristics in the lower and upper bay. In this study, bottom roughness was calibrated based on observed M2 amplitude at ten tidal gauges. Initial bottom roughness values of 0.0001 and 0.0025 m were tested for the entire domain. Final bottom roughness values of 0.0005 m for the coastal ocean to lower bay and 0.0001 m for the middle and upper bay were specified, which gave good calibration results (Figure 3).

<sup>1</sup><https://tpxows.azurewebsites.net/>

The model bathymetry was interpolated based on four different bathymetry data sets from the National Oceanic and Atmospheric Administration (NOAA): (a) 1/9 arc-second resolution (~3.5 m) Continuously Updated Digital Elevation Model (CUDEM, doi: 10.25921/ds9v-ky35), which covers the DBE; (b) the 1/3 arc-second (~10 m) and 1 arc-sec (~30 m) data from the National Centers for Environmental Information (NCEI), which covers the nearshore coastal areas; (c) 3 arc-sec (~90 m) Coastal Relief Model<sup>2</sup> for the less than 300 m deep coastal waters and floodplain; and (d) the 1 arc-min ETOPO1 Global Relief Model (Amante and Eakins, 2009) for the deep ocean. The model vertical datum was referenced to the North American Vertical Datum of 1988 (NAVD88) and any data set that had a different vertical datum was converted to NAVD88 using V-Datum program (Parker et al., 2003; Yang et al., 2008).

<sup>2</sup><https://www.ngdc.noaa.gov/mgg/coastal/crm.html>

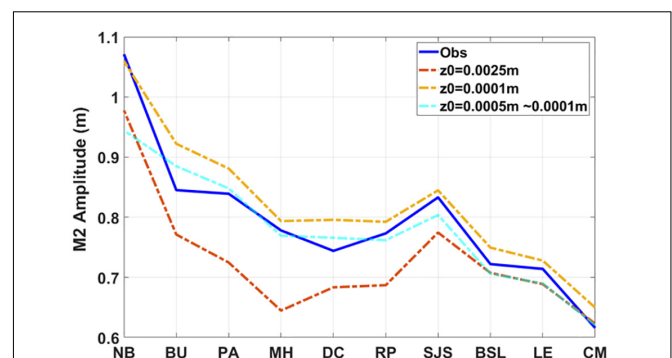


**FIGURE 3 |** Model calibration of bottom roughness based on M2 tidal amplitude.

## TWL and Non-linear Interaction Decomposition

To characterize the non-linear interaction, time series of TWLs were decomposed into astronomical tides, low-frequency surge (LFSs), and non-linear interactions, following the method of Spicer et al. (2019), Spicer et al. (2021). Astronomical tides were obtained from the Tide Only (TO) model run (Table 1). LFS represents the water level setup induced by non-tidal forcing, such as river flow, surface wind, and atmospheric pressure. The total surge level (TSL), which consists of LFS and non-linear interaction, was obtained by subtracting astronomical tides from TWL. LFS was extracted from TSL using a low-pass filter with a cut-off frequency of 35 hr to remove tidal signals (Walters and Heston, 1982). The non-linear interaction was calculated by subtracting LFS from TSL. Figure 4 details the flowchart to decompose the time series of TWL and obtain the non-linear interaction term. The method was first applied at the 10 tidal gauges (Figure 1B) for model calibration and then applied to the whole model domain.

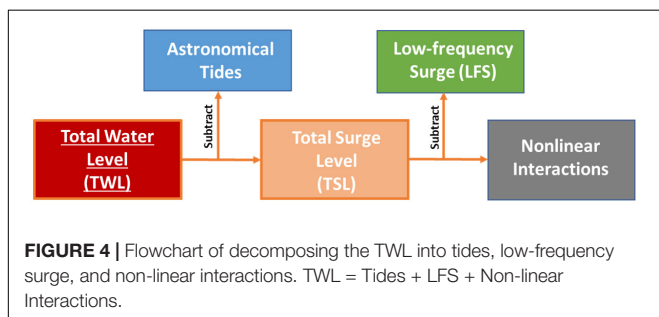
To understand the process of non-linear interaction with tides, the non-linear interaction term is further decomposed based on its specific tidal frequency. A non-stationary tidal analysis method—Complex Demodulation (Gasquet and Wootton, 1997; Jalón-Rojas et al., 2018)—was applied to a non-linear interaction term to estimate the time-dependent amplitude and phase of diurnal (D1), semidiurnal (D2), and high-frequency (D4, D6, and D8) tidal bands. Complex demodulation is based on a wavelet approach and assumes that the time series  $X(t)$  is composed of an oscillating signal with frequency  $\sigma$  and a non-periodic signal  $Z(t)$ :

$$X(t) = A(t) \cos(\sigma t + \vartheta(t)) + Z(t) \quad (1)$$

where, tidal frequency  $\sigma$  is calculated as  $2\pi/24 \text{ rad h}^{-1}$  for D1,  $2\pi/12.4206 \text{ rad h}^{-1}$  for D2,  $2\pi/6.21 \text{ rad h}^{-1}$  for D4,  $2\pi/4.14 \text{ rad h}^{-1}$  for D6, and  $2\pi/3.10 \text{ rad h}^{-1}$  for D8;

TABLE 1 | Design of numerical experiments for non-linear interactions analysis.

Scenario	Forcing	Extreme Events
TO	Tide	N/A
TSR	Tide, Wind, River	Irene, Lee, Sandy, and Isabel
TS	Tide, Wind	Irene
TR	Tide, River	Irene
TSR SensQ	Tide, Wind, 2–500 years ARI River	Irene



time-dependent amplitude  $A$  and phase  $\vartheta$  can be calculated by integrating the frequency  $\sigma$  with respect to time following the steps below (Jalón-Rojas et al., 2018):

a) The time series  $X(t)$  is multiplied by a complex modulation of frequency  $e^{-i\sigma t}$  to get an unfiltered modulated signal in order to shift the frequency of interest to zero:

$$Y(t) = X(t) e^{-i\sigma t} = \frac{A(t)}{2} e^{-i\vartheta(t)} + \frac{A(t)}{2} e^{-i(2\sigma t + \vartheta(t))} + Z(t) e^{-i\sigma t} \quad (2)$$

b)  $Y(t)$  is low-pass filtered to remove frequencies at or above  $\sigma$ , whereas the terms  $\frac{A(t)}{2} e^{-i(2\sigma t + \vartheta(t))} + Z(t) e^{-i\sigma t}$  are removed, thus the oscillation in the original signal  $X(t)$  is effectively removed to get:

$$Y'(t) = \frac{A'(t)}{2} e^{-i\vartheta'(t)} \quad (3)$$

c) The time-varying amplitude  $A'(t)$  and phase  $\vartheta'(t)$  are calculated from the Inverse Fourier Transform (Bloomfield, 2004) of the filtered spectrum  $Y'(t)$  by taking twice the magnitude of  $Y'(t)$  and the arc tangent of the ratio of the imaginary to real parts of  $Y'(t)$ , respectively.

In addition to the wavelet transform method, a spectral technique—the so called singular spectral analysis (SSA) method—is also presented in this study. This method has been demonstrated to be especially efficient for extracting information from short and noisy time series without previous knowledge of the non-linear dynamics affecting the time series (Schoellhamer, 2001, 2002). The SSA method is widely used to quantify the relative contributions made by different processes to the total variance of the time series (Jalón-Rojas et al., 2016, 2017; Xiao et al., 2020). The SSA method decomposes a time series into so-called reconstructed components by sliding a window of width  $M$  down the time series and obtaining an autocorrelation matrix (Vautard et al., 1992). The eigenvalues of the autocorrelation matrix give the contribution of each period to the total variance of the analyzed time-series data set. For further information about the SSA method, the reader is referred to Vautard et al. (1992). Jalón-Rojas et al. (2016) state that a combined approach of wavelet transform method and SSA for short-term analysis complement each other. SSA complements the wavelet transform method in terms of quantification, and the wavelet transform method complements SSA by reconstructing and visualizing the time series of interested periods.

## MODEL VALIDATION AND SIMULATIONS

### Extreme Events and Numerical Experiments Design

The major historical hurricanes since 2000 that have affected the DBE include Isabel (2003), Hurricane Irene (2011), and Hurricane Sandy (2012). Tropical Storms Lee (2011), which followed Hurricane Irene, also brought heavy rainfall to the Delaware River Basin. These extreme events were selected to validate the storm surge model of the DBE Figure 5

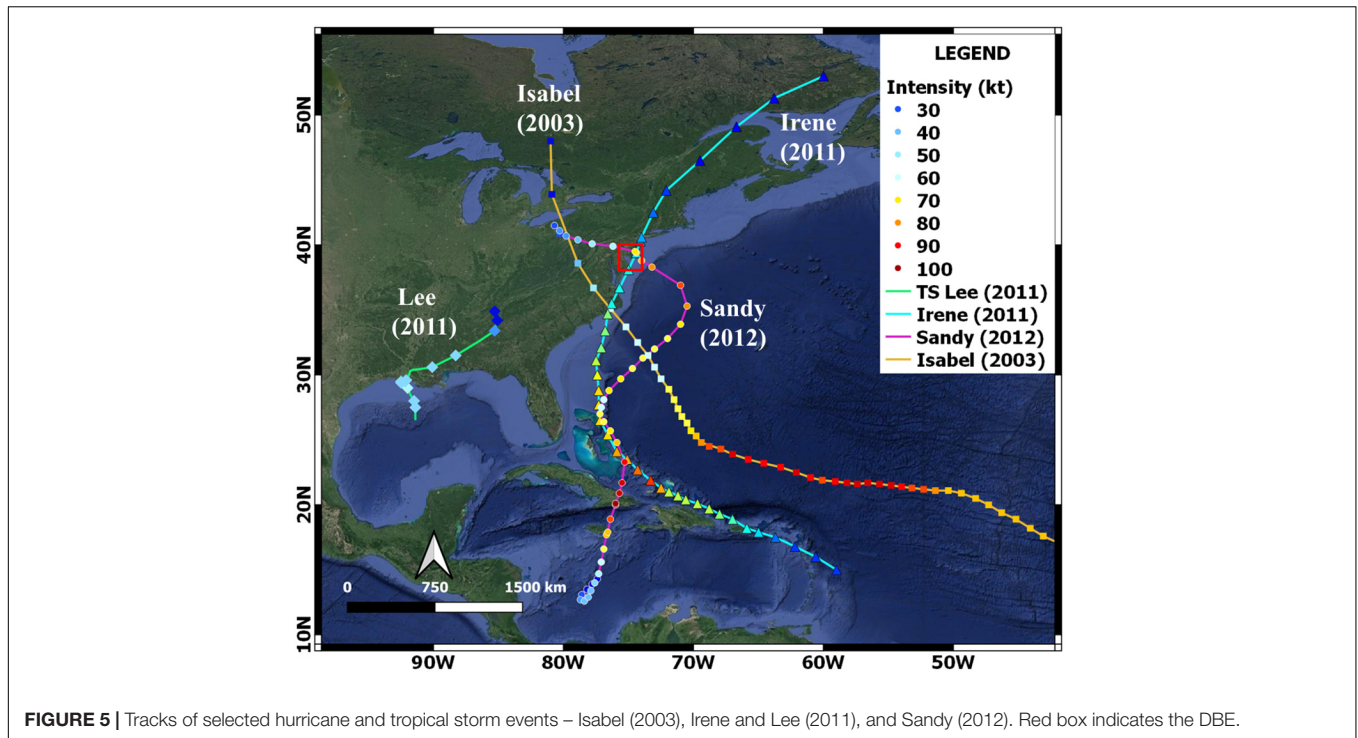


**FIGURE 5** | Tracks of selected hurricane and tropical storm events – Isabel (2003), Irene and Lee (2011), and Sandy (2012). Red box indicates the DBE.

shows the tracks of these hurricanes obtained from the hurricane database (HURDAT) at National Hurricane Center (Landsea and Franklin, 2013).

Hurricane Isabel was formed on September 1, 2003 and intensified to a category 5 hurricane on September 11, 2003, with a maximum sustained wind speed of 145 kts. It made landfall near the banks of North Carolina at 17:00 UTC September 18, 2003, as a slow-moving system, and proceeded on a northwesterly track (**Figure 5**). Isabel produced storm surges of 1.8 m to 2.4 m above normal tides near the point of landfall along the Atlantic coast of North Carolina, with reduced storm surge levels ranging from 0.6 m to 1.2 m along Delaware shorelines.

Hurricane Sandy, one of the largest Atlantic hurricanes on record, made landfall as an extratropical cyclone near New Jersey at 23:30 UTC October 29, 2012, and proceeded on a northeasterly track (**Figure 5**). The maximum sustained wind speed was estimated to be 100 kts and the storm surge peak was 0.9 m to 1.5 m along Delaware shorelines.

Hurricane Irene, one of the costliest hurricanes on record in the U.S., made primary landfall along the US East Coast on the North Carolina shoreline as a category 1 hurricane at 12:00 UTC on August 27, 2011, and another landfall at 09:35 UTC on August 28, 2011, near New Jersey, and continued along the Atlantic coastline (**Figure 5**). The maximum sustained wind speed was about 105 kts and peak storm surges were between 1.2 and 1.8 m along the coast of New Jersey. Hurricane Irene is an example of a compound flooding event during which the combination of storm surge and rainfall-induced freshwater river flooding amplifies the hazardous impacts of individual events (Ye et al., 2020).

Tropical Storm Lee formed over the Gulf of Mexico (**Figure 5**) and made landfall along the coast of southern Louisiana at 10:30 UTC on September 3, 2011. The strongest wind (60 kts) associated with the low pressure occurred primarily over the northern Gulf of Mexico. Lee brought heavy rainfall to the Mid-Atlantic region, which caused some of the most severe flooding in the region's history.

Two large precipitation events associated with Hurricane Irene and Tropical Storm Lee resulted in two peak flows from Delaware River up to 4000 m<sup>3</sup>/s and 5500 m<sup>3</sup>/s on August 28, 2011 and September 9, 2011 at Trenton (USGS, 1463500, **Figure 6A**). The peak flows during Hurricanes Isabel and Sandy were less significant than those during Hurricane Irene and Tropical Storm Lee, which measured up to 1500 m<sup>3</sup>/s (**Figure 6B**) and 800 m<sup>3</sup>/s at Trenton (**Figure 6C**), respectively.

To compare the non-linear terms produced by different forcings during Irene (a compound flooding event), numerical experiments were conducted and are summarized in **Table 1**. Results from two model runs, TO run (driven by tides only) and TSR run (driven by tides, surface winds, and river flow), were processed to extract TSRI following the method described in section "TWL and Non-linear Interaction Decomposition." To distinguish TSI and TRI from TSRI during Hurricane Irene, the TS run (driven by tides and surface winds) and the TR run (driven by tides and river flow) were designed to mimic the Irene event but the individual river flows and surface winds were removed; thus the non-linear interaction induced by TSI only and TRI only during Irene, as well as their effect on TSRI, could be estimated.

Furthermore, a series of sensitivity model runs were conducted to investigate the response of TSRI during Irene with river flows (TSR SensQ) corresponding to different recurrence

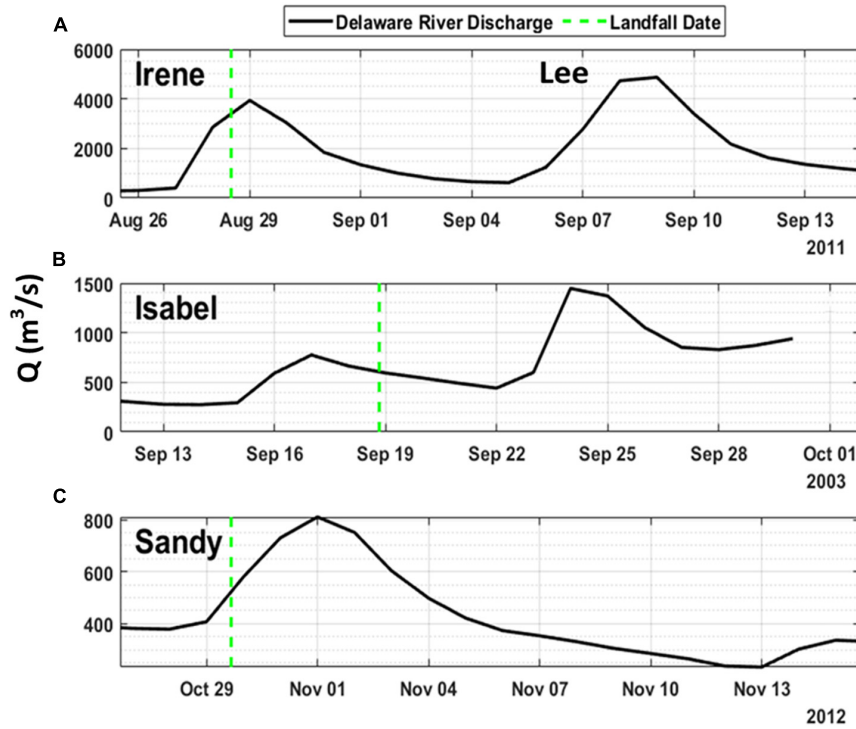


**FIGURE 6 |** Delaware River discharge at Trenton (USGS 1463500, Q1 in **Figure 1B**) during historical extreme events: **(A)** Irene and Lee; **(B)** Isabel; and **(C)** Sandy.

intervals (ARIs), commonly known as return periods, and the impact of TSRI on TWLs. The surface wind field and open boundary of water levels were kept the same as those during Hurricane Irene in the TSR run.

### Model Validation With Water Levels

To validate the storm surge model of DBE, model performance in simulating the TWL during extreme events was evaluated by comparing modeled water levels in the TSR run to observed data at the NOAA 10 tide gauges for three one-month-long periods that corresponded to four extreme events—Hurricane Irene and Tropical Storm Lee (August 20, 2011 to September 20, 2011), Hurricane Sandy (October 20, 2012 to November 20, 2012), and Hurricane Isabel (September 01, 2003 to September 30, 2003).

Model parameters, such as the bottom roughness and open-boundary sponge layer (radius and friction coefficient), were first calibrated based on Hurricane Irene and Tropical Storm Lee and then validated for Hurricanes Sandy and Isabel. **Figure 7** shows the scatter-plot comparisons for simulated and observed water levels at the 10 tide gauges in the DBE for the three simulation periods. Overall, the model-predicted water levels match the observed data variation trend well and the model reproduces the tidal amplification toward upstream inside the DBE. However, the model tends to underpredict the TWL at some locations, such as at the PA station during Sandy and Isabel, and the SJS and CM stations, respectively, during the Irene and Lee events.

To quantify the model’s skill in simulating water level in the DBE, a set of model performance metrics were

calculated. Specifically, the following four error statistical parameters were used.

The root-mean-square-error (*RMSE*) is defined as:

$$RMSE = \sqrt{\frac{\sum_{i=1}^N (P_i - M_i)^2}{N}} \tag{4}$$

where,  $N$  is the number of observations,  $M_i$  is the measured value, and  $P_i$  is the model-predicted value.

The scatter index (*SI*) is the normalized *RMSE* with the average magnitude of measurements:

$$SI = \frac{RMSE}{|M|} \tag{5}$$

The bias (*Bias*) is defined as the mean difference between model predictions and the measurements:

$$Bias = \frac{\sum_{i=1}^N (P_i - M_i)}{N} \tag{6}$$

The linear correlation coefficient (*R*) is a measure of the linear relationship between model predictions and the measurements:

$$R = \frac{\sum_{i=1}^N (P_i - \bar{P})(M_i - \bar{M})}{\sqrt{(\sum_{i=1}^N (M_i - \bar{M})^2)(\sum_{i=1}^N (P_i - \bar{P})^2)}} \tag{7}$$

The error statistics for the simulated water levels at all tide gauges are provided in **Table 2**. The *RMSE* varies within a range between

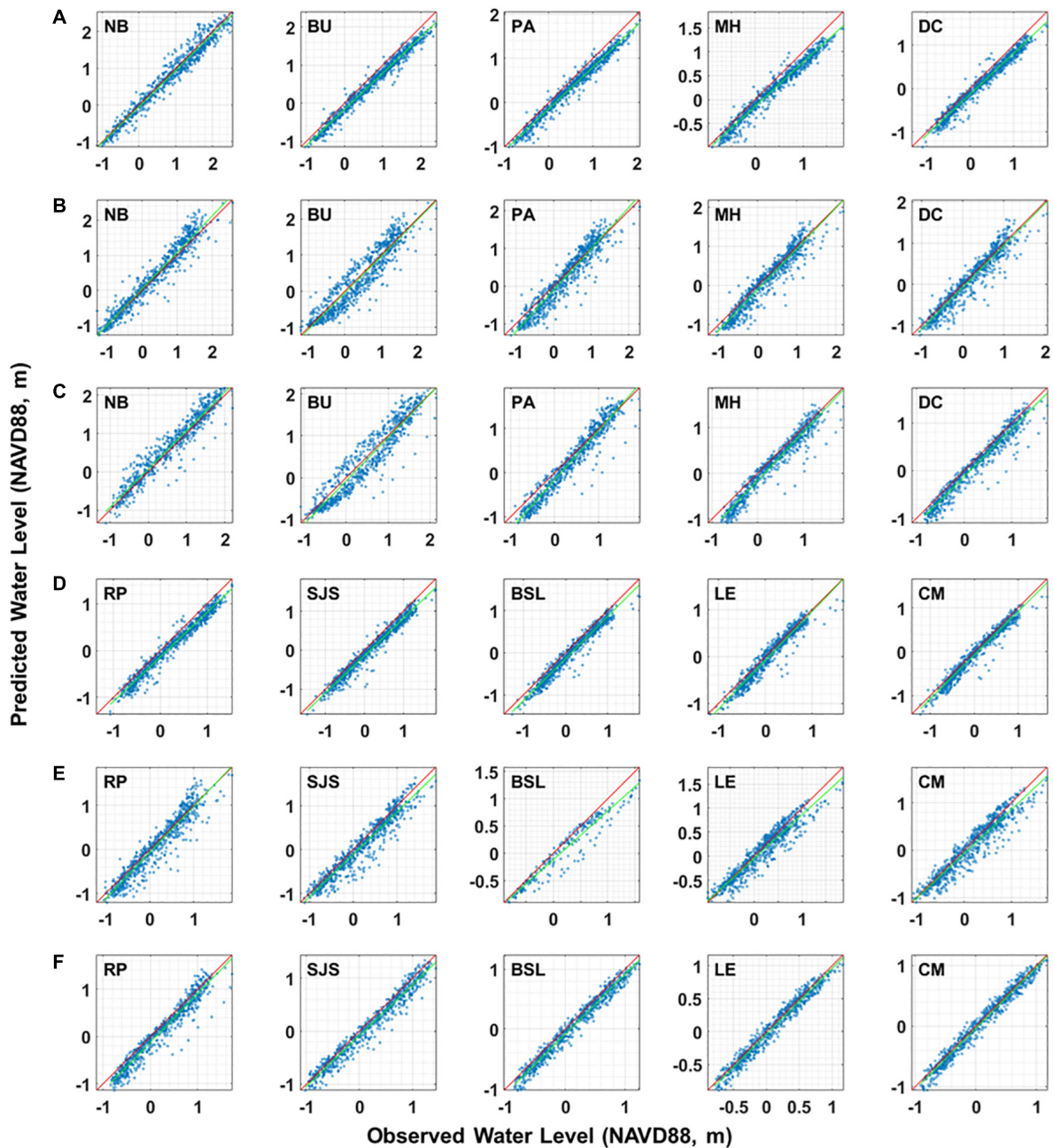


**FIGURE 7 |** Scatter comparisons of simulated and observed water levels at 10 tidal stations during three simulation periods in the DBE; **(A,D)** Irene and Lee: August 20 to September 20, 2011; **(B,E)** Sandy: October 20 to November 20, 2012; **(C,F)** Isabel: September 01 to 30, 2003. The red line represents the 1-to-1 fit and the green line represents the linear correlation between model and data.

0.15 and 0.26 m with an increasing trend in the upstream, likely due to the effects of the complicated geometry of narrow and meandering channels. The *SI* values, which measure the normalized *RMSE*, vary from 0.22 in the estuarine mouth to 0.38 in the river mouth. The *Bias* values at all stations are within a range of  $-0.06$  to  $-0.20$  m, which also suggests the model is slightly underestimating water levels. The linear correlation coefficient *R* is 0.98 at all the stations except at the very upstream

station Newbold (0.97) and the downstream station at Lewes (0.96), indicating the model predictions strongly correlate with field observations.

The simulated major tidal harmonic constant (*M2*) was also compared with observed data at ten tide gauges (Table 3). The maximum difference between simulated and observed *M2* tidal constituent is  $-0.13$  m at NB station, which is about 12.1% underprediction by the model. More accurate bathymetry



**TABLE 2** | Error statistics of water-level predictions in the DBE.

Station ID	RMSE (m)	SI	Bias (m)	R
Newbold (NB)	0.23	0.22	-0.06	0.97
Burlington (BU)	0.26	0.29	-0.20	0.98
Philadelphia (PA)	0.22	0.32	-0.18	0.98
Marcus Hook (MH)	0.22	0.36	-0.17	0.98
Delaware City (DC)	0.20	0.34	-0.14	0.98
Reedy Point (RP)	0.20	0.35	-0.15	0.98
Ship John Shoal (SJS)	0.21	0.35	-0.15	0.98
Brandywine Shoal Light (BSL)	0.18	0.37	-0.14	0.98
Lewes (LE)	0.15	0.38	-0.08	0.96
Cape May (CM)	0.15	0.31	-0.08	0.98

**TABLE 3** | Comparison of observed and modeled M2 tidal amplitude in the DBE.

Station ID	A <sub>M2_obs</sub> (m)	A <sub>M2_mod</sub> (m)	A <sub>M2_mod</sub> - A <sub>M2_obs</sub> (m)	Relative error (%)
Newbold (NB)	1.07	0.94	-0.13	-12.1
Burlington (BU)	0.85	0.88	0.03	3.5
Philadelphia (PA)	0.84	0.85	0.01	1.2
Marcus Hook (MH)	0.78	0.77	-0.01	-1.3
Delaware City (DC)	0.74	0.77	0.03	4.1
Reedy Point (RP)	0.77	0.76	-0.01	-1.3
Ship John Shoal (SJS)	0.83	0.80	-0.03	-3.6
Brandywine Shoal Light (BSL)	0.72	0.71	-0.01	-1.4
Lewes (LE)	0.71	0.69	-0.02	-2.8
Cape May (CM)	0.62	0.62	0	0.0

and high model resolution may be required to improve the model accuracy in very upstream region of the estuary. Model predictions of M2 tide at the rest tide gauges matched the data reasonably well. Therefore, the overall performance of the model in simulating tidal elevation is considered satisfactory.

## RESULTS AND DISCUSSION

### Contribution of TSRI to TWL

Previous studies suggest that TSRI increases the uncertainty in TWL prediction (Doodson, 1956; Proudman, 1957; Rossiter, 1961; Johns et al., 1985; Arns et al., 2020). To understand the effects of TSRI on TWLs and coastal flooding in the DBE, TSRI was derived for the four extreme events.

**Figure 8** shows the time series of the simulated TWL, astronomical tides, LFS, and TSRI—at the NB, PA, and LE stations, located at the upstream, upper bay, and lower bay, respectively. To better understand the effect of TSRI on TWL, the unmodulated total water level (UTWL), which is simply a linear superposition of tide and LFS, was also plotted in **Figure 8**. Comparison of the TWL and UTWL indicates that modulations from TSRI on TWL vary with locations and extreme events. During Hurricane Irene (**Figure 8A**), TSRI was the product of tides interacting with river and storm surges in turn to manifest TWL at a tidal frequency. TSRI at the LE station, which is located

in the downstream of DBE, is storm surge driven for four extreme events, indicating less effect on TWL because there was little difference between TWL and UTWL (**Figure 8C**). TSRI at the NB station is dominated by river flow, showing strong tidal signals (**Figure 8A**). TSRI at NB suppressed tidal variations by more than 50% of the tidal range. TSRI at PA is less river dominant and does not feature prolonged damping on tides (**Figure 8B**).

During Tropical Storm Lee, which featured strong river flow and little storm surge, TWL at NB is significantly elevated up to 2.1 m by LFS, but the tidal range is much reduced (**Figure 8D**), similar to during Hurricane Irene. TSRI at NB had an amplitude (up to 1.2 m) similar to tides during peak river flow but in an opposite phase, resulting in the weakening of the tidal fluctuations. Strong TSRI lasted more than 4 days during high river flow, which demonstrated that TSRI was in a direct proportion to the river flow (Godin and Martinez, 1994; Sassi and Hoitink, 2013). Without the effect of TSRI, as shown in the UTWL, the tidal variations were maintained and the maximum UTWL was up to 1.0 m higher than the maximum TWL (**Figure 8D**). Downstream of NB, the magnitude of TSRI was greatly reduced to a level of 10 to 15% of TWL at PA (**Figure 8E**) and approached zero at LE (**Figure 8F**), because neither river flow nor storm surge affected TWL at the mouth of DBE during Tropical Storm Lee.

Hurricanes Sandy and Isabel featured strong storm surges, but had river flows smaller than those during Irene and Lee. TSRI from downstream (LE) to upstream (PA, NB) were mainly induced by the storm surges, and the peaks of TSRI increased from about 0.2 to 0.8 m as water depth became shallower (**Figures 8G–L**). Wind stress-induced surge magnitude is understood to be significantly greater at low water than at high water (Horsburgh and Wilson, 2007; Rego and Li, 2010; Zheng et al., 2020). The shallower the water depth, the stronger the tidal current magnitude, which resulted in stronger TSRI.

Unmodulated total water level shows both magnitude and phase differences from TWL at PA and NB during landfall of Sandy and Isabel (**Figures 8G,H,I,K**). Previous studies indicated that the effect of TSRI on surges is through magnitude modulation, and the effect on tides is through phase shift (Horsburgh and Wilson, 2007). The peak of TSRI occurred on falling tide during Sandy but on rising tide during Isabel, where TWL propagated faster than UTWL during Sandy but slower than UTWL during Isabel. In an idealized first-order modeling study, Horsburgh and Wilson (2007) discovered that the peak TSRI with respect to high tide does not occur randomly but in clusters on the rising or falling tides, depending on the phase speed between TWL and tides. Therefore when tides lead the TWL (such as Isabel), the TSRI will peak halfway up the rising tide. On the other hand, when tides lag TWL (such as Sandy), TSRI will peak on the falling tide. The changes of phase speeds of surge and tide can be explained by the increase of bottom friction effect due to the reduced water depth (Wolf, 1981).

### Contribution of TSRI to Tidal Modulation

Tides interact with different physical processes and generate non-linear interactions at tidal frequencies, which affect the tidal variations of TWL. This process is seen as tidal modulation by

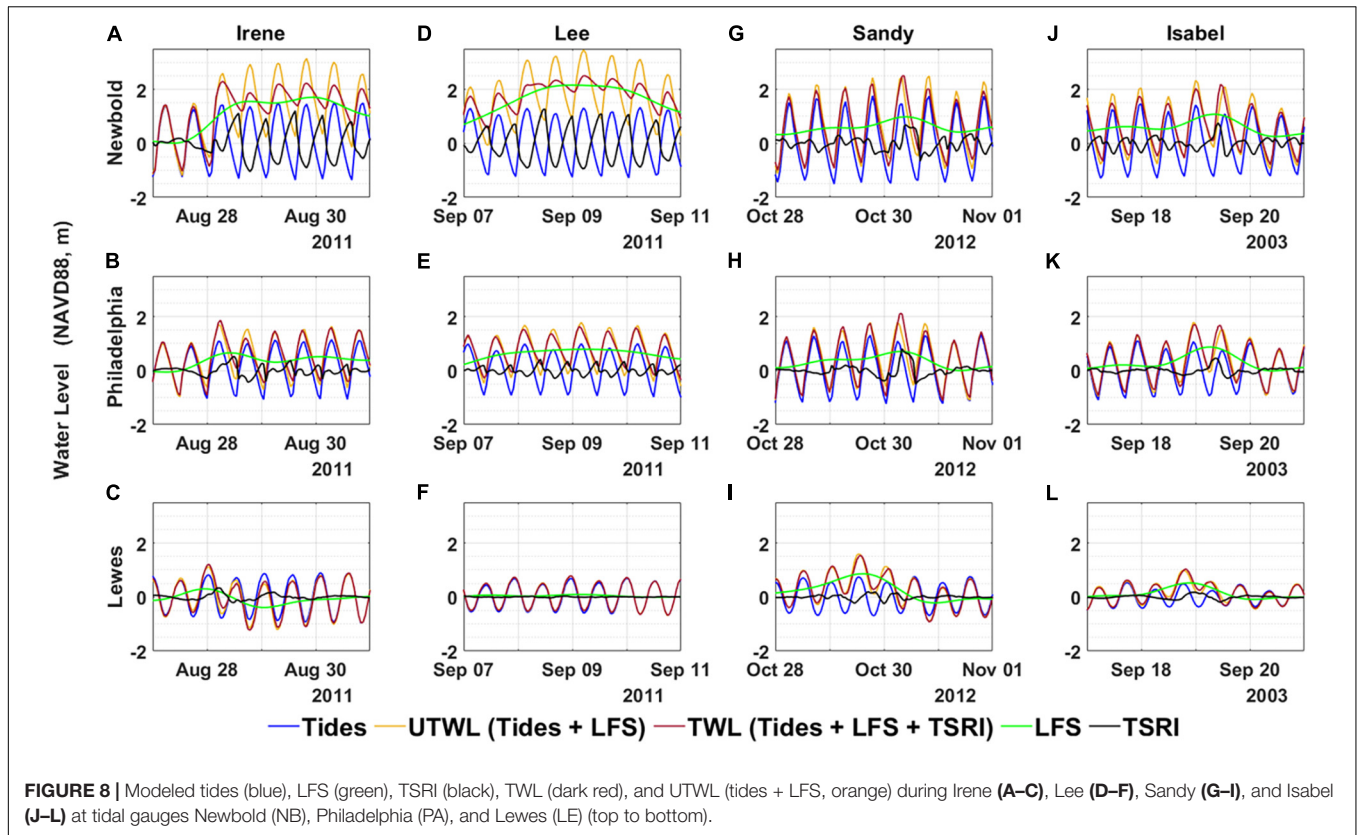


**FIGURE 8 |** Modeled tides (blue), LFS (green), TSRI (black), TWL (dark red), and UTWL (tides + LFS, orange) during Irene (A–C), Lee (D–F), Sandy (G–I), and Isabel (J–L) at tidal gauges Newbold (NB), Philadelphia (PA), and Lewes (LE) (top to bottom).

TSRI on TWL. Because TSRI varies with tidal frequency, it is helpful to conduct frequency analysis of TSRI to understand how different tidal bands interact with LFS. By decomposing the TSRI based on the tidal frequency (mainly focusing on diurnal D1, semidiurnal D2, and quarter-diurnal D4 bands), the effects of tidal modulation by TSRI on TWL were assessed and quantified during the four extreme events. This section describes how non-stationary tidal analysis—Complex Demodulation as described in section “TWL and Non-linear Interaction Decomposition”—was applied to the time series of TSRI to calculate the time-varying amplitude and phase at different tidal frequencies. The reconstructed time series of TSRI at the D1, D2, and D4 bands at the upstream NB station are presented in **Figure 9**.

The amplitude of the D2 component of TSRI during strong river flow (Irene and Tropical Storm Lee) can reach up to 1 m, which is comparable to semidiurnal tides, and the time series is out of phase with a 6-h lag relative to tides (**Figures 9A,D**). Therefore, the tidal modulation by TSRI on TWL at the D2 band has a damping effect. The amplitude of tidal variations of TWL (red line in **Figures 9A,D**) at the D2 band is reduced by more than 50% of the amplitude of semidiurnal tides (blue line in **Figures 9A,D**). The contribution of TSRI to tidal modulation at the D2 band during Sandy and Isabel was insignificant, as shown in **Figures 9G,J**. The amplitude of the D1 component of TSRI can reach up to 0.4 m during strong storm surge events induced by Sandy and Irene, about 2 times greater than diurnal tides (**Figures 9B,H**). The tidal modulation by TSRI on TWL at the D1 band enhanced the diurnal tides in a dominant way.

The amplitude of the D4 component of TSRI is less significant in NB station for all the four extreme events (**Figures 9C,E,I,L**). However, the phase of TSRI at the D4 band works against the tides when the river flow is strong, such as during Irene and Lee (**Figures 9C,F**).

The peak amplitudes of TSRI at the D2, D1, and D4 bands and the corresponding amplitudes for tides, as well as the sum of the two, are plotted in **Figure 10** for 10 tidal gauges, in order from upstream to downstream in the DBE. During Hurricane Irene and Tropical Storm Lee, it is clear that river flow mainly interacts with tides at the D2 band and results in TSRI damping semidiurnal tides until the river flow impact ceases at MH station (**Figures 10A,D**). Therefore, the higher the river flow, the greater the tidal modulation of damping on semidiurnal tides by TSRI, and the smaller the tidal variations of TWL at the D2 band. During Irene and Sandy, storm surges mainly interacted with diurnal tides, and the tidal modulation by TSRI on TWL at the D1 band was amplified. The tidal variations of TWL at the D1 band were enhanced by peak TSRI during Irene and Sandy, resulting in strong storm surges larger than diurnal tides (**Figures 10B,H**). High-frequency TSRI at the D4 band generally enhances tides except at the NB station during high river flow events (e.g., Irene and Lee), and the magnitude is overall not significant (**Figures 10C,E,I,L**).

From upstream to downstream, the tidal modulations by TSRI on TWL at the D2, D1, and D4 bands all show a decreasing trend as water depth increases. The TSRI at the D2 band shows greater variations and larger magnitudes than those at the D1

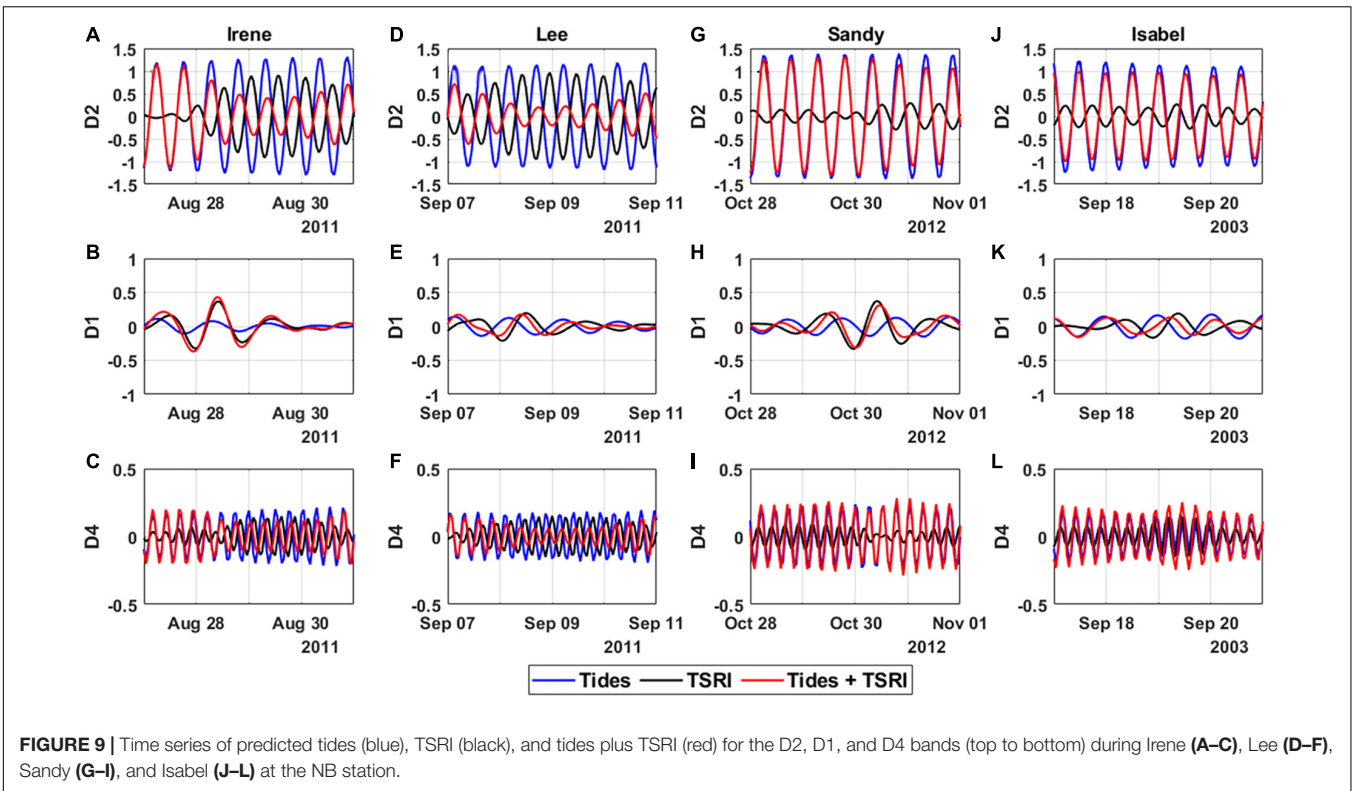


**FIGURE 9 |** Time series of predicted tides (blue), TSRI (black), and tides plus TSRI (red) for the D2, D1, and D4 bands (top to bottom) during Irene (A–C), Lee (D–F), Sandy (G–I), and Isabel (J–L) at the NB station.

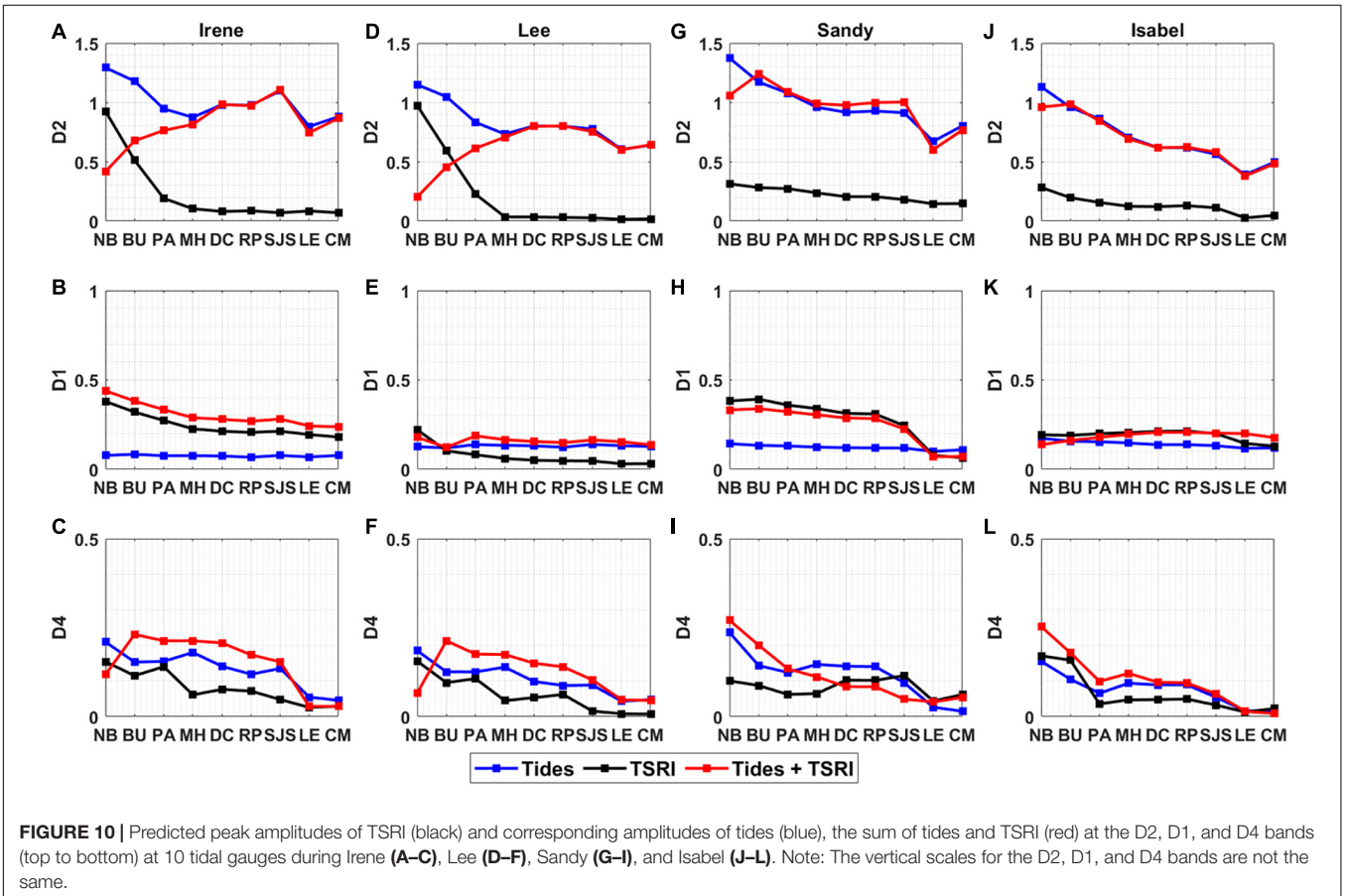


**FIGURE 10 |** Predicted peak amplitudes of TSRI (black) and corresponding amplitudes of tides (blue), the sum of tides and TSRI (red) at the D2, D1, and D4 bands (top to bottom) at 10 tidal gauges during Irene (A–C), Lee (D–F), Sandy (G–I), and Isabel (J–L). Note: The vertical scales for the D2, D1, and D4 bands are not the same.

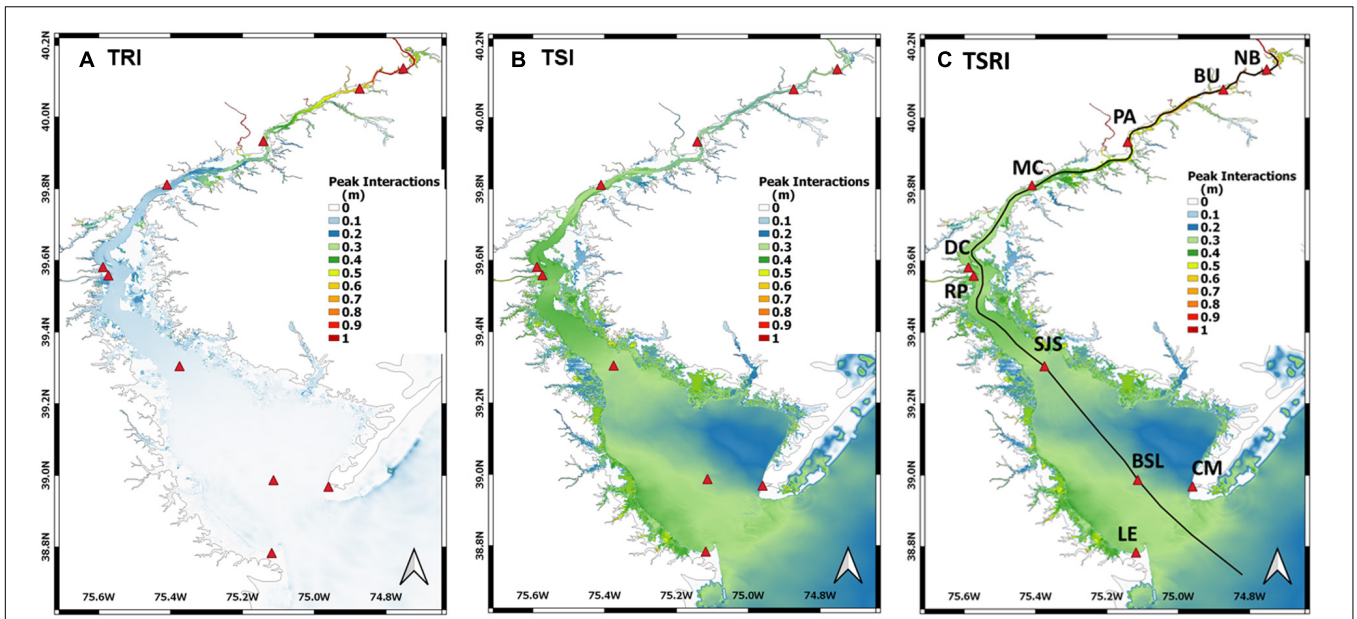


FIGURE 11 | Spatial variations on peak values of (A) TRI, (B) TSI, and (C) TSRI during Hurricane Irene in the DBE. Tide gauges are labeled as red triangles.

band when the impact of river flow is significant. Therefore, the tidal modulation on TWL by TSRI is dominated by the river-induced damping effect during high flow events. Storm surge-induced amplification becomes the dominant effect when river flow is low.

TS is delimiting but TR becomes dominant. The transition zone classification based on TSRI distribution also indicates the estuary-tidal river boundary.

### Effects of River Flow and Storm Surge on Compound Flooding

For Hurricane Irene, which featured high river flow and large storm surge, the effects of river-induced damping by TRI and storm surge-induced amplification by TSI on TWL co-exist during compound flooding (e.g., Figures 10A,B). As indicated in the previous section, TRI mainly damps on semidiurnal tides (D2 band) and TSI enhances diurnal tides (D1 band). To better understand the combined effect of TRI and TSI on the TWL, numerical experiments (TR run and TS run) were conducted to extract TRI and TSI components from TSRI.

The spatial distributions of the peak magnitude of TRI, TSI, and TSRI inside the DBE during Hurricane Irene were compared (Figure 11) and further evaluated along a longitudinal transect. The DBE can be divided into three zones based on the pattern of TSRI: the river zone where TSRI is dominated by TRI in the upstream of the BU station and shows patterns similar to those in Figures 11A,C; the surge zone where TSRI is dominated by TSI downstream of the MH station and exhibits patterns similar to those in Figures 11B,C; and the transition zone where TSRI is influenced by both river flow (TRI) and storm surge (TSI) between the BU and MH stations (Figure 11C). Hoitink and Jay (2016) proposed the definition of boundary between tidal river and estuary using the point of reversal of lowest low waters from spring to neap (typically  $A_{Msf}=A_{S2}$ ). It was found  $A_{Msf}=A_{S2} \approx 0.13\text{m}$  at the PA station where

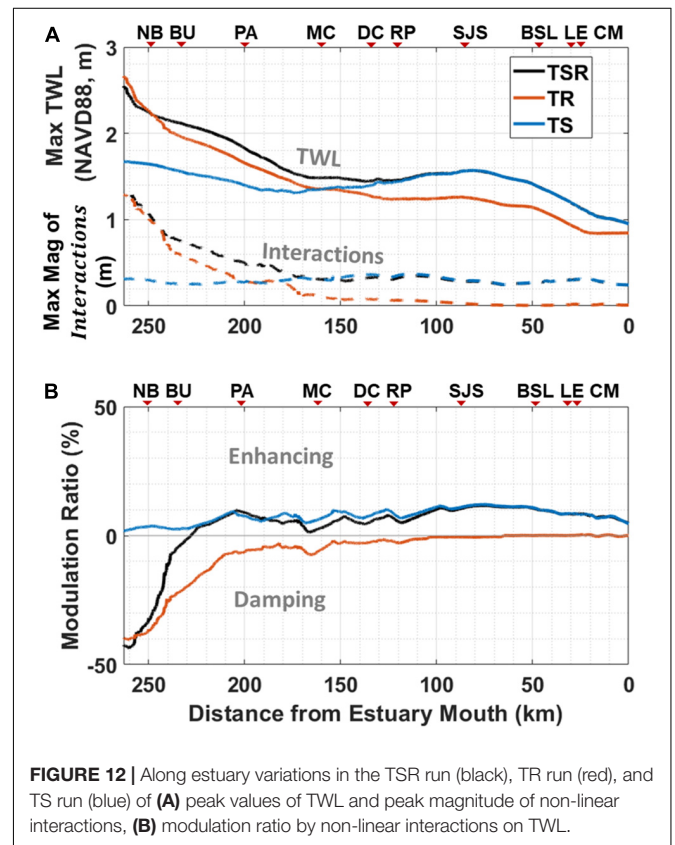


FIGURE 12 | Along estuary variations in the TSR run (black), TR run (red), and TS run (blue) of (A) peak values of TWL and peak magnitude of non-linear interactions, (B) modulation ratio by non-linear interactions on TWL.

To assess the level of impact of TRI, TSI, and TSRI on TWL, the modulation ratio is used, which is defined as:

$$\begin{aligned}
 \text{modulation ratio (\%)} &= \frac{TWL_{max} - UTWL}{TWL_{max}} \times 100 \\
 &= \left(1 - \frac{Tide + LFS}{TWL_{max}}\right) \times 100 \quad (8)
 \end{aligned}$$

where,  $UTWL = Tide + LFS$  at the same timestep of  $TWL_{max}$ . Based on the definition of TWL (Figure 4), Eq. (8) can be further written as:

$$\text{modulation ratio (\%)} = \left(\frac{\text{Nonlinear Interactions}}{TWL_{max}}\right) \times 100 \quad (9)$$

The modulation ratio represents the modulation of non-linear interactions on TWL in terms of magnitude and phase change. Figure 12 shows that when only tide and river flow are considered (TR run, orange line), the TRI damps TWL by up to 40% in the upstream and the damping effect gradually reduces to zero around MH. In TS run (blue line), the TSI enhances TWL by 5–15% in the whole domain, but the effect on the TWL is smaller than the effect of river flow (Figure 12A). In the TSR run, a

transition point of TSRI is shown around 230 km upstream between the PA and BU stations. At the very upstream, TSRI is damping TWL up to 40%, while downstream of the tipping points TSRI is enhancing TWL by 10–15% (Figure 12B).

The frequency analysis in section “Contribution of TSRI to Tidal Modulation” details the variations in TSRI at different tidal frequencies (Figure 9), and the modulation ratio evaluates the impacts of non-linear interactions on TWL under different forcing mechanisms (Figure 12). To further quantify the relative contributions of the D2, D1, and high-frequency (D4+D6+D8) tidal bands to the total variance of TRI, TSI, and TSRI, the SSA method (described in section “TWL and Non-linear Interaction Decomposition”) was applied at 10 tide gauges. Figure 13A shows that TRI is contributed by D2 and high-frequency bands only and the contribution from the D1 band is zero. The D2 band contributes 70 to 90% of the total variability of TRI at the NB and BU stations, while the high-frequency band contributes more than 50% of the total variability of TRI at the PA and MH stations, which indicates the shallow water effect becomes dominant in this area. The lower contribution of the high-frequency band to the total variability of TRI at upstream locations (NB and BU) with respect to D2 was attributed to a faster damping of

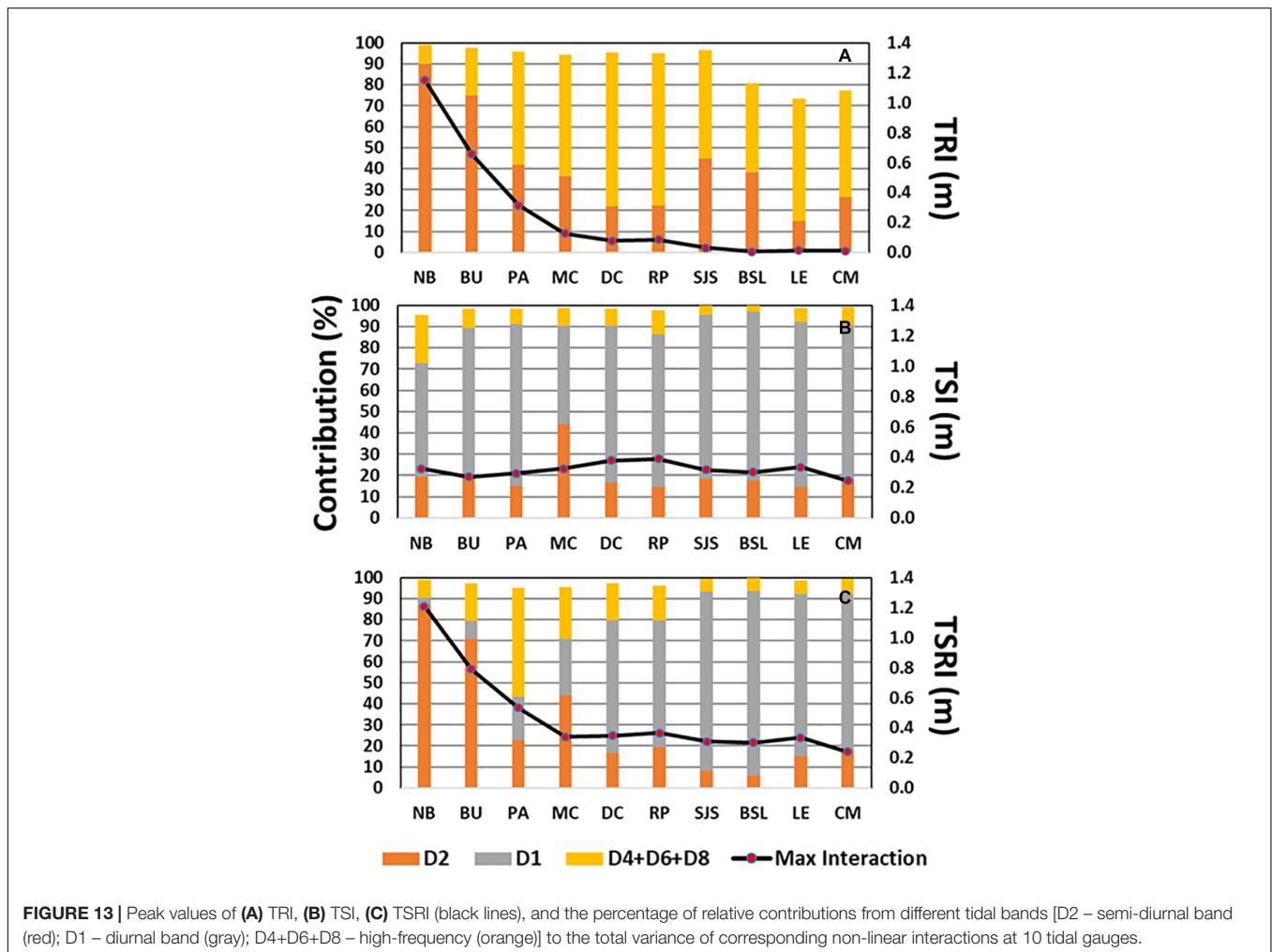


**TABLE 4 |** Relative contributions (%) of the D2, D1, and high-frequency (D4+D6+D8) bands to the total variance of TRI, TSI, and TSRI at 10 tidal gauges.

	TRI				TSI				TSRI			
	Peak	D2	D1	D <sub>4+6+8</sub>	Peak	D2	D1	D <sub>4+6+8</sub>	Peak	D2	D1	D <sub>4+6+8</sub>
ID	(m)	(%)	(%)	(%)	(m)	(%)	(%)	(%)	(m)	(%)	(%)	(%)
NB	1.2	89.8	0.0	9.4	0.3	19.6	53.0	22.8	1.2	86.7	3.7	8.7
BU	0.7	74.9	0.0	22.9	0.3	19.0	70.1	9.4	0.8	71.0	8.2	18.0
PA	0.3	41.9	0.0	53.9	0.3	15.2	75.8	7.2	0.5	22.7	20.7	51.5
MH	0.1	36.5	0.0	57.9	0.3	43.9	46.4	8.4	0.3	44.1	26.9	24.3
DC	0.1	21.9	0.0	73.7	0.4	16.4	73.9	8.0	0.4	16.6	63.1	17.6
RP	0.1	22.2	0.0	72.7	0.4	14.8	71.3	11.7	0.4	19.4	60.4	16.4
SJS	0.0	44.6	0.0	51.9	0.3	18.3	77.2	4.3	0.3	8.1	85.3	6.2
BSL	0.0	38.1	0.0	42.6	0.3	17.5	79.5	2.7	0.3	5.9	87.7	6.1
LE	0.0	15.2	0.0	58.3	0.3	14.7	77.5	6.7	0.3	15.1	77.0	6.8
CM	0.0	26.5	0.0	50.8	0.2	17.9	73.2	8.1	0.2	17.8	74.8	6.8

the higher harmonics by river flow. Further downstream of MH, TRI is less than 0.2 m and becomes negligible. However, for the TS run, TSI is predominantly contributed by the D1 band in a range of 50 to 80% in the entire DBE (Figure 13B). In the TSR run, which considered the combined forcing of tide, river flow, and storm surge, the contribution of TSRI followed a three-zone pattern (Figure 13C), as described in section “Effects of River Flow and Storm Surge on Compound Flooding.” The D2 and D1 bands contribute the most to TSRI in the upstream and downstream of the estuary, respectively. In the transition zone around PA, the high-frequency band contributes up to 60% of the total variance of TSRI (Figure 13C). The contributions to the total variance of TRI, TSI, and TSRI from the identified D2, D1, high-frequency (D4+D6+D8) bands at 10 tidal gauges are summarized in Table 4.

### Sensitivity of River Flow on Compound Flooding

As discussed in previous sections, TSRI is proportional to river flow and has a damping effect on tidal amplitude, which is caused by the bottom friction effect via dissipating tidal energy (Godin, 1999; Horrevoets et al., 2004). However, the relationship between tidal damping and river flow rate can be linear or non-linear in different estuaries. Tidal damping by TSRI is dominated by the river flow in the upstream of tidal estuaries (Godin and Martinez, 1994). Theoretical analysis suggested a linear relationship between tidal damping modulus and river flow in the Columbia River estuary (Kukulka and Jay, 2003). However, Guo et al. (2015) found non-linear tidal decay of principal tides and the modulation of M4 tide with increasing river flow in the Yangtze River estuary. To better understand the relationship between the damping effect and river flow in the DBE, a sensitivity analysis was conducted to evaluate the damping effect of TSRI on TWL in the DBE under different river flow conditions.

To determine the river flow range corresponding to a flood return period, a rating curve of flood frequency for the Delaware River was developed using USGS stream gauge data at Trenton. Figure 14 indicates that Irene is equivalent to a 5 year flood

event while Tropical Storm Lee corresponds to a 10 year flood event. Sensitivity model runs were carried out with stream flows corresponding to flood return periods of 2, 5, 10, 25, 50, 100, and 500 years. The hydrograph shape of the Irene event was used to construct the river flow input by multiplying a ratio to match the peak design flows to simulate Irene-like river flood events. Tide and wind field were kept the same as those used in Hurricane Irene.

The variations of the peak TWL and peak magnitude of TSRI under different river flows from upstream to downstream and the corresponding modulation ratios by TSRI on TWL are shown in Figure 15. The magnitude of TSRI and TWL from upstream to the MH station is affected by river flow changes; the maximum variations of TSRI and TWL in the upstream were approximately in the ranges of 1–2 m and 2.2–5.5 m, respectively (Figure 15A). The larger increase in TWL compared to TSRI is due to the increase in LFS induced by river flow. In general, downstream of station MH, the variation of river flow has little influence on TWL and TSRI, and modulation ratio. However, approximately between stations BU and MH, the effects of river flow rates on TWL, TSRI, and modulation ratio become evident, with TWL and TSRI increasing toward the upstream as a function of flow rate (Figure 15A) and the modulation ratio transitioning from enhancing to damping (Figure 15B). It is also observed that the

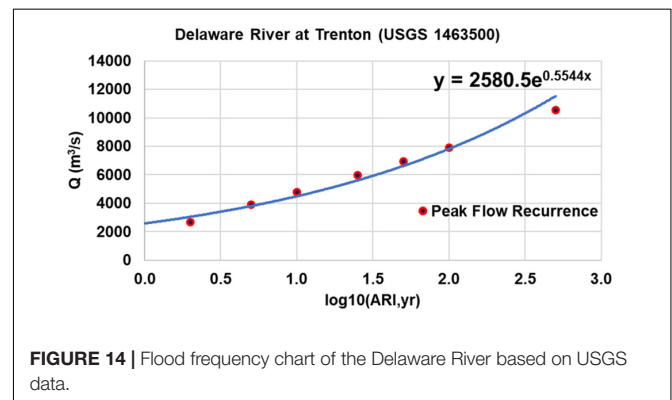
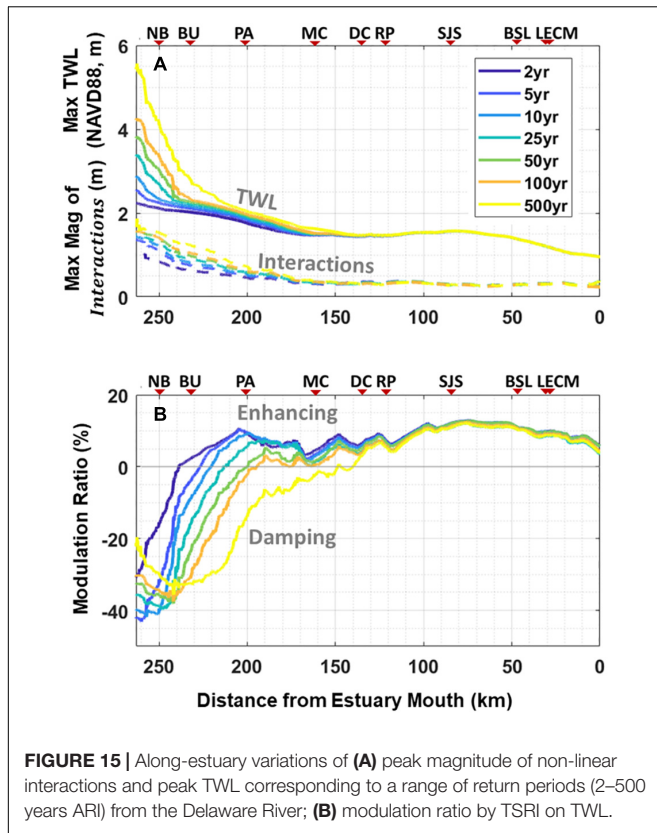


**FIGURE 14 |** Flood frequency chart of the Delaware River based on USGS data.



transition location of the modulation ratio shifts downstream as river flow increases (Figure 15B). It is interesting to see the modulation ratio reaching a minimum (or maximum damping) in the upstream zone and the minimum inversely proportional to the flow rate and ARI (Figure 15B). For example, the respective minimums of the modulation ratio corresponding to ARIs of 5 yr, 25 yr, and 500 yr are approximately  $-43$ ,  $-40$ , and  $-33\%$ . The presence of the minimum of modulation ratio can be explained by its definition in Eq. (9), which is non-linear interactions divided by TWL. In the transition zone, the relative increase in the damping effect from non-linear interactions is greater than the increase in TWL. However, toward the upstream, TWL increases significantly with a greater rate and results in a reduction in the magnitude of the modulation ratio, and consequently the maximum damping.

## SUMMARY AND CONCLUSION

In this study, a 3-D, high-resolution storm surge model was developed to evaluate the non-linear interactions between tidal and non-tidal components of TWLs in the DBE during hurricane events. In particular, focused analysis was conducted to understand the effect of non-linear interactions on coastal compound flooding induced by the co-occurrence of river floods and coastal storm surges. Specifically, storm surge and non-linear interactions induced by historical extreme weather events—Hurricanes Isabel (2003), Irene (2011), Tropical Storm Lee (2011), and Sandy (2012) – were simulated and analyzed.

The model was validated with observed water levels at 10 tide gauges that span the entire DBE. Simulated water levels were decomposed to astronomical tides, LFSs, and non-linear interactions. The effects of non-linear interactions on the TWL were further analyzed using a wavelet approach and a spectral analysis method. TRI and TSI were derived using numerical experiments driven by the corresponding forcing only. The DBE can be divided into three zones: the river-dominated (upstream of the BU station), the storm surge-dominated (downstream of station MH), and the transition zone in between. Analysis results indicate that TRI tends to damp tidal amplitude on the D2 band, by up to 40% of the TWL, in the upstream river-dominated zone, caused by the bottom friction effect via dissipating tidal energy (Godin, 1999; Horrevoets et al., 2004). However, TSI amplifies tides on the D1 band by 10 to 15% of TWL in the entire estuary.

The effect of TSRI on TWL was more noticeable during compound flooding events such as Hurricane Irene. TSRI in the river and surge zones are dominated by TRI and TSI to dampen and enhance TWL, respectively. TSRI in the transition zone is jointly contributed to by TRI and TSI, which yields a tipping point of separating the damping and enhancing effects in the estuary. Sensitivity analysis indicated that the tipping point of TSRI damping and enhancing effects shifts downstream as river flow ARI increases.

## DATA AVAILABILITY STATEMENT

The raw data supporting the conclusions of this article will be made available by the authors, without undue reservation.

## AUTHOR CONTRIBUTIONS

ZY, ZX, and TW contributed to conception and design of the study. ZX, ZY, and TW contributed to the methodology. NS and MW contributed to the river flow analysis. ZX performed the simulations, visualization, and results analysis. DJ provided project administration. ZX and ZY wrote the first draft of the manuscript. All authors contributed to manuscript review, revision, and approved the submitted version.

## FUNDING

This work was supported by the MultiSector Dynamics, Earth System Model Development and Regional and Global Modeling and Analysis program areas of the United States Department of Energy, Office of Science, Office of Biological and Environmental Research as part of the multi-program, collaborative Integrated Coastal Modeling (ICoM) project. All model simulations were performed using resources available through Research Computing at Pacific Northwest National Laboratory.

## ACKNOWLEDGMENTS

The authors thank Dr. Isabel Jalón-Rojas for providing the MATLAB script of the complex demodulation method.

## REFERENCES

- Amante, C., and Eakins, B. W. (2009). *ETOPO1 1 Arc-Minute Global Relief Model: Procedures, Data Sources and Analysis, OAA Technical Memorandum NESDIS, NGDC-24*. 19.
- Aristizabal, M., and Chant, R. (2013). A numerical study of salt fluxes in Delaware bay estuary. *J. Phys. Oceanogr.* 43, 1572–1588. doi: 10.1175/Jpo-D-12-0124.1
- Arns, A., Wahl, T., Wolff, C., Vafeidis, A. T., Haigh, I. D., Woodworth, P., et al. (2020). Non-linear interaction modulates global extreme sea levels, coastal flood exposure, and impacts. *Nat. Commun.* 11:1918. doi: 10.1038/s41467-020-15752-5
- Bevacqua, E., Maraun, D., Vousdoukas, M. I., Voukouvalas, E., Vrac, M., Mentaschi, L., et al. (2019). Higher probability of compound flooding from precipitation and storm surge in Europe under anthropogenic climate change. *Sci. Adv.* 5:eaaw5531. doi: 10.1126/sciadv.aaw5531
- Bloomfield, P. (2004). *Fourier analysis of Time Series: An Introduction. Wiley Series in Probability and Statistics*. Hoboken, NJ: John Wiley.
- Chen, C., Gao, G., Zhang, Y., Beardsley, R. C., Lai, Z., Qi, J., et al. (2016). Circulation in the Arctic Ocean: results from a high-resolution coupled ice-sea nested Global-FVCOM and Arctic-FVCOM system. *Prog. Oceanogr.* 141, 60–80. doi: 10.1016/j.pocean.2015.12.002
- Chen, C. S., Lai, Z. G., Beardsley, R. C., Sasaki, J., Lin, J., Lin, H. C., et al. (2014). The March 11, 2011 Tohoku M9.0 earthquake-induced tsunami and coastal inundation along the Japanese coast: a model assessment. *Prog. Oceanogr.* 123, 84–104. doi: 10.1016/j.pocean.2014.01.002
- Chen, C. S., Liu, H. D., and Beardsley, R. C. (2003). An unstructured grid, finite-volume, three-dimensional, primitive equations ocean model: application to coastal ocean and estuaries. *J. Atmos. Ocean. Technol.* 20, 159–186. doi: 10.1175/1520-0426(2003)020<0159:augfv>2.0.co;2
- Dean, R. G. (1966). “Tides and harmonic analysis,” in *Estuary and Coastline Hydrodynamics*, ed. A. T. Ippen (New York, NY: MGHraw-Hill), 197–229.
- Dinapoli, M. G., Simionato, C. G., and Moreira, D. (2021). Nonlinear interaction between the tide and the storm surge with the current due to the river flow in the rio de la Plata. *Estuaries Coasts* 44, 939–959. doi: 10.1007/s12237-020-00844-8
- Doodson, A. T. (1956). Tides and storm surges in a long uniform gulf. *Proc. R. Soc. Lon. Series A Math. Phys. Sci.* 237, 325–343. doi: 10.1098/rspa.1956.0180
- Dronkers, J. J. (1964). *Tidal Computations in Rivers and Coastal Waters*. Amsterdam: North-Holland Publishing Company.
- Flinchem, E. P., and Jay, D. A. (2000). An introduction to wavelet transform tidal analysis methods. *Estuarine Coastal Shelf Sci.* 51, 177–200. doi: 10.1006/ecss.2000.0586
- Gasquet, H., and Wootton, A. J. (1997). Variable-frequency complex demodulation technique for extracting amplitude and phase information. *Rev. Sci. Instr.* 68, 1111–1114. doi: 10.1063/1.1147748
- Godin, G. (1972). *The Analysis of Tides*. Buffalo, NY: University of Toronto Press, 264.
- Godin, G. (1999). The propagation of tides up rivers with special considerations on the upper saint lawrence river. *Estuarine Coastal Shelf Sci.* 48, 307–324. doi: 10.1006/ecss.1998.0422
- Godin, G., and Martinez, A. (1994). Numerical experiments to investigate the effects of quadratic friction on the propagation of tides in a channel. *Continental Shelf Res.* 14, 723–748. doi: 10.1016/0278-4343(94)90070-1
- Guo, L., van der Wegen, M., Jay, D. A., Matte, P., Wang, Z. B., Roelvink, D., et al. (2015). River-tide dynamics: exploration of nonstationary and nonlinear tidal behavior in the Yangtze River estuary. *J. Geophys. Res. Oceans* 120, 3499–3521. doi: 10.1002/2014JC010491
- Hoitink, A. J. F., and Jay, D. A. (2016). Tidal river dynamics: implications for deltas. *Rev. Geophys.* 54, 240–272. doi: 10.1002/2015rg000507
- Horrevoets, A. C., Savenije, H. H. G., Schuurman, J. N., and Graas, S. (2004). The influence of river discharge on tidal damping in alluvial estuaries. *J. Hydrol.* 294, 213–228. doi: 10.1016/j.jhydrol.2004.02.012
- Horsburgh, K. J., and Wilson, C. (2007). Tide-surge interaction and its role in the distribution of surge residuals in the North Sea. *J. Geophys. Res. Oceans* 112(C8):4033. doi: 10.1029/2006JC004033
- Hsiao, S. C., Chen, H., Chen, W. B., Chang, C. H., and Lin, L. Y. (2019). Quantifying the contribution of nonlinear interactions to storm tide simulations during a super typhoon event. *Ocean Eng.* 194:106661. doi: 10.1016/j.oceaneng.2019.106661
- Idier, D., Bertin, X., Thompson, P., et al. (2019). Interactions between mean sea level, tide, surge, waves and flooding: mechanisms and contributions to sea level variations at the coast. *Surv. Geophys.* 40, 1603–1630. doi: 10.1007/s10712-019-09549-5
- Idier, D., Dumas, F., and Muller, H. (2012). Tide-surge interaction in the English channel. *Nat. Hazard Earth Sys.* 12, 3709–3718. doi: 10.5194/nhess-12-3709-2012
- Jalón-Rojas, I., Schmidt, S., and Sottolichio, A. (2016). Evaluation of spectral methods for high-frequency multiannual time series in coastal transitional waters: advantages of combined analyses. *Limnol. Oceanogr. Methods* 14, 381–396. doi: 10.1002/lom3.10097
- Jalón-Rojas, I., Schmidt, S., and Sottolichio, A. (2017). Comparison of environmental forcings affecting suspended sediments variability in two macrotidal, highly turbid estuaries. *Estuar. Coast. Shelf Sci.* 198, 529–541. doi: 10.1016/j.ecss.2017.02.017
- Jalón-Rojas, I., Sottolichio, A., Hanquiez, V., Fort, A., and Schmidt, S. (2018). To what extent multidecadal changes in morphology and fluvial discharge impact tide in a convergent (Turbid) Tidal River. *J. Geophys. Res. Oceans* 123, 3241–3258. doi: 10.1002/2017jc013466
- Jay, D. A., and Flinchem, E. P. (1997). Interaction of fluctuating river flow with a barotropic tide: a demonstration of wavelet tidal analysis methods. *J. Geophys. Res.* 102, 5705–5720. doi: 10.1029/96jc00496
- Johns, B., Rao, A. D., Dubinsky, Z., Sinha, P. C., and Lighthill, M. J. (1985). Numerical modelling of tide-surge interaction in the Bay of Bengal. *Philos. Trans. Royal Soc. Lond. Series A Math. Phys. Sci.* 313, 507–535. doi: 10.1098/rsta.1985.0002
- Keers, J. F. (1968). An empirical investigation of interaction between storm surge and astronomical tide on the east coast of Great Britain. *Dtsch. Hydrogr. Z.* 21, 118–125. doi: 10.1007/bf02235726
- Kukulka, T., and Jay, D. A. (2003). Impacts of Columbia River discharge on salmonid habitat: 1. A non-stationary fluvial tide model. *J. Geophys. Res.* 108(C9):3293. doi: 10.1029/2002JC001382
- Landsea, C. W., and Franklin, J. L. (2013). Atlantic hurricane database uncertainty and presentation of a new database format. *Mon. Wea. Rev.* 141, 3576–3592. doi: 10.1175/mwr-d-12-00254.1
- Lanzoni, S., and Seminara, G. (1998). On tide propagation in convergent estuaries. *J. Geophys. Res. Oceans* 103(C13), 30793–30812. doi: 10.1029/1998jc900015
- Li, M., Zhang, F., Barnes, S., and Wang, X. (2020). Assessing storm surge impacts on coastal inundation due to climate change: case studies of Baltimore and Dorchester County in Maryland. *Nat. Hazards* 103, 2561–2588. doi: 10.1007/s11069-020-04096-4
- Matte, P., Jay, D. A., and Zaron, E. D. (2013). Adaptation of classical tidal harmonic analysis to nonstationary tides, with application to river tides. *J. Atmos. Oceanic Technol.* 30, 569–589. doi: 10.1175/jtech-d-12-00016.1
- Matte, P., Secretan, Y., and Morin, J. (2014). Temporal and spatial variability of tidal-fluvial dynamics in the St. Lawrence fluvial estuary: an application of nonstationary tidal harmonic analysis. *J. Geophys. Res.* 119, 5724–5744. doi: 10.1002/2014JC009791
- Olbert, A. I., Nash, S., Cunnane, C., and Hartnett, M. (2013). Tide-surge interactions and their effects on total sea levels in Irish coastal waters. *Ocean Dynamics* 63, 599–614. doi: 10.1007/s10236-013-0618-0
- Pareja Roman, L. F. (2019). *Delaware Bay: Hydrodynamics and Sediment Transport in the Anthropocene*. doi: 10.7282/t3-3ss3-kc28 PhD thesis, Rutgers University, New Jersey.
- Parker, B., Hess, K. W., Milbert, D. G., and Gill, S. (2003). A national vertical datum transformation tool. *Sea Technol.* 44, 10–15.
- Pawlowicz, R., Beardsley, B., and Lentz, S. (2002). Classical tidal harmonic analysis including error estimates in MATLAB using T\_TIDE. *Comput. Geosci.* 28, 929–937. doi: 10.1016/s0098-3004(02)00013-4
- Prandle, D., and Wolf, J. (1978). The interaction of surge and tide in the North Sea and River Thames. *Geophys. J. Int.* 55, 203–216. doi: 10.1111/j.1365-246X.1978.tb04758.x
- Proudman, J. (1955). The propagation of tide and surge in an estuary. *Proc. R. Soc. Lond. Series A Math. Phys. Sci.* 231, 8–24. doi: 10.1098/rspa.1955.0153
- Proudman, J. (1957). Oscillations of tide and surge in an estuary of finite length. *J. Fluid Mech.* 2, 371–382. doi: 10.1017/S002211205700018X



- Rego, J. L., and Li, C. (2010). Nonlinear terms in storm surge predictions: effect of tide and shelf geometry with case study from Hurricane Rita. *J. Geophys. Res.* 115:C06020. doi: 10.1029/2009JC005285
- Rossiter, J. R. (1961). Interaction between tide and surge in the thames. *Geophys. J. Int.* 6, 29–53. doi: 10.1111/j.1365-246X.1961.tb02960.x
- Sassi, M. G., and Hoitink, A. J. F. (2013). River flow controls on tides and tide-mean water level profiles in a tidal freshwater river. *J. Geophys. Res. Oceans* 118, 4139–4151. doi: 10.1002/jgrc.20297
- Schoellhamer, D. H. (2001). Singular spectrum analysis for time series with missing data. *Geophys. Res. Lett.* 28, 3187–3190. doi: 10.1029/2000GL012698
- Schoellhamer, D. H. (2002). Variability of suspended-sediment concentration at tidal to annual time scales in San Francisco Bay, USA. *Cont. Shelf Res.* 22, 1857–1866. doi: 10.1016/S0278-4343(02)00042-0
- Sharp, J. (ed.) (1984). *The Delaware Estuary: Research as Background For Estuarine Management and Development*. Delaware River and Bay Authority Rep. University of Delaware College of Marine Studies and New Jersey Marine Sciences Consortium, DEL-SG-03-84. Newark, DE: University of Delaware, 340.
- Sheng, Y. P., Alymov, V., and Paramygin, V. A. (2010). Simulation of storm surge, wave, currents and inundation in the Outer Banks and Chesapeake Bay during Hurricane Isabel in 2003: the importance of waves. *J. Geophys. Res.* 115, 1–27.
- Song, D., Wang, X. H., Cao, Z., and Guan, W. (2013). Suspended sediment transport in the Deepwater Navigation Channel, Yangtze River Estuary, China, in the dry season 2009: 1. Observations over spring and neap tidal cycles. *J. Geophys. Res. Oceans* 118, 5555–5567. doi: 10.1002/jgrc.20410
- Spicer, P., Huguenard, K., Ross, L., and Rickard, L. N. (2019). High-Frequency tide-surge-river interaction in estuaries: causes and implications for coastal flooding. *J. Geophys. Res. Oceans* 124, 9517–9530. doi: 10.1029/2019jc015466
- Spicer, P., Matte, P., Huguenard, K., and Rickard, L. N. (2021). Coastal windstorms create unsteady, unpredictable storm surges in a fluvial Maine estuary. *Shore Beach* 89, 3–10. doi: 10.34237/1008921
- Vautard, R., Yiou, P., and Ghil, M. (1992). Singular-spectrum analysis: a toolkit for short, noisy chaotic signals. *Phys. D* 58, 95–126. doi: 10.1016/0167-2789(92)90103-T
- Walters, R. A., and Heston, C. (1982). Removing tidal-period variations from time-series data using low-pass digital filters. *J. Phys. Oceanogr.* 12, 112–115. doi: 10.1175/1520-0485(1982)012<0112:rtpvft>2.0.co;2
- Wang, T. P., and Yang, Z. Q. (2019). The nonlinear response of storm surge to sea-level rise: a modeling approach. *J. Coast. Res.* 35, 287–294. doi: 10.2112/jcoastres-d-18-00029.1
- Whitney, M. M., and Garvine, R. W. (2006). Simulating the Delaware bay buoyant outflow: comparison with observations. *J. Phys. Oceanogr.* 36, 3–21. doi: 10.1175/jpo2805.1
- Wolf, J. (1978). Interaction of tide and surge in a semi-infinite uniform channel, with application to surge propagation down the east coast of Britain. *Appl. Math. Model.* 2, 245–253. doi: 10.1016/0307-904X(78)90017-3
- Wolf, J. (1981). “Surge-tide interaction in the North Sea and River Thames,” in *Floods due to High Winds and Tides*, ed. D. H. Peregrine (New York, NY: Elsevier), 75–94.
- Wong, K.-C., and Sommerfield, C. K. (2009). The variability of currents and sea level in the upper Delaware estuary. *J. Mar. Res.* 67, 479–501. doi: 10.1357/002224009790741111
- Xiao, Z. Y., Wang, X. H., Song, D., Jalón-Rojas, L., and Harrison, D. (2020). Numerical modelling of suspended-sediment transport in a geographically complex microtidal estuary: Sydney Harbour Estuary, NSW. *Estuar. Coast. Shelf Sci.* 236:106605. doi: 10.1016/j.ecss.2020.106605
- Yang, Z., Myers, E. P., Wong, A. M., and White, S. A. (2008). *VDatum for Chesapeake Bay, Delaware Bay and Adjacent Coastal Water Areas: Tidal datums and Sea Surface Topography*, NOAA Tech. Rep. NOS CS 15. Silver Spring, Md: National Oceanic and Atmospheric Administration, 110.
- Yang, Z., Wang, T., Branch, R., Xiao, Z., and Deb, M. (2021). Tidal stream energy resource characterization in the Salish Sea. *Renewable Energy* 172, 188–208. doi: 10.1016/j.renene.2021.03.028
- Yang, Z., Wang, T., Leung, R., Hibbard, K., Janetos, T., Kraucunas, I., et al. (2014). A modeling study of coastal inundation induced by storm surge, sea-level rise, and subsidence in the Gulf of Mexico. *Nat. Hazards* 71, 1771–1794. doi: 10.1007/s11069-013-0974-6
- Ye, F., Zhang, Y. J., Yu, H., Sun, W., Moghimi, S., Myers, E., et al. (2020). Simulating storm surge and compound flooding events with a creek-to-ocean model: Importance of baroclinic effects. *Ocean Model.* 145:101526. doi: 10.1016/j.oceomod.2019.101526
- Zhang, Y. J., Ye, F., Yu, H., Sun, W., Moghimi, S., Myers, E., et al. (2020). Simulating compound flooding events in a hurricane. *Ocean Dynamics* 70, 621–640. doi: 10.1007/s10236-020-01351-x
- Zheng, P., Li, M., Wang, C., Wolf, J., Chen, X., De Dominicis, M., et al. (2020). Tide-surge interaction in the pearl river estuary: a case study of typhoon hato. *Front. Mar. Sci.* 7:236. doi: 10.3389/fmars.2020.00236

**Conflict of Interest:** The authors declare that the research was conducted in the absence of any commercial or financial relationships that could be construed as a potential conflict of interest.

**Publisher’s Note:** All claims expressed in this article are solely those of the authors and do not necessarily represent those of their affiliated organizations, or those of the publisher, the editors and the reviewers. Any product that may be evaluated in this article, or claim that may be made by its manufacturer, is not guaranteed or endorsed by the publisher.

Copyright © 2021 Xiao, Yang, Wang, Sun, Wigmosta and Judi. This is an open-access article distributed under the terms of the Creative Commons Attribution License (CC BY). The use, distribution or reproduction in other forums is permitted, provided the original author(s) and the copyright owner(s) are credited and that the original publication in this journal is cited, in accordance with accepted academic practice. No use, distribution or reproduction is permitted which does not comply with these terms.



# Evaluation of Wave-Ice Parameterization Models in WAVEWATCH III® Along the Coastal Area of the Sea of Okhotsk During Winter

Shinsuke Iwasaki\* and Junichi Otsuka

Civil Engineering Research Institute for Cold Region, Public Works Research Institute, Sapporo, Japan

## OPEN ACCESS

### Edited by:

Giovanni Besio,  
University of Genoa, Italy

### Reviewed by:

Matjaz Licer,  
National Institute of Biology (NIB),  
Slovenia  
Hajime Mase,  
Kyoto University, Japan

### \*Correspondence:

Shinsuke Iwasaki  
iwasaki-s@ceri.go.jp

### Specialty section:

This article was submitted to  
Coastal Ocean Processes,  
a section of the journal  
Frontiers in Marine Science

**Received:** 24 May 2021

**Accepted:** 12 July 2021

**Published:** 06 August 2021

### Citation:

Iwasaki S and Otsuka J (2021)  
Evaluation of Wave-Ice  
Parameterization Models  
in WAVEWATCH III® Along  
the Coastal Area of the Sea  
of Okhotsk During Winter.  
*Front. Mar. Sci.* 8:713784.  
doi: 10.3389/fmars.2021.713784

Ocean surface waves tend to be attenuated by interaction with sea ice. In this study, six sea ice models in the third-generation wave model WAVEWATCH III® (WW3) were used to estimate wave fields over the Sea of Okhotsk (SO). The significant wave height ( $H_s$ ) and mean wave period ( $T_m$ ) derived from the models were evaluated with open ocean and ice-covered conditions, using SO coastal area buoy observations. The models were validated for a period of 3 years, 2008–2010. Additionally, the impact of sea ice on wave fields was demonstrated by model experiments with and without sea ice. In the open ocean condition, the root-mean square error (RMSE) and correlation coefficient for hourly  $H_s$  are 0.3 m and 0.92, and for hourly  $T_m$  0.97 s and 0.8. In contrast, for the ice-covered condition, the averaged RMSE and correlation coefficient from all models are 0.44 m (1.6 s) and 0.8 (0.6) for  $H_s$  ( $T_m$ ), respectively. Therefore, except for the bias, the accuracy of model results for the ice-covered condition is lower than for the open water condition. However, there is a significant difference between the six sea ice models. For  $H_s$ , the empirical formula whereby attenuation depends on the frequency relatively agrees with the buoy observation. For  $T_m$ , the empirical formula that is a function of  $H_s$  is better than those of other simulations. In addition, the simulations with sea ice drastically improved the wave field bias in coastal areas compared to the simulations without sea ice. Moreover, sea ice changed the monthly  $H_s$  ( $T_m$ ) by more than 1 m (3 s) in the northwestern part of the SO, which has a high ice concentration.

**Keywords:** ocean surface waves, sea ice, Sea of Okhotsk, wave model, WAVEWATCH III

## INTRODUCTION

The Sea of Okhotsk (SO) is a marginal ice zone (defined as the region of an ice cover that is affected by waves and swell penetrating into the ice from the open ocean) and is the southernmost sea with a seasonal ice cover in the Northern Hemisphere. Accurate forecasts of ocean surface waves in the SO are important for navigation planning of ocean transport because it can help identify hazardous areas and ensure safe shipping routes. In addition to its social importance, ocean waves in sea ice play a part in the interaction between sea ice, the ocean, and the atmosphere, and those

attenuations are key to the success of the sea ice-wave coupled model (Roach et al., 2019). In winter, sea ice rapidly extends southeastward from November to March before receding (Figures 1A–G). Sea ice suppresses the wave-wind interaction by reducing fetch. It also modifies the wave dispersion relation, and the wave energy is attenuated through a conservative scattering and non-conservative dissipation phenomenon (Squire, 2020). Although the extent of sea ice in the SO has a large interannual variability, its maximum value has been reported by the Japan Meteorological Agency (JMA) to be decreasing at a rate of 3.9 %/decade<sup>1</sup>. Therefore, it is of great concern that a decrease in sea ice in the SO will result in an increase in the height of ocean surface waves in the future.

(Wavewatch III Development Group (WW3DG), 2019), one of the most widely used third-generation spectral wave models based on the radiative transfer equation for global and regional wave forecasts, implements several parameterizations for wave-ice interaction. In deep water, when currents are absent, the evaluation of wind-generated ocean waves is governed by:

$$\frac{\partial N}{\partial t} + \nabla \cdot C_g N = \frac{S}{\sigma}, \quad (1)$$

where,  $N = E/\sigma$  is the wave action density spectrum, which is a function of the wave number ( $k$ ) or relative angular frequency ( $\sigma = 2\pi f$ ), direction ( $\theta$ ), space ( $x, y$ ), and time ( $t$ ),  $E$  is the wave energy spectral density,  $f$  is the frequency, and  $C_g$  is the group velocity. For the ice-covered region, the source term on the right-hand side of Eq. (1) is defined as follows:

$$S = (1 - C_i)(S_{in} + S_{ds}) + S_{nl} + C_i S_{ice}, \quad (2)$$

where,  $S_{in}$  is the input term by wind,  $S_{ds}$  is the dissipation term induced by wave breaking,  $S_{nl}$  is the nonlinear interaction term among spectral components,  $S_{ice}$  is the wave-ice interaction term, and  $C_i$  is the ice concentration. Both wind input and dissipation terms ( $S_{in}$  and  $S_{ds}$ ) are scaled by the open water fraction ( $1 - C_i$ ), whereas  $S_{ice}$  is scaled by the ice concentration. The effects of ice on ocean waves can be presented as a complex wavenumber  $k = k_r + ik_i$ , with the real part  $k_r$  representing the physical wave number related to the wave length and propagation speeds, producing effects analogous to shoaling and refraction by bathymetry, and the imaginary part  $k_i$  representing the exponential attenuation coefficient  $k_i = k_i(x, y, t, \sigma)$  which depends on the location, time, and radian frequency.  $k_i$  is introduced in the WW3 model as:

$$\frac{S_{ice}}{E} = -C_g \alpha = -2C_g k_i, \quad (3)$$

here,  $\alpha$  is the exponential attenuation rate for wave energy, which is twice that of the amplitude ( $\alpha = 2k_i$ ). The above equation (Eq. 3) is used to calculate the dissipation by ice in WW3, denoted as IC1–5 (except for IC0).

IC0 is based on Tolman (2003) and provides simple energy flux blocking depending on the local ice concentration. Thus, IC0 does not treat the effect as “dissipation” via the  $S_{ice}$  source

term. IC1 allows the user to provide an exponential attenuation rate of amplitude that is uniform in the frequency space (Rogers and Orzech, 2013). IC2 assumes dissipation by friction in the boundary layer below the ice cover (Liu and Mollo-Christensen, 1988). IC3 treats the ice cover as a linear viscoelastic layer based on the model by Wang and Shen (2010). IC4 was introduced by Collins and Rogers (2017) and provides the wave energy dissipation by one of several simple, empirical, and parametric forms through direct fitting with field data. IC4 is different from the other models and needs seven empirical formulas denoted as IC4M1–M7. In addition, IC5 uses a viscoelastic model based on Mosig et al. (2015).  $k_i$  is implemented for source functions in IC1–5. The estimation of  $k_r$  requires IC2, IC3, and IC5 to provide a new dispersion relation. Descriptions of these models are provided in **Supplementary Text 1**.

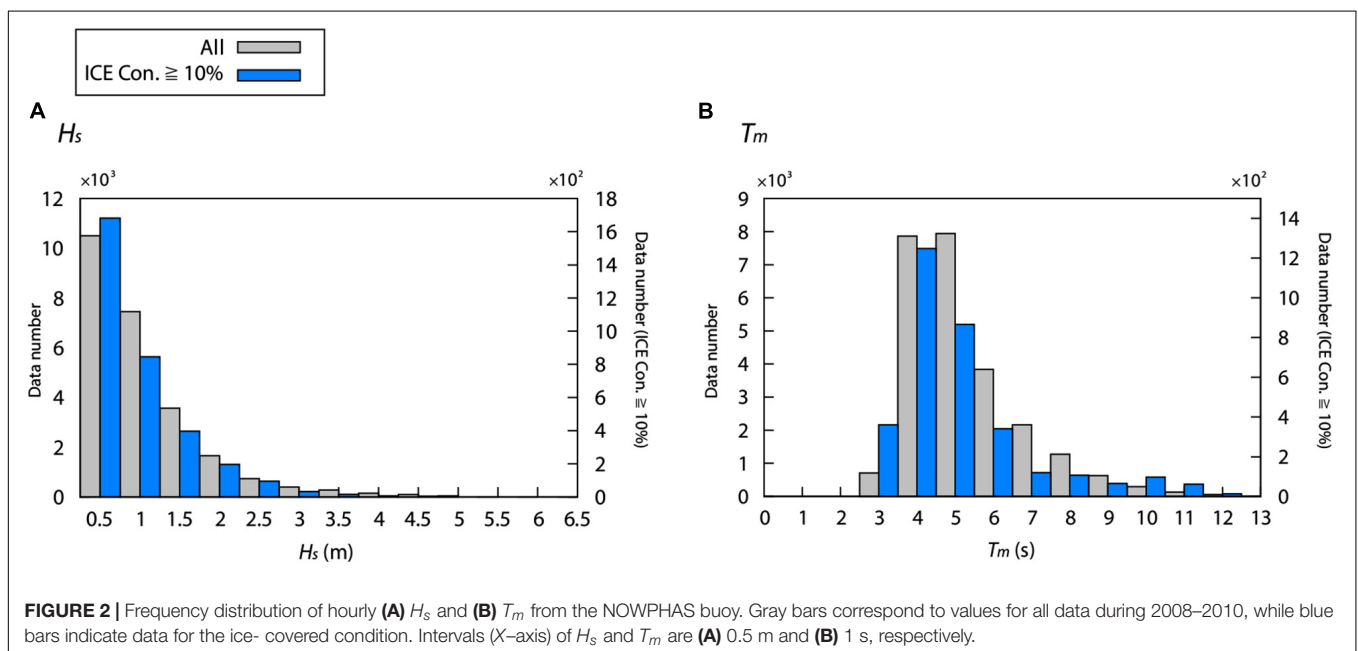
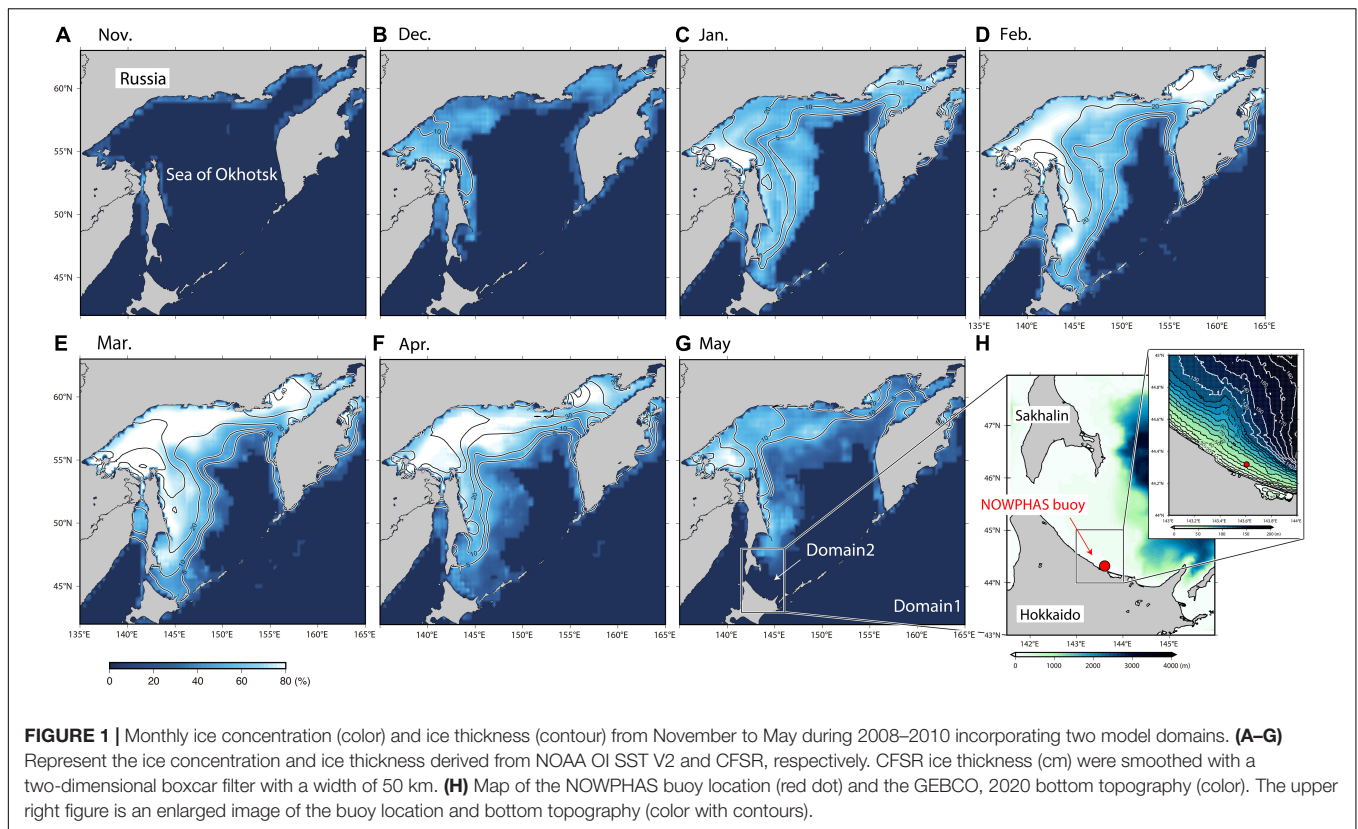
WW3 wave-ice parameterization models were applied in several recent studies on field observations from the Arctic Sea, in regions such as the Barents Sea, Chukchi Sea, and Beaufort Sea (e.g., Cheng et al., 2020; Liu et al., 2020; Nose et al., 2020). Nose et al. (2020) evaluated the uncertainty of wave-ice parameterization models, using three theoretical models (IC2, IC3, and IC5) and the field observations obtained during November in the Chukchi Sea. In addition, Liu et al. (2020) validated the performance of three wave-ice parameterization models (IC2, IC3, and IC4M1–M4) using the field observation from April to May in the Barents Sea. The results suggest that IC3 and IC4M2 corroborate the observations the most. Although sea ice is expected to have a significant impact on the wave fields, no studies have evaluated the effect of sea ice on the wave field in the SO. This study evaluates the wave fields derived from six wave-ice parameterization models (IC0–5 in WW3) using the buoy observations on the north coast of Hokkaido (see **Figure 1H**). In this study, the wave fields derived from the models were also evaluated for both open ocean and ice-covered conditions. Moreover, the impact of sea ice on wave fields using model simulations with and without sea ice was also clarified. This study had two advantages over previous studies. The first is the evaluation of a considerable number of six wave-ice parameterization models. Six empirical models for IC4 (IC4M1–M7 except for IC4M5) were also evaluated in this study. The second advantage is the use of time-rich observation data. The SO exhibits periods of open ocean and ice-covered conditions, and the buoy observation fully covers both periods (3 years in this study). Therefore, considering the accuracy of the modeled wave field, it can be reliably used to compare the open ocean and ice-covered conditions in the same region.

## MATERIALS AND METHODS

### Model Design

Two model domains were created using a nesting process for a horizontal resolution of 0.25° (domain 1) and 0.08° (domain 2) (**Figure 1G**). The outer domain (domain 1) covers the entire SO (42°–63°N, 135°–165°E). The inner domain (domain 2) was used to validate the wave fields in the coastal area (43°–48°N, 141.5°–146°E). The directional resolution was 10°, and the frequency

<sup>1</sup>[https://www.data.jma.go.jp/gmd/kaiyou/english/seaice\\_okhotsk/series\\_okhotsk\\_e.html](https://www.data.jma.go.jp/gmd/kaiyou/english/seaice_okhotsk/series_okhotsk_e.html)



range was 0.035–1.1 Hz, which was logarithmically discretized into 30 increments. GEBCO, 2020<sup>2</sup> was used to provide the bottom topography and coastlines.

<sup>2</sup>[https://www.gebco.net/data\\_and\\_products/gridded\\_bathymetry\\_data/gebco\\_2020](https://www.gebco.net/data_and_products/gridded_bathymetry_data/gebco_2020)

The simulation of domain 1 incorporated 6-hourly surface wind data from the 55-year JMA Reanalysis (JRA55) (Kobayashi et al., 2015). This product is approximately 55 km in latitude and longitude. In addition, the wind data for domain 2 were obtained from the JRA55 dynamic regional downscaling product (DSJRA55) (Kayaba et al., 2016) developed by JMA,

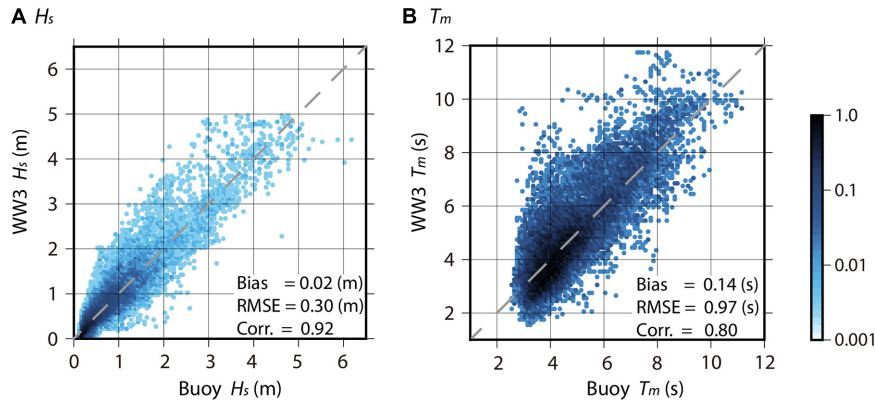


**FIGURE 3** | Scatter diagrams of **(A)**  $H_s$  and **(B)**  $T_m$  between the ST6 model simulation (Y-axis) versus buoy observation (X-axis) for the open water condition. Statistical values are shown in the lower left corner of both panels. In this comparison, we used values only when the ice concentration in the coastal area ( $44^\circ\text{--}46^\circ\text{N}$ ,  $142.5^\circ\text{--}145.5^\circ\text{E}$ ) around the buoy is 0%. IC1 modeled results are used in this figure. Colored shading indicates normalized data density on a  $\log_{10}$ -scale. The number of validation data points (hourly) was 19453. The gray broken line  $y = x$  is added to both panels.

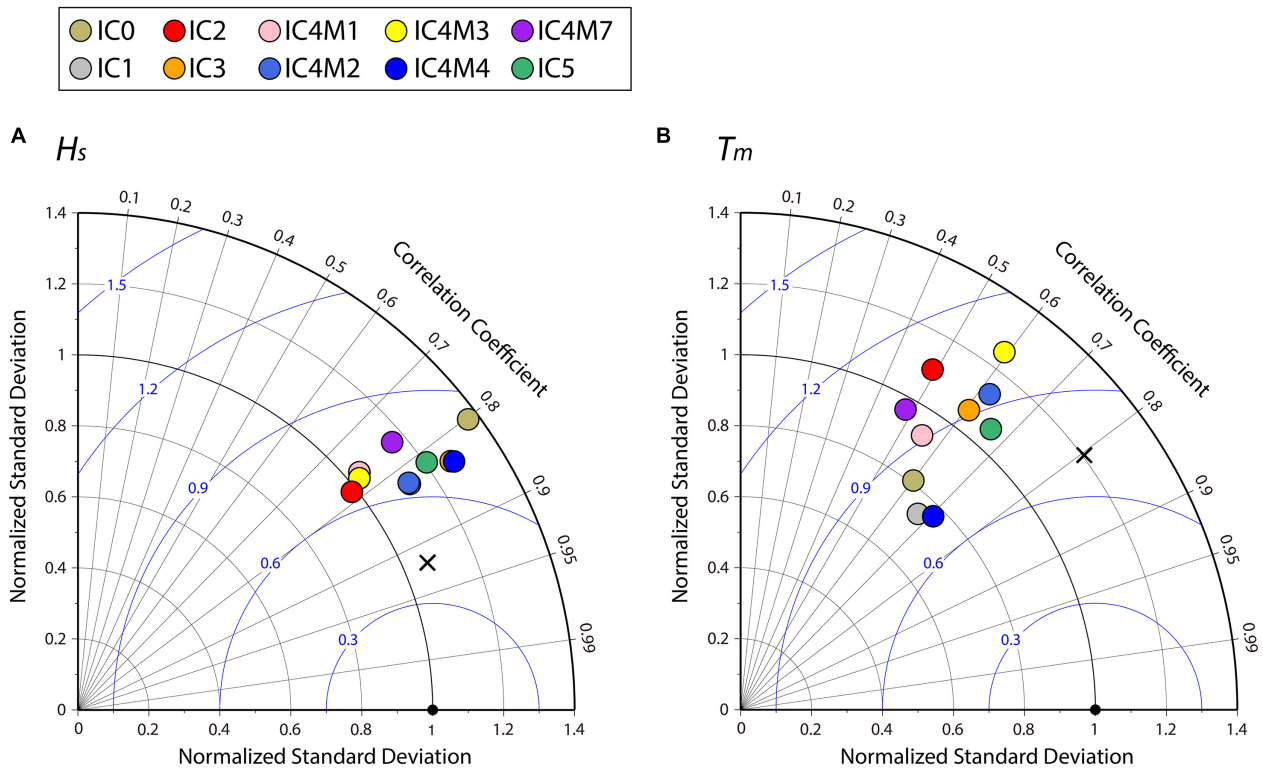


**FIGURE 4** | Taylor diagram summarizing the statistical comparison between the NOWPHAS buoy observation and the model simulations with ST6 for the ice-covered condition: **(A)**  $H_s$  and **(B)**  $T_m$ . The number of validation data points is 3277. The source terms of  $S_{ice}$  are represented by the different colored circles (legend in the upper region of the panel). The black cross shows the modeled results of IC1 simulation for the open water condition (i.e., results of **Figure 3**). The black circle at the bottom indicates the buoy observation. The blue colored contour with an interval of 0.3 denotes the RMSE between the simulations and observations. The RMSE and standard deviations have been normalized by the observed standard deviation. The correlation coefficients between both the fields are shown by the azimuthal position of the simulation field. Note that the position of IC1 (gray circle) overlaps that of IC4M2 (light blue circle) in the left figure.

which has a spatial resolution of 5 km and a temporal resolution of 1 h. Daily ice concentration was obtained from NOAA Optimum Interpolation (OI) sea surface temperature (SST) version 2 high-resolution dataset with a  $0.25^\circ \times 0.25^\circ$  spatial

grid (Reynolds et al., 2007). Ice thickness was incorporated from the Climate Forecast System Reanalysis (CFSR) produced by the National Centers for Environmental Prediction (NCEP) (Saha et al., 2010). The CFSR product has a spatial resolution

**TABLE 1** | Statistical values of  $H_s$  and  $T_m$  between the ST6 model simulations and buoy observations for the ice-covered condition.

	IC0	IC1	IC2	IC3	IC4M1	IC4M2	IC4M3	IC4M4	IC4M7	IC5
<b><math>H_s</math></b>										
bias (m)	0.47	0.10	<b>0.01</b>	0.25	-0.07	<b>0.03</b>	<b>-0.06</b>	0.29	0.10	0.17
RMSE (m)	0.51	<b>0.40</b>	<b>0.41</b>	0.44	0.44	<b>0.40</b>	0.43	0.44	0.47	0.43
Corr.	0.80	<b>0.83</b>	0.78	<b>0.83</b>	0.76	0.82	0.77	<b>0.83</b>	0.76	0.83
<b><math>T_m</math></b>										
Bias (s)	0.82	-0.42	<b>0.22</b>	0.61	-0.97	<b>-0.02</b>	-0.51	0.26	-0.40	<b>0.09</b>
RMSE (s)	<b>1.47</b>	<b>1.33</b>	1.89	1.63	1.63	1.67	1.85	<b>1.27</b>	1.78	1.50
Corr.	0.60	<b>0.67</b>	0.49	0.61	0.55	0.62	0.59	<b>0.71</b>	0.48	<b>0.67</b>

The top three relatively accurate values in the ten model simulations are shown in bold. The number of validation data points is 3277.

of  $0.25^\circ$  at the equator, extending to a global  $0.5^\circ$  beyond the tropics, with a temporal resolution of 6 h. The wind, ice concentration, and thickness data were linearly interpolated to the same spatial grid in the wave simulation of both domains. On the north coast of Hokkaido, a southeastward Soya warm current exists along the coast throughout the year. However, this study does not include the influence of ocean currents in model simulation because the strength of the ocean current fluctuates seasonally, and is weak during winter (Ohshima et al., 2017) which is the focal season of this study. In addition, the buoy observation is located in deep water (see section “Buoy Observation” for observation depth), and the effect of tides is also not considered for our model simulation.

In this study, six models for  $S_{ice}$ , IC0, IC1, IC2, IC3, IC4, and IC5 were used (see **Supplementary Text 1**). In addition, in order to investigate the impact of sea ice on the wave field, simulations that did not incorporate ice concentration were conducted. Hereinafter, the model results without ice concentration are denoted as “Non-ICE.” As shown in **Supplementary Table 1**, the kinematic viscosity ( $\nu$ ) is required for IC2, and the  $\nu$  and the effective shear modulus ( $G$ ) are required for IC3 and IC5 as input parameters. Some theoretical ice parameters ( $\nu$  and  $G$ ) for the theoretical models (IC2, IC3, and IC5) have been proposed by previous studies (see **Supplementary Table 1**). In this study, three, four, and two simulation cases were conducted for IC2, IC3, and IC5, respectively, using the theoretical ice parameters summarized in **Supplementary Table 1**. In addition, various parameters have also been proposed for the binomial fitting of IC4M2 and the step function of IC4M6 based on different observational data (**Supplementary Tables 2, 3**). Therefore, eight and six simulation cases were performed for IC4M2 and IC4M6, respectively. Although IC4M5 and IC4M6 both provide a step function in the frequency space, IC4M6 has more steps than IC4M5. Therefore, IC4M5 was excluded from validation in this study. A simple diffusive scattering model (denoted as IS1 in WW3) was used for these simulations. Another scattering model (denoted as IS2) was implemented in WW3. However, the difference between the scattering models (i.e., IS1 and IS2) was small compared to the difference between the dissipation models (IC0–IC5) (not shown). For terms  $S_{in}$  and  $S_{ds}$ , we used both ST4 (Ardhuin et al., 2010; Raschle and Ardhuin, 2013) and ST6 (Rogers et al., 2012; Zieger et al., 2015; Liu et al., 2019).

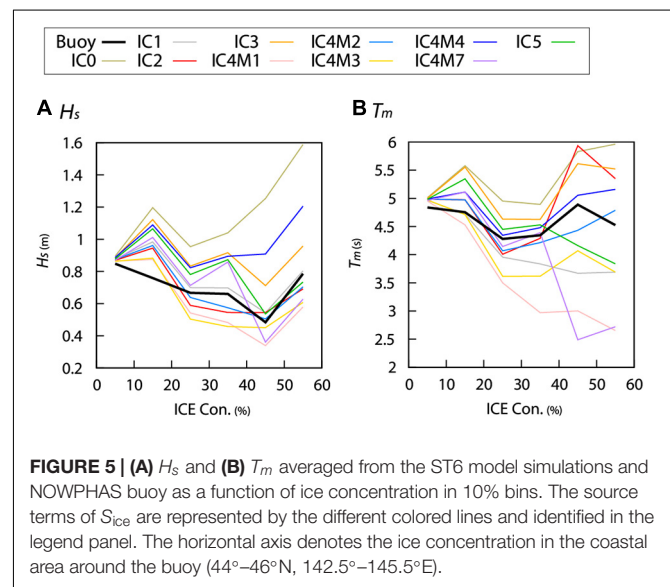


**FIGURE 5** | (A)  $H_s$  and (B)  $T_m$  averaged from the ST6 model simulations and NOWPHAS buoy as a function of ice concentration in 10% bins. The source terms of  $S_{ice}$  are represented by the different colored lines and identified in the legend panel. The horizontal axis denotes the ice concentration in the coastal area around the buoy ( $44^\circ$ – $46^\circ$ N,  $142.5^\circ$ – $145.5^\circ$ E).

In this study, the model results with ST6 are presented in the main text, while the model results with ST4 are presented in **Supplementary Material**.

All simulations were performed over a 3-year period from 2008 to 2010. The significant wave height ( $H_s$ ) and mean wave period ( $T_{m01}$ ) were both recorded every hour during the computation period. To simplify the notation,  $T_{m01}$  is denoted as  $T_m$ . To obtain the modeled value at the buoy position, we bilinearly interpolated the fields to the buoy position using the surrounding four grid values from domain 2.

## Buoy Observation

To validate the model results of the wave field, we used buoy observation data from the Nationwide Ocean Wave Information Network for Ports and Harbors (NOWPHAS)<sup>3</sup>, provided by the Ports and Harbors Bureau, Ministry of Land, Infrastructure, Transport, and Tourism (MLIT). Significant wave height and mean wave period data obtained every 20 min were used for the observation depth of 52.6 m in the Monbetsu (south) Station (red dot in **Figure 1H**). The distance from the coast

<sup>3</sup>[http://www.mlit.go.jp/kowan/nowphas/index\\_eng.html](http://www.mlit.go.jp/kowan/nowphas/index_eng.html)

of the buoy is 8,200 m. Buoy data for 3 years, from 2008 to 2010, were used, same as the modeling period. In the present study, the observation data were averaged from 20 min to 1 h and compared with the simulation results. **Figure 2** shows the frequency distribution of  $H_s$  and  $T_m$  observed by the buoy during 2008–2010. The averages for  $H_s$  and  $T_m$  are 0.83 m and 4.80 s, respectively (gray bars in **Figure 2**). The total number of hourly observation data points was 24909. In the present study, to evaluate the model simulations for the ice-covered condition, we utilized values only when the ice concentration in the coastal area ( $44^\circ$ – $46^\circ$ N,  $142.5^\circ$ – $145.5^\circ$ E) around the buoy was 10% or more. The number of observation data points was 3277 for the ice-covered condition (blue bars in **Figure 2**). The number of data points for the ice-covered conditions is significantly reduced compared to that for all data but it covers the entire observation area (**Figure 2**).

The sea ice in the SO is a one-year ice type and is thinner than that of the Arctic Sea (e.g., Nihashi et al., 2018). Although different from the buoy observation points of this study, the floe size of sea ice up to 5 m accounts for 90% of the total in the northeastern coast of Hokkaido (Kioka et al., 2020).

## RESULTS

### Validation With Buoy

The wave fields for the open water condition were evaluated before comparing them with the wave fields for the ice-covered condition. **Figure 3** shows the scatter diagrams for the open water condition for the model simulation and the buoy observation. The bias, RMSE, and correlation coefficient for  $H_s$  were 0.02, 0.3, and 0.92 m, and for  $T_m$  were 0.14, 0.97, and 0.8 s, respectively. The model results are in close agreement with the buoy observations, and are consistent with the results of a previous study (e.g., Shimura and Mori, 2019). This comparison shows the model results of IC1 because there is no significant difference between the other six models (IC0–5) in the open water condition (not shown). The ST4 model simulation was also calculated with close accuracy to the ST6 model simulation (see **Supplementary Figure 1**).

As shown in **Supplementary Tables 1–3**, previous studies have proposed various parameters for the three theoretical models (IC2, IC3, and IC5), and two empirical models (IC4M2 and IC4M6). Therefore, these five models are evaluated prior to the comparison between the six wave–ice parameterization models. There are no remarkable differences in IC2 depending on the theoretical parameter, but there are significant differences in IC3 and IC5 (see **Supplementary Table 4** for IC2, **Supplementary Table 5** for IC3, and **Supplementary Table 6** for IC5). Hereafter, IC2 is the simulation result of using  $\nu$  by Liu et al. (1991), and the results are almost the same (**Supplementary Table 4**). In addition, IC3 and IC5 are the model results based on  $\nu$  by Liu et al. (2020) and  $G$  by Mosig et al. (2015), and these results demonstrated relatively better accuracy (see **Supplementary Tables 5, 6**). The empirical parameter of Meylan et al. (2014) was employed for IC4M2 because the model results mostly agree with buoy observations (**Supplementary Table 7**). The results of

IC4M6 are not presented here as it can be almost reproduced by the binomial fitting of IC4M2 (see **Supplementary Tables 7, 8**).

To visualize the standard deviation (STD), root mean square error (RMSE), and correlation coefficient between the model simulations and NOWPHAS buoy data, **Figure 4** displays Taylor diagrams between the two fields (Taylor, 2001). In addition, **Table 1** lists the statistical analysis results between the model simulation and buoy observations for  $H_s$  and  $T_m$ . Additionally, **Supplementary Figures 2, 3** display the scatter diagrams for the model simulations and the buoy observations for  $H_s$  ( $T_m$ ). The model accuracies for the ice-covered condition are lower than that for the open water condition except for bias, regardless of the six wave–ice parameterization models (**Figures 3, 4** and **Table 1**). The averaged RMSE and correlation coefficient from all models for the ice-covered condition are 0.44 m and 0.8, for  $H_s$ , respectively, and 1.6 s and 0.6, respectively, for  $T_m$ , respectively. The RMSE and correlation coefficient of  $H_s$  ( $T_m$ ) for the ice-covered condition are 0.14 m and 0.12 (0.63 s and 0.2) and are less accurate compared with those for the open water condition.

For  $H_s$ , all model simulations indicate a correlation coefficient greater than 0.75, a normalized STD between 0.99 and 1.4, and a normalized RMSE (NRMSE) and RMSE of less than 0.83 and 0.52 m, respectively (**Figure 4A**, **Supplementary Figure 2**, and **Table 1**). The bias for all  $H_s$  simulation was within  $\pm 0.3$  m except for IC0 (**Table 1**). In particular, the bias of IC2 and IC4M2 were within 0.03 m, which were simulated with high accuracy (**Table 1**). In addition, the RMSE and the correlation coefficients of IC1 and IC4M2 were 0.4 m and  $>0.81$ , respectively, and were better than those of other simulations (**Table 1**), although the normalized STD of both simulations is slightly overestimated as presented in **Figure 4A**. In contrast, the bias, NRMSE, and RMSE of IC0 were 0.47, 0.82, and 0.51 m, respectively, and were poorly estimated as compared with other simulations (**Figure 4A**, **Supplementary Figure 2**, and **Table 1**).

Overall, for  $T_m$ , all simulations provided corresponding correlation coefficients of less than 0.72, which was relatively worse than those of  $H_s$ , same as the open water condition (**Figure 4B**, **Supplementary Figure 3**, and **Table 1**). In addition, the differences in the statistical values between simulations were large compared to those of  $H_s$  (**Figure 4** and **Table 1**). IC2, IC4M1, IC4M3, and IC4M7 provided poor simulation results, as their RMSE and correlation coefficients for  $T_m$  were greater than 1.62 s and less than 0.6, respectively (**Figure 4B**, **Supplementary Figure 3**, and **Table 1**). In contrast, IC1 and IC4M4 yielded simulations with least amount of error and indicated a NRMSE (RMSE) less than 0.75 (1.34 s) and a correlation coefficient of greater than 0.66, although the normalized STDs for both simulations were less than 0.8 and tend to be underestimated (**Figure 4B**, **Supplementary Figure 3**, and **Table 1**). Moreover, the bias for IC4M2 and IC5 was  $\pm 0.1$  s, smaller than those of other simulations (**Table 1**).

The statistical results, except as shown above for the bias, depend on the averaging interval. **Supplementary Table 9** lists the statistical values between the model simulation and buoy observations for the daily mean. The averaged RMSE for  $H_s$  and  $T_m$  from the all simulations is 0.38 m and 1.24 s, respectively. The correlation coefficient for  $H_s$  and  $T_m$  is 0.82 and 0.7, respectively.

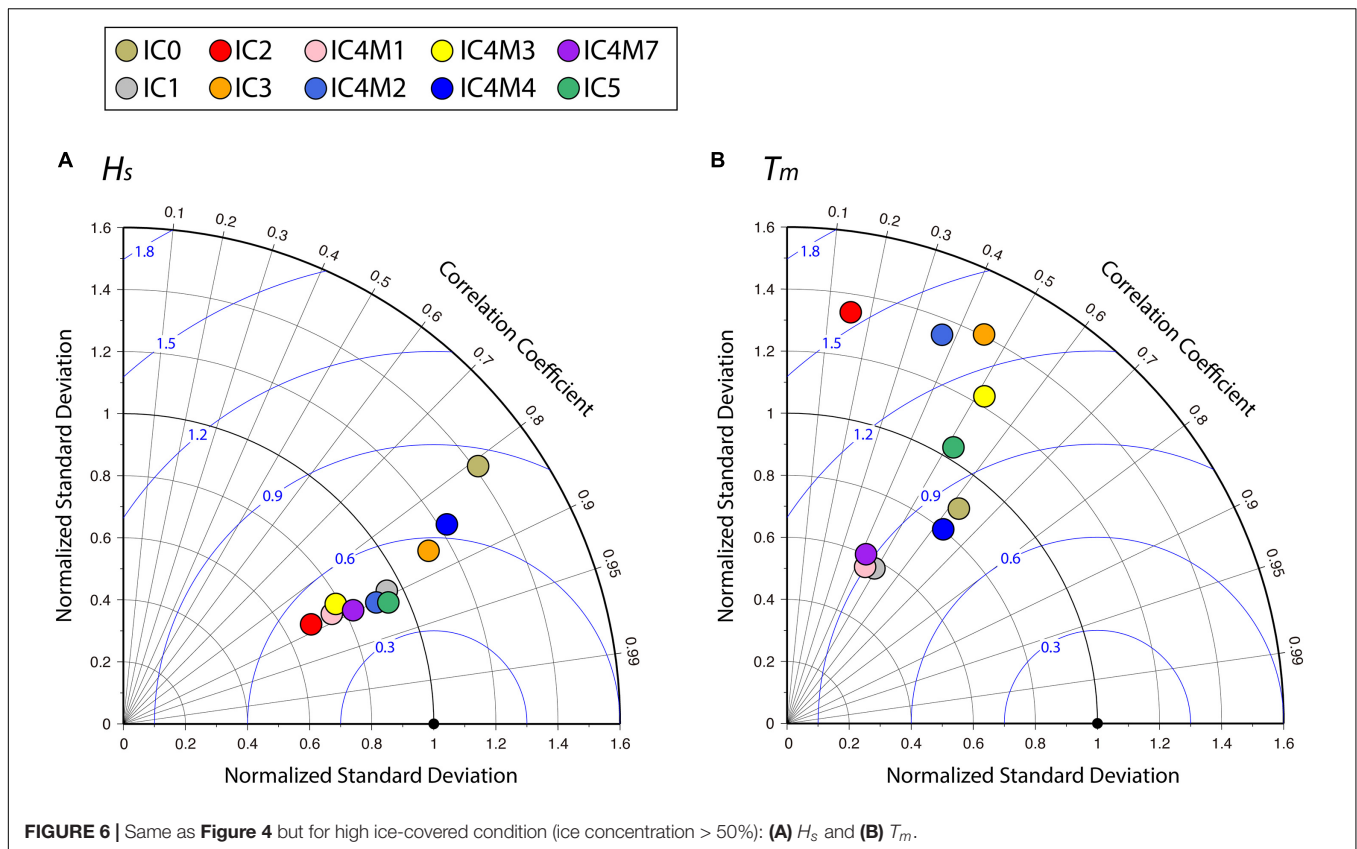


**TABLE 2 |** Same as **Table 1** but for the high ice-covered conditions (ice concentration > 50%).

	IC0	IC1	IC2	IC3	IC4M1	IC4M2	IC4M3	IC4M4	IC4M7	IC5
<b><math>H_s</math></b>										
bias (m)	0.7	<b>0.01</b>	-0.1	0.14	-0.19	<b>-0.09</b>	-0.17	0.36	-0.15	<b>-0.06</b>
RMSE (m)	0.71	<b>0.38</b>	0.43	0.47	0.41	<b>0.36</b>	0.42	0.54	<b>0.38</b>	<b>0.35</b>
Corr.	0.81	0.89	0.88	0.87	0.88	<b>0.9</b>	0.87	0.85	<b>0.9</b>	<b>0.91</b>
<b><math>T_m</math></b>										
Bias (s)	1.28	-0.79	0.71	0.86	-1.74	<b>0.16</b>	-0.81	<b>0.54</b>	-1.67	<b>-0.69</b>
RMSE (s)	<b>1.4</b>	<b>1.49</b>	2.63	2.22	1.54	2.29	1.9	<b>1.36</b>	1.57	1.71
Corr.	<b>0.62</b>	0.49	0.15	0.45	0.45	0.37	<b>0.52</b>	<b>0.63</b>	0.42	<b>0.52</b>

The number of validation data points is 512. The top three relatively accurate values in the ten model simulations are shown in bold.

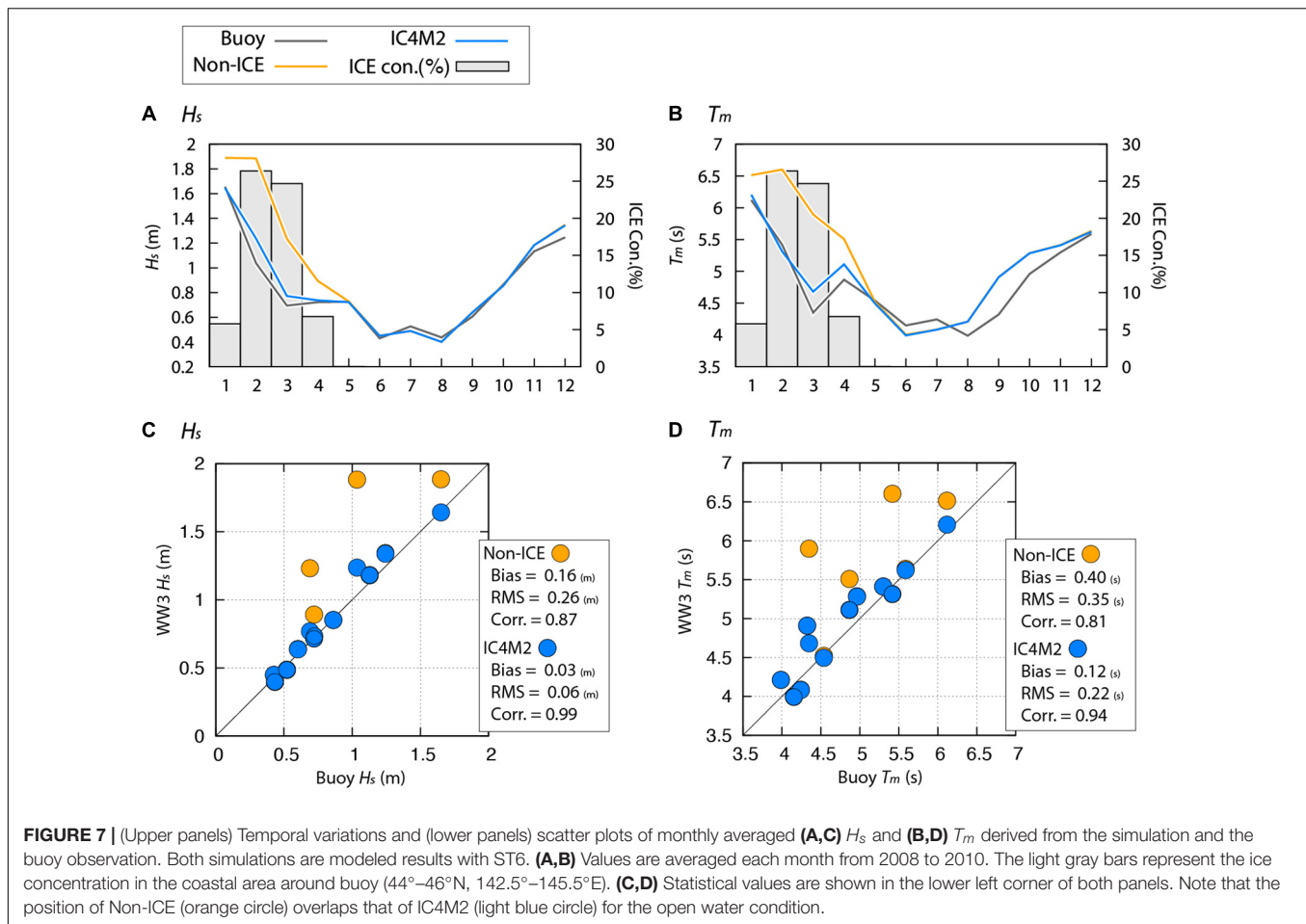
Compared with those for hourly data, the RMSE and correlation coefficient of  $H_s$  ( $T_m$ ) are 0.06 m and 0.02 (0.36 s and 0.1) more accurate, respectively.

Moreover, we validated the model simulations as a function of ice concentration (**Figure 5**). All  $H_s$  simulations were overestimated at low ice concentrations ( $C_i < 20\%$ ) (**Figure 5A**). At high ice concentrations ( $C_i > 20\%$ ), the trend was dependent on the simulation (**Figure 5A**). IC0, IC3, and IC4M4 overestimated, while IC4M1 and IC4M3 tended to underestimate (**Figure 5A**). IC1 and IC4M2 were relatively close to the buoy observations and were simulated with high accuracy, consistent with the comparison results shown in **Figure 4A** and **Table 1**. For  $T_m$ , differences between the simulations became remarkable as the ice concentration increased (**Figure 5B**). IC4M2, IC4M4, and

IC5 were in good agreement with the observations (**Figure 5B**). IC1, IC4M1, IC4M3, and IC4M7 underestimated, especially for IC4M1 and IC4M7 at  $C_i > 40\%$  (**Figure 5B**). On the other hand, the  $T_m$  of IC0 and IC3 were overestimated, regardless of ice concentration (**Figure 5B**).

As described in section “Materials and Methods,” we also evaluated six dissipation models (IC0–IC5) with ST4 (**Supplementary Figures 4, 5** and **Supplementary Table 10**). Overall, there were no significant differences in the wave fields between ST4 and ST6 in the buoy location (**Supplementary Figures 4, 5** and **Supplementary Table 10**). However, the normalized STD for  $H_s$  with ST4 was remarkably reduced (approximately 0.15) compared with that of ST6 (**Supplementary Figure 4A**). When examined as a function of ice concentration,





$H_s$  and  $T_m$  with ST4 were slightly smaller than those with ST6, but the trend in both simulations remained the same (**Supplementary Figure 5**).

As shown in **Figure 5**, the differences between the simulations became significant at high ice concentrations, especially for  $T_m$ . **Figure 6** and **Table 2** show the comparison results between the model simulations and the buoy observations for the high ice-covered condition (ice concentration > 50%). For  $H_s$ , IC1 and IC4M2 were relatively agreed with the buoy observations, similar to their comparison results for the ice-covered condition (ice concentration > 10%) shown in **Table 1**. In addition, the bias, RMSE, and correlation coefficient of IC5 for  $H_s$  were  $-0.06$ ,  $0.35$ , and  $0.91$  m, respectively, and were also close to those of IC1 and IC4M2 simulations (**Figure 6A** and **Table 2**). For  $T_m$ , overall, the qualitative results in **Table 2** were similar to the results shown in **Table 1**, except for quantitative values. IC4M4 results were better than those of other simulations (**Table 2**). Moreover, IC5 results mostly agree with the observations, compared with the other two theoretical models (IC2 and IC3) (**Figure 6B**).

## Sea Ice Impact for Wave Field

To evaluate the impact of sea ice on ocean waves in the SO, we compared the non-ICE simulations and IC4M2, which are relatively accurate, especially in  $H_s$ . **Figure 7** shows time series

and scatter plot of the monthly averaged  $H_s$  and  $T_m$  for the simulation and observation at the buoy position. In general, large  $H_s$  and  $T_m$  were observed in the coastal areas of Hokkaido during winter (**Figures 7A,B**). Interestingly, IC4M2 simulations remarkably mitigated the overestimation of  $H_s$  and  $T_m$  for non-ICE simulations from January to April, when sea ice existed (i.e., ice concentration is not 0%) (**Figures 7A,B**). In addition, the improvement of  $H_s$  and  $T_m$  for IC4M2 is confirmed from the statistical values (**Figures 7C,D**).

**Figure 8** shows the spatial distribution of averaged  $H_s$  and  $T_m$  in February from IC4M2, and the differences between IC4M2 and non-ICE. As expected, the wave fields were strongly dependent on the sea ice field, and  $H_s$  ( $T_m$ ) became smaller (larger) as the ice concentration increased (**Figures 8A,B**). The difference in  $H_s$  ( $T_m$ ) between IC4M2 and non-ICE is greater (less) than 1 m (3 s) at high ice concentrations ( $C_i > 70\%$ ) (**Figures 8C,D**).

## DISCUSSION

As shown in section “Materials and Methods,” various coefficients have been proposed for the binomial fitting of IC4M2 based on different observational data (**Supplementary Table 2**). In the eight simulation results of IC4M2, the biases of IC4M6H1, WA3

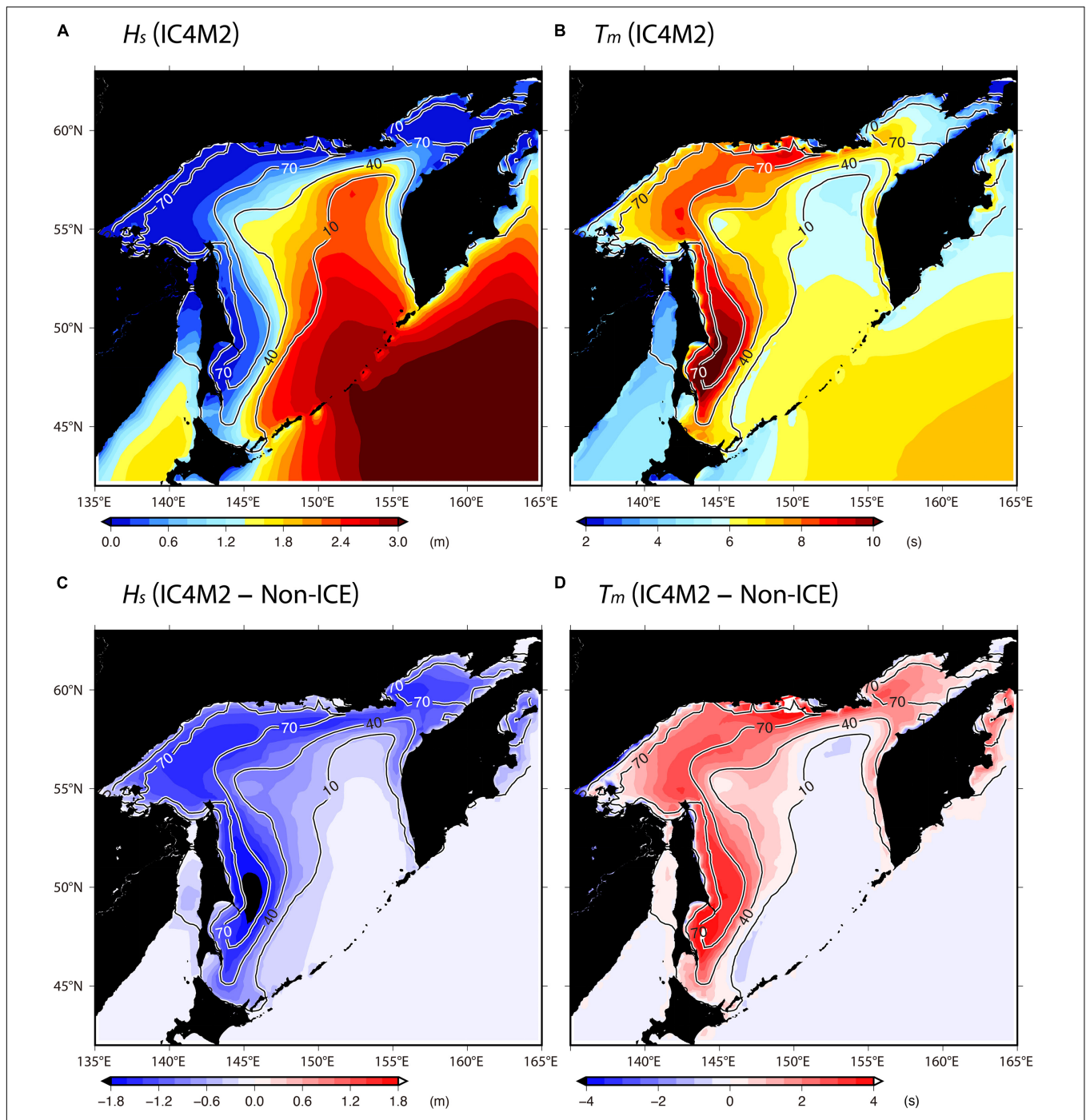
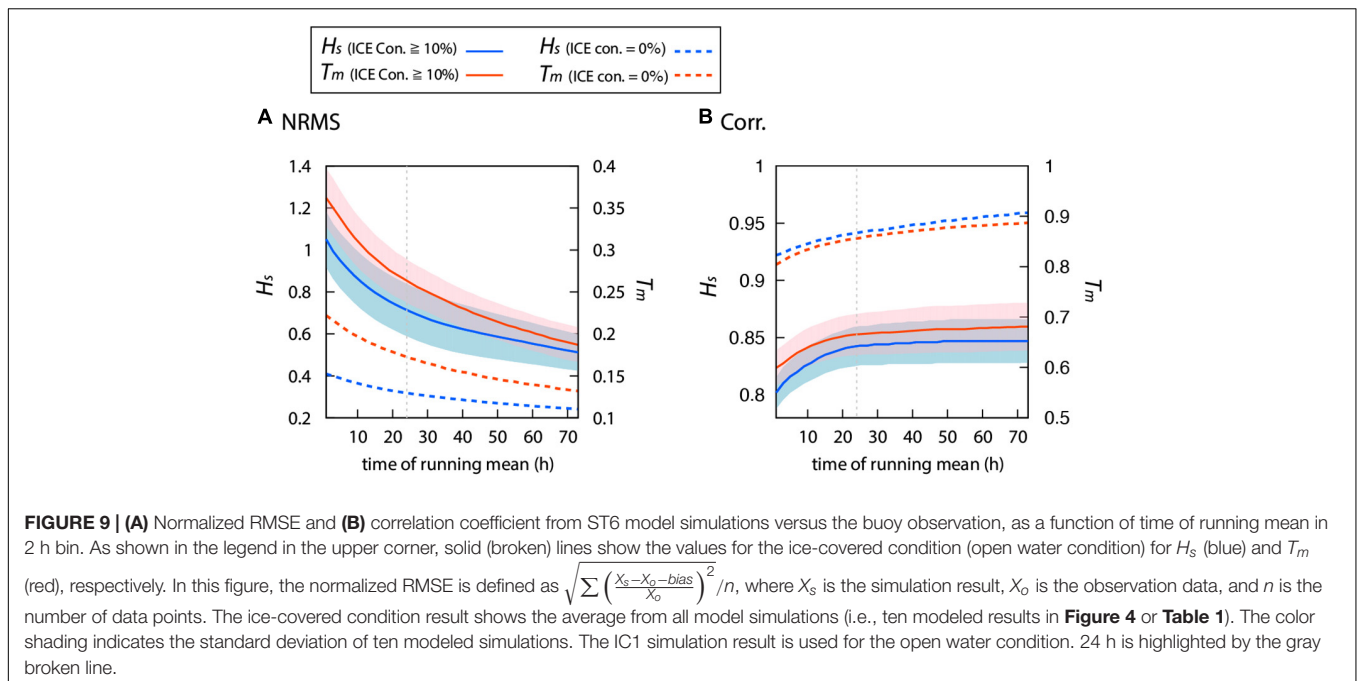


**FIGURE 8 |** Averaged field (color) of (A)  $H_s$  and (B)  $T_m$  computed by IC4M2 in February during 2008–2010; difference (color) between IC4M2 and Non-ICE simulations; (C)  $H_s$ ; (D)  $T_m$ . Both simulations are modeled results with ST6. Spatial smoothing using a box filter of horizontal scale 50 km was performed for the ice concentration (contour) (%). In this figure, we used the model results from domain 1.

UK, and WA3 NIWA were greater than 0.15 m (0.43 s) for  $H_s$  ( $T_m$ ) and were larger than the other simulations (Supplementary Table 7). In fact, the attenuation rates of IC4M6H1, WA3 UK, and WA3 NIWA were lower (Supplementary Figure 6). In addition, we validated that the accuracy of IC4M1, IC4M3, and IC4M7 was poor (especially in  $T_m$ ), and the attenuation rate

was significantly different from that of IC4M2 (Supplementary Figure 7). This is probably because the sea ice conditions based on these parameterizations are different from those of the SO. The sea ice thickness is less than 10 cm in the coastal area of Hokkaido (Figure 1). As mentioned in the previous section, 90% of the floe size of sea ice is within 5 m in the



coastal area of Hokkaido. In contrast, IC4M1 uses field data with sea ice floe sizes ranging from 20 to 30 m. In addition, IC4M3 is based on an ice thickness between 0.5 and 3 m, which is much thicker than the ice conditions in this study. Moreover, IC4M7 is based on observations of only the pancake ice region, although both pancake and frazil ice may exist in the SO. On the other hand, IC4M2 was in good agreement with observations for  $H_s$ , and IC4M4 was relatively close to the observations for  $T_m$ . The IC4M2 (i.e., Meylan et al., 2014) and IC4M4 were based on parameterization data from the same field observation in the Antarctic Sea with ice thickness ranging from 0.5 to 1 m; its ice conditions are relatively close to those of SO. The empirical formula of IC4M4 (Kohout et al., 2014) assumes the attenuation is a function of only  $H_s$  as shown in **Supplementary Text 1**. Recently, Kohout et al. (2020) suggested attenuation considers wave period and ice concentration in addition to  $H_s$ , based on the observation with < 0.5 m ice thickness in the Antarctic Sea. In the future, implementation of this model in WW3 is expected to further improve the accuracy of simulation in thin ice thickness areas such as SO.

Although the simulations of IC5 were relatively worse compared with those of the accurate empirical model (IC4M2 for  $H_s$ , and IC4M4 for  $T_m$ ), IC5 were better than those of two theoretical models (IC2 and IC3), especially for the high ice-covered condition (ice concentration > 50%). The results of these models remarkably depend theoretical parameters ( $v$  for IC2, and  $v$  and  $G$  for IC3 and IC5), as shown in **Supplementary Tables 4–6** (especially in IC3 and IC5). In this study, constant theoretical parameters were used for IC2, IC3, and IC5. However, these parameters are affected by the ice conditions (e.g., Cheng et al., 2017); thus, these are likely changing both spatially and temporally in the real ocean. Theoretical models have the

potential to further improve accuracy in the future, although it is not possible to know the specific types or floe sizes of ice in the entire SO. In other words, the simulation of wave fields under ice-covered conditions depends the accuracy of sea ice used as a model forcing in addition to the accuracy of the model itself, as shown below.

Recently, Nose et al. (2020) revealed that the uncertainty between ice concentration products is greater than the uncertainty between theoretical models (IC2, IC3, and IC5). Thus, it should be noted that our results depend not only on the parameterization for source terms such as  $S_{in}$ ,  $S_{ds}$ , and  $S_{ice}$ , but also on the ice concentration used as forcing. In fact, the results of this study are significantly dependent on the temporal resolution of the ice concentration. For example, **Figure 9** shows the statistical analysis results for  $H_s$  and  $T_m$  as functions of the interval of time averaging. As shown in **Supplementary Table 9**, the NRMS (correlation coefficient) decreases (increases) as the interval of time averaging increases (**Figure 9**). However, up to approximately 24 h, the rate of change of NRMS and the correlation for both wave fields with the ice condition are larger than those for the open water condition. This is probably due to the daily (24 h) ice concentration used in this study. In addition, the theoretical models IC2, IC3, and IC5 also depend on the ice thickness. Moreover, differences in wind data may also be one cause of uncertainty in wave fields.

## CONCLUSION

In this study, we evaluated six WW3 wave–ice parameterization models (IC0–IC5) using buoy observations located in the southern part of the Sea of Okhotsk for 3 years from 2008

to 2010. In this comparison,  $H_s$  and  $T_m$  from the model were evaluated with open ocean and ice-covered conditions. Overall, the accuracy of model results for the ice-covered condition is lower compared to the open water condition, except for the bias. However, in the ice-covered condition, IC4M2 appears to relatively agree with buoy observations for  $H_s$ , and IC4M4 is closest to the observations for  $T_m$ . We also clarified the impact of sea ice on wave fields in the SO. In the coastal areas, the simulation with sea ice drastically improved the bias of the wave fields ( $H_s$  and  $T_m$ ) compared to that without the simulation without sea ice. In addition, the difference between the simulations with and without sea ice is more than 1 m (3 s) for the monthly mean  $H_s$  ( $T_m$ ). The results of the present study can help researchers and engineers perform calculations of wave fields in the Sea of Okhotsk.

## DATA AVAILABILITY STATEMENT

The original contributions presented in the study are included in the article/**Supplementary Material**, further inquiries can be directed to the corresponding author.

## REFERENCES

- Ardhuin, F., Rogers, E., Babanin, A. V., Filipot, J. F., Magne, R., Roland, A., et al. (2010). Semiempirical dissipation source functions for ocean waves. Part I: definition, calibration, and validation. *J. Phys. Oceanogr.* 40, 1917–1941. doi: 10.1175/2010jpo4324.1
- Cheng, S., Rogers, W. E., Thomson, J., Smith, M., Doble, M. J., Wadhams, P., et al. (2017). Calibrating a viscoelastic sea ice model for wave propagation in the arctic fall marginal ice zone. *J. Geophys. Res. Oceans* 122, 8770–8793. doi: 10.1002/2017JC013275
- Cheng, S., Stopa, J., Ardhuin, F., and Shen, H. H. (2020). Spectral attenuation of ocean waves in pack ice and its application in calibrating viscoelastic wave-in-ice models. *Cryosphere* 14, 2053–2069. doi: 10.5194/tc-14-2053-2020
- Collins, C. O., and Rogers, W. E. (2017). *A Source Term for Wave Attenuation by Sea Ice in WAVEWATCH III*, (Technical Memo. NRL/MR7320–17-9726). Washington, D.C.: Naval Research Laboratory.
- Kayaba, N., Yamada, T., Hayashi, S., Onogi, K., Kobayashi, S., Yoshimoto, K., et al. (2016). Dynamical regional downscaling using the JRA-55 (DSJRA-55). *SOLA* 12, 1–5. doi: 10.2151/sola.2016-001
- Kioka, S., Ishida, M., Hasegawa, T., Takeuchi, T., and Saeki, H. (2020). A study of sea ice floe distribution on Okhotsk sea coast of Hokkaido. *Proc. Civ. Eng. Ocean* 76, I\_905–I\_910. doi: 10.2208/jsceoe.76.2\_I\_905
- Kobayashi, S., Ota, Y., Harada, Y., Ebita, A., Moriya, M., Onoda, H., et al. (2015). The JRA-55 reanalysis: general specifications and basic characteristics. *J. Meteorol. Soc. Jpn. Ser. II* 93, 5–48. doi: 10.2151/jmsj.2015-001
- Kohout, A. L., Williams, M. J. M., Dean, S. M., and Meylan, M. H. (2014). Storm-induced sea-ice breakup and the implications for ice extent. *Nature* 509, 604–607. doi: 10.1038/nature13262
- Kohout, A. L., Smith, M., Roach, L. A., Williams, G., Montiel, F., Montiel, F., et al. (2020). Observations of exponential wave attenuation in Antarctic sea ice during the PIPERS campaign. *Ann. Glaciol.* 61, 196–209. doi: 10.1017/aog.2020.36
- Liu, A. K., Holt, B., and Vachon, P. W. (1991). Wave propagation in the marginal ice zone: model predictions and comparisons with buoy and synthetic aperture radar data. *J. Geophys. Res.* 96, 4605–4621. doi: 10.1029/90JC02267
- Liu, A. K., and Mollo-Christensen, E. (1988). Wave propagation in a solid ice pack. *J. Phys. Oceanogr.* 18, 1702–1712. doi: 10.1175/1520-0485(1988)018<1702:wpiasi>2.0.co;2
- Liu, D., Tsarau, A., Guan, C., and Shen, H. H. (2020). Comparison of ice and wind-wave in WAVEWATCH III in the Barents sea. *Cold Reg. Sci. Technol.* 172:103008. doi: 10.1016/j.coldregions.2020.103008
- Liu, Q., Rogers, W. E., Babanin, A. V., Young, I. R., Romero, L., Zieger, S., et al. (2019). Observation-based source terms in the third-generation wave model WAVEWATCH III: updates and verification. *J. Phys. Oceanogr.* 49, 489–517. doi: 10.1175/jpo-d-18-0137.1
- Meylan, M., Bennetts, L. G., and Kohout, A. L. (2014). In situ measurements and analysis of ocean waves in the Antarctic marginal ice zone. *Geophys. Res. Lett.* 41, 5046–5051. doi: 10.1002/2014GL060809
- Mosig, J. E. M., Montiel, F., and Squire, V. A. (2015). Comparison of viscoelastic-type models for ocean wave attenuation in ice-covered seas. *J. Geophys. Res.* 120, 6072–6090. doi: 10.1002/2015JC010881
- Nihashi, S., Kurtz, N. T., Markus, T., Oshima, K., Tateyama, K., and Toyota, T. (2018). Estimation of sea-ice thickness and volume in the Sea of Okhotsk based on ICESat data. *Ann. Glaciol.* 59, 1–11. doi: 10.1017/aog.2018.8
- Nose, T., Waseda, T., Kodaira, T., and Inoue, J. (2020). Satellite-retrieved sea ice concentration uncertainty and its effect on modelling wave evolution in marginal ice zones. *Cryosphere* 14, 2029–2052. doi: 10.5194/tc-14-2029-2020
- Ohshima, K. I., Simizu, D., Ebuchi, N., Morishima, S., and Kashiwase, H. (2017). Volume, heat, and salt transports through the Soya Strait and their seasonal and interannual variations. *J. Phys. Oceanogr.* 47, 999–1019. doi: 10.1175/jpo-d-16-0210.1
- Rasclé, N., and Ardhuin, F. (2013). A global wave parameter database for geophysical applications. Part 2: model validation with improved source term parameterization. *Ocean Model.* 70, 174–188. doi: 10.1016/j.ocemod.2012.12.001
- Reynolds, R. W., Smith, T. M., Liu, C., Chelton, D. B., Casey, K. S., and Schlax, M. G. (2007). Daily high-resolution-blended analyses for sea surface temperature. *J. Clim.* 20, 5473–5496. doi: 10.1175/2007jcli1824.1
- Roach, L. A., Bitz, C. M., Horvat, C., and Dean, S. M. (2019). Advances in modeling interactions between sea ice and ocean surface waves. *J. Adv. Model. Earth Syst.* 11, 4167–4181. doi: 10.1029/2019MS001836
- Rogers, W. E., Babanin, A. V., and Wang, D. W. (2012). Observation consistent input and whitecapping dissipation in a model for wind-generated surface waves: description and simple calculations. *J. Atmos. Ocean Technol.* 29, 1329–1346. doi: 10.1175/JTECH-D-11-00092.1

## AUTHOR CONTRIBUTIONS

SI and JO conceived and designed research. SI supervised the work, analyzed the observational data and model simulations, and wrote the manuscript. Both authors contributed to the article and approved the submitted version.

## ACKNOWLEDGMENTS

We express sincere gratitude to the members of Port and Coastal Research Team, Civil Engineering Research Institute for Cold Region (CERI), Japan, for administrative support. We thank two reviewers for their constructive and fruitful comments.

## SUPPLEMENTARY MATERIAL

The Supplementary Material for this article can be found online at: <https://www.frontiersin.org/articles/10.3389/fmars.2021.713784/full#supplementary-material>

- Rogers, W. E., and Orzech, M. D. (2013). *Implementation and Testing of Ice and Mud Source Functions in WAVEWATCH III*, (Technical Memo. NRL/MR7320-09-9193). Washington, D.C: Naval Research Laboratory.
- Saha, S., Moorthi, S., Pan, H. L., Wu, X., Wang, J., Nadiga, S., et al. (2010). The NCEP climate forecast system reanalysis. *Bull. Am. Meteorol. Soc.* 91, 1015–1058.
- Shimura, T., and Mori, N. (2019). High-resolution wave climate hindcast around Japan and its spectral representation. *Coast. Eng.* 151, 1–9. doi: 10.1016/j.coastaleng.2019.04.013
- Squire, V. A. (2020). Ocean wave interactions with sea ice: a reappraisal. *Annu. Rev. Fluid Mech.* 52, 37–60. doi: 10.1146/annurev-fluid-010719-060301
- Taylor, K. E. (2001). Summarizing multiple aspects of model performance in a single diagram. *J. Geophys. Res.* 106, 7183–7192. doi: 10.1029/2000JD900719
- Tolman, H. L. (2003). Treatment of unresolved islands and ice in wind wave models. *Ocean Model.* 5, 219–231. doi: 10.1016/S1463-5003(02)00040-9
- Wang, R., and Shen, H. H. (2010). Gravity waves propagation into an ice-covered ocean: a viscoelastic model. *J. Geophys. Res.* 115:C06024. doi: 10.1029/2009JC005591
- Wavewatch III Development Group (WW3DG) (2019). *User Manual and System Documentation of WAVEWATCH III Version 6.07*, Technical Note 333, NOAA/NWS/NCEP/MMAB. College Park, MD: WW3DG, 465.
- Zieger, S., Babanin, A. V., Rogers, W. E., and Young, I. R. (2015). Observation-based source terms in the third-generation wave model WAVEWATCH. *Ocean Model.* 96, 2–25. doi: 10.1016/j.ocemod.2015.07.014

**Conflict of Interest:** The authors declare that the research was conducted in the absence of any commercial or financial relationships that could be construed as a potential conflict of interest.

**Publisher's Note:** All claims expressed in this article are solely those of the authors and do not necessarily represent those of their affiliated organizations, or those of the publisher, the editors and the reviewers. Any product that may be evaluated in this article, or claim that may be made by its manufacturer, is not guaranteed or endorsed by the publisher.

Copyright © 2021 Iwasaki and Otsuka. This is an open-access article distributed under the terms of the Creative Commons Attribution License (CC BY). The use, distribution or reproduction in other forums is permitted, provided the original author(s) and the copyright owner(s) are credited and that the original publication in this journal is cited, in accordance with accepted academic practice. No use, distribution or reproduction is permitted which does not comply with these terms.



# Numerical Analysis of the Effect of Binary Typhoons on Ocean Surface Waves in Waters Surrounding Taiwan

Tzu-Yin Chang<sup>1</sup>, Hongey Chen<sup>1,2</sup>, Shih-Chun Hsiao<sup>3</sup>, Han-Lun Wu<sup>3</sup> and Wei-Bo Chen<sup>1\*</sup>

<sup>1</sup> National Science and Technology Center for Disaster Reduction, New Taipei City, Taiwan, <sup>2</sup> Department of Geosciences, National Taiwan University, Taipei City, Taiwan, <sup>3</sup> Department of Hydraulic and Ocean Engineering, National Cheng Kung University, Tainan City, Taiwan

## OPEN ACCESS

### Edited by:

Bahareh Kamranzad,  
Kyoto University, Japan

### Reviewed by:

Yuanjian Yang,  
Nanjing University of Information  
Science and Technology, China  
Yuxiang Ma,  
Dalian University of Technology, China

### \*Correspondence:

Wei-Bo Chen  
wbchen@ncdr.nat.gov.tw

### Specialty section:

This article was submitted to  
Coastal Ocean Processes,  
a section of the journal  
Frontiers in Marine Science

**Received:** 10 August 2021

**Accepted:** 09 September 2021

**Published:** 05 October 2021

### Citation:

Chang T-Y, Chen H, Hsiao S-C,  
Wu H-L and Chen W-B (2021)  
Numerical Analysis of the Effect  
of Binary Typhoons on Ocean Surface  
Waves in Waters Surrounding Taiwan.  
*Front. Mar. Sci.* 8:749185.  
doi: 10.3389/fmars.2021.749185

The ocean surface waves during Super Typhoons Maria (2018), Lekima (2019), and Meranti (2016) were reproduced using hybrid typhoon winds and a fully coupled wave-tide-circulation modeling system (SCHISM-WWM-III). The hindcasted significant wave heights are in good agreement with the along-track significant wave heights measured by the altimeters aboard the SARAL (Satellite with ARGOS and ALtiKa) and Jason-2 satellites. Two numerical experiments pairing Super Typhoons Maria (2018) and Meranti (2016) and Super Typhoons Lekima (2019) and Meranti (2016) were conducted to analyze the storm wave characteristics of binary and individual typhoons. Four points located near the tracks of the three super typhoons were selected to elucidate the effects of binary typhoons on ocean surface waves. The comparisons indicate that binary typhoons not only cause an increase in the significant wave height simulations at four selected points but also result in increases in the one-dimensional wave energy and two-dimensional directional wave spectra. Our results also reveal that the effects of binary typhoons on ocean surface waves are more significant at the periphery of the typhoon than near the center of the typhoon. The interactions between waves generated by Super Typhoons Maria (2018) and Meranti (2016) or Super Typhoons Lekima (2019) and Meranti (2016) might be diminished by Taiwan Island even if the separation distance between two typhoons is <700 km.

**Keywords:** storm wave, super typhoon, binary typhoons, Taiwan Island, wave spectra

## INTRODUCTION

Since the early 1900s, many studies on binary typhoons have been proposed (Fujiwhara, 1921; Dong and Neumann, 1983; Ritchie and Holland, 1993; Carr et al., 1997; Carr and Elsberry, 1998; Prieto et al., 2003; Jang and Chun, 2015; Cha et al., 2021). Carr et al. (1997) categorize the direct tropical cyclone/typhoon interaction into three modes: the first is the one-way influence, in which the motion of the larger tropical cyclone/typhoon is slightly affected by the presence of the smaller tropical cyclone/typhoon; the second is the mutual interaction, in which both tropical cyclones/typhoons experience significant rotation; and finally is the special merger case of two nearly equal-sized tropical cyclones/typhoons that somehow are mutually attracted and become close enough that the two cyclonic/typhoon's circulations merge. Carr and Elsberry (1998) objectively detected three modes of binary tropical cyclone interaction defined by Carr et al. (1997).

Although previous studies have mainly focused on atmospheric science and meteorology, these pioneering works have contributed to a deep understanding of binary typhoons. As the name suggests, binary typhoons involve two typhoons/cyclones/hurricanes that are spatially proximal and occur simultaneously. How close must two typhoons be to be considered binary typhoons? Binary interactions (also known as the Fujiwhara effect) defined by the NHC (National Hurricane Center, National Oceanic and Atmospheric Administration, United States) refer to two typhoons within a certain distance (556–1,389 km depending on the sizes of the cyclones) that begin to rotate around a common midpoint. Ritchie and Holland (1993) indicated that the cores of two typhoons (binary typhoons) might merge once they are as close as 150–300 km. According to the report from Dong and Neumann (1983), the influence of the ITCZ (intertropical convergence zone) flow on relative rotation exceeds the Fujiwhara effect when the separation distance of two typhoons in the ITCZ is more than 650 km; however, the Fujiwhara effect surpasses the ITCZ flow in terms of relative rotation when the separation distance between two typhoons is <650 km.

Dong and Neumann (1983) also demonstrated that the occurrences of binary typhoons are considerably more frequent in the Northwestern Pacific Ocean (NPO) than in the North Atlantic Ocean. Additionally, based on 36 years of recorded data (1964–1981), typhoon pairs subject to binary interaction occur 1.5 times a year on average in the NPO and only 0.33 times in

the Atlantic Ocean. Jang and Chun (2015) utilized the best track and reanalysis data observed in the NPO over 62 years (1951–2012) to investigate the dynamical and statistical characteristics of binary typhoons and found that the number of occurrences of binary typhoons was 98, and was 1.58 a year on average. In fact, the coexistence of two or more typhoons within a certain time and distance was frequent in the NPO from 1951 to 2019, and the highest number of typhoon coexistence instances was five in both 1960 and 1985 (Cha et al., 2021).

In the 2000s, numerous researchers conducted studies on multiple-typhoon interactions using numerical models (Khain et al., 2000; Yang et al., 2008; Wu et al., 2012; Jang and Chun, 2015; Choi et al., 2017). For example, Khain et al. (2000) investigated the motion and evolution of binary tropical cyclone using a coupled tropical cyclone-ocean movable nested grid model. Through a series of sensitivity experiments, their researches recommended that the regimes of binary typhoons interaction depend on the structure of the background flow then. However, few studies focused on the effect of binary typhoons on marine weather, e.g., storm waves, storm tides, and storm surges, and further research is therefore required (Xu et al., 2020). Ocean surface waves induced by wind are a dominant process in coastal and nearshore regions worldwide; moreover, understanding the characteristics of typhoon-driven extreme waves and projecting their future change are important considerations for the sustainable development of coastal and offshore infrastructure and the management of coastal resources

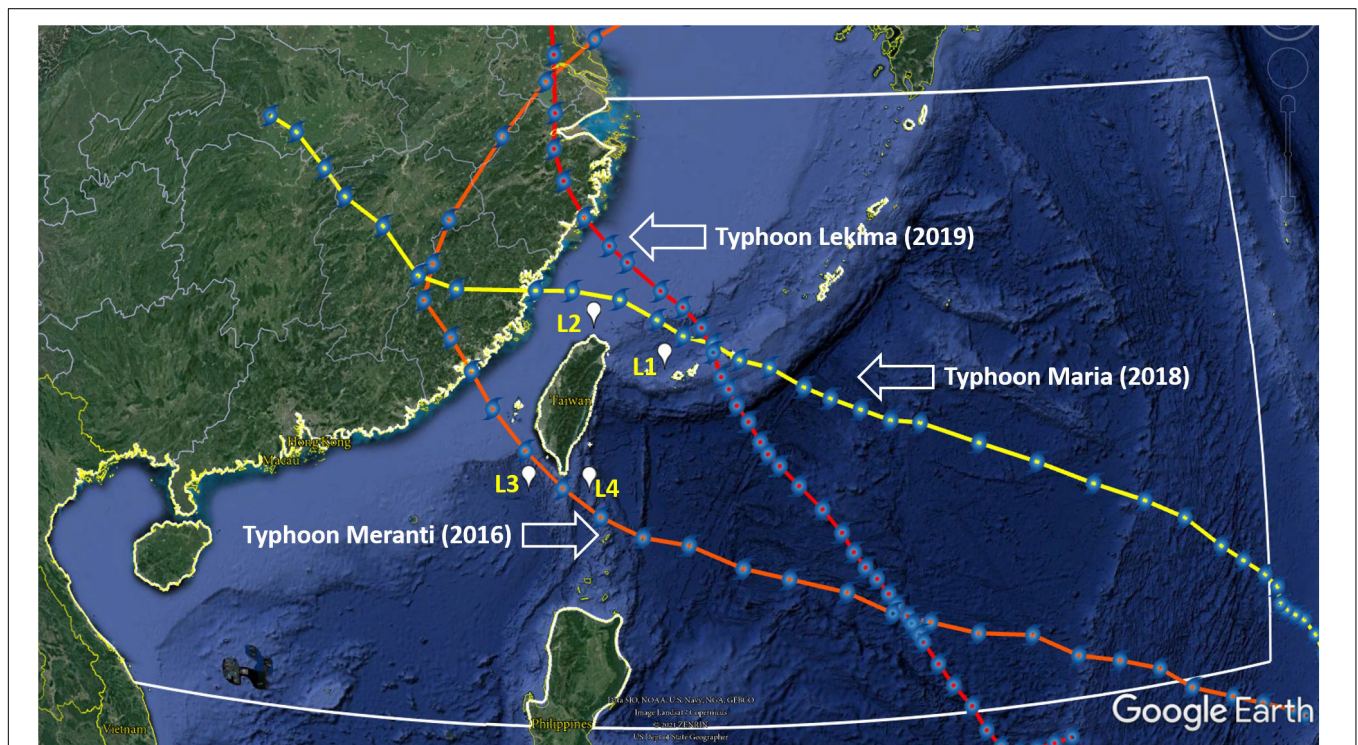
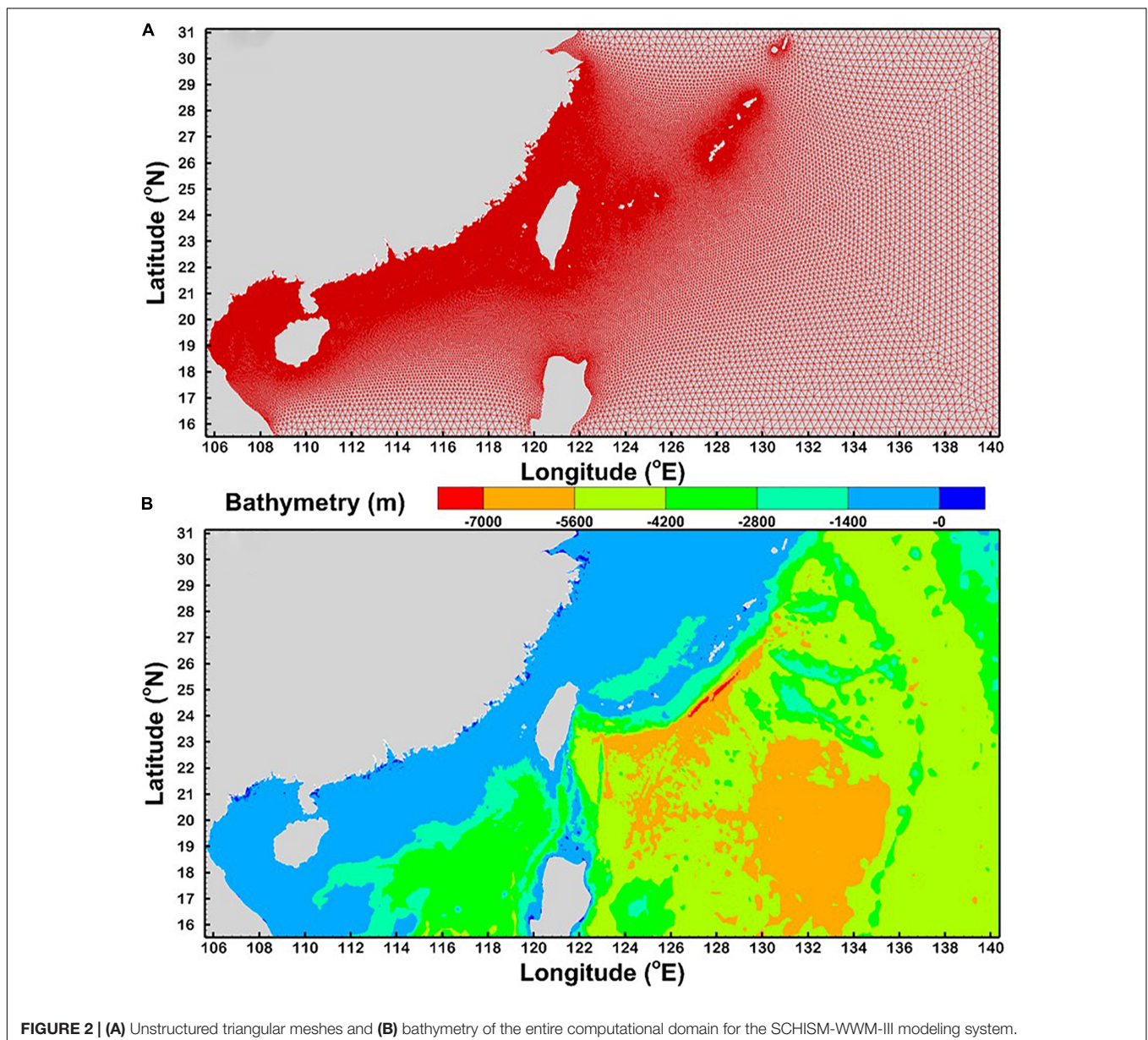


**FIGURE 1 |** The computational domain of the SCHISM-WWM-III modeling system (sea area within the white line). The red, yellow, and orange lines represent the tracks for Super Typhoons Lekima in 2019, Maria in 2018 and Meranti in 2016, respectively. L1, L2, L3, and L4 are selected representative points for elucidating the effects of binary typhoons on ocean surface waves [typhoon tracks: Regional Specialized Meteorological Center (RSMC) Tokyo-Typhoon Center].

and ecosystems, which is particularly true for studies on binary typhoons. Yang et al. (2012) used multiple satellite observations to evaluate the impacts of binary typhoons on upper ocean environments for typhoons Hagibis and Mitag in November 2007. Their results suggested that due to the strong wind stress curls forcing sustained for a long time, the intense Ekman pumping and two mesoscale cold, cyclonic eddies appeared in two certain areas after the trails of binary typhoons. This finding provides convincing evidence that typhoons play an important role in the activities of mesoscale eddies for the South China Sea and NPO.

The present study on ocean surface waves focuses on binary typhoon-generated storm waves as an important component of the Earth's climate system, recognizing that global extreme waves will change with historical and future changes in the frequency,

intensity, and position of the marine typhoons that generate them. This paper aims to study the effect of binary typhoons on ocean surface waves in the waters surrounding Taiwan during the passage of three binary typhoons, pairing Super Typhoons Maria (2018) and Meranti (2016) and Super Typhoons Lekima (2019) and Meranti (2016). This paper is organized as follows: the details of the three selected super typhoons are described in the following section. Section "Data and Methods" presents the measurements, methods for improving the typhoon winds from the reanalysis product and designing the binary typhoon systems and the configuration of the wave-circulation modeling system (i.e., an ocean circulation model, SCHISM-2D, coupled with a wind wave model, WWM-III). The results of the model validation and designed numerical experiments and discussion are presented in section "Results and Discussion." Finally, a





summary and conclusions are provided in section “Summary and Conclusion.”

## SELECTED SUPER TYPHOONS

Super Typhoon Meranti was one of the most intense tropical cyclones on record and one of the three Category 5 (the Saffir–Simpson hurricane wind scale) typhoons in the South China Sea, with the others being Typhoon Pamela in 1954 and Typhoon Rammasun in 2014. Meranti formed as a tropical depression on Sep. 8 near the island of Guam and gradually intensified through Sep. 11. Meranti became a super typhoon on Sep. 12 and reached its peak intensity on Sep. 13 with 1-min sustained winds of 315 km/h as it passed through the Luzon Strait (to the south of Taiwan). The estimated pressure of 890 hPa for Super Typhoon Meranti was also the lowest on record in the Western Pacific after those of Typhoon Megi in 2010 and Typhoon Mangkhut in 2018. Meranti began weakening steadily as a result of land (Taiwan) interaction, and then it struck Fujian Province of China as a Category 2-equivalent typhoon on Sep. 15. Meranti rapidly

weakened after moving inland and dissipated when it arrived over the waters off South Korea. The orange line in **Figure 1** represents the track of Super Typhoon Meranti in 2016.

Super Typhoon Maria was a powerful tropical cyclone that affected Guam (the United States), the Ryukyu Islands (Japan), Taiwan, and East China in early July 2018. Maria became a tropical storm and passed the Mariana Islands on July 4 and rapidly intensified the next day due to favorable environmental conditions. Maria reached its first peak intensity on July 6, and a second stronger peak intensity with 1-min sustained winds of 270 km/h (equivalent to category 5 super typhoon status on the Saffir–Simpson scale) and a minimum pressure of 915 hPa was reached on July 9. Maria finally made landfall over Fujian Province, China, on July 11 after crossing the Yaeyama Islands and passing the northern offshore waters of Taiwan on July 10. The yellow line in **Figure 1** represents the track of Super Typhoon Maria in 2018.

Super Typhoon Lekima originated from a tropical depression that developed in the eastern Philippines on July 30, 2019. Lekima became a tropical storm and was named on August 4. Under favorable environmental conditions, Lekima intensified

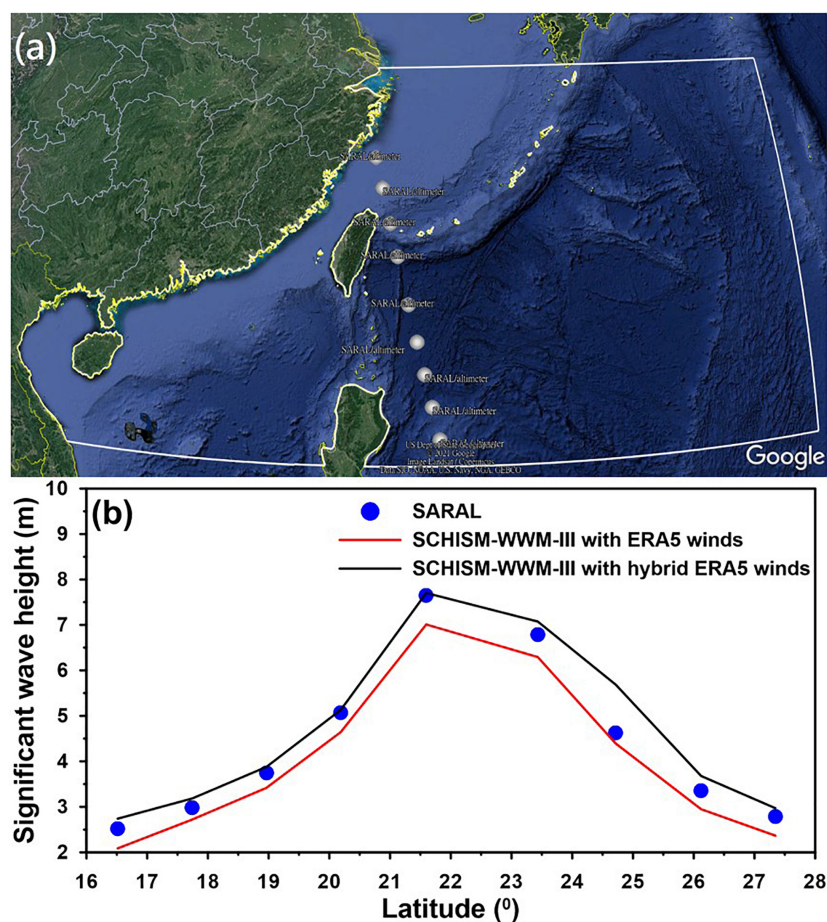


**FIGURE 3 | (a)** Satellite with ARGOS and ALTiKa (SARAL) orbit in the computational domain at UTC 21:30 on Sep. 13, 2016, and **(b)** along-track significant wave heights measured by altimeter on SARAL with hindcasted significant wave heights derived from the original ERA5 and modified ERA5 wind fields for Super Typhoon Meranti in 2016.

and reached its peak with 1-min sustained winds of 250 km/h (equivalent to a category 4 super typhoon status on the Saffir-Simpson scale) and a minimum pressure of 925 hPa on August 8. Lekima made landfall in Zhejiang Province, China, on late August 9 and made its second landfall in Shandong Province, China, on August 11 after moving across eastern China. The track of Super Typhoon Lekima is illustrated using a red line in **Figure 1**.

## DATA AND METHODS

### Measurements of Significant Wave Height From Satellite Altimeters

Satellite altimeter measurement data of ocean significant wave height were utilized for model validation in the present study. The data were collected by two satellites: SARAL (Satellite with ARGos and ALtiKa) is a French (Centre National d'Etudes Spatiales, CNES)/Indian (Indian Space Research Organisation, ISRO) collaborative mission and was launched on 25 February 2013. SARAL performs altimetric measurements designed to study

ocean circulation and sea surface elevation. Jason-2 was an Earth satellite designed to make observations of ocean topography for investigations into sea-level rise and the relationship between ocean circulation and climate change. It was an international Earth observation satellite altimeter joint mission for sea surface height measurements between NASA (National Aeronautics and Space Administration) and CNES.

The main instrument on the SARAL and Jason-2 satellites is a radar altimeter that provides measurements of sea surface height, wind speed at the ocean surface and significant wave height. The data can be used for forecasting hurricanes, improving the safety and efficiency of offshore industry operations, routing ships, managing fisheries, monitoring river and lake levels, and validating the accuracy of ocean and wind wave models.

### Improvement of Typhoon Winds Through a Directed Modified Method

Because of their simplicity, many parametric cyclone wind models have been proposed since the mid-1960s (Jelesnianski, 1965, 1966) and have been widely used to

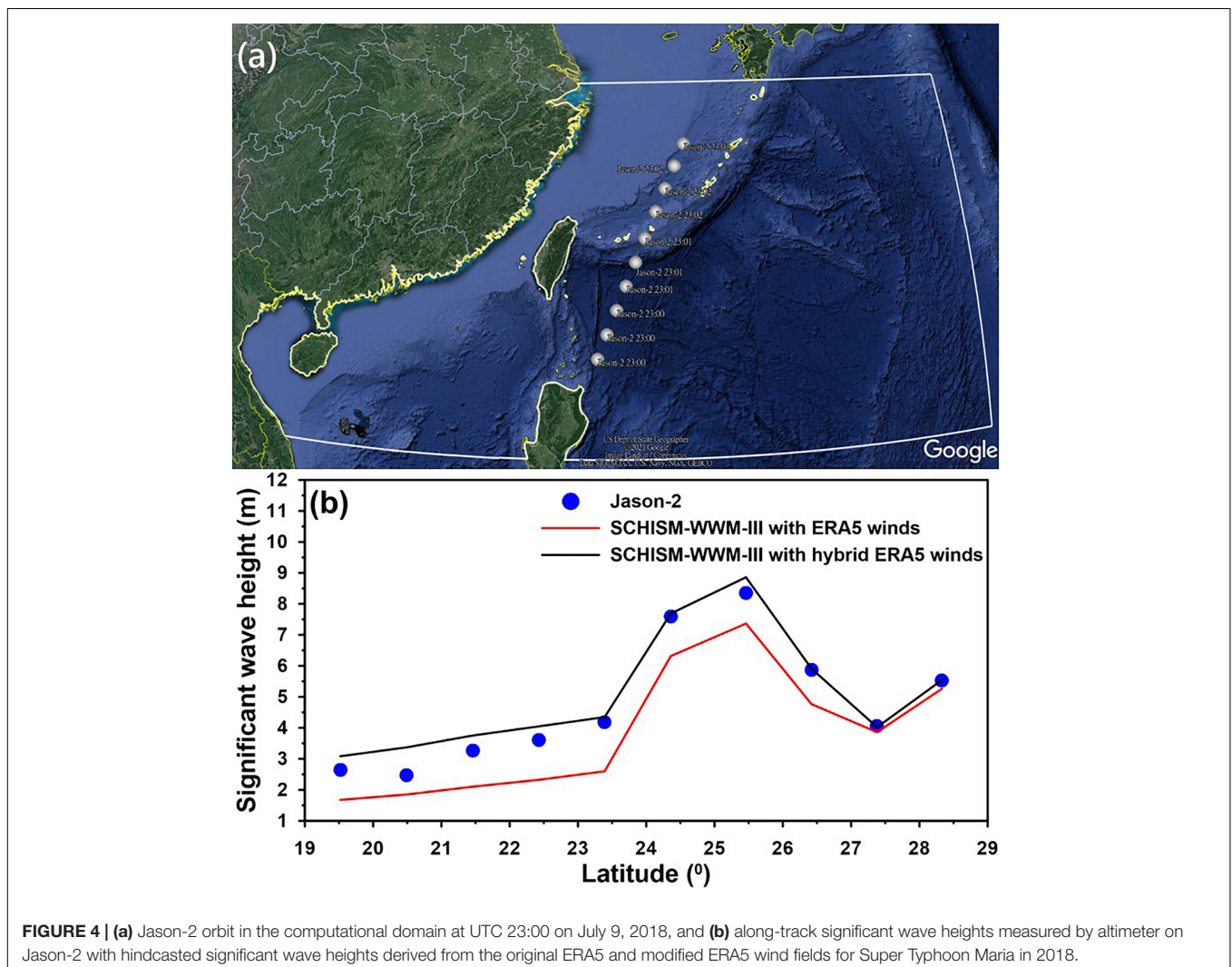


**FIGURE 4 |** (a) Jason-2 orbit in the computational domain at UTC 23:00 on July 9, 2018, and (b) along-track significant wave heights measured by altimeter on Jason-2 with hindcasted significant wave heights derived from the original ERA5 and modified ERA5 wind fields for Super Typhoon Maria in 2018.

reconstruct the wind field of typhoons (Dube et al., 1985; Ginis and Sutyryn, 1995; Lee, 2008; Chen et al., 2012). The wind speeds and their distributions near the center of the typhoon can accurately be reproduced through parametric cyclone wind models; however, their performances are inferior in regions far from the center of the typhoon. Conversely, the typhoon winds derived from an atmospheric reanalysis are superior in areas outside of the typhoon’s center but are generally worse for the maximum typhoon wind speed (Pan et al., 2016; Chen et al., 2019; Hsiao et al., 2019, 2020a,b, 2021a,b). To construct a reliable scale for the entire wind field of a typhoon, a direct modification technique proposed by Pan et al. (2016) was therefore applied in the present study to take advantage of the combination of a parametric cyclone wind model and reanalysis products:

$$W_{DM} = \begin{cases} W_{ERA5} \left[ \frac{r}{R_{max}} \left( \frac{W_{Bmax}}{W_{Emax}} - 1 \right) + 1 \right] & r < R_{max} \\ W_{ERA5} \left[ \frac{R_{trs} - r}{R_{trs} - R_{max}} \left( \frac{W_{Bmax}}{W_{Emax}} - 1 \right) + 1 \right] & R_{max} \leq r \leq R_{trs} \\ W_{ERA5} & r > R_{trs} \end{cases} \quad (1)$$

where  $W_{DM}$  is the wind speed at an arbitrary grid point within the model domain through the direct modification method,  $W_{ERA}$  is the wind speed extracted from ERA5 (the fifth-generation reanalysis of the European Centre for Medium-Range Weather Forecasts for the global climate and weather) at an arbitrary point in the computational grid,  $W_{Bmax}$  is the maximum wind speed of the best track typhoon issued by the Regional Specialized Meteorological Center (RSMC) Tokyo-Typhoon Center,  $W_{Emax}$  is the maximum wind speed of the typhoon among the hourly ERA5 wind fields,  $r$  is the radial distance from an arbitrary grid point within the model domain to the eye of the typhoon,  $R_{trs}$  is the radius of the modified scale (also known as the radius of the transitional zone), and  $R_{max}$  is the radius at the maximum typhoon wind speed.  $R_{max}$  can be expressed as a function of  $W_{Bmax}$  and the latitude of the typhoon’s center:

$$R_{max} = m_0 + m_1 \times W_{Bmax} + m_2 (\phi - 25) \quad (2)$$

where  $\phi$  is the latitude of the typhoon’s center. In Eq. (2),  $m_0$ ,  $m_1$ , and  $m_2$  were set to 38.0 (in n mi), -0.1167 (in n mi  $kt^{-1}$ ), and -0.0040 (in n mi  $o^{-1}$ ), respectively, according to the results derived

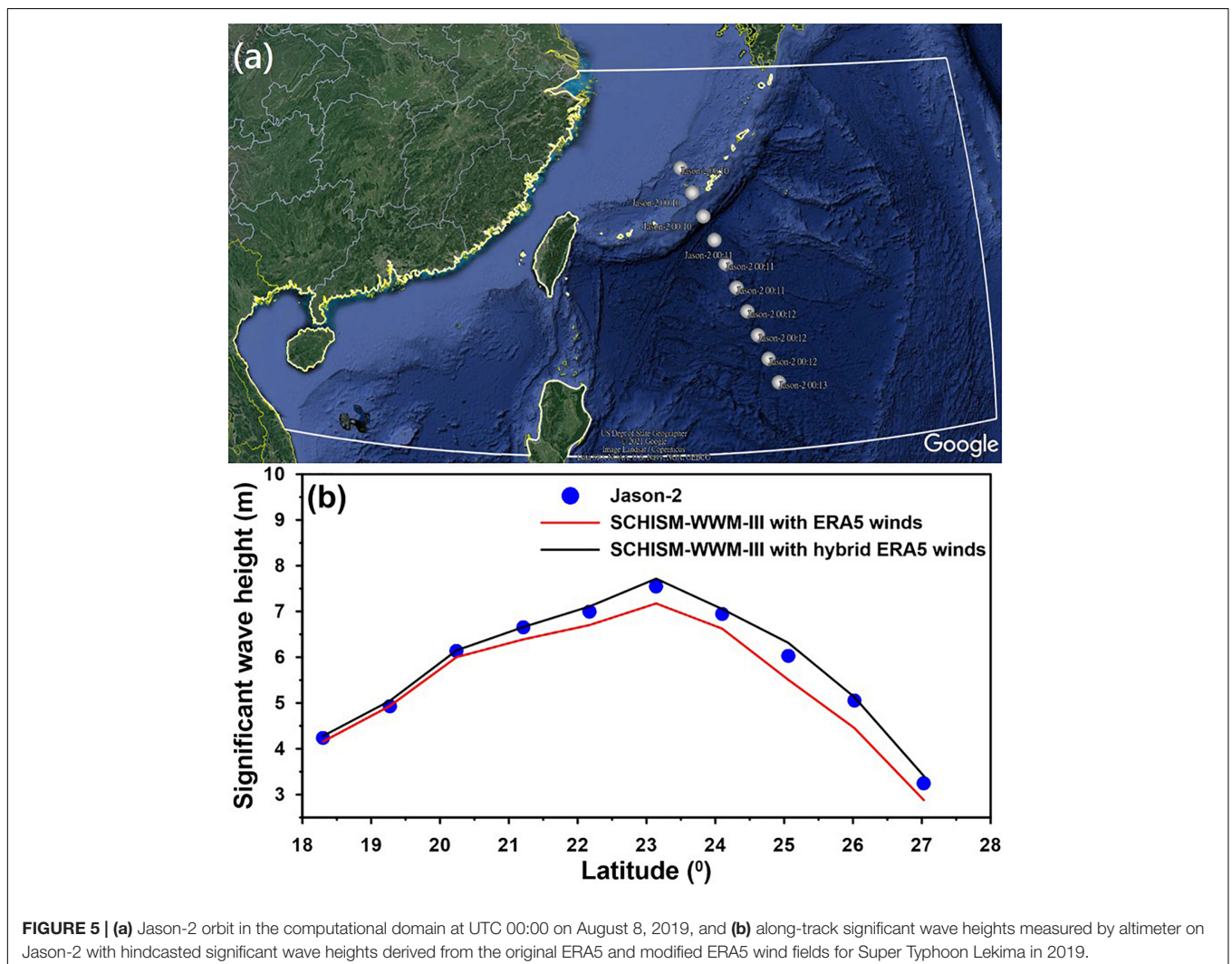


**FIGURE 5 |** (a) Jason-2 orbit in the computational domain at UTC 00:00 on August 8, 2019, and (b) along-track significant wave heights measured by altimeter on Jason-2 with hindcasted significant wave heights derived from the original ERA5 and modified ERA5 wind fields for Super Typhoon Lekima in 2019.

from Knaff et al. (2007) for the Western Pacific typhoon basin. In Eq. (1),  $R_{trs}$  is regarded as an important parameter in determining the accuracy of wind fields.

## Binary Typhoon Design

The creation of wind fields with binary typhoons is not a straightforward task. To ensure that the hourly wind speed at

each grid remained the maximum for the inputs of storm wave hindcasting, an approach proposed by Xu et al. (2020) was employed in the present study. Equation (1) was applied to reconstruct the typhoon wind fields for Super Typhoons Meranti (2016), Maria (2018), and Lekima (2019) individually and then merged the wind fields of Super Typhoons Meranti (2016) and Maria (2018) and the wind fields of Super Typhoons Meranti

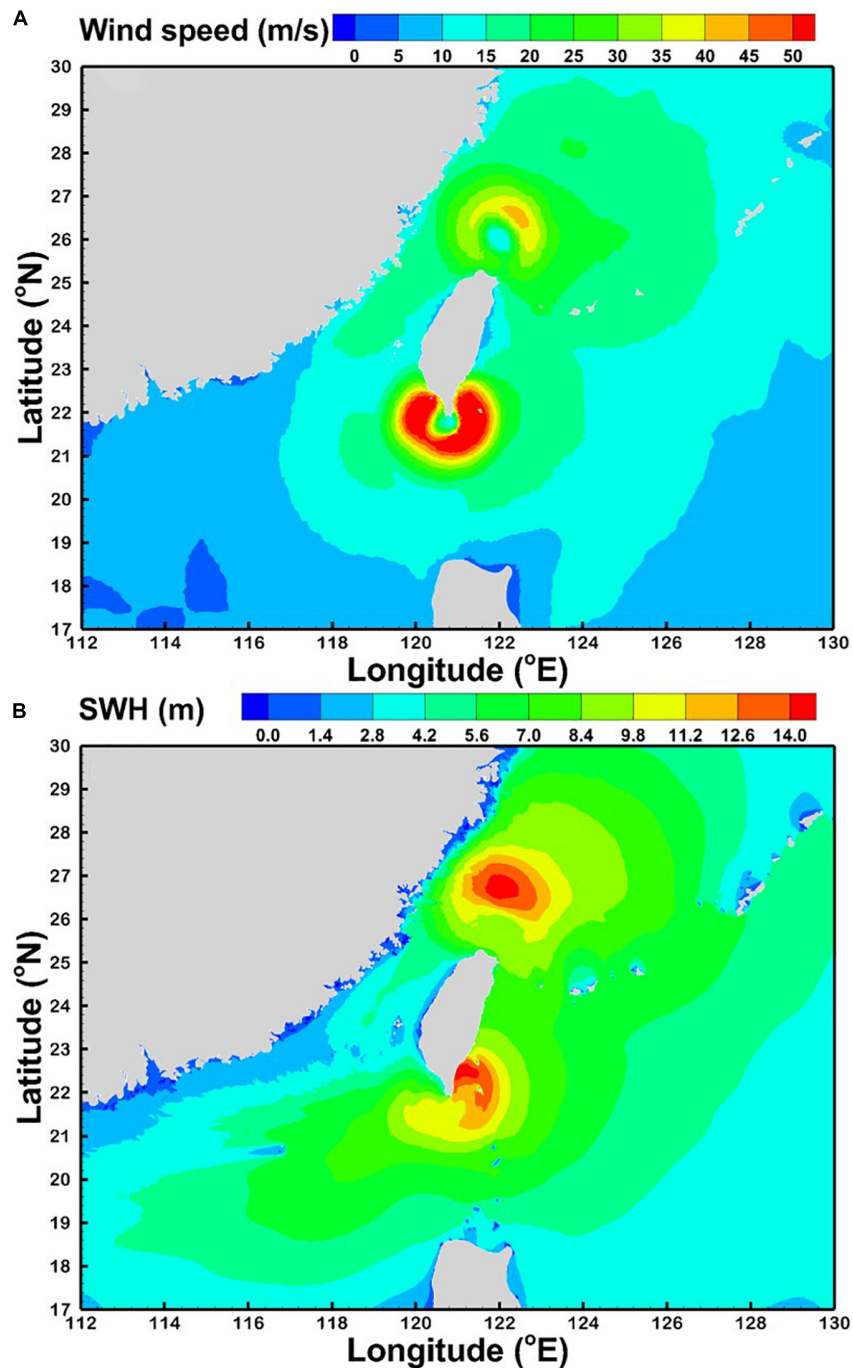


**FIGURE 6** | Spatial distribution of (A) the instantaneous wind field from a superposition of Super Typhoons Maria in 2018 and Meranti in 2016 and (B) the corresponding significant wave heights.

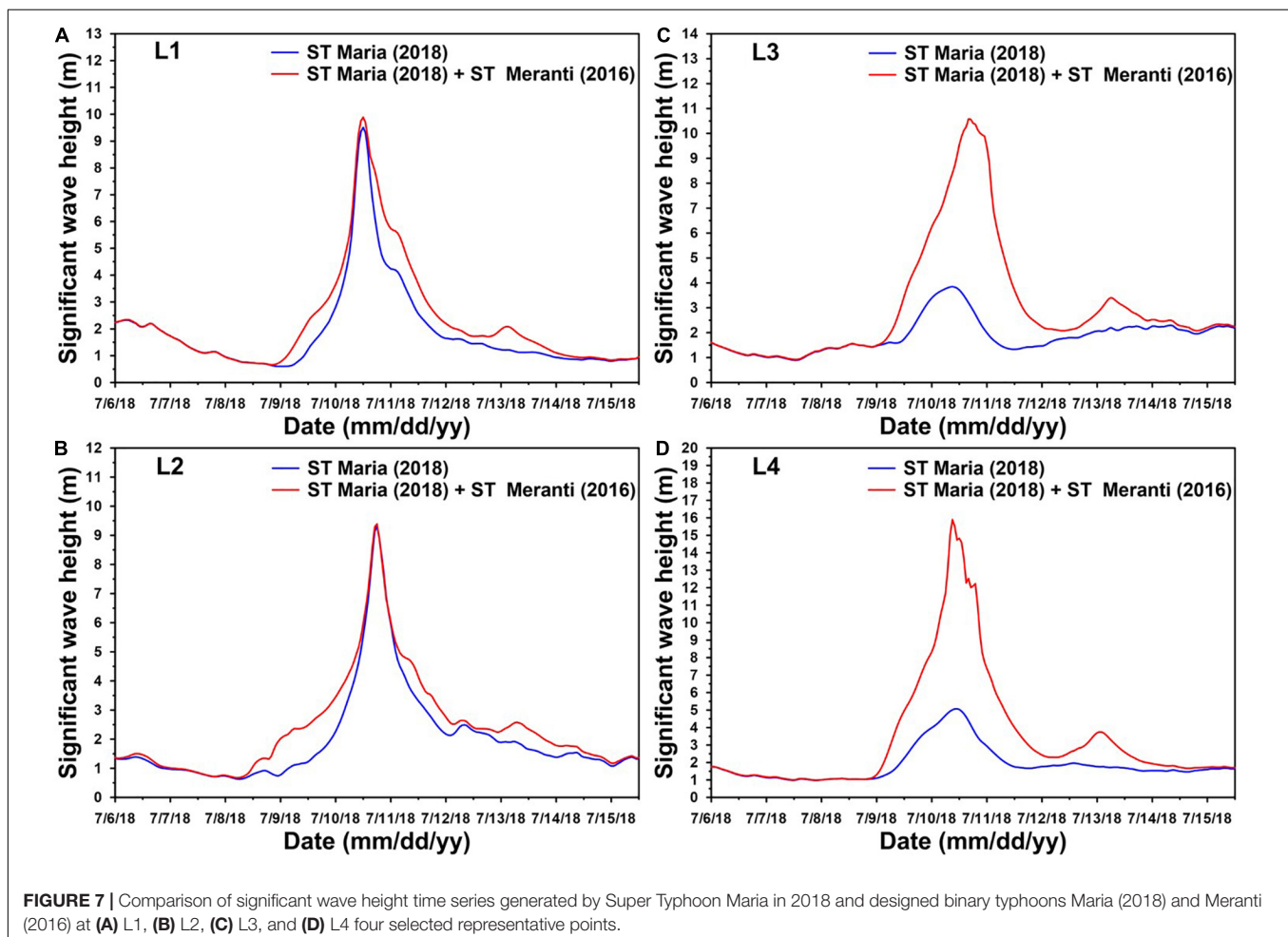
(2016) and Lekima (2019), which are then used as the designed binary typhoon events in the present study.

## Configuration of the SCHISM-WWM-III Modeling System

An ocean circulation model called the SCHISM (Semi-implicit Cross-scale Hydroscience Integrated System Model, Zhang et al., 2016) serves as the core of the wave-tide-circulation modeling system. The SCHISM is an upgraded product of the SELFE (Semi-implicit Eulerian-Lagrangian Finite Element/volume, developed by Zhang and Baptista, 2008) model, and both models are based on the unstructured grids. To eliminate numerical errors originating from the splitting between internal and external modes (Shchepetkin and McWilliams, 2005), the no-mode-splitting technique is employed in the SCHISM. High-performance computations can be performed even if a very high spatial resolution mesh is used in the SCHISM because the severest stability constraint, i.e., the CFL (Courant–Friedrichs–Lewy) condition, is ignored through a highly efficient semi-implicit scheme (Zhang et al., 2020). Typhoon-induced ocean hydrodynamics can be well-mimicked by means of a two-dimensional, depth-averaged ocean circulation. Therefore,

SCHISM-2D (the two-dimensional version of the SCHISM) is adequate to hindcast storm waves in practice. Because of their high scalability, the SCHISM and SELFE modeling systems have been employed to solve water quality and hydrodynamic problems in estuarine and coastal environments in Taiwan. For instance, estuarine residence time, suspended sediment, and fecal coliform transport were simulated (Liu et al., 2008; Chen et al., 2015; Chen and Liu, 2017), storm tide-induced coastal inundation was assessed (Chen and Liu, 2014, 2016), and tidal current energy was evaluated (Chen et al., 2013, 2017a). According to the bathymetric characteristics of the seafloor in the Taiwanese waters and the numerical stability, a time step of 120 s and a Manning coefficient of 0.025 were specified for the SCHISM-2D model.

The WWM-III (Wind Wave Model version III) is a third-generation spectral wave model derived from WWM-II (developed by Roland, 2009). The WWM-III solves the wave action balance equation on unstructured grids by a fractional step method. In the present study, the BJ 78 model proposed by Battjes and Janssen (1978) was utilized in the WWM-III to cope with depth-induced wave breaking in nearshore shallow waters. The wave breaking criterion and bottom friction coefficients are 0.78 and 0.067, respectively. The peak enhancement factor of



3.3 from the JONSWAP spectra (Joint North Sea Wave Project, Hasselmann et al., 1973) is adopted in the WWM-III. The lowest and highest limits of the discrete wave period are 0.04 and 1.0 Hz, respectively, and is divided into 36 frequency bins. The full circle of  $360^\circ$  is taken into account in the WWM-III, the number of bins in the directional space is 36 and consequently the spectral directional resolution is  $360^\circ/36 = 10^\circ$ .

SCHISM-2D and WWM-III share the same subdomains using the same domain decomposition scheme; therefore, interpolation errors from the two models can be avoided. Additionally, the parallelization highly enhances the computational efficiency of SCHISM-2D and WWM-III. The improvement of the coupled model, SCHISM-WWM-III, was accomplished by employing the different time steps in two models, i.e., 120 s for SCHISM-2D

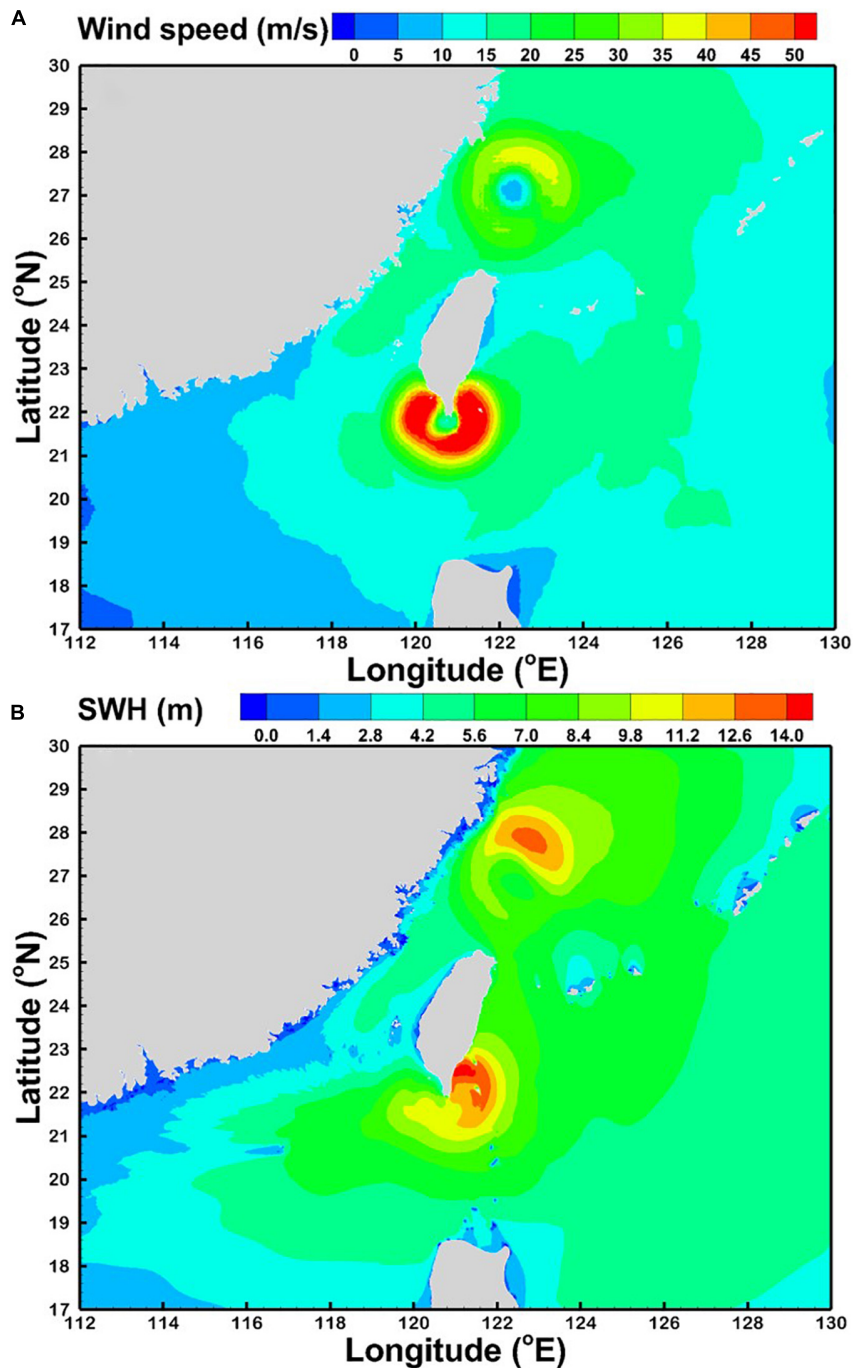


**FIGURE 8** | Spatial distribution of (A) the instantaneous wind field from a superposition of Super Typhoons Lekima in 2019 and Meranti in 2016 and (B) the corresponding significant wave heights.

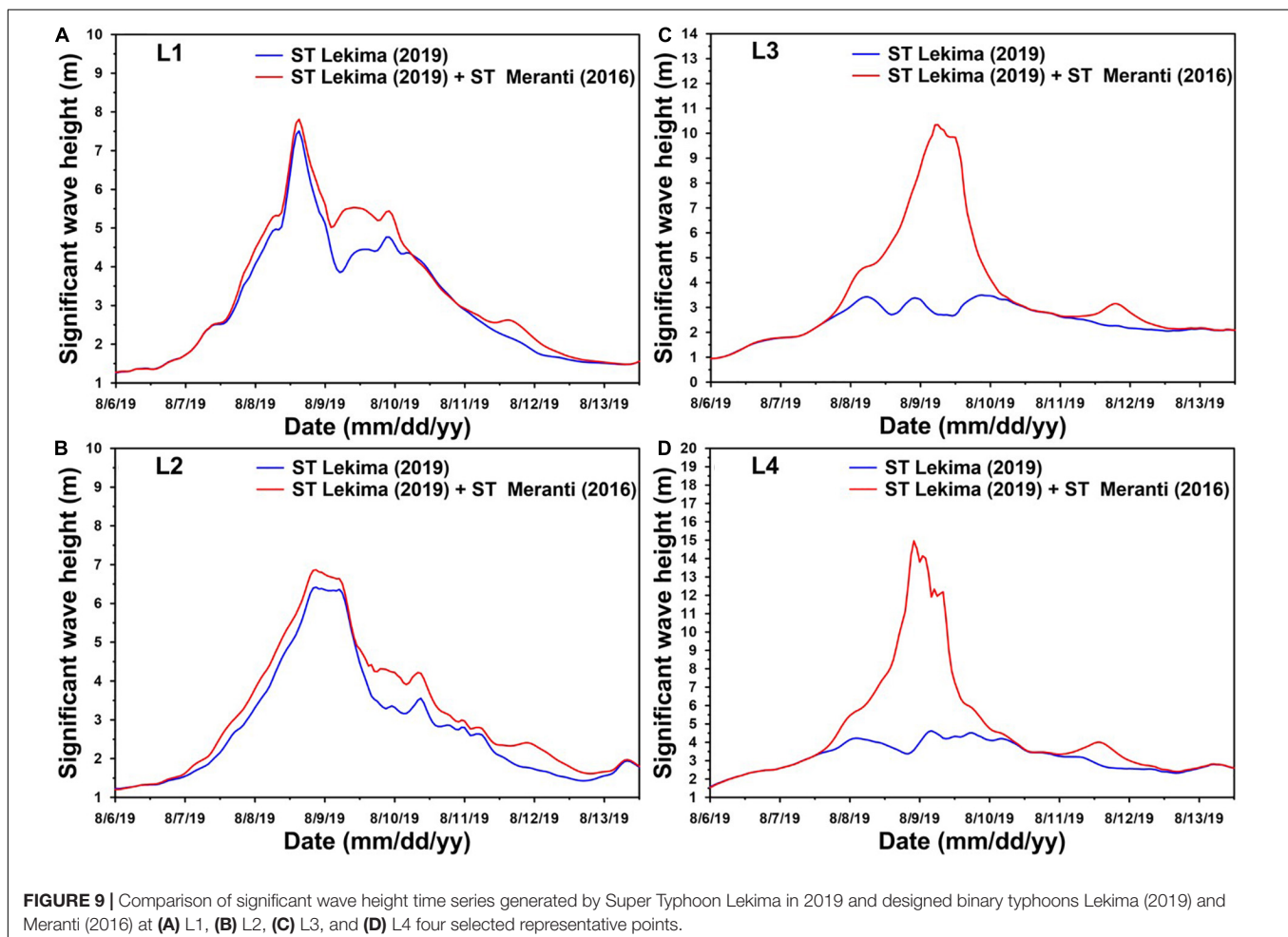
and 600 s for WWM-III. The SCHISM-WWM-III system is a two-way, tightly coupled modeling system, i.e., the SCHISM-2D delivers the wind velocities, depth-averaged currents, and water surface elevations to the WWM-III, and then the wave radiation stresses computed by the WWM-III are used in the SCHISM-2D every 5 hydrodynamic time intervals, and has been used to predict the offshore storm waves and coastal storm tides induced by typhoons and to hindcast the long-term wave parameters in the waters surrounding Taiwan (Chen et al., 2017b, 2019; Shih et al., 2018; Su et al., 2018; Hsiao et al., 2019, 2020a,b, 2021a,b).

To eliminate the effects of the boundary conditions on model simulations, the computational domain for storm surge, storm tide and storm wave modeling must be large enough to accommodate an entire typhoon, including its peripheral circulation (Orton et al., 2012; Zheng et al., 2013; Hsiao et al., 2021a). Hence, the present study created a large computational domain that covers the area from longitudes of 105°E to 140°E and latitudes of 15°N to 31°N (as shown in **Figure 1**) and contains 276,639 vertices and 540,510 triangular elements (as shown in **Figure 2A**). The latest global bathymetric product released by the GEBCO (General Bathymetric Chart of the Oceans), namely, the GEBCO\_2021 Grid, was adopted to

construct the bathymetric data for the SCHISM-WWM-III modeling system in the present study (as shown in **Figure 2B**). GEBCO\_2021 provides global coverage of elevation data in meters at a 15 arc-second spatial resolution. Open boundary conditions for SCHISM-WWM-II were not always required, as the three selected super typhoons are completely covered by the large computational domain (Liu et al., 2012; Hsiao et al., 2020a,b, 2021a). The tidal elevation and horizontal velocity at the open boundaries of SCHISM-WWM-III were driven by eight main tidal constituents ( $M_2$ ,  $S_2$ ,  $N_2$ ,  $K_2$ ,  $K_1$ ,  $O_1$ ,  $P_1$ , and  $Q_1$ ) extracted from a regional inverse tidal model (China Seas and Indonesia; Zu et al., 2008), and the effects of sea level pressure on the boundary tidal elevations were taken into consideration.

## RESULTS AND DISCUSSION

Hsiao et al. (2021b) examined significant wave height simulations for Super Typhoons Maria (2018) and Lekima (2019) at various  $R_{trs}$  and found that acceptable significant wave heights could be hindcasted if  $R_{trs}$  was equal to  $4 R_{max}$ . Therefore, the ERA5 winds were adjusted through the direct modification method (as expressed in Eq. 1) with  $R_{trs} = 4R_{max}$  and were imposed on the



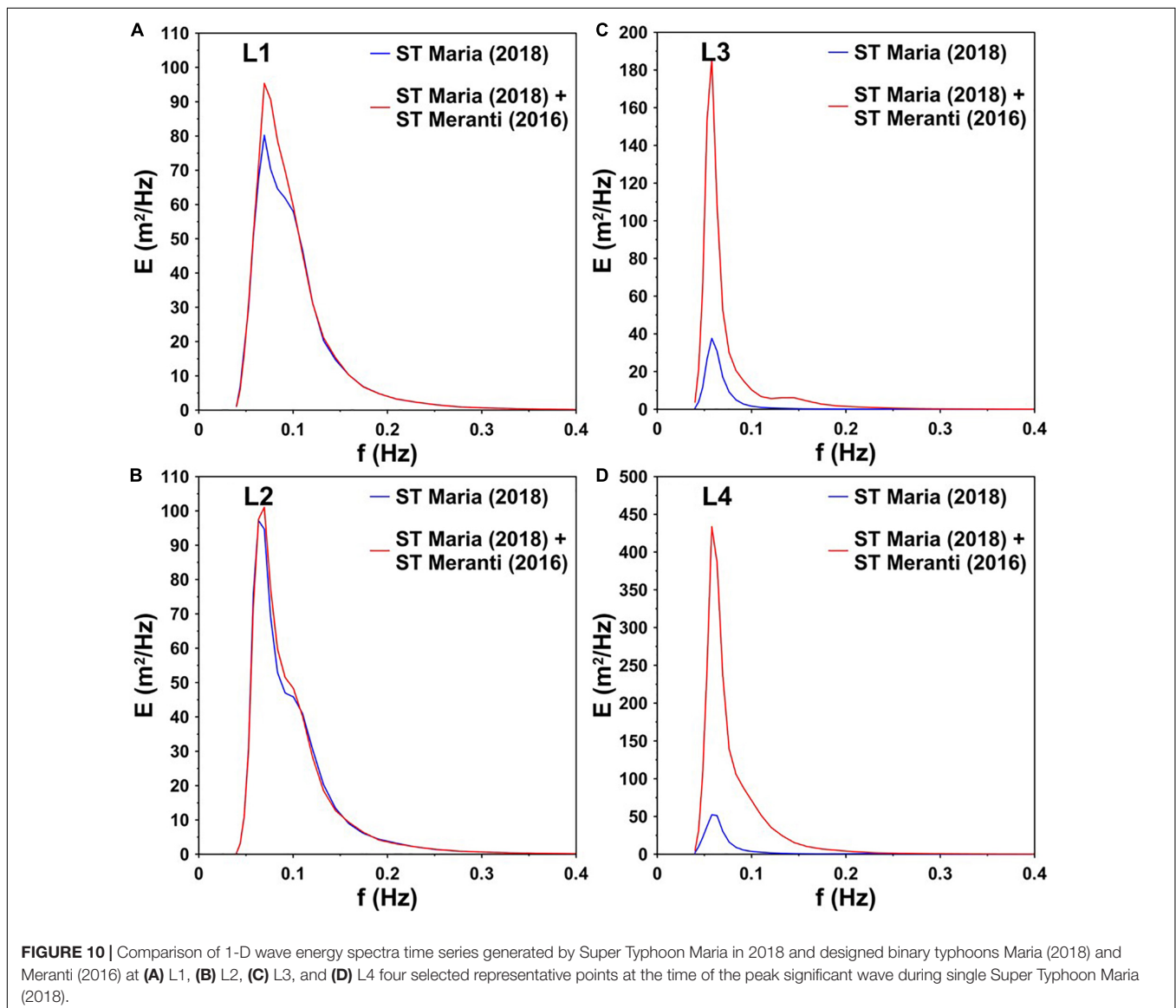
SCHISM-WWM-III modeling system to validate the hindcasts of typhoon-caused storm waves in the present study.

The hourly typhoon winds from ERA5 were adjusted using Eq. (1), transformed from the structured grid (at a spatial resolution of 31 km) into the unstructured grid and served as meteorological data for the SCHISM-WWM-III modeling system. The significant wave height observations measured by the altimeters aboard the SARAL and Jason-2 satellites were used to evaluate the performance of the significant wave heights hindcasted by the SCHISM-WWM-III modeling system for Super Typhoons Meranti (2016), Maria (2018) and Lekima (2019).

## Model Validation of Significant Wave Heights for Individual Super Typhoons

The measurement points of significant wave height (gray solid circle) along the orbit of the SARAL satellite in the computational

domain at UTC 21:30 on Sep. 13, 2016, are shown in **Figure 3a**. The comparison of along-track significant wave heights between observations and model hindcasts is presented in **Figure 3b**. For Super Typhoon Meranti in 2016, the measured significant wave height reached a maximum of 7.65 m at a latitude of 21.6°N (blue solid circle in **Figure 3b**), while the maximal hindcasts were 7.7 m (black line in **Figure 3b**) and 7.01 m (red line in **Figure 3b**) at the same position by using the original and modified hourly ERA5 wind fields, respectively. **Figure 3b** also indicates the underestimations of the significant wave height when the original ERA5 winds were imposed on the SCHISM-WWM-III modeling system. **Figures 4a, 5a** show the measurement points of significant wave height (gray solid circle) along the orbit of the Jason-2 satellite in the computational domain at UTC 23:00 on July 9, 2018, and UTC 00:00 on Aug. 8, 2019, respectively. The hindcasted significant wave heights corresponding to the measured points in **Figures 4a, 5a** are



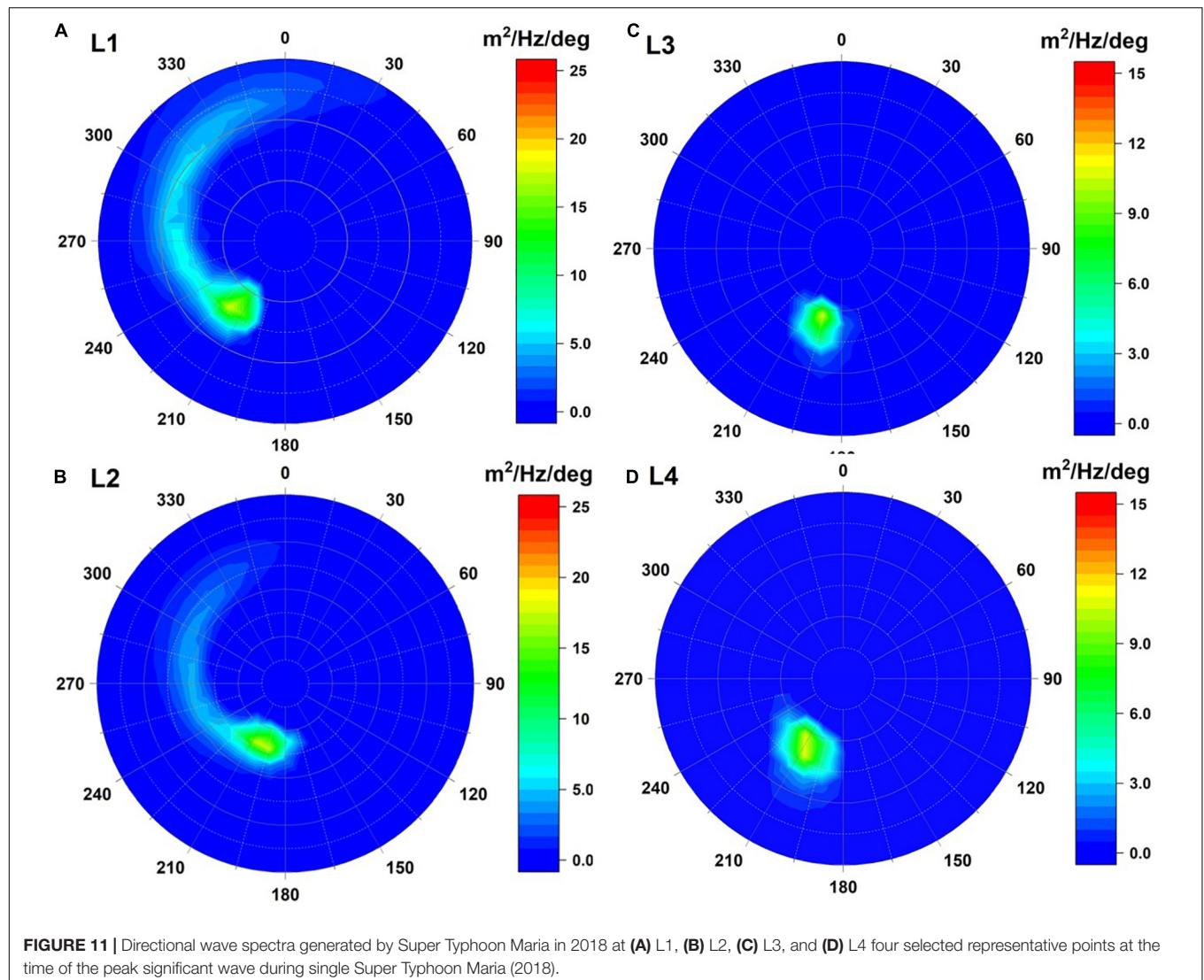


presented in **Figures 4b, 5b** for Super Typhoons Maria (2018) and Lekima (2019), respectively. As shown in **Figures 4b, 5b**, the hindcasts driven by the original and modified hourly ERA5 wind fields match the altimeter data from the Jason-2 satellite for Super Typhoons Maria (2018) and Lekima (2019); this phenomenon is similar to that observed for Super Typhoon Meranti (2016) (**Figure 3b**). The maximum significant wave heights can be captured only when using the modified ERA5 winds, although they are slightly overestimated for Super Typhoon Maria (2018) (**Figure 5b**). The results of the model validations for significant wave height in the present study are consistent with those derived from Xu et al. (2020).

### Variation in Significant Wave Height Between Single Typhoons and Binary Typhoons

Numerical experiments were designed to pair Super Typhoons Maria (2018) and Meranti (2016) and Super Typhoons Lekima

(2019) and Meranti (2016) through the method proposed by Xu et al. (2020) to better understand the effect of binary typhoons on ocean surface waves. The wind fields of the three typhoons were reconstructed individually by means of Eq. (1), and the winds of Super Typhoons Maria (2018) and Meranti (2016) and Super Typhoons Lekima (2019) and Meranti (2016) were then merged separately. The spatial distribution of the instantaneous wind field with a superposition of Super Typhoons Maria (2018) and Meranti (2016) is illustrated in **Figure 6A**. The main structures (areas with higher wind speeds) of the two super typhoons remained unchanged, and the maximum wind speed ranged from 40–45 m/s for Super Typhoon Maria (2018) and could exceed 50 m/s for Super Typhoon Meranti (2016). **Figure 6B** shows the significant wave heights generated by the binary typhoons [Super Typhoon Maria (2018) coupled with Super Typhoon Meranti (2016)] corresponding to the wind field in **Figure 6A**. An interesting phenomenon that should be noted is that the significant wave heights induced by Super Typhoon Maria (2018) in the deeper offshore waters were similar to

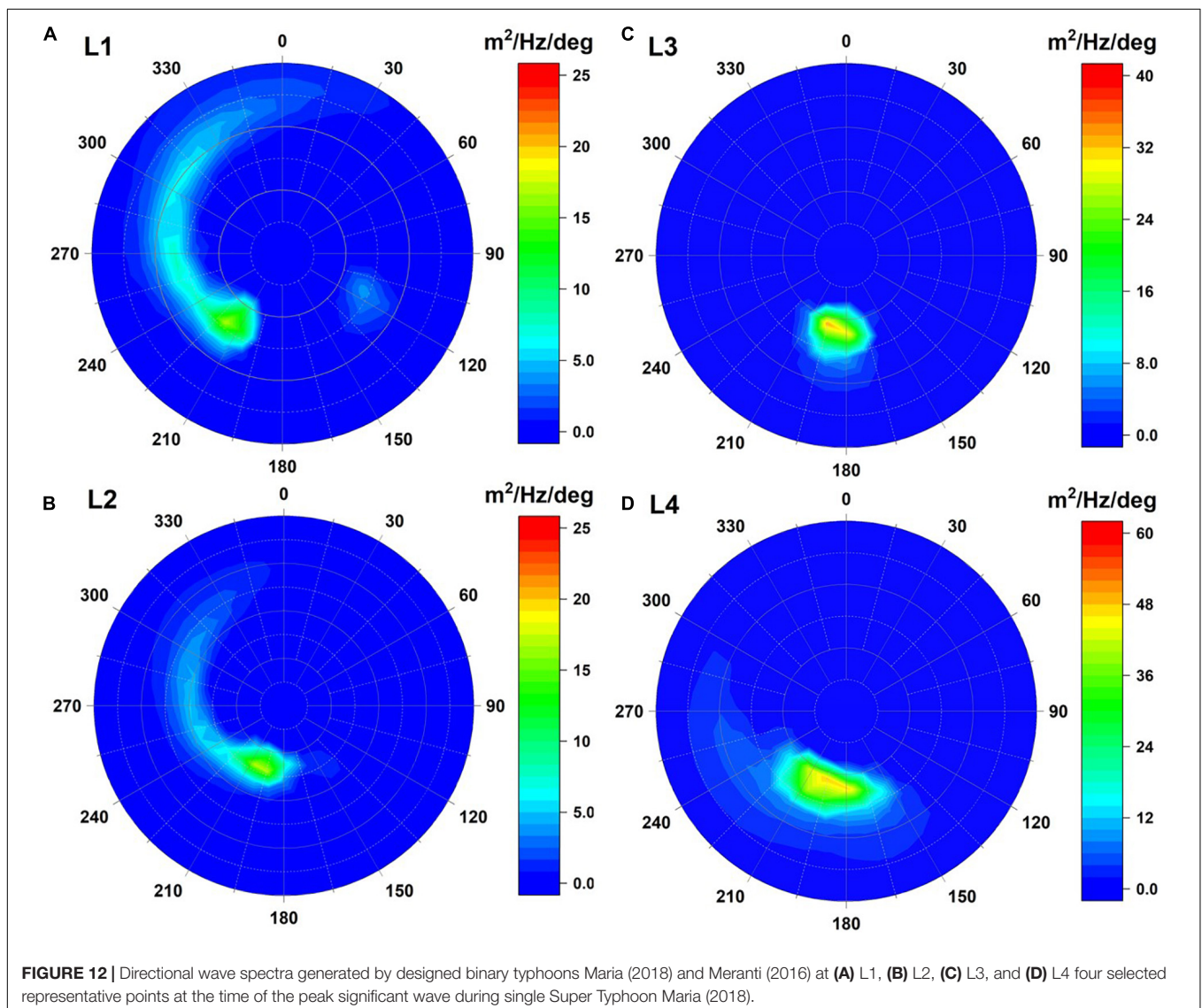


those caused by Super Typhoon Meranti (2016) in the nearshore shallow waters (as shown in **Figure 6B**). This is because the wave heights are attenuated by wave energy dissipation through seabed friction in coastal shallow waters even if the winds are stronger.

The selection of a representative point to illustrate the effects of binary typhoons on ocean surface wave time series is not straightforward. Four points (L1–L4, as shown in **Figure 1**) close to the tracks of the three super typhoons and close to Taiwan are selected to elucidate the effects of binary typhoons on ocean surface waves although this selection might not be comprehensive enough. **Figure 7** presents a comparison of the significant wave height time series driven by a single typhoon [Super Typhoon Maria (2018)] and binary typhoons (Super Typhoon Maria (2018) paired with Super Typhoon Meranti (2016)). The enhancement of peak significant wave heights by the binary typhoon effect for L1 and L2 is weak (**Figures 7A,B**). The percentage increases in the peak significant wave height are only 4 and 0.9% for L1 and L2, respectively. However, the

effect of the binary typhoons on significant wave height is more obvious before and after the peaks when Super Typhoon Maria (2018) approaches L1 and L2. This phenomenon might be due to the presence of Super Typhoon Meranti (2016), which raised the wind speeds in the peripheral circulation of Super Typhoon Maria (2018). As shown in **Figures 7C,D**, there is no doubt that the significant wave heights at L3 and L4 increases dramatically because of the passage of Super Typhoon Meranti (2016).

**Figure 8A** depicts the spatial distribution of the instantaneous wind field from a superposition of Super Typhoons Lekima (2019) and Meranti (2016) and the corresponding significant wave height (**Figure 8B**). The significant wave height time series generated by the single typhoon [Super Typhoon Lekima (2019)] and binary typhoons [Super Typhoon Lekima (2019) paired with Super Typhoon Meranti (2016)] for L1–L4 are presented in **Figure 9** (**Figure 9A** for L1, **Figure 9B** for L2, **Figure 9C** for L3, and **Figure 9D** for L4). Comparison of **Figures 9A–D** with **Figures 7A–D** shows that the effects of binary typhoons on



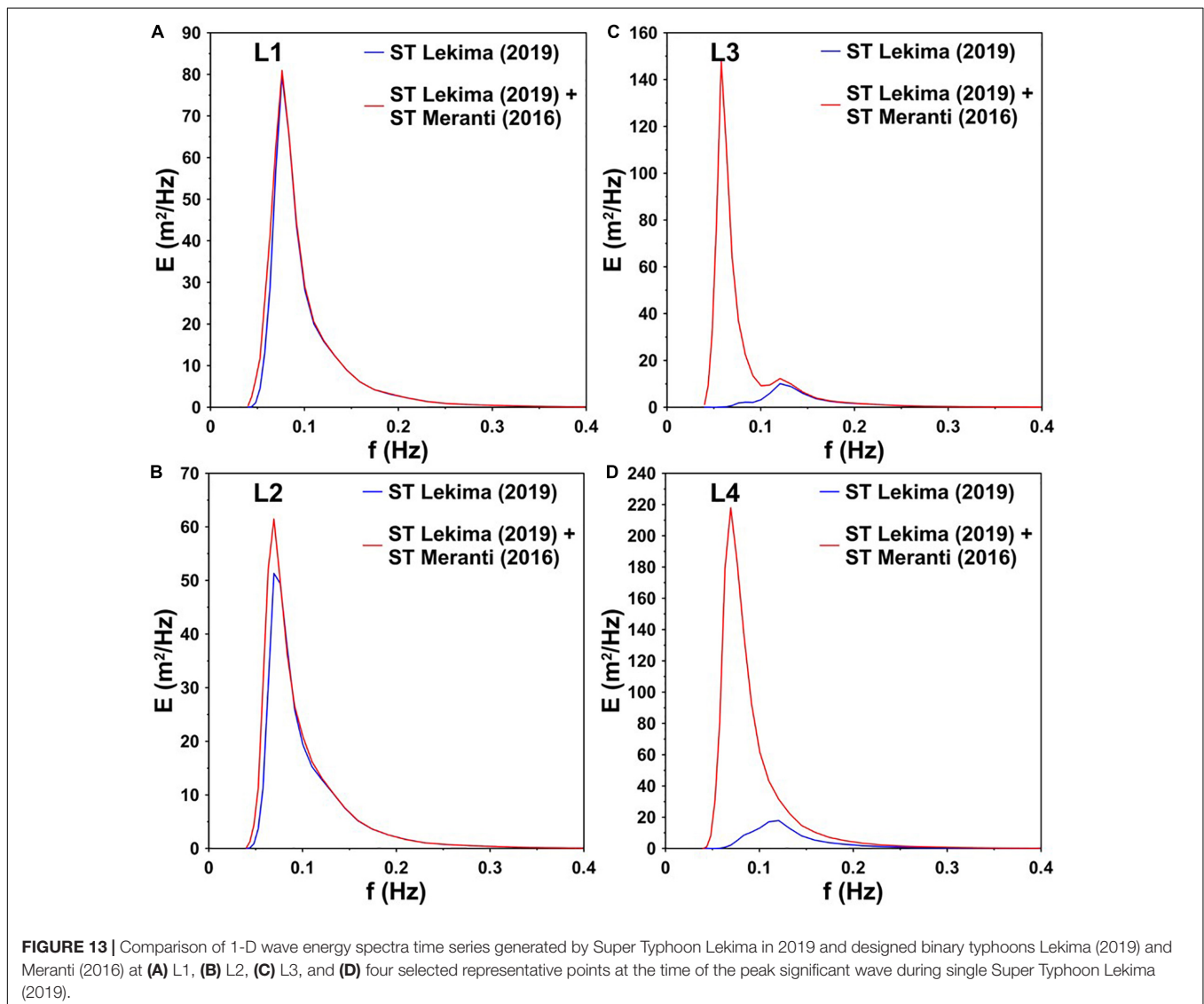
significant wave height derived from the coupled Super Typhoons Lekima (2019) and Meranti (2016) are very similar to those from the coupled Super Typhoons Maria (2018) and Meranti (2016).

## Variation in Wave Spectra Between Single Typhoons and Binary Typhoons

The one-dimensional (1-D) wave spectra of a single typhoon [Super Typhoon Maria (2018)] and designed binary typhoons [Super Typhoon Maria (2018) paired with Super Typhoon Meranti (2016)] at four selected points (L1–L4) are presented in **Figure 10** (**Figure 10A** for L1, **Figure 10B** for L2, **Figure 10C** for L3, and **Figure 10D** for L4) at the time of the peak significant wave that occurred during the single Super Typhoon Maria (2018). Higher wave energy spectra with lower frequency (0.05–0.1 Hz) are observed at points L1–L4 for both the single typhoon and binary typhoons. Additionally, lower-frequency (0.05–0.1 Hz) wind seas are the major component at points L3–L4 (as shown in **Figures 10C,D**) for both the single typhoon

(blue lines in **Figures 10C,D**) and binary typhoons (red lines in **Figures 10C,D**) since the storm waves were primarily generated before or during the passage of the center of typhoons. The percentage increases in wave energy spectra caused by the binary typhoons at L1 and L2 are only 19 and 11%. This phenomenon is dissimilar to that observed at L3 and L4 because the presence of Super Typhoon Meranti (2016) brought high wave energy and generated ocean surface waves.

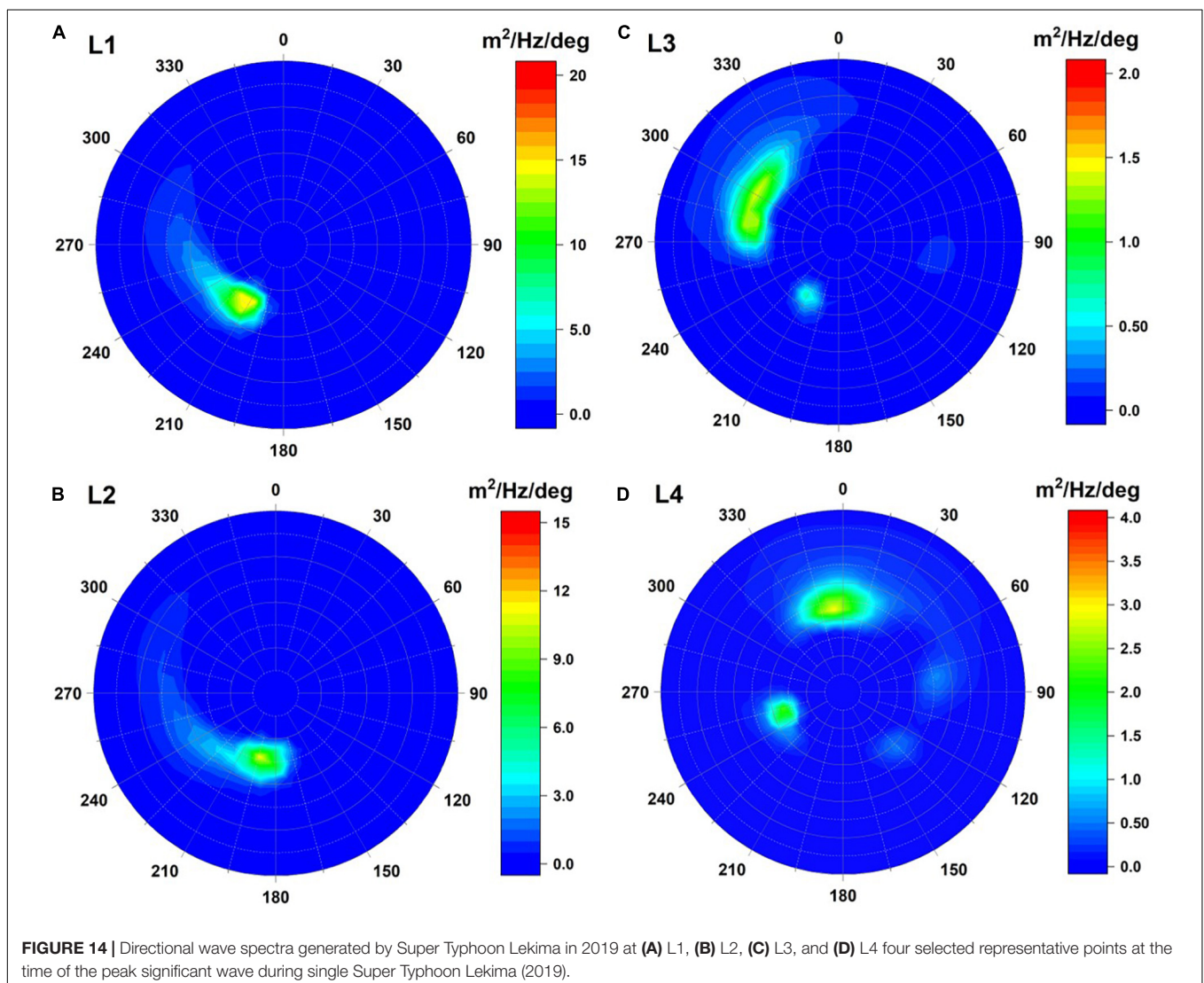
The influence of binary typhoons on wave spectra was also investigated by comparing the single typhoon- and binary typhoon-induced two-dimensional (2-D) directional wave spectra at four selected points (L1–L4). **Figure 11** (**Figure 11A** for L1, **Figure 11B** for L2, **Figure 11C** for L3, and **Figure 11D** for L4) illustrates the 2-D directional wave spectra at the time of the peak significant wave that occurred during the single Super Typhoon Maria (2018). According to the report from Young (2006) and Hu and Chen (2011), most spectra induced by tropical cyclones are monomodal (unidirectional). The simulated



2-D directional wave spectra with the single Super Typhoon Maria (2018) are monomodal at L1–L4, and the results are consistent with previous studies (Young, 2006; Hu and Chen, 2011; Xu et al., 2020). However, a weaker bimodal feature can be found at L1 when binary typhoons [Super Typhoon Maria (2018) paired with Super Typhoon Meranti (2016)] were present (as shown in Figure 12A). Comparison of Figures 11A,B with Figures 12A,B shows that the differences in 2-D directional wave spectra between the single and binary typhoons are minor at L1 and L2. Nevertheless, the magnitudes of the 2-D directional wave spectra for the binary typhoon were three times and four times higher than those for the single typhoon at L3 and L4, respectively (Figures 12C,D), and more widespread.

Figure 13 shows the 1-D wave spectra of the single Super Typhoon Lekima (2019) and designed binary typhoons, i.e., Super Typhoon Lekima (2019) coupled with Super Typhoon Meranti (2016), at four selected points (Figure 13A for L1, Figure 13B for L2, Figure 13C for L3, and Figure 13D for L4) at the time of the peak significant wave that occurred during

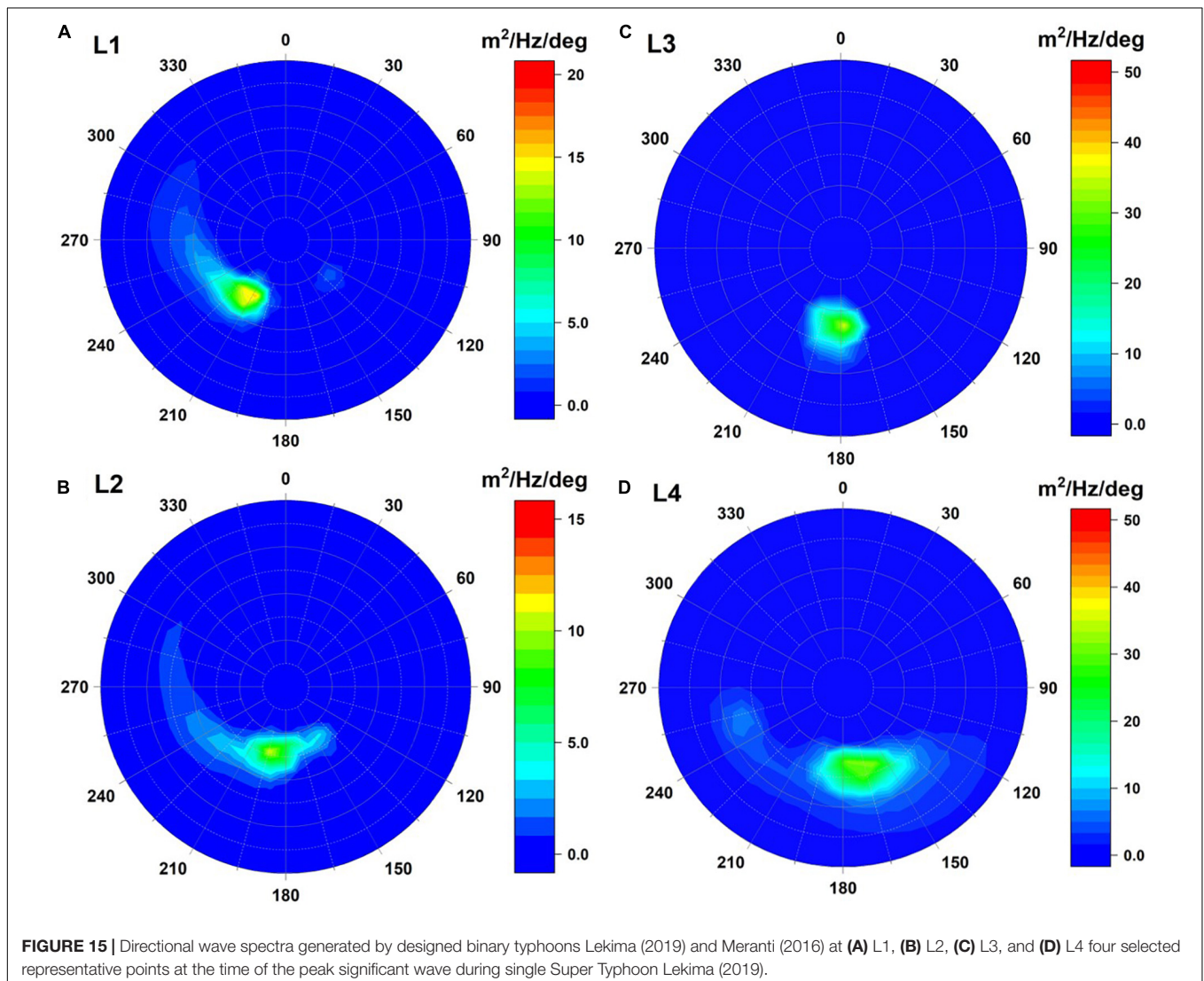
the single Super Typhoon Lekima (2019). The enhancements of the 1-D wave spectra are weaker at L1 and L2 than at L3 and L4 due to the presence of Super Typhoon Meranti (2016). The 1-D wave spectra shown in Figure 13 are similar to those illustrated in Figure 10; higher wave energy spectra with lower frequencies (0.05–0.1 Hz) are observed at points L1–L4 for the binary typhoons (red lines in Figures 10A–D). However, higher-frequency wind seas (>0.1 Hz) were the major component of the 1-D wave spectra for the single Super Typhoon Lekima (2019) at L3 and L4 (blue lines in Figures 13C,D). The 2-D directional wave spectra driven by single Super Typhoon Lekima (2019) for four selected points at the time of the peak significant wave occurrence are displayed in Figure 14 (Figure 14A for L1, Figure 14B for L2, Figure 14C for L3, and Figure 14D for L4). The single Super Typhoon Lekima (2019) formed weaker bimodal features that were detected at L3 and L4 (as shown in Figures 14C,D). Hu and Chen (2011) indicated that most of the hurricane/typhoon-generated 2-D directional wave spectra are monomodal, but the occurrence of bimodal 2-D directional wave



spectra is still 15%. **Figures 15A–C** show the 2-D directional wave spectra of the designed binary typhoons, i.e., Super Typhoon Lekima (2019) coupled with Super Typhoon Meranti (2016) for four selected points. Comparison of the 2-D directional wave spectra of single Super Typhoon Lekima (2019) and those of the designed binary typhoons shows that a weaker bimodal feature is found at L1 for the binary typhoons (**Figure 15A**). The magnitudes of the 2-D directional wave spectra are very similar at L1 and L2 for single typhoons and binary typhoons but slightly more widespread when Super Typhoon Meranti (2016) was present (**Figure 15B**). The increments of 2-D directional wave spectra from the binary typhoon are significant at L3 and L4. As seen in **Figures 15C,D**, the 2-D directional wave spectra of the binary typhoon at L3 and L4 are 26 and 13 times higher than those from Super Typhoon Lekima (2019) alone because of the presence of Super Typhoon Meranti (2016). Additionally, the spectra directions at L3 are also shifted from  $300^\circ$  to  $180^\circ$  for the single typhoon and binary typhoons (comparing **Figure 14C** with **Figure 15C**). A similar phenomenon is also found at L4, and

the spectra directions are changed from  $0^\circ$  to  $180^\circ$  (comparing **Figure 14D** with **Figure 15D**). The occurrence times of peak significant wave height between the single typhoon and binary typhoons at L3 and L4 were shifted (**Figures 9C,D**), and the frequencies of the 1-D wave spectra for the designed binary typhoons at L3 and L4 became lower than those for the single typhoon (**Figures 13C,D**). These variations might cause changes in the directions of the 2-D directional wave spectra.

The results derived from the numerical experiments indicate that the bimodal features of 2-D directional wave spectra are ordinary phenomena when the presence of binary typhoons interaction. The dominating spectral shapes are almost the same at L1 and L2 compared single typhoon to binary typhoons conditions (compared **Figures 11A,B** to **Figures 12A,B**, and compared **Figures 12A,B** to **Figures 13A,B**). The slight differences in 2-D directional wave spectra were distributed in the east-southeast. These bimodal spectral peaks were caused by the swell from the induced by Super Typhoon Meranti (2016). On the contrary, the bimodal features in the 2-D directional wave



spectra returns to the monomodal form when the spectrum is dominated by wind sea generated by the single Super Typhoons Maria (2018) or Lekima (2019). The comparison results also suggest that wave interactions raised by binary typhoons cannot be ignored for simulating the storm waves in Taiwanese waters even if the interactions might be diminished by Taiwan Island.

## SUMMARY AND CONCLUSION

A fully coupled wave-circulation modeling system, SCHISM-WWM-III, with a large computational domain was developed to investigate the effects of binary typhoons on ocean surface waves. SCHISM-WWM-III was validated with significant wave heights measured by altimeters aboard the SARAL and Jason-2 satellites during the period of Super Typhoons Meranti (2016), Maria (2018), and Lekima (2019). Original and modified typhoon wind fields from ERA5 were imposed on SCHISM-WWM-III to hindcast the storm waves induced by three super typhoons. The comparisons indicate that the modified ERA5 winds are far superior to the original ERA5 winds in hindcasting ocean surface waves during typhoon events. Two numerical experiments with modified ERA5 typhoon winds were designed to clarify the influences of binary typhoons on the significant wave height, 1-D wave spectra, and 2-D directional wave spectra simulations. The first numerical experiment paired Super Typhoons Maria (2018) and Meranti (2016), while the second numerical experiment consisted of two typhoons Super Typhoons Lekima (2019) and Meranti (2016). Four representative points (L1–L4) close to the paths of three super typhoons are selected to examine the binary typhoon effects caused by two designed numerical experiments. The significant wave height, 1-D wave spectra, and 2-D directional wave spectra at points L1–L4 for single typhoons and binary typhoons were determined to assess their differences. It is intuitively that the significant wave height will be raised due to the effect of binary typhoons, however, from a scientific perspective, how many percentages of wave height increment is needed to be quantified. This paper reveals that binary typhoons slightly increase the peak significant wave height (<9%) at points L1 and L2 in the two numerical experiments. This is identical to the result from a previous similar study for binary typhoons in the South China Sea. However, the increases in significant wave heights before and after peaks are obvious at points L1 and L2 because the wind speeds in a typhoon's peripheral circulation might be enhanced if another typhoon is present nearby. This finding is particularly noticeable and unique in the present study. At points L3 and L4, the significant wave heights increased dramatically because of the passage of Super Typhoon Meranti (2016) in two numerical experiments. The 1-D wave spectra time series at points L1–L4 for the single typhoons and binary typhoons are similar to the significant wave height time series. Weak bimodal features in the 2-D directional wave spectra are detected at point L1 in two numerical experiments because of the presence of the binary typhoons. The variations in the 2-D directional wave spectra at point L2 are minor but are slightly more widespread. However, the enhancements of the 2-D directional wave spectra at points L3 and L4 are more

significant due to the presence of Super Typhoon Meranti (2016). The two numerical experiments designed in the present study indicate that the ocean surface waves caused by single typhoons are different from those induced by binary typhoons. The results in the present study are identical to those previously reported for the South China Sea. The effects of binary typhoons on ocean surface waves are more significant at the periphery of the typhoon than near the center of the typhoon. However, the interactions between storm waves driven by binary typhoons might be diminished by Taiwan Island even if the separation distance between two typhoons is <700 km. The present study aims to clarify the variations of significant wave height and 1D/2D wave spectra when the presence of binary typhoons. The numerical experiments for examining the effect of binary typhoons on wave simulations are well-designed. The wind speeds for the selected three super typhoons were more violent but did not make their landfall on Taiwan. Although the numerical experiments in the present study are artificially designed and exist certain limitations and uncertainties, they can be very useful for scientists and engineers to manage and develop the coastal and marine environment. The present study not only highlights the effect of binary typhoons on ocean surface waves but also provides a methodology for similar or related studies on oceans where binary typhoons/cyclones/hurricanes may occur, although more designed numerical experiments need to be further analyzed.

## DATA AVAILABILITY STATEMENT

The datasets presented in this study can be found in online repositories. The names of the repository/repositories and accession number(s) can be found below: <https://coastwatch.noaa.gov/cw/satellite-data-products/sea-surface-height/along-track.html>.

## AUTHOR CONTRIBUTIONS

HC, S-CH, and W-BC: conceptualization, writing—original draft, and review and editing. T-YC: data curation. T-YC and H-LW: formal analysis. T-YC and W-BC: methodology. W-BC: model validation. All authors have read and agreed to the published version of the manuscript.

## FUNDING

This research was supported by the National Science and Technology Center for Disaster (NCDR), Ministry of Science and Technology (MOST), Taiwan.

## ACKNOWLEDGMENTS

We would like to thank the National Oceanic and Atmospheric Administration in the United States for providing the survey data and Joseph Zhang at the Virginia Institute of Marine Science, College of William & Mary, for kindly sharing his experiences using the numerical model.

## REFERENCES

- Battjes, J. A., and Janssen, J. P. F. M. (1978). "Energy loss and set-up due to breaking of random waves," in *Proceedings of 16th Conference on Coastal Engineering*, (Hamburg: ASCE), 569–587.
- Carr, L. E. III., and Elsberry, R. L. (1998). Objective diagnosis of binary tropical cyclone interactions for the western North Pacific basin. *Mon. Weather Rev.* 126, 1734–1740. doi: 10.1175/1520-04931998126<1734:ODOBTC>2.0.CO;2
- Carr, L. E. III., Boothe, M. A., and Elsberry, R. L. (1997). Observational evidence for alternate modes of track-altering binary tropical cyclone scenarios. *Mon. Weather Rev.* 125, 2094–2111. doi: 10.1175/1520-04931997125<2094:OEFAMO>2.0.CO;2
- Cha, E. J., Yun, S. G., Moon, I. J., and Kim, D. H. (2021). Binary interaction of typhoons Soulik and Cimaron in 2018 e part I: observational characteristics and forecast error. *Trop. Cyclone Res. Rev.* 10, 32–42. doi: 10.1016/j.tcr.2021.03.001
- Chen, W. B., and Liu, W. C. (2014). Modeling flood inundation induced by river flow and storm surges over a river basin. *Water* 6, 3182–3199. doi: 10.3390/w6103182
- Chen, W. B., and Liu, W. C. (2016). Assessment of storm surge inundation and potential hazard maps for the southern coast of Taiwan. *Nat. Hazards* 82, 591–616. doi: 10.1007/s11069-016-2199-y
- Chen, W. B., and Liu, W. C. (2017). Investigating the fate and transport of fecal coliform contamination in a tidal estuarine system using a three-dimensional model. *Mar. Pollut. Bull.* 116, 365–384. doi: 10.1016/j.marpolbul.2017.01.031
- Chen, W. B., Chen, H., Hsiao, S. C., Chang, C. H., and Lin, L. Y. (2019). Wind forcing effect on hindcasting of typhoon-driven extreme waves. *Ocean Eng.* 188, 106260. doi: 10.1016/j.oceaneng.2019.106260
- Chen, W. B., Chen, H., Lin, L. Y., and Yu, Y. C. (2017a). Tidal current power resources and influence of sea-level rise in the coastal waters of Kinmen Island, Taiwan. *Energies* 10:652. doi: 10.3390/en10050652
- Chen, W. B., Lin, L. Y., Jang, J. H., and Chang, C. H. (2017b). Simulation of typhoon-induced storm tides and wind waves for the northeastern coast of Taiwan using a tide–surge–wave coupled model. *Water* 9:549. doi: 10.3390/w9070549
- Chen, W. B., Liu, W. C., and Hsu, M. H. (2012). Computational investigation of typhoon-induced storm surges along the coast of Taiwan. *Nat. Hazards* 64, 1161–1185. doi: 10.1007/s11069-012-0287-1
- Chen, W. B., Liu, W. C., and Hsu, M. H. (2013). Modeling evaluation of tidal stream energy and the impacts of energy extraction on hydrodynamics in the Taiwan Strait. *Energies* 6, 2191–2203. doi: 10.3390/en6042191
- Chen, W. B., Liu, W. C., Hsu, M. H., and Hwang, C. C. (2015). Modeling investigation of suspended sediment transport in a tidal estuary using a three-dimensional model. *Appl. Math. Model.* 39, 2570–2586. doi: 10.1016/j.apm.2014.11.006
- Choi, Y., Cha, D. H., Lee, M. I., Kim, J., Jin, C. S., Park, S. H., et al. (2017). Satellite radiance data assimilation for binary tropical cyclone cases over the western North Pacific. *J. Adv. Model. Earth Syst.* 9, 832–853. doi: 10.1002/2016MS000826
- Dong, K., and Neumann, C. J. (1983). On the relative motion of binary tropical cyclones. *Mon. Weather Rev.* 111, 945–953. doi: 10.1175/1520-04931983111<0945:OTRMOB>2.0.CO;2
- Dube, S. K., Sinha, P. C., and Roy, G. D. (1985). The numerical simulation of storm surges along the Bangladesh coast. *Dyn. Atmos. Oceans* 9, 121–133. doi: 10.1016/0377-0265(85)90002-8
- Fujiwhara, S. (1921). The natural tendency towards symmetry of motion and its application as a principle in meteorology. *Q. J. R. Meteorol. Soc.* 47, 287–292. doi: 10.1002/qj.49704720010
- Ginis, I., and Sutyryn, G. (1995). Hurricane-generated depth-averaged currents and sea surface elevation. *J. Phys. Oceanogr.* 25, 1218–1242. doi: 10.1175/1520-04851995025<1218:HGDACA>2.0.CO;2
- Hasselmann, K. F., Barnett, T. P., Bouws, E., Carlson, H., Cartwright, D. E., Eake, K., et al. (1973). *Measurements of Wind-Wave Growth and Swell Decay during the Joint North Sea Wave Project (JONSWAP)*. Berlin: Deutsches Hydrographisches Institut.
- Hsiao, S. C., Chen, H., Chen, W. B., Chang, C. H., and Lin, L. Y. (2019). Quantifying the contribution of nonlinear interactions to storm tide simulations during a super typhoon event. *Ocean Eng.* 194:106661. doi: 10.1016/j.oceaneng.2019.106661
- Hsiao, S. C., Chen, H., Wu, H. L., Chen, W. B., Chang, C. H., Guo, W. D., et al. (2020a). Numerical simulation of large wave heights from super typhoon Nepartak (2016) in the eastern waters of Taiwan. *J. Mar. Sci. Eng.* 8:217.
- Hsiao, S. C., Wu, H. L., Chen, W. B., Chang, C. H., and Lin, L. Y. (2020b). On the sensitivity of typhoon wave simulations to tidal elevation and current. *J. Mar. Sci. Eng.* 8:731. doi: 10.3390/jmse8090731
- Hsiao, S. C., Cheng, C. T., Chang, T. Y., Chen, W. B., Wu, H. L., Jang, J. H., et al. (2021a). Assessment of offshore wave energy resources in Taiwan using long-term dynamically downscaled winds from a third-generation reanalysis product. *Energies* 14:653. doi: 10.3390/en14030653
- Hsiao, S. C., Wu, H. L., Chen, W. B., Guo, W. D., Chang, C. H., and Su, W. R. (2021b). Effect of depth-induced breaking on wind wave simulations in shallow nearshore waters off Northern Taiwan during the passage of two Super Typhoons. *J. Mar. Sci. Eng.* 9:706. doi: 10.3390/jmse9070706
- Hu, K., and Chen, Q. (2011). Directional spectra of hurricane-generated waves in the Gulf of Mexico. *Geophys. Res. Lett.* 38, 570–583. doi: 10.1029/2011GL049145
- Jang, W., and Chun, H. Y. (2015). Characteristics of binary tropical cyclones observed in the western North Pacific for 62 years (1951–2012). *Mon. Weather Rev.* 143, 1749–1761. doi: 10.1175/MWR-D-14-00331.1
- Jelenski, C. P. (1965). A numerical calculation of storm tides induced by a tropical storm impinging on a continental shelf. *Mon. Weather Rev.* 93, 343–358. doi: 10.1175/1520-04931993093<0343:ANCOS>2.3.CO;2
- Jelenski, C. P. (1966). Numerical computations of storm surges without bottom stress. *Mon. Weather Rev.* 94, 379–394. doi: 10.1175/1520-04931966094<0379:NCOSW>2.3.CO;2
- Khain, A., Ginis, I., Falkovich, A., and Frumin, M. (2000). Interaction of binary tropical cyclones in a coupled tropical cyclone–ocean model. *J. Geophys. Res.* Atmos. 105, 22337–22354. doi: 10.1029/2000JD900268
- Knaff, J. A., Sampson, C. R., DeMaria, M., Marchok, T. P., Gross, J. M., and McAdie, C. J. (2007). Statistical tropical cyclone wind radii prediction using climatology and persistence. *Weather Forecast.* 22, 781–791. doi: 10.1175/WAF1026.1
- Lee, T. L. (2008). Back-propagation neural network for the prediction of the short-term storm surge in Taichung harbor, Taiwan. *Eng. Appl. Artif. Intell.* 21, 63–72. doi: 10.1016/j.engappai.2007.03.002
- Liu, W. C., Chen, W. B., and Kuo, J. T. (2008). Modeling residence time response to freshwater discharge in a mesotidal estuary, Taiwan. *J. Mar. Syst.* 74, 295–314. doi: 10.1016/j.jmarsys.2008.01.001
- Liu, Z., Wang, H., Zhang, Y. J., Magnusson, L., Loftis, J. D., and Forrest, D. (2012). Cross-scale modeling of storm surge, tide, and inundation in Mid-Atlantic Bight and New York City during Hurricane Sandy, 2012. *Estuar. Coast. Shelf Sci.* 233:106544. doi: 10.1016/j.ecss.2019.106544
- Orton, P., Georgas, N., Blumberg, A., and Pullen, J. (2012). Detailed modeling of recent severe storm tides in estuaries of the New York City region. *J. Geophys. Res. Oceans* 117:C09030. doi: 10.1029/2012JC008220
- Pan, Y., Chen, Y. P., Li, J. X., and Ding, X. L. (2016). Improvement of wind field hindcasts for tropical cyclones. *Water Sci. Eng.* 9, 58–66. doi: 10.1016/j.wse.2016.02.002
- Prieto, R., McNoldy, B. D., Fulton, S. R., and Schubert, W. H. (2003). A classification of binary tropical cyclone-like vortex interactions. *Mon. Weather Rev.* 131, 2656–2666. doi: 10.1175/1520-04932003131<2656:ACOBTC>2.0.CO;2
- Ritchie, E. A., and Holland, G. J. (1993). On the interaction of tropical–cyclone–scale vortices. II: discrete vortex patches. *Q. J. R. Meteorol. Soc.* 119, 1363–1379. doi: 10.1002/qj.49711951407
- Roland, A. (2009). *Development of WWM II: Spectral Wave Modeling On Unstructured Meshes*. Ph.D. thesis, Darmstadt: Technology University Darmstadt.
- Shchepetkin, A. F., and McWilliams, J. C. (2005). The regional oceanic modeling system (ROMS): a split-explicit, free-surface, topography-following-coordinate oceanic model. *Ocean Model.* 9, 347–404. doi: 10.1016/j.ocemod.2004.08.002
- Shih, H. J., Chang, C. H., Chen, W. B., and Lin, L. Y. (2018). Identifying the optimal offshore areas for wave energy converter deployments in Taiwanese waters based on 12-year model hindcasts. *Energies* 11:499. doi: 10.3390/en11030499
- Su, W. R., Chen, H., Chen, W. B., Chang, C. H., Lin, L. Y., Jang, J. H., et al. (2018). Numerical investigation of wave energy resources and hotspots in the

- surrounding waters of Taiwan. *Renew. Energy* 118, 814–824. doi: 10.1016/j.renene.2017.11.080
- Wu, X., Fei, J., Huang, X., Zhang, X., Cheng, X., and Ren, J. (2012). A numerical study of the interaction between two simultaneous storms: goni and morakot in September 2009. *Adv. Atmos. Sci.* 29, 561–574. doi: 10.1007/s00376-011-1014-7
- Xu, F., Cheng, Z., and Xia, M. (2020). Surface wave field under binary typhoons Sarika and Haima (2016) in South China Sea. *Estuar. Coast. Shelf Sci.* 241:106802. doi: 10.1016/j.ecss.2020.106802
- Yang, C. C., Wu, C. C., Chou, K. H., and Lee, C. Y. (2008). Binary interaction between Typhoons Fengshen (2002) and Fungwong (2002) based on the potential vorticity diagnosis. *Mon. Weather Rev.* 136, 4593–4611. doi: 10.1175/2008MWR2496.1
- Yang, Y. J., Sun, L., Duan, A.-M., Li, Y.-B., Fu, Y.-F., Wang, Z.-Q., et al. (2012). Impacts of the binary typhoons on upper ocean environments in November 2007. *J. Appl. Remote Sens.* 6:063583. doi: 10.1117/1.JRS.6.063583
- Young, I. R. (2006). Directional spectra of hurricane wind waves. *J. Geophys. Res. Oceans* 111:C08020. doi: 10.1029/2006JC003540
- Zhang, Y. J., Ye, F., Stanev, E. V., and Grashorn, S. (2016). Seamless cross-scale modeling with SCHISM. *Ocean Model.* 102, 64–81.
- Zhang, Y. J., Ye, F., Yu, H., Sun, W., Moghimi, S., Myers, E., et al. (2020). Simulating compound flooding events in a hurricane. *Ocean Dyn.* 70, 621–640. doi: 10.1007/s10236-020-01351-x
- Zhang, Y., and Baptista, A. M. (2008). SELFE: a semi-implicit Eulerian-Lagrangian finite-element model for cross-scale ocean circulation. *Ocean Model.* 21, 71–96. doi: 10.1016/j.ocemod.2007.11.005
- Zheng, L., Weisberg, R. H., Huang, Y., Luettich, R. A., Westerink, J. J., Kerr, P. C., et al. (2013). Implications from the comparisons between two- and three-dimensional model simulations of the Hurricane Ike storm surge. *J. Geophys. Res. Oceans* 118, 3350–3369. doi: 10.1002/jgrc.20248
- Zu, T., Gan, J., and Erofeeva, S. Y. (2008). Numerical study of the tide and tidal dynamics in the South China Sea. *Deep Sea Res. I Oceanogr. Res. Pap.* 55, 137–154. doi: 10.1016/j.dsr.2007.10.007

**Conflict of Interest:** The authors declare that the research was conducted in the absence of any commercial or financial relationships that could be construed as a potential conflict of interest.

**Publisher's Note:** All claims expressed in this article are solely those of the authors and do not necessarily represent those of their affiliated organizations, or those of the publisher, the editors and the reviewers. Any product that may be evaluated in this article, or claim that may be made by its manufacturer, is not guaranteed or endorsed by the publisher.

Copyright © 2021 Chang, Chen, Hsiao, Wu and Chen. This is an open-access article distributed under the terms of the Creative Commons Attribution License (CC BY). The use, distribution or reproduction in other forums is permitted, provided the original author(s) and the copyright owner(s) are credited and that the original publication in this journal is cited, in accordance with accepted academic practice. No use, distribution or reproduction is permitted which does not comply with these terms.





# Wind Waves in the Mediterranean Sea: An ERA5 Reanalysis Wind-Based Climatology

Francesco Barbariol<sup>1\*</sup>, Silvio Davison<sup>1</sup>, Francesco Marcello Falcieri<sup>1</sup>, Rossella Ferretti<sup>2,3</sup>, Antonio Ricchi<sup>2,3</sup>, Mauro Sclavo<sup>4</sup> and Alvise Benetazzo<sup>1</sup>

<sup>1</sup> Institute of Marine Sciences (ISMAR), Italian National Research Council (CNR), Venice, Italy, <sup>2</sup> Department of Physical and Chemical Sciences, University of L'Aquila, L'Aquila, Italy, <sup>3</sup> Center of Excellence in Telesensing of Environment and Model Prediction of Severe Events (CETEMPS), L'Aquila, Italy, <sup>4</sup> Institute of Polar Sciences (ISP), Italian National Research Council (CNR), Padua, Italy

## OPEN ACCESS

### Edited by:

Giovanni Besio,  
University of Genoa, Italy

### Reviewed by:

Francesco De Leo,  
Cal Poly San Luis Obispo College  
of Engineering, United States  
Lorenzo Mentaschi,  
Joint Research Centre (JRC), Belgium  
Khalid Amarouche,  
National School of Sciences of the  
Sea and Coastal Planning  
(ENSSMAL), Algeria

### \*Correspondence:

Francesco Barbariol  
francesco.barbariol@cnr.it

### Specialty section:

This article was submitted to  
Physical Oceanography,  
a section of the journal  
Frontiers in Marine Science

**Received:** 18 August 2021

**Accepted:** 11 October 2021

**Published:** 16 November 2021

### Citation:

Barbariol F, Davison S,  
Falcieri FM, Ferretti R, Ricchi A,  
Sclavo M and Benetazzo A (2021)  
Wind Waves in the Mediterranean  
Sea: An ERA5 Reanalysis  
Wind-Based Climatology.  
Front. Mar. Sci. 8:760614.  
doi: 10.3389/fmars.2021.760614

A climatology of the wind waves in the Mediterranean Sea is presented. The climate patterns, their spatio-temporal variability and change are based on a 40-year (1980–2019) wave hindcast, obtained by combining the ERA5 reanalysis wind forcing with the state-of-the-art WAVEWATCH III spectral wave model and verified against satellite altimetry. Results are presented for the typical (50th percentile) and extreme (99th percentile) significant wave height and, for the first time at the regional Mediterranean Sea scale, for the typical and extreme expected maximum individual wave height of sea states. The climate variability of wind waves is evaluated at seasonal scale by proposing and adopting a definition of seasons for the Mediterranean Sea states that is based on the satellite altimetry wave observations of stormy (winter) and calm (summer) months. The results, initially presented for the four seasons and then for winter and summer only, show the regions of the basin where largest waves occur and those with the largest temporal variability. A possible relationship with the atmospheric parameter anomalies and with teleconnection patterns (through climate indices) that motivates such variability is investigated, with results suggesting that the Scandinavian index variability is the most correlated to the Mediterranean Sea wind-wave variability, especially for typical winter sea states. Finally, a trend analysis shows that the Mediterranean Sea typical and extreme significant and maximum individual wave heights are decreasing during summer and increasing during winter.

**Keywords:** wave climate, Mediterranean Sea, ERA5, maximum waves, climate indices, climate trends, wave hindcast, WAVEWATCH III (WW3)

## INTRODUCTION

Wind waves are a key factor of the Earth global climate system contributing to the modulation of the exchanges at the atmosphere-ocean interface (Cavaleri et al., 2012b). At the same time, wind waves can significantly influence human activities at global-to-local scales, as they can grow under moderate-to-intense winds provided a sufficient fetch length is available, therefore

impacting offshore structures and navigation as well as coastlines and coastal recreational or productive activities. The largest individual waves of sea states, particularly during storm events, are recognized as a potential risk of structural damage and of goods and even human-life losses at sea. Many accidents have been reported in the past and attributed to the occurrence of very large, sometimes abnormal, wave heights (Dysthe et al., 2008). Therefore, the assessment of the wind-wave climate (i.e., the wind-wave characteristics averaged on a long-term temporal scale) and of its spatio-temporal variability and change is of fundamental importance for coastal and offshore engineering purposes (to design, for instance, littoral protections, oil rigs and wind farms), navigation (ship routing) and for all other activities related to the marine environment (DNV GL–Det Norske Veritas Germanischer Lloyd, 2017). Beside the most widely used significant wave height, information on the maximum wave individual height expected at certain locations is more and more required by the naval and offshore industries for the definition of the environmental loads over the lifetime of a ship or a structure (DNV GL–Det Norske Veritas Germanischer Lloyd, 2017).

In this study, we characterize the long-term wind-wave climate of the Mediterranean Sea (hereinafter MS; **Figure 1**), located in southern Europe, which is a primary source of food, ecosystem services and economic activities for all the countries in the region. It is estimated that one-third of the Mediterranean countries' population lives along the MS coastlines (46,000-km long), and that 30% of the global international tourism is headed to this region, particularly the coastal areas, where large and populated cities have developed (United Nations Environment Programme/Mediterranean Action Plan and Plan Bleu, 2020). The MS is also one of the world's busiest shipping lanes, carrying 20% of seaborne trade (including 17% of the world's oil tank capacity; United Nations Environment Programme/Mediterranean Action Plan and Plan Bleu, 2020), 10% of world container throughput and over 200 million passengers (Piante and Ody, 2015). During MS storms wind waves can grow until threatening heights that may cause naval accidents, as happened to the passenger ships "Voyager" in 2005 (Bertotti and Cavaleri, 2008) and "Louis Majesty" in 2010 (Cavaleri et al., 2012a), both cruising in the western MS. Besides this, the MS basin, with its processes and dynamics, is a pivotal environmental factor for the climate not only of the whole region (Lionello, 2012), but also of the neighboring areas and countries. Given its fragility and exposure to anthropogenic pressure, the MS is considered an early responder to climate change and a hot-spot of its effects and impacts (Giorgi, 2006). Hence, it is essential to assess both the past and present climatologies in order to create a solid reference for studies on the future climate.

The purpose of this paper is to characterize the typical and extreme climate of the MS wind waves, together with its spatio-temporal variability and changes at a long-term spanning four decades (1981–2019). To cope with the requirements of such a complex environment and characterize the wave climate therein, we rely on a long-term and high-resolution wave hindcast, obtained by combining numerical wave modeling and atmospheric reanalysis. We have thus run the WAVEWATCH

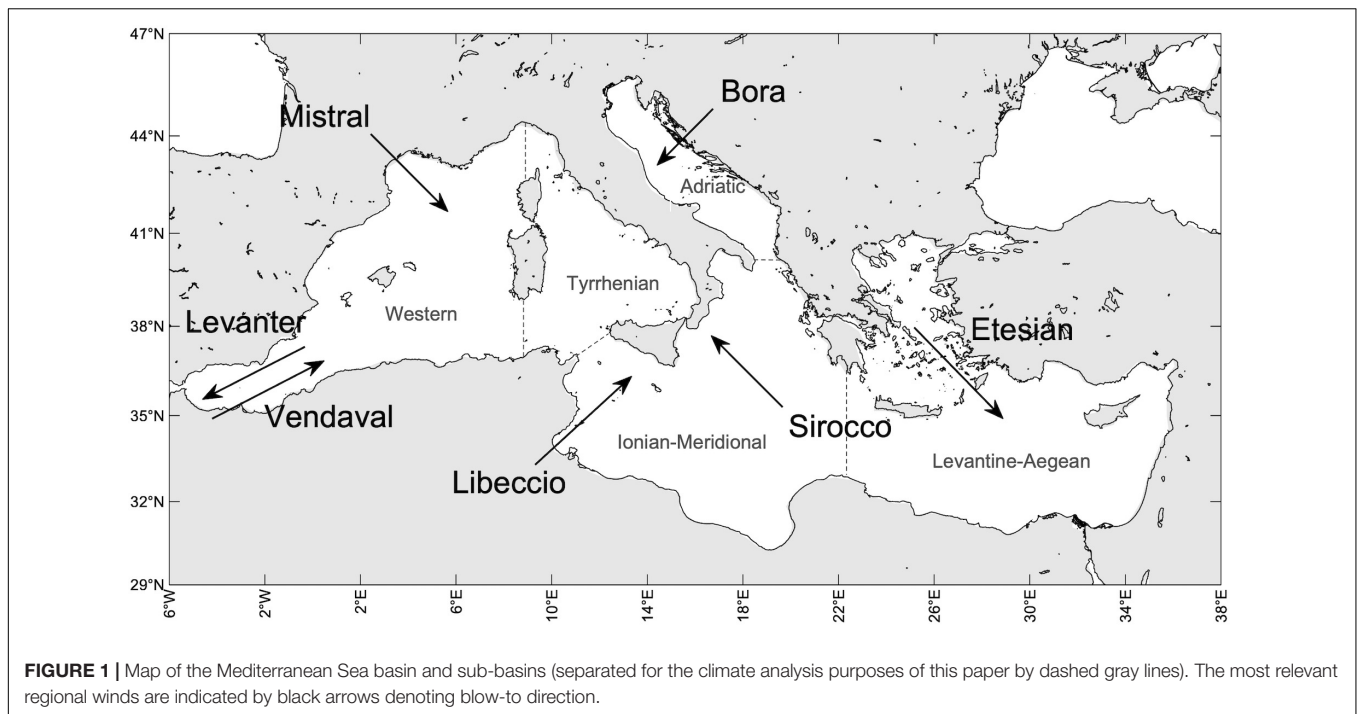
III model [Tolman, 1991; The WAVEWATCH III Development Group [WW3DG], 2019] with the ERA5 reanalysis wind forcing (Hersbach et al., 2018, 2020) and performed a wave climate analysis. In doing so, we do not expect to cover all aspects of the wave climatology of the MS, some of which have been addressed in various studies and publications (an non-exhaustive list of them can be found in Section "The study area"). We rather aim at bestowing new results based on state-of-the-art numerical modeling and reanalysis data, using one of the longest and most recent datasets to date. A novel season definition for the MS states based on observed data is proposed and adopted. Additionally, and most importantly, for the first time, we present and discuss the MS climate of expected maximum individual waves and of the most relevant factors for their development.

The paper is structured as follows. The study area, the wave hindcast and the methodology we have used for the wave climate analysis are detailed in Section "Methodology and Data". In Section "Results" we present the results of this wave climate analysis, which first focuses on the significant wave height of sea states, showing its typical and extreme seasonal climate in the MS, its spatio-temporal variability and change, and then on the expected maximum individual waves and relevant parameters for their estimation (wave steepness and narrow bandedness). Section "Discussion" is a discussion on the limits and strengths of this dataset and on the results of the wave climate analysis, also compared to previous studies in the same region. Conclusions in section "Conclusion" close the paper.

## METHODOLOGY AND DATA

### The Study Area

The MS is a mostly deep (1,500 m on average) semi-enclosed regional sea, connected to the west to the Atlantic Ocean by the narrow Gibraltar Strait and to the east to the Black Sea by the Bosphorus and Gallipoli (Dardanelles) Straits. Geographically, it is located between the European and the African continents and, from a climatic perspective, at the transition between a midlatitude regime zone, to the north, and a subtropical regime zone, to the south. Meteorologically, the MS region is interested by an intense synoptic-scale activity, with a separate branch of the northern hemisphere storm track passing over the region (Lionello and Sanna, 2005). The MS has a complex morphology, with many islands and peninsulas dividing the basin into sub-basins, some of them connected by straits (**Figure 1**). Together with the presence of steep mountain ridges close to the coast, this morphological complexity provides to the MS environment with a spatial heterogeneity, which also reflects on the MS region meteorology and climate, making their successful modeling far from being trivial (Lionello, 2012). In addition, and most important for the topic of this study, the orographic complexity of the MS region plays a fundamental role in the genesis of cyclones. In this context, cyclones typically originate (mostly in the western MS) from the interaction of synoptic-scale flows with the mountains, constraining the flow in the lower troposphere and producing local and often strong winds (Lionello, 2012).



In general, the MS wind climate is characterized by the occurrence of winds with regional spatial structure (200–1,000 km) and seasonal variability (Zecchetto and De Biasio, 2007; Lionello, 2012). In **Figure 1** we have indicated the most relevant winds for the different sub-basins. Levanter and Vendaval winds blow in the westernmost part of the MS (Western sub-basin), respectively, from the north-east and the south-west: the first during all seasons (but most intensely in winter), the second mainly during autumn and spring. Mistral is a cold dry wind jet, stronger during winter, blowing from the north/north-west over the western and Tyrrhenian sub-basins and occasionally reaching the African coasts. Libeccio and Sirocco are southerly winds blowing in the Tyrrhenian and Ionian-Meridional sub-basins: the first mainly in winter from the south-west, the second mainly in autumn and spring from the south-east. Sirocco is also channeled into the Adriatic sub-basin, and it contributes to the intense storm surges that take place in the northern Adriatic Sea and in the Venice lagoon (Cavaleri et al., 2019). The other dominant wind in the Adriatic climate is Bora, a cold and dry north-easterly wind producing jets over the sea after interacting with the local orography. Northerly winds also dominate the climate in the Levantine-Aegean sub-basin: Etesian winds blow from the north/north-west and are particularly strong during summer.

The climate of wind waves in the MS, mostly driven by these regional winds, is subject to the morphological complexity constraints described above, resulting in limited fetches in large parts of the basin (with some exceptions) and in coastal shallow regions relatively proximal to the generation areas. Some regions present peculiar characteristics, for instance the northern Adriatic Sea or the Aegean Sea, where wave propagation experiences either the evolution over a relatively shallow flat

bottom or the shadowing by numerous islands, respectively. Most of the studies on the MS wave climate (including a wind and wave atlas of the MS, Western European Union and Western European Armaments Organisation Research Cell, 2004) based on hindcast or observed data, focused on the extreme significant wave height (e.g., the monthly 99th percentile: Sartini et al., 2015a; Sartini et al., 2015b, 2017; De Leo et al., 2020; Morales-Márquez et al., 2020) with only a few exceptions that focused on the average significant wave height (for instance, Lionello and Sanna, 2005; De Leo et al., 2020). Others were dedicated to the assessment of the wave energy climate at specific locations or over the whole basin, with energy harvesting purposes (Barbariol et al., 2013; Liberti et al., 2013; Arena et al., 2015; Besio et al., 2016). A similar approach to the one presented in this paper, although with a different purpose, can be found in von Schukmann et al. (2021), where Benetazzo et al. have used a shorter portion of our dataset for an assessment of the climate of the maximum individual waves in the MS in the last quarter of a century, focusing on the 2019 anomalies and their physical interpretation. The complexity of the MS climate has also been exploited to test novel approaches for wave climate analysis (Sartini et al., 2015b; Portilla-Yandún et al., 2019). Besides providing the statistics over decadal periods (generally one to three decades), some of the previous studies used statistical and data analysis approaches to obtain accurate return level estimates of the significant wave height (e.g., Sartini et al., 2015a), and to describe the spatio-temporal variability and the long-term change (trends) of the wave climate (e.g., Sartini et al., 2017; De Leo et al., 2020; Morales-Márquez et al., 2020). To interpret inter-annual and inter-decadal variabilities, some studies also tried to relate them to the modes of atmospheric variability, looking for teleconnection patterns and using climate indices (Lionello and Sanna, 2005; Morales-Márquez et al., 2020).

Finally, some studies were devoted to providing projections of the future wave climate under climate change scenarios over the whole basin or sub-basins (see for instance, Benetazzo et al., 2012; De Leo et al., 2021).

## Mediterranean Sea Waves Hindcast Wave Model Setup

The climate of MS wind waves, its spatio-temporal variability and change presented in this paper are grounded on a numerical model hindcast, produced by running the wave model WAVEWATCH III<sup>®</sup> (hereinafter WW3; version 6.07;<sup>1</sup>) for a 40-year long period from 1980 to 2019 over the whole MS basin (Figure 1). WW3 is a third-generation spectral wind-wave model that solves the random-phase spectral action density balance equation for wavenumber-direction spectra [Tolman, 1991; The WAVEWATCH III Development Group [WW3DG], 2019]. Various source-term packages allow computing wave generation by wind, decay by dissipative processes, nonlinear wave-wave interactions, and wave transformation near the coast. For this study, WW3 has been run over a high-resolution structured curvilinear grid with a horizontal spacing of 0.05° (~5 km). WW3 has been forced with the 10-meter wind speed horizontal components ( $u_{10}$ ,  $v_{10}$ ) provided hourly by the ERA5 atmospheric reanalysis, over a 0.25° resolution horizontal structured grid (Hersbach et al., 2018). To represent wave growth and decay in WW3, we have used the state-of-the-art ST4 source-term parameterization of Ardhuin et al. (2010), relying on the default values, but adjusting some coefficients in agreement with the results of TEST405 of the Ardhuin et al. study [The WAVEWATCH III Development Group [WW3DG], 2019] to values that are supposed to perform well for younger seas ( $\beta_{max} = 1.55$  and  $z_{0,max} = 0.002$ ). Wave propagation has been computed using a third-order accurate scheme, together with the discrete interaction approximations for nonlinear wave-wave interactions, and accounting for subgrid-scale obstructions (propagation-based approach; Tolman, 2003), very common in some parts of the MS (e.g., Adriatic and Aegean seas). In shallow waters (i.e., coastal areas and the northern Adriatic Sea) bottom friction has been modeled using the JONSWAP parameterization with default values (Hasselmann et al., 1973), while the depth-induced wave breaking has been parametrized following Battjes and Janssen (1978). To define the bottom topography and coastlines we have used the ETOPO1 relief model (doi: 10.7289/V5C8276M).

## Wave Model Outputs

The model outputs considered in this study, produced at hourly rate, are the significant wave height  $H_s$ , the maximum expected crest height  $\bar{C}_{max}$ , and the maximum expected crest-to-trough height  $\bar{H}_{max}$ . Results for  $H_s$  and  $\bar{H}_{max}$  are presented in the paper, while results for  $\bar{C}_{max}$  are in the **Supplementary Material**. The maximum individual crest and crest-to-trough heights herein considered are computed using the space-time extreme WW3 model implementation distributed since version 5.16 [The WAVEWATCH III Development Group [WW3DG],

2016] which assumes nonlinear (for  $\bar{C}_{max}$ ) and linear (for  $\bar{H}_{max}$ ) constructive interference of directionally spread waves as the leading mechanism for the generation of the largest waves in a sea state. In particular, the WW3 implementation is based on the Tayfun (1980) approximation of the second-order nonlinear model for  $\bar{C}_{max}$  and on the linear Quasi-Determinism model for  $\bar{H}_{max}$  (Benetazzo et al., 2017), such as they can be defined over a given space-time domain as:

$$\bar{C}_{max} = \left( \zeta_0 + \frac{\mu}{2} \frac{\zeta_0^2}{\sigma} \right) + \sigma \gamma \left[ (1 + \mu \zeta_0 \sigma^{-1}) \left( \zeta_0 \sigma^{-1} - \frac{2N_3 \zeta_0 \sigma^{-1} + N_2}{N_3 \zeta_0^2 \sigma^{-2} + N_2 \zeta_0 \sigma^{-1} + N_1} \right)^{-1} \right] \quad (1)$$

$$\bar{H}_{max} = \left[ \zeta_0 + \sigma \gamma \left( \zeta_0 \sigma^{-1} - \frac{2N_3 \zeta_0 \sigma^{-1} + N_2}{N_3 \zeta_0^2 \sigma^{-2} + N_2 \zeta_0 \sigma^{-1} + N_1} \right)^{-1} \right] \sqrt{2(1 + |\psi^*|)} \quad (2)$$

In Equations (1) and (2),  $\zeta_0$  is the mode of the probability density function of linear space-time extremes (Fedele, 2012),  $\sigma = H_s/4$  is the standard deviation of sea surface elevation,  $N_3$ ,  $N_2$  and  $N_1$  are the average numbers of waves in the space-time domain and over its boundaries (Benetazzo et al., 2017),  $\gamma = 0.5772$  is the Euler-Mascheroni constant,  $\mu$  is the wave steepness and  $\psi^*$  is the narrow bandedness parameter. Steepness and bandwidth are sea state characteristics that contribute to the maximum individual wave height characterization.  $\psi^*$  is defined as the absolute value of the first minimum of the autocovariance function of the sea state (Boccotti, 2000). As both  $\mu$  and  $\psi^*$  are not direct outputs of WW3, we have *a posteriori* derived them, as  $\mu = H_s/(gT_m^2/2\pi)$ , with  $T_m$  being the mean zero-crossing spectral wave period produced by WW3, and from  $\bar{H}_{max} = \bar{C}_{max,1} \sqrt{2(1 + \psi^*)}$  (Boccotti, 2000) by deriving the linear estimate of the maximum expected crest height  $\bar{C}_{max,1}$  from  $\bar{C}_{max}$ , using the Tayfun (1980) quadratic equation [Equation (36) of Benetazzo et al., 2017]. Further details on the space-time extreme theoretical framework implemented in WW3 can be found in Barbariol et al. (2017); Benetazzo et al. (2021b) and references therein. A discussion on the role of wave steepness and bandwidth on the maximum individual wave heights during extreme events is given by Benetazzo et al. (2021a).

Our climatology of maximum individual waves deals with the maximum crest height  $\bar{C}_{max}$  and the maximum crest-to-trough height  $\bar{H}_{max}$  that might be expected in 20-min sea states and over a 100 m × 100 m area. This duration and spatial extent point to a customary sea state duration [e.g., measured by *in situ* instruments as a buoy, World Meteorological Organization [WMO], 2018] and to the horizontal sea surface area covered by an offshore structure (e.g., a large oil/drilling rig), respectively.

## Assessment Methodology

The MS wind-wave hindcast has been assessed using satellite altimeter observations of  $H_s$ , starting from 1991. Altimeter

<sup>1</sup><https://polar.ncep.noaa.gov/waves/>

$H_s$  data have been retrieved from the IMOS platform<sup>2</sup> (Ribal and Young, 2019; Young and Ribal, 2019), which provides calibrated and cross-validated data (we have only retained data flagged as “good data,” which according to the authors of those studies proved very reliable). Satellite missions considered in the August 1991–December 2019 period, for a total of 4066142 collocations, are listed in **Supplementary Table 1**. The longest dataset is 14-year long (ERS-2), the shortest is almost 4-year long (SENTINEL-3A). To inter-compare modeled and observed data for validation purposes, wave hindcast data have been bi-linearly interpolated in space and linearly interpolation in time on the satellite data points location and time. The statistical parameters and error metrics used to evaluate the hindcast performance are the model-observation bias  $BIAS = \overline{H}_{s,WW3} - \overline{H}_{s,altimeter}$  (overbar denoting ensemble average), the relative bias  $RBIAS = (\overline{H}_{s,WW3} / \overline{H}_{s,altimeter} - 1) \times 100$ , the Pearson cross-correlation coefficient  $CC$ , the Mean Absolute Error  $MAE = |\overline{H}_{s,WW3} - \overline{H}_{s,altimeter}|$  and the slope of the best-fit line (linear regression).

To assess that the ERA5 climatological signal transferred from the surface wind to waves can represent the intra- and inter-annual climatological variability of MS waves, as well as the trends, we have estimated the correlation between the monthly 50th and 99th percentile  $H_s$  from satellite altimeters and co-located WW3 hindcast and compared the linear trends of observed and modeled data. For these specific latter tasks, we have retained only satellite datasets longer than 10-year (see **Supplementary Table 1**).

Modeled maximum individual waves are generally verified at the short-term (i.e., sea state) time scale (see e.g., Barbariol et al., 2017, 2019; Benetazzo et al., 2021a,b), as there are no observational platforms in the global oceans that are continuously collecting this type of data over a long-term period. In addition, the model-to-observation comparison would require using observations with the same space and time domain sizes used for the hindcast (i.e., 20 min and 100 m  $\times$  100 m), while the sizes used for observations (application dependent and fixed) may be different from those required. Hence, the assessment of the WW3 hindcast in terms of  $\overline{C}_{max}$  and  $\overline{H}_{max}$  can be only done indirectly. We rely here on the assessment of  $H_s$ , which is the pivotal parameter for determining the height of maximum expected individual crest and crest-to-trough heights (Benetazzo et al., 2021b).

## Wave Climate Analysis

The climatology of wind-wave sea states in the MS is presented by using the 50th (i.e., median) and the 99th percentiles of the significant wave height  $H_s$ , which may represent typical and extreme sea-state conditions, respectively. Similarly, the climatology of maximum individual waves is based on the 50th and 99th percentiles of the maximum crest-to-trough height  $\overline{H}_{max}$  (and maximum crest height  $\overline{C}_{max}$  in the **Supplementary Material**).

In order to highlight the effects of intra-annual variability, the 50th and 99th percentiles are estimated at seasonal scale

and averaged over the length of the hindcast to provide an empirical estimate of the expected typical and extreme conditions during the different seasons. In this study, we propose and adopt a novel definition of stormy seasons for the MS wind-wave climate based on the observed  $H_s$  data in the MS, rather than using the canonical meteorological definition based on the air temperature (i.e., winter: December, January, February, DJF; spring: March, April, May, MAM; summer: June, July, August; JJA; autumn: September, October, November, SON). To this end, satellite altimeter observations of  $H_s$  are used (see Section “Assessment Methodology”). Yearly-averaged monthly  $H_s$  values are first computed for each satellite altimeter and then the eight satellites are combined to obtain the ensemble average and standard deviation.

To let the interannual climate variability and climate change due to external forcings emerge, we remove the source of intrinsic intra-annual variability due to seasonality by taking separately into account the different seasons, as done for instance by Morales-Márquez et al. (2020). Therefore, in the result presentation (climate variability and climate change), we shall focus on the two most representative seasons only, i.e., winter and summer. The interannual climate variability is shown in terms of climate anomalies, which are defined as deviations of the winter and summer 50th and 99th percentile values of a generic wave height  $H$  in a specific  $i^{\text{th}}$  year  $H_i^{pp}$  ( $pp = 50, 99$ ) with respect to the winter and summer yearly-averaged 50th and 99th percentiles  $\overline{H}^{pp}$  (overbar denoting average over the years), i.e.,  $H_i^{pp} - \overline{H}^{pp}$ . Further, to assess the spatial distribution of the inter-annual climate variability and highlight the MS sub-basins and regions that have experienced the largest variations in the study period, we have also normalized anomalies with respect to the local yearly averages, thus showing the relative anomalies, i.e.,  $(H_i^{pp} - \overline{H}^{pp}) / \overline{H}^{pp}$ . In order to motivate the inter-annual climate variability of the MS waves, we look for possible teleconnections between the wave climate variability and the principal modes of atmospheric variability, taking into account four northern hemisphere indices (downloaded as monthly averaged values from<sup>3</sup>): North Atlantic Oscillation (NAO), Scandinavian (SCAND), East Atlantic (EA) and East Atlantic-Western Russian (EAWR). Monthly mean data are then combined to obtain seasonal averages.

Finally, in order to assess any potential long-term change in the typical and extreme sea state climate over 1981–2019, the linear trend of winter and summer  $H_s$ ,  $\overline{C}_{max}$  and  $\overline{H}_{max}$  are estimated over the whole MS and sub-basins through the Sen's slope of the 50th and 99th percentiles (Theil, 1950; Sen, 1968), testing the statistical significance at the 90% confidence interval with the Mann–Kendall test (Mann, 1945; Kendall, 1948).

## RESULTS

The characteristics of the MS wind-wave climate obtained from the ERA5 wind forced WW3 hindcast are presented in this Section stemming from the yearly-averaged seasonal 50th

<sup>2</sup><https://catalogue-imos.aodn.org.au>

<sup>3</sup><https://www.cpc.ncep.noaa.gov/data/teledoc/telecontents.shtml>

and 99th percentiles of  $H_s$  (the conventional variable used to describe the wave climate), together with their variability and change. Same analyses are also conducted to investigate the distribution of the crest-to-trough height of the maximum individual waves  $\bar{H}_{\max}$  (results for the crest height of the maximum individual waves  $C_{\max}$  are in the **Supplementary Material**). Before presenting the MS wind-wave climatology a novel definition of seasons for the MS states and the assessment of the wave hindcast performance are introduced.

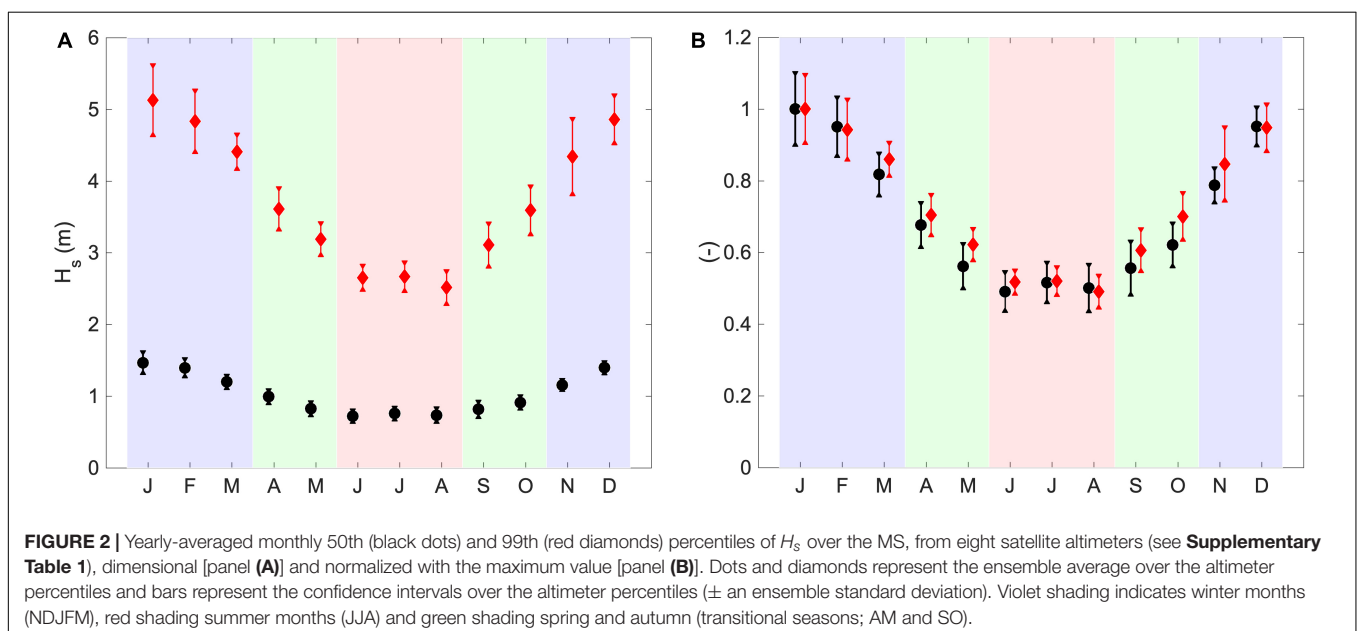
## An Observed Data-Based Definition of Seasons for the Mediterranean Sea States

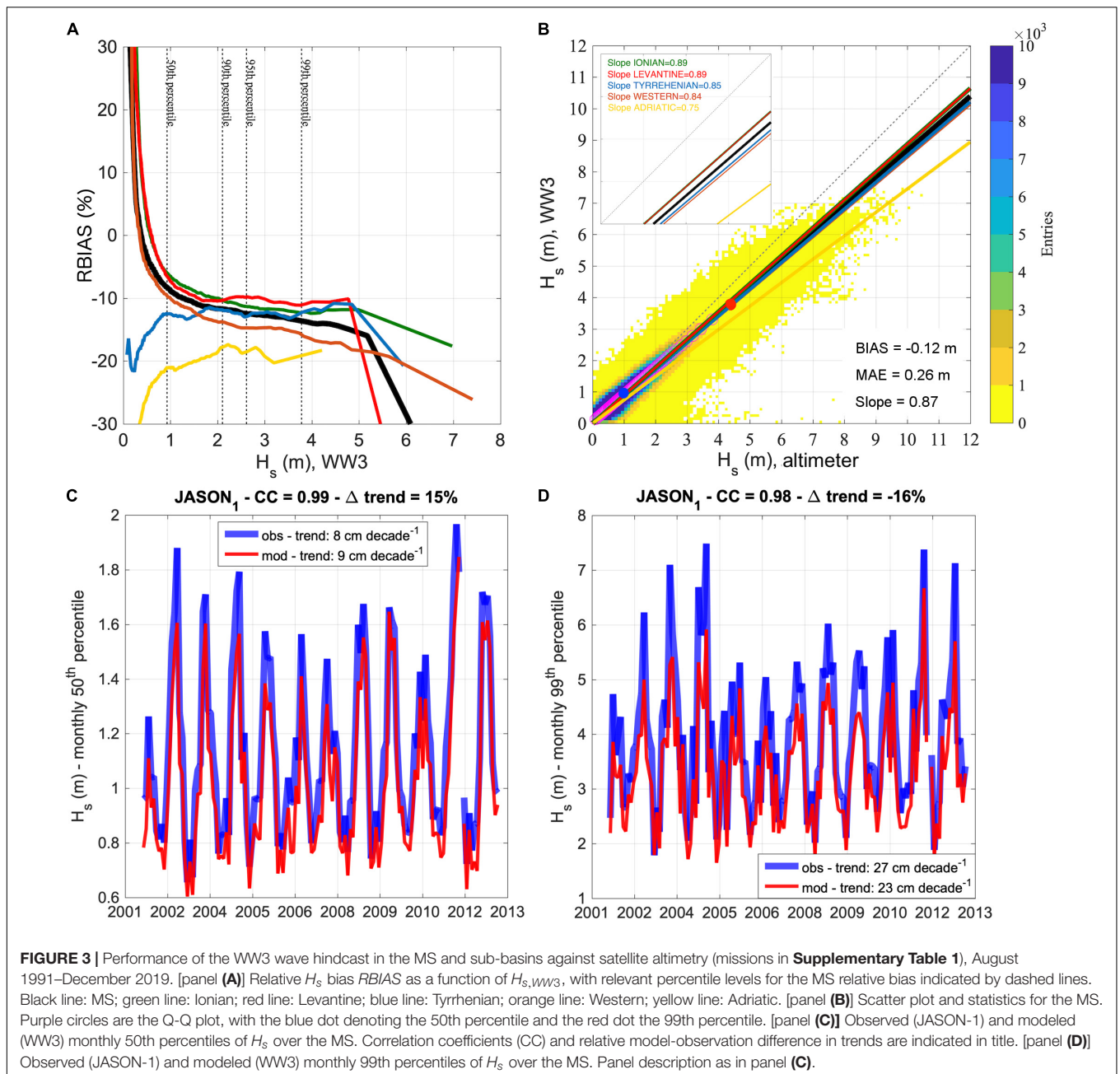
The monthly 50th and 99th percentiles of  $H_s$ , as observed over the MS by the eight satellite altimeters used for the hindcast assessment (**Supplementary Table 1**) are shown in **Figure 2A**. Observations are also normalized with respect to the maximum monthly  $H_s$  percentile (**Figure 2B**), which occurs in January for both the 50th and 99th percentiles. Both typical and extreme sea states clearly show two dominant regimes: a stormy period, from November to March (with values within 20% of the January  $H_s$ ; **Figure 2B**), and a relatively calm period, from June to August (with values within few per cent of the minimum  $H_s$ , occurring in June for the 50th percentile and in August for the 99th percentile). In between, there are two transitional seasons. Following this variability, we define the four sea-state “seasons” as winter (NDJFM), spring (AM), summer (JJA) and autumn (SO). Compared to the classic meteorological definition, we therefore propose a longer winter season, starting in November and ending in March (both showing significantly larger  $H_s$  compared to the other spring and autumn months), and shorter transitional seasons (2-month long), with summer remaining unchanged. This definition applies to the whole basin but still holds if only northern, southern or western sub-basins are considered. If only

the eastern part of MS is accounted for, the relative difference between summer and transitional seasons reduces (not shown here), most likely due to the effect of Etesian wind-waves. This is in agreement with findings of Queffelec and Bentamy (2007) who pointed out differences in western to eastern MS monthly mean  $H_s$  from satellite altimetry, especially during summer season. November and December  $H_s$  values clearly belong to the winter season that accounts for the early months of the following year; therefore, to have an equal number of seasons, we start counting seasons from winter 1981 (beginning with November 1980) to autumn 2019 (ending in October 2019), thus analyzing only 39 years in the whole period (hereinafter 1981–2019).

## Assessment of the Mediterranean Sea Wind-Wave Hindcast

The MS wind-wave hindcast performance in the 1991–2019 period against satellite altimeter observations is summarized in **Figure 3**, which collects information about the relative model-observation bias  $RBIAS$  in the MS and in the sub-basins (**Figure 3A**), the  $H_s$  scatter (**Figure 3B**) and the relation between modeled and observed climate variability and change (**Figures 3C,D**). Modeled  $H_s$  is simulated in the MS with 0.87 best-fit line slope,  $BIAS = -0.12$  m and  $MAE = 0.26$  m. The relative model-observation bias at the 50th percentile of modeled  $H_s$  (0.93 m; blue dot in the **Figure 3B**) is  $-8\%$ , while at the 99th percentile (3.78 m; red dot in the **Figure 3B**) it is  $-14\%$ , denoting a decrease in model performance with  $H_s$ , in agreement with the MS wave hindcast study of Mentaschi et al. (2015; verified against *in situ* wave buoys). The model-observed bias might be partially corrected by calibrating the input/dissipation source term parameterization in WW3. However, the spatial heterogeneity of the MS (with narrow, semi-enclosed sub-basins or/and surrounding orography) makes it difficult to achieve a set of parameters that is optimized to obtain good performance in

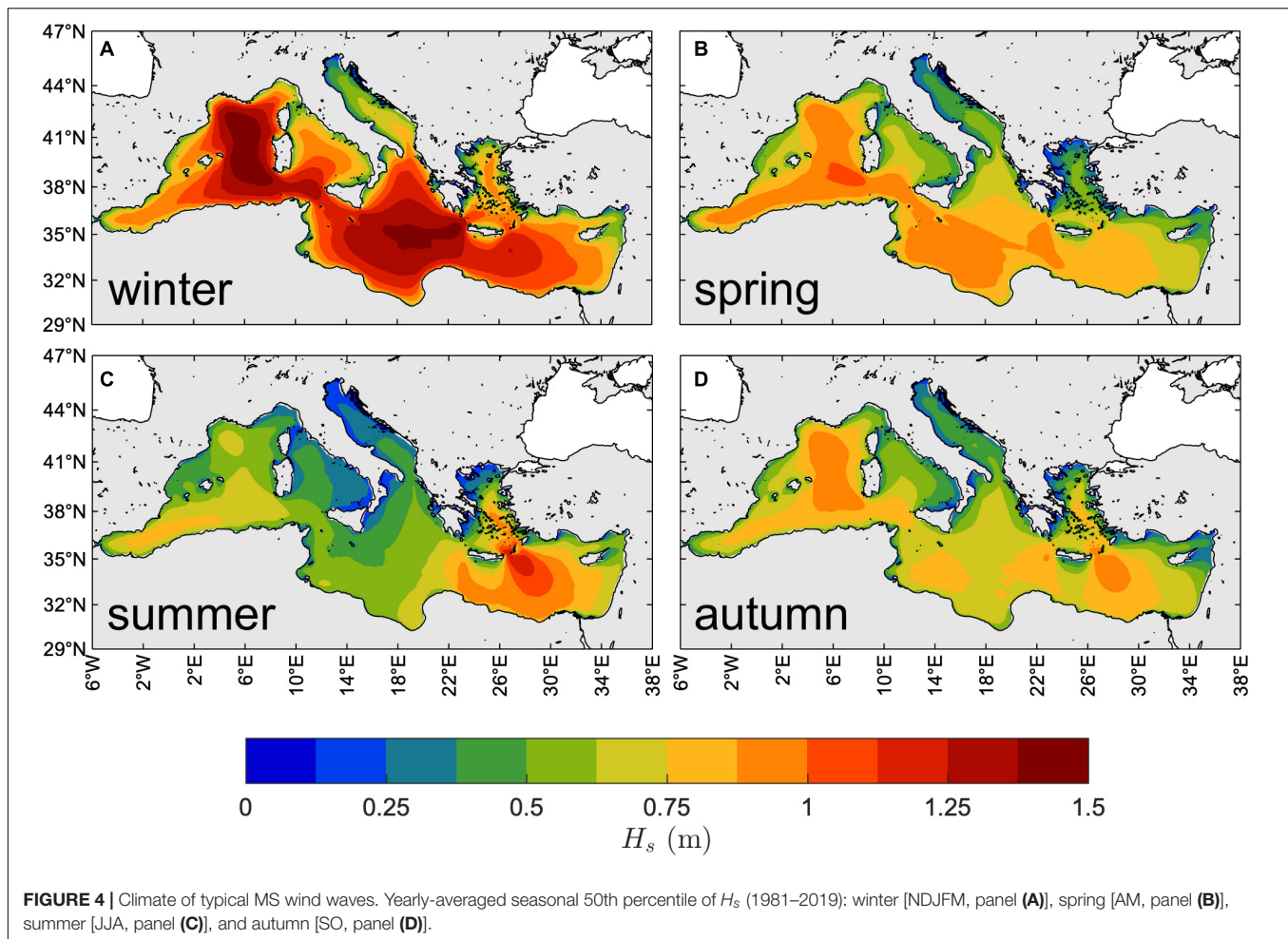




the whole MS basin and in the whole  $H_s$  range (Lionello and Sanna, 2005; Mentaschi et al., 2015; Sartini et al., 2017; Morales-Márquez et al., 2020). This can be seen by comparing the slope of best-fit lines and the relative bias at different percentiles for the MS with those for the sub-basins. Best performance is achieved in the widest sub-basins (Ionian, Levantine), with larger slope and smaller relative bias compared to those obtained in the whole MS. Worst performance are in the Adriatic Sea, where the ERA5 wind is less effective in correctly reproducing wind and then waves due to spatial resolution effects in a narrow basin. These effects are partially visible also in the Tyrrhenian and Western sub-basins (both with islands and narrow parts),

although performance in these sub-basins is comparable to that for the MS.

The average (and standard deviation of) correlation coefficients between the monthly 50th and 99th percentile  $H_s$  from satellite altimeters and co-located WW3 hindcast are:  $0.98 \pm 0.004$  for the 50th percentile and  $0.97 \pm 0.009$  for the 99th percentile. An example of the monthly percentiles time-series for JASON-1 is shown in **Figures 3C,D**, with correlation coefficients larger than or equal to 0.98 for both 50th and 99th percentiles. Also, the linear trends of  $H_s$  estimated from the same satellite altimeters and co-located model data are in agreement, with consistent (i.e., both positive or both negative)



Sen's slope signs and a general tendency for larger model trends for the 50th percentiles and smaller for the 99th percentiles (compared to JASON-1, the relative trend differences are 15 and  $-16\%$  for the 50th and 99th percentile, respectively, while the largest relative difference is  $-43\%$ , between Envisat and model 99th percentile  $H_s$  trends).

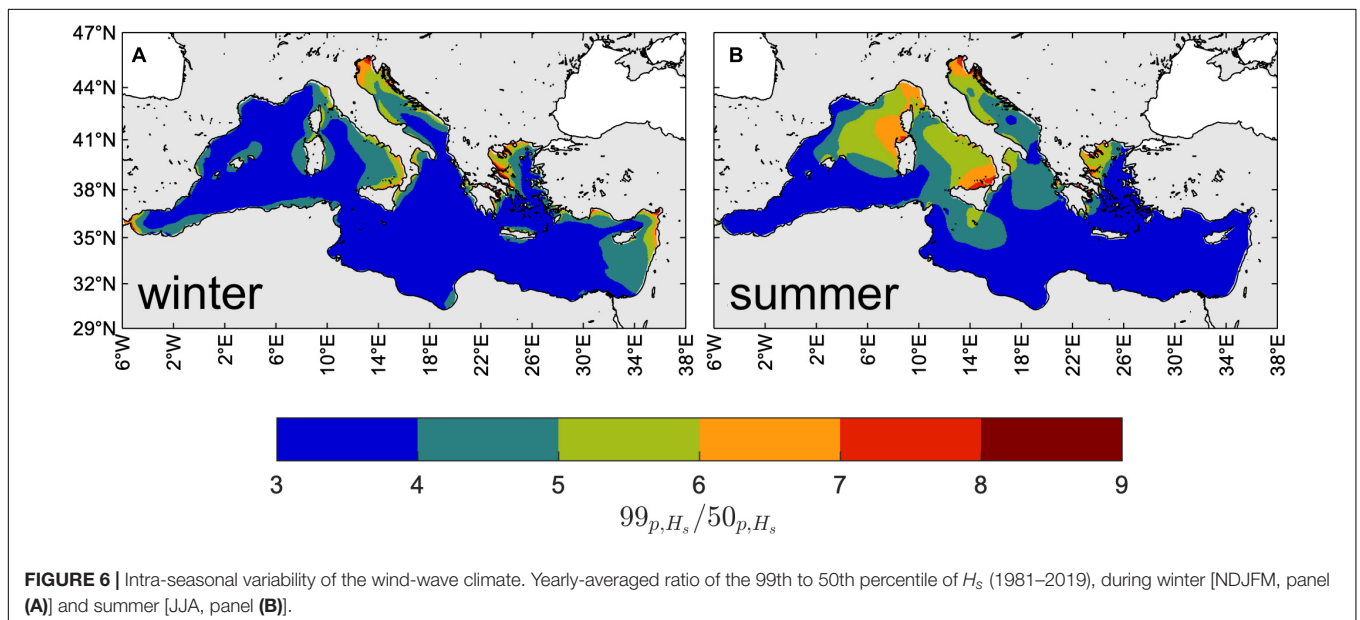
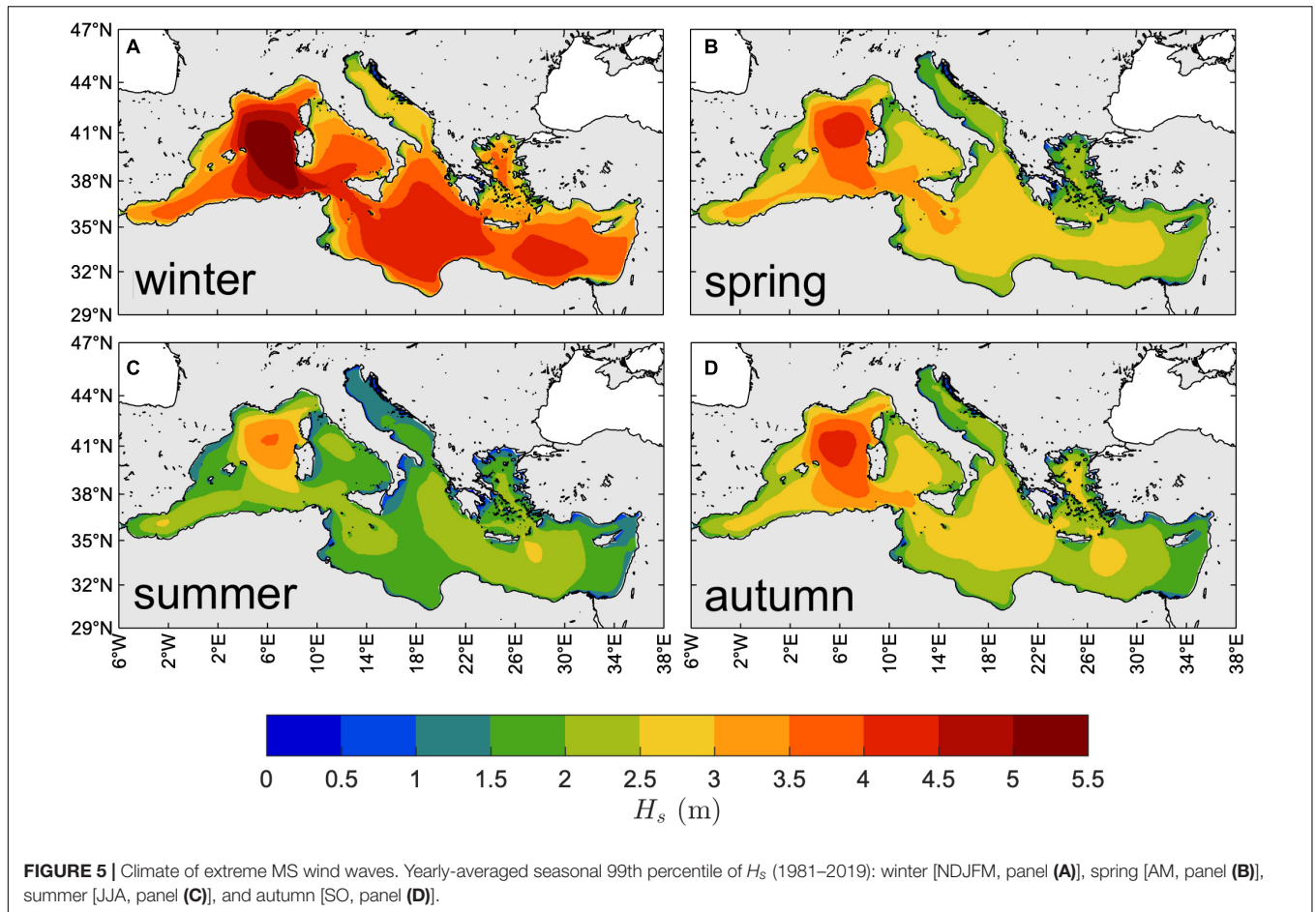
### Mediterranean Sea Wind-Wave Climate

The yearly-averaged seasonal 50th percentile of  $H_s$  is shown in **Figure 4**. As expected, the largest values occur during the winter (NDJFM) season when wind speeds are typically stronger (Zecchetto and De Biasio, 2007). Spatial patterns of the 50th percentile  $H_s$  are rather different in winter and summer (JJA), on the one hand, and very similar in spring (AM) and autumn (SO), on the other hand. The most energetic sea states occur over the western and southern sub-basins in winter (50th percentile up to 1.5 m) and spring (up to about 1 m), and over the eastern and western sub-basins in summer (up to 1.25 m) and autumn (up to 1.0 m). The western basin experiences the largest typical conditions over all seasons except summer, particularly the Sardinian Sea (amid the Gulf of Lyon, Sardinia, the North African coast and the Balearic Islands) where the north-westerly Mistral

wind persistently blows from the French inland (Zecchetto and De Biasio, 2007). In summer, the largest wave heights are attained in the Aegean and Levantine basins (particularly southeast of Crete, with a typical jet-like pattern) with values comparable to those of winter and produced by the north-westerly Etesian winds, typical of late spring, summer and autumn seasons but reaching their maximum intensity during summer (Zecchetto and De Biasio, 2007).

The yearly-averaged seasonal 99th percentile of  $H_s$  is shown in **Figure 5**. The spatial distribution of extreme sea states is different compared to that of typical conditions (**Figure 4**). Indeed, the 99th percentile of  $H_s$  in all seasons have similar spatial patterns, and in particular the sea severities during spring and autumn seem comparable (despite some minor differences, for instance in the Alboran Sea and the Levantine basin). The largest values occur in the Gulf of Lyon and Sardinian Sea (up to 5.5 m in winter, up to 4.0 m in summer, up to 4.5 m in spring and autumn). Other regions with large, though smaller, values are located in the southern (Ionian Sea) and eastern (Levantine Sea) sub-basins, while the summer waves southeast of Crete island (the largest in the summer 50th percentile maps; jet-like pattern) are surpassed by the extreme waves generated by the Mistral wind in the Gulf of Lyon. In the Adriatic Sea, the spatial





pattern changes compared to the 50th percentile, with large values more homogeneously distributed over the whole basin (including in the northern part) and with the largest ones (in

the southern part) off the eastern coast, as a consequence of the south-easterly Sirocco wind storms hitting the Croatia, Albany and Montenegro shorelines.

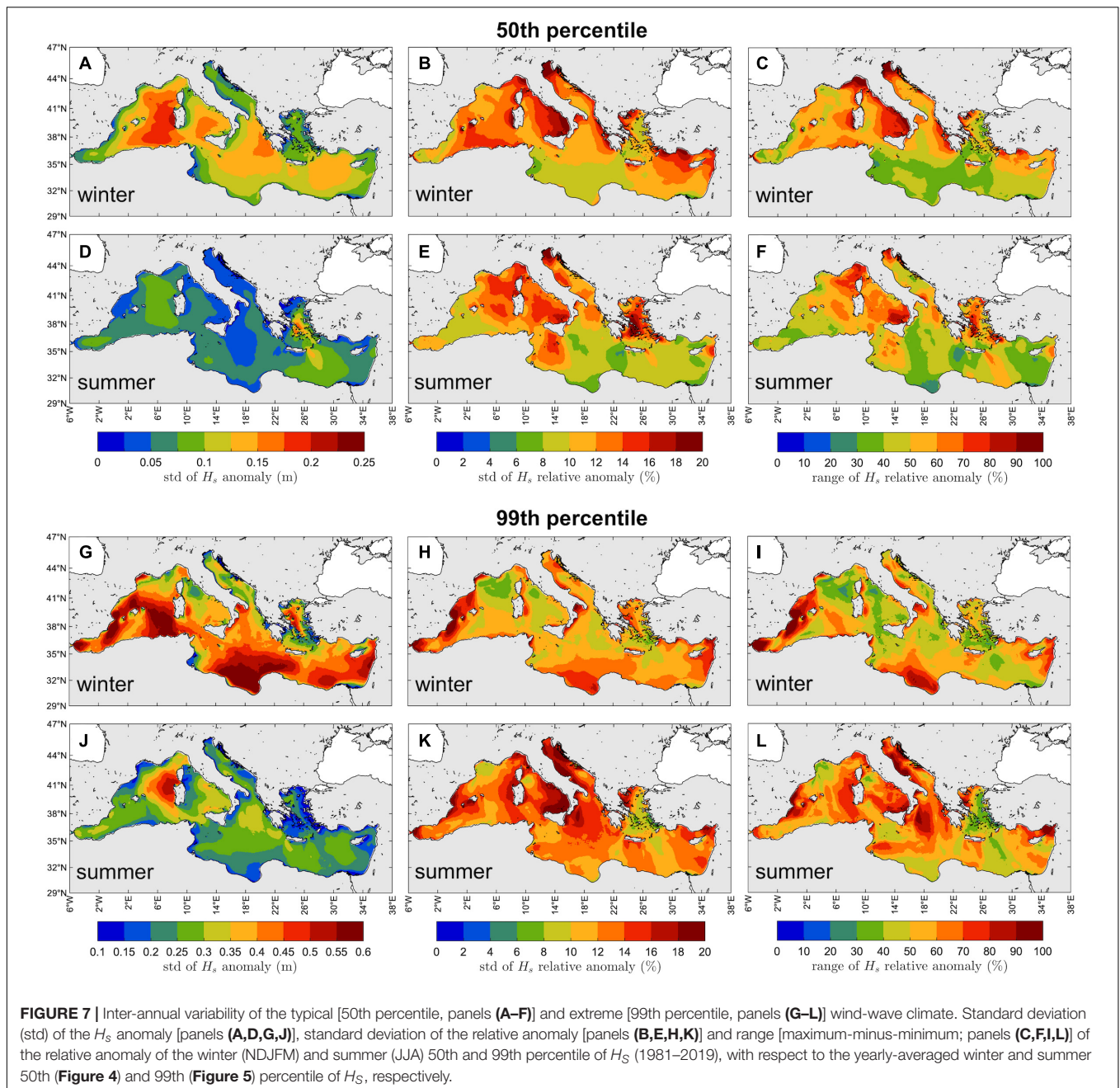
## Variability of the Mediterranean Sea Wind-Wave Climate

The first assessment of the wave climate variability is made by analyzing the intra-seasonal extreme-to-typical condition variations. In **Figure 6** we show the winter (NDJFM) and summer (JJA) ratios  $99_{p,H_s}/50_{p,H_s}$  of the 99th to the 50th percentile of  $H_s$ . This ratio provides a measure of the width of the empirical probability distribution of  $H_s$  at seasonal scale and it is yearly-averaged to obtain an empirical estimate of the expectation. We observe that sea states are much more variable during summer than winter, with the largest values of  $99_{p,H_s}/50_{p,H_s}$ . There is also a larger spatial variability of the ratio during summer with respect to winter. Indeed, during winter extreme conditions are generally up to four times greater than the typical ones, over all the MS basin, with only spatially limited exceptions in the northern Adriatic, southern Tyrrhenian, western Aegean seas and eastern Levantine sub-basin, where they can be up to six times larger (locally, more than six times). During summer, extreme conditions can be more than six times larger than typical ones (up to eight times) over large parts of the central MS, including the Sardinian, Tyrrhenian and Adriatic Seas. The lowest summer variability occurs in the Levantine basin, where the sea states generated by the steady and low-variability Etesian winds are intense but constant over the season.

We now proceed by assessing the interannual variability of the wave climate in the MS region by showing the standard deviation and range of the anomalies of typical and extreme  $H_s$  during winter and summer. We first focus on the standard deviation of the  $H_s$  anomaly, which is used to point out the regions with the largest climate variability over the years. Then, we focus on the standard deviation and range (maximum-minus-minimum) of the relative anomaly (i.e., with respect to the yearly-averaged percentiles of  $H_s$ , see Section “Wave Climate Analysis” for the definition) to show the regions with the largest variability with respect to the local wind-wave climate (and quantify it), allowing to inter-compare regions with different  $H_s$  percentiles. The interannual variability of the 50th percentile of  $H_s$  is presented in **Figure 7**. During winter the largest variability occurs in the Western sub-basin (Mistral wind region, up to 0.25 m standard deviation; **Figure 7A**); in summer, in the Aegean and Levantine sub-basins (Etesian wind region, up to 0.2 m standard deviation; **Figure 7D**). These are also the regions with the largest 50th percentile of  $H_s$  (**Figure 4**) although the spatial distribution of the standard deviation of the  $H_s$  anomaly does not perfectly reflect that of the yearly-averaged 50th percentile of  $H_s$ . Looking at the standard deviation of the relative anomalies (**Figures 7B,E**), it emerges that the regions with the largest variability with respect to the local wave climate are in the Tyrrhenian, Adriatic and Aegean sub-basins during summer, and in the Western, Tyrrhenian, Adriatic, and Levantine sub-basins during winter. The maximum standard deviation of the relative  $H_s$  anomaly, up to 20% of the 50th percentile  $H_s$  in both summer and winter, occurs in the northern Adriatic Sea and the southern Tyrrhenian Sea, where during 1981–2019 winters the range of variability has reached 100% of the local 50th percentile  $H_s$ .

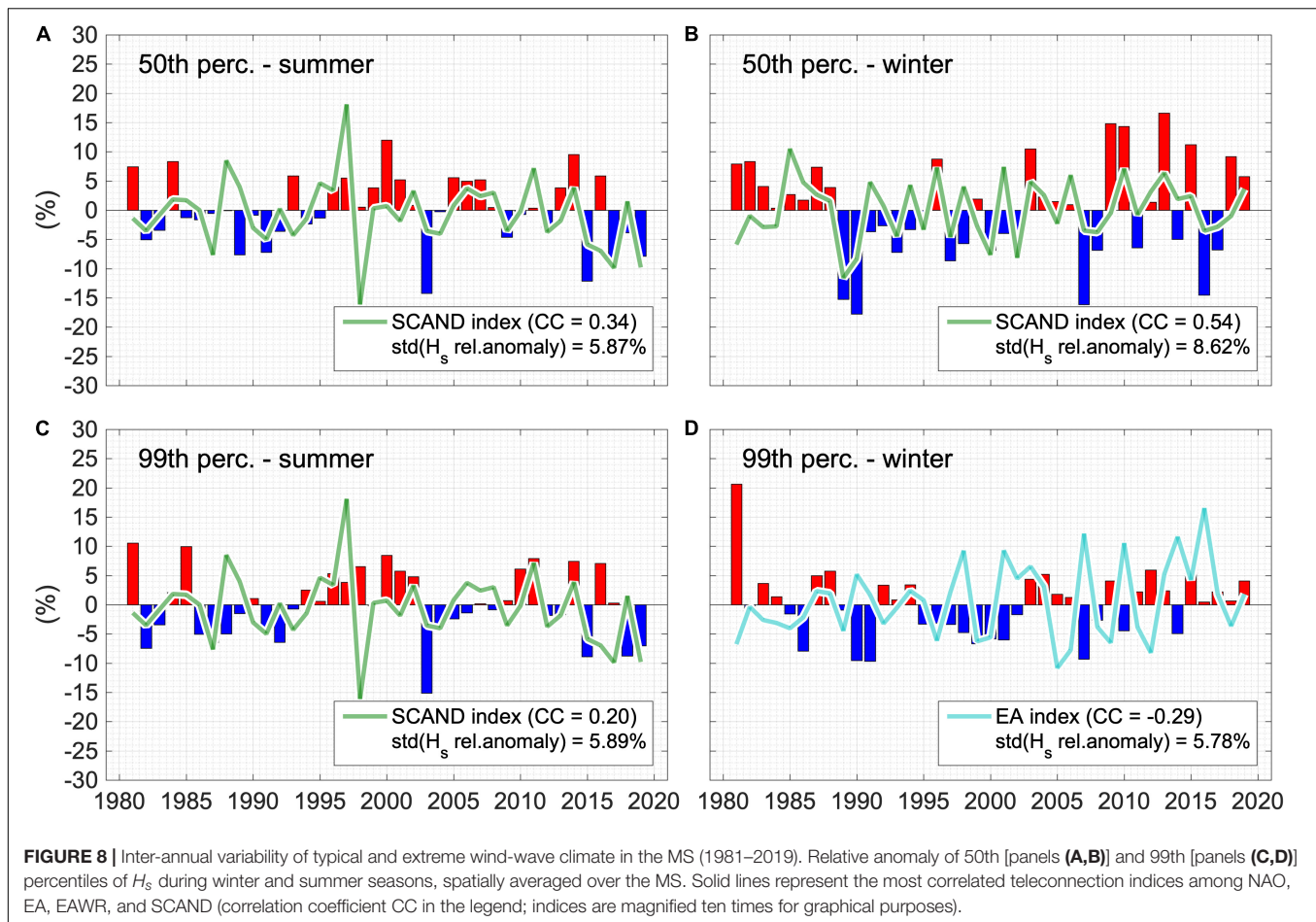
The interannual variability of the 99th percentile of  $H_s$  is presented in **Figure 7**, and show different characteristics with respect to that of the 50th percentile of  $H_s$ . Indeed, in summer the maximum standard deviation of the  $H_s$  anomaly is in the Western sub-basin (Sardinian Sea, 0.6 m; **Figure 7J**), where also the maximum 99th percentile occurs, whereas in winter the maximum standard deviation is in the southernmost (Ionian sub-basin, offshore Libya; **Figure 7G**) and westernmost (Western sub-basin, southeast and southwest of Balearic Islands) parts of the MS, which are not the locations with the maximum 99th percentile of  $H_s$  (Sardinian Sea and Gulf of Lyon, **Figure 5**). Similarly, the largest standard deviation of the relative anomaly (20% of the 99th percentile  $H_s$ ) is in the Western, Tyrrhenian, Adriatic, Aegean and Ionian sub-basins during summer (as for the 50th percentile  $H_s$ ; **Figure 7K**), while in winter the maximum is offshore Libya and southwest of the Balearic Islands (**Figure 7H**). In these regions, the range of the relative anomaly is up to the 100% of the local 99th percentile  $H_s$ .

To provide a synthetic description of the interannual climate variability at the regional scale (i.e., MS basin and sub-basins), in **Figure 8** we show the time series of the spatially averaged relative anomaly of the 50th and 99th percentile of  $H_s$  over the MS (spatial averages over the sub-basins are shown in **Supplementary Figures 1–5**). In general, during 1981–2019 there is an alternation of positive and negative anomalies that, more frequently during winter and especially in some sub-basins, tend to aggregate forming clusters of years with (almost) only positive or negative anomalies. An example of this aggregation is the 1989–1994 anomaly of the winter 50th percentile  $H_s$ . During this period the largest negative anomaly in the MS have occurred (winter 1990,  $-18\%$ ), followed by four more seasons with negative, often considerable, anomalies. The largest negative anomaly at sub-basin scale have occurred in the Tyrrhenian Sea in the same period (winter 1989,  $-36\%$  of the 50th percentile of  $H_s$ ; **Supplementary Figure 1**), but similar pattern can be observed in the Ionian, Adriatic and Western sub-basins, even if with smaller anomalies. During 1989–1994 winters, the atmosphere in the MS region has been very stable, in particular over the Western, Tyrrhenian, Adriatic and Ionian sub-basins (**Supplementary Figures 1–4**; as shown in **Supplementary Figure 6**, displaying the 500 hPa geopotential height, sea level pressure and wind intensity anomalies over western Atlantic, Europe and western Asia from ERA5 atmospheric reanalysis, for some seasons of interest). The cause of this stability can be found in the localization of the pressure fields on a synoptic (European) scale (**Supplementary Figure 6**). The conditions that induce strong atmospheric stability over the MS basin have been marked positive 500 hPa geopotential anomalies and positive sea level pressure (SLP) anomalies over Europe, and negative wind intensity anomalies over the MS basin. Such conditions have occurred in all the 1989–1994 winters (as shown in **Supplementary Figure 6** for 1989 and 1990), and are responsible for the negative  $H_s$  anomalies observed in **Figure 8** for the MS and in **Supplementary Figures 1–5** for sub-basins. The largest positive  $H_s$  anomaly in the MS ( $+21\%$  of the 99th percentile of  $H_s$ ) have occurred in winter 1981, while the largest positive anomaly at sub-basin scale occurred in the Tyrrhenian Sea in summer 2014 ( $+32\%$  of the 50th percentile



of  $H_s$ ). Winter 1981 has been characterized by an average circulation over Europe (Supplementary Figure 6) with positive SLP anomaly over Western Europe, positive 500 hPa geopotential anomaly over Russia and a negative SLP anomaly on central and southern Europe and on Scandinavia. These conditions are associated with the meridional advection of arctic air and intense cyclogenesis over the MS, especially over the western part, as shown in Supplementary Figure 6 with maximum wind intensity anomalies of over 1.5 m/s on the Western and Ionian sub-basin (both showing very large positive extreme  $H_s$  anomalies in winter 1981, Supplementary Figures 3–4). Summer 2014 (Supplementary Figure 6) has been characterized

by geopotential and SLP anomalies in the western MS, with the minimum pressure positioned on central-western Europe. This configuration generates frequent advectations of relatively cold air along the eastern edge of the Azores anticyclone, producing positive wind intensity anomalies (with values between 0.5 and 1.5 m/s, Supplementary Figure 6) in the Western, Tyrrhenian and Adriatic sub-basins, all showing positive  $H_s$  anomalies in summer 2014. The temporal climate variability of typical  $H_s$  in the MS has been the largest in winter typical sea states as shown by the 8.62% standard deviation. At sub-basin scale the largest temporal variability of typical  $H_s$  has occurred in the Tyrrhenian, Adriatic and Western sub-basins, both in



summer and winter (for the Tyrrhenian Sea, 11.3 and 13.6% standard deviation, respectively; see **Supplementary Figure 1**), in agreement with results about typical climate variability in **Figure 7**. Extreme  $H_s$  appears to be most variable in the Tyrrhenian and Adriatic seas during summer, and in the Ionian and Levantine sub-basins during winter, (for the Adriatic Sea summer 11.2% and for the Ionian Sea winter 8.9% standard deviation, respectively; see **Supplementary Figures 2, 4**), in agreement with results for the climate variability shown in **Figure 7**.

The inter-annual climate variability of the MS waves observed in **Figure 8** (and **Supplementary Figures 1–5** for sub-basins) can be partially explained by possible teleconnections between the wave signals and the principal modes of atmospheric variability. To this end, we compare the time series of the relative anomaly with the time series of the NAO, SCAND, EA and EAWR indices. Thus, we have (i) averaged the monthly values of 1981–2019 indices over the winter and summer seasons, respectively, (ii) computed cross-correlation coefficients between the four indices and the MS (and sub-basins)  $H_s$  relative anomalies and then (iii) plotted in **Figure 8** (and **Supplementary Figures 1–5** for sub-basins) the time series of the index showing the highest correlation (in search for teleconnection). Generally, with only a few exceptions, relative anomalies in the MS and sub-basins

are mostly correlated to SCAND positive phases, particularly, but not only, for the 50th percentiles. In the MS, this is observed for winter and summer typical and extreme sea states, except for winter extreme  $H_s$ , which is related to the EA negative phases. The highest correlations are found for the winter 50th percentiles, although the correlation coefficients are generally small, reaching 0.54 at most for the MS (SCAND and winter 50th percentile, **Figure 8**) and 0.65 maximum value for the sub-basins (SCAND and Tyrrhenian Sea winter 50th percentile, **Supplementary Figure 1**). The impact of the SCAND index on the Mediterranean atmosphere dynamics and hence on the MS wave climate can be observed, as an example, in the winter 1989 and 1990 atmospheric configuration (**Supplementary Figure 6**). The persistent low 500 hPa geopotential height and SLP fields over Scandinavia and Eastern Europe (with  $-1.2$  and  $-0.8$  seasonal SCAND index, respectively; **Figure 8**), induce negative anomalies of wind speed over the whole MS, which, in turn, generate negative anomalies of the 50th percentile  $H_s$  ( $-15$  and  $-18\%$ , **Figure 8**).

## Change of the Mediterranean Sea Wind-Wave Climate

We assess here what might have been the climate change of the winter and summer MS sea states over 1981–2019 showing

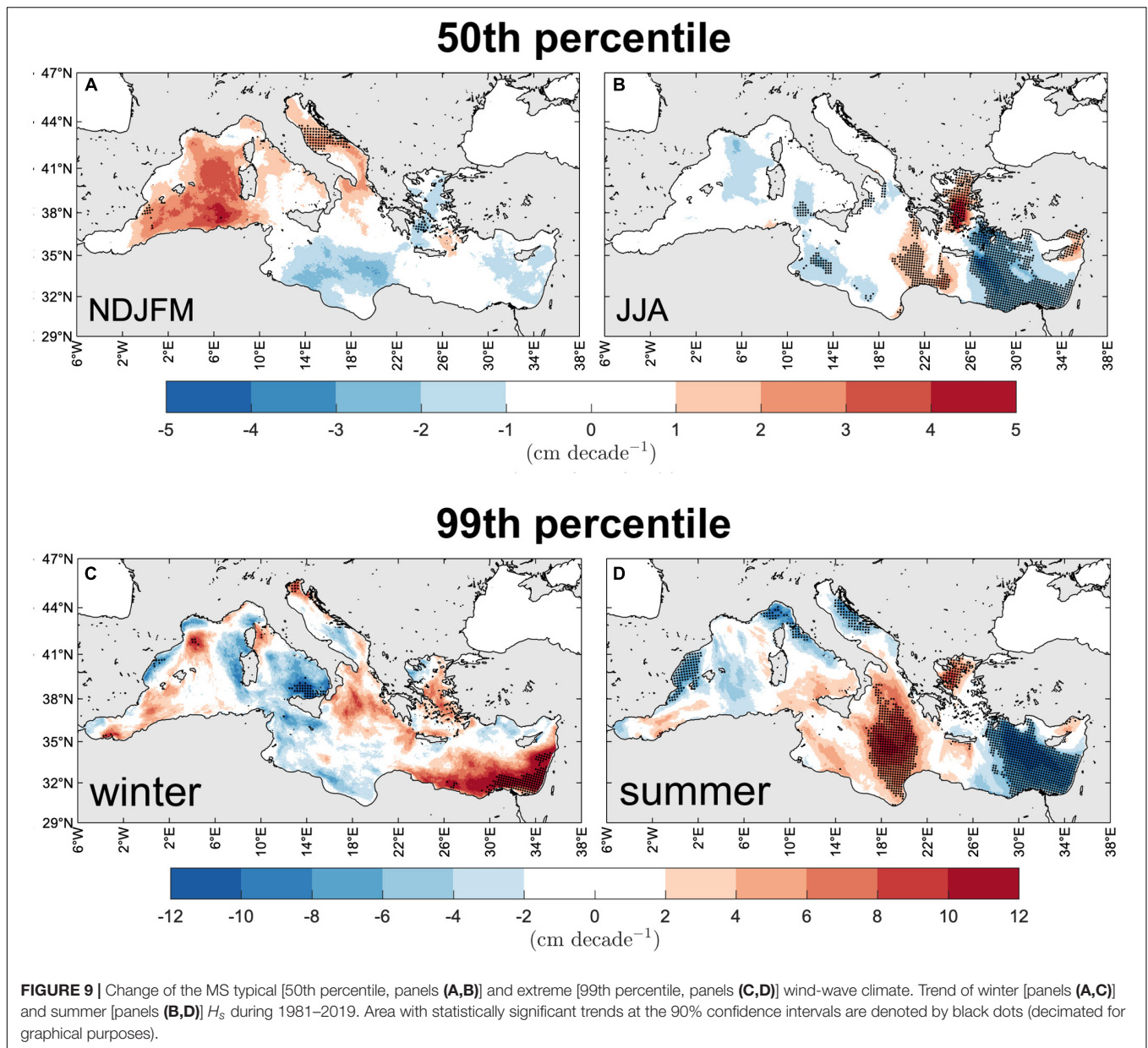


**TABLE 1 |** Spatial averages over the MS and sub-basins of the 50th and 99th percentile  $H_s$  trends shown in **Figure 9** ( $\text{cm decade}^{-1}$ ), during 1981–2019 summer and winter seasons.

	50th Percentile				99th Percentile			
	Summer		Winter		Summer		Winter	
	Significant	All	Significant	All	Significant	All	Significant	All
<i>Mediterranean</i>	-0.8 (22.7%)	-0.4	1.1 (2.4%)	0.3	-1.6 (25.5%)	-0.2	6.5 (4.5%)	0.9
<i>Adriatic</i>	0.5 (3.6%)	0.2	1.9 (28.9%)	1.3	-5.9 (17.1%)	-2.1	5.4 (6.2%)	0.3
<i>Ionian</i>	0.4 (15.5%)	-0.3	-1.3 (0.1%)	-0.7	7.9 (29.8%)	4.2	-4.3 (0.1%)	-0.3
<i>Tyrrhenian</i>	-1.4 (5.0%)	-0.4	0.0 (0.1%)	0.9	-6.9 (4.2%)	0.2	-10.0 (6.6%)	-3.4
<i>Levantine</i>	-1.1 (54.0%)	-0.7	-1.4 (1.9%)	-0.5	-6.6 (41.3%)	-3.0	11.0 (9.5%)	3.9
<i>Western</i>	0.6 (0.5%)	-0.4	2.5 (1.2%)	1.9	-5.4 (9.3%)	-1.6	2.1 (1.5%)	0.1

Averages over the points where the trends are significant (black dots in **Figure 9**; tested with Mann-Kendall test and 90% confidence interval) and over all the points. Value between parentheses is the percentage of points with statistically significant trends in a (sub-) basin with respect to all the points in the (sub-) basin.

the maps of the  $H_s$  linear trends (using the Sen's slope, in cm decade<sup>-1</sup>, evaluated on 39 yearly data) in **Figure 9** and their spatial averages over the basin and sub-basins in **Table 1**. We show both the trends at the points where there is statistically significance (at 90% confidence interval according to the Mann-Kendall test) and at all the points in a (sub-) basin, including where there is no statistical significance.

The winter 50th percentile of  $H_s$  (**Figure 9A** and **Table 1**) shows positive trends over large part of the western and northern sub-basins of the MS, and negative or no trends in the eastern and southern sub-basins, resulting in a substantially net zero trend for the MS typical winter sea states (0.3 cm decade<sup>-1</sup>; **Table 1**). The largest increases are in the Sardinian Sea and offshore Algerian coasts (up to 5 cm decade<sup>-1</sup>) and largest decreases in the southern MS (down to -3 cm decade<sup>-1</sup>). However, only trends offshore the Algerian coasts, in the central Adriatic Sea (Sirocco and middle Bora jets regions) and in small portions of the Aegean and Balearic seas are statistically significant, bringing the spatial average to 1.1 cm decade<sup>-1</sup> (**Table 1**). The summer map (**Figure 9B**) is far different, showing generally smaller Sen's slopes, except in some limited areas in the eastern part of the basin, with statistically significant increases (up to 4 cm decade<sup>-1</sup>) in the Aegean Sea and eastern and western Levantine basin and decreases (down to -4 cm decade<sup>-1</sup>) in the central Levantine basin where the summer Etesian winds blow. As a whole, the MS presents a very mild decreasing trend during typical summer sea states (-0.8 cm decade<sup>-1</sup>; **Table 1**).

The 99th percentile  $H_s$  trends, shown in **Figures 9C,D**, are significantly larger than the 50th percentile trends shown above. During winter the largest statistically significant changes are in the southern Levantine sub-basin with increases up to 12 cm decade<sup>-1</sup> offshore Egypt and Israel (11.0 cm decade<sup>-1</sup> on average in the sub-basin), in the Gulf of Lyon with increases up to 12 cm decade<sup>-1</sup> (Mistral jet region, despite a smaller average trend in the Western sub-basin), in the northern Adriatic Sea (northern Bora jet, increases up to 8 cm decade<sup>-1</sup>) and in the southern Tyrrhenian Sea, the only statistically significant area of negative trend for winter extreme sea states (down to -12 cm decade<sup>-1</sup>, -10.0 cm decade<sup>-1</sup> on average in the Tyrrhenian Sea). In the MS the winter 99th percentile  $H_s$  has increased 6.5 cm decade<sup>-1</sup> (**Table 1**) as a whole. In summer, the trend distribution and sign are quite different from the winter ones. Indeed, globally the 99th percentile  $H_s$  has decreased (-1.6 cm decade<sup>-1</sup>; **Table 1**), and the spatial distribution is quite similar to the distribution of the summer 50th percentile  $H_s$  trends. In particular, a statistically significant increase is observed in the Ionian (up to 12 cm decade<sup>-1</sup>, 7.9 cm decade<sup>-1</sup> on average in the sub-basin) and Aegean seas only. The Levantine basin shows a decrease down to -10 cm decade<sup>-1</sup> and of -6.6 cm decade<sup>-1</sup> on average, while the Balearic, Tyrrhenian (including the Gulf of Genoa) and Adriatic seas show moderate decreasing trends in the summer extreme sea states. Concluding, on average, in 1981–2019 the MS wind-wave climate has decreased during summer seasons and increased during winter seasons (both 50th and 99th percentiles) with the largest changes in the extreme sea states.

## Mediterranean Sea Maximum Individual Wave Climate

In this section we change the focus of the analysis from the climate of the significant wave height of sea states to the MS climate of the maximum individual wave heights and the other (beside significant wave height) relevant parameter for their estimation, i.e., wave steepness and narrow bandedness.

### Maximum Individual Waves

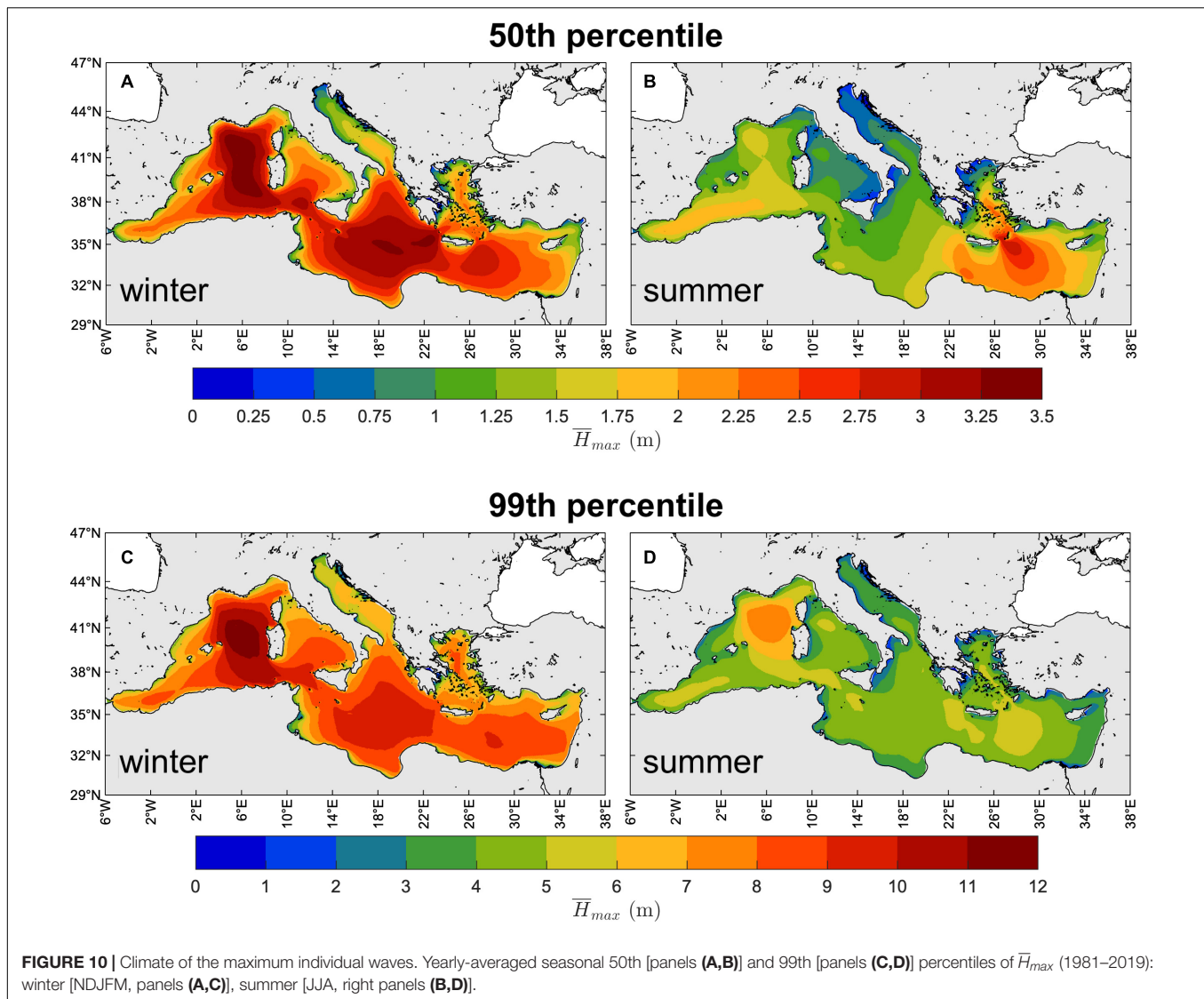
The yearly-averaged winter and summer 50th and 99th percentiles of  $\bar{H}_{max}$  are shown in **Figure 10** (and in **Supplementary Figure 7** for  $\bar{C}_{max}$ ). As expected, seasonal and spatial patterns closely mirror those of  $H_s$ , which is the driving parameter determining the height of maximum individual waves (others, like the steepness for  $\bar{C}_{max}$  and the narrow bandedness parameter for  $\bar{H}_{max}$ , will be discussed in the following). The largest typical crest heights occur in the Sardinian Sea (Western sub-basin) and in the southern MS during winter, reaching up to 3.5 m height, whereas during summer the largest values are found southeast of Crete island in the Levantine basin with heights up to 3 m. The largest extreme wave height (99th percentile) can be found in the same parts of the MS with values up to 12 m in winter and 8 m in summer.

The variability of the maximum individual wave climate ( $\bar{C}_{max}$  and  $\bar{H}_{max}$ ) well matches the variability of the  $H_s$  climate, shown in section "Variability of the Mediterranean Sea Wind-Wave Climate." The extreme-to-typical condition variations at seasonal scale for  $\bar{H}_{max}$  and  $\bar{C}_{max}$  are shown in **Supplementary Figures 8, 9**, respectively. Compared to the  $H_s$  variations in **Figure 6**, they only show minor differences, which do not substantially change the conclusions drawn about the seasonal and regional characteristics of the wave climate variability in the MS, which are also valid for the inter-annual variability.

What deserves more attention is the change in the maximum individual wave climate, expressed using the Sen's slope of the linear trend over 1981–2019. Trends are shown in detail for  $\bar{H}_{max}$  in **Figure 11** (in **Supplementary Figure 10** for  $\bar{C}_{max}$ ) and summarized as spatial averages over the MS and sub-basins in **Table 2** (in **Supplementary Table 2** for  $\bar{C}_{max}$ ). On average, maximum individual waves change more than  $H_s$  (**Table 1**) with slopes larger than  $H_s$  slopes: e.g., on average for the MS in winter 2.5 and 13.9 cm decade<sup>-1</sup> for  $\bar{H}_{max}$ , instead of 1.1 and 6.5 cm decade<sup>-1</sup> for corresponding  $H_s$  values. More than doubled slopes for  $\bar{H}_{max}$  are also observed in **Figure 11**, with winter  $\bar{H}_{max}$  increasing up to 10 cm decade<sup>-1</sup> in the Western sub-basin (50th percentile) and up to 25 cm decade<sup>-1</sup> in the Levantine sub-basin (99th percentile). In general, however, the spatial distribution of the trends for  $\bar{H}_{max}$  (and  $\bar{C}_{max}$  too) reflects the distribution of  $H_s$  trends. The meaning of these trends and how they can be interpreted compared to the  $H_s$  trends will be examined in the Discussion section.

### Wave Steepness and Narrow Bandedness

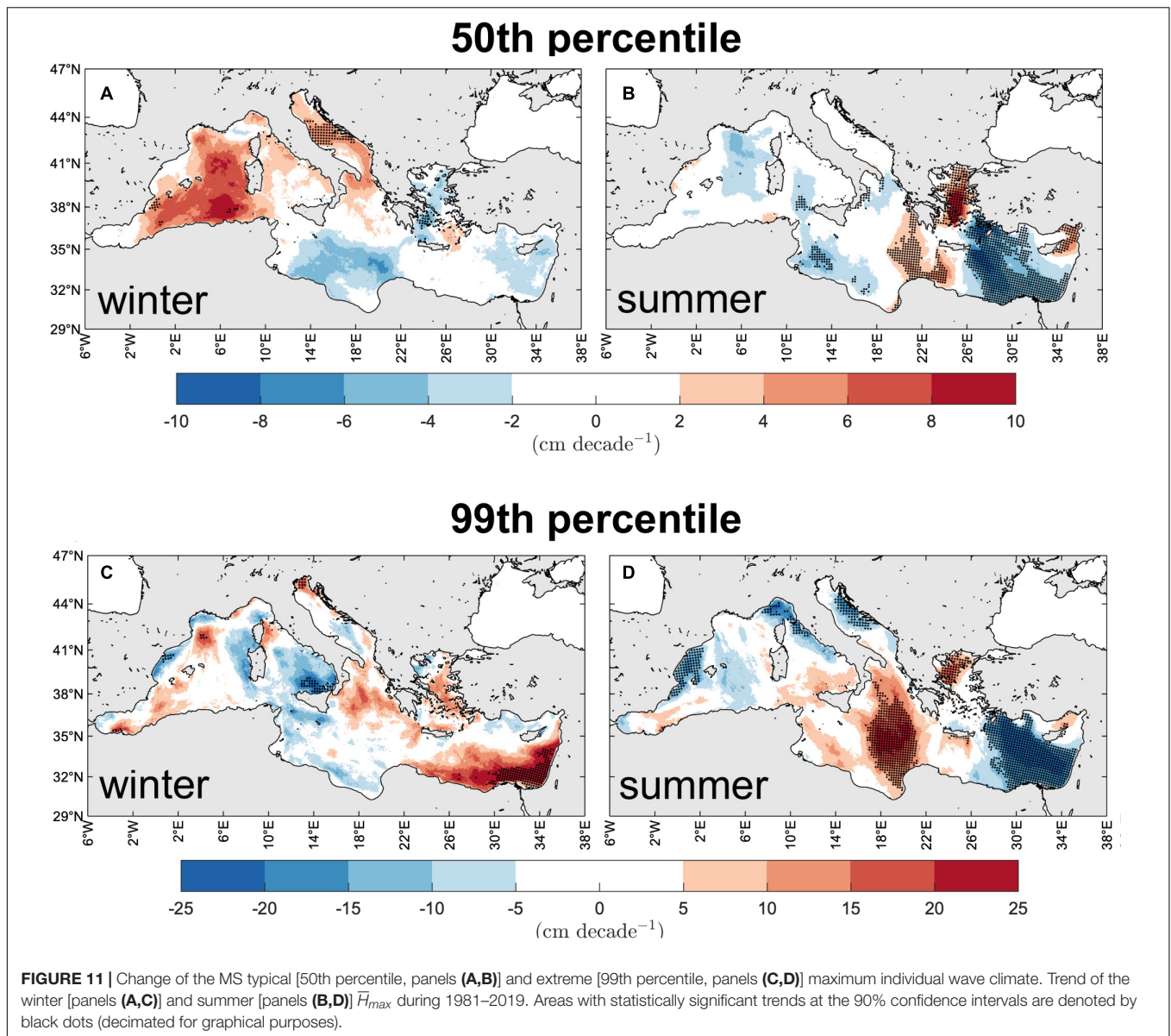
We have shown that, while the maximum individual wave climate displays characteristic typical and extreme values, spatial patterns and variability of the maximum individual wave climate closely mirror those of the significant wave height. The reason is that



maximum crest and wave heights are monotonic functions of significant wave height  $H_s$  [see Equations (1) and (2)]. Therefore, we expect that regions where  $H_s$  is large are also the regions where  $\bar{C}_{max}$  and  $\bar{H}_{max}$  are the highest. This is confirmed by the comparison of **Figure 10** and **Supplementary Figure 7**. At the same time, though with a smaller effect with respect to  $H_s$ ,  $\bar{C}_{max}$  and  $\bar{H}_{max}$  are also monotonic functions of the wave steepness  $\mu$  and the narrow bandedness  $\psi^*$ , respectively [see Equations (1) and (2)]. Therefore, maximum individual wave heights in **Figure 10** and **Supplementary Figure 7** are the result of the combined effect of  $H_s$  (both  $\bar{C}_{max}$  and  $\bar{H}_{max}$ ),  $\mu$  ( $\bar{C}_{max}$ ) and  $\psi^*$  ( $\bar{H}_{max}$ ).

In **Figures 12A,B** we show the yearly-averaged winter and summer 50th percentile of  $\mu$ . As younger waves are generally steeper, largest steepness (up to 0.07) can be found close to the shores where prevailing Mediterranean onshore winds blow from: e.g., in the Gulf of Lyon (Mistral), in the Aegean Sea (Etesian), along the eastern Adriatic coast (Bora), but also on

the leeward side of straits (i.e., Sirocco to the north of Otranto Strait in the Adriatic Sea, Vendaval to the east of Gibraltar Strait, Mistral to the east of Bonifacio Strait in the Tyrrhenian Sea, Etesian to the west of the Bosphorus Strait). Steepness decreases moving off-shore along the wind direction as waves develop. Although the steepest waves occur in winter, the summer Etesian wind waves are as steep as in winter. The 99th percentile of  $\mu$  (**Figures 12C,D**), again larger in correspondence of younger waves, is up to 0.075 over the whole MS except in the Adriatic Sea (up to 0.08) and in very narrow coastal regions where can be up to 0.09. Wind-sea dominated seas typically have steepness values larger than 0.03–0.04, while swell dominated seas may have halved values compared to wind-seas (Barbariol et al., 2019). The steepness values we find in the MS (generally larger than 0.03) denotes the predominance of wind-seas in the MS climate, especially in winter. During summer smaller values (0.02; 50th percentile) can be found in the Gulf of Genoa and in the southern Tyrrhenian Sea, where mature waves driven by south-westerly



winds can develop after frequency- and direction-dispersion along the large distances from the Alboran Sea to these areas (among the longest in the MS).

The yearly-averaged 50th percentile of  $\psi^*$ , shown in **Figures 13A,B**, generally ranges between 0.625 and 0.675 in winter, while can be up to 0.75 in summer. These are values representative of a unimodal wind-sea ( $0.65 \leq \psi^* \leq 0.75$ ; see Boccotti, 2000), denoting the prevailing nature of typical MS sea states. Smaller values can be found in the wide western and southern basins where a local wind-sea may combine with more mature seas coming from different directions. It is worth mentioning that a proper long-term statistical analysis of the sea state characteristics should account for different wave systems separately. That is, wind-sea and swell (if any) should be separated (e.g., using spectral partitioning techniques accounting also for wave direction) and treated independently as

they have a different origin and belong statistically to different populations. However, the range of superimposed wind-sea and swell ( $\psi^* \leq 0.6$ ; Boccotti, 2000) is rather rare in the MS, even if crossing sea states with waves with different wave direction may occur. The 99th percentile values of  $\psi^*$  (**Figures 13C,D**), generally larger than 0.7 and up to 1, denotes the presence of narrow banded sea states, able to produce the largest crest-to-trough excursions according to the Quasi-Determinism theory (Boccotti, 2000; Benetazzo et al., 2017, 2021b), especially in the Adriatic, Tyrrhenian and Aegean seas.

## DISCUSSION

In this section, we first highlight and discuss the limits and strengths of the dataset and of the related climate analysis. Then,



**TABLE 2** | Spatial averages over the MS and sub-basins of the 50th and 99th percentile  $\bar{H}_{max}$  trends shown in **Figure 11** (cm decade<sup>-1</sup>), during 1981–2019 summer and winter seasons.

	50th Percentile				99th Percentile			
	Summer		Winter		Summer		Winter	
	Significant	All	Significant	All	Significant	All	Significant	All
<i>Mediterranean</i>	-1.8 (23.0%)	-1.0	2.5 (2.4%)	0.6	-3.9 (25.4%)	-0.6	13.9 (4.8%)	1.9
<i>Adriatic</i>	1.2 (3.6%)	0.5	4.5 (27.0%)	3.1	-13.3 (17.3%)	-4.6	12.3 (6.4%)	0.9
<i>Ionian</i>	1.0 (16.4%)	-0.7	-3.0 (0.1%)	-1.4	16.9 (28.6%)	8.8	-10.4 (0.1%)	-0.4
<i>Tyrrhenian</i>	-3.0 (4.3%)	-0.9	3.7 (0.1%)	1.9	-15.2 (4.2%)	0.3	-19.7 (6.4%)	-6.7
<i>Levantine</i>	-2.5 (54.1%)	-1.6	-3.6 (2.0%)	-1.1	-14.2 (41.9%)	-6.4	22.6 (10.4%)	8.0
<i>Western</i>	1.2 (0.7%)	-0.8	6.1 (1.4%)	4.4	-12.3 (9.5%)	-3.5	3.7 (1.8%)	0.2

Averages over the points where the trends are significant (black dots in **Figure 11**; tested with Mann-Kendall test and 90% confidence interval) and over all the points. Value between parentheses is the percentage of points with statistically significant trends in a (sub-) basin with respect to all the points in the (sub-) basin.

we comment on the results we have obtained, by also comparing them to those obtained in previous studies for the same area.

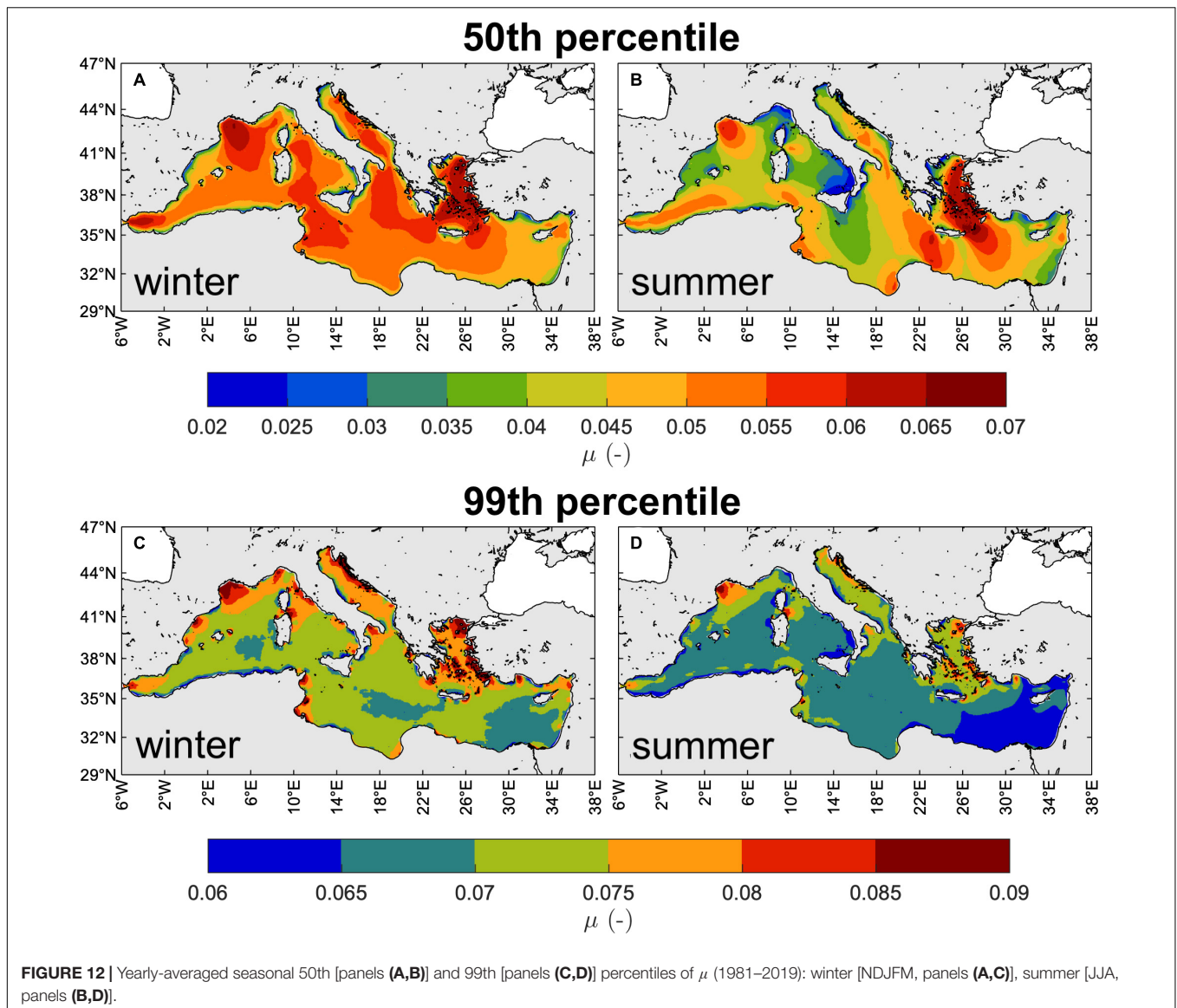
The climatology of MS waves presented in the previous section relies upon the climatology of the ERA5 reanalysis wind. Even if ERA5 horizontal resolution may be poor for representing the dynamical structure of the wind fields in some regional seas, as the narrow semi-enclosed Adriatic or Aegean seas, it currently represents the state-of-the-art of long-term atmospheric reanalysis and hence the best forcing option for the present work. In this context, using a dynamical downscaling of ERA5 winds, Vannucchi et al. (2021) showed an improvement of wind and wave hindcast performance against wind stations and buoys in the MS compared to the original ERA5 data mostly at coastal stations. We have decided to use ERA5 wind and not ERA5 waves, as the latter may be not suitable for long-term climate analyses, at least for studies extending before and after 1992, i.e., the beginning of satellite altimeter data assimilation in the wave models. The introduction of spurious trends is a well-known issue pointed out by Aarnes et al. (2015) for ERA-Interim reanalysis waves (Dee et al., 2011) that may apply also to ERA5. To cope with the resolution issue of ERA5 in the MS and with the potential 1992 singularity in wave products, we have therefore (i) relied on the ERA5 wind forcing (on which we expect a smaller or at least indirect data assimilation effect) and on an *ad hoc* high-resolution (about 5 km) wave hindcast and (ii) verified the wave hindcast results against satellite altimetry. While this has not increased the wind forcing resolution, it has allowed us to produce one of the longest consistent Mediterranean wave hindcasts up to now, providing a detailed representation of the wave climatology in a morphologically complex enclosed sea and assessing its uncertainty compared to observations in the region. Concerning the hindcast performance, the MS wave climate, its (intra- and inter-annual) variability and the trends have shown to be well reproduced by the ERA5 wind forced hindcast. However, the negative modeled-observed  $H_s$  relative bias shown in Section “Assessment of the Mediterranean Sea Wind-Wave Hindcast” should be regarded when using the estimates of the 50th and 99th percentile of the MS wave heights.

Results of the wave hindcast and following wave climate analysis have shown marked regional characteristics of the wave

climate, related to the peculiarities of the regional winds blowing over the Mediterranean sub-basins. Results for the typical and extreme wind-wave climate are in agreement with other studies both for spatial distribution and intensity, albeit with some differences [see e.g., Morales-Márquez et al. (2020) for extreme winter  $H_s$  and Lionello and Sanna (2005) for mean seasonal  $H_s$ , both presenting slightly smaller maxima]. In particular, results have highlighted the MS regions where the largest waves occur, which are in the Western, Ionian and Levantine sub-basins, depending on the season. Indeed, compared to previous studies, in this paper we have provided results at a seasonal scale. We have shown that the variety of the MS wave climate characteristics may be well represented by winter and summer seasons, in terms of intensity and patterns of wave heights, with spring and autumn in-between. This is in agreement with the results of Lionello and Sanna (2005), who argued that the MS climate, including wave climate, is characterized by two main seasons, i.e., winter and summer, with spring and autumn only being transitional seasons.

The definition of seasons we have adopted in this study is based on the wind-wave climate and on the altimeter  $H_s$  observations in particular, rather than on monthly air temperatures, as in the meteorological definition of seasons. This choice is supported by other studies on the MS region climate. Indeed, Trigo et al. (1999) suggested that the traditional four meteorological seasons do not fit well the cyclone occurrence patterns in the MS region. In this context, attempts to objectively define season start/end and duration in the MS region, based on different indices than the largely spatially variable temperature, led to definitions of seasons that generally correspond to the traditional ones, but with longer winters and shorter springs and autumns (Alpert et al., 2004; Kotsias et al., 2021) in agreement with our definition. Also Lionello and Sanna (2005), based on principal component analysis of the modeled  $H_s$ , defined four seasons, again with longer winters (and summers) and shorter springs and autumns.

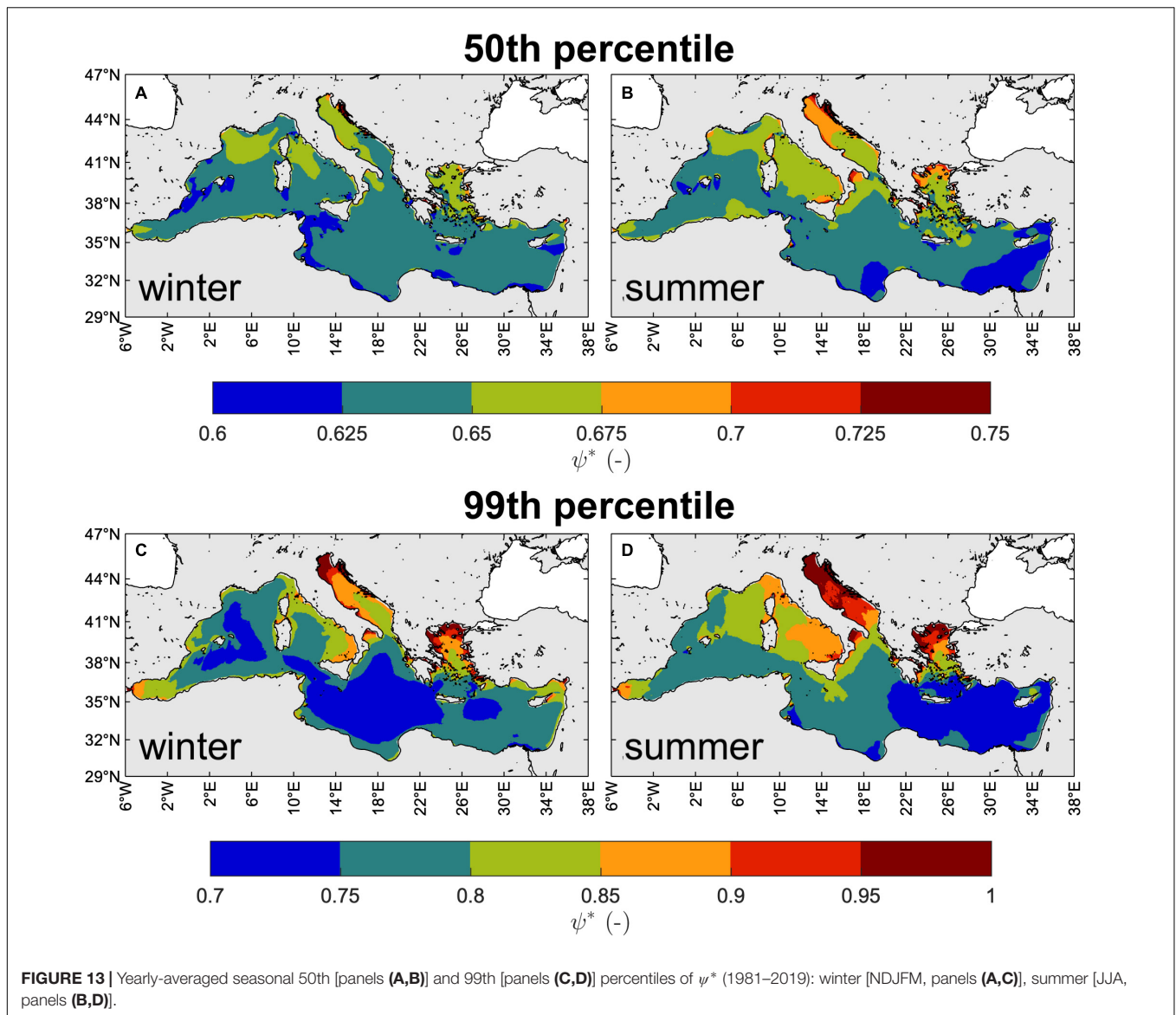
Following the conclusions of previous studies that found that the climate (including wave climate) variability of part of the MS (in particular the northern part with a mid-latitude climate regime) can be partially related to midlatitude climate indices (e.g., Lionello and Sanna, 2005; Morales-Márquez et al., 2020)



we have searched for teleconnections between wave climate variability and the principal modes of atmospheric variability. We have found that MS typical (50th percentile) wave climate variability is generally positively correlated to the SCAND index (i.e., positive  $H_s$  anomalies generally corresponding to positive SCAND phases, and viceversa). This is in accordance with the SCAND positive phases being generally associated with enhanced cyclogenesis in the MS region (Xoplaki, 2002). Extreme wave variability (99th percentile) is also positively correlated to the SCAND index in summer, while it can be negatively correlated to the EA index in winter. The negative phases of EA were also related to extreme waves in the MS by Izaguirre et al. (2010) using satellite data. Over the sub-basins there can be differences, for example the Adriatic Sea, whose wave climate variability is always positively correlated to the SCAND index during winter and to EAWR during summer. In general, our results are in agreement with the results from another study

(Morales-Márquez et al., 2020) and suggest that the MS wave climate variability is mildly-to-slightly related to the variability of large-scale atmospheric structures, which have a more clear influence on the wave climate in other seas (e.g., the North-Atlantic Ocean; Morales-Márquez et al., 2020). We thus share the conclusions of Lionello and Galati (2008) that even if some patterns seem to exert a larger influence with respect to others, this is not sufficient to explain the dominant variability of the wave climate in the MS and its sub-basins, which is the result of a combined effect of large-scale atmosphere dynamics and orography (forcing regional winds).

The observed trend of decreasing  $H_s$  during summer and increasing  $H_s$  during winter (both for typical and extreme wave climate; **Table 1**) seems to disagree with some other past climate change studies in the region, although based on different wind forcing datasets, wave models, trend estimate, and season definition. Indeed, Lionello and Sanna (2005) found a statistically



significant decreasing trend of the mean  $H_s$  in the MS during winter months (December to March,  $-2.4$  cm decade $^{-1}$ ), while we have found a statistically significant increasing trend of the median  $H_s$  in the MS during November to March (Table 1,  $1.1$  cm decade $^{-1}$ ). Also, the spatial distribution and intensity of the 99th percentile winter (December to February)  $H_s$  trend obtained by Morales-Márquez et al. (2020) only partially resembles that shown in Figure 9C. There is instead remarkable agreement, at least in some specific regions, with the trend estimates for the annual maximum  $H_s$  by De Leo et al. (2020). Comparing those estimates with ours for the winter 99th percentile  $H_s$  (the closest to the annual maxima), we see many areas of corresponding increase/decrease: for instance, positive trends in the Gulf of Lyon and other parts of the Western basin, in the northern Adriatic and Tyrrhenian seas and in the easternmost part of the Levantine basin; negative trends in the southern Tyrrhenian Sea, Sardinian Sea and central Adriatic Sea. However, the change in

the wind-wave climate we have found (Figure 9 and Table 1) reflects the change in the ERA5 wind forcing intensity and spatial distribution while for instance Lionello and Sanna (2005) study is based on the ERA-40 reanalysis (Uppala et al., 2005) and Morales-Márquez et al. (2020) and De Leo et al. (2020) on the CFSR reanalysis (Chawla et al., 2013). Hence, the reasons for different trends on the intensity of storms should be searched for in the wind forcings that have generated the wave model results. Changes in ERA5 wind characteristics might be due, for instance, to changes in storm trajectories, as suggested by numerous climatological studies, which investigated not only the intensity and frequency of Mediterranean cyclones but also the variability of their trajectories in the last decades and in the future climate projections (Lionello et al., 2002; Lionello and Giorgi, 2007; Cavicchia et al., 2014; Messmer et al., 2020). We have verified monthly  $H_s$  percentile trends from the ERA5 wind forced wave hindcast at the MS basin scale against trends

from satellite altimeters and found a general agreement in the increasing/decreasing trends as well as in the magnitude of the trends. For  $\bar{H}_{max}$  (and  $\bar{C}_{max}$ ), we have found trends that are larger than the  $H_s$  trends: for instance, for the winter 50th percentile on the whole MS, on average 2.44 times for  $\bar{H}_{max}$ . This can be explained with  $\bar{H}_{max}$  being on average 2.36  $H_s$ . Hence, the linear trend of  $\bar{H}_{max}$ , i.e.,  $\Delta\bar{H}_{max}/\Delta T$ , should be on average  $\Delta\bar{H}_{max}/\Delta T \approx 2.36\Delta H_s/\Delta T$ , the difference between 2.44 and 2.36 being possibly explained with a change in the other wave parameters that  $\bar{H}_{max}$  depends upon.

## CONCLUSION

In this paper, we have taken advantage of the ERA5 atmospheric wind reanalysis and spectral wave modeling to characterize the wind-wave climate of the MS, its spatio-temporal variability and change. The wind-wave dataset we have produced has allowed us to obtain one of the longest wave climate assessments in the MS to date. Also, for the first time we have bestowed an assessment of the maximum individual wave climate in the MS. Our main results are here summarized:

- We have verified the ERA5 wind-based wind-wave hindcast against satellite observations of significant wave height with respect to its performance in reproducing the typical (50th percentile) and extreme (99th percentile)  $H_s$ , and the variability and trend of the MS wind-wave climate. Despite a general tendency to underestimate  $H_s$  (in particular in narrow basins as the Adriatic Sea and for the extremes) the dataset has been shown to properly reproduce the temporal variability and the trends of  $H_s$ .
- We have presented the typical and extreme MS wind-wave climate patterns and characteristics at seasonal scale and, to this end, we have proposed and used a definition of seasons based on the satellite observation of significant wave height over the MS, which presents a stormy season (winter) lasting 5 months, a calm season (summer) lasting 3 months and two transitional seasons (spring and autumn) lasting 2 months each. This definition is in agreement with other objective season definitions in the MS.
- The largest typical waves (both as  $H_s$  and maximum individual waves) occur in the western and southern MS during winter, and in the eastern MS during summer, whereas the largest extreme waves occur in the western MS in all seasons, with maximum values during winter.
- The intra-seasonal variability of MS wind waves (expressed as the ratio of the 99th to the 50th percentile  $H_s$ ) has been shown to be largest during summer and in the Adriatic, Tyrrhenian and Sardinian Seas, indicating these are season and the MS sub-basins that are more prone to the development of large extremes waves compared to the typical ones. On the other hand, the inter-annual variability has proven to be largest where the largest winter and summer waves occur. However, when the inter-annual variability has been expressed with respect to the local climate (i.e., in terms of relative anomaly) it has emerged that the Adriatic and Tyrrhenian Seas are characterized by the largest variability of typical and extreme  $H_s$ , with the Ionian and Levantine sub-basins also showing large variability of extreme  $H_s$ . During the analyzed period (1981–2019) these regions of the MS have experienced variations up to 100% of both the local 50th or 99th percentile  $H_s$ .
- We have motivated the largest positive and negative relative anomalies of  $H_s$  in the MS basin (and sub-basins) thanks to the geopotential height at 500 hPa, mean sea level pressure and wind intensity anomalies and we have related the temporal variability of the relative anomalies in the MS to the principal modes of atmospheric variability. The seasonal Scandinavian index seems the most correlated to the seasonal wind-wave variability in the MS, especially during winter and for the typical  $H_s$ , with positive Scandinavian index phases associated to the largest typical winter  $H_s$  (extreme winter  $H_s$  are best correlated to the Eastern Atlantic index). However, correlations found are not remarkable (0.54 at most for the MS, 0.65 for sub-basins) and this suggests, in agreement with previous studies in the MS, that the wind-wave variability in the MS can only be partially motivated by teleconnections, most likely due to the effects of local orography that, interacting with synoptic scale atmospheric structures, generates cyclones and consequent winds with regional characteristics that partially lose the link with their large-scale source.
- The long-term trends found in the ERA5-wind based hindcast of the MS waves are negative for the summer season and positive for the winter season, both for typical and extreme sea states (and maximum individual waves). These trends are statistically significant though generally modest in magnitude (however, locally up to 12 cm decade<sup>-1</sup> for extreme winter  $H_s$  and 25 cm decade<sup>-1</sup> for extreme winter  $\bar{H}_{max}$ ) and are larger for extreme sea states compared to typical sea states. This suggests the MS wind-wave climate has changed during 1981–2019, with decreasing  $H_s$  (and maximum individual waves) during summer and increasing during winter.
- The climate characteristics (patterns, spatio-temporal variability and change) of maximum individual waves closely mirror those of  $H_s$ , although there are some differences that are motivated by the dependence of  $\bar{H}_{max}$  (and  $\bar{C}_{max}$ ) by other sea state characteristics, i.e., the narrow bandedness parameter and the wave steepness. We have presented their typical and extreme seasonal patterns and intensities, showing that MS sea states are generally dominated by wind waves.

Concluding, this study have proven that the ERA5 wind can be successfully used to hindcast the wind waves in the MS, a crucial task to assess the past and present climate in a regional basin providing environmental and economical services to the whole MS region and where the impacts of climate change are expected to be significant in the near future. As a recommendation for future reanalysis-wind based assessments in a semi-enclosed

basin with similar characteristics (i.e., narrow sub-basins and surrounding orography), in order to reduce the spatial resolution effects in the narrowest basins (as the Adriatic Sea) and close to the coasts, a dynamical downscaling of ERA5 winds would be advisable. This represents one of the further improvements on the hindcast production side. As regards the wave climate analysis, although swell seas are rather rare in the MS, a partitioning analysis of the directional wave spectra determining the different wave systems that may mix in a sea state would allow treating them separately (if necessary) and also characterizing the crossing seas that often pose serious problems to ships in navigation. Finally, further investigations, for instance looking for a change in the direction of cyclonic paths and their intensity, would help disentangling the dominant mechanisms that drive the changing seasonal wave climate we found.

## DATA AVAILABILITY STATEMENT

The raw data supporting the conclusions of this article will be made available by the authors, without undue reservation.

## AUTHOR CONTRIBUTIONS

FB, SD, and AB contributed to the conception and design of the study and produced the dataset. FB and SD performed the dataset assessment. FB and AR performed the analyses. SD, FF, RF, MS, and AB contributed to the analyses. FB wrote the manuscript. All authors contributed to manuscript revision, read, and approved the submitted version.

## REFERENCES

- Aarnes, O. J., Saleh, A., Jean, R. B., and Øyvind, B. (2015). Marine wind and wave height trends at different ERA-interim forecast ranges. *J. Clim.* 28, 819–837. doi: 10.1175/JCLI-D-14-00470.1
- Alpert, P., Osetinsky, I., Ziv, B., and Shafir, H. (2004). A new seasons definition based on classified daily synoptic systems: an example for the Eastern Mediterranean. *Int. J. Climatol.* 24, 1013–1021. doi: 10.1002/joc.1037
- Arduin, F., Rogers, E., Babanin, A. V., Filipot, J.-F., Magne, R., Roland, A., et al. (2010). Semiempirical dissipation source functions for ocean waves. Part I: definition, calibration, and validation. *J. Phys. Oceanogr.* 40, 1917–1941. doi: 10.1175/2010JPO4324.1
- Arena, F., Laface, V., Malara, G., Romolo, A., Viviano, A., Fiamma, V., et al. (2015). Wave climate analysis for the design of wave energy harvesters in the Mediterranean Sea. *Renew. Energy* 77, 125–141. doi: 10.1016/j.renene.2014.12.002
- Barbariol, F., Alves, J. H. G. M., Benetazzo, A., Bergamasco, F., Bertotti, L., Carniel, S., et al. (2017). Numerical modeling of space-time wave extremes using WAVEWATCH III. *Ocean Dyn.* 67, 535–549. doi: 10.1007/s10236-016-1025-0
- Barbariol, F., Benetazzo, A., Carniel, S., and Sclavo, M. (2013). Improving the assessment of wave energy resources by means of coupled wave-ocean numerical modeling. *Renew. Energy* 60, 462–471. doi: 10.1016/j.renene.2013.05.043
- Barbariol, F., Bidlot, J.-R., Cavaleri, L., Sclavo, M., Thomson, J., and Benetazzo, A. (2019). Maximum wave heights from global model reanalysis. *Prog. Oceanogr.* 175, 139–160. doi: 10.1016/j.pocean.2019.03.009
- Battjes, J., and Janssen, J. P. F. M. (1978). “Energy loss and set-up due to breaking of random waves,” in *Proceedings of the 16th International Conference on Coastal*

## FUNDING

This study was partially supported by the Copernicus Marine Environment Monitoring Service (CMEMS) LATEMAR project. CMEMS is implemented by Mercator Ocean in the framework of a delegation agreement with the European Union. This work has also been conducted as part of the bilateral project EOLO-1 (“Extreme oceanic waves during tropical, tropical-like, and bomb cyclones”) between CNR-ISMAR and the University of Tokyo (Japan). Antonio Ricchi funding has been provided by PON Ricerca e Innovazione 2014–2020 “AIM”—Attraction and international mobility program. EU Social Fund and Regional Development Fund; Ministero dell’Istruzione e della Ricerca, grant number AIM1858058.

## ACKNOWLEDGMENTS

Hersbach et al. (2018) was downloaded from the Copernicus Climate Change Service (C3S) Climate Data Store. The results contain modified Copernicus Climate Change Service information, 2020. Neither the European Commission nor ECMWF is responsible for any use that may be made of the Copernicus information or data it contains. We would like to thank Luigi Cavaleri for fruitful discussions on the topic.

## SUPPLEMENTARY MATERIAL

The Supplementary Material for this article can be found online at: <https://www.frontiersin.org/articles/10.3389/fmars.2021.760614/full#supplementary-material>

- Engineering*, Vol. 1 (New York, NY: American Society of Civil Engineers), 569–587. doi: 10.9753/icce.v16.32
- Benetazzo, A., Barbariol, F., Pezzutto, P., Staneva, J., Behrens, A., Davison, S., et al. (2021b). Towards a unified framework for extreme sea waves from spectral models: rationale and applications. *Ocean Eng.* 219:108263.
- Benetazzo, A., Barbariol, F., Bergamasco, F., Bertotti, L., Yoo, J., Shim, J.-S., et al. (2021a). On the extreme value statistics of spatio-temporal maximum sea waves under cyclone winds. *Prog. Oceanogr.* 197:102642. doi: 10.1016/j.pocean.2021.102642
- Benetazzo, A., Barbariol, F., Bergamasco, F., Carniel, S., and Sclavo, M. (2017). Space-time extreme wind waves: analysis and prediction of shape and height. *Ocean Model.* 113, 201–216. doi: 10.1016/j.ocemod.2017.03.010
- Benetazzo, A., Fedele, F., Carniel, S., Ricchi, A., Bucchignani, E., and Sclavo, M. (2012). Wave climate of the adriatic sea: a future scenario simulation. *Nat. Hazards Earth Syst. Sci.* 12, 2065–2076. doi: 10.5194/nhess-12-2065-2012
- Bertotti, L., and Cavaleri, L. (2008). The predictability of the ‘Voyager’ accident. *Nat. Hazards Earth Syst. Sci.* 8, 533–537. doi: 10.5194/nhess-8-533-2008
- Besio, G., Mentaschi, L., and Mazzino, A. (2016). Wave energy resource assessment in the Mediterranean Sea on the basis of a 35-year Hindcast. *Energy* 94, 50–63. doi: 10.1016/j.energy.2015.10.044
- Boccotti, P. (2000). *Wave Mechanics for Ocean Engineering*. New York, NY: Elsevier Science B.V., 496.
- Cavaleri, L., Bajo, M., Barbariol, F., Bastianini, M., Benetazzo, A., Bertotti, L., et al. (2019). The October 29, 2018 storm in Northern Italy – an exceptional event and its modeling. *Prog. Oceanogr.* 178:102178. doi: 10.1016/j.pocean.2019.102178

- Cavaleri, L., Fox-Kemper, B., and Hemer, M. (2012b). Wind waves in the coupled climate system. *Bull. Am. Meteorol. Soc.* 93, 1651–1661. doi: 10.1175/BAMS-D-11-00170.1
- Cavaleri, L., Bertotti, L., Torrisi, L., Bitner-Gregersen, E., Serio, M., and Onorato, M. (2012a). Rogue waves in crossing seas: the Louis Majesty accident. *J. Geophys. Res. Oceans* 117:C00J10. doi: 10.1029/2012JC007923
- Cavicchia, L., Von Storch, H., and Gualdi, S. (2014). Mediterranean tropical-like cyclones in present and future climate. *J. Clim.* 27, 7493–7501. doi: 10.1175/JCLI-D-14-00339.1
- Chawla, A., Spindler, D. M., and Tolman, H. L. (2013). Validation of a thirty year wave hindcast using the climate forecast system reanalysis winds. *Ocean Model.* 70, 189–206. doi: 10.1016/j.ocemod.2012.07.005
- De Leo, F., Besio, G., and Mentaschi, L. (2021). Trends and variability of ocean waves under RCP8.5 emission scenario in the Mediterranean Sea. *Ocean Dyn.* 71, 97–117. doi: 10.1007/s10236-020-01419-8
- De Leo, F., De Leo, A., Besio, G., and Briganti, R. (2020). Detection and quantification of trends in time series of significant wave heights: an application in the Mediterranean Sea. *Ocean Eng.* 202:107155. doi: 10.1016/j.oceaneng.2020.107155
- Dee, D. P., Uppala, S. M., Simmons, A. J., Berrisford, P., Poli, P., Kobayashi, S., et al. (2011). The ERA-interim reanalysis: configuration and performance of the data assimilation system. *Q. J. R. Meteorol. Soc.* 137, 553–597. doi: 10.1002/qj.828
- DNV GL–Det Norske Veritas Germanischer Lloyd (2017). *DNVGL-RP-C205: Environmental Conditions and Environmental Loads. DNV GL Recommended Practice*. Oslo: DNV GL, 1–259.
- Dysthe, K., Krogstad, H. E., and Müller, P. (2008). Oceanic rogue waves. *Annu. Rev. Fluid Mech.* 40, 287–310.
- Fedele, F. (2012). Space–time extremes in short-crested storm seas. *J. Phys. Oceanogr.* 42, 1601–1615.
- Giorgi, F. (2006). Climate change hot-spots. *Geophys. Res. Lett.* 33:L08707. doi: 10.1029/2006GL025734
- Hasselmann, K., Barnett, T. P., Bouws, E., Carlson, H., Cartwright, D. E., Enke, K., et al. (1973). *Measurements of Wind-Wave Growth and Swell Decay During the Joint North Sea Wave Project (JONSWAP)*. Hamburg: Deutsches Hydrographisches Institut Hamburg.
- Hersbach, H., Bell, B., Berrisford, P., Biavati, G., Horányi, A., Muñoz Sabater, J., et al. (2018). *ERA5 Monthly Averaged Data on Single Levels from 1979 to Present. Copernicus Climate Change Service (C3S) Climate Data Store (CDS)*.
- Hersbach, H., Bell, B., Berrisford, P., Hirahara, S., Horányi, A., Muñoz-Sabater, J., et al. (2020). The ERA5 global reanalysis. *Q. J. R. Meteorol. Soc.* 146, 1999–2049. doi: 10.1002/qj.3803
- Izaguirre, C., Mendez, F. J., Menendez, M., Luceño, A., and Losada, I. J. (2010). Extreme wave climate variability in Southern Europe using satellite data. *J. Geophys. Res.* 115:C04009. doi: 10.1029/2009jc005802
- Kendall, M. G. (1948). *Rank Correlation Methods*. London: C. Griffin.
- Kotsias, G., Lolis, C. J., Hatzianastassiou, N., Lionello, P., and Bartzokas, A. (2021). An objective definition of seasons for the Mediterranean region. *Int. J. Climatol.* 41, E1889–E1905. doi: 10.1002/joc.6819
- Liberti, L., Carrillo, A., and Sannino, G. (2013). Wave energy resource assessment in the {M}editerranean, the {I}talian perspective. *Renew. Energy* 50, 938–949. doi: 10.1016/j.renene.2012.08.023
- Lionello, P. (2012). *The Climate of the Mediterranean Region*. Amsterdam: Elsevier. doi: 10.1016/C2011-0-06210-5
- Lionello, P., Dalan, F., and Elvini, E. (2002). Cyclones in the Mediterranean region: the present and the doubled CO2 climate scenarios. *Clim. Res.* 22, 147–159. doi: 10.3354/cr022147
- Lionello, P., and Galati, M. B. (2008). Links of the significant wave height distribution in the Mediterranean sea with the Northern hemisphere teleconnection patterns. *Adv. Geosci.* 17, 13–18. doi: 10.5194/adgeo-17-13-2008
- Lionello, P., and Giorgi, F. (2007). Winter precipitation and cyclones in the Mediterranean region: future climate scenarios in a regional simulation. *Adv. Geosci.* 12, 153–158. doi: 10.5194/adgeo-12-153-2007
- Lionello, P., and Sanna, A. (2005). Mediterranean wave climate variability and its links with NAO and Indian monsoon. *Clim. Dyn.* 25, 611–623. doi: 10.1007/s00382-005-0025-4
- Mann, H. B. (1945). Nonparametric tests against trend. *Econometrica* 13, 245–259. doi: 10.2307/1907187
- Mentaschi, L., Besio, G., Cassola, F., and Mazzino, A. (2015). Performance evaluation of WAVEWATCH III in the Mediterranean sea. *Ocean Model.* 90, 82–94. doi: 10.1016/j.ocemod.2015.04.003
- Messmer, M., Raible, C. C., and ómez-Navarro, J. J. G. (2020). Impact of climate change on the climatology of Vb cyclones. *Tellus Ser. A Dyn. Meteorol. Oceanogr.* 72, 1–18. doi: 10.1080/16000870.2020.1724021
- Morales-Márquez, V., Orfila, A., Simarro, G., and Marcos, M. (2020). Extreme waves and climatic patterns of variability in the Eastern North Atlantic and Mediterranean Basins. *Ocean Sci.* 16, 1385–1398. doi: 10.5194/os-16-1385-2020
- Piante, C., and Ody, D. (2015). *Blue Growth in the Mediterranean Sea: The Challenge of Good Environmental Status. MedTrends Project*. WWF, 192. Available online at: <http://www.developpement-durable.gouv.fr/> (accessed October 20, 2021).
- Portilla-Yandún, J., Barbariol, F., Benetazzo, A., and Cavaleri, L. (2019). On the statistical analysis of ocean wave directional spectra. *Ocean Eng.* 189:106361. doi: 10.1016/j.oceaneng.2019.106361
- Queffelec, P., and Bentamy, A. (2007). Analysis of wave height variability using altimeter measurements: application to the Mediterranean Sea. *J. Atmos. Ocean. Technol.* 24, 2078–2092. doi: 10.1175/2007JTECH0507.1
- Ribal, A., and Young, I. R. (2019). 33 years of globally calibrated wave height and wind speed data based on altimeter observations. *Sci. Data* 6:77. doi: 10.1038/s41597-019-0083-9
- Sartini, L., Besio, G., and Cassola, F. (2017). Spatio-temporal modelling of extreme wave heights in the Mediterranean Sea. *Ocean Model.* 117, 52–69. doi: 10.1016/j.ocemod.2017.07.001
- Sartini, L., Cassola, F., and Besio, G. (2015a). Extreme waves seasonality analysis: an application in the Mediterranean Sea. *J. Geophys. Res. Oceans* 120, 6266–6288. doi: 10.1002/2015JC011061
- Sartini, L., Mentaschi, L., and Besio, G. (2015b). Comparing different extreme wave analysis models for wave climate assessment along the Italian Coast. *Coast. Eng.* 100, 37–47. doi: 10.1016/j.coastaleng.2015.03.006
- Sen, P. K. (1968). Estimates of the regression coefficient based on Kendall's Tau. *J. Am. Stat. Assoc.* 63, 1379–1389. doi: 10.1080/01621459.1968.10480934
- Tayfun, M. A. (1980). Narrow-band nonlinear sea waves. *J. Geophys. Res.* 85, 1548–1552.
- The WAVEWATCH III Development Group [WW3DG] (2016). *User Manual and System Documentation of WAVEWATCH III Version 5.16. Technical Note, MMAB Contribution*.
- The WAVEWATCH III Development Group [WW3DG] (2019). *User Manual and System Documentation of WAVEWATCH III-Version 6.07*. College Park, MD: WW3DG.
- Theil, H. (1950). A rank-invariant method of linear and polynomial regression analysis, part I. *Proc. R. Neth. Acad. Sci.* 53, 386–392.
- Tolman, H. L. (1991). A third-generation model for wind waves on slowly varying, unsteady, and inhomogeneous depths and currents. *J. Phys. Oceanogr.* 21, 782–797.
- Tolman, H. L. (2003). Treatment of unresolved islands and ice in wind wave models. *Ocean Model.* 5, 219–231. doi: 10.1016/S1463-5003(02)00040-9
- Trigo, I. F., Davies, T. D., and Bigg, G. R. (1999). Objective climatology of cyclones in the Mediterranean region. *J. Clim.* 12, 1685–1696. doi: 10.1175/1520-0442(1999)012<1685:OCOCIT>2.0.CO;2
- United Nations Environment Programme/Mediterranean Action Plan and Plan Bleu (2020). *State of the Environment and Development in the Mediterranean*. Nairobi: Marseille Imprimerie.
- Uppala, S. M., Källberg, P. W., Simmons, A. J., Andrae, U., da Costa Bechtold, V., Fiorino, M., et al. (2005). The ERA-40 re-analysis. *Q. J. R. Meteorol. Soc.* 131, 2961–3012. doi: 10.1256/qj.04.176
- Vannucchi, V., Taddei, S., Capecchi, V., Bendoni, M., and Brandini, C. (2021). Dynamical downscaling of Era5 data on the North-Western Mediterranean sea: from atmosphere to high-resolution coastal wave climate. *J. Mar. Sci. Eng.* 9, 1–29. doi: 10.3390/jmse9020208
- von Schuckmann, K., Le Traon, P. Y., Smith, N., Pascual, A., Djavidnia, S., Gattuso, J. P., et al. (2021). Copernicus marine service ocean state

- report, issue 5. *J. Oper. Oceanogr.* 14, 1–185. doi: 10.1080/1755876X.2021.1946240
- Western European Union and Western European Armaments Organisation Research Cell (2004). *Wind and Wave Atlas of the Mediterranean Sea (MEDATLAS)*.
- World Meteorological Organization [WMO] (2018). *Guide to Wave Analysis and Forecasting (WMO-No. 702)*. Geneva: World Meteorological Organization.
- Xoplaki, E. (2002). *Climate Variability Over the Mediterranean*. Bern: University of Bern.
- Young, I. R., and Ribal, A. (2019). Multiplatform evaluation of global trends in wind speed and wave height. *Science* 364, 548–552. doi: 10.1126/science.aav9527
- Zecchetto, S., and De Biasio, F. (2007). Sea surface winds over the Mediterranean basin from satellite data (2000–04): meso- and local-scale features on annual and seasonal time scales. *J. Appl. Meteorol. Climatol.* 46, 814–827. doi: 10.1175/JAM2498.1
- Conflict of Interest:** The authors declare that the research was conducted in the absence of any commercial or financial relationships that could be construed as a potential conflict of interest.
- Publisher's Note:** All claims expressed in this article are solely those of the authors and do not necessarily represent those of their affiliated organizations, or those of the publisher, the editors and the reviewers. Any product that may be evaluated in this article, or claim that may be made by its manufacturer, is not guaranteed or endorsed by the publisher.

Copyright © 2021 Barbariol, Davison, Falcieri, Ferretti, Ricchi, Sclavo and Benetazzo. This is an open-access article distributed under the terms of the Creative Commons Attribution License (CC BY). The use, distribution or reproduction in other forums is permitted, provided the original author(s) and the copyright owner(s) are credited and that the original publication in this journal is cited, in accordance with accepted academic practice. No use, distribution or reproduction is permitted which does not comply with these terms.



# Dynamical Projections of the Mean and Extreme Wave Climate in the Bohai Sea, Yellow Sea and East China Sea

Delei Li<sup>1,2,3\*</sup>, Jianlong Feng<sup>4</sup>, Yuchao Zhu<sup>1,2,3</sup>, Joanna Staneva<sup>5</sup>, Jifeng Qi<sup>1,2,3</sup>, Arno Behrens<sup>5</sup>, Donghyun Lee<sup>6</sup>, Seung-Ki Min<sup>7,8</sup> and Baoshu Yin<sup>1,2,3,9,10\*</sup>

<sup>1</sup> CAS Key Laboratory of Ocean Circulation and Waves, Institute of Oceanology, Chinese Academy of Sciences, Qingdao, China, <sup>2</sup> Pilot National Laboratory for Marine Science and Technology, Qingdao, China, <sup>3</sup> Center for Ocean Mega-Science, Chinese Academy of Sciences, Qingdao, China, <sup>4</sup> College of Marine and Environmental Science, Tianjin University of Science and Technology, Tianjin, China, <sup>5</sup> Institute of Coastal Systems—Analysis and Modeling, Helmholtz-Zentrum Hereon, Geesthacht, Germany, <sup>6</sup> School of Geography and the Environment, Environmental Change Institute, University of Oxford, Oxford, United Kingdom, <sup>7</sup> Division of Environmental Science and Engineering, Pohang University of Science and Technology, Pohang, South Korea, <sup>8</sup> Institute for Convergence Research and Education in Advanced Technology, Yonsei University, Incheon, South Korea, <sup>9</sup> College of Earth and Planetary Sciences, University of Chinese Academy of Sciences, Beijing, China, <sup>10</sup> CAS Engineering Laboratory for Marine Ranching, Institute of Oceanology, Chinese Academy of Sciences, Qingdao, China

## OPEN ACCESS

### Edited by:

Adem Akpinar,  
Uludağ University, Turkey

### Reviewed by:

Piyali Chowdhury,  
Centre for Environment, Fisheries  
and Aquaculture Science (CEFAS),  
United Kingdom  
Tomoya Shimura,  
Kyoto University, Japan

### \*Correspondence:

Delei Li  
deleili@qdio.ac.cn  
Baoshu Yin  
bsyin@qdio.ac.cn

### Specialty section:

This article was submitted to  
Coastal Ocean Processes,  
a section of the journal  
Frontiers in Marine Science

**Received:** 27 December 2021

**Accepted:** 24 January 2022

**Published:** 17 February 2022

### Citation:

Li D, Feng J, Zhu Y, Staneva J,  
Qi J, Behrens A, Lee D, Min S-K and  
Yin B (2022) Dynamical Projections  
of the Mean and Extreme Wave  
Climate in the Bohai Sea, Yellow Sea  
and East China Sea.  
Front. Mar. Sci. 9:844113.  
doi: 10.3389/fmars.2022.844113

Few studies have focused on the projected future changes in wave climate in the Chinese marginal seas. For the first time, we investigate the projected changes of the mean and extreme wave climate over the Bohai Sea, Yellow Sea, and East China Sea (BYE) during two future periods (2021–2050 and 2071–2100) under the RCP2.6 and RCP8.5 scenarios from the WAM wave model simulations with a resolution of 0.1°. This is currently the highest-resolution wave projection dataset available for the study domain. The wind forcings for WAM are from high-resolution (0.22°) regional climate model (RCM) CCLM-MPIESM simulations. The multivariate bias-adjustment method based on the N-dimensional probability density function transform is used to correct the raw simulated significant wave height (SWH), mean wave period (MWP), and mean wave direction (MWD). The annual and seasonal mean SWH are generally projected to decrease (-0.15 to -0.01 m) for 2021–2050 and 2071–2100 under the RCP2.6 and RCP8.5 scenarios, with statistical significance at a 0.1 level for most BYE in spring and for most of the Bohai Sea and Yellow Sea in annual and winter/autumn mean. There is a significant decrease in the spring MWP for two future periods under both the RCP2.6 and RCP8.5 scenarios. In contrast, the annual and summer/winter 99th percentile SWH are generally projected to increase for large parts of the study domain. Results imply that the projected changes in the mean and 99th percentile extreme waves are very likely related to projected changes in local mean and extreme surface wind speeds, respectively.

**Keywords:** wave climate, extreme wave, multivariate bias adjustment, climate projection, Chinese marginal seas



## INTRODUCTION

Ocean waves, especially extreme waves, contain tremendous energy and can greatly impact coastal and offshore industries and marine ecosystems (Hoeke et al., 2013; Toimil et al., 2020). They are also one of the dominant contributors to coastal erosion and flooding (Casas-Prat and Wang, 2020; Melet et al., 2020) along with sea-level rise, storm surge, and precipitation (Camus et al., 2017). Extreme waves have also been a significant threat to human life. For example, they are the deadliest marine hazard in China and have caused ~74% of the total casualties from major marine hazards (including extreme waves, storm surges, tsunamis, and sea ice) during 2000–2015 (Tao et al., 2018).

Under global warming, there have been emerging changes in large-scale atmospheric circulations or climate modes. The western North Pacific subtropical high will likely weaken and retreat eastward in the mid-troposphere at the end of the twenty-first century (He et al., 2015). There was a robust migration of tropical cyclones coastward and poleward in 1982–2018 (Wang and Toumi, 2021). Mei and Xie (2016) revealed that typhoons that impact East and Southeast Asia have intensified by 12–15% during 1977–2014 and indicated that the proportion of category 4 and 5 typhoons has doubled or tripled. All these changes have potential implications for ocean waves or extreme wave events.

Previous studies have investigated the historical changes in the mean or extreme wave conditions globally or regionally (Reguero et al., 2019; Shi et al., 2019; Young and Ribal, 2019). Based on satellite observations, Young and Ribal (2019) revealed small increases in the significant wave height (SWH) and larger increases in the 90th percentiles extreme wave conditions during 1985–2018, especially in the Southern Ocean. Shi et al. (2019) found that the 99th percentile extreme waves increases in most of the Chinese seas by 0.5–3 cm/year in 1979–2017.

However, knowledge of future projected changes in ocean wave climate is limited relative to knowledge of sea surface temperatures or sea levels. This is because most global climate models (GCMs) from the Climate Model Intercomparison Project (CMIP) do not have ocean wave components, with some exceptions, such as FIO-ESM v2.0 (Song et al., 2020). Useful projections of mean and extreme wave climate need to be conducted through dynamical or statistical downscaling (Wang and Swail, 2001, 2006; Mori et al., 2010). Since the launch of the Coordinated Ocean Wave Climate Project (henceforth COWCLIP, Hemer et al., 2012), projected change studies of the ocean wave climate have advanced both regionally and globally (Hemer et al., 2013a; Casas-Prat et al., 2018; Lobeto et al., 2021; O'Grady et al., 2021). From the first community-derived multi-model ensemble of wave-climate projections, Hemer et al. (2013a) revealed the projected changes of SWH, mean wave period (MWP), and mean wave direction (MWD) and found a projected increase in annual mean SWH over 7.1% of the global ocean, predominantly in the Southern Ocean. Based on statistical projections of wave height from sea-level pressure of 20 CMIP5 GCMs, Wang et al. (2014) found increases of SWH in the tropics and high latitudes in the Southern Hemisphere. The occurrence frequency of the present-day 10-year return extreme wave heights are likely to double or triple in several

coastal areas worldwide at end of the twenty-first century under the RCP 8.5 scenario. Morim et al. (2018) conducted a system review on global and regional wind-wave climate projection and established consistent patterns of projected changes in wind-wave climate globally under the global warming. Morim et al. (2019) concluded that approximately 50% of the world's coastline is at risk due to wave climate change, and current wave projection uncertainties are dominated by model-driven uncertainty, encouraging the application of multi-modeling methods on wave climate projections. By using ensembles of global wave model runs driven by 8 CMIP5 GCMs, Meucci et al. (2020) revealed that the intensity of a 100-year return level of the SWH increases by 5–15% in the Southern Ocean by the end of the twenty-first century relative to the 1979–2005 period.

GCMs generally have a coarse resolution, which is not feasible in capturing local or regional wind systems. Li et al. (2016) found that the high-resolution regional climate model (RCM) hindcast can add value in capturing strong wind speeds in the coastal areas of the Bohai Sea and Yellow Sea. Timmermans et al. (2017) revealed that wave modeling driven by high-resolution winds features improvement in capturing extreme waves relative to coarse-resolution winds. In contrast, Chowdhury and Behera (2019) revealed that the wave modeling driven by high-resolution RCMs does not add value to those driven by coarse-resolution GCMs in the Indian Ocean, indicating that the added value of RCMs strongly depends on the regions considered (e.g., Di Luca et al., 2012). The high-resolution wind-driven wave projections have been performed over areas such as the European coast (Laugel et al., 2014; Bricheno and Wolf, 2018; Bonaduce et al., 2019), the southeastern coast of Australia (Hemer et al., 2013b), and the Gulf of St. Lawrence (Wang et al., 2018), however, it is not yet available for the Chinese marginal seas by now.

Wave modeling inevitably demonstrates bias relative to observations, which is a combination of inherited systematic bias from wind forcings and bias generated from wave modeling processes due to inadequate model physics, numerical solution schemes, or unrealistic topography. Different bias-adjustment methods (BAMs), such as the delta method and empirical or parametric quantile mapping method, have been applied in several wave climate studies (Charles et al., 2012; Parker and Hill, 2017; Lemos et al., 2020a,b; Meucci et al., 2020). However, the performances among BAMs show some differences. Lemos et al. (2020a) demonstrated that a quantile-based bias adjustment is better than the delta method in correcting biases in extremes. Parker and Hill (2017) revealed that bivariate BAMs can greatly improve intervariable correlations by comparing them with univariate BAMs. However, wave variables (wave height, wave direction, wave period, etc.) are highly correlated with each other. Multivariate bias adjustment is required to apply on the raw wave outputs, to correct biases in both individual wave variables and multivariate dependence structures.

For the first time, high-resolution regional wave climate projections in the Bohai Sea, Yellow Sea, and East China Sea (hereafter BYE) driven by high-resolution RCM winds are performed. The present study aims to investigate the future projected changes in the annual and seasonal mean and extreme waves in this area during the middle of the twenty-first century

(2021–2050) and the end of the twenty-first century (2071–2100) under the RCP2.6 and RCP8.5 scenarios. A multivariate bias-adjustment method (MBAn, Cannon, 2018) is applied to correct multivariate biases.

This paper is organized as follows. Section “Methodology and Datasets” describes the model and datasets. The results are given in section “Results”, including the wave hindcast evaluation and projected change analyses in the mean and extreme wave conditions. The manuscript ends with conclusions and a discussion (section “Conclusion and Discussion”).

## METHODOLOGY AND DATASETS

### Wave Dynamical Downscaling

In this study, the third-generation WAM cycle 4.7 was used to investigate the impact of climate change on the wave conditions in the BYE area. It maintains the basic physics and numeric of the WAM model used in Li et al. (2021) and is run in a shallow-water mode, with depth refraction considered. The wave model is configured to use 24 directions and 25 frequencies ranging from 0.04118 to 0.41145 Hz. It is implemented on two nested domains: the northwestern Pacific Ocean (NWP) with a spatial resolution of 0.5° and the BYE area with a spatial resolution of 0.1° (Figure 1). Full-wave spectra produced by the larger domain simulations are provided to the smaller domain at the open boundaries with an hourly frequency. The topographic data are obtained from the General Bathymetric Chart of the Oceans 1-min grid.<sup>1</sup>

We conducted wave hindcast simulations over the NWP and BYE forced by ERA5 wind speed (0.25°, Hersbach et al., 2020) during 1979–2019 to validate the model’s ability to capture the wave climate features in the BYE (thereafter ERA5 driven wave hindcast). ERA5 winds have proved to be robust in forcing wave conditions in the study domain (Li et al., 2020). To study the impact of climate change on wave climate, nested WAM simulations are forced by 3-hourly wind outputs (0.22°) from the CCLM-MPIESM RCM simulations (Kim et al., 2020) for the historical climate period (1979–2005) and two future periods (2021–2050 and 2071–2100) under the RCP2.6 and RCP8.5 emission scenarios. The above wind forcings are spatially interpolated to 0.5° and 0.1° resolutions for the NWP and BYE simulations, respectively, and kept constant in time throughout 3-h during wave integration. CCLM-MPIESM regional climate simulations were performed by Pohang University of Science and Technology from the CORDEX-East Asia II framework (Kim et al., 2020) by using the RCM CCLM downscaled from the global climate model MPIESM-LR (Giorgetta et al., 2013). To reduce potential biases on larger-scale circulation patterns, spectral nudging was employed to zonal and meridional winds above the 850 hPa level based on the sensitivity experiment results (Lee et al., 2016). CCLM experimental details are summarized on the CORDEX-East Asia website.<sup>2</sup>

<sup>1</sup>[https://www.gebco.net/data\\_and\\_products/gridded\\_bathymetry\\_data/gebco\\_one\\_minute\\_grid/](https://www.gebco.net/data_and_products/gridded_bathymetry_data/gebco_one_minute_grid/)

<sup>2</sup><http://cordex-ea.climate.go.kr/cordex/>

### Bias Adjustment of Wave Fields

A multivariate bias-adjustment method based on the N-dimensional probability density function transform (MBAn, Cannon, 2018) has been applied to multiple wave variables, including the SWH, MWP, and MWD. As wave direction is a cyclic variable, it was partitioned into two orthogonal components ( $\sin MWD$  and  $\cos MWD$ ) before the application of bias-adjustment. MBAn can correct the biases of the marginal distribution of individual wave variables and multivariate dependence structure. Three steps are involved in the usage of MBAn for bias adjustment of historical and future projected wave variables: (1) applying a uniformly distributed random orthogonal rotation to the simulated and observed data; (2) correcting the marginal distributions of each variable of the rotated simulated data by using the quantile delta mapping method; and (3) applying inverse rotation to the correct data. These steps are repeated until the modeled multivariate distribution has converged to the observed distribution. More details can be found in Cannon (2018).

### Buoy and Satellite Observations

To validate the skills of the wave model in capturing historical wave climate features in the BYE, in-situ observations from five buoy stations (Figure 1) were obtained from the Marine Science Data Center of the Chinese Academy of Sciences for the period approximately from 2010 to 2019. The observed wave variables include SWH, wave direction, and MWP. Furthermore, a daily merged multi-mission along-track L3 satellite product from the Sea State Climate Change Initiative (CCI) dataset v1 (Dodet et al., 2020) is also used as a reference for comparison from 1991 to 2018. The Sea State CCI L3 product retains only valid and good-quality measurements from 10 altimeters (ERS-1, ERS-2, TOPEX, Envisat, GFO, CryoSat-2, Jason-1, Jason-2, Jason-3, and SARAL). The satellite measurements nearest to the WAM model grid points and within 1 h from the simulated full hour were assigned as observations for the specific model grid. All simultaneous pairs between satellite observations and model grid points were used to evaluate the models’ skills in capturing wave conditions.

The statistical metrics used for the comparison between simulated data and observations are the bias, scatter index (SI), correlation coefficient (CORR), and root mean square error (RMSE).

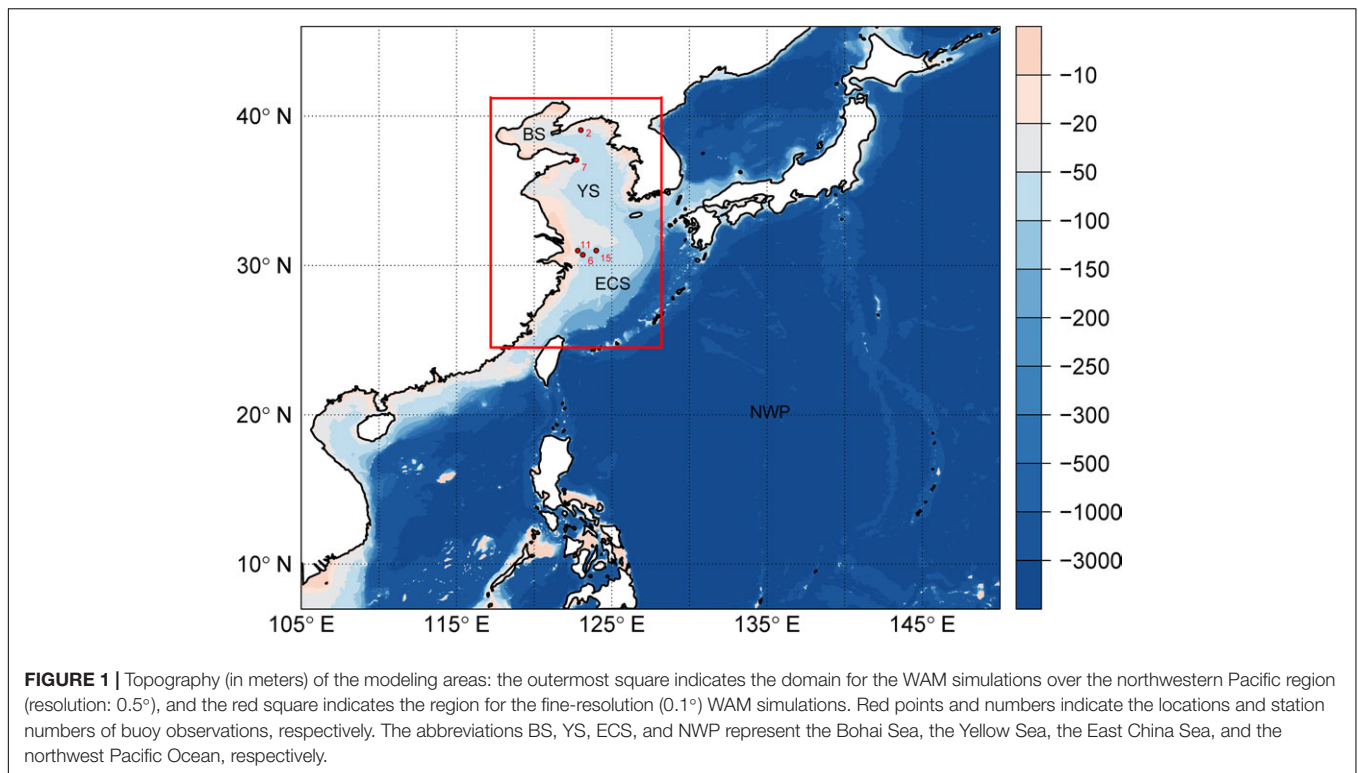
### Calculation of the Intra-Annual and Inter-Annual Variability

We used the robust coefficient of variation (RCoV) to quantify the inter-annual and intra-annual variability in the SWH. RCoV is defined as the median absolute deviation (MAD) divided by the median (Gunturu and Schlosser, 2012):

$$RCoV = \frac{MAD}{Median} = \frac{Median[|SWH_i - median(SWH_i)|]}{median(SWH_i)}$$

where  $SWH_i$  is the bias-adjusted time-series of the SWH.

To compute the intra-annual variability of SWH, we performed the following processes: (1) calculate the monthly mean SWH at each grid point, (2) calculate the median of



monthly SWH and MAD data series for each year, (3) divide the annual MAD with the corresponding annual median SWH to obtain annual RCoV, and (4) calculate the median of the annual RCoV, producing an estimation of the intra-annual variability of SWH. For the calculation of inter-annual variability of SWH, the annual mean SWH was calculated first and the RCoV was calculated based on the annual mean time series.

## RESULTS

### Evaluation of the ERA5-Driven Wave Hindcast and Bias-Adjusted Historical Simulation

We compared the SWH of the ERA5-driven wave hindcast with the Sea State CCI dataset between 1991 and 2018 (**Figure 2**). The results show that the wave hindcast is in good agreement with the observed SWH, with a bias of -0.104 m, correlation coefficient of 0.858, root mean square error of 0.5 m and scatter index of 0.338. Furthermore, we also assessed the wave hindcast annually from 1991 to 2018, with the Sea State CCI dataset as a reference (**Supplementary Table 1**). The statistical metrics are similar among different years in terms of bias, RMSE, and CORR except in 1991, when there are only 204 pairs. It is found that the simulated data tend to overestimate satellite observations for SWH larger than 6 m, which may be due to the underestimation of extreme wave heights by altimeter data in the coastal area (Dodet et al., 2020) or the limited skills of ERA5-driven wave hindcast in capturing very extreme wave heights.

In addition, we compared the wave hindcast with 5 buoy observations in terms of SWH, MWP, and MWD. The comparisons between observed and simulated SWH in **Table 1** show that the biases are mostly within 0.12 m, the CORR values are higher than 0.8, the RMSE is mostly less than 0.4 m, and the normalized standard deviation is larger than 0.86, indicating that the performance of the WAM hindcast is consistent when using different observation datasets as references. Furthermore, the extreme SWH values (i.e., 90th and 99th percentile SWH, hereafter the SWH\_90p and SWH\_99p, respectively) are also well captured by the WAM hindcast.

**Table 2** shows that the WAM hindcast generally overestimates the MWP by values less than 0.46 s and overestimates the temporal variability with nsd larger than 1. However, the CORR values are smaller than those for the SWH in **Table 1**. Regarding the MWD, the biases are within  $\pm 30^\circ$ , except for station S07, where the bias of the simulated MWD is  $58.51^\circ$ . The large bias of MWD at station S07 is possible because the wind forcing or the wave modeling is still too coarse to resolve the coastal wind inhomogeneity or complex bathymetric refraction. Nevertheless, the wave hindcast forced by ERA5 is generally realistic in capturing wave statistics, with both satellite and buoy observations as references.

To assess the skills of MBAn in correcting the biases of multiple variables from raw WAM historical simulation, we compared the climatological biases between the raw WAM simulation and bias-adjusted WAM simulation output for the SWH, SWH\_99p, MWP, and MWD (**Figure 3**). The WAM hindcast driven by the ERA5 wind reanalysis dataset is used as a reference. **Figure 3** shows that the raw WAM

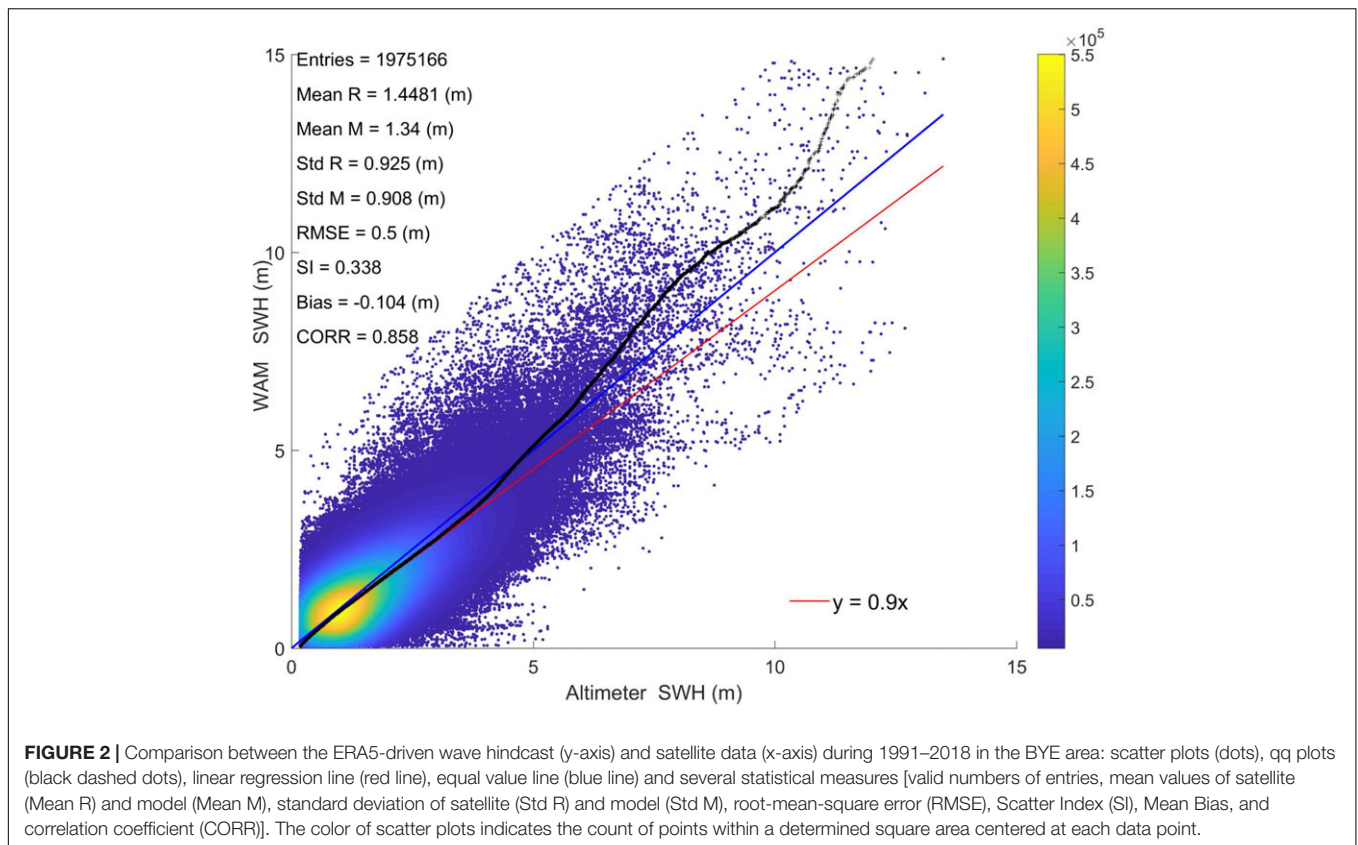


**FIGURE 2** | Comparison between the ERA5-driven wave hindcast (y-axis) and satellite data (x-axis) during 1991–2018 in the BYE area: scatter plots (dots), qq plots (black dashed dots), linear regression line (red line), equal value line (blue line) and several statistical measures [valid numbers of entries, mean values of satellite (Mean R) and model (Mean M), standard deviation of satellite (Std R) and model (Std M), root-mean-square error (RMSE), Scatter Index (SI), Mean Bias, and correlation coefficient (CORR)]. The color of scatter plots indicates the count of points within a determined square area centered at each data point.

**TABLE 1** | Comparison between the ERA5-driven wave hindcast and buoy observations for the SWH.

	num	$M_{obs}$ (m)	$M_{wam}$ (m)	bias (m)	corr	rmse (m)	nsd	$o_{p90}$ (m)	$m_{p90}$ (m)	$o_{99p}$ (m)	$m_{99p}$ (m)
S02	11,939	0.76	0.64	-0.12	0.85	0.28	0.86	1.4	1.2	2.2	1.88
S06	26,598	1.26	1.33	0.07	0.91	0.33	0.99	2.2	2.24	3.9	4.06
S07	21,157	0.51	0.56	0.05	0.8	0.25	0.92	1	1.01	2.1	1.75
S11	15,405	0.96	1.13	0.17	0.83	0.4	0.96	1.8	1.87	3.2	3.22
S15	7,679	1.52	1.49	-0.03	0.91	0.41	0.96	2.8	2.63	4.9	5.01

Here  $M_{obs}$  and  $M_{wam}$  represent the observed and modeled mean SWH, respectively. The nsd is normalized standard deviation, which normalizes simulated standard deviation by the observed standard deviation. The letters o and m indicate observations and modeling, respectively.

simulation generally overestimates the SWH, SWH<sub>99p</sub>, and MWP. There are both positive and negative biases for the raw simulated MWD. As expected, the multivariate bias-adjustment method can greatly reduce the climatological biases of raw simulation, showing negligible biases relative to the WAM hindcast.

## Historical Wave Climate and Projected Changes in the Climatology and Variability of the Wave Climate

The projected changes in the mean and extreme wave climate have been assessed based on bias-adjusted wave datasets under present-day climate (1979–2005) and future projections (2021–2050 and 2071–2100). In addition, a Mann-Whitney *U*-test (Kruskal and Wallis, 1952), a non-parametric test, was used to determine whether the differences in the mean wave

conditions between future projections and present-day climate are statistically significant.

The results show an increase in the climatological annual and seasonal mean SWH from the northwest to southeast in the study domain (Figure 4). Large mean SWHs over 1.6 m are pronounced in the southeastern BYE in autumn and winter. The annual and seasonal mean SWH are generally projected to decrease (-0.15 to -0.01 m) during 2021–2050 and 2071–2100 under the RCP2.6 and RCP8.5 scenarios, with statistical significance at a 0.1 level for most BYE in spring and for most of the Bohai Sea and Yellow Sea in annual and winter/autumn mean. The exceptions are autumn season during 2021–2050 under both scenarios (Figures 4e2,e4), featuring significant increasing changes (0.05–0.15 m) in the East China Sea.

We also observe that the decreases in annual or seasonal mean (except for summer) SWH are more pronounced at the end of the twenty-first century under the RCP8.5 scenario

**TABLE 2** | The same as **Table 1** but for the MWP.

	num	$M_{obs}$ (s)	$M_{wam}$ (s)	bias (s)	corr	rmse (s)	nsd	Bias <sub>MWD</sub> (°)
S02	11,939	4.17	4.62	0.45	0.57	1.2	1.34	23.46
S06	26,598	5.85	6.09	0.24	0.57	1.3	1.05	-28.22
S07	21,157	5.06	5.33	0.27	0.55	1.42	1.32	58.51
S11	15,405	5.76	5.73	-0.03	0.68	0.99	1.32	-26.87
S15	7,679	5.96	6.42	0.46	0.63	1.41	1.24	-11.3

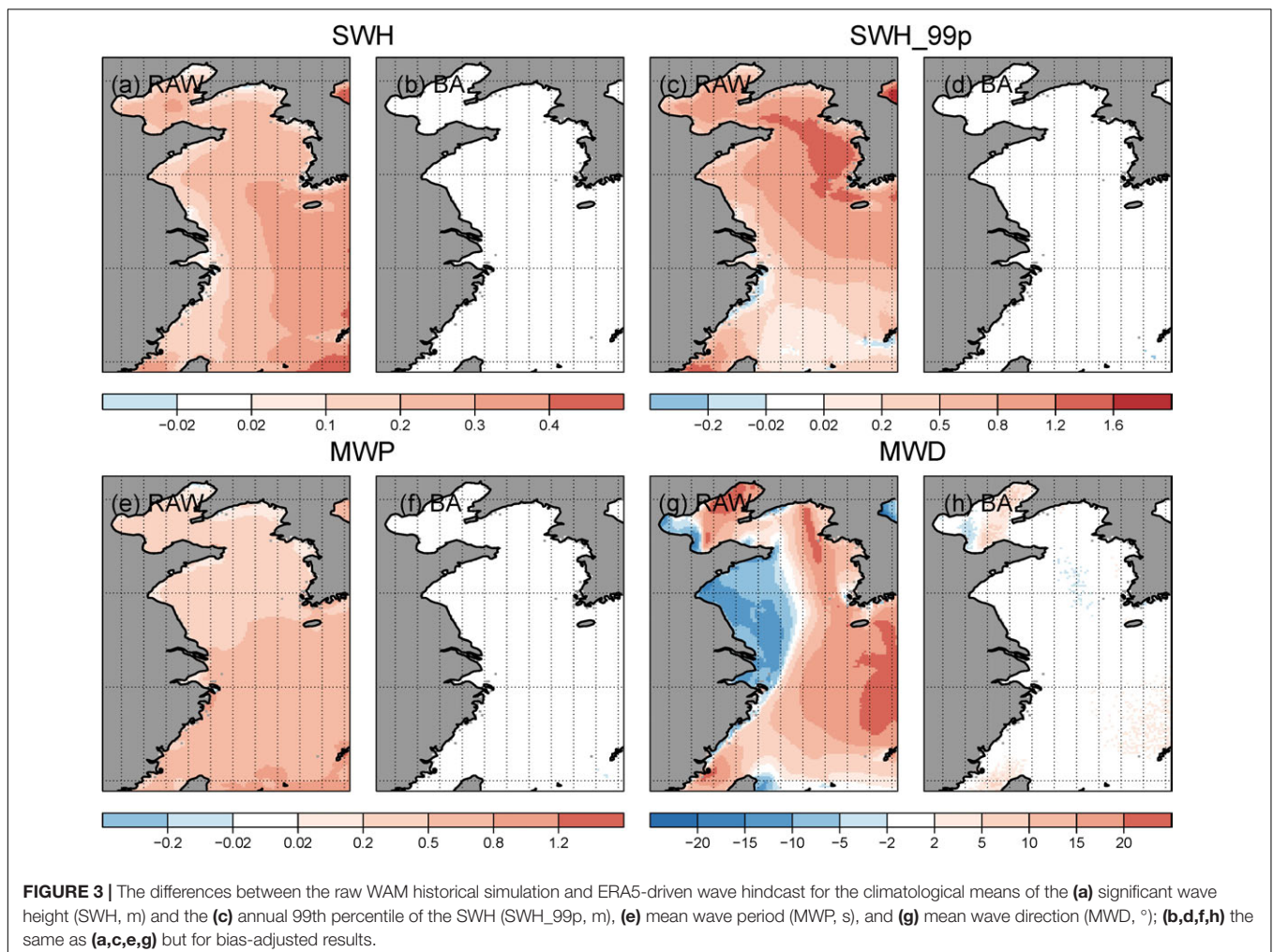
Bias<sub>MWD</sub> indicates the difference between simulated and observed MWD.

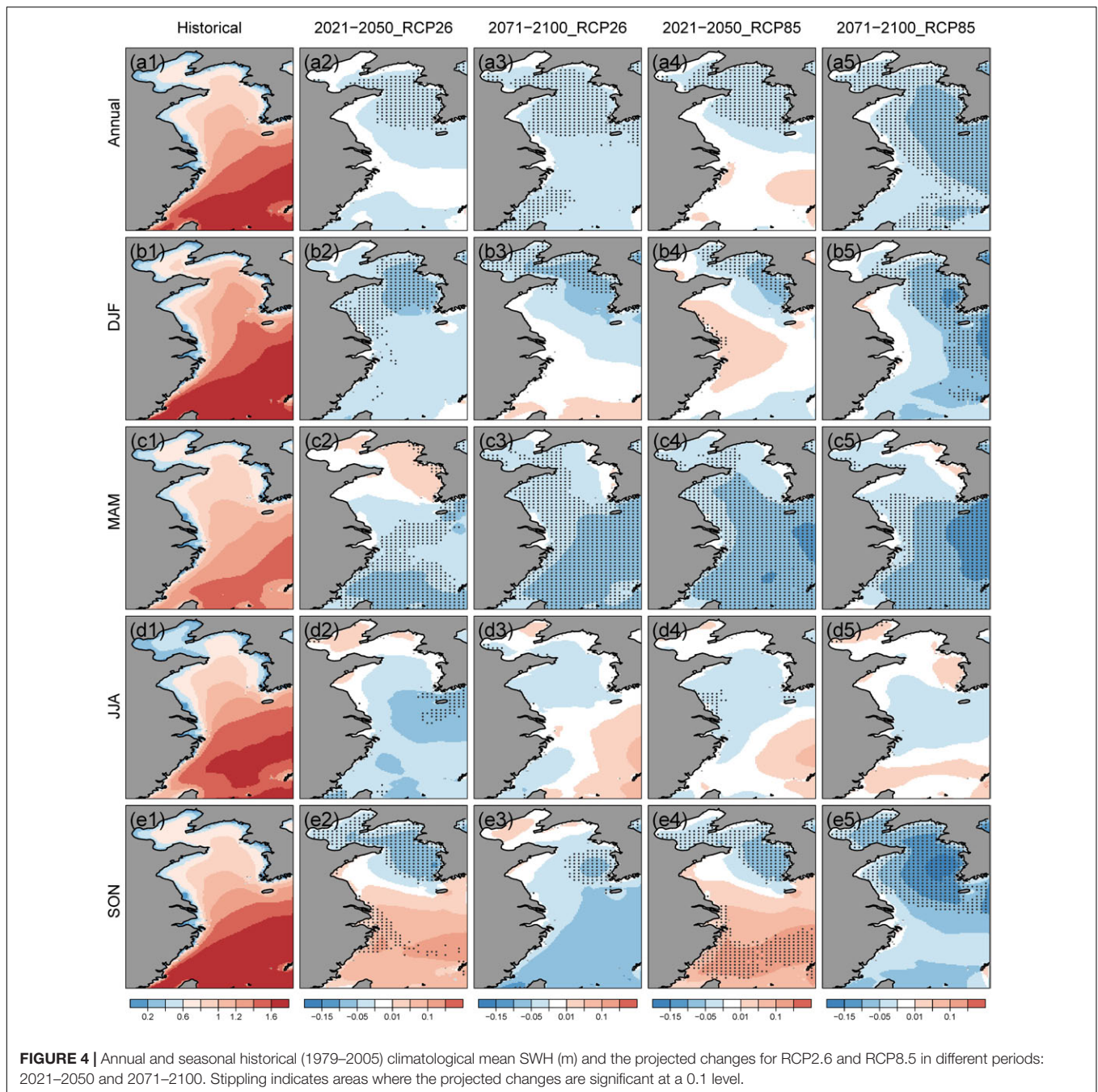
compared with the other counterparts. Furthermore, the spatial patterns of projected changes in the annual mean and seasonal mean SWH resemble those of projected changes in the surface wind speed (**Supplementary Figure 1**), which indicates that the SWH changes in the BYE are highly related to the changes in the local surface wind speeds. The spatially mixed pattern of projected changes in SWH, especially in the Bohai Sea and Yellow Sea in spring (**Figures 4c2,c5**) and in summer (**Figures 4d2-d5**), is also possibly related to the rotation of wind directions (**Supplementary Figure 1**), the impact of which is rather strong

in the marginal seas (Hemer et al., 2010; Kudryavtseva and Soomere, 2017).

**Figure 5** shows that the climatological annual and seasonal MWP also increase from the northwest to the southeast. MWP larger than 6 s is mainly in the southeastern BYE, featuring larger areas in summer and autumn. There are distinct features of projected changes in seasonal MWP. The results indicate a significant decrease in the MWP in spring over almost the entire study domain for both periods and both scenarios, especially for the East China Sea at the end of the twenty-first century under RCP8.5 (**Figure 5c5**). Projected increases are pronounced in large parts of the Yellow Sea and East China Sea in summer at the end of the twenty-first century under RCP2.6 and the middle and end of the twenty-first century under RCP8.5 (**Figures 5d3-d5**); however, the changes are not significant at 0.1 level.

**Figure 6** shows that there is generally low inter-annual variability, with RCoV in the range of 0.03–0.05, while there is stronger intra-annual variability, with RCoV mostly from 0.1 to 0.25. It is noticed that we find that the strong intra-annual variability and low inter-annual variability is a common feature for the global ocean especially in the North Pacific Ocean, North Atlantic Ocean, and some marginal seas, with the exception of





the polar ocean areas (**Supplementary Figure 2**), where the inter-annual variability is much larger than intra-annual variability.

The projected changes in both inter- and intra-annual variability are more pronounced at the end of the twenty-first century than those in the middle of the twenty-first century. In particular, there was a more than 40% increase in inter-annual variability in the southern East China Sea at the end of the twenty-first century under the RCP2.6 scenario (**Figure 6g**) and a more than 30% decrease in inter-annual variability in the southern Yellow Sea and northern ECS at the end of the twenty-first century under RCP8.5 scenario (**Figure 6h**). Furthermore, a

large increase (more than 30%) in intra-annual variability along the southeastern coasts of China and around Jeju Island at the end of the twenty-first century for both scenarios is observed (**Figures 6i,j**).

The spatial patterns of projected changes in the inter-annual variability of SWH resemble those of projected changes in the surface wind speed to some extent, with spatial correlations in the range of 0.36–0.67 (**Supplementary Figure 3**), indicating that the inter-annual variability of SWH is partially determined by the changes in the local surface wind speeds. However, it is not the case for projected

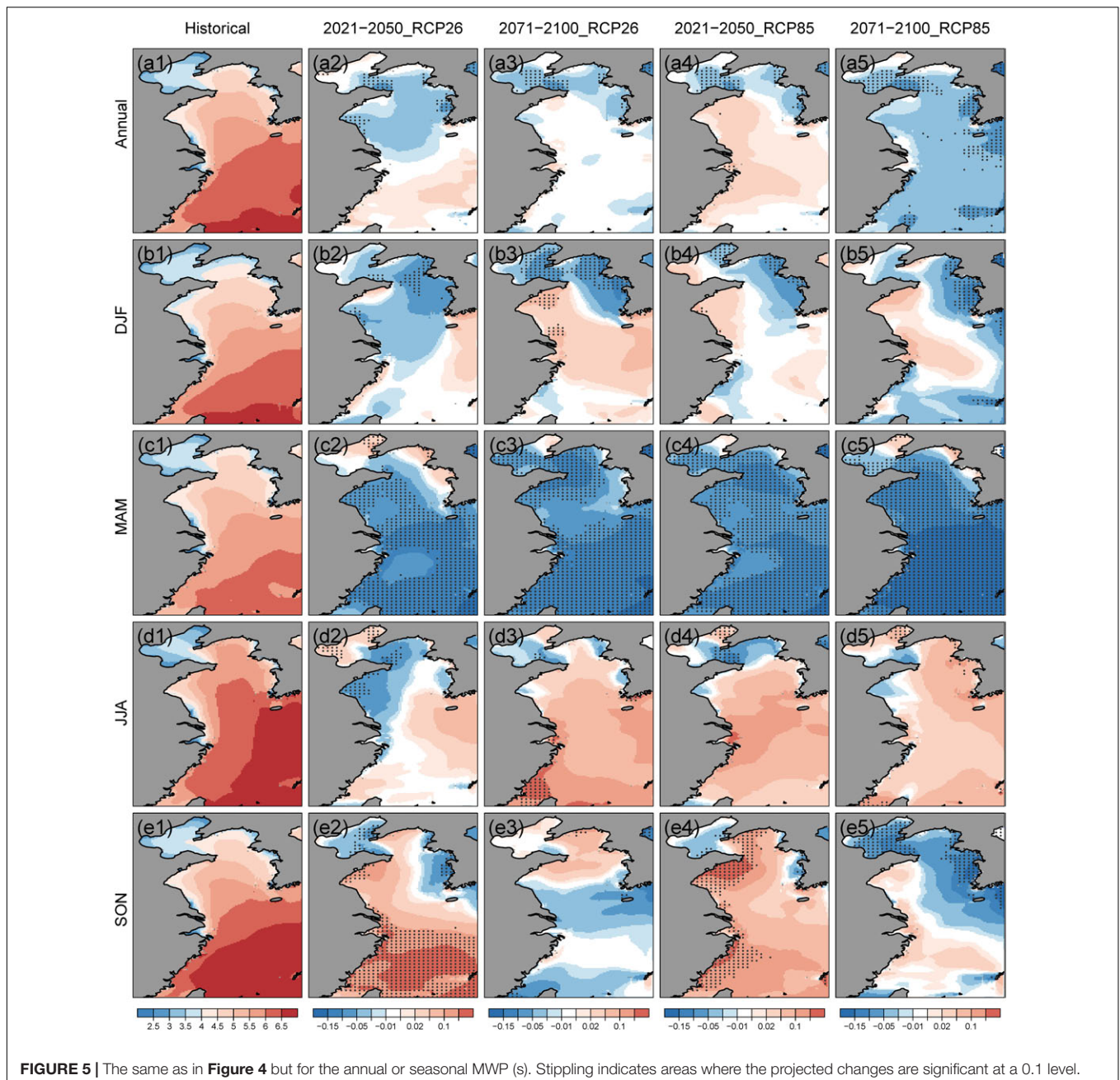


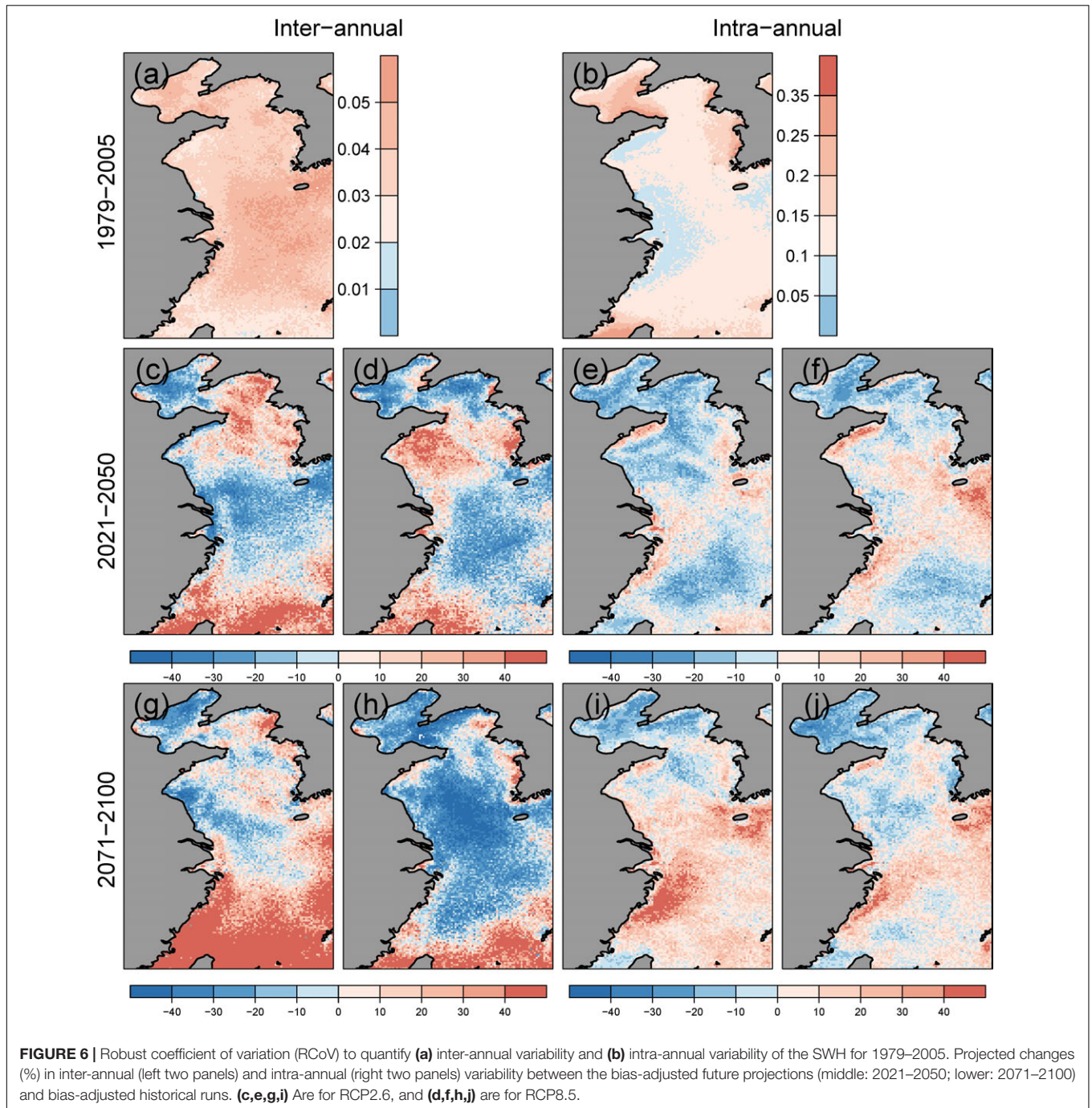
**FIGURE 5 |** The same as in **Figure 4** but for the annual or seasonal MWP (s). Stippling indicates areas where the projected changes are significant at a 0.1 level.

changes of intra-annual variability, which features a very low spatial relationship between SWH and surface wind speed (**Supplementary Figure 3**). Therefore, some other factors such as the migration of cyclone paths or the swell variability generated by a remote wind possibly govern the projected changes in inter-annual and intra-annual variability, which deserves further in-depth study.

### The Projected Changes in the Annual and Seasonal Extreme Wave Climate

The annual or seasonal SWH<sub>99p</sub> shows an increase from the northwest to southeast in the study domain (**Figure 7**). SWH<sub>99p</sub>

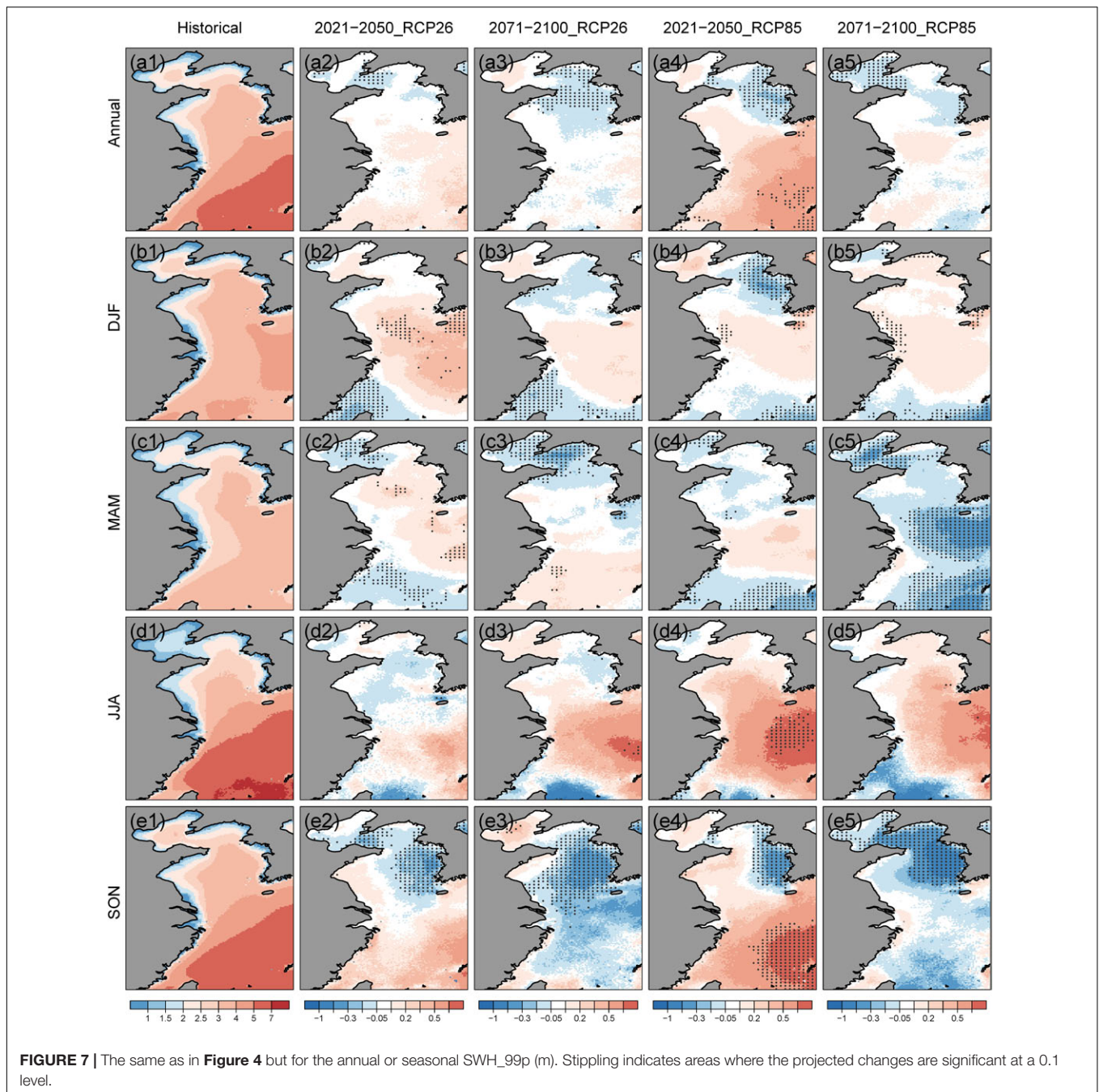
over 5 m is mainly observed in the East China Sea for summer and autumn (**Figures 7d1,e1**), which are supposed to be caused by tropical cyclones. The annual and seasonal SWH<sub>99p</sub> features stronger projected changes than those in the climatological mean SWH. The annual SWH<sub>99p</sub> are projected to increase in the East China Sea in the middle of the twenty-first century under the RCP8.5 scenario (**Figure 7a4**), which are mainly caused by the projected increase in summer and autumn, with a more than 0.5 m intensification in the East China Sea (**Figures 7d4,e4**). For the summer season in 2071–2100 under both scenarios, SWH<sub>99p</sub> shows a projected increase larger than 0.2 m, however, they mostly fail to pass the significance test at 0.1 level. The



projected decreases larger than 0.2 m are mainly in the Yellow Sea in autumn for both periods and both scenarios (Figures 7e2–e5). The BYE shows a significant projected decrease in the SWH<sub>99p</sub> in spring at the end of the twenty-first century under the RCP8.5 scenario (Figure 7c5) in the range of -0.5 to -0.05 m. For winter, we find a projected increase in the SWH<sub>99p</sub> of 0.2–0.5 m in the East China Sea for the middle of the twenty-first century under the RCP2.6 scenario (Figures 7b2–b5). Generally, the projected changes in the SWH<sub>99p</sub> feature strong seasonal variability.

The predominance of wave types can be determined by the wave age parameter. The sea state is dominated by wind sea if the wave age  $A = C_p/U_{10} = gT_p/2\pi U_{10} < 1.2$  and dominated by swell if  $A > 1.2$  (e.g., Smith et al., 1992), where  $C_p$  is the wave peak phase speed,  $U_{10}$  is the 10-m wind speed, and  $T_p$  is the wave peak period. **Supplementary Figure 4** shows the historical simulated and future projected occurrence frequency of swells. The annual and seasonal distribution patterns of occurrence frequencies of swell-dominant waves are similar between the historical simulation and future projections, featuring swell

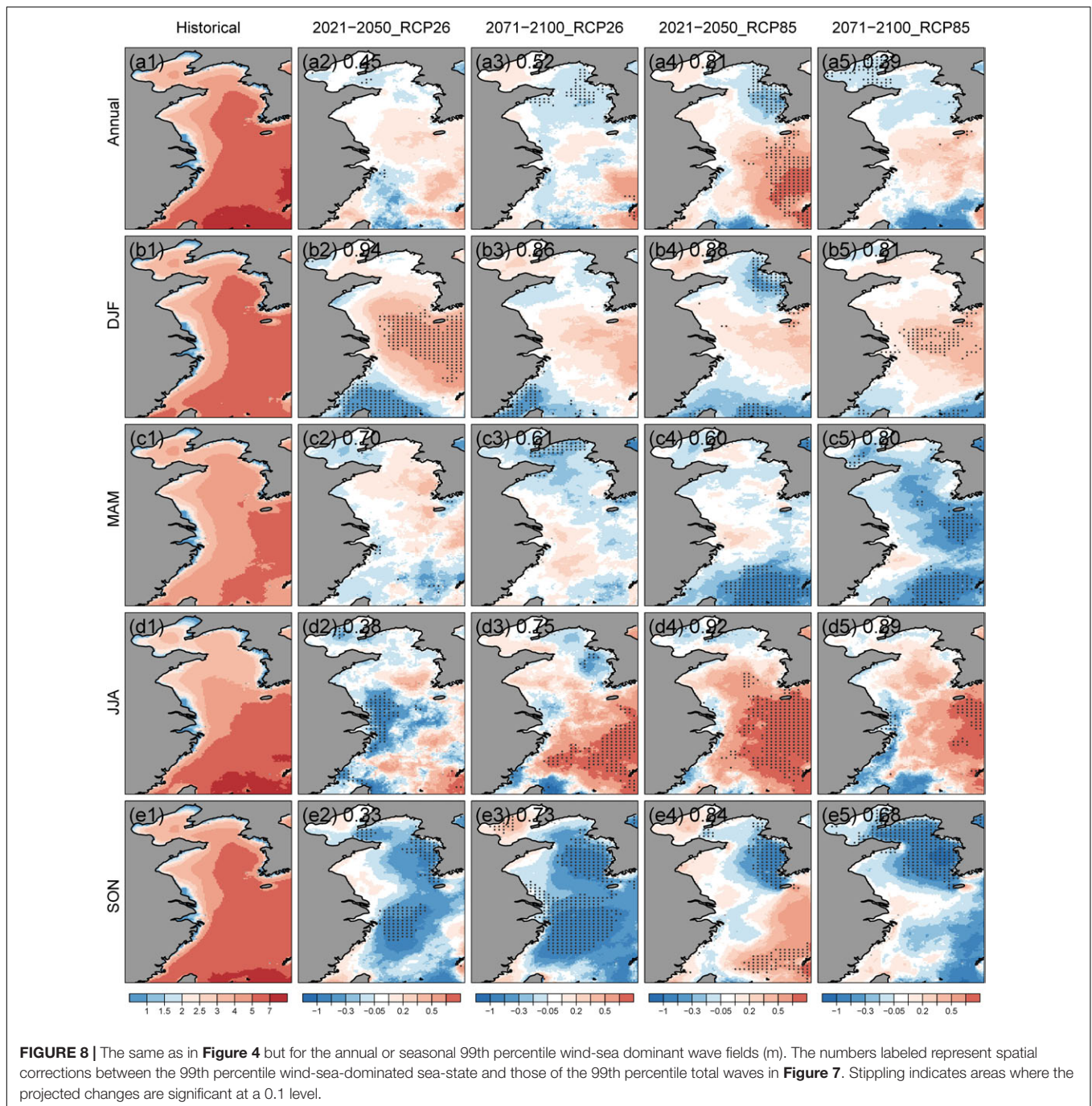




prevalence increases from the Bohai Sea to the East China Sea. Annually, the percentage increases from 30% in the Bohai Sea to more than 80% in the southeastern East China Sea. Swell-dominant waves occur the most frequently in summer and the least frequently in winter, with frequencies larger than 70% for nearly all the Yellow Sea and East China Sea for the former and less than 50% for the Bohai Sea and Yellow Sea for the latter. Except for summer, the Bohai Sea features wind-sea dominant wave fields for the other three seasons.

**Figure 8** shows that the 99th percentile (99p) wind-sea-dominated sea-state are larger than 3 m for most of the study

domain and can be more than 5 m in the southeastern part of the East China Sea in the present-day climate (**Figures 8d1,e1**), which is supposed to be caused by the impacts of tropical cyclones. Projected increases in winter and summer for 99p wind-sea-dominated sea-state are found for large parts of the study domain for both future periods under the RCP2.6 and RCP8.5 scenarios. In particular, 99p wind-sea-dominated sea-state is projected to increase significantly by more than 0.5 m in summer (**Figures 8d3–d5**) and to decrease by more than 0.5 m in autumn in the Yellow Sea or parts of the East China Sea (**Figures 8e2–e5**).



In contrast, we can see that the annual or seasonal 99p swell-dominated sea-state are much smaller than those of extreme wind-sea-dominated sea-state, with the former being larger than 1.5 m for most of the study domain (**Figure 9**). The projected changes in the 99p swell-dominated sea-state are also not as pronounced as those in the 99p wind-sea-dominated sea-state (**Figure 8**). Furthermore, we find projected increases of more than 0.3 m for 99p swell-dominated sea-state in the southern Yellow Sea or the East China Sea in summer and autumn during 2021–2050 under the RCP8.5 scenario, contributing to the total

increases (**Figure 7**). On the other hand, slight decreases in 99p swell-dominated sea-state by 0.05–0.2 m are distributed mainly in the BYE domain for spring except for the one during 2021–2050 under the RCP2.6 scenario (**Figure 9c2**).

Notably, we find that the projected changes in the near future (2021–2050) are generally more pronounced than changes in the far future (2071–2100) under RCP8.5 scenario for annual, summer and autumn SWH<sub>99p</sub> (**Figure 7**), for annual and summer 99p wind-sea-dominated sea-state (**Figure 8**), and for annual, summer and autumn 99p swell-dominated sea-state

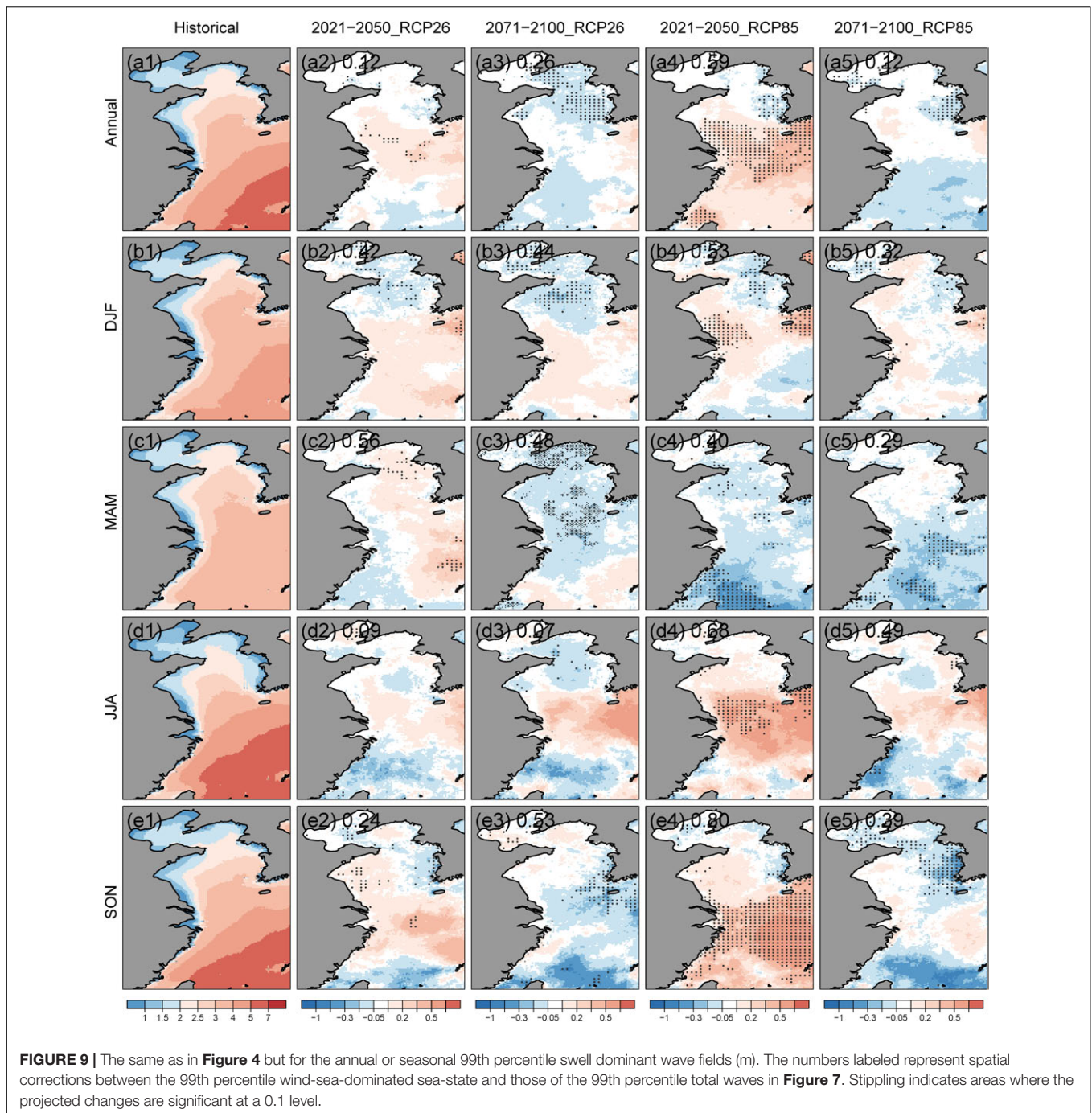


(**Figure 9**). The results are possibly due to the impact of natural variability instead of anthropogenic climate change.

In addition, we calculated the spatial corrections between the 99th percentile wind-sea (swell)-dominated sea-state and those of the 99th percentile total waves, to reveal their spatial consistency. The spatial corrections added in **Figures 8, 9** show that there are generally higher correlations between projected changes of 99p total sea-state (**Figure 7**) and projected changes of 99p wind-sea-dominated sea-state (**Figure 8**). This implies that the local wind-generated sea state mainly causes the projected changes in 99p

extreme waves. This conclusion is further confirmed by the fact that the projected change patterns of the SWH<sub>99p</sub> in **Figure 7** greatly resemble those of the 99th percentile surface wind speeds in the BYE (**Supplementary Figure 5**).

## CONCLUSION AND DISCUSSION

For the first time, we investigate the future changes in the mean and extreme wave climate in the Bohai Sea, Yellow Sea,

and East China Sea. Previous studies have revealed that high-resolution dynamical downscaling can add value to coarse-resolution reanalysis or GCMs in capturing the intensity of strong winds in coastal areas, as well as tropical cyclones (Li et al., 2016; Li, 2017); therefore, we used regional downscaled winds (resolution  $0.22^\circ$ ) to force high-resolution WAM wave model simulations in the study domain for the present-day climate (1979–2005) and future climate (2021–2050, 2071–2100) under the RCP2.6 and RCP8.5 scenarios. The WAM simulations feature a resolution of  $0.1^\circ$ , which is the highest-resolution wave climate projection dataset available for the study domain. We applied a multivariate bias-adjustment method based on the N-dimensional probability density function transform (MBAn) to correct biases in the raw simulated SWH, MWP, and MWD. The projected changes in the mean and extreme wave climate in the middle (2021–2050) and end of the (2071–2100) twenty-first century were evaluated, with the present-day wave climate during 1979–2005 serving as a reference. The main conclusions are summarized as follows:

(1) The WAM hindcast with 0.1-degree resolution driven by ERA5 winds shows robust skills in capturing wave statistics compared with the buoy and satellite observations. The MBAn method proves to be skillful in reducing substantial biases of the historical WAM simulation in the climatological mean SWH, MWP, MWD, and 99p extreme wave heights.

(2) The annual and seasonal mean SWH are generally projected to decrease ( $-0.15$  to  $-0.01$  m) for the 2021–2050 and 2071–2100 periods under the RCP2.6 and RCP8.5 scenarios, with statistical significance at a 0.1 level for most BYE in spring and for most of the Bohai Sea and Yellow Sea in annual and winter/autumn mean. A significant decrease in MWP in spring for both periods under both scenarios is found. The projected changes in inter-annual and intra-annual variabilities are more pronounced at the end of the twenty-first century than those in the mid- twenty-first century.

(3) The annual, and winter/summer 99th percentile SWHs are projected to increase for large parts of the study domain, and the autumn 99th percentile SWH are projected to decrease for the Yellow Sea, with the former mostly failing to pass the significance test. Results imply that the projected changes in the mean and 99th percentile extreme waves are very likely related to the projected changes in local mean and extreme surface wind speeds.

The significant contribution of this study is that we, for the first time, revealed the projected changes of mean and extreme waves, with a focus on the Chinese marginal seas. This is also the first study to apply the multivariate bias-adjustment method on the simulated wave variables. The high-resolution wave projection data produced in this study can provide support for a comprehensive assessment of marine energy resource under climate change (e.g., Lira-Loarca et al., 2021). They can also be used for estimating wave induced loads for appropriate design, construction, and operations of offshore and coastal structures (e.g., Kumar et al., 2018). Furthermore, extreme waves can cause extensive modification of the shoreline environment and landforms, and threaten human life (Hansom et al., 2015). Hence, integrating multivariate extreme wave conditions into comprehensive assessments of coastal hazards and vulnerability

is paramount to effective coastal climate adaptation planning (Morim et al., 2020).

Based on reconstructed SWH over the Chinese marginal seas by using a multivariate regression model and the twentieth-century reanalysis ensemble of the mean sea level pressure, Wu et al. (2014) revealed that the annual and seasonal SWH trends during 1911–2010 are dominantly negative over the Chinese marginal seas, and the summer maximum SWHs seem to have increased in the East China Sea. Our study implies that these trends are likely to continue in the future.

Being consistent with Fan et al. (2014), both the historical and future projected wave fields are dominated by the swell wave. However, the high spatial correlation of projected changes in mean or extremes between wind and wave fields in our study indicated that the projected changes in the mean and extreme waves are mainly related to the projected changes in local surface wind speeds in the Bohai Sea, Yellow Sea and East China Sea, annually and seasonally. The conclusion is partially consistent with Fan et al. (2014), who showed a more pronounced increase in the wind-sea energy than swell energy in July to December at the end of the twenty-first century in our study domain. While for the other global oceans, whether the changes in total waves being determined by swell or by wind-sea are regionally dependent (Fan et al., 2014).

The projected changes of mean, especially the extremes wave heights, for large parts of our study domain, do not pass the significance test at 0.1 level, implying that these changes may be related to sampling uncertainty. Nevertheless, we find strong consensus between our study and many other global-scale studies regarding the projected decrease and its intensity for the annual mean and winter mean SWH in the study domain. The projected decrease of annual mean or winter significant mean wave heights are generally less than  $-0.1$  m or  $-10\%$  in the middle and end of the twenty-first century under different scenarios including A1B (Mori et al., 2010; Semedo et al., 2013; Shimura et al., 2016), A2 (Hemer et al., 2013c), RCP4.5 and RCP8.5 (Wang et al., 2014; Shimura et al., 2016; Lemos et al., 2019; Morim et al., 2019), based on either single-GCM forcing (e.g., Mori et al., 2010) or ensemble-GCM forcing wave simulations (e.g., Shimura et al., 2016). The consensus proves the robustness of projected decrease of annual mean or winter significant mean.

However, the projected changes in summer mean SWH as well as extreme wave heights, lack consensus among studies in this area. Semedo et al. (2013) showed decreasing changes in summer mean SWH under A1B emission scenario, while Wang et al. (2014) revealed increases for projected summer mean SWH and summer maximum wave heights at the end of the twenty-first century under RCP8.5 scenario, and Morim et al. (2019) showed an increase in summer mean SWH and a decrease in annual 99th percentile wave heights under RCP4.5 and RCP8.5 scenario. Similarly, their projected changes in summer mean or extreme wave heights in the study domain generally do not pass the significance test. The dissimilarity of projected changes in summer mean SWH and extreme wave heights is supposed to stem from different sources including internal variability, GCMs or RCMs wind forcing, wind-wave modeling method, and scenario uncertainty (Deser et al., 2012; Morim et al., 2019).

The note is that this study only adopts a single wind forcing for each future period and scenario and does not consider the complete uncertainty sources. This is because of the limited availability of high-resolution wind forcings during the conduction of the wave simulations. With the release of more high-resolution RCM datasets through the Coordinated Regional Climate Downscaling Experiment (Sørland et al., 2021), ensemble of high-resolution wave projections are in demand for the Chinese marginal seas. Furthermore, it is also interesting to investigate the capacity of these high-resolution RCMs in simulating tropical cyclones and in driving cyclone-related extreme waves. The projected changes of cyclones and cyclone-related extreme waves and their uncertainties, are worthy of further efforts.

## DATA AVAILABILITY STATEMENT

The data that support the findings of this study are available from the corresponding author upon reasonable request.

## AUTHOR CONTRIBUTIONS

DL and BY contributed to the conception and designed of the study. DL, JS, AB, DHL, and S-KM contributed to the methodology and modeling. DL performed the dataset analyses, and visualization, with contributions from JF, YZ, and JQ. DL prepared the manuscript draft. All authors contributed to manuscript revision, read, and approved the submitted version.

## FUNDING

The study was supported through the National Natural Science Foundation of China (42176203), the National Key Research

and Development Program of China (2017YFA0604100), the Strategic Priority Research Program of the Chinese Academy of Sciences (XDB42000000), the NSFC-Shandong Joint Fund (U1806227), and the National Natural Science Foundation of China (42076022 and 41706019). Seung-Ki Min was supported by the Korea Meteorological Administration Research and Development Program under Grant KMI2020-01413.

## ACKNOWLEDGMENTS

We acknowledge the Oceanographic Data Center of the Institute of Oceanology Chinese Academy of Sciences and the German Climate Computing Center (DKRZ) for providing the computer hardware for the simulations and subsequent analyses. We thank the buoy observations provided by the Yellow Sea ocean/East China Sea observation and a research station of OMORN. The wind forcings for wave simulations have been generated using the COSMO model in CLimate Mode (CCLM). CCLM is the community model of the German regional climate research jointly further developed by the CLM-Community. We acknowledge the members of the community for their common efforts to envelop the model and to find right setups. The reanalysis dataset ERA5 is available at <https://cds.climate.copernicus.eu/#!/search?text=ERA5&type=dataset>. The Sea State CCI data is accessed at [https://data.ceda.ac.uk/neodc/esacci/sea\\_state/data/v1.1\\_release/l3/v1.1/](https://data.ceda.ac.uk/neodc/esacci/sea_state/data/v1.1_release/l3/v1.1/).

## SUPPLEMENTARY MATERIAL

The Supplementary Material for this article can be found online at: <https://www.frontiersin.org/articles/10.3389/fmars.2022.844113/full#supplementary-material>

## REFERENCES

- Bonaduce, A., Staneva, J., Behrens, A., Bidlot, J. R., and Wilcke, R. A. I. (2019). Wave climate change in the North Sea and Baltic Sea. *J. Mar. Sci. Eng.* 7:166. doi: 10.3390/jmse7060166
- Bricheno, L. M., and Wolf, J. (2018). Future wave conditions of Europe, in response to high-end climate change scenarios. *J. Geophys. Res. Oceans* 123, 8762–8791. doi: 10.1029/2018jc013866
- Camus, P., Losada, I. J., Izaguirre, C., Espejo, A., Menendez, M., and Perez, J. (2017). Statistical wave climate projections for coastal impact assessments. *Earths Future* 5, 918–933.
- Cannon, A. J. (2018). Multivariate quantile mapping bias correction: an N-dimensional probability density function transform for climate model simulations of multiple variables. *Clim. Dyn.* 50, 31–49. doi: 10.1007/s00382-017-3580-6
- Casas-Prat, M., Wang, X. L., and Swart, N. (2018). CMIP5-based global wave climate projections including the entire Arctic Ocean. *Ocean Model.* 123, 66–85.
- Casas-Prat, M., and Wang, X. L. (2020). Projections of extreme Ocean waves in the Arctic and potential implications for coastal inundation and erosion. *J. Geophys. Res. Oceans* 125:e2019JC015745.
- Charles, E., Idier, D., Delecluse, P., Déqué, M., and Le Cozannet, G. (2012). Climate change impact on waves in the Bay of Biscay. France. *Ocean Dyn.* 62, 831–848.
- Chowdhury, P., and Behera, M. R. (2019). Evaluation of CMIP5 and CORDEX derived wave climate in Indian Ocean. *Clim. Dyn.* 52, 4463–4482. doi: 10.1007/s00382-018-4391-0
- Deser, C., Phillips, A., Bourdette, V., and Teng, H. (2012). Uncertainty in climate change projections: the role of internal variability. *Clim. Dyn.* 38, 527–546. doi: 10.1007/s00382-010-0977-x
- Di Luca, A., de Elia, R., and Laprise, R. (2012). Potential for added value in precipitation simulated by high-resolution nested regional climate models and observations. *Clim. Dyn.* 38, 1229–1247. doi: 10.1007/s00382-011-1068-3
- Dodet, G., Piolle, J. F., Quilfen, Y., Abdalla, S., Accensi, M., Ardhuin, F., et al. (2020). The Sea State CCI dataset v1: towards a sea state climate data record based on satellite observations. *Earth Syst. Sci. Data* 12, 1929–1951.
- Fan, Y., Lin, S., Griffies, S. M., and Hemer, M. A. (2014). Simulated global swell and Wind-Sea climate and their responses to Anthropogenic climate change at the end of the twenty-first century. *J. Clim.* 27, 3516–3536. doi: 10.1175/jcli-d-13-00198.1
- Giorgetta, M. A., Jungclaus, J., Reick, C. H., Legutke, S., Bader, J., Böttinger, M., et al. (2013). Climate and carbon cycle changes from 1850 to 2100 in MPI-ESM simulations for the coupled model intercomparison project phase 5. *J. Adv. Model. Earth Syst.* 5, 572–597.
- Gunturu, U. B., and Schlosser, C. A. (2012). Characterization of wind power resource in the United States. *Atmos. Chem. Phys.* 12, 9687–9702. doi: 10.5194/acp-12-9687-2012

- Hansom, J. D., Switzer, A. D., and Pile, J. (2015). "Chap. 11—Extreme waves: causes, characteristics, and impact on coastal environments and society," in *Coastal and Marine Hazards, Risks, and Disasters*, eds J. F. Shroder, J. T. Ellis, and D. J. Sherman (Boston, MA: Elsevier), 307–334.
- He, C., Zhou, T., Lin, A., Wu, B., Gu, D., Li, C., et al. (2015). Enhanced or weakened Western North Pacific Subtropical High under Global Warming? *Sci. Rep.* 5:16771. doi: 10.1038/srep16771
- Hemer, M. A., Church, J. A., and Hunter, J. R. (2010). Variability and trends in the directional wave climate of the Southern Hemisphere. *Int. J. Climatol.* 30, 475–491. doi: 10.1002/joc.1900
- Hemer, M. A., Fan, Y., Mori, N., Semedo, A., and Wang, X. L. (2013a). Projected changes in wave climate from a multi-model ensemble. *Nat. Clim. Chang.* 3, 471–476. doi: 10.1038/nclimate1791
- Hemer, M. A., McInnes, K. L., and Ranasinghe, R. (2013b). Projections of climate change-driven variations in the offshore wave climate off south eastern Australia. *Int. J. Climatol.* 33, 1615–1632. doi: 10.1002/joc.3537
- Hemer, M. A., Katzfey, J., and Trenham, C. E. (2013c). Global dynamical projections of surface ocean wave climate for a future high greenhouse gas emission scenario. *Ocean Model.* 70, 221–245. doi: 10.1016/j.ocemod.2012.09.008
- Hemer, M. A., Wang, X. L., Weisse, R., and Swail, V. R. (2012). Advancing wind-waves climate science: the COWCLIP project. *Bull. Am. Meteorol. Soc.* 93, 791–796. doi: 10.1175/bams-d-11-00184.1
- Hersbach, H., Bell, B., Berrisford, P., Hirahara, S., Horányi, A., Muñoz-Sabater, J., et al. (2020). The ERA5 global reanalysis. *Q. J. R. Meteorol. Soc.* 146, 1999–2049.
- Hoeke, R. K., McInnes, K. L., Kruger, J. C., McNaught, R. J., Hunter, J. R., and Smithers, S. G. (2013). Widespread inundation of Pacific islands triggered by distant-source wind-waves. *Glob. Planet. Change* 108, 128–138. doi: 10.1016/j.gloplacha.2013.06.006
- Kim, J.-U., Kim, T.-J., Kim, D.-H., Kim, J.-W., Cha, D.-H., Min, S.-K., et al. (2020). Evaluation of performance and uncertainty for multi-RCM over CORDEX-East Asia phase 2 region. *Atmosphere* 30, 361–376.
- Kruskal, W. H., and Wallis, W. A. (1952). Use of ranks in one-criterion variance analysis. *J. Am. Stat. Assoc.* 47, 583–621. doi: 10.1080/01621459.1952.10483441
- Kudryavtseva, N., and Soomere, T. (2017). Satellite altimetry reveals spatial patterns of variations in the Baltic Sea wave climate. *Earth Syst. Dyn.* 8, 697–706. doi: 10.5194/esd-8-697-2017
- Kumar, N. K., Savitha, R., and Al Mamun, A. (2018). Ocean wave characteristics prediction and its load estimation on marine structures: a transfer learning approach. *Mar. Struct.* 61, 202–219. doi: 10.1016/j.marstruc.2018.05.007
- Laugel, A., Menendez, M., Benoit, M., Mattarolo, G., and Mendez, F. (2014). Wave climate projections along the French coastline: dynamical versus statistical downscaling methods. *Ocean Model.* 84, 35–50. doi: 10.1016/j.ocemod.2014.09.002
- Lee, D., Park, C., Kim, Y.-H., and Min, S.-K. (2016). Evaluation of the COSMO-CLM for East Asia climate simulations: sensitivity to spectral nudging. *J. Clim. Res.* 11, 69–85. doi: 10.14383/cr.2016.11.1.69
- Lemos, G., Menendez, M., Semedo, A., Camus, P., Hemer, M., Dobrynin, M., et al. (2020a). On the need of bias correction methods for wave climate projections. *Glob. Planet. Change* 186:103109. doi: 10.1016/j.gloplacha.2019.103109
- Lemos, G., Semedo, A., Dobrynin, M., Menendez, M., and Miranda, P. M. A. (2020b). Bias-corrected CMIP5-derived single-forcing future wind-wave climate projections toward the end of the Twenty-First Century. *J. Appl. Meteorol. Climatol.* 59, 1393–1414. doi: 10.1175/jamc-d-19-0297.1
- Lemos, G., Semedo, A., Dobrynin, M., Behrens, A., Staneva, J., Bidlot, J. R., et al. (2019). Mid-twenty-first century global wave climate projections: results from a dynamic CMIP5 based ensemble. *Glob. Planet. Change* 172, 69–87. doi: 10.1016/j.gloplacha.2018.09.011
- Li, D. (2017). Added value of high-resolution regional climate model: selected cases over the Bohai Sea and the Yellow Sea areas. *Int. J. Climatol.* 37, 169–179.
- Li, D., Staneva, J., Bidlot, J.-R., Grayek, S., Zhu, Y., and Yin, B. (2021). Improving regional model skills during Typhoon events: a case study for super Typhoon lingling over the Northwest Pacific Ocean. *Front. Mar. Sci.* 8:613913. doi: 10.3389/fmars.2021.613913
- Li, D., Staneva, J., Grayek, S., Behrens, A., Feng, J., and Yin, B. (2020). Skill Assessment of an Atmosphere–Wave Regional Coupled Model over the East China Sea with a focus on Typhoons. *Atmosphere* 11:252. doi: 10.3390/atmos11030252
- Li, D., von Storch, H., and Geyer, B. (2016). High-resolution wind hindcast over the Bohai Sea and the Yellow Sea in East Asia: evaluation and wind climatology analysis. *J. Geophys. Res. Atmos.* 121, 111–129. doi: 10.1002/2015jd024177
- Lira-Loarca, A., Ferrari, F., Mazzino, A., and Besio, G. (2021). Future wind and wave energy resources and exploitability in the Mediterranean Sea by. *Appl. Energy* 302:117492. doi: 10.1016/j.apenergy.2021.117492
- Lobeto, H., Menendez, M., and Losada, I. J. (2021). Future behavior of wind wave extremes due to climate change. *Sci. Rep.* 11:7869. doi: 10.1038/s41598-021-86524-4
- Mei, W., and Xie, S.-P. (2016). Intensification of landfalling typhoons over the northwest Pacific since the late . *Nat. Geosci.* 9, 753–757.
- Melet, A., Almar, R., Hemer, M., Le Cozannet, G., Meyssignac, B., and Ruggiero, P. (2020). Contribution of wave setup to projected Coastal Sea level changes. *J. Geophys. Res. Oceans* 125:e2020JC016078. doi: 10.1371/journal.pone.0133409
- Meucci, A., Young, I. R., Hemer, M., Kirezci, E., and Ranasinghe, R. (2020). Projected 21<sup>st</sup> century changes in extreme wind-wave events. *Sci. Adv.* 6:eaa7295. doi: 10.1126/sciadv.aaz7295
- Mori, N., Yasuda, T., Mase, H., Tom, T., and Oku, Y. (2010). Projection of extreme wave climate change under Global Warming. *Hyd. Res. Lett.* 4, 15–19. doi: 10.3178/hr.4.15
- Morim, J., Hemer, M., Cartwright, N., Strauss, D., and Andutta, F. (2018). On the concordance of 21<sup>st</sup> century wind-wave climate projections. *Glob. Planet. Change* 167, 160–171.
- Morim, J., Hemer, M., Wang, X. L. L., Cartwright, N., Trenham, C., Semedos, A., et al. (2019). Robustness and uncertainties in global multivariate wind-wave climate projections. *Nat. Clim. Change* 9, 711–718. doi: 10.1038/s41558-019-0542-5
- Morim, J., Trenham, C., Hemer, M., Wang, X. L. L., Mori, N., Casas-Prat, M., et al. (2020). A global ensemble of ocean wave climate projections from CMIP5-driven models. *Sci. Data* 7:105. doi: 10.1038/s41597-020-0446-2
- O'Grady, J. G., Hemer, M. A., McInnes, K. L., Trenham, C. E., and Stephenson, A. G. (2021). Projected incremental changes to extreme wind-driven wave heights for the twenty-first century. *Sci. Rep.* 11:8826. doi: 10.1038/s41598-021-87358-w
- Parker, K., and Hill, D. F. (2017). Evaluation of bias correction methods for wave modeling output. *Ocean Model.* 110, 52–65.
- Reguero, B. G., Losada, I. J., and Mendez, F. J. (2019). A recent increase in global wave power as a consequence of oceanic warming. *Nat. Commun.* 10:205. doi: 10.1038/s41467-018-08066-0
- Semedo, A., Weisse, R., Behrens, A., Sterl, A., Bengtsson, L., and Gunther, H. (2013). Projection of Global Wave Climate Change toward the End of the Twenty-First Century. *J. Clim.* 26, 8269–8288.
- Shi, J., Zheng, J., Zhang, C., Joly, A., Zhang, W., Xu, P., et al. (2019). A 39-year high resolution wave hindcast for the Chinese coast: model validation and wave climate analysis. *Ocean Eng.* 183, 224–235.
- Shimura, T., Mori, N., and Hemer, M. A. (2016). Variability and future decreases in winter wave heights in the Western North Pacific. *Geophys. Res. Lett.* 43, 2716–2722.
- Smith, S. D., Anderson, R. J., Oost, W. A., Kraan, C., Maat, N., DeCosmo, J., et al. (1992). Sea surface wind stress and drag coefficients: the HEXOS results. *Boundary Layer Meteorol.* 60, 109–142.
- Song, Z., Bao, Y., Zhang, D., Shu, Q., Song, Y., and Qiao, F. (2020). Centuries of monthly and 3-hourly global ocean wave data for past, present, and future climate research. *Sci. Data* 7:226. doi: 10.1038/s41597-020-0566-8
- Sørland, S. L., Brogli, R., Pothapakula, P. K., Russo, E., Van de Walle, J., Ahrens, B., et al. (2021). COSMO-CLM Regional climate simulations in the CORDEX framework: a review. *Geosci. Model. Dev. Discuss.* 14, 5125–5154.
- Tao, A., Shen, Z., Li, S., Xu, X., and Zhang, Y. (2018). Research progress for disastrous waves in China. *Sci. Technol. Rev.* 36, 26–34.
- Timmermans, B., Stone, D., Wehner, M., and Krishnan, H. (2017). Impact of tropical cyclones on modeled extreme wind-wave climate. *Geophys. Res. Lett.* 44, 1393–1401. doi: 10.1002/2016gl071681
- Toimil, A., Losada, I. J., Nicholls, R. J., Dalrymple, R. A., and Stive, M. J. F. (2020). Addressing the challenges of climate change risks and adaptation in coastal areas: a review. *Coast. Eng.* 156:103611. doi: 10.1016/j.coastaleng.2019.103611
- Wang, L., Perrie, W., Long, Z. X., Blokhina, M., Zhang, G. S., Toulany, B., et al. (2018). The impact of climate change on the wave climate in the Gulf of St. Lawrence. *Ocean Model.* 128, 87–101. doi: 10.1016/j.ocemod.2018.06.003

- Wang, S., and Toumi, R. (2021). Recent migration of tropical cyclones toward coasts. *Science* 371, 514–517. doi: 10.1126/science.abb9038
- Wang, X. L., Feng, Y., and Swail, V. R. (2014). Changes in global ocean wave heights as projected using multimodel CMIP5 simulations. *Geophys. Res. Lett.* 41, 1026–1034. doi: 10.1002/2013gl058650
- Wang, X. L. L., and Swail, V. R. (2001). Changes of extreme wave heights in Northern Hemisphere oceans and related atmospheric circulation regimes. *J. Clim.* 14, 2204–2221. doi: 10.1175/1520-0442(2001)014<2204:coewhi>2.0.co;2
- Wang, X. L. L., and Swail, V. R. (2006). Climate change signal and uncertainty in projections of ocean wave heights. *Clim. Dyn.* 26, 109–126.
- Wu, L. L., Wang, X. L. L., and Feng, Y. (2014). Historical wave height trends in the South and East China Seas. *J. Geophys. Res. Oceans* 119, 4399–4409. doi: 10.1002/2014jc010087
- Young, I. R., and Ribal, A. (2019). Multiplatform evaluation of global trends in wind speed and wave height. *Science* 364, 548–552. doi: 10.1126/science.aav9527

**Conflict of Interest:** The authors declare that the research was conducted in the absence of any commercial or financial relationships that could be construed as a potential conflict of interest.

**Publisher's Note:** All claims expressed in this article are solely those of the authors and do not necessarily represent those of their affiliated organizations, or those of the publisher, the editors and the reviewers. Any product that may be evaluated in this article, or claim that may be made by its manufacturer, is not guaranteed or endorsed by the publisher.

Copyright © 2022 Li, Feng, Zhu, Staneva, Qi, Behrens, Lee, Min and Yin. This is an open-access article distributed under the terms of the Creative Commons Attribution License (CC BY). The use, distribution or reproduction in other forums is permitted, provided the original author(s) and the copyright owner(s) are credited and that the original publication in this journal is cited, in accordance with accepted academic practice. No use, distribution or reproduction is permitted which does not comply with these terms.



# Atmosphere-Ocean Coupled Variability in the Arabian/Persian Gulf

Fahad Al Senafi\*

Department of Marine Science, College of Science, Kuwait University, Kuwait City, Kuwait

The Arabian Gulf comprises one of the world's most unique and fragile marine ecosystems; it is susceptible to the adverse effects of climate change due to its shallow depth and its location within an arid region that witnesses frequent severe atmospheric events. To reproduce these effects in numerical models, it is important to obtain a better understanding of the region's sea surface temperature (SST) variability patterns, as SST is a major driver of circulation in shallow environments. To this end, here, empirical orthogonal function (EOF) decomposition analysis was conducted to investigate interannual to multi-decadal SST variability in the Gulf from 1982 to 2020, using daily Level 4 Group for High Resolution SST (GHRSST) data. In this way, three dominant EOF modes were identified to contribute the Gulf's SST variability. Significant spatial and temporal correlations were found suggesting that throughout the 39-year study period, SST variability could be attributed to atmospheric changes driven by the El Nio-Southern Oscillation (ENSO), Atlantic Multi-decadal Oscillation (AMO), and Indian Ocean Dipole (IOD) climate modes. Spatial and temporal analyses of the dataset revealed that the average SST was 26.7°C, and that the warming rate from 1982 to 2020 reached up to 0.59°C/decade. A detailed examination of SST changes associated with heat exchange at the air-sea interface was conducted using surface heat fluxes from fifth generation (ERA5) European Centre for Medium-Range Weather Forecasts (ECMWF). Despite the SST warming trend, the accumulation of heat during the study period is suggesting that there was an overall loss of heat (cooling). This cooling reverted into heating in 2003 and has since been increasing.

**Keywords:** sea surface temperature, climate indices, climate change, Arabian Gulf, Persian Gulf

## OPEN ACCESS

### Edited by:

Adem Akpinar,  
Uludağ University, Turkey

### Reviewed by:

Prasad Bhaskaran,  
Indian Institute of Technology  
Kharagpur, India  
Antonio Ricchi,  
University of L'Aquila, Italy

### \*Correspondence:

Fahad Al Senafi  
fahad.alsenafi@ku.edu.kw

### Specialty section:

This article was submitted to  
Physical Oceanography,  
a section of the journal  
Frontiers in Marine Science

**Received:** 04 November 2021

**Accepted:** 31 January 2022

**Published:** 24 February 2022

### Citation:

Al Senafi F (2022) Atmosphere-Ocean  
Coupled Variability in the  
Arabian/Persian Gulf.  
*Front. Mar. Sci.* 9:809355.  
doi: 10.3389/fmars.2022.809355

## 1. INTRODUCTION

Owing to its strategic location and its susceptibility to extremely high temperatures and salinities (Johns et al., 2003; Khan et al., 2021), the Arabian Gulf (hereafter Gulf) is one of the most important, yet fragile, marine ecosystems on Earth. This important region may be susceptible to the adverse effects of climate change. Unfortunately, increasing water temperatures driven by global warming, as well as contaminants (oil spills, waste waters, and industrial waste) (Uddin et al., 2021; Stöfen-O'Brien et al., 2022), have severely affected and degraded the Gulf's marine ecosystems, such as its sabkhas, mudflats, mangrove swamps, sea grasses, and coral reefs (Burt et al., 2011; Vaughan et al., 2021). These ecosystems support various endangered marine species, such as dugongs and turtles (Sale et al., 2010). Thus, understanding the driving forces of the Gulf's circulation mechanism is critical to preserving these natural habitats. In relation to the preservation of climate balance in the Gulf, coupled atmosphere-ocean dynamics play a major role in determining regional and global



climate conditions. They are characterized by multiple spatial and temporal patterns that can be identified by analyzing trends in sea surface temperature (SST) (Messié and Chavez, 2011). Despite its importance, the coupled atmosphere-ocean dynamics within the Gulf are poorly understood and only few studies exist in the published literature, largely due to the paucity of oceanographic and meteorological measurements. A study by Purkis and Riegl (2005) investigated the effects of the Gulf's water temperatures on coral assemblages, while relating SST anomalies to the El Niño-Southern Oscillation (ENSO). Moradi and Kabiri (2015), meanwhile, analyzed the spatio-temporal variability of SST and chlorophyll-a in the Gulf for a 10-year period, finding no clear SST modes. Another study by Noori et al. (2019), used the daily Optimum Interpolation SST anomaly (OISSTA) generated by the National Oceanic and Atmospheric Administration (NOAA) to examine the Gulf spatio-temporal SST trends from 1982 to 2016 and link these to ENSO and NAO. Most other studies (Arun et al., 2005; Nezhlin et al., 2010; Almazroui, 2012; Huang et al., 2021) have focused on the impacts of major climate modes (ENSO, Indian Ocean Dipole [IOD], and North Atlantic Oscillation [NAO]) on the Gulf's air temperature and precipitation. Provided with these contexts, the Gulf's SST modes were analyzed and their relationships to regional and global climate patterns were explored in aim of improving understanding of interannual to multi-decadal SST variability within the Gulf, and to determine its relation to major climate modes. Understanding these patterns will refine the cognizance of current ocean dynamics and predictive capabilities of ocean circulation models, consequently aiding studies into the sustainability of ocean ecosystems globally.

The remainder of this manuscript is organized as follows. Section 2 describes the study area. Section 3 describes the dataset employed in this study and the analytical approach. Section 4 presents the Gulf's SST spatial and temporal variabilities between the years 1982 and 2020. In addition, this section also presents the identification and discussion of the three major SST modes in the Gulf and relates them to the Atlantic Multi-decadal Oscillation (AMO), ENSO, and IOD climate modes. A summary and conclusions are then detailed in Section 5.

## 2. STUDY AREA

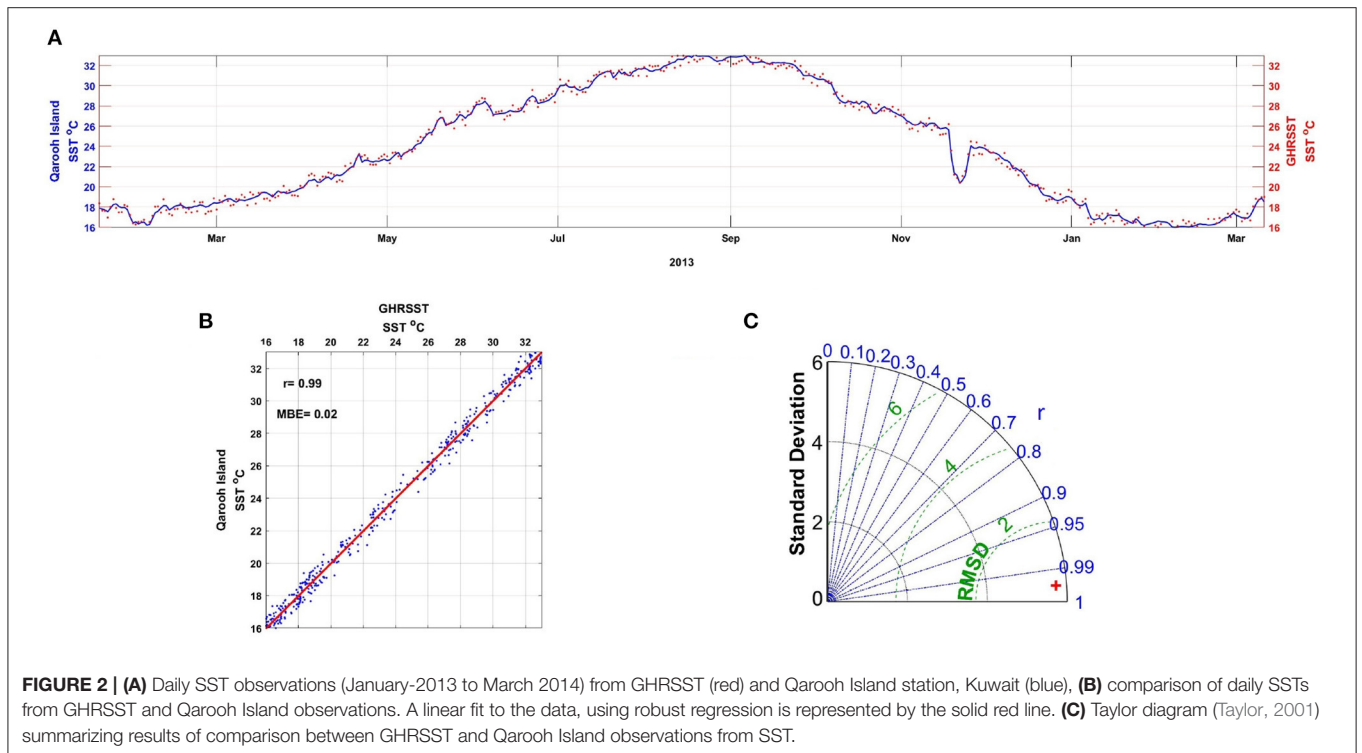
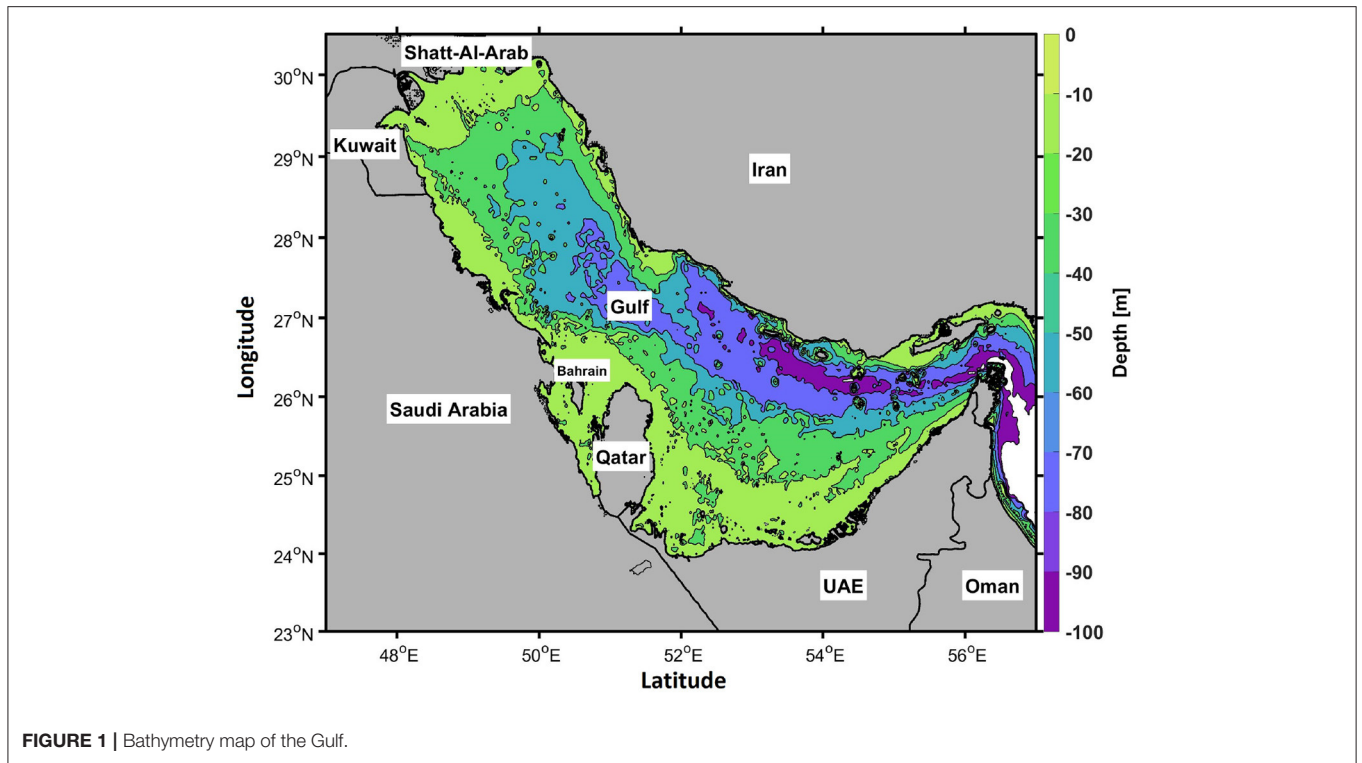
The Gulf's basin has an average depth of 36 m, with the maximum depth (100 m) occurring near the Strait of Hormuz (Figure 1). The Gulf is 990 km long and 338 km wide, with an estimated surface area and volume of 239,000 km<sup>2</sup> and 8,630 km<sup>3</sup>, respectively. Tectonic driven subsidence increased the seafloor depths at the shelf break that connects the Strait of Hormuz to the Gulf of Oman and Indian Ocean to become 200–300 m, while localized seafloor depressions generated 70–95 m troughs along the Iranian coastline. It is situated in the subtropical high pressure belt region (25–30°N), within which the Earth's harshest deserts are found (Al Senafi and Anis, 2015). Descending dry air in this region creates arid desert conditions, while the Gulf is exposed to extra-tropical weather systems from the northwest. The most well-known weather phenomena in the Gulf are Shamal wind events (Rao et al., 2001, 2003) and dust

storms (Kutiel and Furman, 2003). Shamal ("north" in Arabic) designates strong (up to 20 m/s; Rao et al., 2003) northwesterly winds that blow over the Gulf in summer (June to August; associated with the relative strengths of the Indian and Arabian thermal lows) and in winter (November to March; related to synoptic weather systems to the northwest) (Aboobacker et al., 2011). These meteorological phenomena occur at a rate of 10 events per year and substantially impact the natural environment and human health. They also cause abrupt changes in the Gulf's circulation, mixing intensities, heat-budget, and SST patterns (Al Senafi and Anis, 2015; Li et al., 2020b) similar to the Mistral winds that blow towards the Gulf of Lion in the Mediterranean (Bosse et al., 2021), and the Bora wind events that blow towards the Adriatic Sea (Ferrarin et al., 2019). In addition, SST changes resulting from these meteorological events also likely play a major role in the formation and location of the Gulf Deep Water (GDW). Driven by surface water cooling, GDW flows out of the Gulf close to its bottom, before spilling out into the Indian Ocean via the Strait of Hormuz. GDW is critical in regulating the Gulf's salinity and flushing its contaminants (Swift and Bower, 2003; Yao et al., 2014).

The arid regional meteorological conditions and shallow depths described above produce large variations in sea temperatures, which can range from 11°C in winter to 38°C in summer (Alosairi et al., 2020). Moreover, the excess evaporation over precipitation and river discharge can cause hyper-saline conditions, with salinities up to 70 PSU (Sheppard et al., 2010). The long-term circulation in the Gulf is, as in other semi-enclosed basins (e.g., Mediterranean and Red Sea), is a combined product of wind stress, buoyancy (Al Senafi and Anis, 2020b), freshwater runoff, tides (Al Senafi and Anis, 2020a; Li et al., 2020a), as well as the restricted exchange with the open ocean that results in an inverse estuarine circulation (Thoppil and Hogan, 2010a; Yao and Johns, 2010a,b). Thus, better understanding the region's interannual to multi-decadal SST variability could better reveal the Gulf's surface and deep circulations.

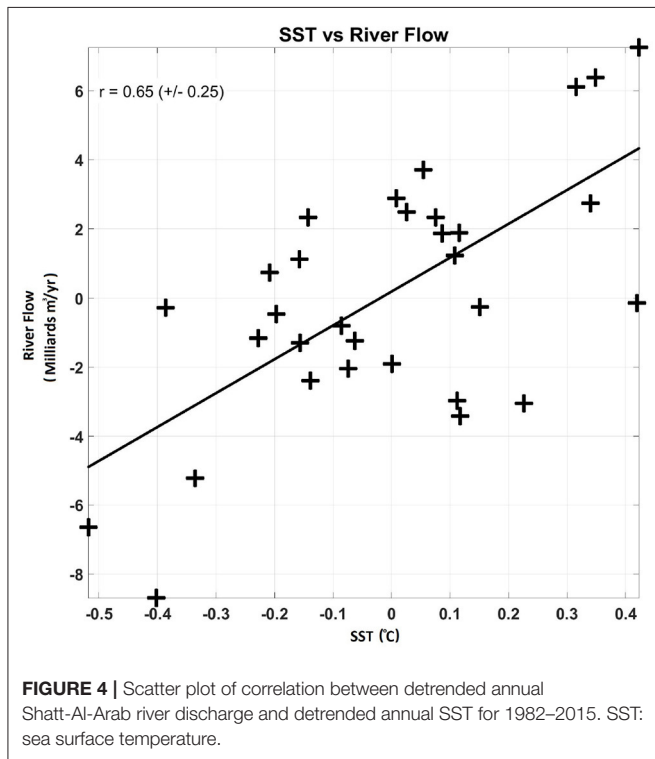
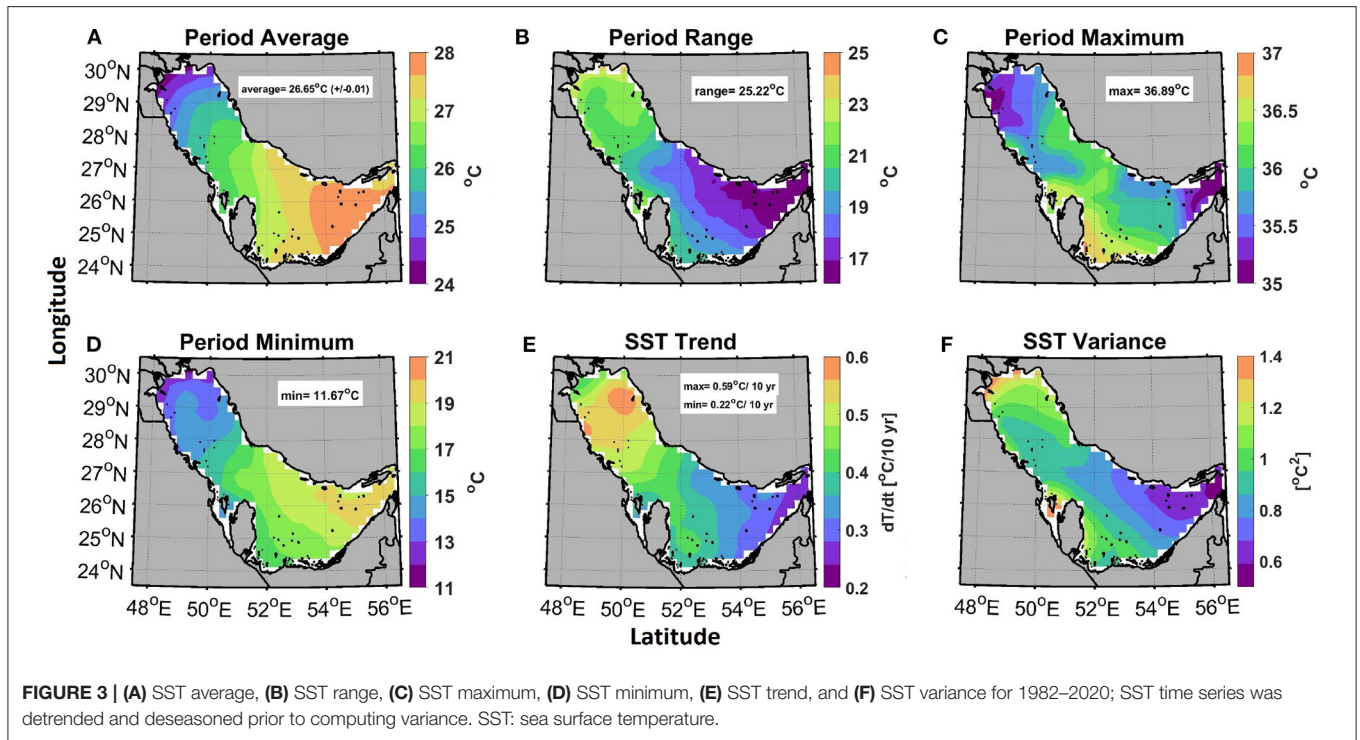
## 3. METHODOLOGY

The Gulf's daily SST was studied for the period of January 1982 to December 2020. The dataset employed in this study was obtained using the Level 4 Group for High Resolution Sea Surface Temperature (GHRSSST) that is freely available online through NASA's Physical Oceanography Distributed Active Archive Center (PO.DAAC) (<https://podaac.jpl.nasa.gov>). This product interpolates and extrapolates SST observations from various sources, creating a smoothly gridded database that contains temporally and spatially homogeneous daily SST images at a spatial resolution of 0.25° (Reynolds et al., 2007; National Centers for Environmental Information, 2016). The GHRSSST dataset has been assessed by Nesterov et al. (2021) using *in-situ* measurements in the southern Gulf. Results of this assessment found a good agreement between both datasets with correlation coefficients exceeding 0.99. Furthermore, *in-situ* measurements at Qaroon Island,



Kuwait described in Al Senafi and Anis (2020b) were used to evaluate the accuracy of the GHRSSST dataset in the northern Gulf (Figure 2A). Results of this evaluation demonstrate that the GHRSSST dataset is well correlated ( $r$

$= 0.99$ ) with the observations and displayed a Mean Bias Error (MBE) of  $0.02^{\circ}\text{C}$  (Figures 2B,C) capturing seasonal variability and the SST's changes associated with various meteorological events.



Using the GHRSSST dataset described above, a total number of 14,244 images were retained and organized in an  $M \times N$  matrix, where  $M$  and  $N$  represent the spatial and temporal elements,

respectively. This dataset was used to describe the space ( $x$ ) and time ( $t$ ) variability of SST in the Gulf, using statistical measures (average, range, variance, trend, minimum, and maximum) and the traditional Empirical Orthogonal Function (EOF) decomposition. EOF analysis reconstructs a gridded time series of the specified modes from eigenmode maps of variability and a corresponding principal component (PC) time series. In an EOF analysis, the temporally and spatially varying SST,  $T(x, t)$ , can be expressed in an orthogonal expansion of PCs in the form

$$T(x, t) = \sum_{n=1}^N F_n(x) a_n(t), \tag{1}$$

where  $F_n(x)$  is the spatial loading (EOF) and  $a_n(t)$  is the temporal varying functions (PC). Prior to EOF analysis, it was first necessary to detrend the daily SST images temporally to remove long term trends and emphasize temporal variance,

$$T'(x, t) = T(x, t) - \frac{1}{N} \sum_{t=1}^N T(x, t), \tag{2}$$

where  $T'(x, t)$  represent the residual SST anomalies. Alternatively, the spatial trend was also removed,

$$T'(x, t) = T(x, t) - \frac{1}{M} \sum_{x=1}^M T(x, t). \tag{3}$$

After the dominant SST modes were defined based on spatio-temporal characteristics, their correlations with major climate

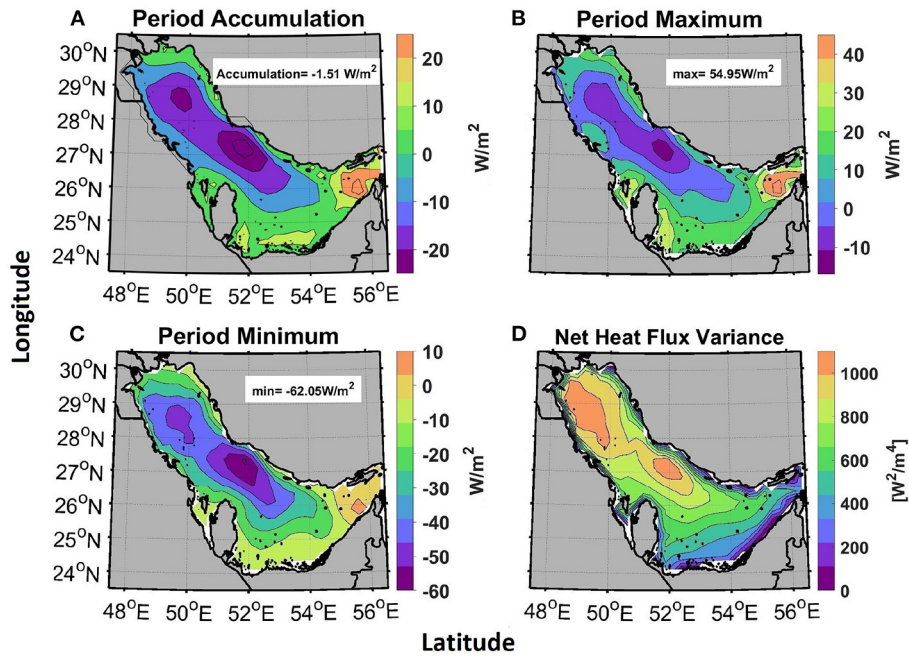


**FIGURE 5 | (A)**  $J_q^0$  average, **(B)**  $J_q^0$  minimum, **(C)**  $J_q^0$  maximum, and **(D)**  $J_q^0$  variance for 1982–2020;  $J_q^0$  time series was detrended and deseasoned prior to computing variance.

modes, including AMO, ENSO, and IOD, were investigated. This type of analysis has been widely adopted in studies with unknown modes of variability and their associations with major modes of climate variability globally (e.g., Fauchereau et al., 2003 over the Atlantic and Indian Oceans, Carleton, 2003 over the Southern Ocean, and Wu et al., 2020 over the Pacific Ocean). Other climates modes were excluded from detailed analysis as overall they exhibited insignificant correlations with the Gulf’s SST modes. These modes included Arctic Oscillation (AO), North Atlantic Oscillation (NAO), and Pacific decadal oscillation (PDO). Climate mode datasets were obtained from the National Oceanic and Atmospheric Administration (NOAA) Physical Sciences Laboratory website (<https://www.psl.noaa.gov/data/climateindices>).

The thermal conservation equation was used to approximate the contribution to SST changes associated with heat exchange at the air-sea interface, as follows:

$$\Delta T = \frac{1}{\rho_w h C_p} \int J_q^0 dt, \tag{4}$$

where  $T$  is temperature,  $\rho_w$  is the surface density (1024–1030 kg/m<sup>3</sup>) taken from Reynolds (1993),  $h$  is the surface mixed layer depths (5–20 m) taken from Reynolds (1993),  $C_p$  is the specific heat capacity constant of seawater, and  $J_q^0$  is the net heat flux.

$$J_q^0 = J_q^{sw} + J_q^{lw} + J_q^L + J_q^S, \tag{5}$$

where  $J_q^{sw}$  is the net shortwave radiation,  $J_q^{lw}$  is the net longwave radiation,  $J_q^L$  is the latent heat flux, and  $J_q^S$  is the sensible heat

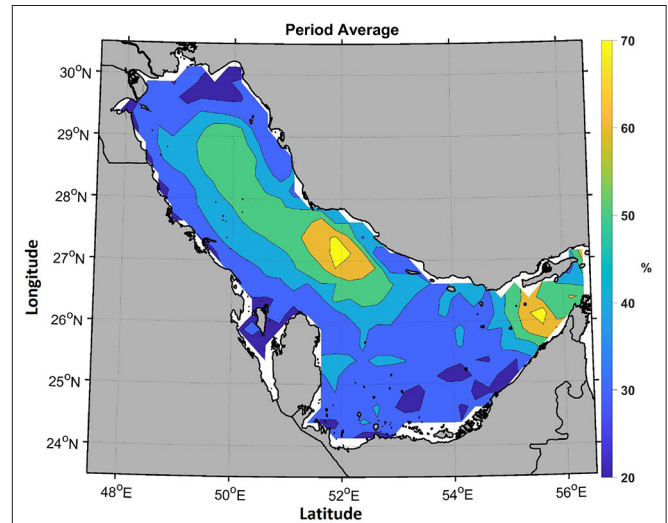


**FIGURE 6 |** Percentage SST changes associated with heat exchange at air-sea interface. SST: sea surface temperature.

flux. The four heat flux components were obtained from the fifth generation (ERA5; Hersbach et al., 2018) of the European Centre for Medium-Range Weather Forecasts (ECMWF) atmospheric reanalysis of global climate for the period of 1982 to 2020, at a spatial resolution of 31 km. The ERA5 dataset is freely available online through the Copernicus Climate Change Service (<https://climate.copernicus.eu>).

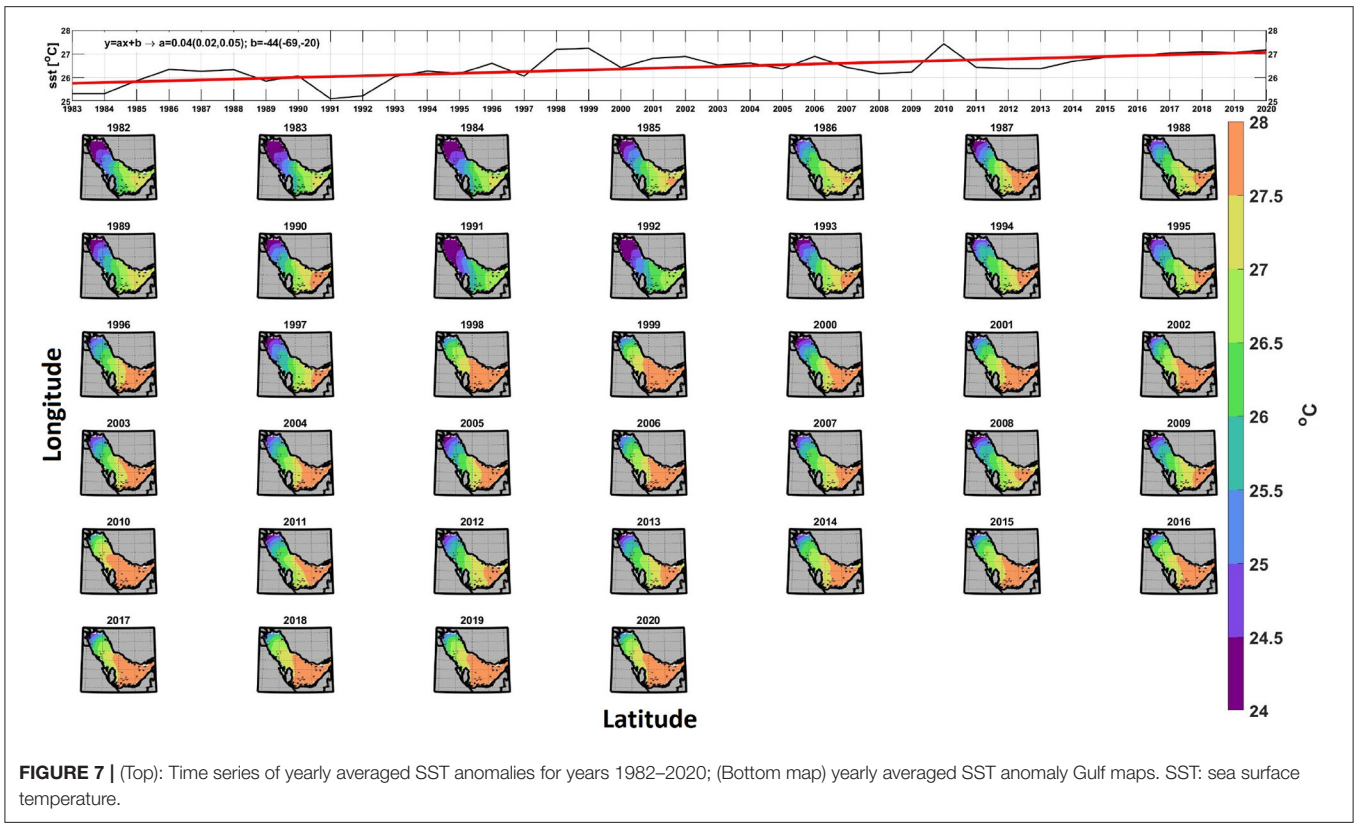


**FIGURE 7 |** (Top): Time series of yearly averaged SST anomalies for years 1982–2020; (Bottom map) yearly averaged SST anomaly Gulf maps. SST: sea surface temperature.

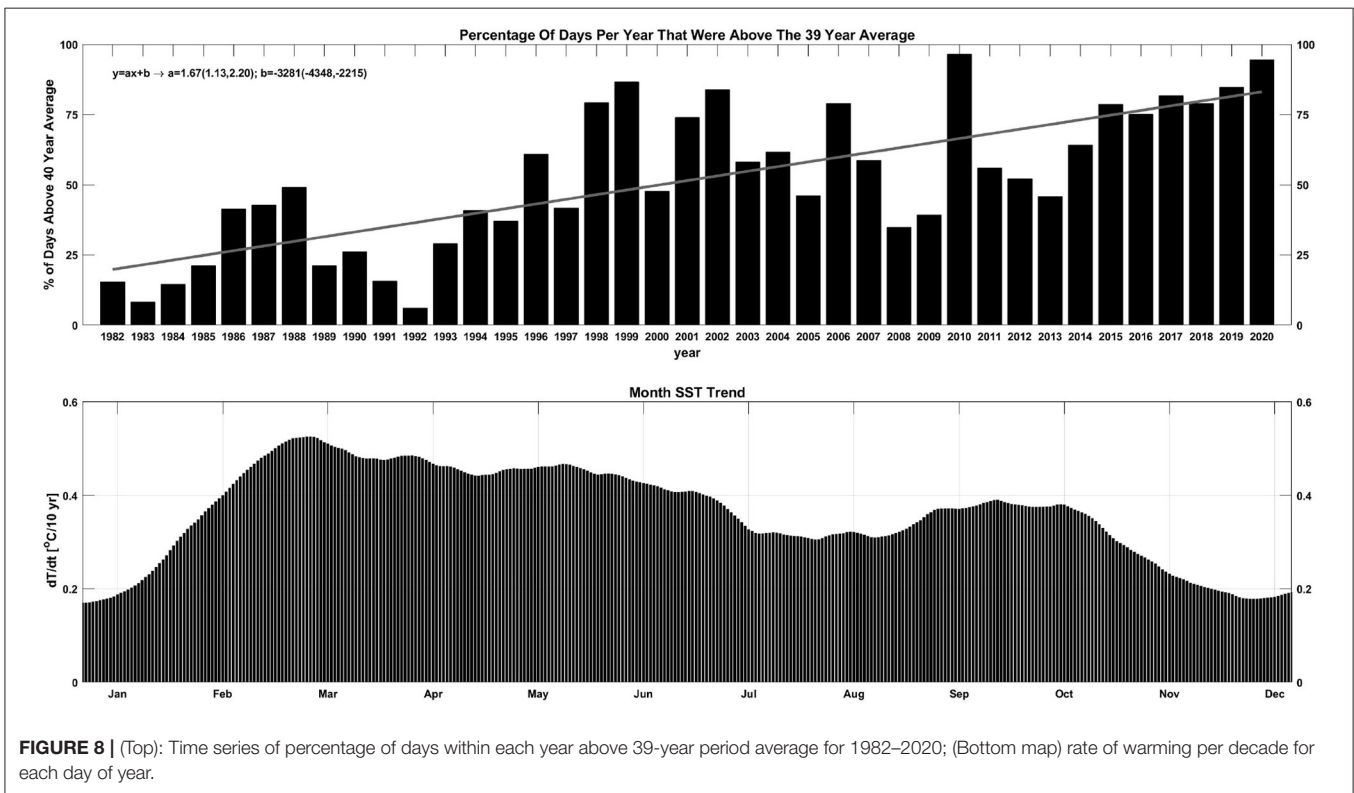
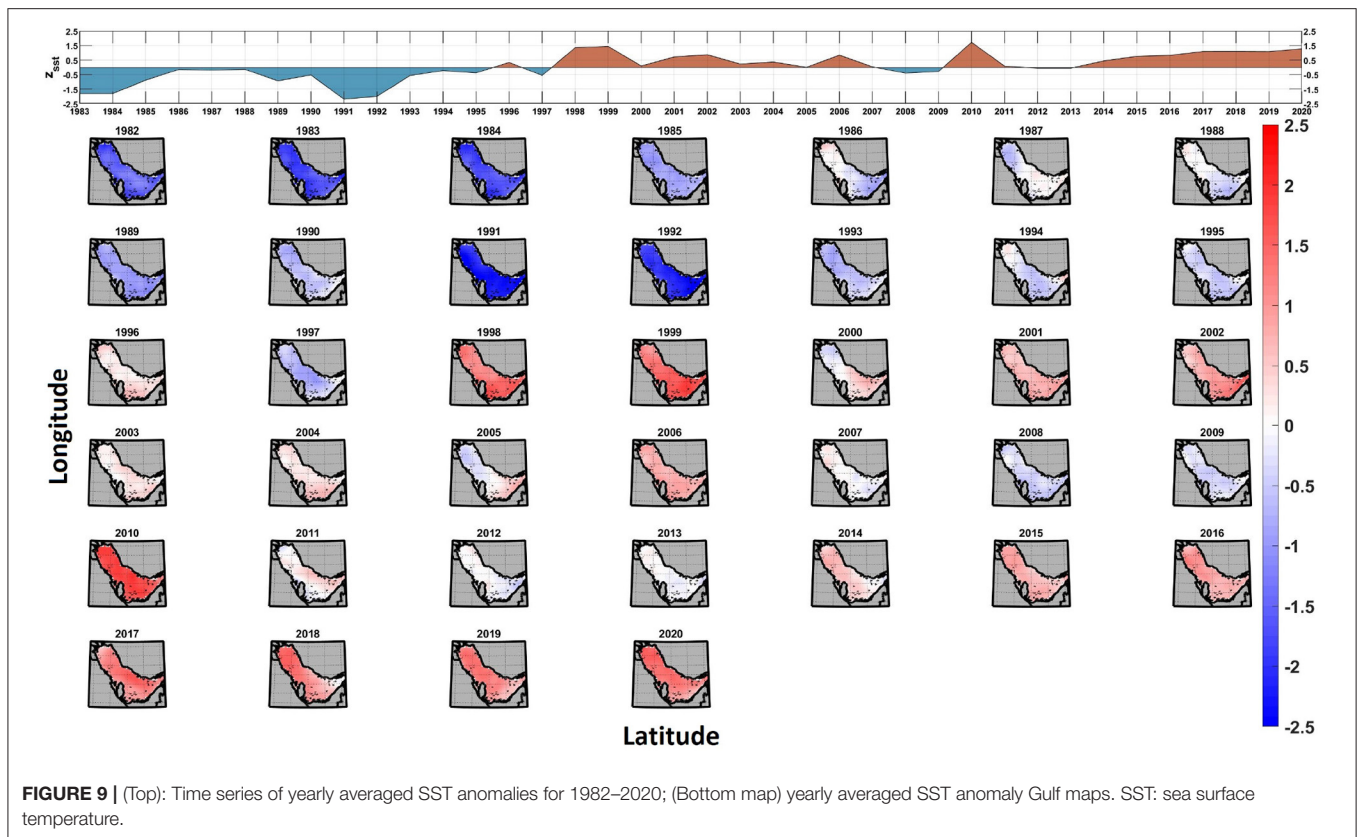


**FIGURE 8 |** (Top): Time series of percentage of days within each year above 39-year period average for 1982–2020; (Bottom map) rate of warming per decade for each day of year.



In a detailed one year study conducted by Al Senafi et al. (2019), ERA5 heat fluxes were validated and shown to be the most suitable data for the Gulf, with an error of  $4.5 \text{ W/m}^2$  and a correlation of 0.9. Based on the thermal conservation approximation, the percentage of change in SST that could be explained by air-sea heat exchange was determined from the overall observed SST changes; Al Senafi and Anis (2020b) used a similar approach to study the Gulf's advection processes.

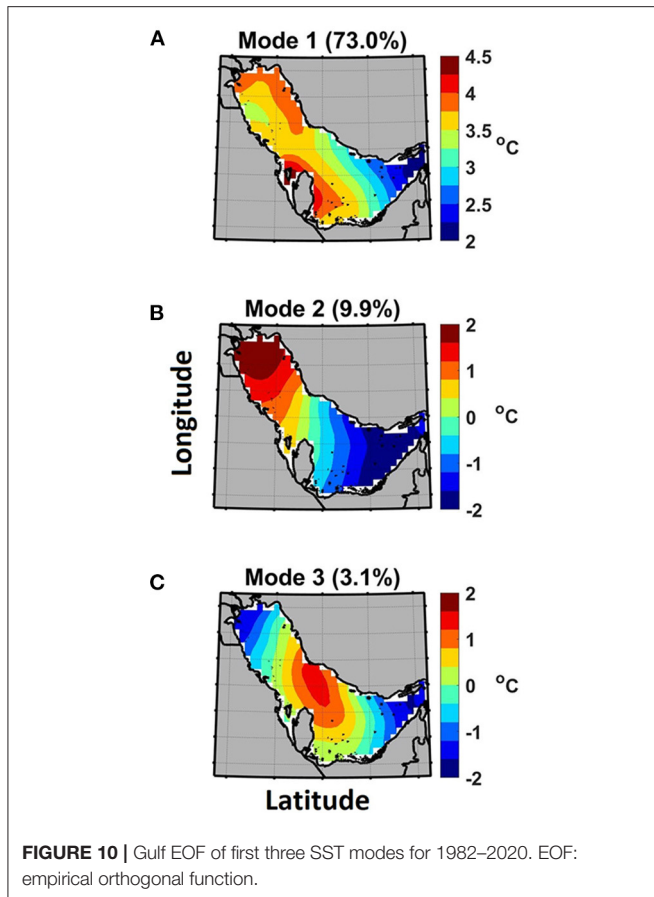
## 4. RESULTS AND DISCUSSION

### 4.1. SST Spatial Variability in the Gulf (1982–2020)

The Gulf daily SST time series for the period of 1982 to 2020 revealed that the spatial period average was  $26.7^\circ\text{C}$  (Figure 3A), and that it displayed a latitudinal gradient of cooler temperatures from south to north. The Gulf was shown to be warmer than other semi-enclosed seas such as the Mediterranean Sea, which has an annual average SST of  $19.7^\circ\text{C}$  (Shaltout and Omstedt, 2014), but cooler than the Red Sea, which has an annual average SST of  $27.1^\circ\text{C}$  (Krokos et al., 2019). However, unlike the Red Sea, which has an average depth of 450 m (Shaked and Genin, 2011), the Gulf is shallower, with an average depth of 36 m (Pous et al., 2012). This results in the Gulf experiencing larger seasonal swings in SST; they can reach up to  $25.2^\circ\text{C}$ , with the range being higher in shallower regions (i.e., the northern half and along the western coast) than in deeper areas (the southern half and eastern coast;

Figures 1, 3B). The Gulf's maximum SST ( $36.7^\circ\text{C}$ ) was recorded on July 1996 in the vicinity of Makasib Island, which is located between Qatar and the United Arab Emirates (UAE; Figure 3C). The currents here are stagnant and the waters are shallow ( $< 10 \text{ m}$ ) (Reynolds, 1993; Thoppil and Hogan, 2010b). The Gulf's maximum SST was found to be warmer than that of the Red Sea (maximum of  $33^\circ\text{C}$  recorded at Bab-el-Mandab Strait; Chaidez et al., 2017). In addition, various studies in the Gulf have recorded single point measurements of  $37.6$  and  $34.6^\circ\text{C}$  in Kuwaiti waters (Alosairi et al., 2020; Al Senafi and Anis, 2020a). In contrast, the Gulf's minimum SST was  $11.7^\circ\text{C}$  (recorded in Kuwaiti waters; Figure 3D), which was cooler than the minimum SST observed in the Mediterranean and Red Seas:  $15^\circ\text{C}$  (Criado-Aldeanueva et al., 2008; Shaltout, 2019). This emphasizes the Gulf's large temperature swings.

The non-seasonal SST intensity of change was examined by focusing on the SST variance shown in Figure 3F. This approach also emphasized the regions within the Gulf that experienced the highest non-seasonal fluctuations during the 39-year study period; these areas are likely to be relatively susceptible to the influence of climate change. The results presented in Figure 3F distinctively show that variance was stronger in the northern tip, where Shatt-Al-Arab river discharge occurs, and in the waters surrounding Qatar. These two regions also feature the shallowest waters, which may explain their relatively quick response to external forcing (e.g., sea surface heat and mass transfer), compared to other regions in the Gulf (Figure 3B). In



addition to their shallow nature, the strong variance observed at the northern tip could also be explained by the variability of the Shatt-Al-Arab river discharge rates; they fluctuated between 8.2 and 46.6 milliards  $\text{m}^3/\text{year}$  throughout the study period (Al-Saadi, 2021). After detrending both riverine discharge rates and SST observations at the Gulf's northern tip to remove long-term linear biases, a correlation of 0.65 was found between both datasets, suggesting that an increase in flow was followed by an increase in SST (Figure 4). Whereas, the stagnate currents and shallow nature explain the high variances in the region surrounding Qatar.

#### 4.2. Gulf's Warming Rate

Compared to the global and Red Sea SST warming rates of 0.07 and 0.17 (max 0.45)  $^{\circ}\text{C}/\text{decade}$  (Lough, 2012; Chaidez et al., 2017), respectively, the Gulf's warming rate was found here to be 0.41 ( $\pm 0.14$ )  $^{\circ}\text{C}/\text{decade}$ . Hereher (2020) determined the Gulf's warming trend to be 0.7  $^{\circ}\text{C}/\text{decade}$  using observations from Moderate Resolution Imaging Spectroradiometer (MODIS) images for the period of 2003 to 2018; this is similar to the observations obtained here for the same time period (0.67  $^{\circ}\text{C}/\text{decade}$ ). In addition, the results obtained here showed that the Gulf's spatial SST warming trend displayed a latitudinal gradient of 0.22 to 0.59  $^{\circ}\text{C}/\text{decade}$ , with steeper trends from south to north. The only exception to this trend occurred in

the northern tip near the Shatt-Al-Arab riverine discharge; here, the warming rate (0.41  $^{\circ}\text{C}/\text{decade}$ ) was slower than that of the surrounding northern water ( $\geq 0.5$   $^{\circ}\text{C}/\text{decade}$ ; Figure 3E). In agreement with the results reported here, Al-Rashidi et al. (2008) concluded that Kuwaiti waters warmed at a rate of 0.6  $^{\circ}\text{C}/\text{decade}$  for the period of 1985 to 2002.

#### 4.3. Temporal and Spatial Variabilities in Gulf's Air-Sea Net Heat Fluxes

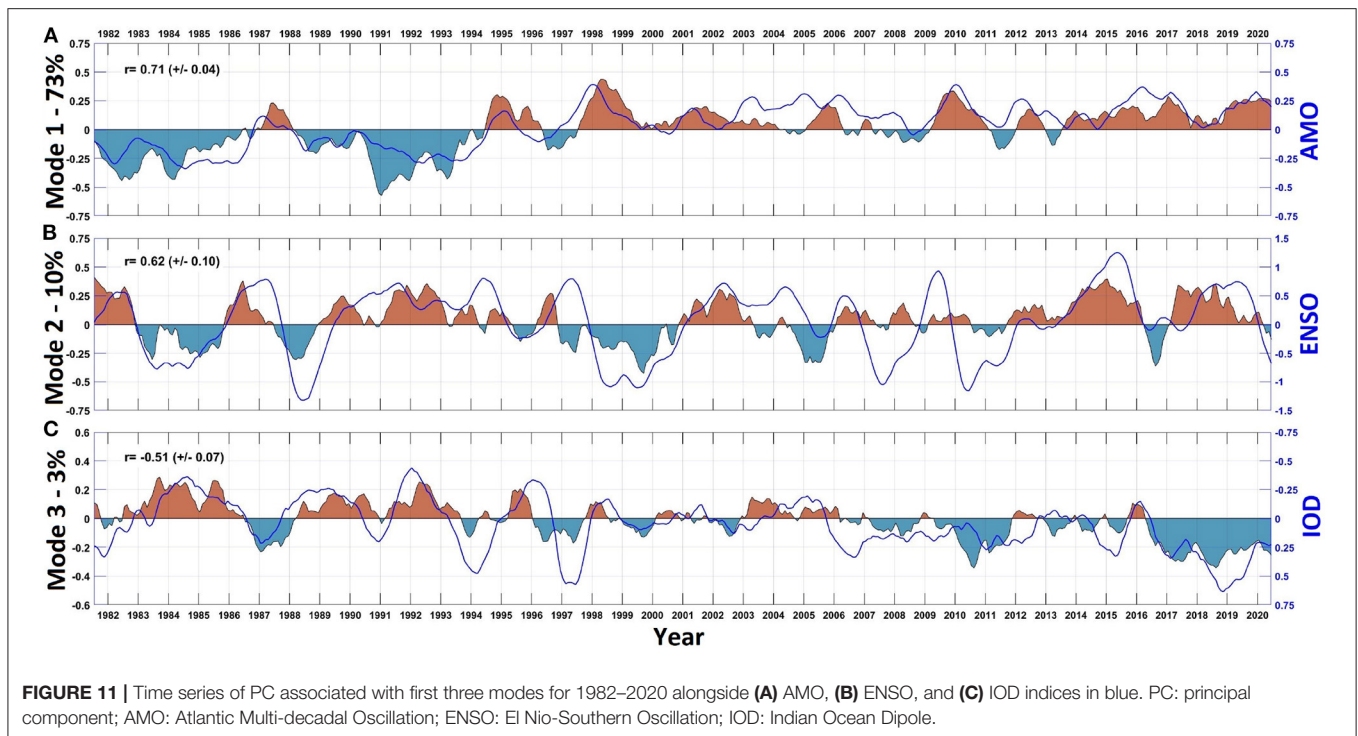
Analyzing the region's air-sea net heat fluxes revealed that the accumulated air-sea net heat flux during the study period throughout the Gulf was  $-1.52 \text{ W}/\text{m}^2$  (Figure 5A). However, since 2003 the Gulf has gained 0.5  $\text{W}/\text{m}^2$  of heat at the air-sea interface; this trend is likely to continue to increase by 0.3  $\text{W}/\text{m}^2$  every year, assuming that a similar trend persists.

Spatially, the Gulf was found to lose heat at the center during the 39-year study period ( $< 0 \text{ W}/\text{m}^2$ ), as indicated by the cooler colors (blue and purple colors) in Figure 5A. The coastal regions and the Strait of Hormuz (to the south) gained heat ( $> 0 \text{ W}/\text{m}^2$ ), as indicated by the green, yellow, and orange colors in Figure 5A. The net heat flux at the Gulf's center exhibited the highest range (up to 51  $\text{W}/\text{m}^2$ ); this was double the range in the coastal regions. Despite the high range of the net heat flux at the Gulf's center, the maximum net heat flux continuously remained below zero, indicating that persistent cooling occurred throughout the 39-year study period (Figure 5B); the minimum flux was  $-62 \text{ W}/\text{m}^2$  (Figure 5C). These results signify the crucial role of the Gulf's center region in cooling the region's waters; it acts as a regulator in reducing the high net heat flux intake within the coastal waters. Though the Gulf continuously lost heat at its center, the net heat flux trend showed that this cooling decreased at a rate of 7.71  $\text{W}/\text{m}^2$  per decade. This is critical, as the Gulf's waters are likely to warm faster in the future should this trend continue. This heating trend was observed throughout the Gulf, ranging between 0.64 and 7.71  $\text{W}/\text{m}^2$  per decade. The strongest heat flux variances were also found in the Gulf's center region, emphasizing that this area exhibited the largest changes (Figure 5D).

As shown in Figure 6, air-sea heat exchange explained up to 70% of SST variance in the Gulf's center and in the Strait of Hormuz (where SST variance was weakest; Figure 3F). The air-sea heat exchange only explained up to 25% of SST variance in the coastal regions, however, where the SST variances were strongest. This suggests that air-sea heat exchange was least pronounced in the shallow and dynamic areas of the Gulf.

#### 4.4. SST Temporal Variability and SST Modes in the Gulf (1982–2020)

The yearly averaged SST time series showed clear interannual variability at a warming rate of 0.41 ( $\pm 0.14$ )  $^{\circ}\text{C}/\text{decade}$  (Figure 7). The SST in the warmest and coolest years was 27.43  $^{\circ}\text{C}$  in 2010 and 25.11  $^{\circ}\text{C}$  in 1991, respectively. Furthermore, the last seven years (2014–2020) were all within the top ten warmest years, with an average SST of 27.02  $^{\circ}\text{C}$ . Moreover,  $> 75\%$  of days within those seven years experienced SSTs that were warmer than the 39-year average. Furthermore, the number of warmer days increased at a rate of  $\sim 2\%$  per year (Figure 8). This



warming trend displayed seasonal variability; SST warming was slowest in mid-winter (December–January) and mid-summer (July–August) at a rate of  $< 0.3^{\circ}\text{C}/\text{decade}$ . This rate then doubled during the fall (September–October) and spring (March–April). The faster warming trends during the fall and spring periods will likely further energize extreme storm events, which are common during these transitional seasons in the Gulf, should this warming rate continue (Al Senafi and Anis, 2015; Al Senafi et al., 2019).

In addition to the air-sea cooling at the Gulf’s center, as explained in Section 4.3, GDW is another regulator of the Gulf’s temperature. Although GDW is poorly understood, various studies (e.g., Thoppil and Hogan, 2010a,b; Li et al., 2020b) have suggested that it is convectively driven by cooling of the sea surface in the northern Gulf, and that it is more pronounced during late winter-spring, when vertical density stratification is weakest (Reynolds, 1993). GDW formation was found to occur within the vicinity of where the Gulf’s SST warming rate was fastest (Figure 3E); furthermore it occurred within those months when the warming rate was also fastest (Figure 8). This suggests that the formation of this deep water mass could possibly be disturbed should this warming trend continue.

The SST-standardized anomalies presented in Figure 9 clearly indicate that 1997 was the period’s “tipping point,” where SST inverted from being persistently cooler (negative anomalies) to being warmer (positive anomalies), with the exception of 2008 and 2009, within the 39-year baseline. The computation of EOF showed that the first three modes together explained 86% of the variance observed in SST anomalies. The remaining EOF modes explained less than 3% each of the total SST anomaly variances. These remaining EOF modes were excluded from

further analysis, as they did not pass the North et al. (1982) criteria, where the difference between the third and fourth eigenvalues are proportional to their sampling error magnitude; thus, the error size is comparable with the EOF themselves.

The EOF (spatial patterns) and PC (time series) for first three modes are presented in Figures 10, 11, respectively. The PC time series of the first mode of SST explained 73% of the total variance, displaying clear positive (e.g., 1995, 1998, and 2010) and negative (e.g., 1982, 1984, and 1991) anomaly peaks that were well correlated (0.71) with the AMO index. Further analysis of the lead-lag correlation revealed a 1–3 month lag, where the AMO index was found to lead the PC time series of mode 1 (Figure 11A). The warming of the Gulf’s SST in response to the AMO warming peaks was consistent with the findings of Alawad et al. (2020) within the Red Sea; it is likely attributable to changes in the upper troposphere (200 hPa) meridional winds (namely the Circum-Global Teleconnection; Ding and Wang, 2005). These changes impose warm air temperatures (Lu et al., 2002; Hong et al., 2017) across the Eurasian continents. This may explain why the strong mode 1 signatures of  $> 3.5^{\circ}\text{C}$  (Figure 10A; yellow-to-red shading) were located in the Gulf’s shallowest regions (Figure 1), while the strongest signature  $> 4^{\circ}\text{C}$  (Figure 10A; red shading) was located in the shallowest and weakest currents, off the coast of Qatar. The second EOF mode of SST explained 9.9% of the total variance, demonstrating a latitudinal gradient (Figure 10B). The PC time series of this mode displayed positive (e.g., 1982, 1986, and 2015) and negative (e.g., 1983, 1988, and 1999) peaks that were consistent with the ENSO index, with a significant correlation of 0.63 and a lag of 4 months (Figure 11B). The strong latitudinal signature of EOF mode



2 may be attributable to fluctuations in regional precipitation following peak ENSO periods. A detailed 40-year study by Al Senafi and Anis (2015) of the Mesopotamia (Kuwait, Iran, Iraq, Syria, and Turkey) and Gulf regions concluded that peak ENSO periods shifted the tropical convection cells eastwards; this in turn disturbed the moisture-bearing jet stream and increased precipitation. Wetter ENSO periods would increase Shatt-Al-Arab discharge; as described in Section 4.1; this would lead to warming of SSTs in the region's northern waters.

The third EOF mode explained 3.1% of the total SST anomaly variance. The strongest signature of the third EOF was located in the Gulf's center, where the influence of air-sea heat exchange was highest (Figure 6). The PC time series of the third mode displayed positive (e.g., 1983, 1985, and 1992) and negative (e.g., 1987, 2010, and 2018) peaks that were consistent with the IOD index, with a significant correlation of -0.51 and a lag of 5 months. This is similar to the lag period observed by Arun et al. (2005) for the Gulf region (Figure 11C). Further analysis of the air-sea net heat fluxes showed that during IOD peak phases, the heat loss from the Gulf was eight times lower than average. This was mainly attributed to the reduction of latent heat loss, which explained 61% of the net heat flux. This reduction in latent heat flux likely arose from an increase in the moisture influx into the Gulf from Africa, via Saudi Arabia, during positive IOD periods (Arun et al., 2005).

## 5. CONCLUSIONS

The study focused on the Arabian Gulf's interannual to multi-decadal SST variability over the period of 1982 to 2020, using daily Level 4 GHRSSST images. The findings presented here indicate that the average SST of the Gulf over the last 39 years was 26.7°C, and that warming occurred at rates of 0.22 to 0.59°C/decade during this time. The overall warming displayed seasonal variations; warming during the extreme storm transitional periods (fall and spring) occurred at double the rate than in winter and summer. Large swings in seasonal SST were observed, with minimum and maximum recorded SSTs of 11.7°C and 26.7°C, respectively.

The results presented here indicate that despite the observed warming trend, the accumulation of heat during the study period was  $-1.52 \text{ W/m}^2$ , suggesting an overall loss of heat (cooling). This cooling is critical in lowering the Gulf's extreme water temperatures, which could otherwise result in coral bleaching and undesired stress to other marine species (Burt et al., 2013; Sheppard, 2016). However, detailed analysis of the air-sea net heat fluxes indicated that a reversal from cooling (negative)

to heating (positive) occurred in 2003; this heating rate will continue to rise at a rate of  $0.3 \text{ W/m}^2$  per year.

EOF analysis was conducted to characterize the multiple spatial and temporal patterns of the Gulf's SST variability. Local trends were subtracted prior to EOF analysis to emphasize interannual to multi-decadal SST variability. In this way, three dominant EOF modes were identified that contributed to 86% of the Gulf's SST variability. The significant spatial and temporal correlations ( $r > 0.51$ ) suggest that throughout the 39-year study period, the SST variability could be attributed to atmospheric changes imposed by the AMO, ENSO, and IOD climate modes. Nonetheless, the findings of this study have to be seen in light of some limitations that could be addressed in future research. This study uses ERA5 and GHRSSST datasets that have been validated only in the northern part of the Gulf and during a 1 year period.

A better understanding of the Gulf's SST modes can help reveal the region's circulation more clearly, within which GDW plays a major role. The formation and circulation of dense GDW have been linked to cooler surface waters (Swift and Bower, 2003; Yao et al., 2014). GDW is critical in regulating salinity and flushing contaminants that are introduced into the Gulf. Thus, it is critical to conduct a detailed observational study to resolve spatial and temporal variations in sea surface heat, momentum, and mass transfer. The influence of spatial and temporal variability in SST, as reported in the present study, should also be investigated regarding GDW.

## DATA AVAILABILITY STATEMENT

The raw data supporting the conclusions of this article will be made available by the author, without undue reservation.

## AUTHOR CONTRIBUTIONS

The author confirms sole responsibility for the following: study conception and design, data collection, analysis and interpretation of results, and manuscript preparation.

## ACKNOWLEDGMENTS

I thank NASA (POODAC) for providing the SST data. I also thank ECMWF for providing online access to reanalysis data and NOAA (PSL) for the online teleconnection pattern data. I would like to express my special thanks of gratitude to Dr Hala Al Jassar (Kuwait University) as well as the Kuwait Sat 1 team for inspiring the project idea.

## REFERENCES

- Aboobacker, V. M., Vethamony, P., and Rashmi, R. (2011). Shamal swells in the Arabian Sea and their influence along the west coast of India. *Geophys. Res. Lett.* 38:L03608. doi: 10.1029/2010GL045736
- Al Senafi, F., and Anis, A. (2015). Shamals and climate variability in the Northern Arabian/Persian Gulf from 1973 to 2012. *Int. J. Climatol.* 35, 4509–4528. doi: 10.1002/joc.4302
- Al Senafi, F., and Anis, A. (2020a). Internal waves on the continental shelf of the Northwestern Arabian Gulf. *Front. Marine Sci.* 6, 1–19. doi: 10.3389/fmars.2019.00805
- Al Senafi, F., and Anis, A. (2020b). Wind-driven flow dynamics off the Northwestern Arabian Gulf Coast. *Estuarine Coastal Shelf Sci.* 233:106511. doi: 10.1016/j.ecss.2019.106511
- Al Senafi, F., Anis, A., and Menezes, V. (2019). Surface heat fluxes over the northern Arabian Gulf and the northern red sea: evaluation of

- ECMWF-ERA5 and NASA-MERRA2 reanalyses. *Atmosphere* 10, 1–30. doi: 10.3390/atmos10090504
- Alawad, K. A., Al-Subhi, A. M., Alsaafani, M. A., and Alraddadi, T. M. (2020). Decadal variability and recent summer warming amplification of the sea surface temperature in the Red Sea. *PLoS ONE* 15, 1–11. doi: 10.1371/journal.pone.0237436
- Almazroui, M. (2012). Temperature variability over Saudi Arabia and its association with global climate indices. *J. King Abdulaziz University Meteorol. Environ. Arid Land Agric. Sci.* 23, 85–108. doi: 10.4197/MWR.23-1.6
- Alosairi, Y., Alsulaiman, N., Rashed, A., and Al-Houti, D. (2020). World record extreme sea surface temperatures in the northwestern Arabian/Persian Gulf verified by in situ measurements. *Marine Pollut. Bull.* 161:111766. doi: 10.1016/j.marpolbul.2020.111766
- Al-Rashidi, T. B., El-Gamily, H. I., Amos, C. L., and Rakha, K. a. (2008). Sea surface temperature trends in Kuwait Bay, Arabian Gulf. *Nat. Hazards* 50, 73–82. doi: 10.1007/s11069-008-9320-9
- Al-Saadi, N. (2021). Water resources decrease of river euphrates and its impacts on the environment in Iraq. *Int. J. Ecol. Environ. Sci.* 33, 33–60.
- Arun, C., Swadhin, B., Mujumdar, M., Ohba, R., and Yamagata, T. (2005). Diagnosis of tropospheric moisture over Saudi Arabia and influences of IOD and ENSO. *Month. Weather Rev.* 134, 598–617. doi: 10.1175/MWR3085.1
- Bosse, A., Testor, P., Damien, P., Estournel, C., Marsaleix, P., Mortier, L., et al. (2021). Wind-forced submesoscale symmetric instability around deep convection in the northwestern mediterranean sea. *Fluids* 6, 1–26. doi: 10.3390/fluids6030123
- Burt, J., Al-Harthi, S., and Al-Cibahy, A. (2011). Long-term impacts of coral bleaching events on the world's warmest reefs. *Marine Environ. Res.* 72, 225–229. doi: 10.1016/j.marenvres.2011.08.005
- Burt, J. A., Al-Khalifa, K., Khalaf, E., AlShuwaikh, B., and Abdulwahab, A. (2013). The continuing decline of coral reefs in Bahrain. *Marine Pollut. Bull.* 72, 357–363. doi: 10.1016/j.marpolbul.2012.08.022
- Carleton, A. M. (2003). Atmospheric teleconnections involving the Southern Ocean. *J. Geophys. Res. Oceans* 108:JC000379. doi: 10.1029/2000JC000379
- Chaidez, V., Dreano, D., Agusti, S., Duarte, C. M., and Hoteit, I. (2017). Decadal trends in Red Sea maximum surface temperature. *Sci. Rep.* 7, 1–8. doi: 10.1038/s41598-017-08146-z
- Criado-Aldeanueva, F., Del Río Vera, J., and García-Lafuente, J. (2008). Steric and mass-induced Mediterranean sea level trends from 14 years of altimetry data. *Glob. Planetary Change* 60, 563–575. doi: 10.1016/j.gloplacha.2007.07.003
- Ding, Q., and Wang, B. (2005). Circumglobal teleconnection in the Northern Hemisphere summer. *J. Clim.* 18, 3483–3505. doi: 10.1175/JCLI3473.1
- Fauchereau, N., Trzaska, S., Richard, Y., Roucou, P., and Camberlin, P. (2003). Sea-surface temperature co-variability in the southern Atlantic and Indian Oceans and its connections with the atmospheric circulation in the Southern Hemisphere. *Int. J. Climatol.* 23, 663–677. doi: 10.1002/joc.905
- Ferrarin, C., Davolio, S., Bellafiore, D., Ghezzi, M., Maicu, F., Mc Kiver, W., et al. (2019). Cross-scale operational oceanography in the Adriatic Sea. *J. Operat. Oceanography* 12, 86–103. doi: 10.1080/1755876X.2019.1576275
- Hereher, M. E. (2020). Assessment of climate change impacts on sea surface temperatures and sea level rise-The Arabian Gulf. *Climate* 8, 50. doi: 10.3390/cli8040050
- Hersbach, H., Bell, B., Berrisford, P., Biavati, G., Horányi, A., Muñoz Sabater, J., et al. (2018). ERA5 hourly data on single levels from 1979 to present. Copernicus Climate Change Service (C3S) Climate Data Store (CDS). doi: 10.24381/cds.adbb2d47
- Hong, X., Lu, R., and Li, S. (2017). Amplified summer warming in Europe-West Asia and Northeast Asia after the mid-1990s. *Environ. Res. Lett.* 12:094007. doi: 10.1088/1748-9326/aa7909
- Huang, Y., Liu, X., Yin, Z. Y., and An, Z. (2021). Global impact of ENSO on dust activities with emphasis on the key region from the Arabian Peninsula to Central Asia. *J. Geophys. Res. Atmosph.* 126, 1–24. doi: 10.1029/2020JD034068
- Johns, W., Yao, F., Olson, D., Josey, S., Grist, J., and Smeed, D. (2003). Observations of seasonal exchange through the Straits of Hormuz and the inferred heat and freshwater budgets of the Persian Gulf. *J. Geophys. Res.* 108, 3391. doi: 10.1029/2003JC001881
- Khan, S., Piao, S., Khan, I. U., Xu, B., Khan, S., Ismail, M. A., et al. (2021). Variability of SST and ILLD in the Arabian Sea and Sea of Oman in Association with the Monsoon Cycle. *Math. Problems Eng.* 2021:9958257. doi: 10.1155/2021/9958257
- Krokos, G., Papadopoulos, V. P., Sofianos, S. S., Ombao, H., Dybczak, P., and Hoteit, I. (2019). Natural climate oscillations may counteract red sea warming over the coming decades. *Geophys. Res. Lett.* 46, 3454–3461. doi: 10.1029/2018gl081397
- Kutiel, H., and Furman, H. (2003). Dust storms in the middle east: sources of origin and their temporal characteristics. *Indoor Built Environ.* 12, 419–426. doi: 10.1177/1420326X03037110
- Li, D., Anis, A., and Al Senafi, F. (2020a). Neap-spring variability of tidal dynamics in the Northern Arabian Gulf. *Continental Shelf Res.* 197:104086. doi: 10.1016/j.csr.2020.104086
- Li, D., Anis, A., and Al Senafi, F. (2020b). Physical response of the Northern Arabian Gulf to winter Shamals. *J. Marine Syst.* 203:103280. doi: 10.1016/j.jmarsys.2019.103280
- Lough, J. M. (2012). Small change, big difference: sea surface temperature distributions for tropical coral reef ecosystems, 1950–2011. *J. Geophys. Res. Oceans* 117, 1950–2011.
- Lu, R.-Y., Oh, J.-H., and Kim, B.-J. (2002). A teleconnection pattern in upper-level meridional wind over the North African and Eurasian continent in summer. *Tellus Dyn. Meteorol. Oceanography* 54, 44–55. doi: 10.3402/tellusa.v54i1.12122
- Messié, M., and Chavez, F. (2011). Global modes of sea surface temperature variability in relation to regional climate indices. *J. Clim.* 24, 4314–4331. doi: 10.1175/2011JCLI3941.1
- Moradi, M., and Kabiri, K. (2015). Spatio-temporal variability of SST and Chlorophyll-a from MODIS data in the Persian Gulf. *Marine Pollut. Bull.* 98, 14–25. doi: 10.1016/j.marpolbul.2015.07.018
- National Centers for Environmental Information (2016). *Daily LA Optimally Interpolated SST (OISST) In situ and AVHRR Analysis. Ver. 2.0.* PO.DAAC, CA, USA. doi: 10.5067/GHAAO-4BC02
- Nesterov, O., Temimi, M., Fonseca, R., Nelli, N. R., Addad, Y., Bosc, E., et al. (2021). Validation and statistical analysis of the group for high resolution sea surface temperature data in the Arabian Gulf. *Oceanologia* 63, 497–515. doi: 10.1016/j.oceano.2021.07.001
- Nezlin, N., Polikarpov, I., Al-Yamani, F., Subba Rao, D., and Ignatov, A. (2010). Satellite monitoring of climatic factors regulating phytoplankton variability in the Arabian (Persian) Gulf. *J. Marine Syst.* 82, 47–60. doi: 10.1016/j.jmarsys.2010.03.003
- Noori, R., Tian, F., Berndtsson, R., Abbasi, M. R., Naseh, M. V., Modabberi, A., et al. (2019). Recent and future trends in sea surface temperature across the persian gulf and gulf of Oman. *PLoS ONE* 14, 1–19. doi: 10.1371/journal.pone.0212790
- North, G. R., Bell, T. L., Cahalan, R. F., and Moeng, F. J. (1982). Sampling Errors in the Estimation of Empirical Orthogonal Functions. *Month. Weather Rev.* 110, 699–706. doi: 10.1175/1520-0493(1982)110<0699:SEITEO>2.0.CO;2
- Pous, S., Carton, X., and Lazure, P. (2012). A process study of the tidal circulation in the persian gulf. *Open J. Marine Sci.* 2, 131–140. doi: 10.4236/ojms.2012.24016
- Purkis, S. J., and Riegl, B. (2005). Spatial and temporal dynamics of Arabian Gulf coral assemblages quantified from remote-sensing and in situ monitoring data. *Marine Ecol. Progr. Series* 287, 99–113. doi: 10.3354/meps287099
- Rao, G., Al-Sulaiti, M., and Al-Mulla, A. (2001). Winter shamals in Qatar, Arabian Gulf. *Weather* 56, 444–451. doi: 10.1002/J.1477-8696.2001.TB06528.X
- Rao, G., Al-Sulaiti, M., and Al-Mulla, A. (2003). Summer shamals over the Arabian Gulf. *Weather* 58, 471–478.
- Reynolds, M. (1993). Physical oceanography of the persian gulf, strait of hormuz, and the gulf of oman results from the mt. mitchell expedition. *Marine Pollut. Bull.* 27, 35–59.
- Reynolds, R. W., Smith, T. M., Liu, C., Chelton, D. B., Casey, K. S., and Schlax, M. G. (2007). Daily high-resolution-blended analyses for sea surface temperature. *J. Clim.* 20, 5473–5496. doi: 10.1175/2007JCLI1824.1
- Sale, P. F., Feary, D. A., Burt, J. A., Bauman, A. G., Cavalcante, G. H., Drouillard, K. G., et al. (2010). The growing need for sustainable ecological management of marine communities of the persian Gulf. *Ambio* 40, 4–17.
- Shaked, Y., and Genin, A. (2011). “Red sea and gulf of Aqaba,” in *Encyclopedia of Modern Coral Reefs: Structure, Form and Process*, ed D. Hopley (Dordrecht: Springer), 839–843.

- Shaltout, M. (2019). Recent sea surface temperature trends and future scenarios for the Red Sea. *Oceanologia* 61, 484–504. doi: 10.1007/s13280-010-0092-6
- Shaltout, M., and Omstedt, A. (2014). Recent sea surface temperature trends and future scenarios for the Mediterranean Sea. *Oceanologia* 56, 411–443. doi: 10.5697/oc.56-3.411
- Sheppard, C. (2016). Coral reefs in the Gulf are mostly dead now, but can we do anything about it? *Marine Pollut. Bull.* 105, 593–598. doi: 10.1016/j.marpolbul.2015.09.031
- Sheppard, C., Al-Husiani, M., Al-Jamali, F., Al-Yamani, F., Baldwin, R., Bishop, J., et al. (2010). The Gulf: a young sea in decline. *Marine Pollut. Bull.* 60, 13–38. doi: 10.1016/j.marpolbul.2009.10.017
- Stöfen-O'Brien, A., Naji, A., Brooks, A. L., Jambeck, J. R., and Khan, F. R. (2022). Marine plastic debris in the Arabian/Persian Gulf: challenges, opportunities and recommendations from a transdisciplinary perspective. *Marine Policy* 136:104909. doi: 10.1016/j.marpol.2021.104909
- Swift, S. A., and Bower, A. (2003). Formation and circulation of dense water in the Persian/Arabian Gulf. *J. Geophys. Res.* 108:3004. doi: 10.1029/2002JC001360
- Taylor, K. E. (2001). Summarizing multiple aspects of model performance in a single diagram. *J. Geophys. Res.* 106, 7183–7192. doi: 10.1029/2000JD900719
- Thoppil, P., and Hogan, P. (2010a). Persian Gulf response to a wintertime shamal wind event. *Deep Sea Res. Part I Oceanograph. Res. Papers* 57, 946–955. doi: 10.1016/j.dsr.2010.03.002
- Thoppil, P. G., and Hogan, P. J. (2010b). A modeling study of circulation and eddies in the Persian Gulf. *J. Phys. Oceanography* 40, 2122–2134. doi: 10.1175/2010JPO4227.1x
- Uddin, S., Fowler, S. W., Saeed, T., Jupp, B., and Faizuddin, M. (2021). Petroleum hydrocarbon pollution in sediments from the Gulf and Omani waters: status and review. *Marine Pollut. Bull.* 173:112913. doi: 10.1016/j.marpolbul.2021.112913
- Vaughan, G. O., Shiels, H. A., and Burt, J. A. (2021). Seasonal variation in reef fish assemblages in the environmentally extreme southern Persian/Arabian Gulf. *Coral Reefs* 40, 405–416. doi: 10.1007/s00338-020-02041-2
- Wu, Z., Jiang, C., Conde, M., Chen, J., and Deng, B. (2020). The long-term spatiotemporal variability of sea surface temperature in the northwest Pacific and China offshore. *Ocean Sci.* 16, 83–97. doi: 10.5194/os-16-83-2020
- Yao, F., Hoteit, I., Pratt, L. J., Bower, A. S., Zhai, P., Köhl, A., et al. (2014). Seasonal overturning circulation in the Red Sea: 1. model validation and summer circulation. *J. Geophys. Res. Oceans* 119, 2238–2262. doi: 10.1002/2013JC009004
- Yao, F., and Johns, W. (2010a). A HYCOM modeling study of the Persian Gulf: 2. formation and export of Persian Gulf Water. *J. Geophys. Res.* 115:C11018. doi: 10.1029/2009JC005788
- Yao, F., and Johns, W. E. (2010b). A HYCOM modeling study of the Persian Gulf: 1. model configurations and surface circulation. *J. Geophys. Res.* 115:C11017. doi: 10.1029/2009JC005781

**Conflict of Interest:** The author declares that the research was conducted in the absence of any commercial or financial relationships that could be construed as a potential conflict of interest.

**Publisher's Note:** All claims expressed in this article are solely those of the authors and do not necessarily represent those of their affiliated organizations, or those of the publisher, the editors and the reviewers. Any product that may be evaluated in this article, or claim that may be made by its manufacturer, is not guaranteed or endorsed by the publisher.

Copyright © 2022 Al Senafi. This is an open-access article distributed under the terms of the Creative Commons Attribution License (CC BY). The use, distribution or reproduction in other forums is permitted, provided the original author(s) and the copyright owner(s) are credited and that the original publication in this journal is cited, in accordance with accepted academic practice. No use, distribution or reproduction is permitted which does not comply with these terms.



# The Skill Assessment of Weather and Research Forecasting and WAVEWATCH-III Models During Recent Meteotsunami Event in the Persian Gulf

*Mohsen Rahimian, Mostafa Beyramzadeh and Seyed Mostafa Siadatmousavi\**

*School of Civil Engineering, Iran University of Science and Technology, Tehran, Iran*

## OPEN ACCESS

### Edited by:

Adem Akpinar,  
Bursa Uludağ University, Turkey

### Reviewed by:

Sanil Kumar,  
National Institute of Oceanography  
(CSIR), India  
Umesh Pranavam Ayyappan Pillai,  
University of Bologna, Italy

### \*Correspondence:

Seyed Mostafa Siadatmousavi  
siadatmousavi@iust.ac.ir

### Specialty section:

This article was submitted to  
Physical Oceanography,  
a section of the journal  
Frontiers in Marine Science

**Received:** 13 December 2021

**Accepted:** 10 February 2022

**Published:** 11 March 2022

### Citation:

Rahimian M, Beyramzadeh M and  
Siadatmousavi SM (2022) The Skill  
Assessment of Weather  
and Research Forecasting  
and WAVEWATCH-III Models During  
Recent Meteotsunami Event  
in the Persian Gulf.  
*Front. Mar. Sci.* 9:834151.  
doi: 10.3389/fmars.2022.834151

This study aims to use a fully realistic high-resolution mesoscale atmospheric and wave model to reproduce met-ocean conditions during a meteotsunami in the Persian Gulf. The atmospheric simulations were performed with the Weather and Research Forecasting (WRF) model by varying planetary boundary layer, microphysics, cumulus, and radiations parameterizations. The atmospheric results were compared to the meteorological observations (e.g., air pressure and wind speed) from the coastal and island synoptic and buoy stations of the nearest area to the meteotsunami event. The results show that using Mellor-Yamada-Nakanishi-Niino (MYNN) scheme for planetary boundary and surface layer had the best performance for stations over the water, whereas applying Mellor-Yamada-Janjic scheme for planetary boundary and Eta similarity surface layer had the best performance for stations over the land. For wave simulations, the WAVEWATCH-III model was employed with the well-known WAM-Cycle4 formulation and a more recent ST6 package. Six WRF experiments and ERA5 wind data were used to force the wave models. The new error parameter was introduced to identify the optimum wind data for wave simulation. EXP4 configuration which uses the MYNN scheme for planetary boundary and surface layer was led to minimum error, while ERA5 severely underestimated  $H_s$  and  $T_p$  parameters. For the first time, the Gaussian Quadrature Method (GQM) was implemented in the WAVEWATCH-III model and combined with a depth scale to be used in the Persian Gulf. This method is more accurate for non-linear wave-wave interaction than the default Discrete Interaction Approximation (DIA) method. Lower coefficients for dissipation term were required for GQM and the resulted bulk wave parameters were improved compared to the DIA method. The calibrated ST6 formulation with GQM resulted in a more realistic prediction of wave spectrum than the default settings of the WAVEWATCH-III.

**Keywords:** meteotsunami, Persian Gulf (PG), ERA5 data, ST3, ST6, DIA, GQM

## INTRODUCTION

The Persian Gulf is one of the most important oil tanker highways in the world, which has been protected from waves induced by tropical storms and tsunamis over the past few decades (El-Sabh and Murty, 1989; Al-Hajri, 1990; Lin and Emanuel, 2016). Although the easterly coastal region in Iran is more susceptible to tsunami by active faults in the Indian Ocean, there is no major earthquake fault in the Persian Gulf region that can produce large tsunami (Ambraseys, 2008). Moreover, tsunami waves produced in the Indian Ocean rarely propagate into the Persian Gulf (Rabinovich and Thomson, 2007; Heidarzadeh et al., 2008); hence, harsh weather is not common in this region (Nadim et al., 2008; Modarress et al., 2012). On 19 March 2017, an unexpected ~3-m-long wave struck the northern shores of the Persian Gulf, and at least five people were killed in the port of Dayyer (see **Figure 1** for its location). It also led to extended damages to ships, residential areas, and coastal facilities adjacent to this port (Salaree et al., 2018; Heidarzadeh et al., 2020; Kazeminezhad et al., 2021). Salaree et al. (2018) conducted a field study on the damaged coastline and reconstructed the initial picture of the whole event. They explained the physical mechanisms generating the strong long waves during this event and concluded that a meteorological tsunami was responsible for this event. Heidarzadeh et al. (2020) studied this meteorological event using satellite imageries, atmospheric reanalysis products, and *in situ* measurements, including sea level data and high-resolution air pressure data along the southern Persian Gulf. The rainfall intensity, maximum reflection, and echo top height images provided by the weather radar confirmed that a strong convergent system, including the middle and upper troposphere, had entered the northern Persian Gulf approximately 4 h before the event and moved to the east (Kazeminezhad et al., 2021). Then, 2 h before its landfall, the convection system deformed into a narrow and long hurricane with 70–130 km length, less than 10 km width, and a transverse speed of 24 m/s.

Meteotsunami are shallow-water waves or water level fluctuations due to atmospheric interactions, which typically last from minutes to hours (Monserrat et al., 2006). The development of these long waves depends upon several factors and has a multi-stage process; but meteotsunami generally begin with a sudden change in air pressure and/or wind (the effect of atmospheric turbulence) and are usually accompanied by mesoscale systems such as frontal passages, storms and strong winds (squalls), thunderstorms and gravitational waves of the atmosphere (Monserrat et al., 2006; Shi et al., 2020). The occurrence of meteotsunami long waves, especially when followed by high energetic wind-induced waves cause severe damage to the coastal environment, destroy infrastructure, and are potentially considered a large threat for local people since they are generally unexpected (Rabinovich, 2020).

Concerning the nature of the meteotsunami phenomenon, simulation of meteotsunami requires a high-resolution atmospheric model to provide a precise estimation of wind stress and pressure disturbances at the sea level (Shi et al., 2019). In addition, having an unembellished atmospheric model is critical in the accurate simulation of meteotsunami

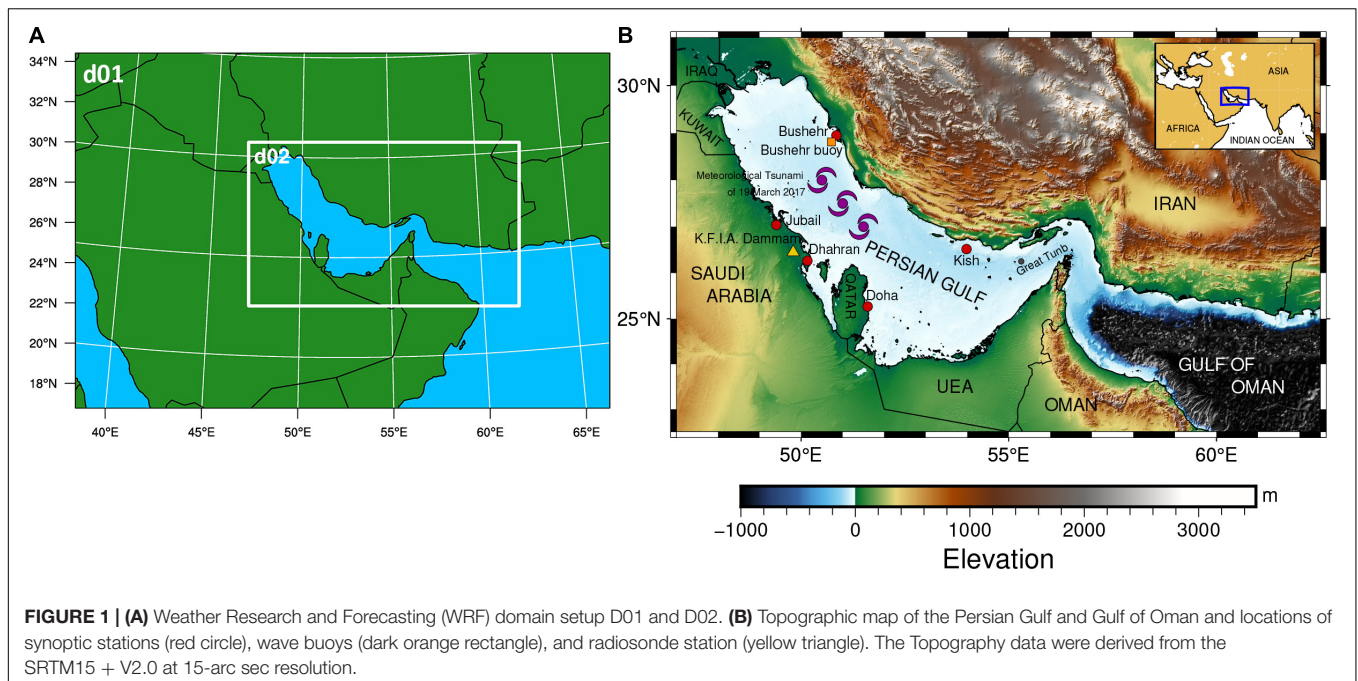
waves (Horvath et al., 2018; Shi et al., 2019) which depends on various factors such as grid resolution, physics, initial conditions, and selected boundaries in the simulation (Borge et al., 2008). Considering the non-linear and turbulent nature of the atmosphere, small differences in initial condition or model parameters lead to different representations of perturbations (Shi et al., 2019, 2020; Mourre et al., 2021). A common approach to deal with these sensitivities and forecast uncertainties in numerical weather models is to use an ensemble prediction (Borge et al., 2008; Horvath and Vilibić, 2014; Mourre et al., 2021). Horvath and Vilibić (2014) in their study on meteotsunami Boothbay, examined the sensitivity of high-resolution weather conditions and its relationship with model parameters, time step, initial and boundary conditions, and nested strategy. Belušić et al. (2007) studied meteotsunami events in the Adriatic Sea in 2003 and found that the wave-convection system is very sensitive to the microphysics used in the model. Mourre et al. (2021) evaluated different physical parameterizations in the implementation of a high-resolution atmospheric-ocean model with a nested network to predict a meteotsunami that occurred in Ciutadella (Spain). The results indicate the success of the extensive expansion of ensemble simulations regarding the prediction of the ultimate magnitude of meteotsunami. However, the small-scale characteristics of these disturbances were highly sensitive to the tuning parameters, which led to significant differences in the magnitude of the simulated response at sea level.

This study aims to assess the performance of different parameterizations for physical processes in a high-resolution numerical model in simulating the meteorological characteristics and wind-induced waves during the dominance of meteotsunami in the Persian Gulf. These simulations were carried out using Weather Research and Forecasting (WRF) model to determine the atmospheric parameters, and WAVEWATCH-III model to determine the wave spectrum. The wind and wave regimes of the Persian Gulf for a 31-yearly period were evaluated by Kamranzad (2018). The results indicated that monthly mean and extreme wave height for Bushehr station in March were lower than 6 m and higher than 3 m, respectively. As will be shown in section “Skill Assessment of WAVEWATCH-III,” the recorded wave height exceeds 1.5 m during the dominance of the meteotsunami (19–20 March); hence, the skill assessment of the WAVEWATCH-III model using different wind data is another goal of the study. The weather stations and buoy measurements were used for the models’ assessment. The study area, modeling system, and experimental approach are described in section “Materials and Methods”. Section “Results” includes the skill assessment of models, followed by conclusions in section “Conclusion.”

## MATERIALS AND METHODS

### Study Area and Observations

The Persian Gulf is a semi-closed marginal sea on a continental shelf extended in a northwest-southeast direction and is located within the 24–30°N latitude and 47–52°E longitude, respectively



(see **Figure 1**). The average depth of this water body is 37 m and it has access to the Gulf of Oman as well as the Indian Ocean through the Strait of Hormuz. The length of the Persian Gulf is approximately 1,000 km, its maximum width is 336 km and its maximum depth is approximately 90 meters near the Great Tunb Island; Also, the west and south side of the Persian Gulf is relatively shallow and has mild slopes (Reynolds, 1993). The Strait of Hormuz restricts the interaction of the Persian Gulf with open oceans (Liao and Kaihatu, 2016). Nayak et al. (2016) showed that the waves formed in the Gulf of Oman have negligible effects on the evolution of waves in the Persian Gulf due to energy loss during their crossing the Strait of Hormuz.

Mixed tides with a height of 1 to 2 m dominate most of the Persian Gulf (Akbari et al., 2016). The climate of the Persian Gulf is divided into two important seasons and two transitional periods. The summer season happens from May to September. In contrast, the winter season starts in November and finishes in March (Athar and Ammar, 2016). The winds are mainly from the northwest throughout the year. In winters, between November and February, wind speeds (mean value  $\sim 5$  m/s) are stronger than in summer (mean value  $\sim 3$  m/s) (Thoppil and Hogan, 2010). The most famous climatic phenomenon in the Persian Gulf region is the north-northwest wind called Shamal wind. It is a monsoon, systematic, continuous, and strong wind in the Persian Gulf. In summer, it blows mainly between May and July while in winter, it occurs between December and early March. However, this phenomenon is often not accompanied by coastal floods and generally causes waves between 0.25 to 0.4 meters in the northernmost coastal areas of the Persian Gulf (Thoppil and Hogan, 2010; Kazeminezhad et al., 2021).

The meteotsunami on 19 March 2017 occurred during a calm and cloudy day (Heidarzadeh et al., 2020). At 8:00 AM (+ 4:30 GMT), large long waves affected an area of about 100 km on the northern coasts of the Persian Gulf and caused more than 1 km

of inundation in coastal and urban zones of Dayyer and Kangan. Pieces of evidence and field studies show that the height of the forerunner low-frequency wave exceeded 3 m near the port of Dayyer and has caused extensive damages in terms of life and economy in this region (Salaree et al., 2018).

Atmospheric systems generally produce meteotsunami with a spatial scale of hundreds of kilometers and a time scale of several hours, which is called mesoscale systems. Because small disturbances of atmospheric pressure (less than 1 hPa) and wind speed changes (10 m/s) in mesoscale systems usually cause disturbances at sea level on a scale of several centimeters, reinforcement mechanisms are required for large meteotsunami. Wave velocity in shallow water is highly dependent on water depth. Most meteotsunamis are reported to occur in semi-enclosed environments such as gulfs, which indicates the importance of the shape and geometry of the region (Williams, 2020). Appropriate bathymetry condition (water depth less than 100 m) and appropriate mesoscale atmospheric phenomenon [e.g., fronts reported by Heidarzadeh et al. (2020)] led to the 2017 meteotsunami event in the Persian Gulf.

The data from several synoptic stations and one radiosonde station were used to validate the simulation results in the period of 15–23 March 2017. Surface data were obtained from 5 airport synoptic stations via Hourly Global Surface (DS3505) datasets of the National Climatic Data Center (NCDC). Also, hourly data from Bushehr wave recorder buoy were provided by the Port and Maritime Organization of Iran<sup>1</sup>. Upper air atmospheric station data from the radiosonde data archive of NOAA-ESRL database were available from the King Fahd International Airport (K.F.I.A.-Dammam) WMO station code 40417, which were retrieved from the Wyoming radiosonde database<sup>2</sup>. All these

<sup>1</sup><http://www.pmo.ir/en/home>

<sup>2</sup><http://weather.uwyo.edu>

stations are shown in **Figure 1B**. Among many parameters recorded at synoptic stations, wind speed and air pressure are more important for a meteotsunami study (Šepić et al., 2015; Vilibić et al., 2016; Horvath et al., 2018; Shi et al., 2019, 2020).

In addition to these ground meteorological data, hourly ERA5 reanalysis data were available *via*<sup>3</sup>. This dataset has been produced by the European Center for Middle-range Weather Forecast (ECMWF) with a 31-km resolution over the Persian Gulf. The variations in air pressure measured at different stations were compared to the ERA5 data during the period 15–23 March 2017 in **Figure 2**.

Fluctuations of atmospheric pressure on 19 March are following the period in which meteotsunami has occurred. Recorded pressure changes at Bushehr (synoptic and buoy) stations, Kish (synoptic and buoy), Daharan, Doha, and Jubail on 15–23 March 2017 are shown in **Figure 2**. Average air pressure begins to decrease at the end of 18 March 2017 and reaches its minimum value in the middle of 19 March in the shown period. At northern stations of the Persian Gulf, such as Bushehr and Kish, air pressure changes sharply and decreases by 4–8 hPa a few hours after the collision of tsunami-like waves (6:00 UTC). At Jubail and Daharan stations located in the southern part of the Persian Gulf, ~2 hPa decrease in air pressure occurred last hours of 18 March followed by another drop in a range of 4 hPa, early morning on 19 March. It indicates that the low-pressure front was moving from the southwest of the Persian Gulf to its northeast part. The synoptic conditions of the Persian Gulf region and its areas at 4:00 and 6:00 AM on 19 March 2017 are shown in **Figure 3** when tsunami-like waves were formed and hit the northern coasts of the Persian Gulf. Parameters such as average sea level pressure, the 10 m wind vectors, and wind gusts were obtained from the reanalysis dataset of ERA5. Since the cyclone was located in the northwest of the Persian Gulf at this moment, ERA5 data show the northeast wind direction over the Persian Gulf; i.e., in the opposite direction to the waves reaching the northern coasts of the Persian Gulf. The wind direction has been evaluated at Bushehr and Kish stations and the same pattern was observed. Thus, the ERA5 results were of good quality during this event based on stations located in the northern part of the Persian Gulf (both synoptic station and buoy of Bushehr). No strong gust wind was observed at these hours over the Persian Gulf; hence it is more likely that long waves during this meteotsunami phenomenon were created by atmospheric pressure fluctuations, which was in accordance with previous studies (Heidarzadeh et al., 2020; Kazeminezhad et al., 2021).

## Modeling System

The wind and wave simulations were performed as explained in this section.

### Wind Model

In this study, the fully compressible, non-hydrostatic mesoscale Advanced Research WRF (ARW) version 4.3<sup>4</sup> (Skamarock et al., 2019) is used on a Lambert conformal

projection during 15–23 March 2017. It uses the Arakawa-C grid and a terrain-following hybrid sigma–pressure coordinate in the vertical direction for solving the governing equations. Runge–Kutta scheme is also utilized for the discretization in time-space. The model incorporates several parameterization schemes for physical processes including microphysics, cumulus convection, planetary boundary layer, land surface, and short and longwave radiations. In this study, WRF is configured with two nested domains with a horizontal grid spacing of 9 km (D01) and 3 km (D02), with 231 × 220 and 502 × 304 grid points (see **Figure 1A**). The domain center was located on the Kish Island. The vertical structure in both domains consists of 45 vertical levels from the sea surface to 50 hPa with varying vertical resolution such that, grid sizes are smaller near the ground and become coarser with increasing altitude.

High-quality initial and boundary conditions are crucial to have accurate simulations. These data were derived from the ECMWF IFS CY41r2 High-Resolution Operational Forecasts dataset<sup>5</sup>, which has 0.08° spatial and 6-h temporal resolution. The time step of the model simulation was set as 27 s in D01 and as 9 s in D02. The WRF Preprocessing System (WPS) in version 4.0.3<sup>6</sup> was used to prepare the input data for the model together with the WPS V4 Geographical Static Data. To improve the accuracy of geographical data in the model, the modified IGBP 21-category, 15 arc-seconds, MODIS LULC database was adopted. The domain size and computational period were selected according to Heidarzadeh et al. (2020). The model was initialized at 6:00 PM on 14 March 2017, and the first 6 h of the simulation were taken as spin-up time.

Although the wind field of atmospheric models has high quality on the oceans and offshore areas, their performance in semi-closed and closed areas with complex geomorphology still needs improvements. The wind speed from a model in such conditions is less than observations in many cases (Cavaleri and Bertotti, 2003, 2006). Factors such as the position and size of the simulation domain, spatial resolution, and initial conditions affect the model results. In addition to selecting the appropriate dynamic configuration, testing and selecting the appropriate physical parameterization also reduce the uncertainties of atmospheric models in calculating the wind field (Belušić et al., 2007; Vilibić et al., 2008, 2016; Šepić et al., 2009; Horvath and Vilibić, 2014; Horvath et al., 2018; Linares et al., 2019; Shi et al., 2019, 2020; Mourre et al., 2021). There are many physical designs in the WRF model which make it flexible for different climatic conditions with optimal performance for a range of temporal and spatial resolutions (Skamarock et al., 2019).

A subset of physical parameterization including the planetary boundary layer (PBL), cumulus (CU), and the microphysics (MP), which has been used in previous meteotsunami studies, were used to optimize the model performance (Belušić et al., 2007; Šepić et al., 2009; Renault et al., 2011; Horvath and Vilibić, 2014; Horvath et al., 2018; Denamiel et al., 2019; Shi et al., 2019; Mourre et al., 2021). To be more specific, the following schemes have been used; (MP): the Thompson

<sup>3</sup><http://www.ecmwf.int/en/forecasts/datasets/reanalysis-datasets/era5>

<sup>4</sup><https://github.com/wrf-model/WRF>

<sup>5</sup><http://rda.ucar.edu/datasets/ds113.1>

<sup>6</sup><https://github.com/wrf-model/WPS/releases>

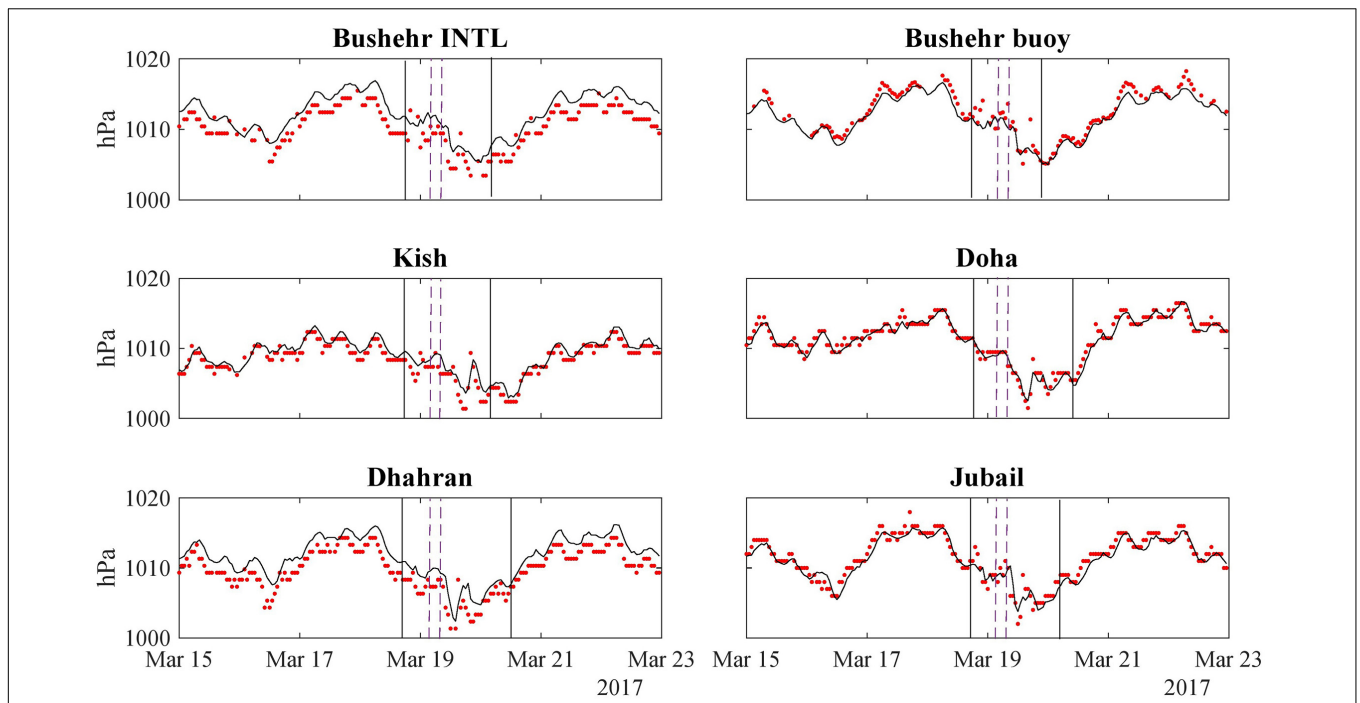


**FIGURE 2 |** Atmospheric air pressure records during 15–23 March 2017, at the Persian Gulf coastal stations. The red dotted lines denote measured data from synoptic and buoy station and the black continuous line denote ERA5 data. The black lines denote distinct air pressure disturbances and the purple dashed line indicates the time of the Persian Gulf meteotsunami.

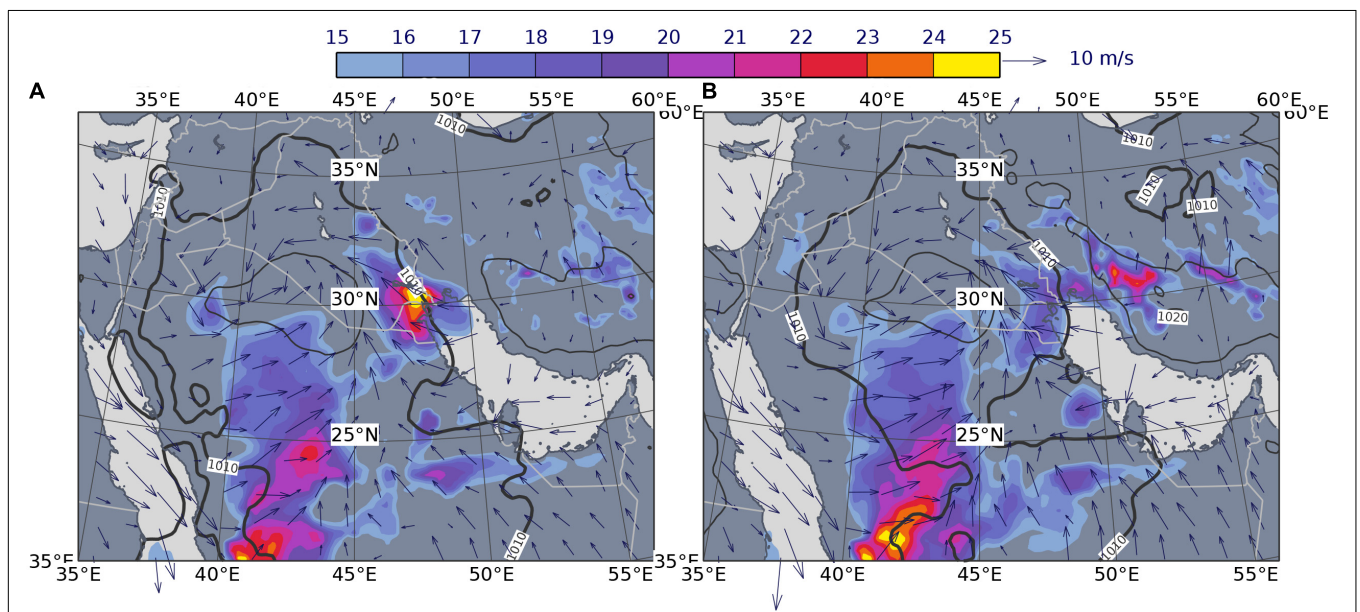


**FIGURE 3 |** Mean sea level pressure contours, wind vectors at 10 m, and wind gust (shown by colors) at (A) 4:00 AM UTC; (B) 6:00 AM UTC.

6-class graupel scheme (Thompson et al., 2008) and the WSM6-class scheme (Hong and Lim, 2006); (CU): the Grell–Devenyi ensemble scheme (Grell and Dévényi, 2002), the New Tiedtke Scheme (Zhang and Wang, 2017) and the Kain–Fritsch scheme (Kain, 2004); (PBL): the Yonsei University scheme

(Hong et al., 2006), the Mellor–Yamada–Janjic (MYJ) scheme (Janjić, 1994) and the Mellor–Yamada–Nakanishi–Niino (MYNN) 2.5 scheme (Nakanishi and Niino, 2006). The YSU PBL scheme was used along with the revised MM5 similarity theory surface layer (Jiménez et al., 2012), while the MYJ and MYNN PBL



scheme was used along with the Eta similarity scheme (Monin and Obukhov, 1954) and MYNN scheme (Nakanishi and Niino, 2006) respectively. For all simulations, the Noah-MP (Niu et al., 2011) land surface scheme was used. The Goddard scheme for shortwave (Chou and Suarez, 1994) and the Rapid Radiative Transfer Model [RRTM; Mlawer et al. (1997)] for longwave radiation was used. Since domain resolution was less than 5 km, the cumulus parameterization was switched off for the local domain in all simulations according to Athukorala et al. (2021). The parameterization schemes incorporated into the model are summarized in **Table 1**.

### Wave Model

The WAVEWATCH-III (hereinafter WWIII) is a state-of-the-art, phase-averaged model which numerically solves the conservation of wave action as below:

$$\frac{dN}{dt} = \frac{S_{tot}}{\sigma} \tag{1}$$

The left-hand side of Eq. (1) includes the local rate of change in wave action, wave propagation in  $x$  and  $y$  dimensions, and wave propagation in  $\sigma$  and  $\theta$  spaces. The wave action  $N$  is equal to  $\frac{E}{\sigma}$ , where  $E$  is wave energy density and  $\sigma$  is the angular frequency. The term  $S_{tot}$  incorporates a sink and source terms among which the exponential wind-wave growth ( $S_{in}$ ), non-linear quadruplet ( $S_{nl}$ ), and dissipation due to white capping ( $S_{ds}$ ) are important in deep waters (WAVEWATCH III Development Group WW3DG, 2016).

Several packages are available for  $S_{in}$  and  $S_{ds}$  in WWIII. Janssen (1991) parameterized wind input term as a function of  $\frac{u_*}{C}$ , wave-supported stress, and wind logarithmic profile; where  $u_*$  is friction velocity and  $C$  is phase speed velocity, respectively. This method needs an iterative process to obtain  $u_*$  which is valid simultaneously in both wave-supported stress and wind profile. This method is known as WAM-Cycle4 or  $ST3$  formulation in WWIII.

The whitecap dissipation in  $ST3$  includes weighted linear and non-linear dependency to wave numbers using  $\delta_1$  and  $\delta_2 = 1 - \delta_1$  coefficients. The  $C_{ds}$  is a tuning parameter in this formulation while  $\bar{k}$ ,  $\bar{\sigma}$ ,  $\bar{\alpha}$  are mean wave number, mean angular frequency and mean steepness, respectively.

$$S_{ds}(k, \theta) = C_{ds} (\bar{\alpha}^2) \bar{\sigma} \left[ \delta_1 \frac{k}{\bar{k}} + \delta_2 \left( \frac{k}{\bar{k}} \right)^2 \right] N(k, \theta) \tag{2}$$

In this research  $\delta_1$  and  $C_{ds}$  will be considered as tuning parameters.

The most recent package for wind input and energy dissipation implemented in WWIII is  $ST6$ . The wind input term includes two parts that depend on wave direction ( $\theta$ ), wind direction ( $\theta_w$ ), wind velocity ( $U$ ), and  $C$ . The  $w_1$  part controls the wind input term when  $\cos(\theta - \theta_w)$  is greater than 0; otherwise  $w_2$  will be dominant which includes ‘negative wind input’ (Donelan et al., 2006).

$$\begin{aligned} w_1 &= \max^2 \left\{ 0, \frac{U}{C} \cos(\theta - \theta_w) - 1 \right\}, \\ w_2 &= \min^2 \left\{ 0, \frac{U}{C} \cos(\theta - \theta_w) - 1 \right\} \\ w &= w_1 - a_0 w_2 \end{aligned} \tag{3}$$

In this study,  $a_0$  was set to 0.09 according to Liu et al. (2017). In Eq. (3),  $U$  could be scaled with  $32u_*$  to avoid overestimation of energy levels at high frequencies (Liu et al., 2019). This scale was used in many recent research [e.g., Christakos et al. (2020), Kalourazi et al. (2020), Beyramzadeh et al. (2021)].

The whitecap dissipation in  $ST6$  includes  $T_1$  term which presents the inherent breaking term, and  $T_2$  term which describes the cumulative effects of short-wave breaking due to longer waves [Rogers et al. (2012), Zieger et al. (2015)]:

$$S_{ds}(k, \theta) = [T_1(k, \theta) + T_2(k, \theta)] N(k, \theta) \tag{5}$$

These  $T_1$  and  $T_2$  terms have tuning coefficients  $a_1$  and  $a_2$  which were used for calibration.

Wind vectors, bathymetry, and open boundary conditions are crucial for wave models. Besides six introduced wind experiments presented in **Table 1**, the original ERA5 wind data were used as wind input for wave simulations. The temporal resolution for all wind data was 1 hour. Both  $ST3$  and  $ST6$  formulations were used to reproduce  $H_s$  and  $T_p$ . Default values for tuning parameters in  $ST3$  were  $C_{ds} = -4.5$  and  $\delta_1 = 0.5$ . For  $ST6$  formulation,  $a_1 = 4.75 \times 10^{-6}$  and  $a_2 = 7 \times 10^{-5}$  were default values. These  $ST3$  and  $ST6$  formulations were calibrated against AD measurements and altimeter data using ERA5 wind in the Persian Gulf and the Gulf of Oman by Beyramzadeh et al. (2021) (hereafter BSD2021). Their suggested values for tuning parameters were also used which are  $C_{ds} = -1.5$  and  $\delta_1 = 0$  for  $ST3$ , and  $a_1 = 1.05 \times 10^{-7}$  and  $a_2 = 1.74 \times 10^{-6}$  for  $ST6$ . Therefore, ERA5 wind data will be

**TABLE 1** | List of the physical options for WRF modeling.

Ensemble	Microphysics	Cumulus	Planetary boundary layer	Longwave radiation	Shortwave radiation	Surface layer physics	Land Surface physics
EXP1	Thompson	New Tiedtke	YSU	RRTM	Goddard	Revised MM5	Noah-MP
EXP2		Grell-Devenyi	MYJ	RRTM	Goddard	Eta Similarity	Noah-MP
EXP3		Kain-Fritsch	MYNN	RRTM	Goddard	MYNN	Noah-MP
EXP4	WSM6	Kain-Fritsch	MYNN	RRTM	Goddard	MYNN	Noah-MP
EXP5		New Tiedtke	YSU	RRTM	Goddard	Revised MM5	Noah-MP
EXP6		Grell-Devenyi	MYJ	RRTM	Goddard	Eta Similarity	Noah-MP

assessed using two sets of coefficients: (1) described default tuning values for *ST3* and *ST6* formulations (2) suggested calibration values by BSD2021 for the Persian Gulf.

The bathymetry data were extracted from The General Bathymetric Chart of the Oceans (GEBCO) which were released with high spatial resolution  $0.004^\circ$  in 2019. Hourly boundary conditions were extracted in the form of directional wave spectra from a global wave modeling. Directional wave spectra were implemented along the southern ( $23^\circ\text{N}$ ,  $59.2^\circ - 61^\circ\text{E}$ ) and eastern ( $61^\circ\text{E}$ ,  $23^\circ - 25.2^\circ\text{N}$ ) open boundaries of the computational domain. More details about the global model were presented in BSD2021.

The computational grid in the WWIII model covers  $47.2^\circ - 61^\circ\text{E}$  and  $23^\circ - 31^\circ\text{N}$  using a rectangular grid with  $0.04^\circ \times 0.04^\circ$  resolution. Following Siadatmousavi et al. (2012), 30 frequencies with geometrical distribution were considered in the range of 0.04–0.63 Hz. Moreover, 36 directions with  $10^\circ$  resolution were applied. Four time-steps are needed in the WWIII model: (1) maximum global time-step was set as 360 s; (2) the maximum CFL time-step for x-y was set as 180 s; (3) the maximum CFL time-step for k-theta was set as 360 s; (4) time-step for source term was set as 30 s.

The non-linear quadruplet wave-wave interaction ( $S_{nl}$ ) mainly controls wave spectrum evolution in wave models. It is the most time-consuming term in simulations; therefore, the DIA (Discrete interaction Approximation) method proposed by Hasselmann et al. (1985) has been presented for operational applications. Resio and Perrie (2008) and Perrie et al. (2013) compared the obtained  $S_{nl}$  term for the JONSWAP spectrum with different peak enhancement parameters ( $\gamma = 1, 3.3, \text{ and } 7$ ) against the exact solution (Webb-Resio-Tracy method). For fully developed spectrum ( $\gamma = 1$ ), the positions of positive and negative lobes are identical with the exact solution, but the DIA overestimates (underestimates) positive (negative) lobes. As a consequence, more dissipation and more wind input energy are needed on forward and rear faces, respectively. Simulated  $S_{nl}$  term with the DIA deviates from the exact solution with increasing  $\gamma$  parameter. Furthermore, spurious positive and negative lobes have appeared on the rear face of the spectrum. It is inferable that the deficiencies of the DIA method in reproducing  $S_{nl}$  the term should be compensated with other sink and source terms ( $S_{in}$  and  $S_{ds}$ ). It is expected that the wind input and whitecap calibration with the DIA method might result in unrealistic coefficient values.

The Gaussian Quadrature Method (GQM) is a recent method to estimate  $S_{nl}$  term in deep water conditions, developed by Lavrenov (2001) and implemented as a portable Fortran module in the TOMWAC model by Benoit (2005). The GQM method strongly depends on the integration resolution. Rough, medium, and fine resolutions were evaluated in duration and fetch limited test cases, slanting fetch, and test cases with varying wind direction. More agreement with the exact solution is expected when medium and fine resolutions were applied, while they are more expensive than rough resolution and the DIA method (Benoit, 2005, 2007; Gagnaire-Renou et al., 2009; Gagnaire-Renou et al., 2010). For the first time, the GQM with the medium resolution was implemented in the WWIII model and used to

simulate wind waves during the presence of meteotsunami in the Persian Gulf. Similar to the DIA, this method was combined with a depth scale proposed by Komen et al. (1994) to be used in the shallow water of the Persian Gulf.

## Statistical Indices

For this part, three statistical indices were applied to skill assess the WRF and WWIII models against measurements: mean bias error (*MBE*), root mean square error (*RMSE*), and index of agreement (*d*) presented by Willmott (1982):

$$MBE = \frac{\sum(M_i - O_i)}{N} \quad (6)$$

$$RMSE = \sqrt{\frac{1}{N} \sum(M_i - O_i)^2} \quad (7)$$

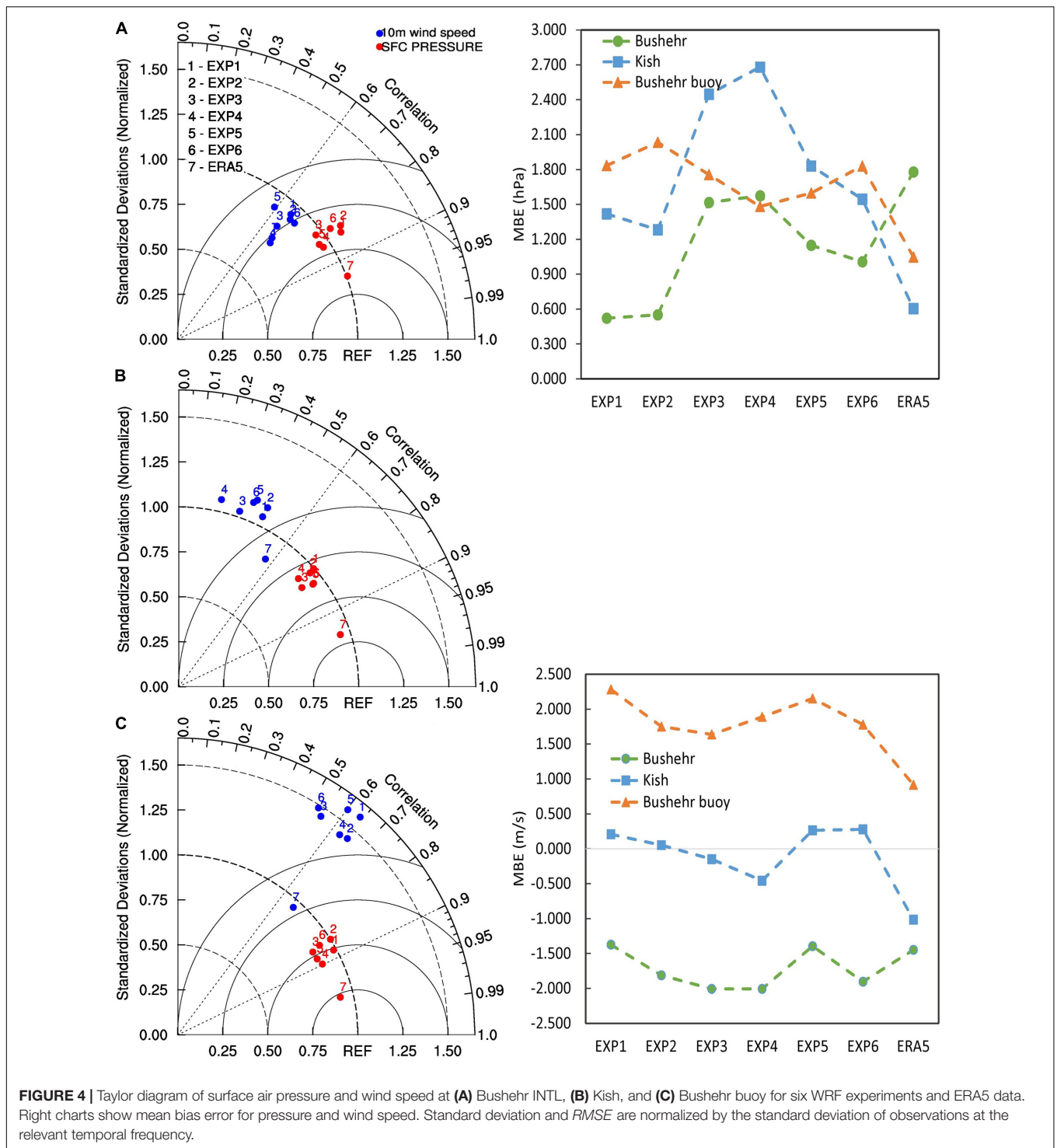
$$d = 1 - \frac{(M_i - O_i)^2}{\sum(|M_i - \bar{O}| + |O_i - \bar{O}|)^2} \quad (8)$$

in which  $M_i$  and  $O_i$  are modeled and observed data, respectively.  $N$  is the total number of observations. All indicators are calculated with hourly data. Note that  $d$  is a dimensionless index that quantifies the agreement between the two series of data; the value of  $d$  index larger than 0.5 indicates good performance of the model.

## RESULTS

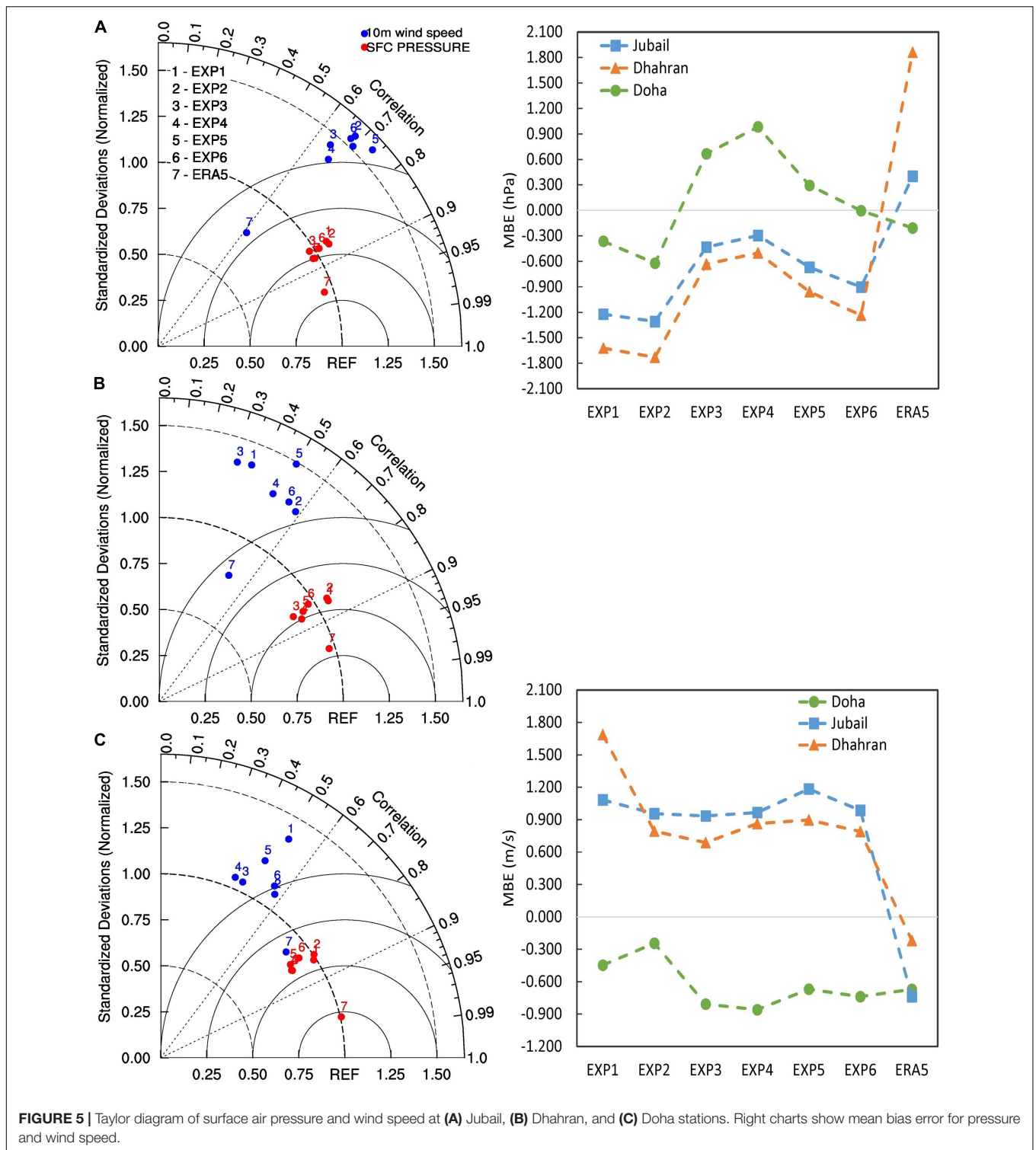
### Skill Assessment of Weather and Research Forecasting Model

Taylor diagram and statistical parameters (*MBE*) for different stations and different experiments are designated in **Figures 4, 5**. Also, the value of the agreement coefficient parameter ( $d$ ) for each station is given in **Table 2**. Taylor diagram is a statistical summary that presents the correlation coefficient, normalized standard deviation and root mean square error (Taylor, 2001). As seen from **Figure 4**, EXP1 and EXP2 were superior to other experiments at Bushehr and Kish stations for predicting wind pressure and speed. The agreement index and the correlation for wind speed for all experiments at Bushehr station were more than 0.6, indicating that all of them had acceptable performance according to Borge et al. (2008). The correlation coefficients between wind speed data from observations and simulations at Kish station were less than 0.5. At Bushehr buoy station, EXP4 had good performance for pressure, and EXP2 and EXP4 had good performance for wind speed. The *MBE* values of surface air pressure at Bushehr synoptic station, Bushehr buoy, and Kish station indicate that pressure values are generally overestimated. No trend exists for wind speed; e.g., the wind speed at Bushehr synoptic station is underestimated while it is overestimated at Bushehr buoy station. At Kish station, unlike other experiments, the *MBE* values for EXP3 and EXP4 were negative. The *MBE* value for EXP2 at this station was close to zero. In general, according to **Figure 4** and **Table 2**, at northern



Gulf stations, EXP3 and EXP4 (using Mellor-Yamada-Nakanishi-Niino scheme for planetary boundary layer and surface layer) slightly overestimated the surface pressure at the ground level stations and underestimated the wind speed. In contrast, over the water body (i.e., at Bushehr buoy), they tend to reduce the amount of surface pressure and relatively increase the wind speed compared to other schemes.

As shown in **Figure 5**, at Daharan, Jubail, and Doha stations, EXP2 and EXP4 configurations were more successful than other combinations for surface pressure and wind speed estimation, respectively. At these ground-level stations, the MYNN boundary layer scheme increased surface pressure and relatively decreased wind speed compared to YSU and MYJ schemes. The results of combining the MYNN planetary boundary layer scheme and the



Thompson microphysics scheme were better than the MYNN and WSM6 microphysics scheme for pressure and wind speed estimation. Unlike stations of the northern Persian Gulf, at these stations (except the three ensembles No. 3, 4, and 5 at Doha station), the estimation of surface pressure was less than the observations. Wind speed was underestimated at Doha station

and overestimated at Jubail and Daharan stations. In general, the MYJ boundary layer scheme, which is a local influenced scheme, resulted in a better estimation of wind speed than two non-local YSU and local MYNN schemas in the Persian Gulf meteotsunami occurrence period. Regarding the index of the agreement for pressure and wind speed obtained from

**TABLE 2** | Index of agreement (d) between model results and *in situ* observations at the different synoptic stations and wave buoys considered in the present study.

Parameter	Ensemble	Bushehr INTL	Bushehr buoy	Kish	Jubail	Dhahran	DOHA
				<b>d</b>			
<b>Surface pressure</b>	EXP1	<b>0.903</b>	0.920	0.802	0.887	0.866	<b>0.913</b>
	EXP2	0.892	0.902	<b>0.811</b>	0.888	0.855	0.900
	EXP3	0.828	0.917	0.700	0.914	0.901	0.892
	EXP4	0.846	<b>0.942</b>	0.666	<b>0.930</b>	<b>0.919</b>	0.876
	EXP5	0.870	0.932	0.778	0.921	0.893	0.892
	EXP6	0.869	0.914	0.803	0.904	0.875	0.897
	ERA5	<u>0.852</u>	<u>0.957</u>	<u>0.922</u>	<u>0.964</u>	<u>0.825</u>	<u>0.941</u>
<b>Wind speed</b>	EXP1	<b>0.750</b>	0.673	0.668	0.773	0.537	0.696
	EXP2	0.726	<b>0.727</b>	<b>0.673</b>	0.764	<b>0.727</b>	<b>0.755</b>
	EXP3	0.685	0.660	0.615	0.762	0.562	0.654
	EXP4	0.682	0.703	0.535	0.777	0.666	0.620
	EXP5	0.706	0.688	0.641	<b>0.787</b>	0.657	0.675
	EXP6	0.727	0.661	0.637	0.763	0.703	0.734
	ERA5	<u>0.735</u>	<u>0.772</u>	<u>0.721</u>	<u>0.756</u>	<u>0.694</u>	<u>0.850</u>

The bold numbers show the best experiments at each station which can be easily compared with ERA5 shown underlined.

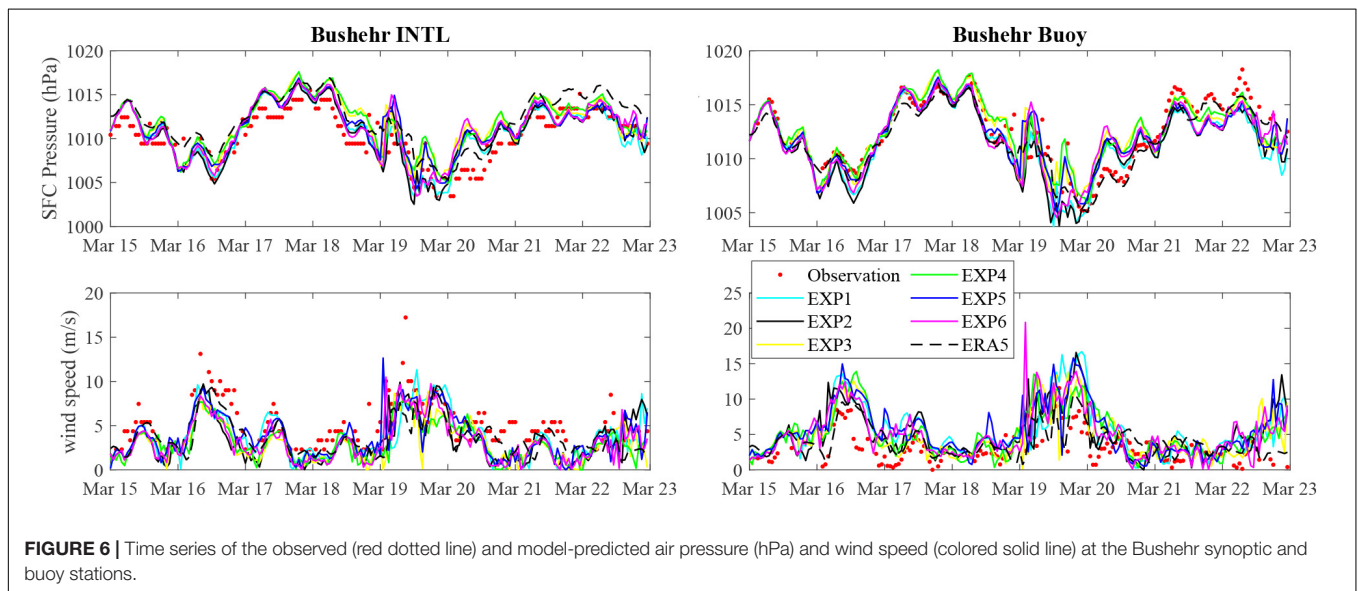


**FIGURE 6** | Time series of the observed (red dotted line) and model-predicted air pressure (hPa) and wind speed (colored solid line) at the Bushehr synoptic and buoy stations.

different ensembles of the WRF model as well as ERA5 data, improvements at some stations were obtained using WRF model ensembles compared to ERA5 data.

The time series of pressure and wind speed from different WRF configurations and ERA5 data at two synoptic stations and Bushehr buoy are designated in **Figure 6**. The transverse of a low-pressure system has been resolved by all scenarios on 19 March and 20 March in all simulations.

Regarding *MBE* at these two stations, which is also characterized in **Figure 4**, the predicted pressure values in all simulations were greater than the observations. The EXP4 had better estimates of pressure changes on the water surface than on land. Wind speed time-series changes also indicated that the overall trends of simulations were close to observations; however, all of them underestimated the wind speed during peaks (including meteotsunami occurrence) at the Bushehr synoptic

station. The configurations EXP2 and EXP1 outperformed others in reproducing wind speed at this station. In contrast, all experiments overestimated the wind speed at the Bushehr buoy. The worst-case was EXP6 which predicted 20 m/s wind speed at the moment of meteotsunami occurrence.

The results of the WRF simulated and measured radiosounding data at 12 UTC on 19 March 2017, are compared and presented in **Figure 7**. In general, all simulations accurately reproduced the temperature and moisture content of the atmosphere but overestimated the moisture content in the upper troposphere. Also, at pressure levels less than 250 hPa, the temperature value was overestimated in all simulations. The same occurred near the ground surface by EXP1 and EXP2 parametrizations. The temperature changes were smooth in EXP3. This configuration showed a sudden temperature inversion in the middle of 500–700 hPa pressure level; however,

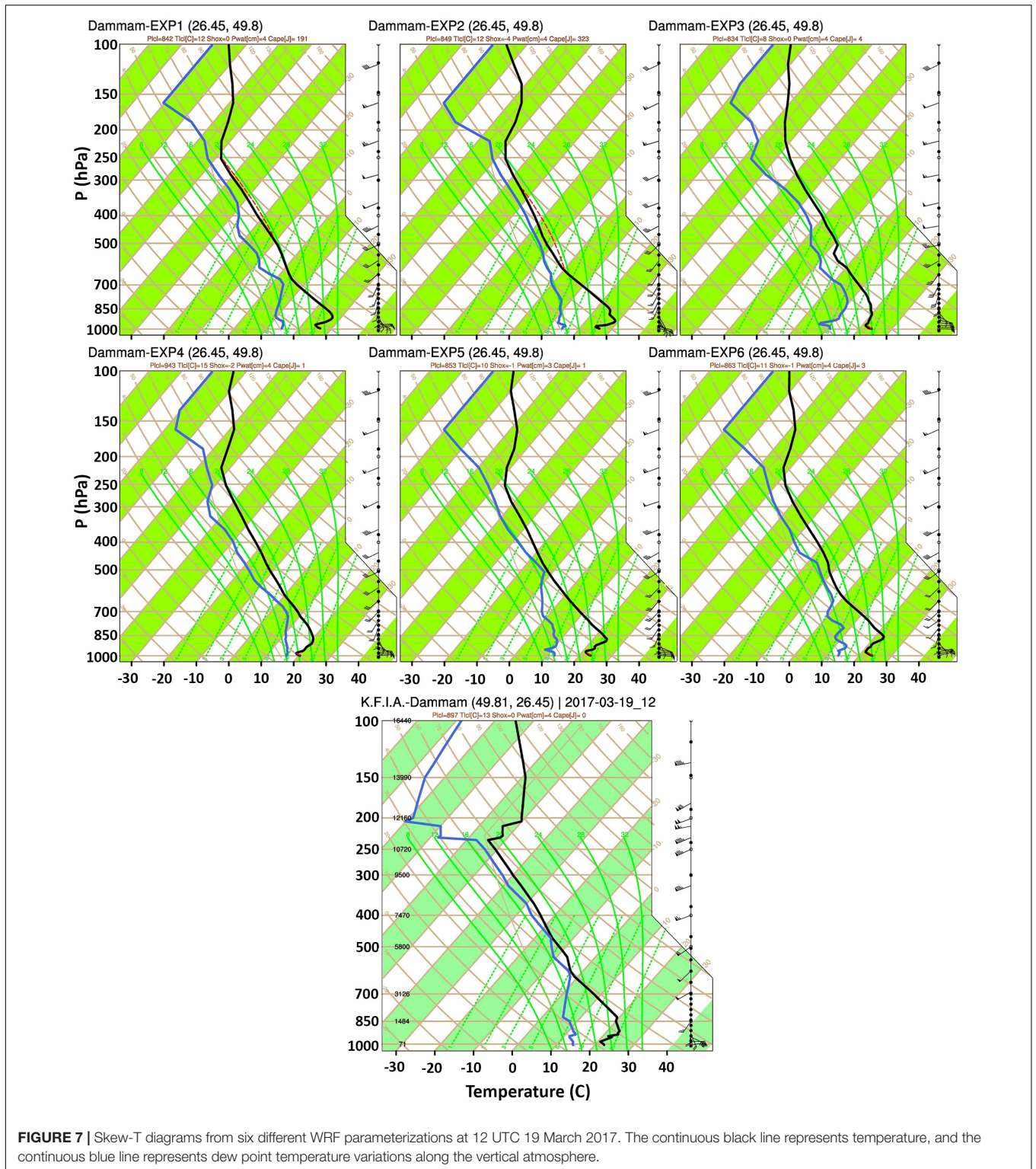


**FIGURE 7** | Skew-T diagrams from six different WRF parameterizations at 12 UTC 19 March 2017. The continuous black line represents temperature, and the continuous blue line represents dew point temperature variations along the vertical atmosphere.

this configuration was not able to simulate temperature changes in the upper troposphere. EXP2 parameterization had a better ability to estimate moisture content in the atmosphere. The closeness of the dew point temperature to the air temperature at pressure levels of 300–700 hPa was well simulated by this

parameterization. The maximum wind speed was observed at a pressure level of 250 hPa at the measuring station; however, it was estimated to occur close to 500 hPa in all simulations. In sum, the EXP2 configuration (using Mellor-Yamada-Janjic scheme for the planetary boundary layer, Grell–Devenyi cumulus

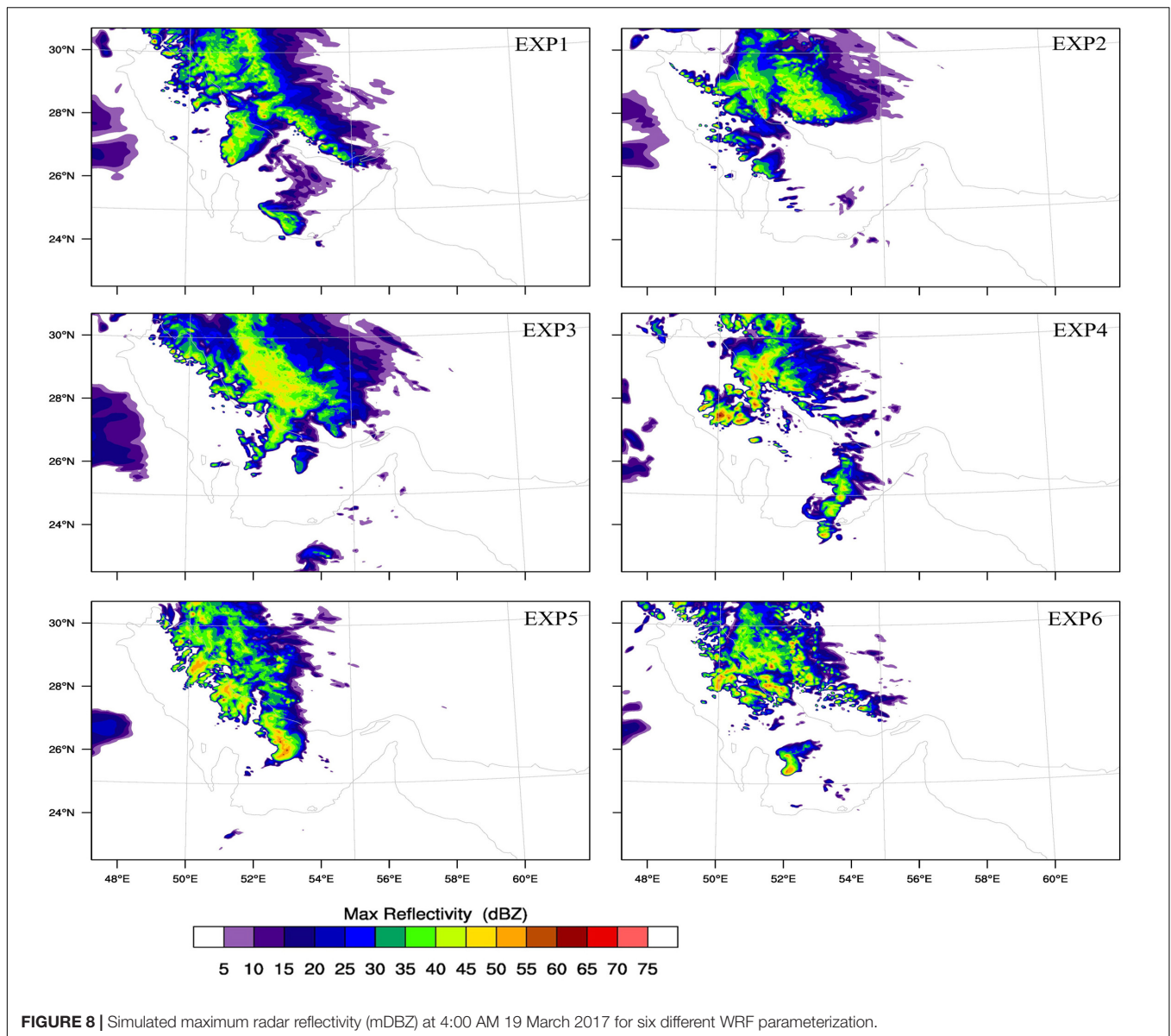


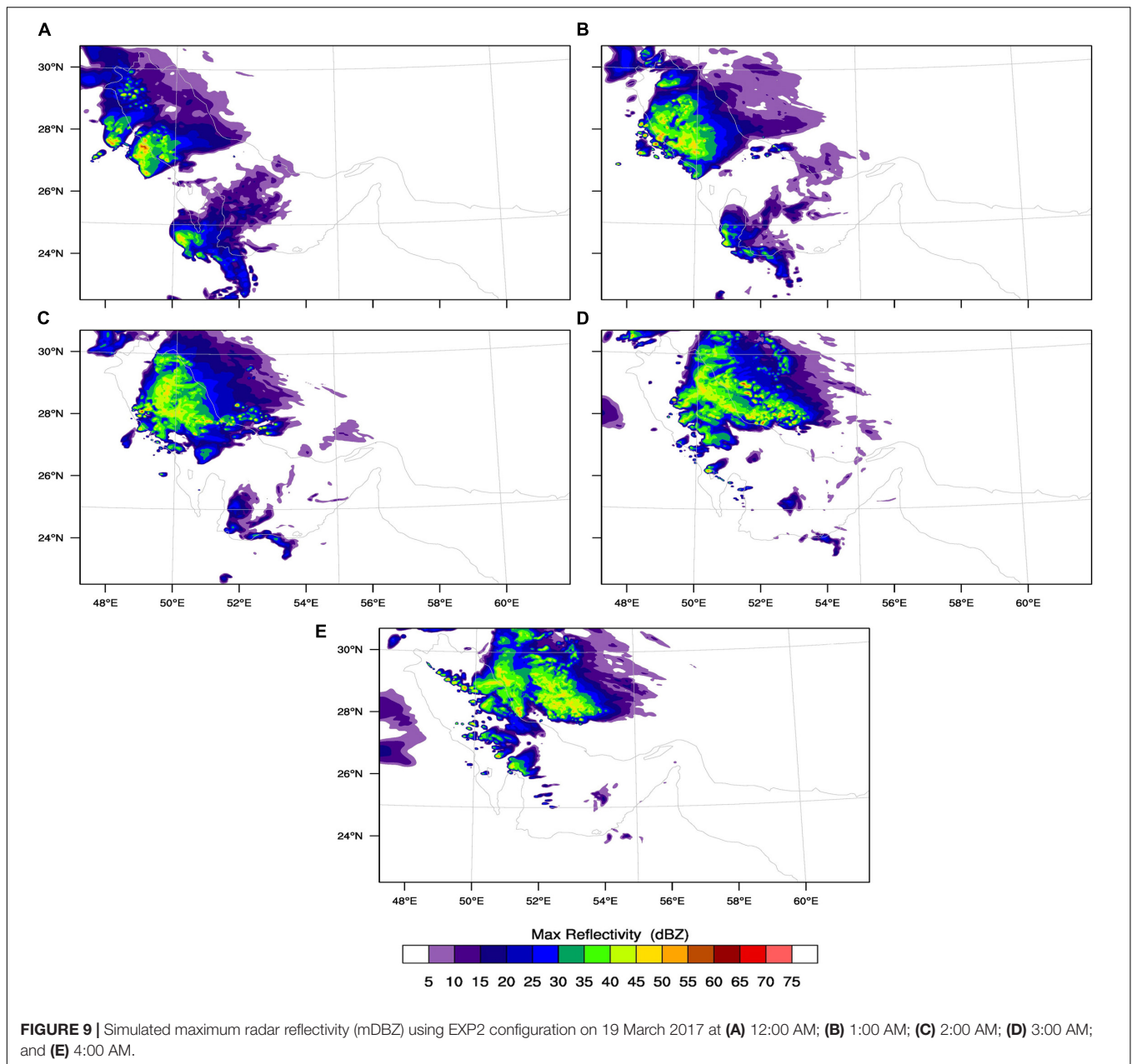
**FIGURE 8** | Simulated maximum radar reflectivity (mDBZ) at 4:00 AM 19 March 2017 for six different WRF parameterization.

scheme, and Thompson microphysics scheme) provided the most realistic results regarding atmospheric moisture content and vertical temperature parameter in the Persian Gulf during the period of meteotsunami event on 19 March 2017.

The maximum radar reflectivity has been investigated to further evaluate the intensity and structure of convective clouds and assess the sensitivity of the mesoscale simulations to the choice of the microphysics and convective parameterization (see **Figure 8**). The results from the innermost model domain were used. Note that in both outermost and innermost domains, heat and moisture tendencies were determined by microphysics parameterization. Therefore, the effects of convective parameterization propagated from the outermost domain to the innermost domain. Model-derived maximum radar reflectivity at 4:00 AM 19 March 2017 showed that simulations with WSM6 microphysics produced slightly stronger reflectivity, especially in the southern part of the domain.

Comparisons with radar data showed that in this area, both WSM6 and Thompson microphysics provided excessive reflectivity [cf. Figure 10 in Kazeminezhad et al. (2021)]. Also, simulations with the Kain–Fritsch scheme provided too intense radar reflectivity. The overall shape of maximum reflectivity distribution at this moment was well simulated by EXP2 parametrizations.

The maximum reflectivity index greater than 60 dbz was introduced by Šepić and Rabinovich (2014) and Kazeminezhad et al. (2021) as a signature for convective cells which followed with meteotsunami formation in the domain; however, a lower value of 40 dbz was also considered as a meteotsunami source in the Gulf of Mexico (e.g., Shi et al., 2019). The hourly simulated maximum reflectivity index was presented in **Figure 9** using EXP2 from 12:00 to 4:00 AM UTC 19 March. Two nearly horizontal and vertical convective systems were entered the Persian Gulf at 12:00 AM from west and south, respectively.



As time passed, the southerly vertical system weakened and eventually disappeared, while the westerly horizontal system strengthened to 55–60 dbz and spatially extended from 1:00 to 02:00 AM. It slightly decreased at 3:00 AM UTC; however, increased to 55–60 dbz at 4:00 AM UTC again as it moved eastward. Described pattern for simulated maximum reflectivity from 12:00 to 4:00 AM is in agreement with Bushehr radar data described by Kazeminezhad et al. (2021).

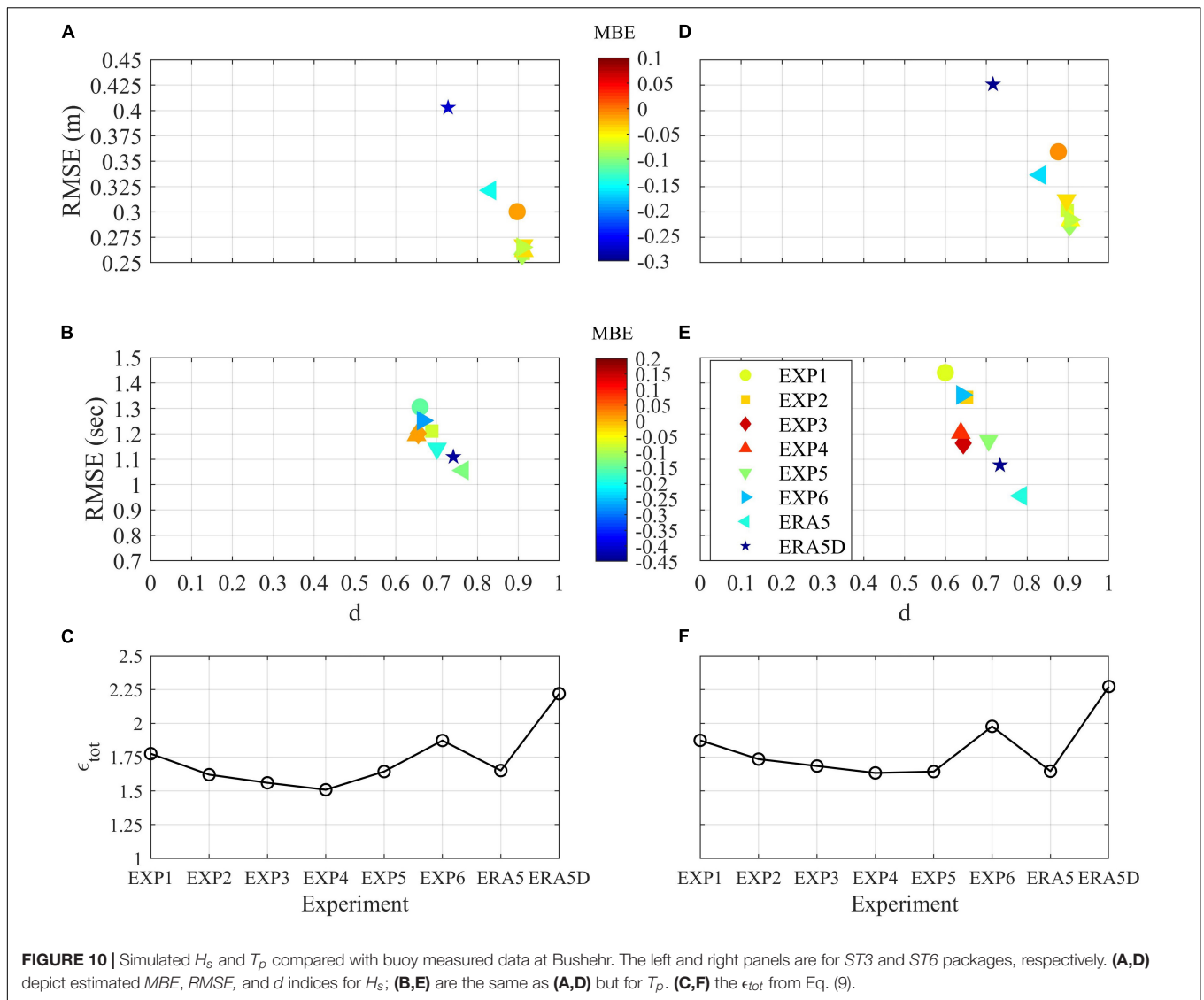
### Skill Assessment of WAVEWATCH-III

In **Figure 10**, Simulated  $H_s$  and  $T_p$  parameters with  $ST3$  and  $ST6$  packages of WWIII model for eight experiments were compared to buoy measurements at Bushehr during 15–23 March. The

performance of the model using WRF experiments was close with small differences; e.g., EXP1 parameterizations resulted in the lowest absolute  $MBE$  and high  $RMSE$  for  $H_s$  hindcast. Also, EXP3 led to  $\sim 0.1 H_s$  underestimation and low  $RMSE$ . Unlike  $H_s$ , EXP1 parameterization has severely underestimated  $T_p$ . The most successful configuration for reproducing  $T_p$  was EXP3.

Furthermore, ERA5 data with default coefficients of the model (ERA5D hereafter) severely underestimated  $H_s$  and  $T_p$  parameters. This experiment presented the worst performance in reproducing  $H_s$ . Unlike ERA5D, applying ERA5 wind data with the calibrated tuning values (ERA5 experiment) proposed for the Persian Gulf by BSD2021, considerably improved both  $H_s$  and  $T_p$  predictions. It is worth mentioning that the  $ST6$  is more





sensitive than  $ST3$  to wind experiments. To determine the best configuration, the following error parameter  $\epsilon_{tot}$  was defined:

$$\epsilon_{tot} = |MBE|_{H_s} + RMSE_{H_s} + |MBE|_{T_p} + RMSE_{T_p} \quad (9)$$

This error parameter was evaluated for eight experiments and results are presented in **Figures 10C,F**.  $EXP4$  parameterizations using  $ST3$  resulted in the lowest  $\epsilon_{tot}$ , while  $EXP4$ ,  $EXP5$  parameterizations and  $ERA5$  experiments using  $ST6$  could result in a similar low  $\epsilon_{tot}$  value at Bushehr buoy; hence  $EXP4$  at Bushehr station could be selected as the optimum configuration when either  $ST3$  or  $ST6$  was applied.  $ERA5D$  using both  $ST3$  and  $ST6$  packages led to high  $\epsilon_{tot}$  which emphasized the importance of model calibration. The accuracy of  $ST3$  was slightly better than  $ST6$  at this station which is in accordance with BSD2021.

The time series of simulated and measured  $H_s$ ,  $T_p$  and mean wave direction were presented in **Figure 11**. According to wind evaluations presented in **Figure 10**,  $EXP4$  and  $ERA5$

parameterizations were selected for further investigations using  $ST3$  and  $ST6$  formulations. As it is clear,  $H_s$  was underestimated by the  $ERA5$  experiment at Bushehr buoy during events on 16–17 March and 19–20 March. In contrast, bulk wave parameters from  $EXP4$  were in good agreement with the trend of measurements; hence, the  $ERA5$  wind data was not suitable for wave hindcast during the dominance of meteotsunami in the Persian Gulf, while  $EXP4$  parameterization led to reasonable performance when either  $ST3$  or  $ST6$  package was used with the default tuning values.

In **Table 3**, simulated  $H_s$  and  $T_p$  were used to assess the importance of  $S_{nl}$  term in the model. In this evaluation, both  $ST3$  and  $ST6$  packages were used with  $EXP4$  wind data. Since the GQM has been applied with  $ST3$  and  $ST6$  for the first time in this study, a calibration was performed; hence  $C_{ds} = -4$  and  $\delta_1 = 0$  were obtained for  $ST3$ , and  $a_1 = 2.75 \times 10^{-6}$  and  $a_2 = 5 \times 10^{-5}$  were determined for  $ST6$ . For each package, four setups were considered: (1) Default tuning values for  $S_{ds}$  term and the DIA method for  $S_{nl}$  term; (2) Default tuning values for  $S_{ds}$  term

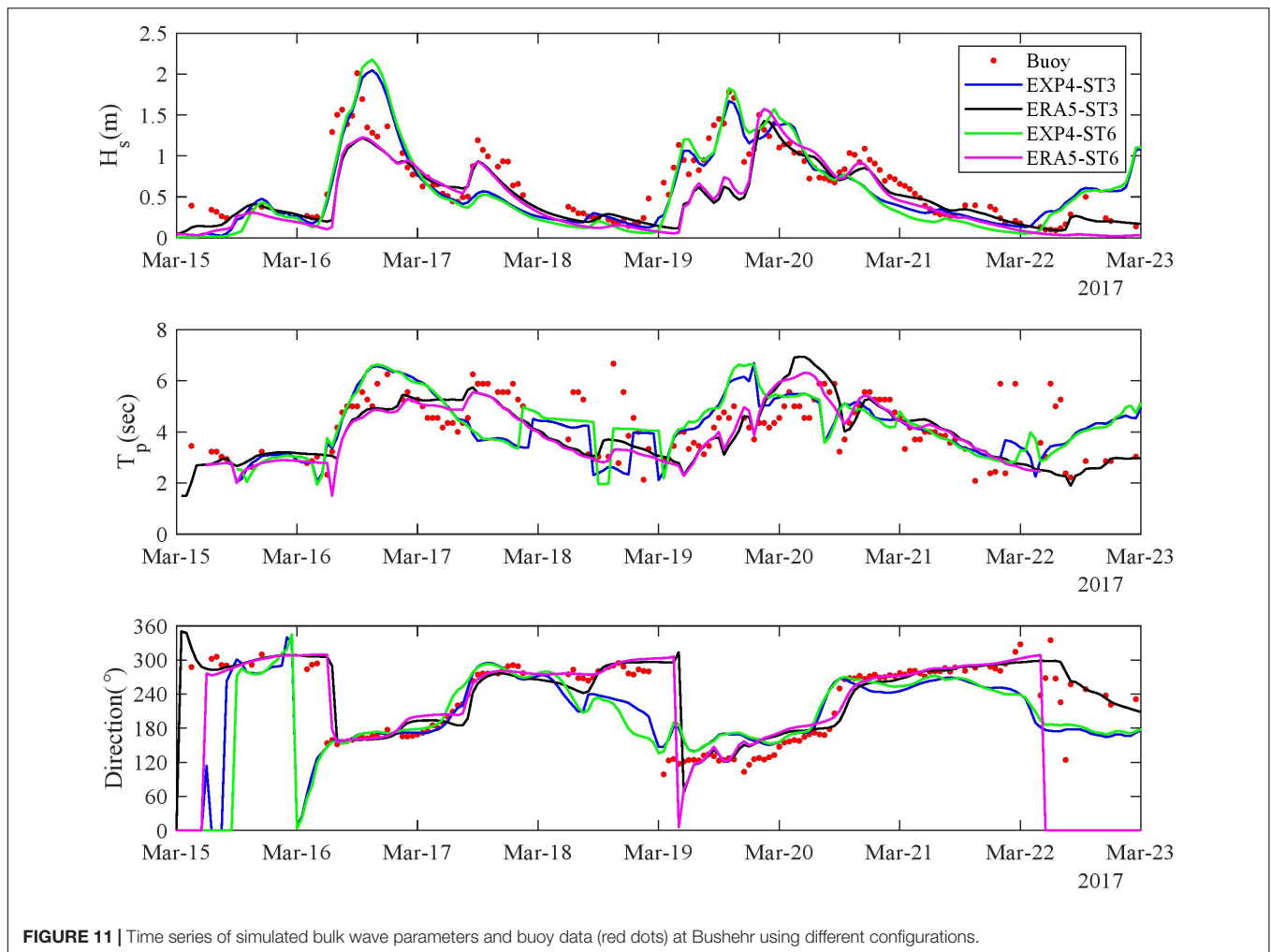


**FIGURE 11** | Time series of simulated bulk wave parameters and buoy data (red dots) at Bushehr using different configurations.

and GQM method for  $S_{nl}$  term; (3) Calibrated values for  $S_{ds}$  and the DIA method for  $S_{nl}$  term; (4) Calibrated values for  $S_{ds}$  and the GQM method for  $S_{nl}$  term.

Following results inferred from **Table 3**: (1) use of calibrated values for  $C_{ds}$  and  $\delta_1$  ( $C_{ds} = -4$  and  $\delta_1 = 0$ ) with the GQM were resulted in  $t_{ot} = 1.5085$  which was identical to the employment of default values ( $C_{ds} = -4.5$  and  $\delta_1 = 0.5$ ) and the DIA method ( $t_{ot} = 1.5087$ ). The value of  $\delta_1 = 0$  with the GQM was in agreement with the findings of Rogers et al. (2003). Default tuning values in  $S_{ds}$  term with the GQM and calibrated tuning values for  $S_{ds}$  term with the DIA method for  $S_{nl}$  term were the worst cases with highest  $t_{ot}$ . (2) Similar to  $ST3$ , obtained tuning values ( $a_1 = 2.75 \times 10^{-6}$ ,  $a_2 = 5 \times 10^{-5}$ ) for  $ST6$  when the GQM was considered for  $S_{nl}$  term were lower than default values ( $a_1 = 4.75 \times 10^{-6}$ ,  $a_2 = 7 \times 10^{-5}$ ). The GQM using calibrated values outperformed other setups according to  $t_{ot}$ ; the improvement was marginal compared to the DIA method with default values though.

The wave spectrum evolution simulated by  $ST3$  and  $ST6$  packages using the GQM and DIA methods were compared in **Figure 12**. Based on results presented in **Table 3**, default tuning values for white capping terms were applied in combination with

the DIA, while calibrated values were considered when the GQM was employed. The highest energy density occurred during 16–17 March. The GQM method in the model has resulted in sharper peaks in the spectrum than the DIA method. As shown in several studies, the spectral peak was estimated smoother and lower than reality by the DIA (Gagnaire-Renou et al., 2010; Rogers and Van Vledder, 2013), and the GQM could improve this deficiency in the wave model.

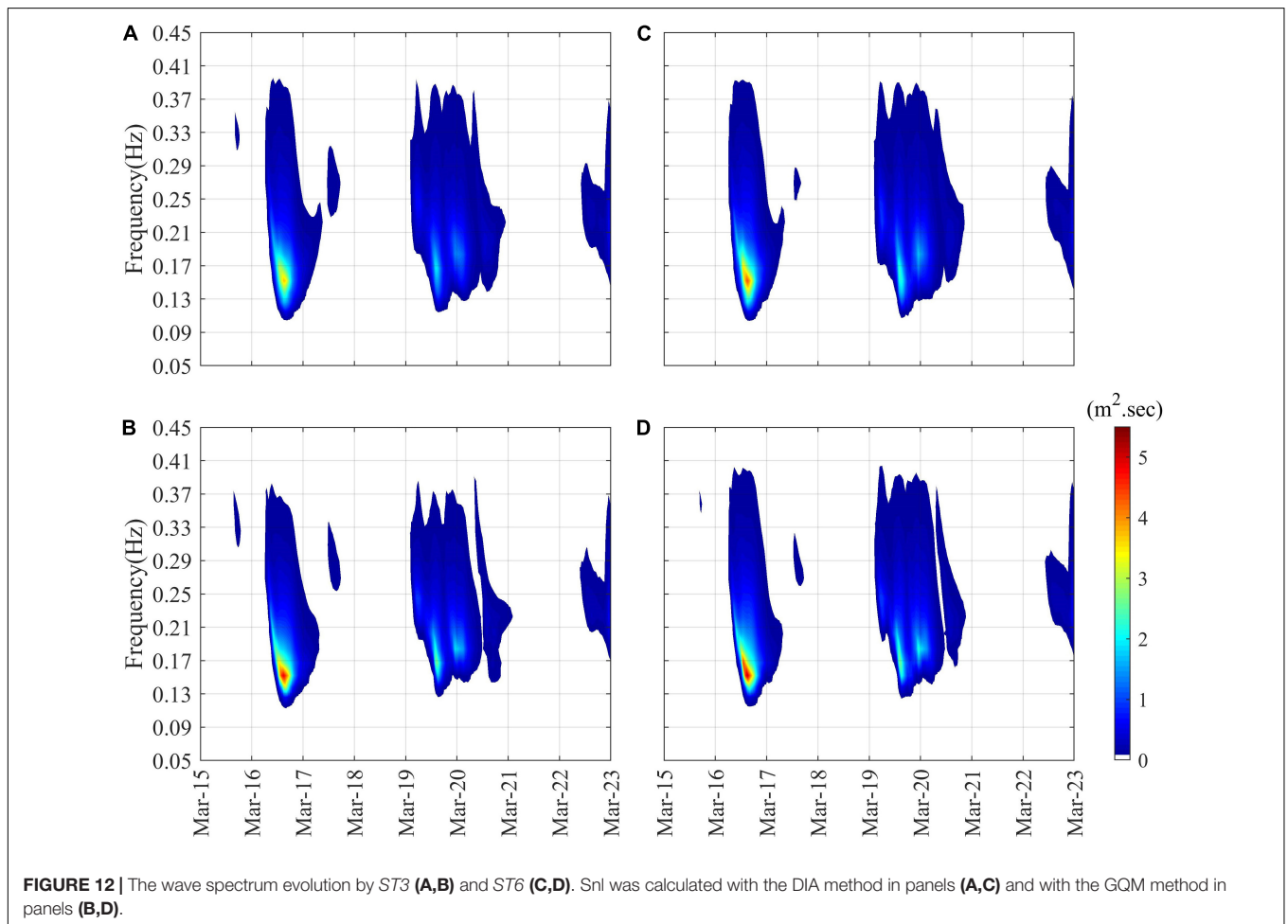
The energy content close to the peak of the spectrum was also more intense for  $ST6$  than  $ST3$ . During the high energy event of 16–17 March,  $ST6$  resulted in higher energy content, even in the high-frequency tail of the spectrum. It is following the results of Kalourazi et al. (2020) who compared different formulations during hurricane Ivan's passage over the Gulf of Mexico. This pattern was also confirmed by ideal and field tests in previous studies (e.g., Zieger et al., 2015; van Vledder et al., 2016). Having more energetic predictions over the entire frequency band also occurred for other events during 19–20 March when  $ST6$  with the GQM was used as compared with other combinations.

The main reason for deviation in the model performance by  $ST3$  and  $ST6$  packages could be explained by the contribution of  $S_{in}$ ,  $S_{ds}$ , and  $S_{nl}$  terms to  $S_{tot}$  in Eq. (1). The spectrum evolution of

**TABLE 3** | The ST3 and ST6 packages using EXP4 wind data with two methods DIA and GQM for  $S_{nl}$  term were evaluated against buoy measured data at Bushehr.

Bushehr Buoy		$H_s$			$T_p$			
Methods	Setup	MBE	RMSE	$d$	MBE	RMSE	$d$	<i>tot</i>
ST3	Default/DIA	-0.0427	0.2612	0.9138	0.0111	1.1937	0.6509	<b><u>1.5087</u></b>
	Default/GQM	-0.0873	0.2630	0.9095	-0.1362	1.1636	0.6726	1.6501
	$C_{ds} = -4.0, \delta_1 = 0$ /DIA	-0.0409	0.2656	0.9123	0.1104	1.2006	0.6679	1.6175
	$C_{ds} = -4.0, \delta_1 = 0$ /GQM	-0.0591	0.2650	0.9123	0.0322	1.1522	0.6667	<b><u>1.5085</u></b>
ST6	Default/DIA	-0.0525	0.2917	0.9059	0.0861	1.2028	0.6377	1.6331
	Default/GQM	-0.0908	0.2931	0.9019	-0.0393	1.1744	0.6476	1.5976
	$a_1 = 2.75 \times 10^{-6}, a_2 = 5 \times 10^{-5}$ /DIA	-0.0275	0.3020	0.9034	0.1326	1.2121	0.6346	1.6742
	$a_1 = 2.75 \times 10^{-6}, a_2 = 5 \times 10^{-5}$ /GQM	-0.0620	0.2989	0.9026	0.0191	1.1827	0.6436	<b><u>1.5627</u></b>

The optimum setups were identified by bold-underlined.



$S_{tot}$  (not shown here) indicates that the energy content is close to the peak of  $S_{tot}$  was higher for ST6 than for ST3. This explains the peak wave period overestimation by ST6. Also, when the GQM was used for  $S_{nl}$  instead of DIA, a concentrated positive lobe at slightly higher frequencies occurred. Furthermore, the negative lobe was less extended to higher frequencies for the GQM than for the DIA method. As a consequence, more energy is transferred to high frequencies when GQM was employed which alleviated the wave peak period overestimation.

### CONCLUSION

Ensemble prediction is a practical approach to handle uncertainties in numerical model predictions. This is essential during complex meteorological conditions such as meteotsunamis due to the importance of small-scale atmospheric processes (Mourre et al., 2021). This study skill assessed the performance of the WRF physics ensemble of a high-resolution modeling system in retrieving atmospheric processes which led to

recent meteotsunami in the Persian Gulf. Numerical experiments with initial and boundary conditions driven from the ECMWF IFS CY41r2 high-resolution operational analysis database were used to study the detailed representation of surface air pressure and wind speed during 15–23 March 2017 in the Persian Gulf. Six experiments were used with 2 microphysics (Thompson and WSM6), 3 cumulus physics schemes (New Tiedtke, Kain-Fritsch, and Grell–Devenyi), and 3 planetary boundary layer schemes (YSU, MYJ, and MYNN) along with Goddard and RRTM as short-wave and long-wave radiation schemes.

Using Mellor–Yamada–Nakanishi–Niino scheme for planetary boundary layer and surface layer, EXP3 and EXP4 parameterizations overestimated surface pressure at the ground level stations and underestimated the wind speed. However, for stations inside the water body, it results to lower surface pressure and relatively higher wind speed compared to other experiments. The results indicated that combining MYNN planetary boundary layer scheme and the Thompson microphysics scheme provided the most reliable results for pressure and wind speed predictions. Also, wind speed is estimated better for either the MYJ or MYNN boundary layer scheme than non-local YSU during the Persian Gulf meteotsunami event. It implied that the turbulent eddies during this time period were small over the Persian Gulf and localized in nature. In general, EXP4 parameterization (using MYNN scheme for planetary boundary layer and surface layer) had the best performance at stations over water and EXP2 parameterization (using MYJ scheme for planetary boundary layer and Eta similarity for surface layer) had the best performance at stations on land.

Additional numerical experiments were performed to evaluate the sensitivity of WRF simulations to the selection of microphysics and convective parameterization using heat and moisture content in the atmosphere and maximum radar reflectivity. The results showed that all simulations were successful in reproducing temperature and moisture content in the atmosphere, but they overestimated the moisture content in the upper troposphere. Also, simulations with WSM6 microphysics produced slightly stronger reflectivity, especially at the southern part of the domain. Radar data indicated that in that area, both WSM6 and Thompson microphysics provided excessive reflectivity.

Both *ST3* and *ST6* packages in the WWIII model were used with six WRF experiments and ERA5 wind data to reproduce  $H_s$  and  $T_p$  during 15–23 March 2017. Two sets of tuning parameters were used when ERA5 wind data were used: (1) default tuning values; (2) calibrated tuning values proposed by BSD2021. Buoy measurements at Bushehr were used for model assessments. A new error parameter was introduced to determine the most suitable wind data for the wave model during the dominance of

meteotsunami in the Persian Gulf. The lowest error was obtained when wind data were produced by the EXP4 parameterization. The ERA5 data led to the severe underestimation of  $H_s$  and  $T_p$  in the model.

For the first time, the exact GQM was implemented in the WWIII model to compensate for the deficiencies of the DIA in deep water. The GQM could be faster than available exact solutions in the third-generation wave models. The preliminary calibration of tuning parameters for  $S_{ds}$  the term was performed when the GQM was applied for  $S_{nl}$  term in the wave model. It is inferable that slightly better performances of the model relative to the DIA method were achieved when lower tuning values were applied.

Conducting two-way coupling between atmosphere, ocean, and wave models using the new implemented  $S_{nl}$  term for reproducing meteotsunami forerunner longwave and its interaction with high-frequency wind waves would be the next step to better study this meteotsunami event.

## DATA AVAILABILITY STATEMENT

The data analyzed in this study is subject to the following licenses/restrictions: Part of data comes from Iran Meteorological Organization and the Port and Maritime Organization (PMO) of Iran; and any user should directly asked data from them. ERA5 data can be downloaded directly from their website. Requests to access these datasets should be directed to <https://marinedata.pmo.ir/>; <https://cds.climate.copernicus.eu/cdsapp#!/search?type=dataset>.

## AUTHOR CONTRIBUTIONS

MR and SS contributed to conception and design of the study. MR performed WRF and COAWST simulations while MB performed wave modeling. MR and MB provided the first draft of the manuscript and it was finalized by SS. All authors contributed to manuscript revision, read, and approved the submitted version.

## ACKNOWLEDGMENTS

We thank the Iran Meteorological Organization for providing synoptic data. The wave buoys data were provided by the Port and Maritime Organization (PMO) of Iran, respectively. ERA5 reanalysis data were downloaded from the ECMWF dataset. We should appreciate Eftekhari who revisited the manuscript from the point of view of the English proficiencies.

## REFERENCES

- Akbari, P., Sadrasab, M., Chegini, V., and Siadatmousavi, M. (2016). Tidal constituents in the Persian Gulf, Gulf of Oman and Arabian Sea: a numerical study. *Indian J. Geo Mar. Sci.* 45, 1010–1016.
- Al-Hajri, K. R. (1990). *The Circulation of the Arabian (Persian) Gulf: a Model Study of its Dynamics*. Washington, DC: The Catholic University of America.
- Ambraseys, N. N. (2008). “Descriptive catalogues of historical earthquakes in the Eastern Mediterranean and the Middle East; revisited,” in *Historical Seismology*, eds J. Frechet and M. Meghraoui (Berlin: Springer).
- Athar, H., and Ammar, K. (2016). Seasonal characteristics of the large-scale moisture flux transport over the Arabian Peninsula. *Theor. Appl. Climatol.* 124, 565–578. doi: 10.1007/s00704-015-1437-7

- Athukorala, R., Thol, T., Neluwala, P., Petri, M., Sengxeu, S., Lattada, L., et al. (2021). Evaluating the performance of a WRF physics ensemble in simulating rainfall over Lao PDR during wet and dry seasons. *Adv. Meteorol.* 2021:6630302. doi: 10.1155/2021/6630302
- Belušić, D., Grisogono, B., and Klaić, Z. B. (2007). Atmospheric origin of the devastating coupled air-sea event in the east Adriatic. *J. Geophys. Res. Atmospheres* 112:14. doi: 10.1029/2006JD008204
- Benoit, M. (2005). "Evaluation of methods to compute the non-linear quadruplet interactions for deep-water wave spectra," in *Proceedings 5th International Symposium Ocean Wave Measurement and Analysis* (Israel: WAVES), 3–7.
- Benoit, M. (2007). "Implementation and Test of Improved Methods for Evaluation of Nonlinear Quadruplet Interactions in a Third Generation Wave Model," in *Coastal Engineering 2006*, ed. J. M. Smith, Vol. 5. Singapore: World Scientific, 526–538. doi: 10.1142/9789812709554\_0046
- Beyramzadeh, M., Siadatmousavi, S. M., and Derkani, M. H. (2021). Calibration and skill assessment of two input and dissipation parameterizations in WAVEWATCH-III model forced with ERA5 winds with application to Persian Gulf and Gulf of Oman. *Ocean Eng.* 219:108445. doi: 10.1016/j.oceaneng.2020.108445
- Borge, R., Alexandrov, V., Del Vas, J. J., Lumbreras, J., and Rodríguez, E. (2008). A comprehensive sensitivity analysis of the WRF model for air quality applications over the Iberian Peninsula. *Atmos. Environ.* 42, 8560–8574. doi: 10.1016/j.atmosenv.2008.08.032
- Cavaleri, L., and Bertotti, L. (2003). The characteristics of wind and wave fields modelled with different resolutions. *Quart. J. R. Meteorol. Soc.* 129, 1647–1662. doi: 10.1256/qj.01.68
- Cavaleri, L., and Bertotti, L. (2006). The improvement of modelled wind and wave fields with increasing resolution. *Ocean Eng.* 33, 553–565. doi: 10.1016/j.oceaneng.2005.07.004
- Chou, M.-D., and Suarez, M. J. (1994). *An Efficient Thermal Infrared Radiation Parameterization for Use in General Circulation Models*, NASA Tech. Memo. 104606. Linthicum Heights, MD: NASA Center for Aerospace Information, 85.
- Christakos, K., Björkqvist, J.-V., Tuomi, L., Furevik, B. R., and Breivik, Ø (2020). Modelling wave growth in narrow fetch geometries: the white-capping and wind input formulations. *Ocean Model.* 157:101730. doi: 10.1016/j.ocemod.2020.101730
- Denamiel, C., Šepić, J., Ivanković, D., and Vilibić, I. (2019). The Adriatic Sea and Coast modelling suite: evaluation of the meteotsunami forecast component. *Ocean Model.* 135, 71–93. doi: 10.1016/j.ocemod.2019.02.003
- Donelan, M. A., Babanin, A. V., Young, I. R., and Banner, M. L. (2006). Wave-follower field measurements of the wind-input spectral function. Part II: parameterization of the wind input. *J. Phys. Oceanogr.* 36, 1672–1689. doi: 10.1175/JPO2933.1
- El-Sabh, M., and Murty, T. (1989). Storm surges in the Arabian Gulf. *Nat. Hazards* 1, 371–385. doi: 10.1007/BF00134834
- Gagnaire-Renou, E., Benoit, M., and Forget, P. (2009). "Modeling waves in fetch-limited and slanting fetch conditions using a quasi-exact method for nonlinear four-wave interactions," in *Coastal Engineering 2008*, Vol. 5, ed. J. M. Smith (Singapore: World Scientific), 496–508. doi: 10.1142/9789814277426\_0042
- Gagnaire-Renou, E., Benoit, M., and Forget, P. (2010). Ocean wave spectrum properties as derived from quasi-exact computations of nonlinear wave-wave interactions. *J. Geophys. Res. Oceans* 115. doi: 10.1029/2009JC005665
- Grell, G. A., and Dévényi, D. (2002). A generalized approach to parameterizing convection combining ensemble and data assimilation techniques. *Geophys. Res. Lett.* 29, 38–31–38–34. doi: 10.1029/2002GL015311
- WAVEWATCH III Development Group WW3DG (2016). *User Manual and System Documentation of Wavewatch III version 5.16*. Technical Note 329. Washington, DC: NOAA
- Hasselmann, S., Hasselmann, K., Allender, J., and Barnett, T. (1985). Computations and parameterizations of the nonlinear energy transfer in a gravity-wave spectrum. Part II: parameterizations of the nonlinear energy transfer for application in wave models. *J. Phys. Oceanogr.* 15, 1378–1391. doi: 10.1175/1520-0485(1985)015<1378:CAPOTN>2.0.CO;2
- Heidarzadeh, M., Pirooz, M. D., Zaker, N. H., Yalciner, A. C., Mokhtari, M., and Esmaeily, A. (2008). Historical tsunami in the Makran Subduction Zone off the southern coasts of Iran and Pakistan and results of numerical modeling. *Ocean Eng.* 35, 774–786. doi: 10.1016/j.oceaneng.2008.01.017
- Heidarzadeh, M., Šepić, J., Rabinovich, A., Allahyar, M., Soltanpour, A., and Tavakoli, F. (2020). Meteorological tsunami of 19 March 2017 in the Persian Gulf: observations and analyses. *Pure Appl. Geophys.* 177, 1231–1259. doi: 10.1007/s00024-019-02263-8
- Hong, S.-Y., and Lim, J.-O. J. (2006). The WRF single-moment 6-class microphysics scheme (WSM6). *Asia Pac. J. Atmos. Sci.* 42, 129–151.
- Hong, S.-Y., Noh, Y., and Dudhia, J. (2006). A new vertical diffusion package with an explicit treatment of entrainment processes. *Mon. Weather Rev.* 134, 2318–2341. doi: 10.1175/MWR3199.1
- Horvath, K., and Vilibić, I. (2014). "Atmospheric mesoscale conditions during the Boothbay meteotsunami: a numerical sensitivity study using a high-resolution mesoscale model," in *Meteorological Tsunamis: the US East Coast and Other Coastal Regions*, eds I. Vilibić and S. Monserrat (Berlin: Springer), 55–74. doi: 10.1007/978-3-319-12712-5\_4
- Horvath, K., Šepić, J., and Prtenjak, M. T. (2018). Atmospheric forcing conducive for the Adriatic 25 June 2014 meteotsunami event. *Pure Appl. Geophys.* 175, 3817–3837. doi: 10.1007/s00024-018-1902-1
- Janjić, Z. I. (1994). The step-mountain eta coordinate model: further developments of the convection, viscous sublayer, and turbulence closure schemes. *Mon. Weather Rev.* 122, 927–945. doi: 10.1175/1520-0493(1994)122<0927:TSMECM>2.0.CO;2
- Janssen, P. A. (1991). Quasi-linear theory of wind-wave generation applied to wave forecasting. *J. Phys. Oceanogr.* 21, 1631–1642. doi: 10.1175/1520-0485(1991)021<1631:QLTOWW>2.0.CO;2
- Jiménez, P. A., Dudhia, J., González-Rouco, J. F., Navarro, J., Montávez, J. P., and García-Bustamante, E. (2012). A revised scheme for the WRF surface layer formulation. *Mon. Weather Rev.* 140, 898–918. doi: 10.1175/MWR-D-11-00056.1
- Kain, J. S. (2004). The Kain–Fritsch convective parameterization: an update. *J. Appl. Meteorol.* 43, 170–181. doi: 10.1175/1520-0450(2004)043<0170:TKCPAU>2.0.CO;2
- Kalourazi, M. Y., Siadatmousavi, S. M., Yeganeh-Bakhtiari, A., and Jose, F. (2020). WAVEWATCH-III source terms evaluation for optimizing hurricane wave modeling: a case study of Hurricane Ivan. *Oceanologia* 63, 194–213. doi: 10.1016/j.oceanol.2020.12.001
- Kamranzad, B. (2018). Persian Gulf zone classification based on the wind and wave climate variability. *Ocean Eng.* 169, 604–635. doi: 10.1016/j.oceaneng.2018.09.020
- Kazeminezhad, M. H., Vilibić, I., Denamiel, C., Ghafarian, P., and Negah, S. (2021). Weather radar and ancillary observations of the convective system causing the northern Persian Gulf meteotsunami on 19 March 2017. *Nat. Hazards* 106, 1747–1769. doi: 10.1007/s11069-020-04208-0
- Komen, G., Cavaleri, L., Donelan, M., Hasselmann, K., Hasselmann, S., and Janssen, P. (1994). *Dynamics and Modelling of Ocean Waves*. Cambridge: Cambridge University Press. doi: 10.1017/CBO9780511628955
- Lavrenov, I. V. (2001). Effect of wind wave parameter fluctuation on the nonlinear spectrum evolution. *J. Phys. Oceanogr.* 31, 861–873. doi: 10.1175/1520-0485(2001)031<0861:EOWWPF>2.0.CO;2
- Liao, Y.-P., and Kaihatu, J. M. (2016). The effect of wind variability and domain size in the Persian Gulf on predicting nearshore wave energy near Doha. *Qatar. Appl. Ocean Res.* 55, 18–36. doi: 10.1016/j.apor.2015.11.012
- Lin, N., and Emanuel, K. (2016). Grey swan tropical cyclones. *Nat. Clim. Change* 6, 106–111. doi: 10.1038/nclimate2777
- Linares, Á, Wu, C. H., Bechle, A. J., Anderson, E. J., and Kristovich, D. A. R. (2019). Unexpected rip currents induced by a meteotsunami. *Sci. Rep.* 9. doi: 10.1038/s41598-019-38716-2
- Liu, Q., Babanin, A., Fan, Y., Zieger, S., Guan, C., and Moon, I.-J. (2017). Numerical simulations of ocean surface waves under hurricane conditions: assessment of existing model performance. *Ocean Model.* 118, 73–93. doi: 10.1016/j.ocemod.2017.08.005
- Liu, Q., Rogers, W. E., Babanin, A. V., Young, I. R., Romero, L., Zieger, S., et al. (2019). Observation-based source terms in the third-generation wave model WAVEWATCH III: updates and verification. *J. Phys. Oceanogr.* 49, 489–517. doi: 10.1175/JPO-D-18-0137.1
- Mlawer, E. J., Taubman, S. J., Brown, P. D., Iacono, M. J., and Clough, S. A. (1997). Radiative transfer for inhomogeneous atmospheres: RRTM, a validated correlated-k model for the longwave. *J. Geophys. Res. Atmos.* 102, 16663–16682. doi: 10.1029/97JD00237
- Modarress, B., Ansari, A., and Thies, E. (2012). The effect of transnational threats on the security of Persian Gulf maritime petroleum transportation. *J. Transportation Security* 5, 169–186. doi: 10.1007/s12198-012-0090-y

- Monin, A. S., and Obukhov, A. M. (1954). Basic laws of turbulent mixing in the surface layer of the atmosphere. *Contrib. Geophys. Inst. Acad. Sci. USSR* 151:e187.
- Monserrat, S., Vilibić, I., and Rabinovich, A. B. (2006). Meteotsunamis: atmospherically induced destructive ocean waves in the tsunami frequency band. *Nat. Hazards Earth Syst. Sci.* 6, 1035–1051. doi: 10.5194/nhess-6-1035-2006
- Mourre, B., Santana, A., Buils, A., Gautreau, L., Lièer, M., Jansá, A., et al. (2021). On the potential of ensemble forecasting for the prediction of meteotsunamis in the Balearic Islands: sensitivity to atmospheric model parameterizations. *Nat. Hazards* 106, 1315–1336. doi: 10.1007/s11069-020-03908-x
- Nadim, F., Bagtzoglou, A. C., and Iranmahboob, J. (2008). Coastal management in the Persian Gulf region within the framework of the ROPME programme of action. *Ocean Coast. Manag.* 51, 556–565. doi: 10.1016/j.ocecoaman.2008.04.007
- Nakanishi, M., and Niino, H. (2006). An improved Mellor–Yamada level-3 model: its numerical stability and application to a regional prediction of advection fog. *Boundary Layer Meteorol.* 119, 397–407. doi: 10.1007/s10546-005-9030-8
- Nayak, S., Sandeepan, B., and Panchang, V. (2016). “Effect of high resolution winds on wind-wave simulations in Arabian Gulf,” in *Qatar Foundation Annual Research Conference Proceedings Volume 2016 Issue 1*, (Qatar: Hamad bin Khalifa University Press). doi: 10.5339/qfarc.2016.EEPP2869
- Niu, G.-Y., Yang, Z.-L., Mitchell, K. E., Chen, F., Ek, M. B., Barlage, M., et al. (2011). The community Noah land surface model with multiparameterization options (Noah-MP): 1. model description and evaluation with local-scale measurements. *J. Geophys. Res. Atmos.* 116:19. doi: 10.1029/2010JD015139
- Perrie, W., Toulany, B., Resio, D. T., Roland, A., and Auclair, J.-P. (2013). A two-scale approximation for wave–wave interactions in an operational wave model. *Ocean Model.* 70, 38–51. doi: 10.1016/j.ocemod.2013.06.008
- Rabinovich, A. B. (2020). Twenty-seven years of progress in the science of meteorological tsunamis following the 1992 Daytona Beach event. *Pure Appl. Geophys.* 177, 1193–1230. doi: 10.1007/s00024-019-02349-3
- Rabinovich, A. B., and Thomson, R. E. (2007). “The 26 December 2004 Sumatra tsunami: analysis of tide gauge data from the world ocean Part I. Indian Ocean and South Africa,” in *Tsunami and its Hazards in the Indian and Pacific Oceans*, eds K. Staake, E. A. Okal, and J. C. Borrero (Berlin: Springer), 261–308. doi: 10.1007/978-3-7643-8364-0\_2
- Renault, L., Vizoso, G., Jansá, A., Wilkin, J., and Tintoré, J. (2011). Toward the predictability of meteotsunamis in the Balearic sea using regional nested atmosphere and ocean models. *Geophys. Res. Lett.* 38:7. doi: 10.1029/2011GL047361
- Resio, D. T., and Perrie, W. (2008). A two-scale approximation for efficient representation of nonlinear energy transfers in a wind wave spectrum. Part I: theoretical development. *J. Phys. Oceanogr.* 38, 2801–2816. doi: 10.1175/2008JPO3713.1
- Reynolds, R. M. (1993). Physical oceanography of the Gulf, Strait of Hormuz, and the Gulf of Oman—results from the Mt Mitchell expedition. *Mar. Pollut. Bull.* 27, 35–59. doi: 10.1016/0025-326X(93)90007-7
- Rogers, W. E., and Van Vledder, G. P. (2013). Frequency width in predictions of windsea spectra and the role of the nonlinear solver. *Ocean Model.* 70, 52–61. doi: 10.1016/j.ocemod.2012.11.010
- Rogers, W. E., Babanin, A. V., and Wang, D. W. (2012). Observation-consistent input and whitecapping dissipation in a model for wind-generated surface waves: description and simple calculations. *J. Atmos. Oceanic Technol.* 29, 1329–1346. doi: 10.1175/JTECH-D-11-00092.1
- Rogers, W. E., Hwang, P. A., and Wang, D. W. (2003). Investigation of wave growth and decay in the SWAN model: three regional-scale applications. *J. Phys. Oceanogr.* 33, 366–389. doi: 10.1175/1520-0485(2003)033<0366:IOGWAD>2.0.CO;2
- Salaree, A., Mansouri, R., and Okal, E. A. (2018). The intriguing tsunami of 19 March 2017 at Bandar Dayyer, Iran: field survey and simulations. *Nat. Hazards* 90, 1277–1307. doi: 10.1007/s11069-017-3119-5
- Šepić, J., and Rabinovich, A. B. (2014). “Meteotsunami in the Great Lakes and on the Atlantic coast of the United States generated by the “derecho” of June 29–30, 2012,” in *Meteorological Tsunamis: the US East Coast and Other Coastal Regions*, eds I. Vilibic, S. Monserrat, and A. B. Rabinovich (Berlin: Springer), 75–107. doi: 10.1007/978-3-319-12712-5\_5
- Šepić, J., Vilibić, I., and Belušić, D. (2009). Source of the 2007 Ist meteotsunami (Adriatic Sea). *J. Geophys. Res. Oceans* 114:14. doi: 10.1029/2008JC005092
- Šepić, J., Vilibić, I., Rabinovich, A. B., and Monserrat, S. (2015). Widespread tsunami-like waves of 23–27 June in the Mediterranean and Black Seas generated by high-altitude atmospheric forcing. *Sci. Rep.* 5:11682. doi: 10.1038/srep11682
- Shi, L., Olabarrieta, M., Nolan, D. S., and Warner, J. C. (2020). Tropical cyclone rainbands can trigger meteotsunamis. *Nat. Commun.* 11:678. doi: 10.1038/s41467-020-14423-9
- Shi, L., Olabarrieta, M., Valle-Levinson, A., and Warner, J. C. (2019). Relevance of wind stress and wave-dependent ocean surface roughness on the generation of winter meteotsunamis in the Northern Gulf of Mexico. *Ocean Model.* 140:101408. doi: 10.1016/j.ocemod.2019.101408
- Siadatmousavi, S. M., Jose, F., and Stone, G. (2012). On the importance of high frequency tail in third generation wave models. *Coast. Eng.* 60, 248–260. doi: 10.1016/j.coastaleng.2011.10.007
- Skamarock, C., Klemp, B., Dudhia, J., Gill, O., Liu, Z., Berner, J., et al. (2019). *A Description of the Advanced Research WRF Model Version 4*.
- Taylor, K. E. (2001). Summarizing multiple aspects of model performance in a single diagram. *J. Geophys. Res. Atmos.* 106, 7183–7192. doi: 10.1029/2000JD900719
- Thompson, G., Field, P. R., Rasmussen, R. M., and Hall, W. D. (2008). Explicit forecasts of winter precipitation using an improved bulk microphysics scheme. Part II: implementation of a new snow parameterization. *Mon. Weather Rev.* 136, 5095–5115. doi: 10.1175/2008MWR2387.1
- Thoppil, P. G., and Hogan, P. J. (2010). Persian Gulf response to a wintertime shamal wind event. *Deep Sea Res. Part I Oceanogr. Res. Papers* 57, 946–955. doi: 10.1016/j.dsr.2010.03.002
- van Vledder, G. P., Hulst, S. T. C., and McConochie, J. D. (2016). Source term balance in a severe storm in the Southern North Sea. *Ocean Dyn.* 66, 1681–1697. doi: 10.1007/s10236-016-0998-z
- Vilibić, I., Monserrat, S., Rabinovich, A., and Mihanović, H. (2008). Numerical Modelling of the Destructive Meteotsunami of 15 June, 2006 on the Coast of the Balearic Islands. *Pure Appl. Geophys.* 165, 2169–2195. doi: 10.1007/s00024-008-0426-5
- Vilibić, I., Šepić, J., Rabinovich, A. B., and Monserrat, S. (2016). Modern approaches in Meteotsunami research and early warning. *Front. Mar. Sci.* 3:57. doi: 10.3389/fmars.2016.00057
- Williams, D. A. (2020). *Meteotsunami Generation, Amplification and Occurrence in North-West Europe*. England: The University of Liverpool.
- Willmott, C. J. (1982). Some comments on the evaluation of model performance. *Bull. Am. Meteorol. Soc.* 63, 1309–1313. doi: 10.1175/1520-0477(1982)063<1309:SCOTEO>2.0.CO;2
- Zhang, C., and Wang, Y. (2017). Projected future changes of tropical cyclone activity over the Western North and South Pacific in a 20-km-mesh regional climate model. *J. Clim.* 30, 5923–5941. doi: 10.1175/JCLI-D-16-0597.1
- Zieger, S., Babanin, A. V., Rogers, W. E., and Young, I. R. (2015). Observation-based source terms in the third-generation wave model WAVEWATCH. *Ocean Model.* 96, 2–25. doi: 10.1016/j.ocemod.2015.07.014

**Conflict of Interest:** The authors declare that the research was conducted in the absence of any commercial or financial relationships that could be construed as a potential conflict of interest.

**Publisher's Note:** All claims expressed in this article are solely those of the authors and do not necessarily represent those of their affiliated organizations, or those of the publisher, the editors and the reviewers. Any product that may be evaluated in this article, or claim that may be made by its manufacturer, is not guaranteed or endorsed by the publisher.

Copyright © 2022 Rahimian, Beyramzadeh and Siadatmousavi. This is an open-access article distributed under the terms of the Creative Commons Attribution License (CC BY). The use, distribution or reproduction in other forums is permitted, provided the original author(s) and the copyright owner(s) are credited and that the original publication in this journal is cited, in accordance with accepted academic practice. No use, distribution or reproduction is permitted which does not comply with these terms.



# Sea Levels Dynamical Downscaling and Climate Change Projections at the Uruguayan Coast

Michelle Jackson\*, Monica Fossati and Sebastian Solari

*Instituto de Mecánica de los Fluidos e Ingeniería Ambiental, Facultad de Ingeniería, Universidad de la República, Montevideo, Uruguay*

## OPEN ACCESS

### Edited by:

Adem Akpinar,  
Uludag University,  
Turkey

### Reviewed by:

Ricardo de Camargo,  
University of São Paulo, Brazil  
Matthew Dudley Palmer,  
Met Office Hadley Centre (MOHC),  
United Kingdom

### \*Correspondence:

Michelle Jackson  
mjackson@fing.edu.uy

### Specialty section:

This article was submitted to  
Coastal Ocean Processes,  
a section of the journal  
Frontiers in Marine Science

**Received:** 31 December 2021

**Accepted:** 02 March 2022

**Published:** 25 March 2022

### Citation:

Jackson M, Fossati M and Solari S  
(2022) Sea Levels Dynamical  
Downscaling and Climate Change  
Projections at the Uruguayan Coast.  
*Front. Mar. Sci.* 9:846396.  
doi: 10.3389/fmars.2022.846396

This work implements a dynamical downscaling approach, based on a set of nested two-dimensional hydrodynamic models, to quantify the expected changes in the total sea level climate and its components for the Uruguayan coast, using surface wind and sea level pressure projections from global climate models generated during the Phase 5 of the Coupled Models Inter-Comparison Project, considering three time horizons: historical period (1986-2005), short term (2027-2045) and long term (2082-2100), and the future scenarios RCP 4.5 and RCP 8.5. It is concluded that the main contribution to the projected changes in the area is the regional mean sea level rise, followed in importance by the effect that the increase in the water depth has on the amplitude of the tidal components. Moreover, it is concluded that changes in the meteorological residuals (or surges), associated with potential changes in the atmospheric circulation patterns, are negligible in the study area. The obtained results reinforce the need to resort to dynamic downscaling for projecting total sea level changes in areas characterized by wide and shallow continental shelves and estuaries, as this approach allows to resolve the interactions that may arise between tides, surges and the mean sea level rise, something that cannot be addressed with an approach based solely on statistical downscaling.

**Keywords:** sea level rise, dynamical downscaling, climate change, tide-surge interaction, non-linear effect

## 1 INTRODUCTION

The planning of coastal adaptation measures to climate change requires projections of the changes that are expected to occur in the maritime agents (i.e. waves and sea level) in the future under different scenarios and for different time horizons. There are several studies aimed at quantifying future changes in the waves and sea level climates at global or regional scales (e.g. Hemer et al., 2015; Vousdoukas et al., 2016; Camus et al., 2017; Casas-Prat et al., 2017; Wandres et al., 2017; Meucci et al., 2020). All these studies share a common line of work where results from global climate models (GCM), such as surface winds and sea level pressures (SLP), are used to project changes in the variables of interest in a certain domain, resorting to one of the two methodologies available to this end, known as statistical and dynamic downscaling.

Statistical downscaling methods are based in training statistical models that relate predictor (winds and SLP) and predictand (waves and/or sea levels) variables. These methods are inexpensive

from a computational point of view, which makes it possible to use a large number of GCMs, allowing to improve the quantification of the uncertainty involved and the consensus of the projected changes (Perez et al., 2015). In fact, the studies using statistical downscaling methods usually use all GCM results available (e.g. Wang et al., 2014; Camus et al., 2017). On the other hand, dynamic downscaling is based on the use of physics-based numerical models that are forced with wind and SLP fields time series obtained from the GCM, resulting in high computational costs and, also, in more demanding requirements in terms of spatial and temporal resolution of the GCM used to force the models (e.g. Vousdoukas et al., 2016).

When looking at changes in the sea level, an advantage of the dynamical downscaling over the statistical downscaling is that the use of physic-based numerical models allows for considering the non-linear interactions between the different components that make up the total sea level and its change, namely: mean sea level rise, astronomical tides (or tides) and meteorological residuals (or surges). Unlike dynamical downscaling, the statistical downscaling approach can only determine changes directly associated with changes in atmospheric patterns (see e.g. Camus et al., 2014).

Uruguay has more than 600 km of coast, encompassing both the Río de la Plata estuary and the Atlantic Ocean (**Figure 1**). Along the coast, meteorological residuals and astronomical tides have the same order of magnitude and are important components of the total sea level (Santoro et al., 2013). The main component of the astronomical tide is M2, with amplitudes of up to 15 cm, followed by component O1 in most of the coast (Fernández & Piedra-Cueva, 2011). Regarding the variability of the M2 amplitude along the coast, there is a tendency of higher amplitudes around Colonia and Montevideo, and lower

amplitudes between these and towards the ocean. Studies based on *in situ* measured sea level data showed that the magnitude of the meteorological residuals (or surges) decrease from the inner part of the estuary towards the ocean (Fossati et al., 2013; Santoro et al., 2013).

Despite the importance of specifically knowing how total sea level will change along the Uruguayan coast, there are few studies in relation to this. While there are global studies about mean sea level change projections (e.g. IPCC, 2013; Slangen et al., 2014; Carson et al., 2016), there are no global or regional studies that determine the change in the total sea level climate for this zone.

The objective of this work is to quantify the expected changes in the total sea level climate and its components for the Uruguayan coast, using surface wind and SLP projections from GCM generated during the Phase 5 of the Coupled Models Inter-Comparison Project (CMIP5) (Taylor et al., 2012) in the framework of the WRCP (World Climate Research Program), which are presented in the IPCC fifth report (IPCC, 2013). At the moment, the latest report published by the IPCC is the AR6 (only draft, final publication is expected on September 2022) where the CMIP6 (Eyring et al., 2016) is presented, providing the state of the art climate models; in addition, the Special Report on the Ocean and Cryosphere in a Changing Climate (IPCC, 2019) brings together recent research regarding sea level projections. Nevertheless, at the time of initiating this work only information from IPCC AR5 was available, so this is the one used. Three time horizons are considered: historical period (1986-2005), short term (2027-2045) and long term (2082-2100), and two future scenarios RCP 4.5 and RCP 8.5 (Moss et al., 2010). Given characteristics of the continental shelf and of the Río de la Plata estuary (**Figure 1**), it is expected that non-linear interactions between sea level rise and tides and surges would play a significant role in the estimation of projected changes, so a dynamic downscaling scheme is adopted in this work.

The rest of the document is organized as follows. Sections 2 and 3 describes the methodology and the data used in this study. Obtained results are presented in section 4 and discussed in section 5, while section 6 summarizes the main conclusions.

## 2 METHODS

### 2.1 General Methodology

To obtain sea level projections in the study area, a dynamic downscaling methodology is adopted, based on the implementation of two nested hydrodynamic models. The nested models are called regional and local model, and are forced by the inflows from the tributaries of the Río de la Plata estuary, surface winds and SLP, and tides at its outer oceanic boundaries.

To determine the future sea level climate, the hydrodynamic models are forced with the wind and SLP projections of the GCMs listed in **Table 3**. Results are obtained for three time-horizons: historical, short term (2027-2045) and long term (2082-2100); and for two representative concentration

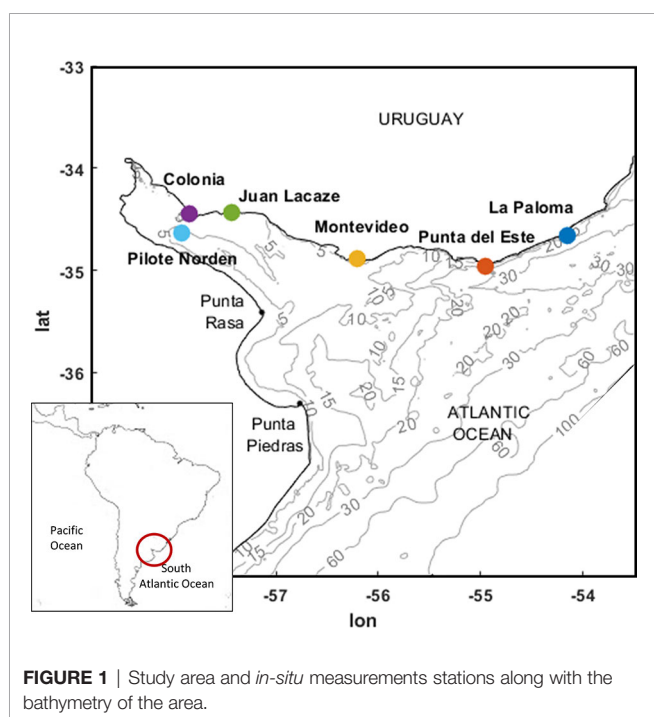


**FIGURE 1** | Study area and *in-situ* measurements stations along with the bathymetry of the area.



pathways scenarios: RCP 4.5 and RCP 8.5. **Figure 2** shows an outline of the methodology. On the one hand, the models are forced with winds and SLP from the CFSR reanalysis (Saha et al., 2010). Sea level time series obtained with this forcing are validated using measured data to later be considered as the ground true (**Figure 2**, left panel). On the other hand, models are forced with GCM winds and SLP for both the historical period and the future periods. First, results from the historical period are used to evaluate whether the models correctly represent the sea level climate in the study area when forced with GCMs. Then, changes in the sea level climate are quantified by comparing historical and future periods for each GCM (**Figure 2**, right panel).

## 2.2 Hydrodynamic Models Setup

Hydrodynamic modeling is carried out by means of two nested numerical models. **Figure 3** shows the domains used in the two models, along with a detail of the inner part of the Río de la Plata estuary.

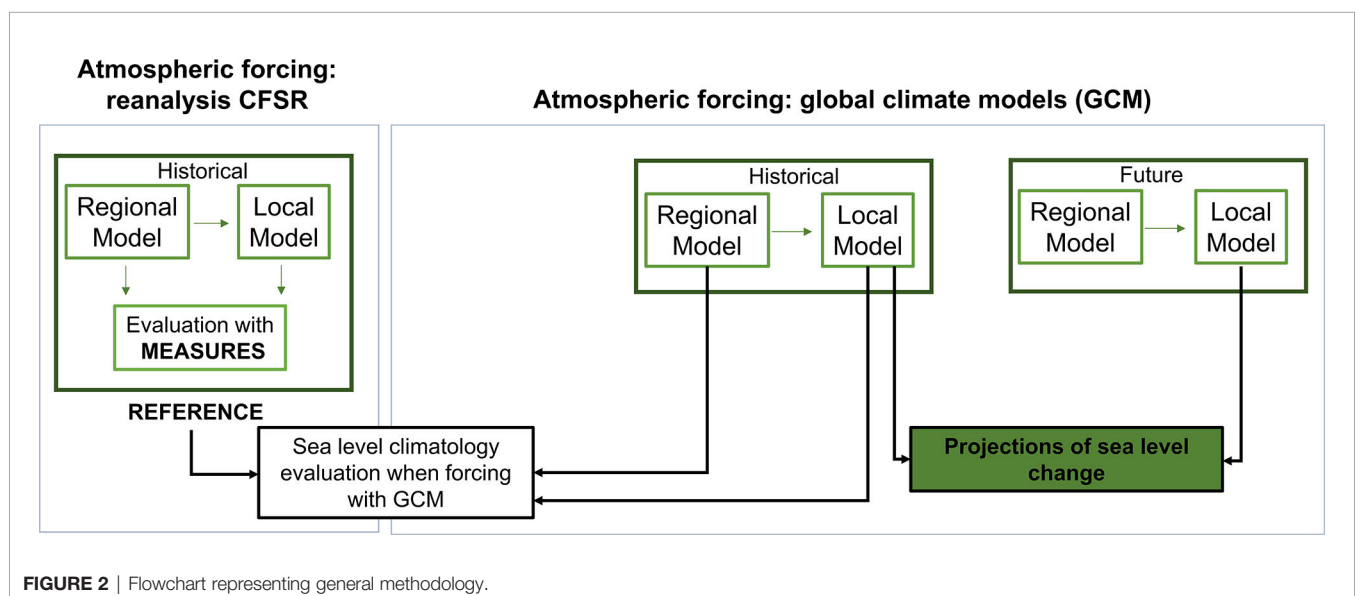
The first model encompasses the domain comprised by the South Atlantic Ocean (regional model; **Figure 3**, left panel), and is forced by astronomical tides at the ocean boundaries, average inflows from the Paraná and Uruguay rivers, and by surface winds and SLP in the free surface. In particular, the astronomical tide is imposed at the ocean boundaries as the superposition of 13 tidal components (M2, N2, S2, K2, 2N2, O1, Q1, K1, P1, Mf, Mm, Mtm, MSqm) obtained from FES2004 global ocean tide atlas (Lyard et al., 2006). The objective of the regional model is to generate the total sea levels time series to be imposed at the oceanic boundaries of the local model (**Figure 3**; central panel). The regional model is based on MOHID (Mateus and Neves, 2013) and was previously calibrated and validated for this domain (Martínez et al., 2015; Jackson et al., 2021). The most relevant characteristics of its implementation are presented in **Table 1**.

The local model is an implementation of TELEMAC-MASCARET (Hervouet, 2007), in its 2D version, to a domain that includes the estuary of the Río de la Plata and its continental shelf (**Figure 3**, central panel). TELEMAC has been successfully applied in several estuarine dynamics studies (Briere et al., 2007; Jones and Davies, 2008; Guillou & Chapalain, 2012; Huybrechts et al., 2012; Huybrechts & Villaret, 2013; Luo et al., 2013; Sathish Kumar & Balaji, 2015). The vertically integrated two-dimensional hydrodynamic TELEMAC-2D model solves the momentum and continuity equations using finite elements on unstructured meshes. The equations are simplified assuming incompressible fluid, vertical homogeneity, and hydrostatic pressure distribution. The model is forced by surface winds and SLP on the free surface, mean inflows from the Uruguay, Paraná and Santa Lucía rivers (**Figure 3**, right panel), and from the sea level time series coming from the regional model at the open oceanic boundaries. The time step used for running the model is 60 seconds and results are saved at every node of the mesh every 1 hour. **Table 1** summarizes most relevant characteristics of the implementation of the local model.

## 2.3 Calibration and Validation of the Local Model

The calibration of the model was carried out using data measured during the period 1985 to 2005, forcing the models with the CFSR reanalysis, varying the Manning number and testing different formulations for the wind shear stress. More than 40 calibration simulations were carried out, comparing the obtained results against sea levels measured at 3 stations on the Uruguayan coast, namely: La Paloma, Montevideo and Colonia (see **Figure 1**).

Validation is performed by comparing the results obtained with the calibrated model and the sea level data measured at the 6 stations shown in **Figure 1**. The goodness of the model is analyzed by estimating bias (BIAS), mean square error (RMSE)



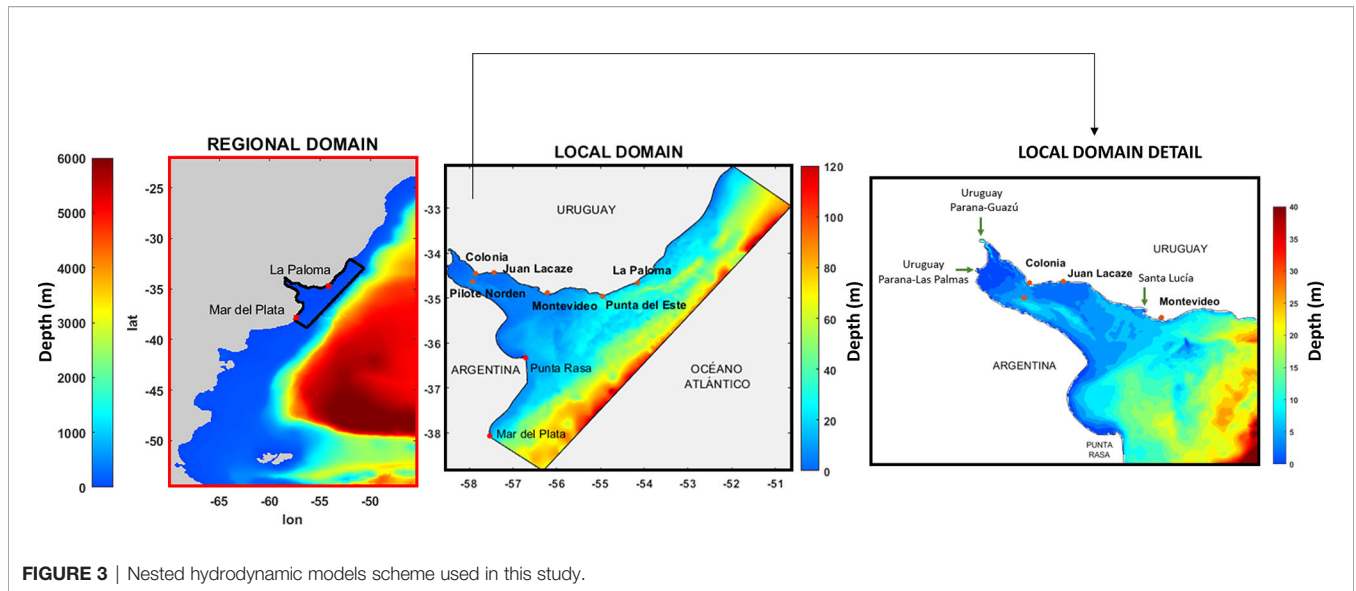


FIGURE 3 | Nested hydrodynamic models scheme used in this study.

TABLE 1 | Features of the setup for both regional and local hydrodynamic models.

MODELS FEATURES		
	REGIONAL	LOCAL
<b>Model</b>	MOHID - 2D	TELEMAC-2D
<b>Grid</b>	Structured; Latitude-Longitude with constant discretization of 0.1°	Finite volumes; From 7 km side triangles in the ocean border to 1 km in the Uruguayan coast
<b>Boundary Conditions</b>	Tributary flows (Uruguay, Paraná and Santa Lucia); Surface pressure and winds (10 m); Astronomical tide in open boundary	Tributary flows (Uruguay, Paraná and Santa Lucia); Surface pressure and winds (10 m); Sea level elevation from regional model in open boundary
<b>Flow rates</b>	Uruguay-Paraná Guazú 20.000 m3/s; Paraná Las Palmas 5.000 m3/	Uruguay-Paraná Guazú 20.547 m3/s; Uruguay- Paraná Las Palmas 5.825 m3/s; Santa Lucia 180 m3/s
<b>Atmospheric forcing</b>	NCEP-CFSR (model validation and reference data, 6 hr resolution); CMIP5 (projections, 3 hr resolution)	NCEP-CFSR (model validation and reference data, 1hr resolution); CMIP5 (projections, 3 hr resolution)
<b>Time step</b>	180 s	60 s
<b>Periods and climate scenarios simulated</b>	Historical (1985-2005); Short term (2026-2045, RCP 4.5 RCP 8.5); Long term (2082-2100, RCP 4.5 RCP 8.5)	
<b>Mean sea level</b>	Historical: 0,91 m; Short and long term: according to IPCC et al., 2013.	
<b>Model output</b>	Sea level every 1 hr for all grid points	

and correlation coefficient ( $r$ ) at each station, as expressed by equations 1, 2 and 3 respectively,

$$BIAS = \bar{y}_m - \bar{y}_o \quad \text{Equation 1}$$

$$RMSE = \sqrt{(y_m - y_o)^2} \quad \text{Equation 2}$$

$$R = \frac{\sum(y_m - \bar{y}_m) - (y_o - \bar{y}_o)}{\sqrt{\sum(y_m - \bar{y}_m)^2} \sqrt{\sum(y_o - \bar{y}_o)^2}} \quad \text{Equation 3}$$

where  $y_m$  refers to the modeled data and  $y_o$  to the measured (observed) data. In addition, scatter diagrams are presented for total sea level and for the meteorological residual, showing data density according to a color scale, superimposed by a quantile-quantile plot (25 quantiles are considered, evenly spaced on the

Gumbel scale, between 0.001 and 0.999). Once validated, results of the model are considered the ground true for subsequent analyzes.

## 2.4 Projections of Change in Sea Level Climate

The analysis of the sea level projections obtained by forcing the numerical models with the GCM is carried out focusing on different spatial and temporal scales, using a series of evenly spaced nodes located along the Uruguayan coast, from Conchillas to Chuy (see e.g. Figure 8A).

Table 2 lists the different components of the total sea level that are considered in the analysis. Total Sea Level (TSL) is arguably the most important variable to be considered when analyzing changes in sea level climate from a coastal engineering and coastal management viewpoint. However, to better understand these changes, their origin and their interactions, other variables are analyzed as well, namely:

**TABLE 2** | Sea level components considered in the analysis.

Sea level components considered in the analysis	
<b>MSL</b>	Mean sea level
<b>MSL<sub>imposed</sub></b>	Regional mean sea level, imposed as boundary condition
<b>MSL<sub>model</sub></b>	Model mean sea level $MSL_{model} = MSL - MSL_{imposed}$
<b>T<sub>met</sub></b>	Meteorological tide
<b>T<sub>ast</sub></b>	Astronomical tide
<b>SLWR</b>	Sea level without regional sea level rise $SLWR = MSL_{model} + M_{met} + M_{ast}$
<b>TSL</b>	Total sea level $TSL = MSL_{imposed} + SLWR$

sea level without regional sea level rise (SLWR), model mean sea level ( $MSL_{model}$ ), meteorological residuals (surge or meteorological tides;  $T_{met}$ ) and tides (or astronomical tides;  $T_{ast}$ ).

$MSL_{imposed}$  is the imposed regional sea level rise and in consequence is uniform in the entire domain and does not depend on atmospheric forcing. On the other hand,  $MSL_{model}$  does depend on atmospheric forcing, but it has a spatial scale similar to that of the analysis region, being approximately uniform throughout the local domain. Both  $MSL_{imposed}$  and  $MSL_{model}$  are removed from the results to better analyze the other components of the sea level signal.

Changes in  $T_{met}$  and  $T_{ast}$  are analyzed separately because they have different origin. While  $T_{met}$  depends on the atmospheric forcing,  $T_{ast}$  does not depend on the atmospheric forcing but can be affected by the nonlinear interactions with  $T_{met}$  and by the change in the MSL.

To obtain  $T_{met}$  at each point, first  $MSL_{model}$  is subtracted from the SLWR in order to avoid the influence of sea level components of spatial and temporal scales greater than that of the meteorological events (synoptic scale), and then the Doodson filter (Pugh, 1987) is applied to filter out astronomical tides from the signal. To obtain  $T_{ast}$ , an harmonic analysis is carried out using T-Tide toolbox (Pawlowicz et al., 2002), and only the amplitudes of the M2 and O1 components is analyzed, as these are the two most relevant components along the Uruguayan coast (Fossati et al., 2013).

For each variable the projected changes are evaluated by looking at changes in its mean value and in the 1% and 99% quantiles (the latter two representatives of extreme low and high conditions). Changes are evaluated considering results from each GCM separately and also by looking at the ensemble of the results.

## 2.5 Significance of the Projected Changes

The significance of the changes is analyzed only for the SLWR and its components. To analyze the significance of the changes projected by each GCM, the Student-t test was applied to the series of annual values of the three analyzed statistics (i.e. series of annual mean and of 1% and 99% quantiles; see e.g. Casas-Prat et al., 2017 and Hemer et al., 2013). Null hypothesis in this test is that the distribution of the annual statistics is the same in the historical period and in the future periods.

On the other hand, for the analysis of the ensemble of the results, the significance of the change is determined following a methodology similar to that used in Wandres et al. (2017) and Camus et al. (2017). For each model, the difference between the statistic estimated from projections and the one estimated in the historical period is calculated. Then, if the mean of the differences is greater than the standard deviation, and if at least 6 of the 7 models project the same direction of the change (increase or decrease), then the change in is said to be significant (i.e. when working with the ensemble of the results, a change is considered significant if both conditions are met).

## 3 DATA

### 3.1 Measured Sea Level Series

Sea level data measured at six stations located in the study area are used for the calibration and validation of the local model. Of these, five stations are located along the Uruguayan coast and one in the inner part of the Río de la Plata estuary (**Figure 1**). Only years with less than 50% missing data are used in this study, considering the time period 1985-2005. **Figure 4** shows the data availability at each station.

**FIGURE 4** | Measured data available in each station (only years with less than 50% missing data are considered).

**TABLE 3** | CMIP5 models used in this study: name, institution, country and spatial resolution.

Model	Institute	Spatial resolution [°latx°lon]
<b>S1.0</b>	CSIRO-BOM (Australia)	1.25 x 1.9
<b>CMCC-CM</b>	Centro Euro-Mediterraneo per I cambiamenti Climatici (Italy)	0.75 x 0.75
<b>CNRM-CM5</b>	Centre National de Recherches Meteorologiques (France)	1.4 x 1.4
<b>GFDL-ESM2G</b>	NOAA Geophysical Fluid Dynamics Laboratory (USA)	2 x 2.5
<b>HadGEM2-ES</b>	Met Office Hadley Centre (UK)	1.25 x 2
<b>IPSL-CM5A-MR</b>	Institut Pierre-Simon Laplace (France)	1.25 x 2.5
<b>MIROC5</b>	MIROC (Japan)	1.4 x 1.4

### 3.2 Reanalysis CFSR

The calibration and validation of the hydrodynamic model is carried out by forcing it with hourly wind and SLP fields from the atmospheric reanalysis of the National Centers for Environmental Prediction NCEP-CFSR of USA (Saha et al., 2010). Wind data have a spatial resolution of  $0.205^{\circ} \times 0.204^{\circ}$ , and SLP data have a spatial resolution of  $0.312^{\circ} \times 0.312^{\circ}$ <sup>1</sup>. Here, only the data covering the historical period (1985-2005) is used.

### 3.3 Global Climate Models (GCMs)

To obtain sea level projections, the 2D hydrodynamic models are forced with wind and SLP fields of the seven GCM from the CMIP5 listed in **Table 3**. The selection of these models is made on the basis that these were the only models (at the moment of downloading, January 2019) having the required variables with temporal resolution of three-hours or higher. In all cases only r11p1 runs were used, and all data was downloaded through the Earth System Grid Federation<sup>2</sup>.

### 3.4 Mean Sea Level Rise

Regional sea level rise projections from IPCC AR5 (Church et al., 2013; IPCC, 2013) are used for climate scenarios RCP 4.5 and RCP 8.5 (data available from the Hamburg University<sup>3</sup>). Regional mean sea level rise data, relative to the baseline period 1986-2005, is available in a global domain with a  $1^{\circ} \times 1^{\circ}$  resolution. In this work, the increase in mean sea level (we considered mean values of increase from the data set) is considered as uniform in space and is added to the boundary condition of the hydrodynamic model. This uniform regional mean sea level rise value is estimated as the spatial mean of the regional mean sea level rise within the computational domain of the hydrodynamic model, which includes the Rio de la Plata and part of the Atlantic Ocean [lat (-54.2, -22) lon (-70, -45.5); see **Figure 2**].

**Table 4** summarizes the estimated values of the regional sea level rise for four time-horizons and the mean rise for 2081-2100 period, for the two scenarios analyzed. It is noted that these values are in agreement with the values obtained when considering the regional sea level rise at the nodes closest to the Uruguayan coast (i.e. average regional sea level rise within the computational domain is in agreement with sea level rise projected for the Uruguayan coast and the Rio de la Plata estuary).

<sup>1</sup> <https://rda.ucar.edu/>.

<sup>2</sup> <https://esgf-node.llnl.gov>.

<sup>3</sup> [https://icdc.cen.uni-hamburg.de/thredds/catalog/ftpthredds/ar5\\_sea\\_level\\_rise/catalog.html](https://icdc.cen.uni-hamburg.de/thredds/catalog/ftpthredds/ar5_sea_level_rise/catalog.html).

## 4 RESULTS

### 4.1 Local Model Calibration and Validation

The calibration of the local model results in choosing the Flather (1976) formulation for the wind shear stress and a non-uniform Manning number for the domain (0.007 in the inner zone of the estuary and 0.15 in outer and middle zones). Regarding validation, **Figures 5, 6** show the scatter plots and the quantile-quantile plots for each station for total sea level (TSL) and meteorological residuals (or surge,  $T_{met}$ ; see *Projections of Change in Sea Level Climate*), respectively. In addition, **Table 5** lists RMSE and correlation coefficient for the different stations for both variables, along with the bias for the TSL.

In **Figure 5** it is observed that in all the stations the scatter points are aligned with the line 1-1 (indicated in red). In the case of Punta del Este, it is observed that the quantile-quantile plot shows a negative bias for all quantiles, in agreement with the high bias and RMSE and low correlation estimated for the TSL for this station (see **Table 5**). TSL at the rest of the stations present high correlation coefficients and RMSE values around 25 cm (**Table 5**). In **Figure 6** it is noted that the scatter plots tend to be aligned with the identity line, although some points depart from the trend in some stations; in all cases the quantile-quantile plots are clearly aligned with the identity line. This is consistent with the large correlation coefficients listed for  $M_{met}$  in **Table 5**, although in this case the lowest correlations are obtained Punta del Este and La Paloma stations. Regarding astronomical tide, the model overestimates the amplitudes, reaching around 0.07 m and 0.04 m global RMSE values for M2 and O1 constituents respectively (considering only the coastal stations from **Figure 1**). Differences between measured and modeled amplitude and phase for each station are shown in **Table S1**. Nevertheless the model represents correctly the regional trend of the tide.

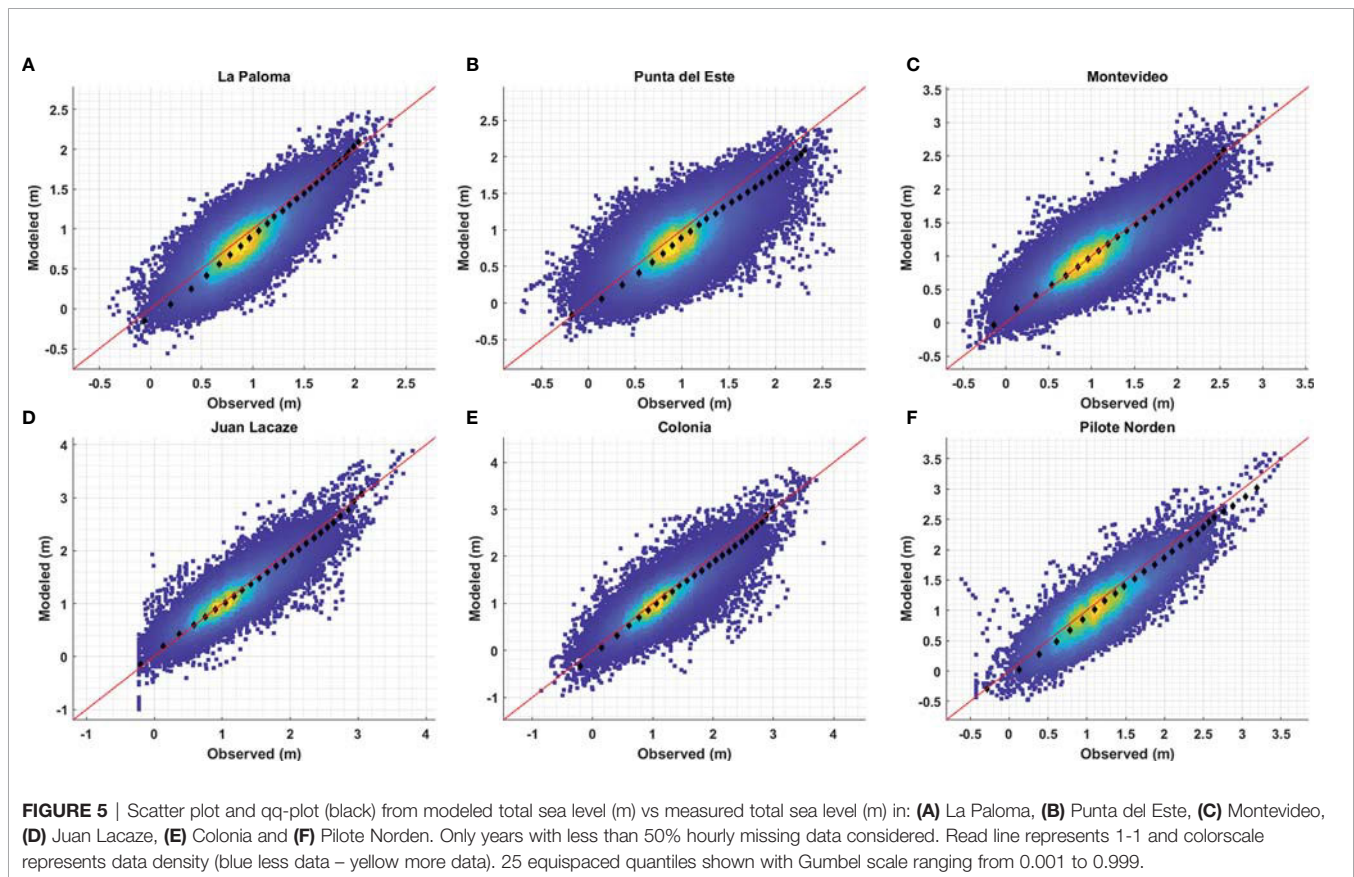
In general terms, the model correctly represents both the total sea levels and the meteorological component along the entire coast. These validated results are considered as the reference results from now on.

### 4.2 GCMs Historical Period

**Figure 7** shows the quantile-quantile plots comparing TSL series obtained with the GCM with the reference series obtained with the CFSR at the 6 coastal stations presented in **Figure 1**, for the historical period. For the sake of readability, from now on when referring to results of a GCM, reference is made to the results obtained with the hydrodynamic model forced with that

**TABLE 4** | Mean sea level change used in this work for RCP 4.5 y RCP 8.5 scenarios.

Mean sea level change (m)	RCP 4.5	RCP 8.5
2026	0.100	0.103
2045	0.189	0.204
2081	0.385	0.505
2100	0.492	0.729
2081-2100 mean	0.458	0.635



particular GCM. It is observed that the results get worse for the stations located at the inner part of the estuary (Colonia, Juan Lacaze and Pilote Norden).

For the stations located at the outer part of the estuary and at the oceanic coast, a good performance is observed for all the GCM for low and middle quantiles; however, most of the GCM underestimate the high quantiles, with underestimations of up to 40 cm in La Paloma and 60 cm in Montevideo for the GFDL-ESM2G model. Exceptions are results from the MIROC5 and CMCC-CM models, for which the highest quantiles are well represented and tend to improve from La Paloma to Montevideo.

On the other hand, for stations at the inner part of the estuary, good results are observed for the MIROC5 and CMCC-CM models in the entire range of quantiles, while the rest of the models overestimate (underestimate) low (high) quantiles:

lowest quantiles are overestimated by up to 30 cm, while highest quantiles are underestimated by up to 90 cm.

## 4.3 Projections

### 4.3.1 Changes in TSL

**Figure 8** shows changes in the mean (left panels), 1% quantile (center panels) and 99% quantile (right panels) of the TSL, for both the short term (2027-2045) and long term (2082-2100) projections, and for both RCP scenarios. For the mean, a constant change is projected along the coast, while for the 1% and 99% quantiles it is observed that the projections of change vary along the coast.

For the 1% quantile, a pattern of spatial variability is observed with a maximum around Colonia and a minimum between Juan Lacaze and Montevideo. In the short term, the range of projected

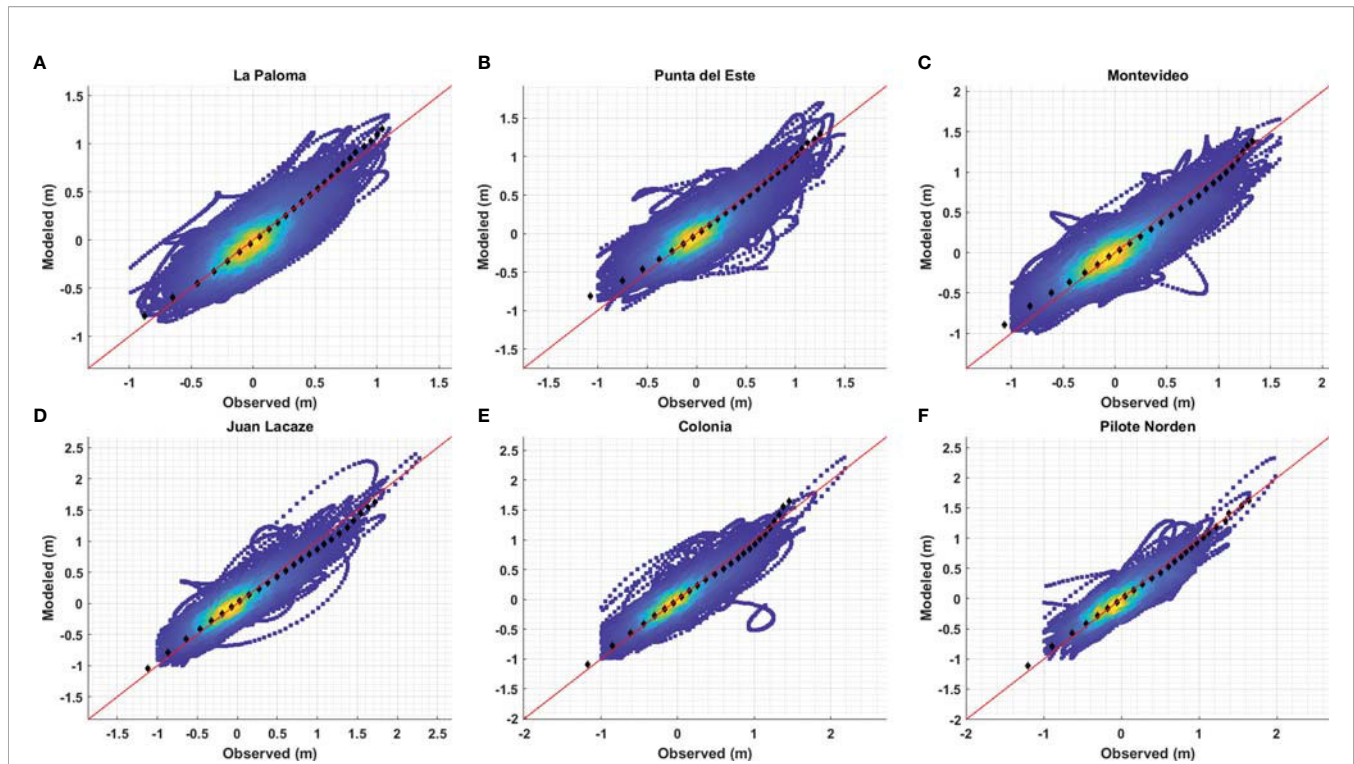


**FIGURE 6** | Scatter plot and qq-plot (black) from modeled meteorological tide (m) vs measured meteorological tide (m): **(A)** La Paloma, **(B)** Punta del Este, **(C)** Montevideo, **(D)** Juan Lacaze, **(E)** Colonia and **(F)** Pilote Norden. Only years with less than 50% hourly missing data considered. Read line represents 1-1 and colorscale represents data density (blue less data – yellow more data). 25 equispaced quantiles shown with Gumbel scale ranging from 0.001 to 0.999.

**TABLE 5** | Statistics obtained comparing modeled total sea level (BIAS, RMSE and  $r$ ) and meteorological tide (RMSE and  $r$ ) with measures in La Paloma, Punta del Este, Montevideo, Colonia, Juan Lacaze and Pilote Norden.

Station	Total sea level			Meteorological tide	
	BIAS (m)	RMSE (m)	$r$	RMSE (m)	$r$
La Paloma	-0.09	0.24	0.77	0.18	0.78
Punta del Este	-0.12	0.31	0.65	0.2	0.79
Montevideo	-0.002	0.25	0.8	0.19	0.85
Colonia	-0.08	0.28	0.82	0.19	0.88
Juan Lacaze	-0.02	0.25	0.84	0.19	0.87
Pilote Norden	-0.11	0.29	0.84	0.19	0.87

changes is similar for both RCP scenarios. In the long term, the same spatial pattern is observed as in the short term, but with different ranges of variation for the different RCP (associated with differences in the mean sea level rise), and with larger differences between maximums and minimums.

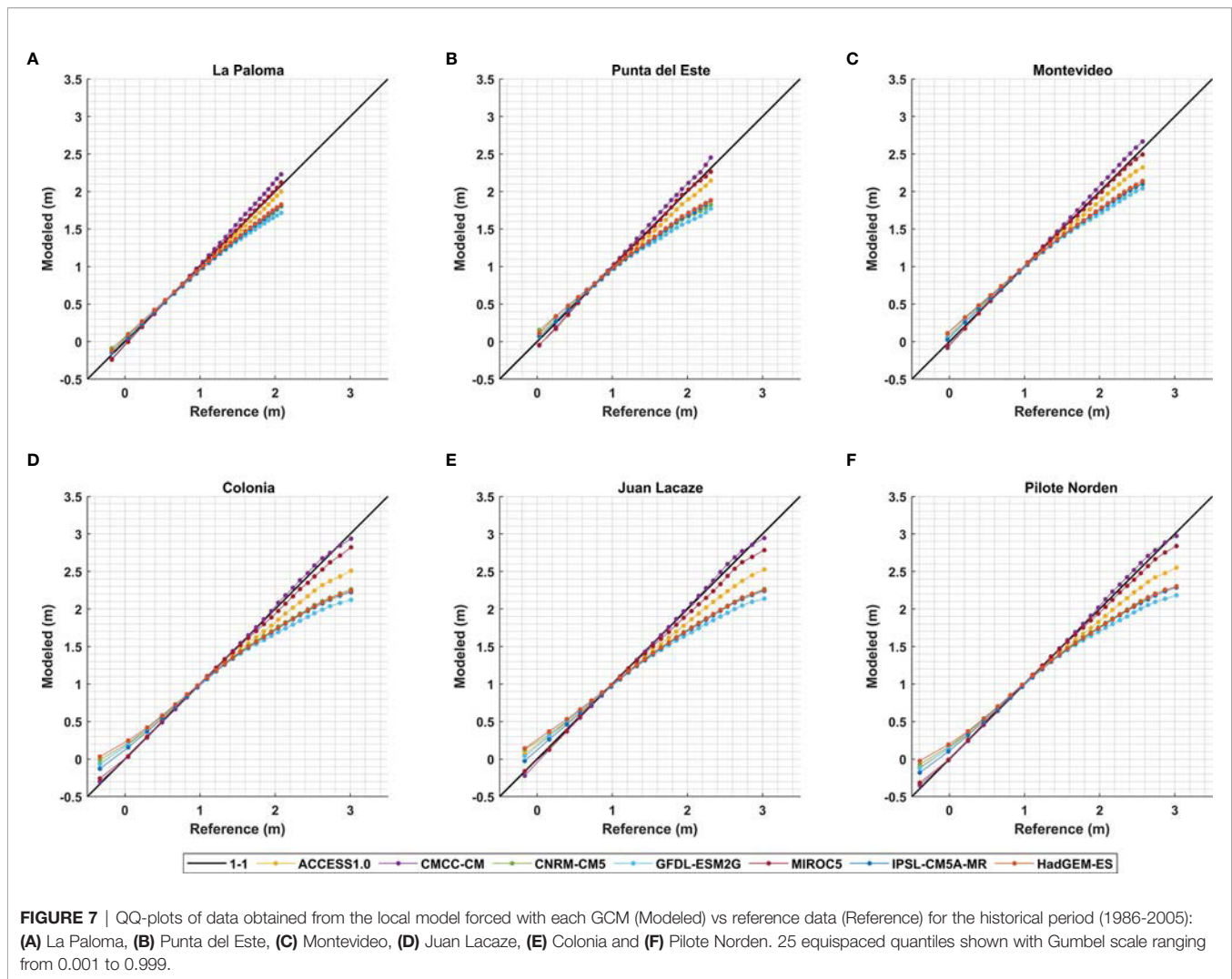
On the other hand, changes in the short term of the 99% quantile shows a very similar range for the two scenarios and a relatively uniform pattern all along the coast. Whereas in the long term a marked spatial distribution is observed, with maximum values in the inner area of the estuary and a relative maximum around Montevideo, with similar behavior observed for both scenarios, although with different ranges of values.

From **Figure 8** it is clear that the mean sea level rise dominates the projected changes in the TSL, therefore it is

relevant to analyze changes in the *SLWR* and its components to better quantify and understand other sources of changes and their interactions.

#### 4.3.2 Changes in the *SLWR*

**Figure 9** shows the projected changes in the mean and in the 1% and 99% quantiles of the *SLWR*, for the long and short term and for both RCP scenarios, as well as the significance of the changes. It should be noted that the Student-t test, applied to each member of the ensemble, rejected the null hypothesis (i.e. changes are statistically significant) for all the nodes and for all the models and scenarios analyzed (for *SLWR* and for the variables  $T_{met}$  and  $T_{ast}$  analyzed next); therefore in **Figure 9** and in those that follow, only the result of the significance of the changes in the ensembles is included.



The change in the mean of the SLWR assembly is practically null and not significant along the entire coast, except for the innermost nodes in the long term, which indicates that the change in the mean of the TSL comes almost entirely from the increase in the mean sea level. On the other hand, the change in the 1% and 99% quantiles shows the same spatial patterns observed in the TSL.

The 1% quantile of the SLWR shows values very close to 0 in the short term along the entire coast for every scenario, although some significant negative changes are observed in the ensemble (less than 5 cm) for the RCP 8.5 scenario. In the long term, the spatial pattern of the changes is clearer, and the changes in the ensemble are significant in the inner zone of the estuary, between Juan Lacaze and Montevideo, as well as on the oceanic coast, from La Paloma to the East, for both scenarios. These changes show a minimum in the inner zone of the estuary, a relative minimum between Juan Lacaze and Montevideo, as well as a decrease from Punta del Este towards the east. It is noted that in the long term all the models show the same spatial pattern.

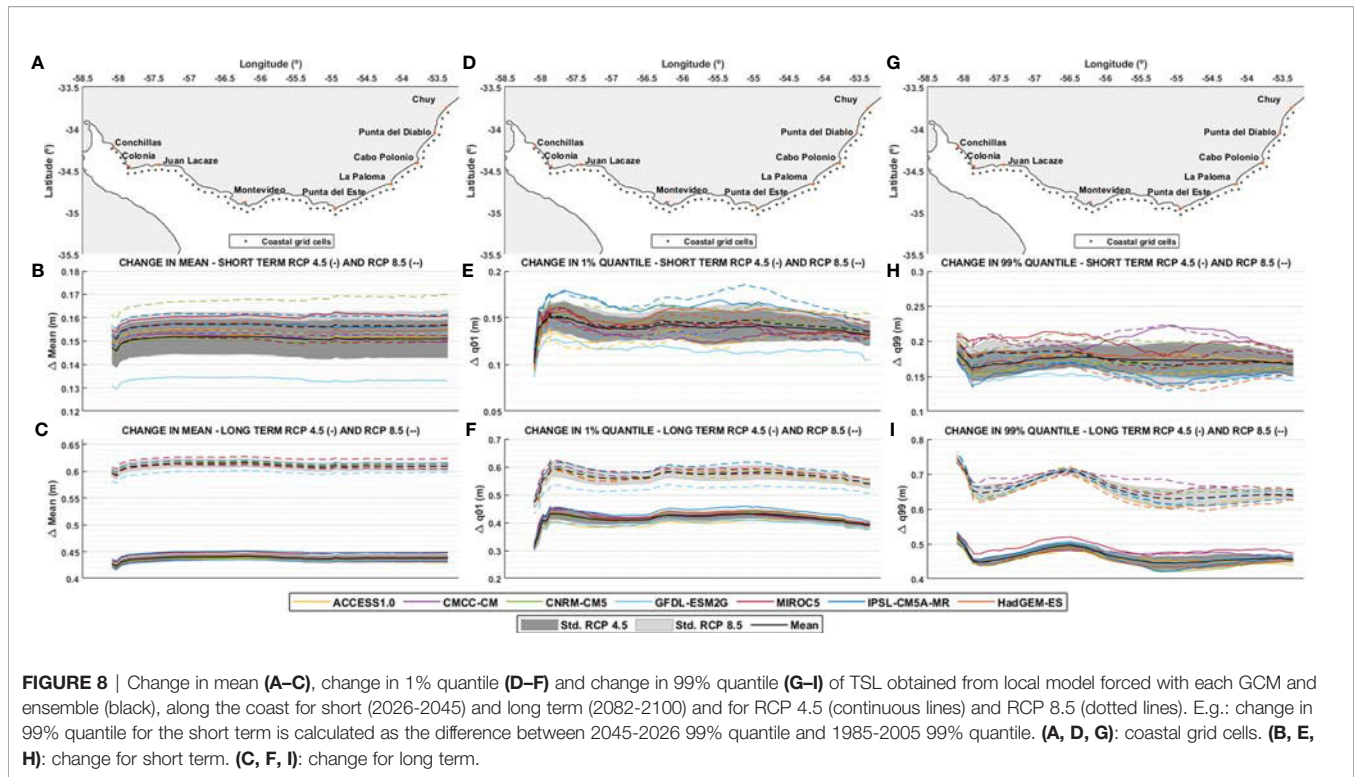
The 99% quantile of the SLWR shows significant changes in most of the coast for both future horizons and both scenarios. In

the short term, the change is practically uniform along the coast for both scenarios, and the ensemble shows positive changes of less than 5 cm. In the long term, the same spatial pattern as for the change in TSL is observed, although in this case the maximums in the RCP8.5 scenario are more pronounced, which could be associated to either changes in the atmospheric patterns or to non-linear effects produced by the depth increase due to the mean sea level rise.

#### 4.3.3 Change in the Meteorological Residuals ( $T_{met}$ )

Figure 10 shows the changes in the 1% and 99% quantiles of the  $T_{met}$  (by its definition, the mean value of  $T_{met}$  is always zero). The objective of analyzing this variable is to focus attention on the changes in sea level produced by changes in the atmospheric patterns in the region.

It is observed that the projected change for the 1% quantile is small along the entire coast for all models and RCP scenarios, barely exceeding one centimeter in the short term and two centimeters in the long term. The maximum change in the 1% quantile occurs for the GFDL-ESM2G model in the long term



and for the RCP 8.5 scenario, with a decrease of only 2 cm. It is noted that changes in the ensemble are not significant in all cases.

In general terms, the changes in the 99% quantile are small, although there is a slight trend towards positive changes towards the east, reaching values that exceed 5 cm in the short and long term for some of the models. In the inner area of the estuary, changes are negligible for all models. The model that shows the greatest changes is the CMCC-CM in all cases. The ensemble shows a clear trend to larger positive changes towards the east, with values not exceeding 2 cm in any case. As in the previous case, changes in the ensemble are not significant, mainly due to the great dispersion of the results.

#### 4.3.4 Changes in the Astronomical Components ( $T_{ast}$ )

Figure 11 shows the projected changes in the amplitude of the tidal components M2 (right panel) and O1 (left panel), including the amplitude of both components for the historical period.

In the case of the M2 amplitude, it is seen that the spatial pattern of the changes along the coast is repeated in the short and long term, showing mostly positive changes for the amplitude of this component along almost the entire coast, with increases of about 1 cm in the short term and between 2 cm and 5 cm in the long term. It is noted that both the amplitude calculated for the historical period and the projected change have the same pattern, with relative maxima and minima almost coinciding in space. There is a relative minimum between Colonia and Juan Lacaze, with zero change in both the short and long term; then, there is another minimum in the amplitude between Montevideo and Punta del Este, also associated with zero change. In turn, near

Punta del Este there is a significant negative change in both the short and long term. On the other hand, the largest projected changes occur for the largest amplitudes, in the inner zone of the estuary, where the maximum change in the short term reaches 1.5 cm and in the long term exceeds 4 cm for RCP 4.5 and 6 cm for RCP 8.5. Between Juan Lacaze and Montevideo there is a relative maximum in the amplitude of the M2 component that exceeds 30 cm; the changes for both time horizons also present a relative maximum in this zone, with short-term changes barely reaching one centimeter, and long-term changes exceeding 2 cm for RCP 4.5 and 4 cm for RCP 8.5. It should be noted that within each scenario and time horizon the dispersion of the results of the different models is small, resulting in all projected changes being significant for practically the entire coast. In addition, in the short term there is almost no difference in the projected changes for the different scenarios, while in the long term there are some differences between the scenarios, particularly in the magnitude of the projected changes.

The O1 component shows a similar behavior to that observed for the M2 component: the spatial pattern of the projected changes is similar to that of the amplitudes, with greater changes projected in the zones of higher amplitudes. Short-term changes show greater dispersion between models (with respect to that observed in M2), although they do not exceed one centimeter in any case. In the long term, there is a slight difference between scenarios, and the maximum change does not reach 4 cm for the RCP 4.5 scenario and barely exceeds 4 cm for the RCP 8.5 scenario, where the amplitude of the component is approximately 20 cm. As for the M2 component, the changes in the ensemble are significant along the coast.



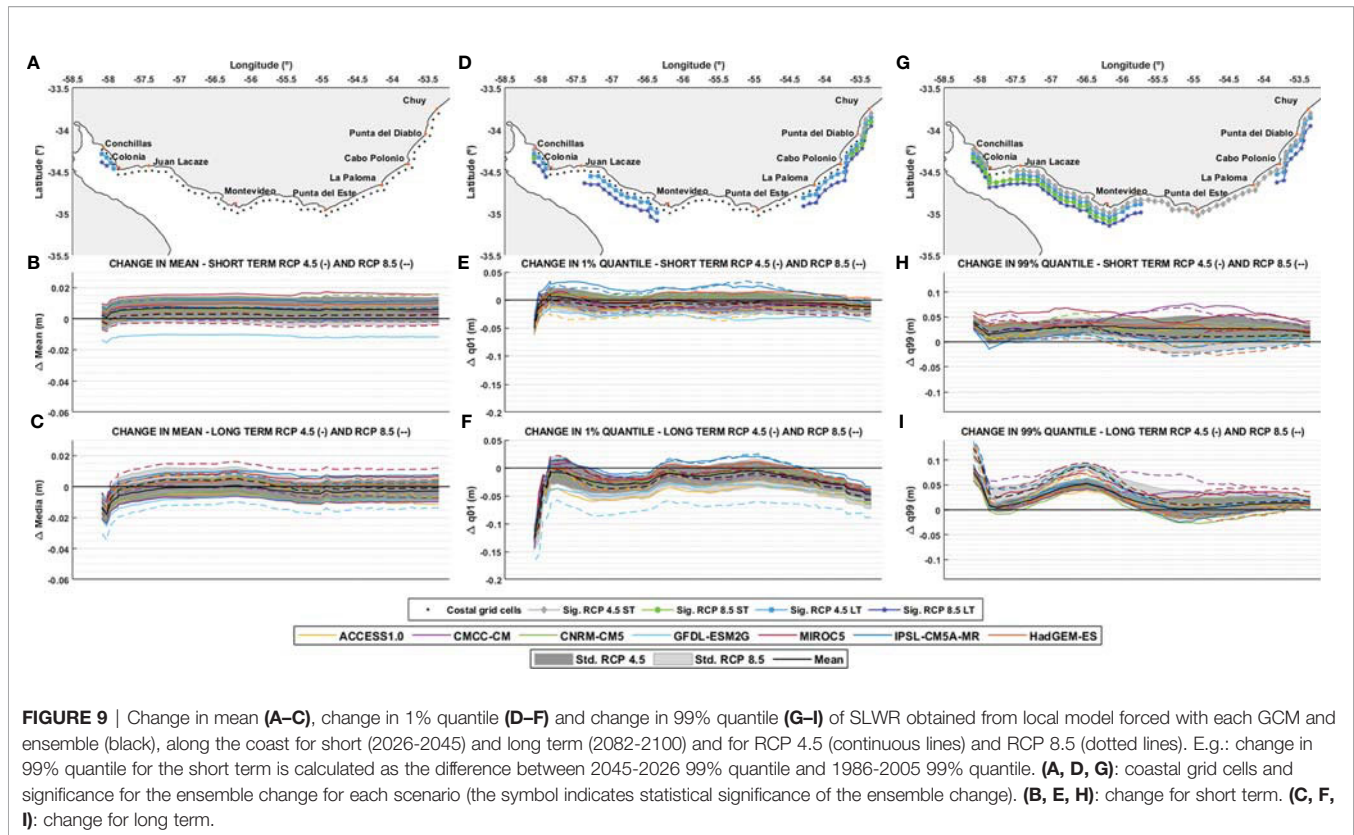


**FIGURE 9** | Change in mean (A–C), change in 1% quantile (D–F) and change in 99% quantile (G–I) of SLWR obtained from local model forced with each GCM and ensemble (black), along the coast for short (2026–2045) and long term (2082–2100) and for RCP 4.5 (continuous lines) and RCP 8.5 (dotted lines). E.g.: change in 99% quantile for the short term is calculated as the difference between 2045–2026 99% quantile and 1986–2005 99% quantile. (A, D, G): coastal grid cells and significance for the ensemble change for each scenario (the symbol indicates statistical significance of the ensemble change). (B, E, H): change for short term. (C, F, I): change for long term.

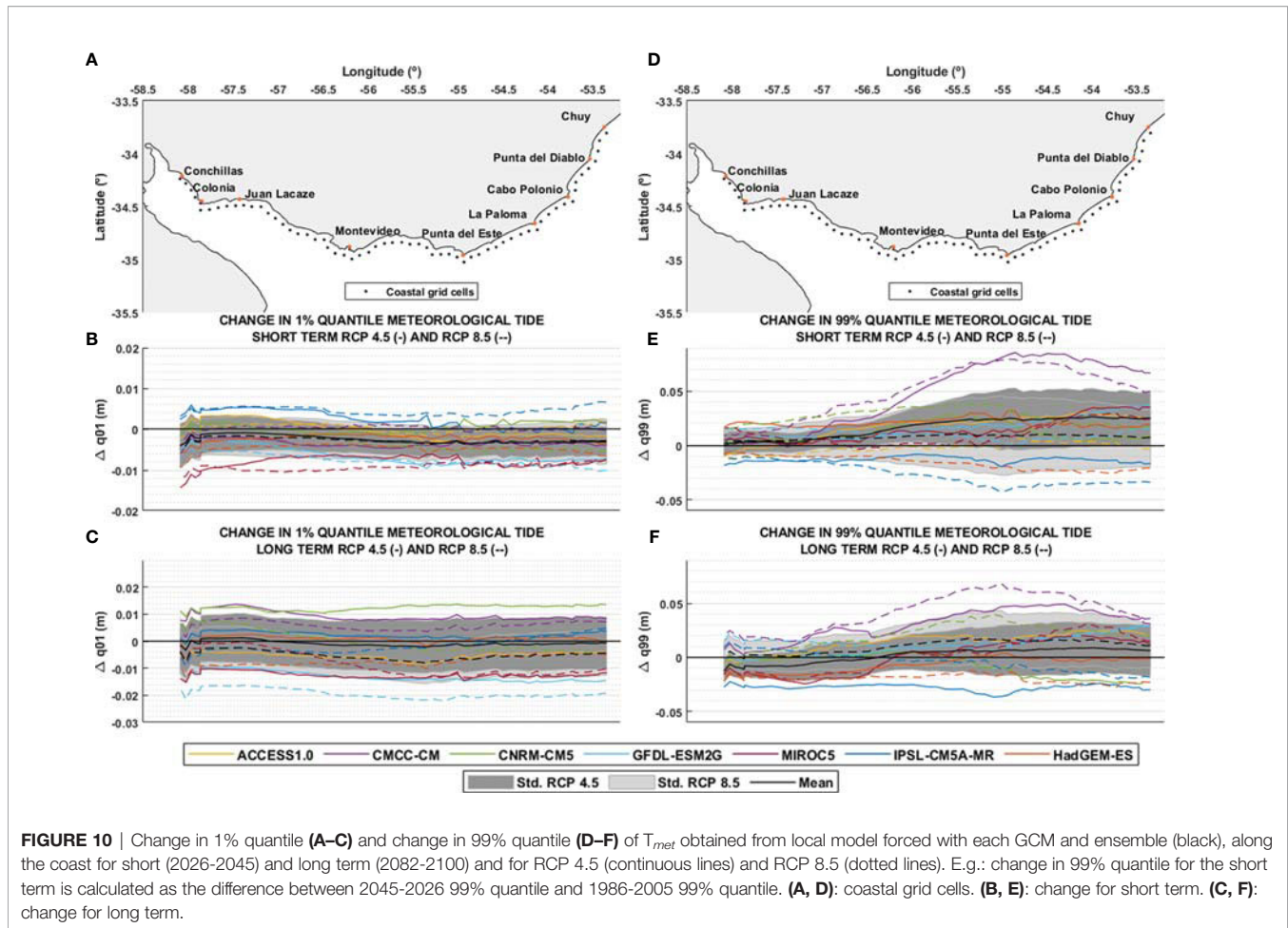
## 5 DISCUSSION

The results obtained by modeling the historical period, forcing the hydrodynamic models with the GCMs, show that a better representation of the sea level climate is achieved at the stations located in the outer estuary zone and in the oceanic coast. In particular, most GCMs underestimate the higher quantiles at all stations (except CMCC-CM at La Paloma, Punta del Este and Montevideo, and MIROC 5 at La Paloma), while the lower quantiles are well represented at the outer stations and overestimated at the inner stations. The models that best represent current sea level climate in the region are MIROC5 and CMCC-CM, which have a spatial resolution of  $1.4^{\circ} \times 1.4^{\circ}$  (the lowest resolution among the 7 GCMs used) and  $0.75^{\circ} \times 0.75^{\circ}$  (the highest resolution), respectively; thus, there seems to be no dependence between the resolution of the GCMs and their performance in modeling sea level climate. In any case, none of the models present results clearly at odds with the reference climatology, therefore it is reasonable to retain all of them when analyzing projections of change in order to have the widest possible range of results.

When analyzing the changes in TSL for all scenarios and future periods, it is observed that the change in the mean is uniform along the coast, dominated mainly by the increase in regional mean sea level. When analyzing the changes in the 1% and 99% quantiles of the SLWR, the influence of other components is observed, with a spatial pattern of changes that is not always uniform along the coast, which also emerge when

analyzing the 1% and 99% quantiles of the TSL. The analysis of SLWR allows focusing attention on the changes induced in the tidal and surge wave dynamics resulting from the increase in the water depths due to the regional mean sea level rise. While the distribution of the 1% SLWR quantile does not yield additional information to that already observed in the distribution of the 1% TSL quantile (the SLWR shows almost overlapping changes for both scenarios, both in the short and long term), the analysis of the 99% SLWR quantile shows that in the long term for the RCP 8.5 scenario the change intensifies, obtaining differences of more than 5 cm between the maximum changes of the ensemble for each RCP scenario. It is possible to relate the latter to the interaction between tidal wave propagation and mean sea level rise, as in the future the difference between the mean sea level rise for both scenarios increase (see **Table 4**).

Regarding the meteorological residuals, both the 1% and 99% quantiles show changes close to 0 and not significant along the coast, for both the short and the long term. This indicates that the changes observed in the TSL are not associated with changes in the atmospheric circulation patterns. There are no previous studies of this type for our region, neither at global nor regional scales, but it is interesting to note that Vousedoukas et al., 2016) reach the opposite conclusion for the European coasts: these authors perform a dynamic downscaling of sea levels, forced with surface winds and SLP from 8 GCMs (without considering astronomical tides), finding that the increase in extreme levels associated with meteorological events along the European coast range from 15% to 40% in certain regions.



On the other hand, the changes in the amplitude of the M2 and O1 astronomical components along the coast were shown to be very similar between models. The general trend is to have large changes in areas of large tidal amplitude, and larger ratio between change and current amplitude for the O1 component than for the M2 component, with the former showing changes that reaches 4 cm for a current amplitude of 20 cm. It is also noted that the change in the astronomical components is not influenced by the atmospheric, as the 7 GCMs projected quite similar changes forcing (i.e. there are no strong tide-surge interaction affecting the changes), implying that changes in the astronomical tide amplitudes are due to the imposed regional mean sea level rise and the resulting increase in water depths.

From the previous analysis, it is clear that the main contribution to the change in the TSL is the regional mean sea level rise. Then, the analysis of the signals obtained by subtracting this contribution (SLWR and its components), shows that the change in the astronomical tide resulting from the increase in the regional mean sea level is especially important, and that it is from this interaction that arises the spatial patterns observed in the 1% and 99% quantiles (mainly in the latter). Moreover, since the change in  $MSL_{model}$  is constant along the coast, it is understood that it does not contribute significantly to

the observed spatial patterns. On the other hand, the changes in the 99% quantile of the meteorological residual does not present the spatial pattern observed in TSL and SLWR, but shows minimum values along the coast towards the inner zone of the estuary and grows outwards. In contrast, the change along the coast in the tidal components does present a spatial pattern that agrees with that observed in the SLWR, especially in the inner zone of the estuary, where the change for the M2 and O1 component are maximum. In particular, the M2 component presents a relative maximum that encompasses the zone of maximum change around Montevideo observed in the TSL and SLWR, which leads to think that it may also be contributing significantly to these, although for the M2 component the zone of change extends almost to Punta del Este, unlike for the SLWR. All the above agrees with the fact that changes in the 99% quantile intensify in the long term with the more severe scenario, given that the difference in regional mean sea level rise between scenarios increases in the long term. It is noted that this result is consistent with that of Pickering et al. (2012); Pelling et al. (2013) and Idier et al. (2017) for the European shelf, where they analyzed the effect of the mean sea level rise on the astronomical tide, confirming the importance of the interaction between the mean sea level change and the tides:

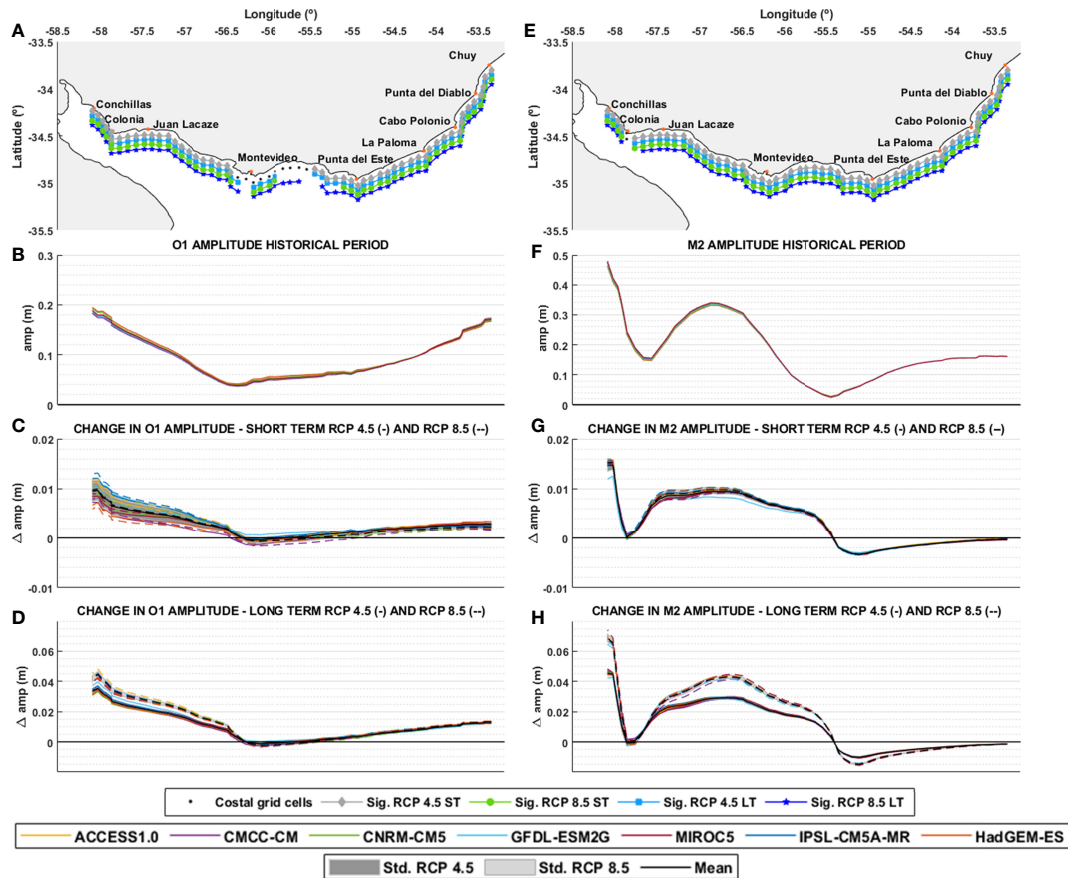


**FIGURE 11** | Change in O1 component amplitude (A–D) and change in M2 component amplitude (E–H) obtained from local model forced with each GCM and ensemble (black), along the coast for short (2026–2045) and long term (2082–2100) and for RCP 4.5 (continuous lines) and RCP 8.5 (dotted lines). E.g.: change in M2 component for the short term is calculated as the difference between 2045–2026 M2 amplitude and 1986–2005 M2 amplitude. (A, E) coastal grid cells coastal grid cells and significance for the ensemble change for each scenario (the symbol indicates statistical significance of the ensemble change), (B, F): component amplitude, (C, G): change for short term, (D, H): change for long term.

Idier et al. (2017) concludes that changes of up to  $\pm 15\%$  are reached in the amplitudes of the most important tidal components in the region, such as M2, S2, N2, among others; Pickering et al. (2017) investigated the effect of mean sea level rise on the tides globally, concluding that significant changes occur in the M2 and S2 constituents in most shelf seas. Moreover, Haigh et al. (2020) does a comprehensive review of past and future non-astronomical changes in tides, concluding regional increases and decreases in tides are likely to occur in response to MSL rise, changes in coastal morphology and variations in ice sheets extension, affecting particularly shelf seas and coastal waters; Howard et al. (2019) provided a synthesis of results of projections of 21<sup>st</sup> century change in extreme sea levels around the coast of the United Kingdom and reached similar conclusions as this work, finding projections dominated by the effects of the mean sea level rise and changes in tidal amplitudes induced by it, also noting that the tidal changes do not depend on the atmospheric forcing (i.e. on the GCM forcing model), being these highly uncertain, what makes changes in tidal amplitudes more robust.

There are certain limitations in this work that are worth highlighting. First, the number of GCMs available for analysis was relatively small, which is detrimental to the robustness of the projections; although criteria have been implemented to determine when a change is significant, having a small number of models increases the risk of not being able to differentiate between climate trends and the internal variability of the GCMs used. In any case, this problem may be overcome in future studies using the growing number of GCM results made available by CMIP for dynamic downscaling. A second limitation is related to the use of two-dimensional models, since they cannot capture variations in mean sea level due to changes in the baroclinic structure of the oceans; Hermans et al., 2020 have shown that this effect is significant in the case of the North Sea, so it should be included in future studies in order to analyze its relevance in this region. Lastly, this work used sea level rise projections corresponding to AR5 (IPCC, 2013), which were improved in the SROCC (IPCC, 2019) and for AR6 (Fox-Kemper et al., 2021). However, comparison of CMIP5 and CMIP6 shows that there are no qualitative differences in sea

level rise projections, and that quantitative differences are limited to a few centimeters (see e.g. Hermans et al., 2020, Lyu et al., 2020), so it seems that updated regional sea level rise values would lead to similar results in our work.

## 6 CONCLUSIONS

From the analysis of the changes projected for the different components of the total sea level along the Uruguayan coast, it is concluded that the main contribution to the projected changes is the regional mean sea level rise, followed in importance by the effect that the increase in the water depth has on the amplitude of the tidal components. Moreover, it is concluded that changes in the meteorological residuals, associated with potential changes in the atmospheric circulation patterns, are negligible in the study area. This in turn reinforces the need to resort to dynamic downscaling for studies of these characteristics, since this approach allows to resolve the interactions that may arise between tides, surges and the mean sea level rise, something that cannot be addressed with an approach based solely on statistical downscaling.

Regarding the magnitude of the projected changes for the Uruguayan coast, there are two regions along the coast that deserve special attention, as there is where the greatest increases in the 99% quantile of the TSL is projected: from Colonia towards the inner part of the estuary and the coastal zone around Montevideo. In the long term (2082–2100) the ensemble shows increases of up to 52 cm in Colonia and 50 cm around Montevideo for RCP 4.5, with around 46 cm explained by the 2081–2100 mean sea level rise. For RCP 8.5, the ensemble shows increases up to 74 cm in Colonia towards the inner part of the estuary and 71 cm around Montevideo, where 64 cm comes from 2081–2100 mean sea level rise.

## REFERENCES

- Briere, C., Abadie, S., Bretel, P., and Lang, P. (2007). Assessment of TELEMAC System performances, a Hydrodynamic Case Study of Anglet, France. *Coast Eng.* 54, 345–356. doi: 10.1016/j.coastaleng.2006.10.006
- Camus, P., Losada, I. J., Izaguirre, C., Espejo, A., Menéndez, M., and Pérez, J. (2017). Statistical Wave Climate Projections for Coastal Impact Assessments. *Earth's Future* 5, 918–933. doi: 10.1002/2017EF000609
- Camus, P., Menéndez, M., Méndez, F. J., Izaguirre, C., Espejo, A., Cánovas, V., et al. (2014). A Weather-Type Statistical Downscaling Framework for Ocean Wave Climate. *J. Geophys. Res.: Oceans* 119, 7389–7405. doi: 10.1002/2014JC010141
- Carson, M., Kohl, A., Stammer, D., Slangen, A. B. A., Katsman, C. A., Van de Wal, R. S. A., et al. (2016). Coastal Sea Level Changes, Observed and Projected During the 20<sup>th</sup> and 21<sup>st</sup> Century. *Clim. Chang.* 134, 269–218. doi: 10.1007/s10584-015-1520-1
- Casas-Prat, M., Wang, X. L., and Swart, N. (2017). CMIP5-Based Global Wave Climate Projections Including the Arctic Ocean. *Ocean Model.* 123, 66–85. doi: 10.1016/j.ocemod.2017.12.003
- Church, J., Clark, P., Cazenave, A., Gregory, J., Jevrejeva, S., Merrifield, M., et al. (2013). “Sea Level Change, Pages 1137–1216. Climate Change 2013: The Physical Science Basis,” in *Contribution of Working Group I to the Fifth Assessment Report of the Intergovernmental Panel on Climate Change*, vol. 13. (Cambridge, UK and New York, NY, USA: Cambridge University Press), 1137–1216.
- Eyring, V., Bony, S., Meehl, G. A., Senior, C. A., Stevens, B., Stouffer, R. J., et al. (2016). Overview of the Coupled Model Intercomparison Project Phase 6

## DATA AVAILABILITY STATEMENT

The raw data supporting the conclusions of this article will be made available upon reasonable request. Requests to access the datasets should be directed to Michelle Jackson, mjackson@fing.edu.uy.

## AUTHOR CONTRIBUTIONS

MJ, MF, and SS designed the research and wrote the paper. MJ performed the research, process the data and analyzed the results. MF and SS advised all the research and analysis. All authors contributed to the article and approved the submitted version.

## ACKNOWLEDGMENTS

We acknowledge the World Climate Research Programme's Working Group on Coupled Modelling, which is responsible for CMIP, and we thank the climate modeling groups (listed in **Table 3** of this paper) for producing and making available their model output. For CMIP the U.S. Department of Energy's Program for Climate Model Diagnosis and Intercomparison provides coordinating support and led development of software infrastructure in partnership with the Global Organization for Earth System Science Portals.

## SUPPLEMENTARY MATERIAL

The Supplementary Material for this article can be found online at: <https://www.frontiersin.org/articles/10.3389/fmars.2022.846396/full#supplementary-material>

- (CMIP6) Experimental Design and Organization. *Geosci. Model Dev.* 9, 1937–1958. doi: 10.5194/gmd-9-1937-2016
- Fernández, M., and Piedra-Cueva, I. (2011). “Revisión De Un Modelo Regional De Marea Astronómica Implementado Sobre La Región Suroeste Del Océano Atlántico,” in *Tesis De Maestría En Mecánica De Los Fluidos*. (Montevideo, Uruguay: Universidad de la República).
- Flather, R. (1976). *Results From Surge Prediction Model of the North-West 15uantifi Continental Shelf for 15uant, 15uantifi and 15uantifi 1973. Report 24* (Wormley, UK: Institute of Oceanography (UK)).
- Fossati, M., Santoro, P., Mosquera, R., Martínez, C., Ghiardo, F., Ezzatti, P., et al. (2013). Dinámica De Flujo, Del Campo Salino Y De Los Sedimentos Finos En El Río De La Plata. *RIBAGUA-Revista Iberoam. del Agua* 1, 48–63. doi: 10.1016/S2386-3781(15)30007-4
- Fox-Kemper, B., Hewitt, H. T., Xiao, C., Aðalgeirsdóttir, G., Drijfhout, S. S., Edwards, T. L., et al. (2021). “Ocean, Cryosphere and Sea Level Change,” in *Climate Change 2021: The Physical Science Basis. Contribution of Working Group I to the Sixth Assessment Report of the Intergovernmental Panel on Climate Change*. Eds. V. Masson-Delmotte, P. Zhai, A. Pirani, S. L. Connors, C. Péan, S. Berger, N. Caud, Y. Chen, L. Goldfarb, M. I. Gomis, M. Huang, K. Leitzell, E. Lonnoy, J. B. R. Matthews, T. Waterfield, O. Yelekçi, R. Yu and B. Zhou (Cambridge University Press).
- Guillou, N., and Chapalain, G. (2012). Modeling Penetration of Tide-Influenced Waves in Le Havre Harbor. *J. Coast Res.* 28, 945–955. doi: 10.2112/JCOASTRES-D-11-00192.1

- Haigh, I. D., Pickering, M. D., Green, J. M., Arbic, B. K., Arns, A., Dangendorf, S., et al. (2020). The Tides They are A-Changin': A Comprehensive Review of Past and Future Nonastronomical Changes in Tides, Their Driving Mechanisms, and Future Implications. *Rev. Geophys.* 58 (1). doi: 10.1029/2018RG000636
- Hemer, M. A., Katzfey, J., and Trenham, C. (2013). Global Dynamical Projections of Surface Ocean Wave Climate for a Future High Greenhouse Gas Emission Scenario. *Ocean Modell.* 70, 221–245. doi: 10.1016/j.ocemod.2012.09.008
- Hemer, M. A., and Trenham, C. E. (2015). Evaluation of a CMIP5 Derived Dynamical Global Wind Wave Climate Model Ensemble. *Ocean Modell.* 103, 190–203. doi: 10.1016/j.ocemod.2015.10.009
- Hermans, T. H. J., Tinker, J., Palmer, M. D., Katsman, C. A., Vermeersen, B. L. A., and Slangen, A. B. A. (2020). Improving Sea-Level Projections on the Northwestern European Shelf Using Dynamical Downscaling. *Climate Dyn.* 54(3–4), 1987–2011. doi: 10.1007/s00382-019-05104-5
- Hervouet, J. M. (2007). *Hydrodynamics of Free Surface Flows: Modelling With the Finite Element Method* (Chichester, UK: John Wiley & Sons Ltd).
- Howard, T., Palmer, M. D., and Bricheno, L. M. (2019). Contributions to 21st Century Projections of Extreme Sea-Level Change Around the Uk. *Environ. Res. Commun.* 1 (9), 095002. doi: 10.1088/2515-7620/ab42d7
- Huybrechts, N., and Villaret, C. (2013). Large Scale Morphodynamic Modeling of the Gironde Estuary. *Proc. Inst. Civ. Eng. Marit. Eng.* 166 (2), 51–62. doi: 10.1680/maen.2012.18
- Huybrechts, N., Villaret, C., and Lyard, F. (2012). Optimized Predictive 2D Hydrodynamic Model of the Gironde Estuary (France). *J. Waterw. Port Coast. Ocean Eng.* 138 (4), 312–322. doi: 10.1061/(ASCE)WW.1943-5460.0000129
- Idier, D., Paris, F., Le Cozannet, G., Boulahya, F., and Dumas, F. (2017). Sea-Level Rise Impacts on the Tides of the European Shelf. *Cont. Shelf Res.* 137, 56–71. doi: 10.1016/j.csr.2017.01.007
- IPCC (2013). *Climate Change 2013: The Physical Science Basis. Contribution of Working Group I to the Fifth 17uantifica Report of the Intergovernmental Panel on Climate Change* (Cambridge, United Kingdom and New York, NY, USA: Cambridge University Press).
- IPCC (2019). *Summary for Policymakers. Special Report on the Ocean and Cryosphere in a Changing Climate* (Cambridge, United Kingdom and New York, NY, USA: Cambridge University Press).
- Jackson, M., Fossati, M., and Solari, S. (2021). *Cuantificación De Los Efectos Del Cambio Climático Sobre El Régimen Medio Y Extremal Del Nivel De Mar En La Costa Uruguaya. Tesis De Maestría En Mecánica De Los Fluidos (In Spanish)*. (Montevideo, Uruguay: Universidad de la República).
- Jones, J. E., and Davies, A. M. (2008). Storm Surge Computations for the West Coast of Britain using a Finite Element Model (TELEMAC). *Ocean Dyn* 58, 337–363. doi: 10.1007/s10236-008-0140-y
- Luo, J., Li, M., Sun, Z., and O'Connor, B. A. (2013). Numerical Modelling of Hydrodynamics and Sand Transport in the Tide-Dominated Coastal-to-Estuarine Region. *Mar. Geol* 342, 14–27. doi: 10.1016/j.margeo.2013.06.004
- Lyard, F., Lefevre, F., Letellier, T., and Francis, O. (2006). Modelling the Global Ocean Tides: Modern Insights From FES2004. *Ocean Dyn Vol.* 56 pp, 394–415. doi: 10.1007/s10236-006-0086-x
- Lyu, K., Zhang, X., and Church, J. A. (2020). Regional Dynamic Sea Level Simulated in the CMIP5 and CMIP6 Models: Mean Biases, Future Projections, and Their Linkages. *J. Climate* 33 (15), 6377–6398. doi: 10.1175/JCLI-D-19-1029.1
- Martínez, C., Silva, J. P., Dufrechou, E., Santoro, P., Fossati, M., Ezzati, P., et al. (2015). "Towards a 3D Hydrodynamic Numerical Modeling System for Long Term Simulations of the Rio De La Plata Dynamic," in *E-proceedings of the 36th IAHR World Congress, The Hague, the Netherlands*.
- Mateus, M., and Neves, R. (2013). *Ocean Modelling for Coastal Management – Case Studies With MOHID* (Lisbon, Portugal: IST Press).
- Meucci, A., Young, I. R., Hemer, M., Kirezci, E., and Ranasinghe, R. (2020). Projected 21st Century Changes in Extreme Wind-Wave Events. *Sci. Adv.* 6, 7295–7305. doi: 10.1126/sciadv.aaz7295
- Moss, R. H. co-authors (2010). The Next Generation of Scenarios for Climate Change Research and Assessment. *Nature* 463, 747–756. doi: 10.1038/nature08823
- Pawłowicz, R., Beardsley, B., and Lentz, S. (2002). Classical Tidal Harmonic Analysis Including Error Estimates in MATLAB Using T\_TIDE. *Comput. Geosci.* 28, 929–937. doi: 10.1016/S0098-3004(02)00013-4
- Pelling, H., Green, M., and Ward, S. (2013). Modelling Tides and Sea-Level Rise: To Flood or Not to Flood. *Ocean Modell.* 63, 21–29. doi: 10.1016/j.ocemod.2012.12.004
- Perez, J., Menendez, M., Camus, P., Mendez, F. J., and Losada, I. J. (2015). Statistical Multi-Model Climate Projections of Surface Ocean Waves in Europe. *Ocean Modell.* 96, 161–170. doi: 10.1016/j.ocemod.2015.06.001
- Pickering, M., Horsburgh, K., Blundell, J. R., Hirschi, J., Nicholls, R. J., Verlaan, M., et al. (2017). The Impact of Future Sea-Level Rise on the Global Tides. *Cont. Shelf Res.* 142, 50–68. doi: 10.1016/j.csr.2017.02.004
- Pickering, M., Wells, N., Horsburgh, K., and Green, M. (2012). The Impact of Future Sea-Level Rise on the European Shelf Tides. *Cont. Shelf Res.* 35, 1–15. doi: 10.1016/j.csr.2011.11.011
- Pugh, D. T. (1987). *Tides, Surges and Mean Sea Level* (Swindon, UK: Natural Environment Research Council).
- Saha, S., Moorthi, S., Pan, H.-L., Wu, X., and Wang, J. (2010). The NCEP Climate Forecast System Reanalysis. *Bull. Am. Meteorol. Soc.* 91 (8), 1015–1058. doi: 10.1175/2010BAMS3001.1
- Santoro, P., Fossati, M., and Piedra-Cueva, I. (2013). Study of the Meteorological Tide in the Rio De La Plata. *Cont. Shelf Res.* 60, 51–63. doi: 10.1016/j.csr.2013.04.018
- Sathish Kumar, S., and Balaji, R. (2015). Effect of Bottom Friction on Tidal Hydrodynamics Along Gulf of Khambhat, India. *Estuarine Coastal Shelf Sci.* 154, 129. doi: 10.1016/j.ecss.2015.01.012
- Slangen, A. B. A., Carson, M., Katskman, C. A., van de Wal, R. S. W., Kohl, A., Vermeersen, L. L. A., et al. (2014). Projecting Twenty-First Century Regional Sea-Level Changes. *Clim. Chang.* 124, 317–332. doi: 10.1007/s10584-014-1080-9
- Taylor, K. E., Stouffer, R. J., and Meehl, G. A. (2012). An Overview of CMIP5 and the Experiment Design. *Bull. Am. Meteorol. Soc.* 93, 485–498. doi: 10.1175/BAMS-D-11-00094.1
- Vousdoukas, M. I., Voukouvalas, E., Annunziato, A., Giardino, A., and Feyen, L. (2016). Projections of Extreme Storm Surge Levels Along Europe. *Climate Dyn.* 47, 3171–3190. doi: 10.1007/s00382-016-3019-5
- Wandres, M., Pattiaratchi, C., and Hemer, M. A. (2017). Projected Changes of the Southwest Australian Wave Climate Under Two Atmospheric Greenhouse Gas Concentration Pathways. *Ocean Modell.* 117, 70–87. doi: 10.1016/j.ocemod.2017.08.002
- Wang, X. L., Feng, Y., and Swail, V. R. (2014). Changes in Global Ocean Wave Heights as Projected Using Multimodel CMIP5 Simulations. *Geophys. Res. Lett.* 41, 1026–1034. doi: 10.1002/2013GL058650

**Conflict of Interest:** The authors declare that the research was conducted in the absence of any commercial or financial relationships that could be construed as a potential conflict of interest.

**Publisher's Note:** All claims expressed in this article are solely those of the authors and do not necessarily represent those of their affiliated organizations, or those of the publisher, the editors and the reviewers. Any product that may be evaluated in this article, or claim that may be made by its manufacturer, is not guaranteed or endorsed by the publisher.

Copyright © 2022 Jackson, Fossati and Solari. This is an open-access article distributed under the terms of the Creative Commons Attribution License (CC BY). The use, distribution or reproduction in other forums is permitted, provided the original author(s) and the copyright owner(s) are credited and that the original publication in this journal is cited, in accordance with accepted academic practice. No use, distribution or reproduction is permitted which does not comply with these terms.



# Long-Term and Seasonal Variability of Wind and Wave Extremes in the Arctic Ocean

Isabela S. Cabral<sup>†</sup>, Ian R. Young and Alessandro Toffoli\*

Department of Infrastructure Engineering, The University of Melbourne, Parkville, VIC, Australia

## OPEN ACCESS

### Edited by:

Giovanni Besio,  
University of Genoa, Italy

### Reviewed by:

Francesco De Leo,  
Cal Poly San Luis Obispo College of  
Engineering, United States

Jose A. A. Antolínez,  
Delft University of Technology,  
Netherlands

Frederic Dias,  
University College Dublin, Ireland

### \*Correspondence:

Alessandro Toffoli  
toffoli.alessandro@gmail.com

### <sup>†</sup>Present address:

Isabela S. Cabral,  
Bureau of Meteorology,  
Melbourne, VIC, Australia

### Specialty section:

This article was submitted to  
Physical Oceanography,  
a section of the journal  
Frontiers in Marine Science

Received: 26 October 2021

Accepted: 25 March 2022

Published: 19 May 2022

### Citation:

Cabral IS, Young IR and Toffoli A  
(2022) Long-Term and Seasonal  
Variability of Wind and Wave  
Extremes in the Arctic Ocean.  
Front. Mar. Sci. 9:802022.  
doi: 10.3389/fmars.2022.802022

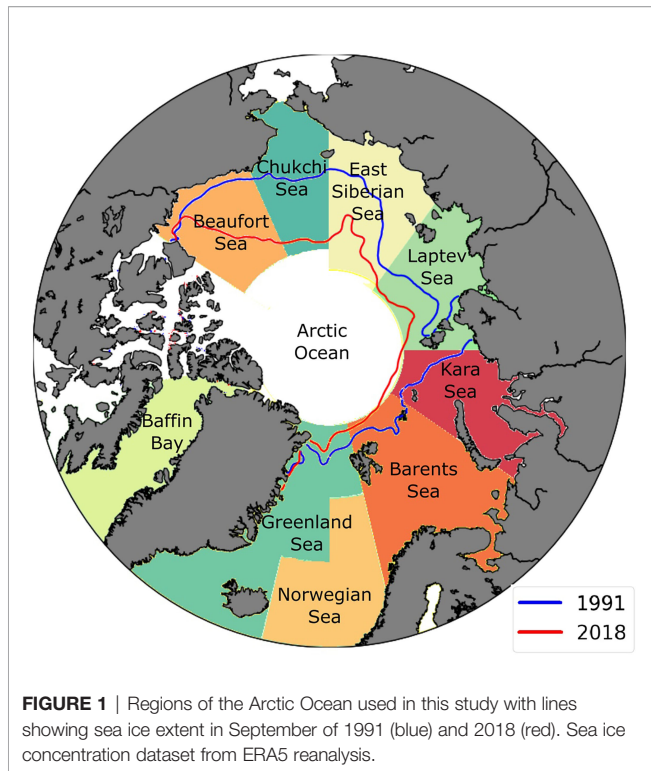
Over recent decades, the Arctic Ocean has experienced dramatic variations due to climate change. By retreating at a rate of 13% per decade, sea ice has opened up significant areas of ocean, enabling wind to blow over larger fetches and potentially enhancing wave climate. Considering the intense seasonality and the rapid changes to the Arctic Ocean, a non-stationary approach is applied to time-varying statistical properties to investigate historical trends of extreme values. The analysis is based on a 28-year wave hindcast (from 1991 to 2018) that was simulated using the WAVEWATCH III wave model forced by ERA5 winds. Despite a marginal increase in wind speed (up to about 5%), results demonstrate substantial seasonal differences and robust positive trends in extreme wave height, especially in the Beaufort and East Siberian seas, with increasing rates in areal average of the 100-year return period up to 60%. The reported variations in extreme wave height are directly associated with a more effective wind forcing in emerging open waters that drives waves to build up more energy, thus confirming the positive feedback of sea ice decline on wave climate.

**Keywords:** wind extremes, wave extremes, Arctic Ocean, climate change, non-stationary statistics

## 1 INTRODUCTION

Arctic sea ice extent has been declining sharply at a rate of 13% per decade and with thickness reducing about 66% over the past 60 years (see IPCC, 2019). Variations of the sea ice cover have been the cause of notable changes to meteorological and oceanographic conditions in the Arctic Ocean (e.g. Thomson and Rogers, 2014; Liu et al., 2016; Stopa et al., 2016; Thomson et al., 2016; Waseda et al., 2018; Casas-Prat and Wang, 2020). Emerging open waters—see the minimum sea ice extent in September 1991 and September 2018 in **Figure 1**—provide longer fetches for surface waves to build up more energy and increase in magnitude (Thomson and Rogers, 2014; Thomson et al., 2016). Concurrently, an increase of wave height impacts profoundly on the already weak sea ice cover by enhancing breakup and melting processes in a feedback mechanism (Thomson et al., 2016; Dolatshah et al., 2018; Passerotti et al., 2022). In addition, coastlines and coastal communities have been impacted by intensifying erosion with coastline retreat rates up to 25 m per year (e.g. Jones et al., 2009; Gunther et al., 2015).

Ocean climate evaluated from satellite observations (Liu et al., 2016) for the months of August and September—the period of minimum ice coverage—reveals weak or even negative trends of average offshore wind speeds over the period between 1996 and 2015, while notable upward trends



were detected in the higher 90<sup>th</sup> and 99<sup>th</sup> percentiles across the entire Arctic Ocean, except for the Greenland sea. Unlike winds, waves showed more substantial increasing rates even for average values, especially in the Chukchi, Laptev, Kara seas and Baffin Bay.

Satellite observations have temporal and spatial limitations, which are exacerbated in the Arctic where most of the altimeter sensors do not usually cover latitudes higher than 82°. Numerical models, on the contrary, provide more consistent data sets for climate analysis in this region. Stopa et al. (2016) estimated trends using a 23-year model hindcast and found that simulated average wind speed exhibits a weak increasing trend, especially in the Pacific sector of the Arctic Ocean, slightly differing from the satellite-based observations in Liu et al. (2016). Average wave heights, however, were found to be consistent with altimeter data. Waseda et al. (2018) used the ERA-Interim reanalysis database (Dee et al., 2011) to evaluate the area-maximum wind speed and wave height in the months of August, September and October from the period 1979–2016 in the Beaufort, Chukchi, East Siberian and Laptev seas. Their analysis indicated robust increasing trends for both variables, with most significant changes in October:  $\approx 0.06\text{ms}^{-1}$  per year for wind speed and  $\approx 2\text{cm}$  per year for mean significant wave height. Recently, Casas-Prat and Wang (2020) simulated historical (1979–2005) and future (2081–2100) sea state conditions to evaluate changes in regional annual maximum significant wave height, under high baseline emission scenarios (RCP8.5). Their results indicated that wave height is projected to increase at a rate of

approximately 3 cm per year, which is more than 0.5% per year in terms of annual maxima.

Previous assessments of ocean climate in the Arctic have focused on annual or monthly values and often paid specific attention to summer months. A comprehensive evaluation of climate and related changes cannot, however, ignore extremes. Classically, extreme metocean conditions are estimated with an extreme value analysis (EVA), where observations are fitted to a theoretical probability distribution to extrapolate values at low probability levels, such as those occurring on average once every 100 years (normally referred to as the 100-year return period event, see Ochi, 2005; Bitner-Gregersen and Toffoli, 2014; Thomson and Emery, 2014; Clancy et al., 2016; Meucci et al., 2020, for examples of applications in different fields of ocean engineering, physical oceanography and climate). Therefore, the EVA has to rely on long records spanning over one or more decades (observations typically cover more than a 1/3 of the return period), to be statistically significant. Motivated by the need of very long time series, the EVA requires the fundamental assumption that the statistical properties of a specific variable do not change over time, namely the process is stationary. For the strongly seasonal and rapidly changing Arctic environment, however, the hypothesis of stationarity cannot hold for an extended period of time. The inevitable time-dependency of the statistical distribution of a certain environmental stochastic process translates into a time-dependency of the parameters of the associated extreme value distribution (see more details in e.g. Renard et al., 2013; De Leo et al., 2021), invalidating the fundamental assumption of the EVA.

An alternative approach that better fits the highly dynamic nature of the Arctic is the estimation of time-varying extreme values with a non-stationary analysis (see, for example, Coles et al., 2001; Mendez et al., 2006; Galiatsatou and Prinos, 2011; Cheng et al., 2014; Mentaschi et al., 2016; De Leo et al., 2021, for a general overview). There are a number of methods for the estimation of time-varying extreme value distributions from non-stationary time series. A functional approach is the transformed-stationary extreme value analysis (TS-EVA) proposed by Mentaschi et al. (2016). The method consists of transforming a non-stationary time series with a normalisation based on the time-varying mean and standard deviation into a stationary counterpart, for which the classical EVA theory can be applied. Subsequently, an inverse transformation allows the conversion of the EVA results to time-varying extreme values.

Here we apply the TS-EVA method to assess time-varying extremes in the Arctic Ocean. The assessment is performed on a data set consisting of a long-term hindcast—from January 1991 to December 2018—that was obtained using the WAVEWATCH III (WW3, Tolman, 2009) spectral wave model forced with ERA5 reanalysis wind speeds (Hersbach et al., 2019). A description of the model and its validation is reported in Section 2.1. Model data are processed with the TS-EVA to determine extreme values for wind forcing and wave height. Long-term trends are investigated with a nonseasonal approach; seasonal variability is considered with a concurrent seasonal method (Section 2.2). Results are discussed in terms of regional distributions and areal

averages in Sections 3 and 4. Concluding remarks are presented in the last Section.

## 2 METHOD

### 2.1 Wave Hindcast

A 28-year (from 1991 to 2018) wave hindcast of the Arctic Ocean (Cabral et al., 2021) was carried out with the WAVEWATCH III (WW3) spectral wave model—version 6.07—to build a database of sea state conditions, which is consistent in space and time. A regional model domain covering the area above latitude 53.17°N was set up in an Arctic Polar Stereographic Projection with a horizontal resolution varying from 9 to 22 km (this configuration was found to optimise the accuracy of model results in relation to recorded data and computational time). The bathymetry was extracted from the ETOPO1 database (Amante and Eakins, 2009). The regional set up was then forced with ERA5 atmospheric data and sea ice coverage (Hersbach et al., 2019). The model physics were defined by the observation-based ST6 source term package (Liu et al., 2019), which accounts for wind-wave interaction and white capping dissipation processes, and the discrete interaction approximation (DIA, see Komen et al., 1984), which describes nonlinear interactions. The model was run without wave-ice interaction modules as the focus is on the open ocean and not the marginal ice zone; regions of sea ice with concentration larger than 25% were therefore treated as land. Note that higher thresholds of sea ice concentration are not ideal as they would produce significant wave attenuation (see for

example Kohout et al., 2020; Alberello et al., 2021), requiring specific waves-in-ice physics. Boundary conditions were imposed on the regional model to account for energetic swells coming from the North Atlantic. To this end, boundaries were forced by incoming sea states from WW3 global runs with 1-degree spatial resolution (see Zieger et al., 2015, for general details of the set up). The global model used ERA5 wind forcing and the ST6 source term package. Simulations were run with a spectral domain of 32 frequency and 24 directional bins (directional resolution of 15 degrees). The minimum frequency was set at 0.0373 Hz and the frequency increment factor was set at 1.1, providing a frequency range of 0.0373–0.715 Hz. Grid outputs were stored every 3 hours.

Calibration of the ST6 source terms only requires adjustments of the wind-wave growth parameter (CDFAC, see e.g. Fernandez et al., 2021, for a discussion on model sensitivity to this parameter). This was performed by testing the model outputs (significant wave height) against altimeter data across six different satellite missions (ERS1, ERS2, ENVISAT, GFO, CRYOSAT-2 and Altika SARAL, see Queffeuou and Croize-Fillon, 2015) and for the period August–September 2014. The best agreement for the regional set up was achieved for CDFAC = 1.23 with correlation coefficient  $R=0.95$ , scatter index  $SI \approx 1\%$  and root mean square error  $RMSE \approx 0.3\text{mm}$  (see e.g. Thomson and Emery, 2014, for details on error metrics). The configuration was further validated by comparing all modelled significant wave height values against matching altimeter observations for an independent period of four years from 2012 to 2016. **Figure 2A** shows the regional model outputs versus collocated altimeter

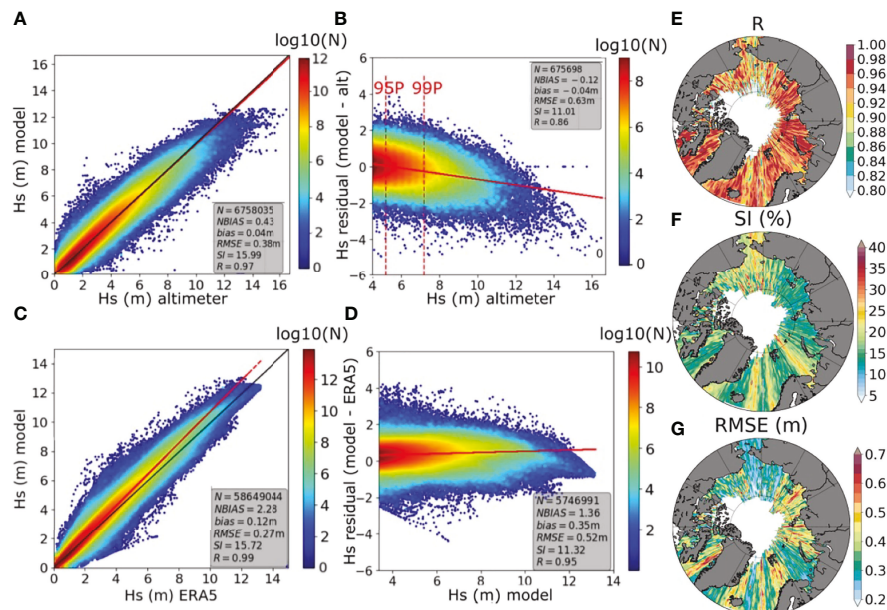


**FIGURE 2** | Validation of significant wave height for the period 2012–2016 with ST6 core physics. Comparison against altimeter observations: **(A)** all data and **(B)** 90th percentile. Comparison against ERA reanalysis: **(C)** all data and **(D)** 90th percentile and above. The black line represents the 1:1 agreement and the red lines are the linear regression. Regional distribution of error metrics (in relation to altimeter observations and data in the 90th percentile): **(E)** correlation, **(F)** scatter index, and **(G)** root mean square error.



data for the validation runs. Generally, the model correlates well with observations:  $R = 0.97$ ,  $SI = 16\%$ , and  $RMSE = 0.38m$ . The residuals between model and altimeters as a function of the observations are reported in **Figure 2B** for data in the 90<sup>th</sup> percentile. The comparison indicates a satisfactory level of agreement for the upper range of wave heights ( $H_s > 4m$ ):  $R = 0.86$ ,  $SI = 11\%$ , and  $RMSE = 0.63m$ . Model outputs are also consistent with ERA5 reanalysis, with a  $R = 0.99$ ,  $RMSE = 0.27m$  and NBIAS of 2.3% for all data (**Figure 2C**), and  $R = 0.95$ ,  $RMSE = 0.52m$  and NBIAS of 1.4% for the upper percentiles (**Figure 2D**). Note, however, that the WW3 model hindcast used herein predicts slightly higher wave heights and is marginally more accurate in replicating satellite observations than ERA5 (see assessment of ERA5 performance in Law-Chune et al., 2021) due to enhanced spatial and temporal resolution, making it more suitable for the present analysis.

The regional distribution of model errors (with respect to altimeter observations and for data in the 90<sup>th</sup> percentile) is reported in **Figures 2E–G**. The model performed well across the entire Arctic Ocean with no specific regions affected by significant errors, noting that the analysis is limited to deep water regions where altimeter data is not contaminated by land.

The validation above considers matches of collocated values in time and space. An extreme value analysis applied to model results would require a further validation of e.g. 100-year return period significant wave height against *in-situ* or remotely sensed observations. Long duration (more than 20-years) *in-situ* buoy records are not available in the Arctic. Although altimeter data can be used for long term statistical analysis (Vinoth and Young, 2011; Takbash et al., 2019), low observation density and contamination of land and sea ice in the satellite footprints result in significant under-sampling and thus uncertainties of extreme value estimates (Takbash and Young, 2019). Thereby, the lack of reliable independent long term observations hampers a thorough verification of an extreme value analysis.

## 2.2 Transformed Stationary Extreme Value Analysis

The TS-EVA method developed by Mentaschi et al. (2016) is applied herein without any modifications, to extract time-varying information on climate extremes. In this section,

we only provide a brief summary of the approach, while a more detailed discussion can be found in Mentaschi et al. (2016); De Leo et al. (2021).

The method is based on three main steps. In the first step, the original non-stationary time series (see an example of significant wave height for the Kara sea in **Figure 3A**, where an initial downward trend between 1993 and 1999 is followed by a clear positive trend) is transformed into a stationary counterpart that can be processed using classical EVA methods. The transformation is based on the following equation:

$$x(t) = \frac{y(t) - T_y(t)}{S_y(t)} \quad (1)$$

where  $y(t)$  is the non-stationary time-series,  $x(t)$  is the stationary counterpart,  $T_y(t)$  is the trend of  $y(t)$  and the  $S_y(t)$  is its standard deviation. Computation of  $T_y(t)$  and  $S_y(t)$  relies on algorithms based on running means and running statistics. This approach acts as a low-pass filter, which removes the variability within a specified time window  $W$  (hereafter this approach is referred to as nonseasonal). The time window has to be short enough to incorporate the desired variability, but long enough to eliminate noise and short-term variability; the optimal length for  $W$  was found to be 5 years due to the rapid sea ice melting occurring in the last few decades. The transformation results in time series with zero trend, zero mean and a standard deviation of one. In order to further verify stationarity, Mentaschi et al. (2016) also recommend that the skewness and kurtosis are approximately constant as a function of time. In the present application, representative transformed time series for each of the major Arctic Ocean basins (**Figure 1**) were examined and their skewness and kurtosis evaluated. In all cases these values varied by less than 15% over the full duration of the model data set, in agreement with test results reported by Mentaschi et al. (2016). Thereby, we concluded that the transformed time series are approximately stationary.

In the second step, the stationary time-series  $x(t)$  is processed with a standard EVA approach. Herein, a peaks-over-threshold method (POT, see e.g. Thomson and Emery, 2014, for a general overview) was applied to extract extreme values from the records with a threshold set at the 90<sup>th</sup> percentile. A Generalised Pareto Distribution (GPD, e.g. Thomson and Emery, 2014).

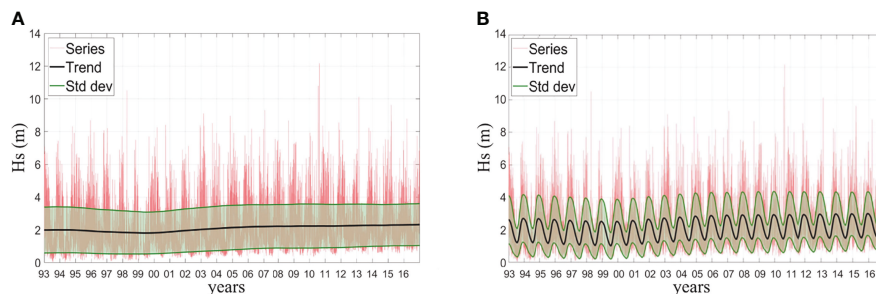


**FIGURE 3** | TS-EVA of the projections of significant wave height for a point located in the Kara Sea. The time series of  $H_s$  (m), its long-term trend and standard deviation computed with a time window of 5 years obtained with **(A)** the nonseasonal approach and **(B)** with the seasonal approach.

$$F(x) = 1 - \left[ 1 + k \left( \frac{x - A}{B} \right)^{\frac{-1}{k}} \right] \quad (2)$$

where  $A$  is the threshold and  $B$  and  $k$  are the scale and shape parameters respectively, was fitted to the data in order to derive an extreme value distribution; a Kolmogorov Smirnov test (see e.g. Chu et al., 2019) was applied to validate the fit. Note that the parameters  $A$  and  $B$  are time-dependent and change with trends, standard deviation, and seasonality in the TS-EVA approach. To ensure statistical independence, peaks were selected at least 48 hours apart. Furthermore, to ensure a stable probability distribution, a minimum of 1000 peaks was selected for each grid point of the model domain (Meucci et al., 2018), meaning that regions free of sea ice less than about two months per year were excluded from the analysis.

It should be noted that the selection of the threshold affects the estimate of extreme values. The threshold has to be neither too high, in order to include sufficient data points and hence ensure a stable fit of equation 2, nor too low, so that non-extreme values are excluded from the analysis. For significant wave height, the threshold is normally a percentile value from 90<sup>th</sup>, as in this study, to 95<sup>th</sup> percentile or a value that sets a minimum number of events (e.g. 1,000) (Alves and Young, 2003; Cairns and Sterl, 2005; Vinoth and Young, 2011; Takbash et al., 2019; Meucci et al., 2018). Extensive sensitivity analysis against buoy data (Vinoth and Young, 2011; Takbash et al., 2019) suggests these thresholds result in unbiased estimates of extreme value significant wave height.

The third and final step consists of back-transforming the extreme value distribution into a time-dependent one by reincorporating the trends that were excluded from the original non-stationary time series. As the resulting distribution is different for each year within the time series, the TS-EVA method enables extrapolation of partial return period values for any specific year. Therefore, after fitting a GPD distribution to the stationary time series and transforming to a time-varying distribution, it is possible to obtain the  $N$ -year return levels for any specific year within the original time series. For this study, we use the 100-year return level, which is commonly used in climate and ocean engineering applications (see, e.g. Ochi, 2005; Bitner-Gregersen and Toffoli, 2014; Bitner-Gregersen et al., 2014; Thomson and Emery, 2014; Clancy et al., 2016; Bitner-Gregersen et al., 2018; Meucci et al., 2020).

Effects of the seasonal cycle (see e.g. Figure 3B) can be accounted for by incorporating seasonal components in the stationary time-series  $x(t)$ . To this end, trend  $T_y(t)$  and standard deviation  $S_y(t)$  in equation (1) are expressed as  $T_y(t) = T_{0y}(t) + s_T(t)$  and  $S_y(t) = S_{0y}(t) \times s_S(t)$ , where  $T_{0y}(t)$  and  $s_T(t)$  are the long-term and seasonal components of the trend and  $S_{0y}(t)$  and  $s_S(t)$  are the long-term and seasonal components of the standard deviation. Parameters  $T_{0y}(t)$  and  $S_{0y}(t)$  are computed by a running mean acting as a low-pass filter within a given time window ( $W$ ). The seasonal component of the trend  $s_T(t)$  is computed by estimating the average monthly anomaly of the de-trended series. The seasonal component of the standard deviation  $s_S(t)$  is evaluated as the monthly average of the ratio between the fast and slow

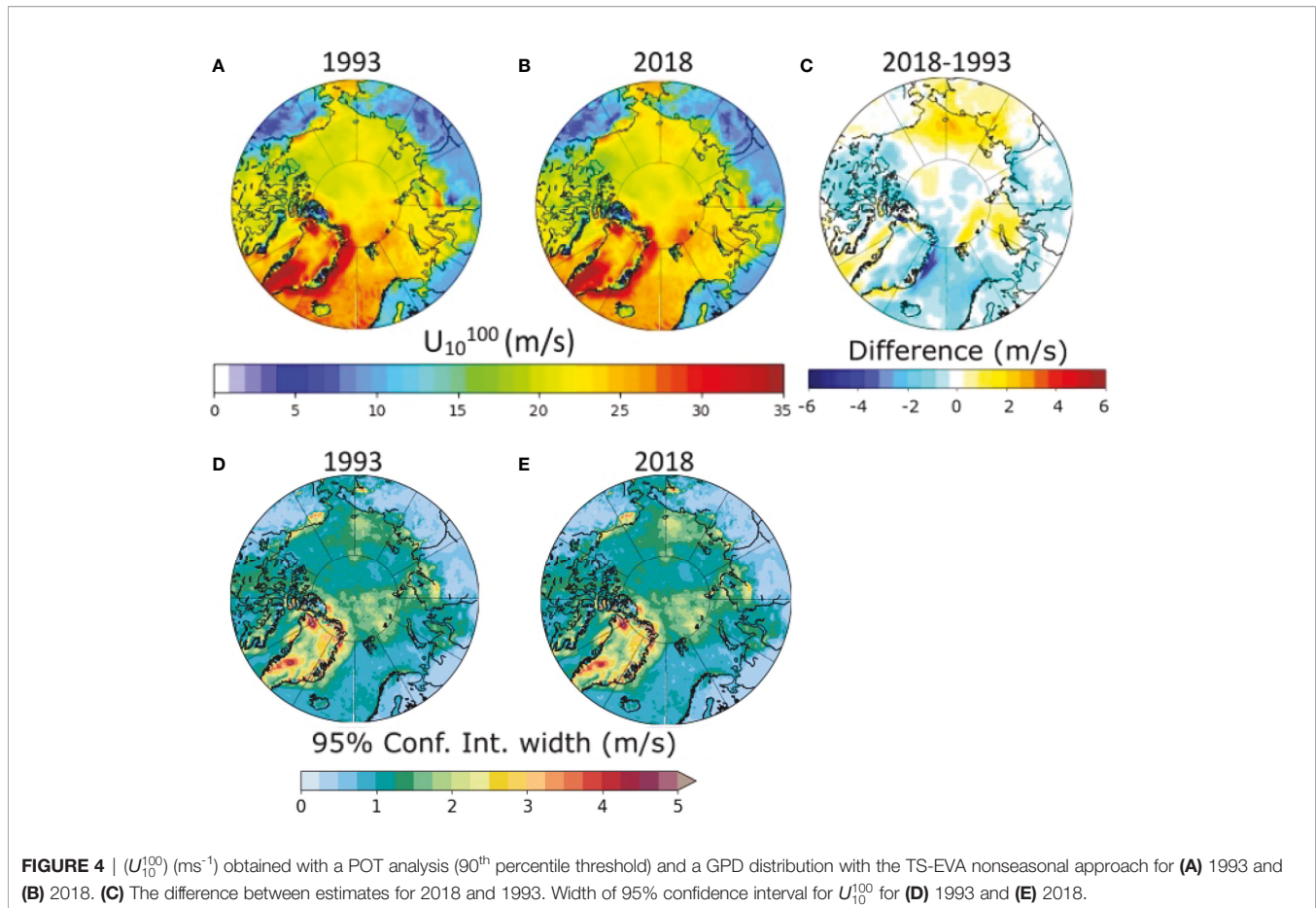
varying standard deviations,  $S_{sn}(t)/S_{0y}(t)$ , where  $S_{sn}$  is computed by another running mean standard deviation on a time window  $W_{sn}$  much shorter than one year. As for the non-seasonal approach, the time window  $W$  was set to 5 years to estimate the long-term components, while a time window  $W_{sn}$  of 2 months was applied to evaluate the intra-annual variability (seasonal components). Note that the length of the seasonal window  $W_{sn}$  is chosen to maximise accuracy and minimise noise. The resulting stationary time series  $x(t)$  is analysed with an EVA approach to fit an extreme value distribution, which is then back-transformed to a time-dependent one. The seasonal approach enables the extrapolation of partial extreme values such as the 100-year return period levels for each month.

## 3 NONSEASONAL TRENDS

### 3.1 Wind Extremes

Atmospheric forcing over the ocean is described by the wind speed at 10 metres above the sea surface, ( $U_{10}$ , see e.g. Holthuijsen 2007), and it is applied herein to investigate the 100-year return levels for wind extremes. Figure 4 shows examples of regional distribution of the 100-year return period levels for wind speed  $U_{10}^{100}$  and 95% confidence interval (CI95) width for the years 1993 and 2018, i.e. beginning and end of the considered period. The regional distribution of the differences between the two years is also displayed in the figure to highlight the substantial change that has occurred. Extreme winds are estimated to reach approximately  $25\text{ms}^{-1}$  in the Baffin Bay, Greenland, Barents and Kara seas (i.e. the Atlantic sector of the Arctic Ocean, see Figure 1 for the geographical location of sub-regions), with peaks up to  $40\text{ms}^{-1}$  along the Eastern coast of Greenland. Extreme winds in the Pacific Sector, i.e. the Beaufort, Chukchi, East Siberian and Laptev seas recorded lower  $U_{10}^{100}$ , reaching values up to  $20\text{ms}^{-1}$ . Confidence intervals were normally narrow over the ocean with extremes varying within the range of  $\pm 2.5\text{ms}^{-1}$  (peaks up to  $\pm 5\text{ms}^{-1}$  were reported over land, especially in Greenland). The magnitude of extreme wind speeds predicted here is generally consistent with values determined with classical EVA methods in the Atlantic sector of the Arctic Ocean (Breivik et al., 2014; Gallagher et al., 2016; Bitner-Gregersen et al., 2018).

The TS-EVA analysis, nevertheless, shows that extremes have only been changing marginally for the past three decades (Figure 4). The long term trends of  $U_{10}^{100}$  are shown in Figure 5, which reports areal averages as a function of time for each sub-region. In the Atlantic sector,  $U_{10}^{100}$  showed a weak drop in the Norwegian and Greenland seas, with a total decrease of about  $3\text{ms}^{-1}$  over the period 1993-2018 (a rate of  $-0.12\text{ms}^{-1}$  per year). More significant drops were recorded along the Western coast of Greenland (i.e. Fram Strait, Eastern Greenland sea), where  $U_{10}^{100}$  reduced at a rate of  $-0.24\text{ms}^{-1}$  per year. The Baffin Bay and the Barents sea showed negligible changes, with  $U_{10}^{100}$  remaining approximately constant. The opposite trend was reported on the Eastern side of the Atlantic sector (i.e. the Kara sea), where wind speed showed a weak increase with a



rate of  $0.04\text{ms}^{-1}$  per year. The Pacific sector, on the contrary, was subjected to more consistent trends across the sub-regions. The East Siberian and Chukchi seas show weak positive trends of about  $0.16$  and  $0.12 \text{ms}^{-1}$  per year, respectively. A similar increase was also observed in the Western part of the Beaufort sea. The Laptev sea recorded the lowest rate of increase in the Pacific sector, with  $U_{10}^{100}$  increasing at a rate of  $0.04\text{ms}^{-1}$  per year.

### 3.2 Wave Extremes

The energy content of the sea state is historically represented by the significant wave height ( $H_s$ , see Holthuijsen 2007), which is used to describe wave extremes. **Figure 6** shows the 100-year return levels for significant wave height ( $H_s^{100}$ ), confidence intervals and differences between years 1993 and 2018. It should be noted that regions covered by sea ice for most of the year are not considered in this analysis and thus they are color-coded with white in the figure. The Atlantic sector experiences high  $H_s^{100}$  ( $>10 \text{m}$ ) due to the energetic North Atlantic swell penetrating the Arctic Ocean. Likewise, the Pacific sector experiences significant values of  $H_s^{100}$  ( $>5 \text{m}$ ), despite a substantial sea ice cycle that limits fetch lengths for a large fraction of the year. Generally, the 95% confidence intervals vary within  $\pm 1.5\text{m}$  at the beginning of the examined period (1993) and widen in more recent years (2018) in regions of significant

sea ice decline (see **Figures 6D, E**), with range increasing up to  $\pm 2.5\text{m}$ .

There is a clear difference of  $H_s^{100}$  between 1993 and 2018. More specifically,  $H_s^{100}$  increases substantially, up to  $4 \text{m}$ , in the emerging open waters of the Pacific sector (the Beaufort, Chukchi and East Siberian seas, cf. sea ice margins in **Figure 1**). Variations are typically smaller in the Laptev and Kara seas, with increments of about  $2 \text{m}$ , on average. Notable increases of  $H_s^{100}$  (up to  $6 \text{m}$ ) occur nearby the sea ice margins. Here, the seasonal sea ice cycle is still significant, introducing uncertainties related to the exact position of sea ice and limiting the amount of data available for the analysis that result in larger confidence intervals (up to  $\pm 4 \text{m}$ ). Extremes in the Atlantic sector, surprisingly, show an overall decrease, with  $H_s^{100}$  dropping by about  $1\text{-}2 \text{m}$ . Note, however, that this is a region in which the sea ice extent has not changed dramatically over this period and the decrease is a direct consequence of the drop of wind speed (see **Figure 4**). Similarly to the Laptev and Kara seas, regions closer to sea ice such as the Fram straits and the Northern part of the Barents sea experienced a sharp growth, with  $H_s^{100}$  increasing up to  $5 \text{m}$  between 1993 and 2018 (but with notably large uncertainties).

Temporal variations of the aerial average of  $H_s^{100}$  are reported in **Figure 5** for different basins. A consistent increase of  $H_s^{100}$  is

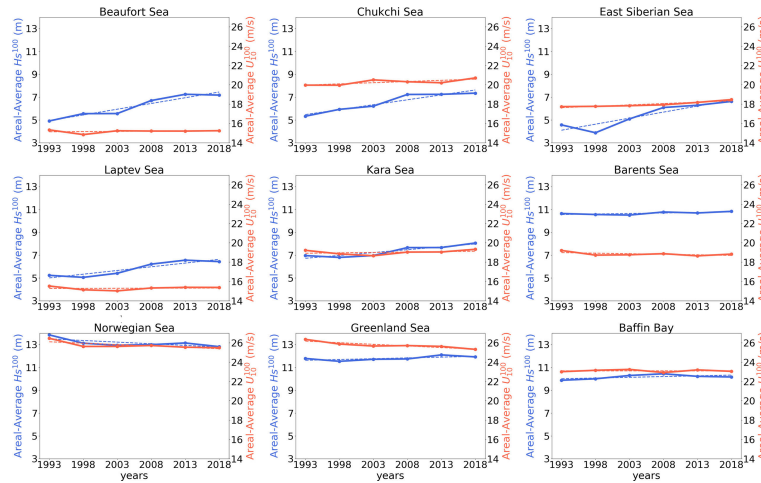


**FIGURE 5** | Temporal variation of the Areal-averages of  $H_s^{100}$  (blue) and  $U_{10}^{100}$  (red) estimated by nonseasonal TS-EVA approach for each sea in the Arctic Ocean.

evident in the emerging open waters of the Beaufort, Chukchi, East Siberian, Laptev and Kara seas. Variations in the Beaufort and East Siberian seas are the largest, with a total increase over the period 1993-2018 of approximately 16 cm per year. The

Chukchi and Laptev seas also experienced a substantial growth of  $H_s^{100}$ , with an increase of 6 cm per year, while  $H_s^{100}$  increased by approximately 4 cm per year in the Kara sea. In contrast, the Atlantic sector reports only weak upward trends, with the Baffin

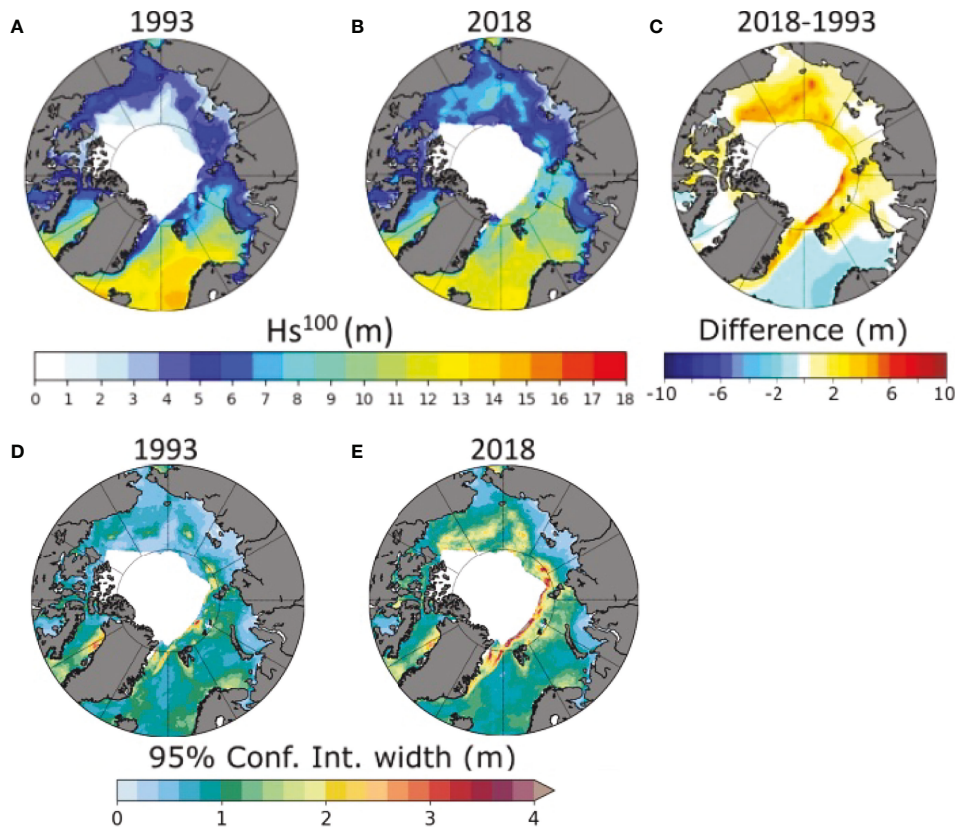


**FIGURE 6** |  $H_s^{100}$  (m) obtained with a POT analysis (90<sup>th</sup> percentile threshold) and a GPD distribution in the TS-EVA nonseasonal approach for (A) 1993 and (B) 2018. (C) The difference between estimations for 2018 and 1993. Width of 95% confidence interval for  $H_s^{100}$  for (D) 1993 and (E) 2018.

Bay and Greenland sea showing an increase of 1.6 cm per year. The Barents sea experienced no notable long-term variations, while the Norwegian sea reported a drop in  $H_s^{100}$  of about 4 cm per year. We note that, as these latter regions are predominantly free from sea ice, the downward trends are associated with the decline of wind speeds over the North Atlantic (results are consistent with finding in Breivik et al., 2013; Bitner-Gregersen et al., 2018). It is worth noting that negative trends for the North Atlantic are expected to continue in the future as indicated by projections based on RCP 4.5 and RCP 8.5 emission scenarios (Aarnes et al., 2017; Morim et al., 2019). Wave height, however, is predicted to increase at high latitudes of the Norwegian and Barents seas over the next decades as a result of ice decline (Aarnes et al., 2017), confirming the positive trend in wave extremes that is already arising close the ice edge (see **Figure 6**). The contrast between an overall decrease of wave height as a result of wind speed decline and the increase of wave height due to emerging open waters in winter is also a distinct feature in the North Pacific (cf. Shimura et al., 2016).

The increase in  $U_{10}^{100}$  is small over the modelled period (up to about 5% and confined to the Chukchi and Kara Seas; **Figure 4C**) and it cannot fully explain the more substantial increase of  $H_s^{100}$  (up to about 60%; **Figure 6C**) that is observed around the entire Arctic Ocean, with the Beaufort, Chukchi, East Siberian and Laptev seas being the most significant examples. Nevertheless, it can still be argued that the increase in  $H_s^{100}$  is caused by an increase in magnitude/frequency of storms or changes in wind direction. It should be noted, however, that increases in either the magnitude or frequency of storms would also results in notable changes in  $U_{10}^{100}$ , which are not reported herein. Changes in the prevailing wind directions over Beaufort, Chukchi and East Siberian seas have been reported but are only marginal (Stegall and Zhang, 2012), further suggesting that direct contributions from the wind field are negligible. Conversely, sea ice decline correlates more robustly with the increase of  $H_s^{100}$  as substantiated by the temporal variation of the yearly, aerial average of sea ice area in **Figure 7**

and aerial average of  $H_s^{100}$  in **Figure 5** (see also the remarkable agreement between regions where  $H_s^{100}$  has increased significantly, **Figure 6C**, and the areas where sea-ice has decreases, **Figure 1**). Therefore, negative trends of sea ice area remain the most robust cause for longer fetches in emerging open waters, contributing to more effective atmospheric forcing and driving waves to grow in magnitude. This coincides with an enhanced stage of development for the wave fields associated with the 100-year return level, as demonstrated by positive trends of the 100-year wave age ( $WA^{100}$ ; **Figure 7**). The latter is a measure of the strength of the wind forcing and wave growth, and it is computed as  $C_p^{100} / U_{10}^{100}$ , where  $C_p^{100}$  is the phase speed linked to the 100-year peak wave period, which is estimated from a population of peak wave periods associated with the selected significant wave height events (cf. Ochi, 2005). In addition, it is also worth mentioning that regions mostly free of sea-ice, such as the Greenland Sea, have shown very little change in  $H_s^{100}$  and  $WA^{100}$  (**Figures 5, 7**).

## 4 SEASONAL VARIABILITY

### 4.1 Wind Extremes

**Figures 8, 9** show the monthly values of  $U_{10}^{100}$  for 1993 and 2018, respectively. During the autumn and winter season (October to February),  $U_{10}^{100}$  ranges between 20 and 30ms<sup>-1</sup>, with peaks along the Greenland coast (Denmark and Fram Straits) up to 50ms<sup>-1</sup>. In the spring and summer months (March to September),  $U_{10}^{100}$  ranges between 10 and 30ms<sup>-1</sup> with again the highest winds reported in the western Greenland sea. Note that the seasonal approach returns a geographical distribution of extremes that is similar to the one obtained with the nonseasonal approach, but it captures more extreme season-related events. The seasonal component tends to shift the tail of the time-varying extreme value distribution into higher frequencies, resulting in higher estimated extremes for all seasons (months).

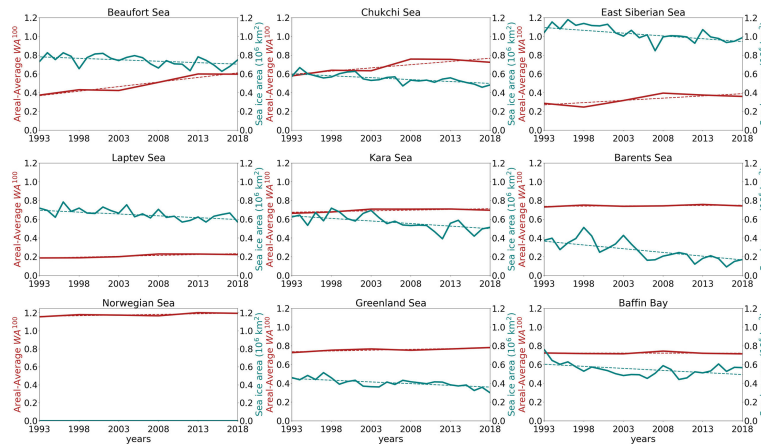


**FIGURE 7** | Temporal variation of the yearly areal-average of sea ice area (sea ice extent, blue line) and aerial-average of wave age associated with 100-year events (red line). Areal trends are shown as dashed lines.

Differences between  $U_{10}^{100}$  for 1993 and 2018 are reported in **Figure 10**. Generally, differences range between 1 and  $3\text{ms}^{-1}$  and are quite consistent across all seasons. The Pacific sector experiences an increase, while the Atlantic sector and the central Arctic are subjected to a reduction of  $U_{10}^{100}$ . The most significant changes are observed in the western Greenland sea during the winter season (December to February), where reductions up to  $-5\text{ms}^{-1}$  were detected. It is interesting to note that the regional distribution of differences is similar for each month, denoting a homogeneous change of extreme winds across the Arctic Ocean throughout the year. Note also that differences obtained with the seasonal approach are consistent with those estimated with the nonseasonal method.

### 4.2 Wave Extremes

The seasonal variations of  $H_s^{100}$  are presented in **Figures 11, 12** for 1993 and 2018, respectively. The minimum sea ice coverage in 1991-1993 is shown as a dashed lines in **Figure 12**. Extreme wave height, as expected, is subjected to a substantial seasonal variation. The highest values are found in the region encompassing the Greenland and Norwegian Seas, where energetic swells coming from the North Atlantic Ocean propagate into the region (cf. Liu et al., 2016; Stopa et al., 2016). The highest  $H_s^{100}$  in this region reaches values up to 18 m in the winter months (December to February), concomitantly with strong winds (**Figures 8, 9**), and reduces to about 5 m in the summer (June and July). Over the past three decades, however, the general trend shows a consistent reduction in this region at a rate of 4 cm per year regardless of the season (see maps of differences in **Figure 13** and trends of areal-averages in **Figure 14**). These results are in agreement with the results obtained with the nonseasonal approach. Nevertheless, extreme waves

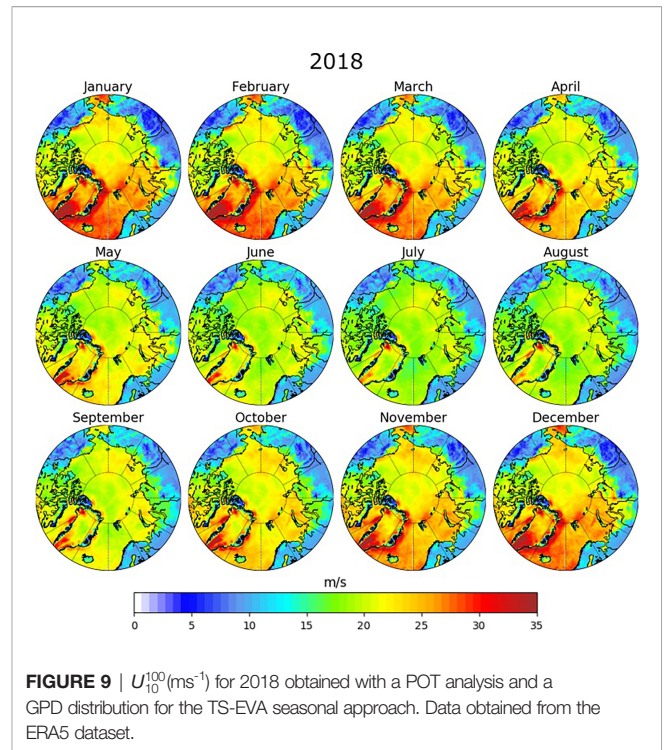


**FIGURE 9** |  $U_{10}^{100}(\text{ms}^{-1})$  for 2018 obtained with a POT analysis and a GPD distribution for the TS-EVA seasonal approach. Data obtained from the ERA5 dataset.

penetrate further North in the emerging open waters of the Northern Greenland, Barents and Kara seas, especially during the autumn (September to November) and winter (December to February) seasons in recent years. Consequently, there is a dramatic increase of  $H_s^{100}$  in these regions with values up to 13 m in 2018. This corresponds to an average increasing rate of approximately 12 cm per year, with peaks of about 35 cm per

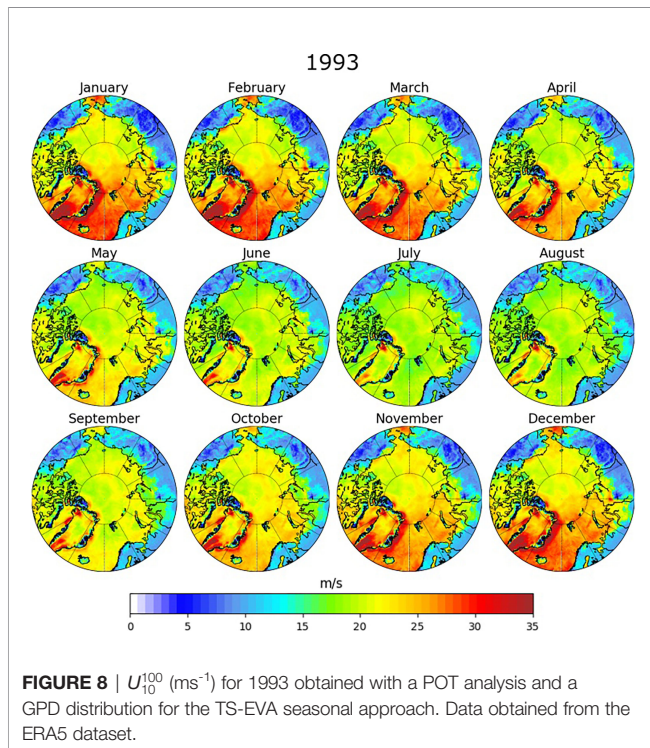


**FIGURE 8** |  $U_{10}^{100}(\text{ms}^{-1})$  for 1993 obtained with a POT analysis and a GPD distribution for the TS-EVA seasonal approach. Data obtained from the ERA5 dataset.

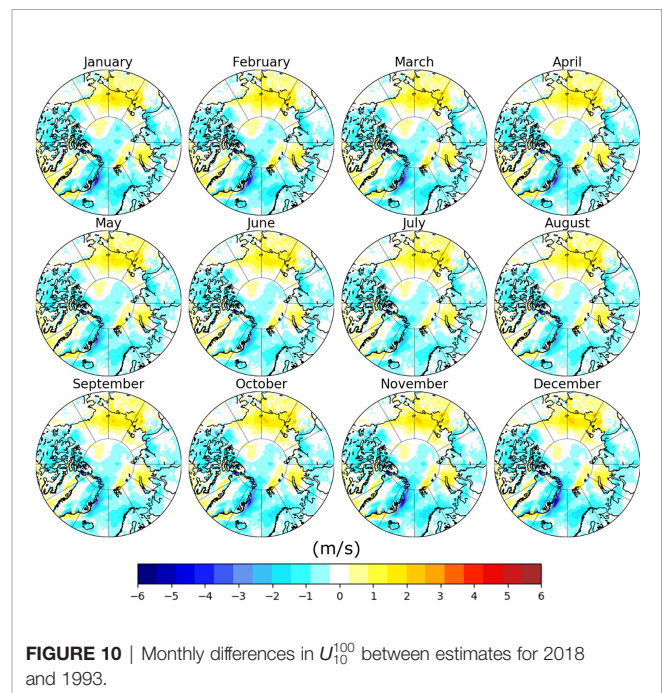
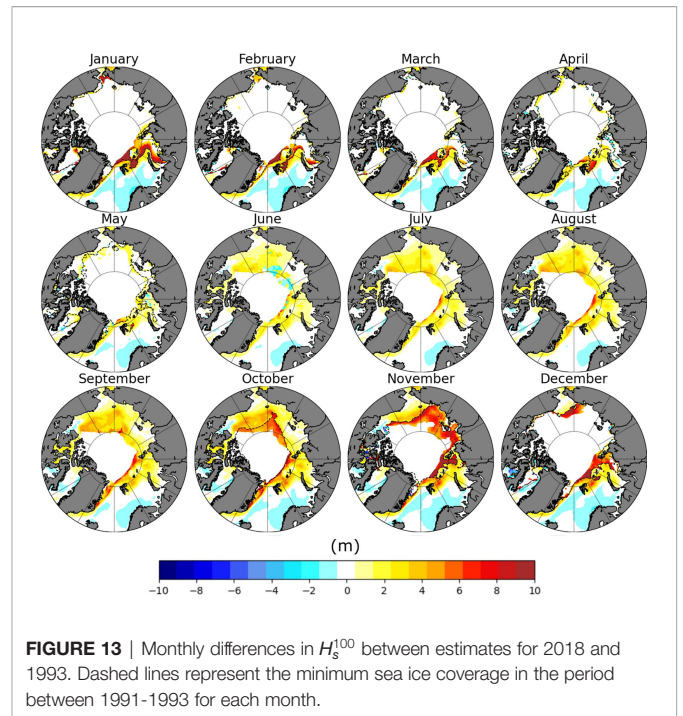
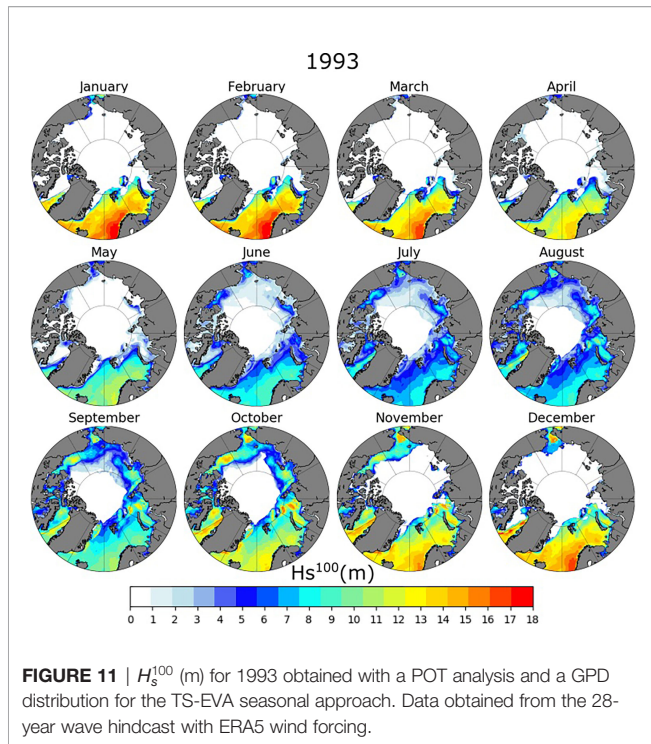


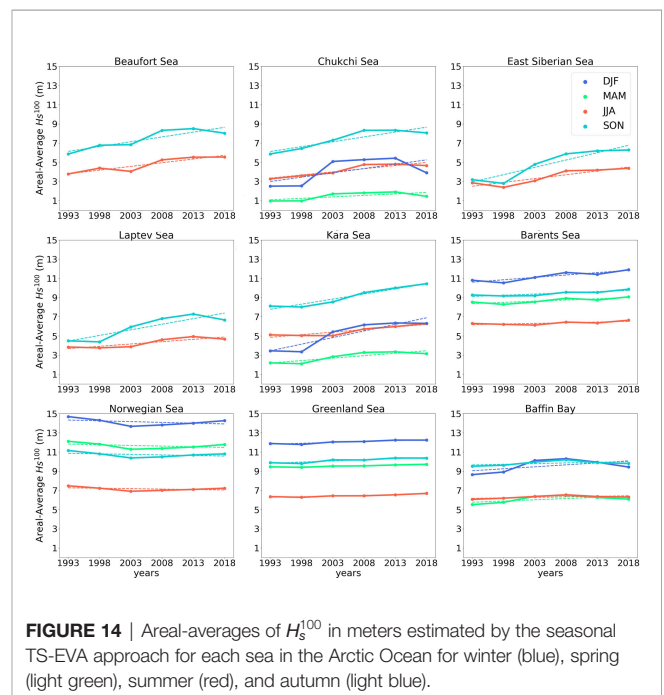
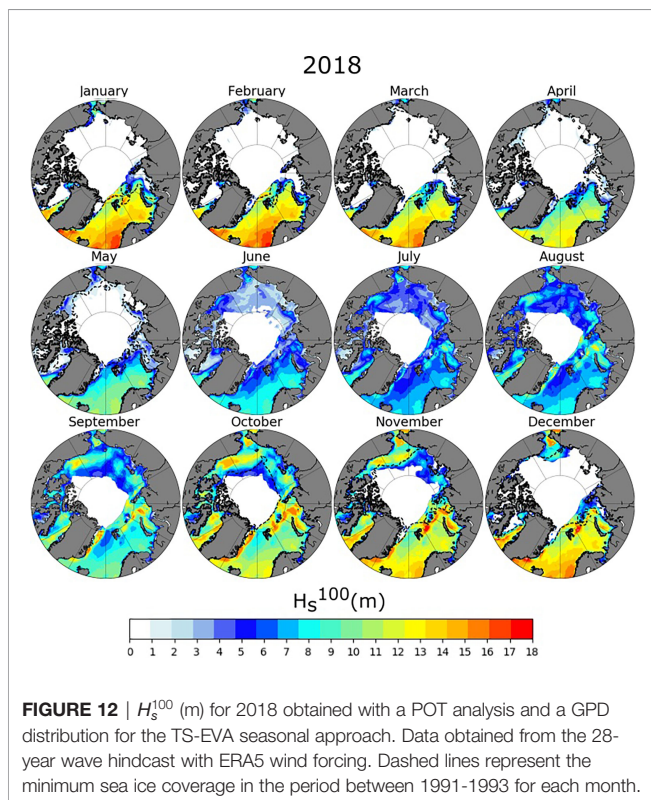
**FIGURE 10** | Monthly differences in  $U_{10}^{100}$  between estimates for 2018 and 1993.



year nearby the sea ice margins. Based on future projection, this positive trend is expected to continue (Aarnes et al., 2017).

In regions subjected to the sea ice cycle, wave extremes in 1993 used to build up in late spring or early summer (June), and

reach their maximum of up to 12 m in a confined area of the Beaufort sea in autumn (October). In more recent years (2018), extreme waves already have a significant presence earlier in spring (May), primarily in the coastal waters of the Beaufort sea and the East Siberian sea (Figure 13). From June to November, there is a rapid intensification of the sea state and extremes span from a few metres in June to about 16 m in



November, with an average growth rate of 12 cm per year, over a region encompassing the whole Beaufort, Chukchi and East Siberian seas. These secluded areas, which are the most prone to positive long-term variations of wind speed (Figure 10) and sea ice retreat (see Figure 7 and Strong and Rigor, 2013), are now experiencing sea state extremes comparable to those reported in the North Atlantic. It is also worth noting that significant changes are also apparent for the western part of the East Siberian sea and the nearby Laptev sea at the end of autumn (November). These regions, which used to be entirely covered by sea ice by November in the earliest decade, are now still completely open with  $H_s^{100}$  recording changes up to 8 m (a rate of 32 cm per year since 1993).

## 5 DISCUSSION

A non-stationary extreme value analysis (TS-EVA, Mentaschi et al., 2016) was applied to assess long-term and seasonal variability of wind and wave extremes (100-year return period levels) in the Arctic Ocean. This non-conventional approach is dictated by the highly dynamic nature of the Arctic, which has been undergoing profound changes over the past decades (Liu et al., 2016; Stopa et al., 2016) and invalidating the basic hypothesis of stationarity that is fundamental for classical extreme value analysis. Estimation of extremes was based on a 28-year (1991–2018) database of 10-metre wind speed and significant wave height, with a temporal resolution of three hours. Wind speed was obtained from the ERA5 reanalysis database and subsequently used to force the WAVEWATCH III spectral wave model. An Arctic Polar Stereographic Projection grid with a horizontal resolution spanning from 9 to 22 km was applied. The model was calibrated and validated against satellite altimeter observations, producing good agreement with a correlation coefficient  $R = 0.97$ , scatter index  $SI = 16\%$  and root mean squared error  $RMSE = 0.036\text{m}$ .

The TS-EVA extreme value analysis consisted of transforming the original non-stationary time series of wind speed and wave height into a stationary counterpart and then applying standard peak-over-threshold methods to evaluate extreme values with a return period of 100 years over a running window of 5 years. Non-stationarity was then reinstated by back-transforming the resulting extreme value distribution. Two different approaches were applied to the data sets: a nonseasonal approach, which returns yearly estimates of extremes and enables evaluation of long-term variability; and a seasonal approach, which incorporates a seasonal variability enabling estimation of extremes for specific months.

The nonseasonal approach showed a weak long term variability for the 100-year return period values of wind speed. An increase of approximately  $3\text{ms}^{-1}$  from 1993 to 2018 (a rate of  $\approx 0.12\text{ms}^{-1}$  per year since 1993) was reported in the Pacific sector, especially in the regions of the Chukchi and East Siberian seas and, more marginally, in the Beaufort sea and part of the Laptev sea. A decrease of roughly  $31\text{ms}^{-1}$  ( $-0.12\text{ms}^{-1}$  per year) was found in most of the remaining regions of the Arctic, with peaks

in the Eastern part of the Greenland sea ( $\approx -0.2\text{ms}^{-1}$  per year). Conversely, the growth in wave extremes is dramatic and it cannot be attributed to these mild trends in wind extremes, noting that the latter also exclude feedback from possible increases in magnitude/frequency of storms. As wind direction is steady over the Arctic Ocean, changes in the wave field are primarily driven by the substantially longer fetches emerging from sea ice decline that allow waves to build up more energy despite a marginal increase of wind speed. Large changes, in this respect, were found in the Pacific sector encompassing the area between the Beaufort and East Siberian seas, where wave height extremes have been increasing at a rate of approximately 12 cm per year, which results in an overall increase of  $\approx 60\%$  from 1993 to 2018. The enhanced wave climate in the Beaufort sea is particularly remarkable since wind extremes are stable and sea ice area is reduced by about 13% during the past three decades (Figures 5, 7), reinforcing the argument that sea ice decline exerts a positive feedback on fetches and, concurrently, wave growth as substantiated by the robust increasing trend of wave age, a measure of the strength of wind forcing and wave growth (Figure 7). The Atlantic sector, on the contrary, experienced a notable decrease of wave extremes at the rate of  $-4\text{cm}$  per year; this is consistent with a reduction of wind extremes and with general climate trends observed in Liu et al. (2016). For regions closer to the sea ice edge, where emerging open waters have been replacing pack ice, the 100-year return period levels of wave height exhibit the opposite trend, with a sharp increase of wave extremes at an extremely large local rate of 35 cm per year. It should be noted, however, that estimates of long term trends closer to the sea ice edge are more uncertain due to lack of data in the earlier years, where sea ice covered the ocean more substantially. Nevertheless, it is worth reflecting on the consequences that a sharp upward trend of wave extremes can have on already weak sea ice. As extremes become more extreme, there is negative feedback accelerating sea ice dynamics (Vichi et al., 2019; Alberello et al., 2020; Alberello et al., 2021), break up (Passerotti et al., 2022) and melting processes (Dolatshah et al., 2018), further contributing to sea ice retreat.

The seasonal approach shows a more detailed picture of climate, providing a combined seasonal and long-term variability. Wind extremes distribute uniformly over the Arctic, with peaks in the autumn and winter periods spanning from  $20\text{ms}^{-1}$  in the Pacific sector to  $30\text{ms}^{-1}$  in the North Atlantic. Spring and summer months still exhibit significant extremes up to  $20\text{ms}^{-1}$ , with a more homogeneous regional distribution. Over the entire 28-year period, trends are mild and stable through the seasons, consistent with those found with the nonseasonal approach. Variability of wave extremes is again more substantial than wind. In the Pacific sector, the decline of sea ice extent allows a rapid intensification of extremes in the spring (May and June); average growth rates span from 1 cm per year in spring to 12 cm per year in late summer and early autumn. In the Atlantic sector, in response to a notable drop of wind speed, a consistent decrease of wave extremes results all year-round. Nevertheless, the emerging waters of northern Greenland and Barents sea showed the opposite trend with an increase of wave



height at a very large rate up to 32 cm per year closer to the sea ice margin.

## DATA AVAILABILITY STATEMENT

The datasets presented in this study can be found at <https://doi.org/10.5281/zenodo.5592192>.

## AUTHOR CONTRIBUTIONS

All authors conceived the manuscript. IC set up the wave model, performed numerical simulations and analysed model output. All authors contributed to the data interpretation and to the

writing of the manuscript. All authors contributed to the article and approved the submitted version.

## FUNDING

This research was partially supported by the Victoria Latin America Doctoral Scholarship (VLADS) program.

## ACKNOWLEDGMENTS

AT acknowledge technical support from the Air-Sea-Ice Lab initiative.

## REFERENCES

- Aarnes, O. J., Reistad, M., Breivik, Ø., Bitner-Gregersen, E., Ingolf Eide, L., Gramstad, O., et al. (2017). Projected Changes in Significant Wave Height Toward the End of the 21st Century: Northeast Atlantic. *J. Geophys. Res.: Oceans* 122, 3394–3403. doi: 10.1002/2016JC012521
- Alberello, A., Bennetts, L., Heil, P., Eayrs, C., Vichi, M., MacHutchon, K., et al. (2020). Drift of Pancake Ice Floes in the Winter Antarctic Marginal Ice Zone During Polar Cyclones. *J. Geophys. Res.: Oceans* 125, e2019JC015418. doi: 10.1029/2019JC015418
- Alberello, A., Dolatshah, A., Bennetts, L. G., Onorato, M., Nelli, F., and Toffoli, A. (2021). A Physical Model of Wave Attenuation in Pancake Ice. *Int. J. Offshore Polar Eng.* 31, 263–269. doi: 10.17736/ijope.2021.ik08
- Alves, J. H. G., and Young, I. R. (2003). On Estimating Extreme Wave Heights Using Combined Geosat, Topex/Poseidon and ERS-1 Altimeter Data. *Appl. Ocean Res.* 25, 167–186. doi: 10.1016/j.apor.2004.01.002
- Amante, C., and Eakins, B. W. (2009). ETOPO1 Arc-Minute Global Relief Model: Procedures, Data Sources and Analysis. (Boulder, Colo: U.S. Dept. of Commerce, National Oceanic and Atmospheric Administration, National Environmental Satellite, Data, and Information Service, National Geophysical Data Center, Marine Geology and Geophysics Division).
- Bitner-Gregersen, E. M., Bhattacharya, S. K., Chatjigeorgiou, I. K., Eames, I., Ellermann, K., Ewans, K., et al. (2014). Recent Developments of Ocean Environmental Description With Focus on Uncertainties. *Ocean Eng.* 86, 26–46. doi: 10.1016/j.oceaneng.2014.03.002
- Bitner-Gregersen, E. M., and Toffoli, A. (2014). Occurrence of Rogue Sea States and Consequences for Marine Structures. *Ocean Dynamics* 64, 1457–1468. doi: 10.1007/s10236-014-0753-2
- Bitner-Gregersen, E. M., Vanem, E., Gramstad, O., Hørte, T., Aarnes, O. J., Reistad, M., et al. (2018). Climate Change and Safe Design of Ship Structures. *Ocean Eng.* 149, 226–237. doi: 10.1016/j.oceaneng.2017.12.023
- Breivik, Ø., Aarnes, O. J., Abdalla, S., Bidlot, J.-R., and Janssen, P. A. (2014). Wind and Wave Extremes Over the World Oceans From Very Large Ensembles. *Geophys. Res. Lett.* 41, 5122–5131. doi: 10.1002/2014GL060997
- Breivik, Ø., Aarnes, O. J., Bidlot, J. R., Carrasco, A., and Saetra, Ø. (2013). Wave Extremes in the Northeast Atlantic From Ensemble Forecasts. *J. Climate* 26, 7525–7540. doi: 10.1175/JCLI-D-12-00738.1
- Cabral, L., Young, I. R., and Toffoli, A. (2021). Arctic Wave Hindcast. doi: 10.5281/zenodo.5592193
- Caires, S., and Steri, A. (2021). 100-year return value estimates for ocean wind speed and significant wave height from the era-40 data. *J. Climate* 18, 1032–1048.
- Casas-Prat, M., and Wang, X. L. (2020). Sea-Ice Retreat Contributes to Projected Increases in Extreme Arctic Ocean Surface Waves. *Geophys. Res. Lett.* 47, e2020GL088100. doi: 10.1029/2020GL088100
- Cheng, L., AghaKouchak, A., Gilleland, E., and Katz, R. W. (2014). Non-Stationary Extreme Value Analysis in a Changing Climate. *Climatic Change* 127, 353–369. doi: 10.1007/s10584-014-1254-5
- Chu, J., Dickin, O., and Nadarajah, S. (2019). A Review of Goodness of Fit Tests for Pareto Distributions. *J. Comput. Appl. Math.* 361, 13–41. doi: 10.1016/j.cam.2019.04.018
- Clancy, C., O'Sullivan, J., Sweeney, C., Dias, F., and Parnell, A. C. (2016). Spatial Bayesian Hierarchical Modelling of Extreme Sea States. *Ocean Modelling* 107, 1–13. doi: 10.1016/j.ocemod.2016.09.015
- Coles, S., Bawa, J., Trenner, L., and Dorazio, P. (2001). *An Introduction to Statistical Modeling of Extreme Values* 208, 208. (London: Springer).
- Dee, D. P., Uppala, S. M., Simmons, A. J., Berrisford, P., Poli, P., Kobayashi, S., et al. (2011). The ERA-Interim Reanalysis: Configuration and Performance of the Data Assimilation System. *Q. J. R. Meteorol. Soc.* 137, 553–597. doi: 10.1002/qj.828
- De Leo, F., Besio, G., Briganti, R., and Vanem, E. (2021). Non-Stationary Extreme Value Analysis of Sea States Based on Linear Trends. Analysis of Annual Maxima Series of Significant Wave Height and Peak Period in the Mediterranean Sea. *Coastal Eng.* 167, 103896. doi: 10.1016/j.coastaleng.2021.103896
- Dolatshah, A., Monbaliu, J., and Toffoli, A. (2022). Interactions Between Irregular Wave Fields And Sea Ice: A Physical Model For Wave Attenuation And Ice Breakup In An Ice Tank, *J Phys Oceanogr* (published online ahead of print 2022), doi: 10.1175/JPO-D-21-0238.1
- Dolatshah, A., Nelli, F., Bennetts, L. G., Alberello, A., Meylan, M. H., Monty, J. P., et al. (2018). Hydroelastic Interactions Between Water Waves and Floating Freshwater Ice. *Phys. Fluids* 30, 091702. doi: 10.1063/1.5050262
- Emery, W. J., and Thomson, R. E. (2014). *Data Analysis Methods in Physical Oceanography* (Amsterdam: Elsevier).
- Fernández, L., Calvino, C., and Dias, F. (2021). Sensitivity Analysis of Wind Input Parametrizations in the Wavewatch Iii Spectral Wave Model Using the St6 Source Term Package for Ireland. *Appl. Ocean Res.* 115, 102826. doi: 10.1016/j.apor.2021.102826
- Galiatsatou, P., and Prinos, P. (2011). Modeling Non-Stationary Extreme Waves Using a Point Process Approach and Wavelets. *Stoch. Env. Res. Risk A* 25, 165–183. doi: 10.1007/s00477-010-0448-2
- Gallagher, S., Gleeson, E., Tiron, R., McGrath, R., and Dias, F. (2016). Twenty-First Century Wave Climate Projections for Ireland and Surface Winds in the North Atlantic Ocean. *Adv. Sci. Res.* 13, 75–80. doi: 10.5194/asr-13-75-2016
- Günther, F., Overduin, P. P., Yakshina, I. A., Opel, T., Baranskaya, A. V., and Grigoriev, M. N. (2015). Observing Muostakh Disappear: Permafrost Thaw Subsidence and Erosion of a Ground-Ice-Rich Island in Response to Arctic Summer Warming and Sea Ice Reduction. *Cryosphere* 9, 151–178. doi: 10.5194/tc-9-151-2015
- Hersbach, H., Bell, B., Berrisford, P., Horányi, A., Sabater, J. M., Nicolas, J., et al. (2019). Global Reanalysis: Goodbye ERA-Interim, Hello ERA5. *ECMWF Newsl* 159, 17–24. doi: 10.21957/vf291hehd7
- Holthuijsen, L. H. (2007). *Waves in Oceanic and Coastal Waters* (Cambridge: Cambridge University Press). doi: 10.1017/CBO9780511618536
- IPCC. (2019). *IPCC Special Report on the Ocean and Cryosphere in a Changing Climate*. Pörtner, H. O., Roberts, D. C., Masson-Delmotte, V., Zhai, P., Tignor,

- M., Poloczanska, E., et al. (eds.) In Press. (Cambridge: Cambridge University Press). doi: 10.1017/CBO9780511618536
- Jones, B. M., Arp, C. D., Jorgenson, M. T., Hinkel, K. M., Schmutz, J. A., and Flint, P. L. (2009). Increase in the Rate and Uniformity of Coastline Erosion in Arctic Alaska. *Geophys. Res. Lett.* 36, L03503. doi: 10.1029/2008GL036205
- Kohout, A. L., Smith, M., Roach, L. A., Williams, G., Montiel, F., and Williams, M. J. M. (2020). Observations of Exponential Wave Attenuation in Antarctic Sea Ice During the Pipers Campaign. *Ann. Glaciol.* 61, 196–209. doi: 10.1017/aog.2020.36
- Komen, G. J., Hasselmann, K., and Hasselmann, K. (1984). On the Existence of a Fully Developed Wind-Sea Spectrum. *J. Phys. oceanogr.* 14, 1271–1285. doi: 10.1175/1520-0485(1984)014<1271:OTEAF>2.0.CO;2
- Law-Chune, S., Aouf, L., Dalphin, A., Levier, B., Drillet, Y., and Drevillon, M. (2021). Waverys: A Cmems Global Wave Reanalysis During the Altimetry Period. *Ocean Dynamics* 71, 357–378. doi: 10.1007/s10236-020-01433-w
- Liu, Q., Babanin, A. V., Zieger, S., Young, I. R., and Guan, C. (2016). Wind and Wave Climate in the Arctic Ocean as Observed by Altimeters. *J. Climate* 29, 7957–7975. doi: 10.1175/JCLI-D-16-0219.1
- Liu, Q., Rogers, W. E., Babanin, A. V., Young, I. R., Romero, L., Zieger, S., et al. (2019). Observation-Based Source Terms in the Third-Generation Wave Model WAVEWATCH III: Updates and Verification. *J. Phys. Oceanogr.* 49, 489–517. doi: 10.1175/JPO-D-18-0137.1
- Méndez, F. J., Menéndez, M., Luceño, A., and Losada, I. J. (2006). Estimation of the Long-Term Variability of Extreme Significant Wave Height Using a Time-Dependent Peak Over Threshold (Pot) Model. *J. Geophys. Res.: Oceans* 111, C07024. doi: 10.1029/2005JC003344
- Mentaschi, L., Voudoukas, M., Voukouvalas, E., Sartini, L., Feyen, L., Besio, G., et al. (2016). The Transformed-Stationary Approach: A Generic and Simplified Methodology for Non-Stationary Extreme Value Analysis. *Hydrol. Earth System Sci.* 20, 3527–3547. doi: 10.5194/hess-20-3527-2016
- Meucci, A., Young, I. R., and Breivik, Ø. (2018). Wind and Wave Extremes From Atmosphere and Wave Model Ensembles. *J. Climate* 31, 8819–8842. doi: 10.1175/JCLI-D-18-0217.1
- Meucci, A., Young, I. R., Hemer, M., Kirezci, E., and Ranasinghe, R. (2020). Projected 21st Century Changes in Extreme Wind-Wave Events. *Sci. Adv.* 6, eaaz7295. doi: 10.1126/sciadv.aaz7295
- Morim, J., Hemer, M., Wang, X. L., Cartwright, N., Trenham, C., Semedo, A., et al. (2019). Robustness and Uncertainties in Global Multivariate Wind-Wave Climate Projections. *Nat. Climate Change* 9, 711–718. doi: 10.1038/s41558-019-0542-5
- Ochi, M. K. (2005). *Ocean Waves: The Stochastic Approach* (Cambridge: Cambridge Ocean Technology Series). doi: 10.1017/CBO9780511529559
- Queffelec, P., and Croizé-Fillon, D. (2015). Global Altimeter SWH Data Set, Version 11.1. Tech. Rep.
- Renard, B., Sun, X., and Lang, M. (2013). “Bayesian Methods for Non-Stationary Extreme Value Analysis,” in *Extremes in a Changing Climate* (Dordrecht: Springer), 39–95.
- Shimura, T., Mori, N., and Hemer, M. A. (2016). Variability and Future Decreases in Winter Wave Heights in the Western North Pacific. *Geophys. Res. Lett.* 43, 2716–2722. doi: 10.1002/2016GL067924
- Stegall, S.T., and Zhang, J. (2012). Wind Field Climatology, Changes, And Extremes In The Chukchi-beaufort Seas And Alaska North Slope During 1979–2009. *J. Climate* 25, 8075–8089.
- Stopa, J. E., Ardhuin, F., and Girard-Ardhuin, F. (2016). Wave Climate in the Arctic 1992–2014: Seasonality and Trends. *Cryosphere* 10, 1605–1629. doi: 10.5194/tc-10-1605-2016
- Strong, C., and Rigor, I. G. (2013). Arctic Marginal Ice Zone Trending Wider in Summer and Narrower in Winter. *Geophys. Res. Lett.* 40, 4864–4868. doi: 10.1002/grl.50928
- Takbash, A., and Young, I. R. (2019). Global Ocean Extreme Wave Heights From Spatial Ensemble Data. *J. Climate* 32, 6823–6836.
- Takbash, A., Young, I.R., and Breivik, Ø. (2019). Global Wind Speed And Wave Height Extremes Derived From Long-duration Satellite Records. *J. Climate* 32, 109–126.
- Thomson, R. E., and Emery, W. J. (2014). *Data Analysis Methods in Physical Oceanography* (Newnes). Amsterdam, Elsevier.
- Thomson, J., Fan, Y., Stammerjohn, S., Stopa, J., Rogers, W. E., Girard-Ardhuin, F., et al. (2016). Emerging Trends in the Sea State of the Beaufort and Chukchi Seas. *Ocean modelling* 105, 1–12. doi: 10.1016/j.ocemod.2016.02.009
- Thomson, J., and Rogers, W. E. (2014). Swell and Sea in the Emerging Arctic Ocean. *Geophys. Res. Lett.* 41, 3136–3140. doi: 10.1002/2014GL059983
- Tolman, H. L. (2009). User Manual and System Documentation of WAVEWATCH III TM Version 3.14. *Tech. note MMAB Contribution* 276, 220.
- Vichi, M., Eayrs, C., Alberello, A., Bekker, A., Bennetts, L., Holland, D., et al. (2019). Effects of an Explosive Polar Cyclone Crossing the Antarctic Marginal Ice Zone. *Geophys. Res. Lett.* 46, 5948–5958. doi: 10.1029/2019GL082457
- Vinoth, J., and Young, I.R. (2011). Global Estimates of Extreme Wind Speed and Wave Height. *J. Climate* 24, 1647–1665.
- Waseda, T., Webb, A., Sato, K., Inoue, J., Kohout, A., Penrose, B., et al. (2018). Correlated Increase of High Ocean Waves and Winds in the Ice-Free Waters of the Arctic Ocean. *Sci. Rep.* 8, 4489. doi: 10.1038/s41598-018-22500-9
- Zieger, S., Babanin, A. V., Rogers, W. E., and Young, I. R. (2015). Observation-Based Source Terms in the Third-Generation Wave Model WAVEWATCH. *Ocean modelling* 96, 2–25. doi: 10.1016/j.ocemod.2015.07.014

**Conflict of Interest:** The authors declare that the research was conducted in the absence of any commercial or financial relationships that could be construed as a potential conflict of interest.

**Publisher’s Note:** All claims expressed in this article are solely those of the authors and do not necessarily represent those of their affiliated organizations, or those of the publisher, the editors and the reviewers. Any product that may be evaluated in this article, or claim that may be made by its manufacturer, is not guaranteed or endorsed by the publisher.

Copyright © 2022 Cabral, Young and Toffoli. This is an open-access article distributed under the terms of the Creative Commons Attribution License (CC BY). The use, distribution or reproduction in other forums is permitted, provided the original author(s) and the copyright owner(s) are credited and that the original publication in this journal is cited, in accordance with accepted academic practice. No use, distribution or reproduction is permitted which does not comply with these terms.



# A Generalized Two-Scale Approximation for Ocean Wave Models

William Perrie\*, Bechara Toulany and Michael Casey

Fisheries and Oceans Canada, Bedford Institute of Oceanography, Dartmouth, NS, Canada

## OPEN ACCESS

### Edited by:

Adem Akpinar,  
Uludağ University,  
Turkey

### Reviewed by:

Prabhakar V.,  
Vellore Institute of Technology (VIT),  
India  
Wei-Bo Chen,  
National Science and Technology  
Center for Disaster Reduction (NCDR),  
Taiwan

Prasad Bhaskaran,

Indian Institute of Technology  
Kharagpur, India

### \*Correspondence:

William Perrie  
william.perrie@dfo-mpo.gc.ca

### Specialty section:

This article was submitted to  
Physical Oceanography,  
a section of the journal  
Frontiers in Marine Science

Received: 01 February 2022

Accepted: 06 May 2022

Published: 30 June 2022

### Citation:

Perrie W, Toulany B and  
Casey M (2022) A Generalized  
Two-Scale Approximation  
for Ocean Wave Models..  
Front. Mar. Sci. 9:867423.  
doi: 10.3389/fmars.2022.867423

The two-scale approximation (hereafter, TSA) was previously presented as a new method to approximate and estimate transfer rates in wind – wave spectra. It was shown to perform well for a variety of idealized and observed sea state conditions and to compare well with respect to the total Boltzmann integral for nonlinear quadruplet wave-wave interactions. Here, we present a generalized formulation of TSA, allowing for multiple peaked spectra, sheared spectra, sea – swell combinations, etc. This formulation is implemented in a modern operational wave model, WAVEWATCHIII™, and shown to provide a significant improvement over the standard approximation used in wave models, the discrete interaction approximation (DIA). Additional tests involve the simulation of waves generated in Hurricane Teddy (2020).

**Keywords:** ocean surface waves, nonlinear wave-wave interactions, two-scale approximation, wind-generated waves, WAVEWATCHIII (WW3) wave model

## 1 INTRODUCTION

In operational forecast models for surface waves, like WAVEWATCHIII™ also denoted WW3, the quadruplet nonlinear wave-wave interactions  $S_{nl}$  have a central role for the growth and development of ocean waves. This is suggested by several earlier studies such as SWAMP Group (1985); Komen et al. (1994); Holthuijsen (2007), whereby  $S_{nl}$  contributes energy to the ‘forward face’ of the spectrum, where frequencies are less than the spectral peak  $f_p$ , transferring energy from elsewhere in the spectrum. This accounts for the spectral down-shifting process in growing seas (Hasselmann et al., 1973). By comparison, the other source terms for the development and evolution of wind - waves, such as wind forcing input  $S_{in}(f, \theta)$  and wave dissipation,  $S_{ds}(f, \theta)$  largely operate locally in spectral space, adding or subtracting local energy at given frequency – direction locations,  $(f, \theta)$ , (Komen et al., 1994; Holthuijsen, 2007; WW3DG, 2016). There is a long history of studies related to these latter physical processes in simulations of ocean surface waves, like workshops reported by Swail et al. (2021), or specific studies like that given by Hsiao et al. (2020).

In recent years several formulations have been constructed for  $S_{nl}$ . These include the Discrete Interaction Approximation (DIA) from Hasselmann and Hasselmann (1985), which provides the operational parameterization used in most modern spectral waves models, such as WAM by WAMDI Group (1988), WAVEWATCHIII™, hereafter WW3, (WW3DG, 2016) and SWAN by Booij et al. (1999). Although there are known biases in the DIA formulation (Tolman, 2013), it continues to be used in forecasts because new formulations for  $S_{nl}$  have yet to be found that can

surpass DIA in combined forecast skill, computational efficiency and stability. A generalization of DIA was presented by Tolman and Grumbine (2013). Besides DIA, the WW3 model also has a formulation for the full integration for the Boltzmann integral based on Webb (1978); Tracy and Resio (1982); Resio and Perrie (1991), and Van Vledder (2006), denoted WRT (for Webb, Resio, and Tracy). More recently, motivated by deficiencies in DIA, Resio and Perrie (2008) proposed the Two-Scale Approximation, TSA, to represent the nonlinear transfer,  $S_{nl}$ . This has been implemented into WW3 by Perrie et al. (2013).

In the TSA approach, the wave spectrum is assumed to be decomposed into a 1<sup>st</sup> order or ‘broad-scale’ component, and a 2<sup>nd</sup> order or ‘local-scale’ component. The broad-scale term is given a parametric spectral representation, and the local-scale term is defined as the residual of the spectrum, once the broad-scale term is subtracted out. The local-scale term in the approximation is quite important because it provides the degrees of freedom needed in the detailed balance source-term formulation that were preserved by the 2<sup>nd</sup> order local-scale term in the approximation, as discussed by Resio and Perrie (2008), motivated by earlier presentations, for example Komen et al. (1994).

Resio and Perrie (2008) showed that, compared to DIA, the TSA can give significantly increased accuracy for the nonlinear spectral transfers,  $S_{nb}$ , using tests with idealized wave spectra that were motivated by the Joint North Sea Wave Project (JONSWAP) of Hasselmann et al. (1973). Additional confirmation was given by Perrie and Resio (2009) using measured wave spectra from field experiments in Currituck Sound (North Carolina, U.S.A.), and observed open-ocean waverider buoy data off the U.S. Army Field Research Facility (Duck, North Carolina) during Hurricane Wilma (2005).

Perrie et al. (2013) implemented TSA into WW3, and performed tests for wave spectra based on field measurements and waves generated during Hurricane Juan (2001), confirming that results from TSA can surpass those of DIA. They concluded that TSA can generally work well in situations where its basic assumptions are met, that the broad-scale term represents most of the spectrum and the rest of the spectrum can be represented by the local-scale term. These conditions are largely met in tests based on JONSWAP-type spectra, or evolutionary cases where winds are generally constant, spatially and temporarily, or some conditions during storm-generated waves like Hurricanes Juan or Wilma.

However, there are clearly more complicated cases of ocean-surface waves that go beyond TSA’s basic assumptions. These include severe cases of complex wave systems, such as storm cases where the winds rapidly change speed or direction, with combinations of intense windsea-swell interactions, multiple spectral wave peaks and strong directional shears. In these situations, TSA does not represent the development of a secondary, or tertiary spectral peak well, because the 1<sup>st</sup> order broad-scale term may be dominated by the low-frequency ( $f_{p1}$ ) energy, and the 2<sup>nd</sup> order local-scale term focuses on representing the developing wind-sea component of the wave spectra. We address these cases in the present study.

Here, we propose a slight generalization to TSA in order to give a *second* 1<sup>st</sup> order broad-scale term, corresponding to a *second* broad-scale peak ( $f_{p2}$ ), with a peak direction ( $\theta_{p2}$ ) that may differ from that of the first broad-scale term ( $\theta_{p1}$ ). This approach is denoted ‘multiple TSA’ or mTSA, which can be further generalized with additional 1<sup>st</sup> order broad-scale terms. Section 2 gives a presentation of the mTSA methodology. Implementation within WW3 and hypothetical test cases are considered in section 3. Simulations of waves generated during extratropical Hurricane Teddy (2020) are given in section 4. Discussion and conclusions are given in section 5.

## 2 GENERALIZATION OF THE TSA METHODOLOGY

### (a) The Wave Model

Models for simulation of ocean surface waves, such as WW3, are formulated in terms of parameterizations for the nonlinear wave-wave interactions,  $S_{nl}(f, \theta)$ , with other source terms, such as wind input to waves,  $S_{in}(f, \theta)$ , and wave dissipation,  $S_{ds}(f, \theta)$ . WW3 is based on the well-known balance equation for spectral action density, expressed as  $n(f, \theta)$ , where ( $f, \theta$ ) denote frequency and direction; it is an open-source modern 3<sup>rd</sup> generation wave model (WW3DG, 2016). Version 5.16 is used in this study. Detailed discussion of WW3 model physics and characteristics is given by WW3DG (2016) for both regional and global applications. As noted in the Introduction, the basic three source terms in deep water are the nonlinear wave-wave term  $S_{nl}(f, \theta)$ , wind input,  $S_{in}(f, \theta)$ , and wave dissipation,  $S_{ds}(f, \theta)$ . As described by Perrie et al. (2013), the implementation of TSA within WW3 follows the methodology used in implementing DIA or WRT in third generation wave models like WAM and WW3, respectively (WAMDI Group, 1988; Van Vledder, 2006; Tolman, 2009). We assume an explicit forward – time scheme for the difference equations, for the 2-dimensional ocean wave spectrum  $F(f, \theta)$ . In terms of the nonlinear wave-wave interactions  $S_{nb}$ , the integration is semi-implicit, requiring a diagonal term to estimate  $S_{nl}$  at succeeding time-steps. This term is the diagonal of the partial derivative of  $S_{nl}(f, \theta)$  with respect to spectral energy  $F(f, \theta)$ , where  $f, \theta$  are spectral frequency and direction. Thus, only array elements with equal  $f$  and  $\theta$  in both the source and spectrum terms are used; the diagonal term may be written as  $\Lambda_i$ , where

$$\Lambda_i = \frac{\partial(S_{nl})}{\partial F} \quad (1)$$

which must now be determined for TSA.

### (b) The Two-Scale Approximation

In evolving wind and wave conditions, the TSA formulation works well in many sea state conditions, for example, simple fetch-limited or duration-limited wave growth. However, when the wind direction changes rapidly, the TSA formulation needs to be modified to allow the broad-scale term to take into account

more complicated spectral situations such as multi-peaked spectra. If there is a significant misalignment of TSA's broad-scale term with respect to waves generated by sudden wind direction changes, the original TSA formulation of Resio and Perrie (2008) may not be able to provide a reliable representation of the nonlinear transfer,  $S_{nl}$ .

In its original formulation, TSA is based on the WRT formulation for  $S_{nl}(f, \theta)$ , which is due to Webb (1978); Tracy and Resio (1982) and Resio and Perrie (1991). In this approach, the nonlinear transfer of action density from one spectral wavenumber  $k_3$  to another,  $k_1$ , is represented by a transfer function  $T(k_1, k_3)$ ,

$$\frac{\partial n(k_1)}{\partial t} = \iint T(k_1, k_3) dk_3 \tag{2}$$

which may be expressed as

$$\begin{aligned} T(\underline{k}_1, \underline{k}_3) &= 2\phi[n_1 n_3(n_4 - n_2) + n_2 n_4(n_3 - n_1)]C(\underline{k}_1, \underline{k}_2, \underline{k}_3, \underline{k}_4)\vartheta \\ &\quad (|\underline{k}_1 - \underline{k}_4| - |\underline{k}_1 - \underline{k}_3|) \left| \frac{\partial W}{\partial \eta} \right|^{-1} ds \\ &\equiv \sim 2\phi N^3 C\vartheta \left| \frac{\partial W}{\partial \eta} \right|^{-1} ds \end{aligned} \tag{3}$$

where  $\vartheta$  is the Heaviside function,  $k_4 = k_1 + k_2 - k_3$  where  $k_2 = k_2(s, k_1, k_3)$ . Here,  $n_i$  is the action density at  $k_i$ , and the locus of possible wave-wave interactions is specified by the contour  $s$  satisfying the resonance condition,

$$W = \omega_1 + \omega_2 - \omega_3 - \omega_4 = 0 \tag{4}$$

and where  $\eta$  is the local orthogonal to contour  $s$ .

In the original TSA of Resio and Perrie (2008), a given spectrum  $n_i$  is decomposed into a 1<sup>st</sup> order, or broad-scale, term  $\hat{n}_i$  and a 2<sup>nd</sup> order, local-scale term  $n'_i$ , where  $\hat{n}_i$  is given a parametric JONSWAP-type form following Hasselmann et al. (1973), thereby depending on only a few parameters. The local-scale term  $n'_i$  is the residual,

$$n'_i = n_i - \hat{n}_i \tag{5}$$

with the same number of degrees of freedom as the input spectrum  $n_i$ . TSA becomes quite accurate if the parameterization for  $\hat{n}_i$  can be selected so that  $\hat{n}_i$  is small. However, to have optimal computational efficiency, the methodology will try to minimize the number of parameters used for  $\hat{n}_i$  because application of large multi-dimensional sets of pre-computed matrices for  $\hat{n}_i$  is time-consuming.

For complicated wave conditions, for example multi-peaked spectra  $n_i$ , the challenge of selecting  $\hat{n}_i$  is dependent on a relatively small parameter set can be somewhat mitigated by application of multiple broad-scale terms, or for example in this paper, two broad-scale terms,

$$\hat{n}_i = \hat{n}_{1i} + \hat{n}_{2i} \tag{6}$$

where  $\hat{n}_{1i}$  and  $\hat{n}_{2i}$  are both given JONSWAP-type parametric forms, corresponding to two peaks,  $f_{p1}$  and  $f_{p2}$ , in the given spectrum  $n_i$ . Therefore, following the original TSA methodology, the residual local-scale  $n'_i$  term may be determined by subtracting,

$$n'_i = n_i - \hat{n}_{1i} - \hat{n}_{2i} \tag{7}$$

Thus, in the usual manner of Resio and Perrie (2008), we partition the action density term,  $n_i$ , and write the transfer integral  $T$  in equation (3) in terms of the sum of interactions involving broad-scale terms, which we pose as  $\hat{n}_{1i} + \hat{n}_{2i}$ , denoted  $B$ , local-scale terms  $n'_i$ , denoted  $L$ , and the cross interactions among  $\hat{n}_{1i} + \hat{n}_{2i}$  and  $n'_i$ , denoted  $X$ . Thus, the nonlinear transfer interactions  $S_{nl}$  can still be represented as,

$$S_{nl}(f, \theta) = B + L + X \tag{8}$$

and  $B$  can be pre-computed and depends on JONSWAP-type parameters  $x_i$ ,

$$S_{nl}(f, \theta)_{broad-scale} = B(f, \theta, x_1, \dots, x_n) \tag{9}$$

The objective of this slightly generalized TSA is to accurately, efficiently approximate  $L+X$ , by neglecting terms involving  $n'_2$  and  $n'_4$  thereby simplifying equation (8). This follows Resio and Perrie (2008) in assuming that the local-scale terms ( $n'_2$  and  $n'_4$ ) are deviations around the associated broad-scale terms ( $\hat{n}_2$  and  $\hat{n}_4$ ) which capture most of the spectral energy; and with their positive/negative differences and products, the former tend to cancel, as we move along the interaction loci. This approach is validated by mTSA's ability to give results that compare well with those of WRT.

Thus, Resio and Perrie (2008) show that eliminating  $n'_2$  and  $n'_4$  gives

$$S_{nl}(k_1) = B + L + X = B + \iint \phi N_*^3 C \left| \frac{\partial w}{\partial n} \right|^{-1} ds k_3 d\theta_3 dk_3 \tag{10}$$

where  $N_*^3$  is given by

$$\begin{aligned} N_*^3 &= \hat{n}_2 \hat{n}_4 (n'_3 - n'_1) + n'_1 n'_3 (\hat{n}_4 - \hat{n}_2) + \hat{n}_1 n'_3 (\hat{n}_4 - \hat{n}_2) \\ &\quad + n'_1 \hat{n}_3 (\hat{n}_4 - \hat{n}_2) \end{aligned} \tag{11}$$

and they use known scaling relations to obtain

$$\begin{aligned} \frac{\partial n_1}{\partial t} &= \left( \frac{k}{k_0} \right)^{-19/2} \left\{ B \left( \frac{\zeta}{\zeta_0} \left( \frac{k}{k_0} \right)^p \right)^3 \right. \\ &\quad + \left[ \frac{\zeta}{\zeta_0} \left( \frac{k}{k_0} \right)^p \iint (\hat{n}_1 n'_3 + n'_1 \hat{n}_3 + n'_1 n'_3) \Lambda_p k_* d\theta_* dk_* \right. \\ &\quad \left. \left. + \left( \frac{\zeta}{\zeta_0} \left( \frac{k}{k_0} \right)^p \right)^2 \iint (n'_1 - n'_3) \Lambda_d k_* d\theta_* dk_* \right] \right\} \end{aligned} \tag{12}$$

with

$$\begin{aligned} \Lambda_p &= \oint C \left| \frac{\partial W}{\partial n} \right|^{-1} (\hat{n}_4 - \hat{n}_2) ds \\ \Lambda_d &= \oint C \left| \frac{\partial W}{\partial n} \right|^{-1} (\hat{n}_2 \hat{n}_4) ds \end{aligned} \tag{13}$$

where the so-called ‘pumping’ and ‘diffusion’ terms are  $\Lambda_p$  and  $\Lambda_d$  following Webb (1978)’s notation. Here, superscript  $p$  is the equilibrium-range power law, for example  $f^4$  or  $f^5$ , and  $(\zeta/\zeta_0)$  is related to a linear scaling coefficient for the  $\hat{n}_i$  terms;  $(k/k_0)$  is the ratio of the spectral peak wavenumber for the spectrum being integrated to that of the reference spectrum. Coordinates  $\theta_*$  and  $k_*$  are

$$\theta_* = \theta_3 - \theta_1; k_* = (k_3 - k_1)/k_p. \tag{14}$$

For a  $f^5$  JONSWAP spectrum,  $\zeta$  is the Phillips’ coefficient in equation (12), whereas for an  $f^4$ -type spectrum like  $E(f) \approx \beta f^4$ , then  $\zeta$  is  $\beta$ , and generally any linear multiplicative term that scales the spectrum. The power of  $\zeta$  is the number of broad-scale densities ( $\hat{n}_i$ ) in the integrals used in matrices,  $\Lambda_d$  and  $\Lambda_p$ . The scaling factor for wavenumber  $k$  is from the wavenumber dimensions of the coupling coefficient ( $\sim k^6$ ), Jacobian ( $\sim k^{1/2}$ ), and the phase space terms ( $dsdk \sim k^3$ ).

From equations (12) and (13), the diagonal terms for WRT are,

$$\begin{aligned} \Lambda|n_1 &= \frac{\partial S_{nl}}{\partial n_1} = 2 \iint \phi [n_3(n_4 - n_2) - n_2 n_4] C \vartheta \left| \frac{\partial W}{\partial n} \right|^{-1} dsdk_3 \\ \Lambda|n_3 &= \frac{\partial S_{nl}}{\partial n_3} = 2 \iint \phi [n_1(n_4 - n_2) + n_2 n_4] C \vartheta \left| \frac{\partial W}{\partial n} \right|^{-1} dsdk_3 \end{aligned} \tag{15}$$

and neglecting of terms involving  $n'_2$  and  $n'_4$ , we find for TSA, or in this case, mTSA,

$$\begin{aligned} \Lambda^{TSA}|n_1 &= \frac{\partial S_{nl}^{TSA}}{\partial n_1} = 2 \iint \phi [(\hat{n}_3 + n'_1)(\hat{n}_4 - \hat{n}_2) - \hat{n}_2 \hat{n}_4] C \vartheta \left| \frac{\partial W}{\partial n} \right|^{-1} dsdk_3 \\ \Lambda^{TSA}|n_3 &= \frac{\partial S_{nl}^{TSA}}{\partial n_3} = 2 \iint \phi [(\hat{n}_1 + n'_1)(\hat{n}_4 + n'_2) + \hat{n}_2 \hat{n}_4] C \vartheta \left| \frac{\partial W}{\partial n} \right|^{-1} dsdk_3 \end{aligned} \tag{16}$$

These terms are central to the mTSA semi-implicit implementation within WW3.

### (c) Equilibrium Range Constraints

Operational wave models like WW3 are restricted in the sense that they have a finite discrete spectral grid. mTSA’s broad-scale terms  $\hat{n}_{1i} + \hat{n}_{2i}$  typically depend on a few parameters for each broad scale term, such as peak frequency  $f_p$ , peak direction,  $\theta_p$ , Phillips coefficient  $\beta$ , peakedness  $\gamma$ , spectral width parameters  $\sigma_a$  and  $\sigma_b$  for the forward and rear faces of the

spectral peak, and a spreading distribution,  $\sim \cos^m(\theta - \theta_p)$  around the spectral peak direction  $\theta_p$ . However, when the spectral peak  $f_p$  is too close to the highest frequency of the discrete spectral computational grid, it is not possible to define  $\beta$  in terms of the equilibrium range of the spectrum, in the usual manner,

$$\beta = \left\langle \frac{E(f) C_g(f) k^{2.5}}{2\pi} \right\rangle_{equilibrium-range} \tag{17}$$

where the equilibrium range is assumed as  $\sim 2$  or  $3 \times f_p$ , and  $C_g$  is the group velocity (Donelan et al., 1985). In these cases, a simple practical approach is to define  $\beta$  in terms the highest discrete frequency above  $f_p$ , and below the equilibrium range, which may be nonexistent in this case (more on this below). This is an approximation in terms of the expected value for  $\beta$ ; had the frequency grid extended to a higher limit with an equilibrium range, a more accurate estimate would be possible. In this way, a modified definition of  $\beta$  allows the WW3 forecast model to continue with the computation, providing an estimate for  $\beta$ . This approach is consistent with that of previous third generation wave models. However, the issue regarding the calculation of  $\beta$  can become critical if there are multiple spectral peaks, particularly regarding the region between two spectral peaks.

The mTSA approach allows generalization of the broad-scale term, allowing more than one broad-scale parametric term, corresponding to multi-peaked spectra. It is shown in test cases in the next section, that this modification allows the mTSA approach to rather accurately represent a fully integrated formulation of the nonlinear wave-wave transfer, in terms of the WRT estimates. For example, in test cases involving windsea-swell interactions, with two or more changing spectral peaks, each with differing peak frequency directions, we represent the double peak as two separate peaks in the mTSA formulation, and invoke the broad-scale parameterization twice to simulate each separately. The procedure for determining JONSWAP parameters for two broad-scale terms for a double-peaked spectrum is given in the Appendix.

An issue is the high-frequency equilibrium range. When there is only a single peak frequency, the equilibrium range is typically about 2~3 times the peak frequency  $f_p$  and is represented by spectral tail with  $f^{-4}$  variation, following Resio et al. (2004), and earlier studies. The  $f^{-4}$  spectral tail is matched to the upper limit of the discrete frequency spectrum, which allows an equilibrium range Phillips coefficient to be defined, denoted  $\beta$  in the notation of Resio et al. (2004). This is a key term in the broad-scale parameterization. Moreover, there are clearly instances where a given wind-wave spectrum may have a spectral tail which does not follow the  $f^{-4}$  distribution. But that is not a problem for the mTSA methodology. In any case, whatever the distribution of the spectral tail, whether  $f^{-4}$  or  $f^{-5}$  or  $f^{-4.5}$  etc., we construct the broad-scale spectrum using a JONSWAP-type parameterization as discussed in this section and in the Appendix. Whatever mismatch occurs is then reconciled by the residual local-scale term, as identified in equation (7).

In the mTSA formulation, while there may be two or more peaks, we represent the spectrum in terms of just two peaks in this paper, where the second peak  $f_{p2}$  is required to be more than

2 frequency bins higher than the first peak  $f_{p1}$ ; otherwise we represent the spectrum with a single broad-scale term, and mTSA becomes just the standard TSA formulation. For the second peak  $f_{p2}$ , the upper part of the spectrum above  $f_{p2}$  is used to define the equilibrium range and the Phillips coefficient  $\beta$ , in the usual manner. If there are enough frequency bins between the two peaks, we define an equilibrium range  $\sim 2-3 \times f_{p2}$ , and calculate a Phillips-type coefficient, denoted here as " $\beta^*$ ". Otherwise we just use the highest frequency bin above  $f_{p2}$ , as a proxy to define the  $\beta$  term, to allow the simulation to proceed.

The region between the two peaks ( $f_{p1}$  and  $f_{p2}$ ) is a challenge. The peaks must be separated by at least one frequency bin, to allow definition of two broad-scale terms. In this case, if there are enough frequency bins between  $f_{p1}$  and  $f_{p2}$ , we define an equilibrium range  $\sim 2-3 \times f_{p2}$ , and calculate a Phillips-type coefficient  $\beta$  for the broad-scale term associated with  $f_{p1}$ , in the usual manner. However, if  $f_{p1}$  and  $f_{p2}$  are separated by only a very small region, then for the lower of the two spectral peaks,  $f_{p1}$ , we represent the energy of its equilibrium range by the minimum spectral energy between  $f_{p1}$  and  $f_{p2}$ , thus defining  $\beta$  for the lower of the two spectral peaks. Thus, each of the two peaks,  $f_{p1}$  and  $f_{p2}$ , has its own  $\beta$  coefficient, peak direction,  $\theta_{p1}$  and  $\theta_{p2}$ , and its own broad-scale term.

For an assumed two-peaked spectrum, each of the two broad-scale terms requires a directional spreading distribution function. As with the original TSA formulation, the directional spreading distribution for each of the two broad-scale terms is assumed to be of the form  $\sim \cos^m(\theta - \theta_p)$  where the integral exponent  $m$  is selected so that the broad-scale spreading at the respective spectral peak ( $f_{p1}$  or  $f_{p2}$ ) can approximate that of the given input spectrum  $F(f_p, \theta)$ , for whatever directional distribution this is.

### 3 HYPOTHETICAL TEST CASES

#### (a) Sheared Spectrum

The initial test case considers a sheared spectrum, with swell propagating to the west at  $0^\circ$ , and higher frequency wind-waves at higher frequency propagating to the north at  $270^\circ$  as shown in **Figure 1C**. Within WW3, the convention for winds is always the Meteorological Convention; direction from, clockwise from North. For waves, it is direction to, counterclockwise from East.

**Figure 1** shows comparisons for the 1-D (1-dimensional) and 2-D action density and nonlinear transfer,  $S_{nb}$ , for the three formulations, namely DIA, multiple-TSA (denoted mTSA), and WRT. We do not show the single TSA (denoted sTSA) case, because as in the more basic JONSWAP-type cases considered by Perrie et al. (2013), the broad-scale term  $\hat{n}_i$  is able to fit the swell spectral peak region rather well (**Figure 1A**), and therefore sTSA and mTSA are essentially the same in this case.

However, this case shows that there is a notable mismatch between  $\hat{n}_i$  and the given test case action,  $n_r$ , in the high-frequency region, where the energy is almost zero. Thus, the role for the local-scale term  $n'_i$  is relatively important in this latter region. Resultant 1-D estimates for the nonlinear transfer  $S_{nl}$  given by mTSA are able to match those of WRT well, compared

to DIA, as shown in **Figure 1B**, as well for 2-D results shown in **Figures 1D–F**. By comparison, DIA results have magnitudes that are too large in the positive and negative lobe regions as shown in **Figure 1B**. While detailed patterns for mTSA and WRT are shown to compare well in **Figures 1D, E**, DIA results appear distorted in **Figure 1F**, particularly in the high frequency portion of the spectrum.

#### (b) Evolving Sheared Spectrum, No Wind or Dissipation

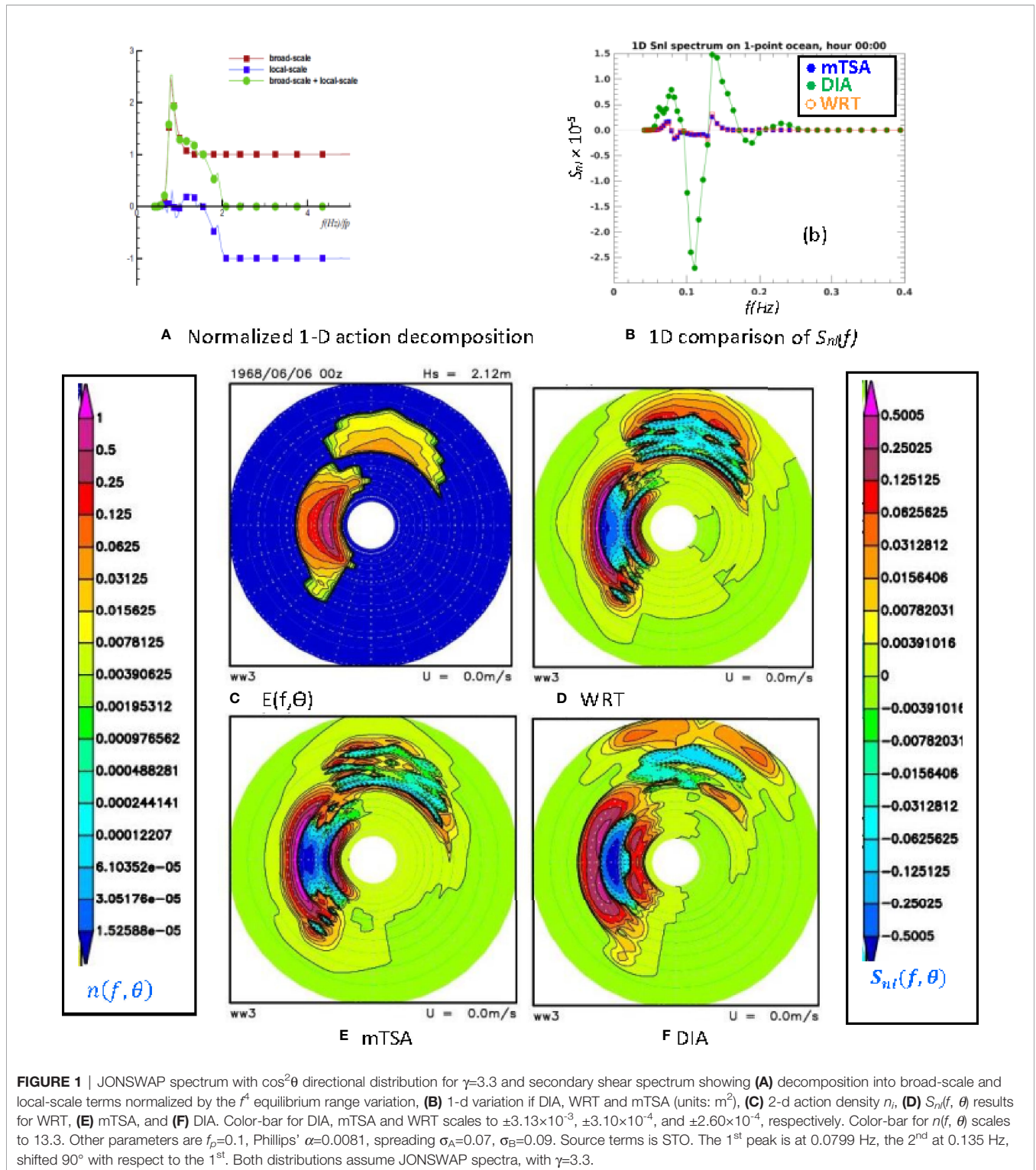
The second test case consists of simply letting the sheared spectrum in case 1 evolve, without wind input or wave dissipation, or other source terms, like the propagation of swell waves. As the nonlinear transfer is conservative, no change in total energy is expected. 2-D results are presented in **Figure 2** after time evolution of 5 hours. Here, we see that, as in the initial conditions given in **Figure 1**, estimates for the nonlinear transfer  $S_{nl}$  given by both sTSA and mTSA are able to match those of WRT well, compared to DIA. As in the first test case, compared to the results from TSA and WRT, (which compare well with each other), DIA results have detailed patterns that appear distorted, particularly in the high frequency portion of the spectrum. The implications of these differences particularly appear to show up as energy growth in high frequency regions of the spectrum as indicated in **Figure 2**, e.g. the smaller waves that might be central to satellite backscattering from synthetic aperture radars.

#### (c) Evolving Sheared Spectrum, Growing Wind-Sea Opposing Swell Direction

The third test case considers the same initial wave spectrum as in the first case in **Figure 1**; however there is now a constant west-to-east wind blowing opposite the main westward swell direction, at 20 m/s, with an initial secondary wind-sea to the north, as shown in **Figure 1**, orthogonal to the assumed wind direction. See **Figure 3**. The main low-frequency swell direction is to the west. The formulations for wind input,  $S_{im}$ , and wave dissipation,  $S_{ds}$ , are given by the ST4 source terms of Ardhuin et al. (2010), as implemented within WW3.

Results are shown after the system has evolved for 10 hours. The wind speed of 20 m/s is relatively strong. After 10 hours of time evolution, the new wind-generated waves are the dominant feature in the spectrum of this system. However, in each of the simulations shown in **Figure 3**, we see that westward propagating swell remains mostly unchanged by the nonlinear transfer  $S_{nb}$ , regardless of which formulation is used, WRT, sTSA, mTSA, or DIA. Minor variations are obtained in the swell results, due to DIA formulation and more so in the sTSA results, compared to results from WRT or mTSA.

By comparison, results for the eastward propagating wind-sea driven by 20 m/s wind, imposed on the initial conditions of a northward wind-sea, and a westward propagating swell are a different story. We see that the results for the 2-D action density and the nonlinear transfer  $S_{nb}$ , given by mTSA, are largely able to compare to those of WRT relatively well, compared to those of DIA or sTSA. Differences between results of WRT and mTSA are comparatively minor.



By comparison, DIA results have variations in frequency regions around the spectra peak of the northward-propagating wind-sea region. In terms of direction, these effects are most notable in the northeastward direction, approximately diagonal between the northward propagating wind sea, and

the new eastward-propagating wind-generated waves. Results from sTSA show notable biases throughout much of the spectrum, although the overall shape of the 2-D action density is rather similar to that of mTSA. For varying 2D distributions, it is not completely clear how to assign a single



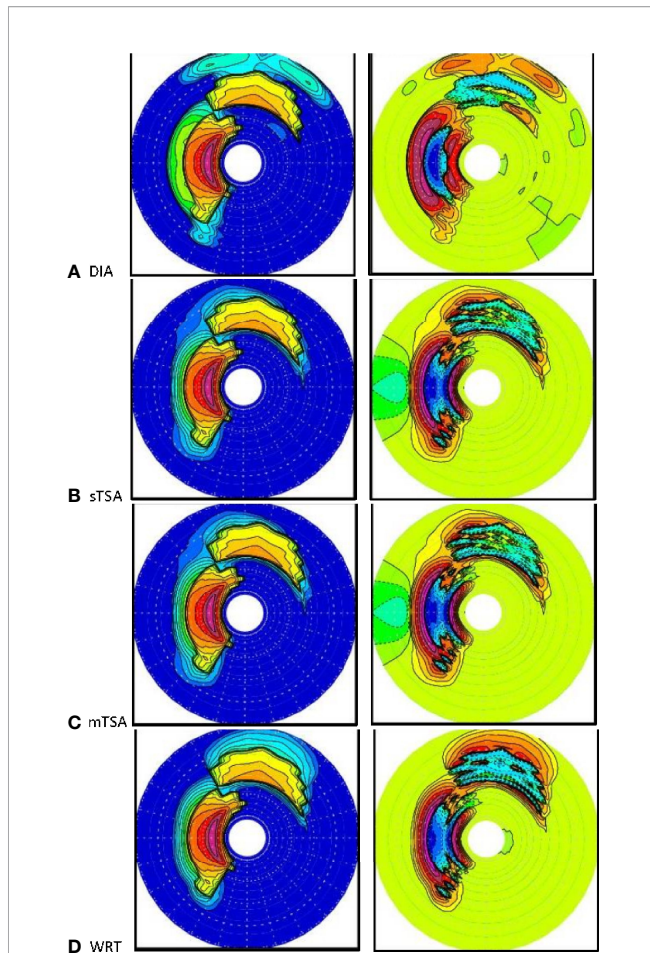


**FIGURE 2** | Evolving spectra starting with initial conditions as **Figure 1**, after time of 5 hours evolution, with no wind: **(A)** DIA, **(B)** single-TSA, or sTSA, **(C)** multiple TSA, or mTSA, **(D)** WRT, showing 2-D energy in the left column and 2-D  $S_{nl}$  in the right. Same color bars and scales as **Figure 1**.  $H_s$  remains constant. Total energy is conserved;  $H_s$  is 2.12m.

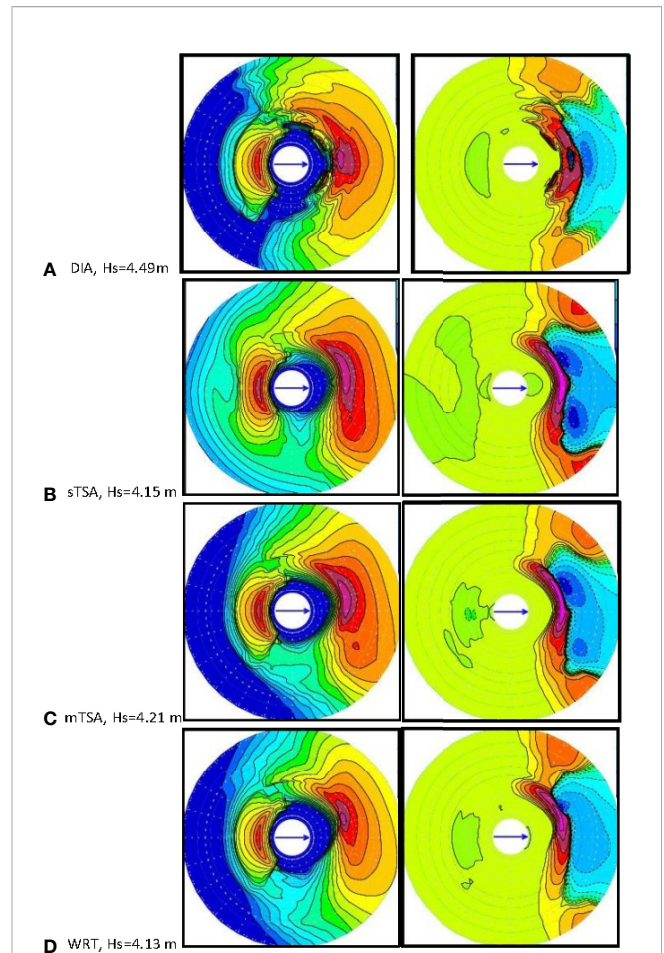


**FIGURE 3** | Evolving spectra starting with initial conditions as **Figure 1**, after time of 10 hours evolution, with 20m/s wind opposing the swell, from west to east and ST4 source terms: **(A)** DIA, **(B)** single-TSA, or sTSA, **(C)** multiple TSA, or mTSA, **(D)** WRT, showing 2-D energy in the left column and 2-d  $S_{nl}$  in the right.  $H_s$  (m) as indicated. Same color bars and scales as **Figure 1**.

number to express error. If we take maximum  $H_s$  as a kind of qualitative expression of mismatch, then relative to WRT, mTSA has an error of about 1.9% in maximum  $H_s$ , compared to 8.7% for DIA.

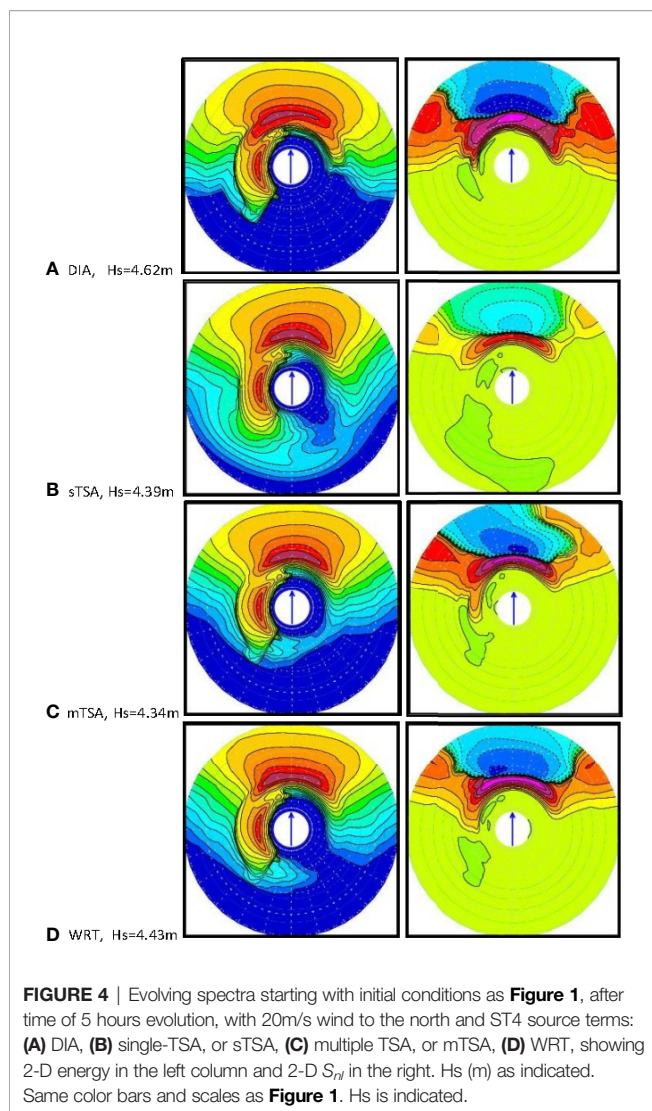
The overall dominance of the new wind-generated waves propagating to the east is clear after 10 hours. The effects of nonlinear wave-wave interactions between the new wind-generated waves propagating to the east, and the initial conditions involving wind-sea propagating in the northern direction are relatively minor.

#### (d) Evolving Sheared Spectrum, Growing Wind-Sea Parallel to Initial Wind-Sea

The fourth test case is similar to the third case, except now the 20 m/s wind is blowing south to north, orthogonal to the main east-to-west swell direction, and parallel to the initial secondary wind-sea, also to the north. See **Figure 4**. The formulations for wind input,  $S_{im}$ , and wave dissipation,  $S_{ds}$ , are given by the ST4 source terms of Ardhuin et al. (2010), as implemented within WW3. The simulation is for 5 hr.

As in test case 3, we see that westward-propagating swell remains largely unchanged by the nonlinear transfer  $S_{nl}$ , regardless of the formulation; WRT, sTSA, mTSA or DIA. Minor variations are obtained in the swell spectrum due to the DIA formulation, particularly in the southwestern direction, and more so for the results from sTSA, which shows apparent ‘smoothing’ of the westward swell spectrum. Results for the northward propagating wind-sea imposed on the initial conditions and the new generating north-propagating wind-sea waves are dominant features of the simulations.

As in the previous test cases (**Figures 1–3**), we see again that simulation results given by mTSA are able to match those of WRT rather well, compared to those from DIA or sTSA. By comparison, DIA results have more northerly-propagating wind-sea region and more directional spreading than results suggested by mTSA and WRT; these similar tendencies for more directional spreading and more smoothing are also notable in results from sTSA. The initial wind-sea in the northern direction is effectively ‘assimilated’ into the new wind-generated waves propagating in the northern



direction. There is no apparent impact of the west-propagating swell on the newly-generated north-propagating wind-sea.

As in test case 3, the wind speed of 20 m/s is relatively strong, and after 5 hours of time evolution, the new wind-generated waves are the dominant feature in the 2-D spectrum of this system. The effect of the west-propagating swell on the new wind-sea is rather minor and only evident in directional components in the northwest direction, adjacent to the swell propagation direction. However, variations due to differing formulations for  $S_{nl}$  are evident. We see that after 5 hours evolution, the results for the simulation given by mTSA are able to match those of WRT relatively well, compared to DIA or sTSA.

By comparison, DIA results have magnitudes that are too large, in both the negative high frequency regions, and also in frequencies of the region around the spectra peak of the north-propagating wind-sea region. In terms of direction, the DIA effects result in more broadly distributed directional spreading of the new wind-sea, rather than to have dominantly north-propagating waves. This tendency of bias and excessive

directional spreading is accentuated in the sTSA results. In terms of error, if we take maximum  $H_s$  as a qualitative expression for mismatch, then relative to WRT, mTSA has an error of about 2.0% in maximum  $H_s$ , compared to 4.3% for DIA.

The overall dominance of the new wind-generated waves propagating northward is clear after the 5-hour time evolution. The effects of nonlinear wave-wave interactions between the new wind-generated waves propagating to the north, and the initial conditions involving swell propagating to the west are relatively minor.

## 4 HURRICANE TEDDY (2020)

A detailed discussion of Hurricane Teddy's development is given by Blake (2021). Teddy began as a strong tropical wave off the west coast of Africa on 10 September, 2020, accompanied by a large area of deep convection, which eventually led to the formation of a tropical depression near 0600 UTC 12 September to the southwest of the Cabo Verde Islands. The "best track" of Teddy's path is given in **Figure 5A**. Rapid intensification started late on 15 September and Teddy became a hurricane on 16 September, about 1300 km east-northeast of Barbados as it turned northwestward.

By 16 September Teddy's intensity levelled off at about 85 kt, and with changing shear conditions, it started another intensification by the next day. Teddy strengthened into a major hurricane near 1200 UTC 17 September while centered about 900 km east-northeast of Guadeloupe, reaching a peak of 120 kt near 0000 UTC on 18 September and then beginning to weaken, due to an eyewall replacement, and later due to an increased shear. Teddy dropped below major hurricane status by 0000 UTC 20 September and continued to steadily weaken that day, although its 50-kt and hurricane-force wind fields remained large.

On 20 September, Teddy was centered about 700 km southeast of Bermuda when the synoptic environment changed, causing it to turn northward and then north-northeastward on 21 September, when it passed about 370 km east of Bermuda. The weakening trend stopped late on 21 September due to interactions with a negatively tilted trough, causing an increase in its maximum wind speed and size. Thereafter, Teddy moved rapidly northward and then north-northwestward due to the flow around the trough, and it became a very large cyclone. The extent of tropical-storm-force winds from 0000 UTC 22 September to 1200 UTC that day more than doubled in size in only 12 hours, as confirmed by aircraft and scatterometer data, and a secondary peak intensity of 90 kt between 0600 and 1200 UTC was achieved.

This trough interaction also started Teddy's extratropical transition process. Teddy's wind field became more asymmetric, frontal features formed away from the center, and the convection became less centralized. As Teddy moved across cooler water it lost deep convection in the core, and quickly weakened and transitioned to an extratropical low after 0000 UTC 23 September. At this point it was centered about 300 km south of Halifax, Canada. Teddy turned northward and then north-northeastward and made landfall near Ecum Secum, Nova Scotia, Canada, at 1200 UTC that day, with

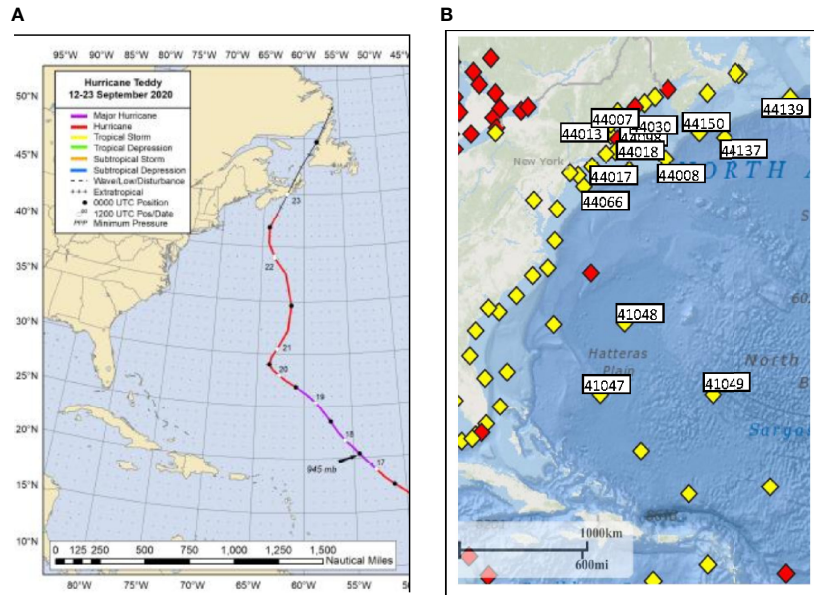


**FIGURE 5 | (A)** Figure 5 Best track for Hurricane Teddy, 12-23 September 2020. **(B)** Fourteen NDBC and Canadian buoys used in this study.

sustained winds of 55 kt. It continued to weaken as it moved across eastern Nova Scotia and the Gulf of St. Lawrence, and was later absorbed by a larger low-pressure system.

Surface wave and meteorological conditions were compared with model estimates at four buoys (41049, 44008, 44137, and 44139) deployed by the National Data Buoy Center (NDBC) and Environment Climate Change Canada (ECCC). These are located in **Figure 5B**. The peak wind speed at 41049, the most southern of these buoys, was about 22 m/s at 06:00 UTC on Sept 20. Wave conditions increased rapidly as Hurricane Teddy approached, with significant wave heights ( $H_s$ ) reaching about 9 m at this buoy.

**(a) The Wave Model**

The computational domain for implementation of WW3 for the simulation of waves generated by Hurricane Teddy consists of the nested grid system shown below in **Figure 6**. This nested system has a relatively coarse-resolution (0.5°) large-scale grid which extends from 20°N to 65°N, and from 40°W to 75°W for the Northwest Atlantic. Within this domain, a relatively high-resolution subdomain is nested from 42°N to 52°N and from 55°W to 72°W, focused on the waters off northern New England and the Canadian Maritimes Provinces, as shown in **Figure 6**. These grid resolutions are selected to provide a relatively reliable degree of accuracy in simulating swell and wind-generated waves energy. The directional resolution is 10° and 29 frequency bins are used, spaced logarithmically using  $f_{n+1} = 1.10 f_n$  ranging from 0.04118 Hz to 0.5939 Hz. The model global time step is 600 s. As mentioned earlier, the ST4 source terms are used following Ardhuin et al. (2010), for wind input  $S_m$  and wave dissipation  $S_{ds}$ .

**(b) Winds**

Wind fields to drive the wave models for Hurricane Teddy are obtained from Environment and Climate Change Canada (ECCC). For the coarse-grid Northwest Atlantic domain, 3-hourly ECCC global wind products are used with 0.24 resolution on a latitude-longitude grid. For the high-resolution Atlantic Canada domain, 1-hourly ECCC regional wind products are used with 10 km resolution based on a polar-stereographic projection. These are routine forecast products that are posted daily by ECCC (<https://dd.weather.gc.ca/>). The ECCC global wind data are already on a latitude-longitude grid, and so need no further processing. The ECCC regional model has wind components on the polar-stereographic grid of the weather model simulation, and need to be rotated to our latitude-longitude reference frame in order to be ingested into WW3, which then performs interpolations in space and time as needed.

**(c) Wave Model Estimates**

**Figure 6** compares significant wave height distributions from WW3 using the four formulations implemented for the nonlinear wave-wave transfer  $S_{nl}$  term. These are the three formulations used in this study; DIA, WRT, and mTSA. A fourth simulation is denoted mTSA4, which uses the tuning for ST4 for the Northwest Atlantic as determined by Perrie et al. (2018); the latter was a study of waves generated by three intense nor'easter storms, and different wave models implemented on coarse- and fine-resolution nested grid systems that are similar to those used in **Figure 6**. The tuning of ST4 reflects regional characteristics of the Northwest Atlantic and the southern Gulf of Maine, and was shown to give enhanced results.

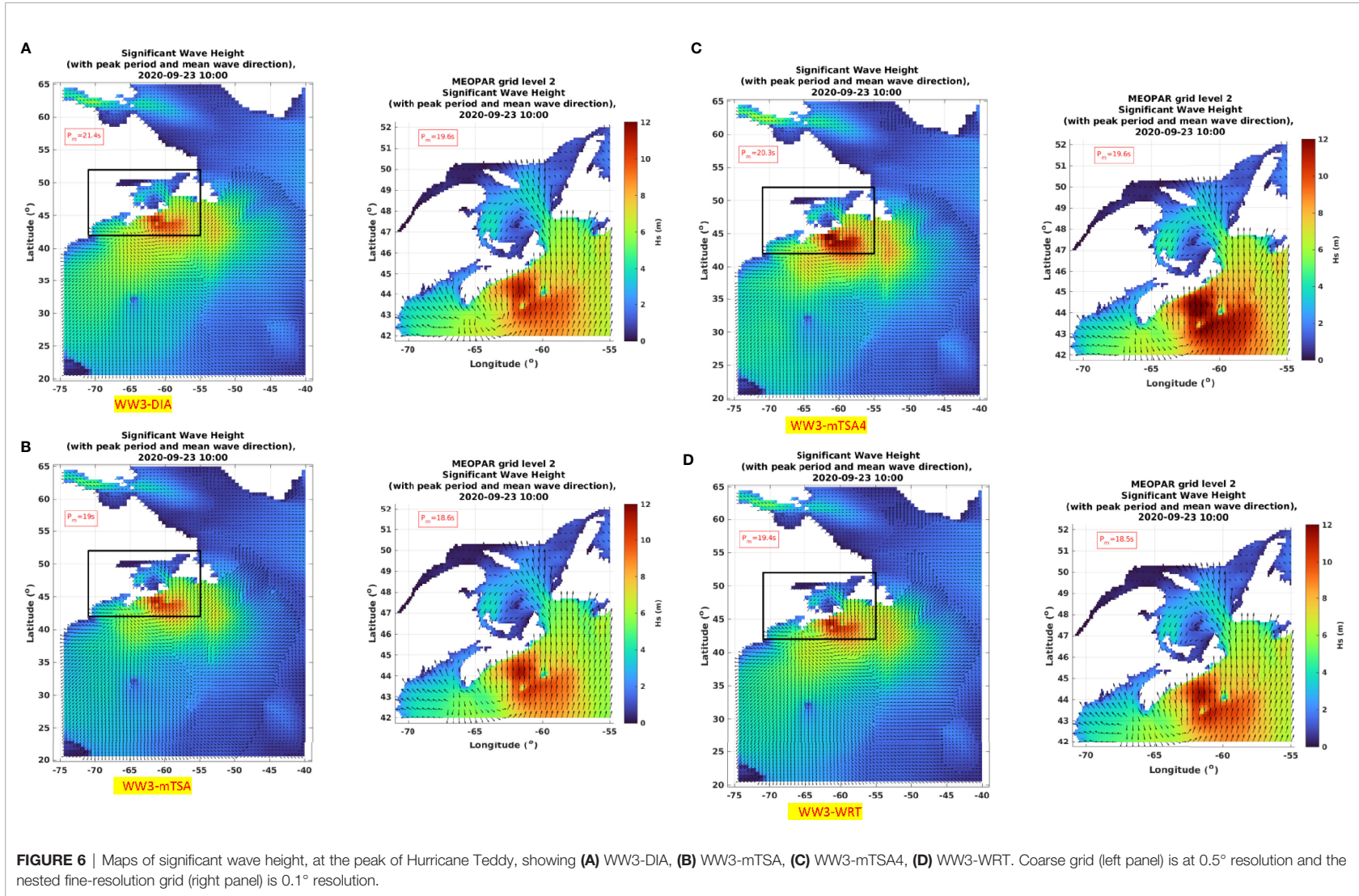


**FIGURE 6** | Maps of significant wave height, at the peak of Hurricane Teddy, showing (A) WW3-DIA, (B) WW3-mTSA, (C) WW3-mTSA4, (D) WW3-WRT. Coarse grid (left panel) is at  $0.5^{\circ}$  resolution and the nested fine-resolution grid (right panel) is  $0.1^{\circ}$  resolution.

In these simulations, WW3 is driven by the ECCC wind fields as Teddy propagated from the area around Bermuda, to Nova Scotia as described in the previous section. In terms of the  $H_s$  spatial distributions, the results from DIA and WRT appear to exhibit slightly larger  $H_s$  values than those of mTSA. However, as expected, this can be compensated for by applying the ST4 tuning suggested by Perrie et al. (2018), which results in higher values in the simulation results for mTSA4.

Overall, the qualitative features of the  $H_s$  area distributions and wave directions are similar in these four simulations, with respect to the propagation of the wave fields, the overall directional patterns of the waves, and the peak wave directions. Consistent with fetch-limited growth results reported in previous studies by Perrie et al. (2013), mTSA appears to give results that are biased low, whereas results from DIA are biased high compared to those of WRT, using the standard ST4 source terms. These differences in results from respective different  $S_{nl}$  formulations may be somewhat modulated by the inherent nonlinearity, numerical instability etc. present in the WW3 model system.

### (d) Comparison of $H_s$ Time Series

To estimate the reliability of the model simulations using the different nonlinear transfer  $S_{nl}$  formulations, we conducted comparisons with measured significant wave heights,  $H_s$ , with observations at four buoys in the model domain whose locations are shown in Figure 5B. Comparisons were made between time series of buoy measurements of significant wave heights,  $H_s$ , and the model simulations for Hurricane Teddy, using the implemented  $S_{nl}$  formulations; DIA, mTSA, mTSA4 and WRT. Buoy observations are generally reported at 30-minute intervals.

Figure 7 shows  $H_s$  time series and scatter plots at four selected buoys along Teddy's storm track. These are buoy

41049 near Bermuda, 44008 off Cape Cod, 44137 off Nova Scotia and 44139 near the southern tip of the Grand Banks. These four were selected in order to have additional discussion regarding 1-D and 2-D spectra, in the sections that follow. A summary of statistics for specifically these 4 buoys, plus an additional 10 other buoys along, or near, the storm track of Teddy, indicated in Figures 5A, B is presented in Table 1, in terms of root mean square error (RMSE), bias, correlation coefficient (corr), and scatter index (SI). In this computation of statistics, only data within  $\pm 3$  days of the passage of the storm by a given buoy are used; these data are indicated in Figure 7. Note that the full observational time series are indicated by red stars (\*), with the points used to calculate statistics (within  $\pm$  three days of the peak) marked by black circles  $\odot$  overlaying the red stars (\*).

In terms of capturing the storm peak values and model biases, the  $H_s$  time series and scatterplots in Figure 7 appear to suggest similar behaviors for all formulations, DIA, mTSA, mTSA4 and WRT. Statistical indices in Table 1 also reflect this finding, with mTSA4 tending to overpredict the peak  $H_s$  values and mTSA tending to underpredict these values. This suggests the general approach, that in implementing WW3 for specific regional applications, it is important to perform some careful tuning of the basic ST4 source terms of Ardhuin et al. (2010), to reflect the associated regional characteristics. This trend is also reported in the statistical indices in Tables 1 and 2 for the 14 buoys shown in Figure 5B along, or near, Teddy's storm track. mTSA4 is able to outperform mTSA in terms of improved RMSE, reduced bias, improved correlation coefficient, and scatter index. However, although results from mTSA4 appear to compare somewhat favorably with measurements at buoys 41049 and 44008, the mTSA4 results at buoys 44137 and 44139 appear to have notable overestimates. Thus, the performance is not unequivocal.

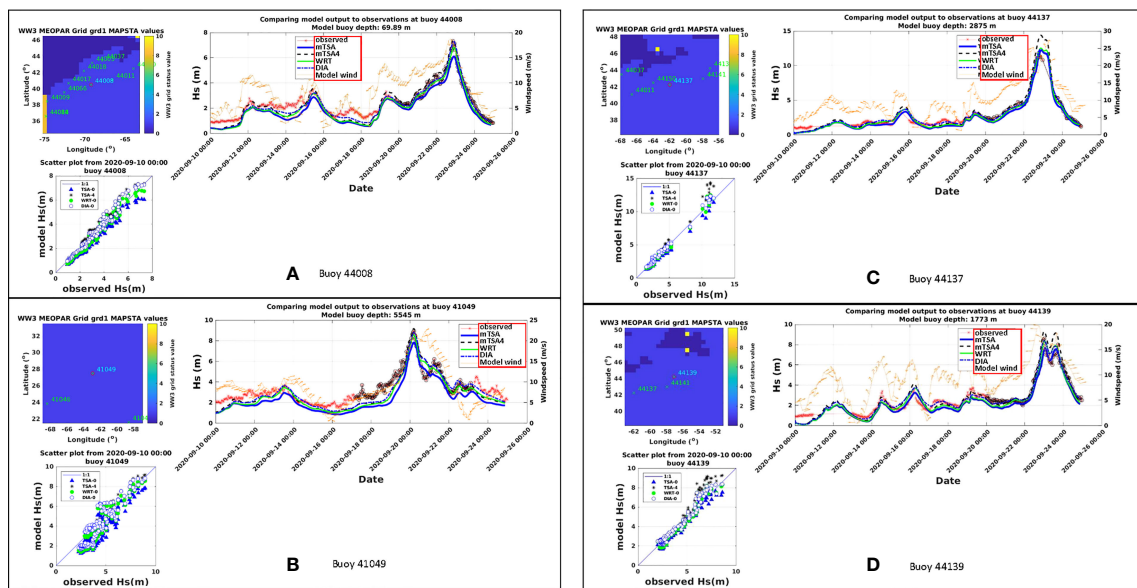


FIGURE 7 | Time series comparisons for significant wave heights  $H_s$  for Hurricane Teddy in 2020; shown for buoys: (A) 41049, (B) 44008, (C) 44137, (D) 44139.

**TABLE 1 |** Statistics for Hs (m) from WW3 wave model compared to measurements at 14 buoys along or near the storm track of Hurricane Teddy, for root mean square error (RMSE), bias, correlation coefficient (corr) and scatter index (SI).

Model	RMSE	Bias	Corr	SI (%)
mTSA	0.651	-0.526	0.930	32.02
mTSA4	0.495	-0.195	0.937	24.19
WRT	0.532	-0.357	0.936	26.54
DIA	0.438	-0.181	0.941	21.80

**(e) Impacts of Model Tuning**

Because ST4 was originally tuned for DIA by Arduin et al. (2010) for simulation of waves for global ocean studies it tends to perform well. In fact, statistical indices in **Table 1** suggest that DIA can outperform the other simulations; those using mTSA, mTSA4 and WRT. Occasionally, for some of the statistical indices, mTSA4 can outperform the other simulations, for example at buoy 44066 at the edge of the Continental Shelf off the coast of Delaware USA.

As reported by Perrie et al. (2018) the tuning of ST4 consists of adjustments to parameters BETAMAX, the wind-wave growth parameter, and ZALP, the wave age shift of the long waves to account for gustiness, respectively, 1.75 and 0.008, to give optimal simulation skill for waves generated by three nor'easters for the Northwest Atlantic and Gulf of Maine region. It is anticipated that additional tuning could also produce more improvements to the performance of mTSA4. But that is not the objective of this study. In any case, it is interesting to compare the results from mTSA4 with those from mTSA and WRT. **Table 2** suggests that for the four selected buoys, results from mTSA4 are generally better than those from WRT or mTSA.

**(f) 1-D Wave Spectra**

Comparisons between 1-D wave spectra at the peak of the buoy measurements are shown in **Figure 8** for Hurricane Teddy. The simulated 1-D spectra are all essentially dominated by single-peaked spectra. Some of the comparisons show large discrepancies between model simulations and observed data. It is evident that as the peak of the storm passes the buoy locations, each will experience changing wind directions, and therefore interactions between swell and wind-waves are present. These interactions are evident in the comparisons that are shown.

We consider the simulations from the different  $S_{nl}$  formulations. Buoy 41049 off Bermuda shows a dominant peak near 0.07 Hz and a secondary peak near 0.09 Hz. Only mTSA4 shows any (minor) indication of the secondary peak. All simulations underestimate the primary peak. mTSA provides a notable underestimate compared to the observations or compared to the other simulations like mTSA, DIA and WRT.

Results for buoy 44008 off Cape Cod are somewhat similar to those of 41049. The observed data indicate some indication of a secondary spectral peak at about 0.11 Hz, and a primary peak at about 0.07 Hz. All model simulations tend to also have indications

**TABLE 2 |** Statistics for Hs (m) from WW3 wave model compared to measurements at 4 buoys along or near the storm track of Hurricane Teddy, for root mean square error (RMSE), bias, correlation coefficient (corr) and scatter index (SI).

Buoy41049				
	RMSE	Bias	Corr	SI (%)
mTSA	1.014	-0.874	0.936	31.03
mTSA4	0.736	-0.401	<b>0.941</b>	22.55
WRT	0.782	-0.53	0.936	23.93
DIA	<b>0.678</b>	<b>-0.3</b>	0.932	20.77
Buoy44008				
Model				
mTSA	0.595	-0.508	0.97	24.81
mTSA4	0.466	<b>-0.123</b>	0.972	19.43
WRT	0.482	-0.351	0.977	20.12
DIA	<b>0.389</b>	-0.178	<b>0.978</b>	16.25
Buoy44137				
Model				
mTSA	0.56	-0.408	0.984	21.75
mTSA4	0.643	0.043	<b>0.987</b>	25.01
WRT	0.486	-0.206	0.983	18.9
DIA	<b>0.409</b>	<b>0.009</b>	0.985	15.91
Buoy44139				
Model				
mTSA	0.539	-0.388	<b>0.978</b>	19.61
mTSA4	0.64	0.095	<b>0.978</b>	23.28
WRT	0.516	-0.19	0.973	18.8
DIA	<b>0.467</b>	<b>0.013</b>	0.972	17

Values in bold denote best results.

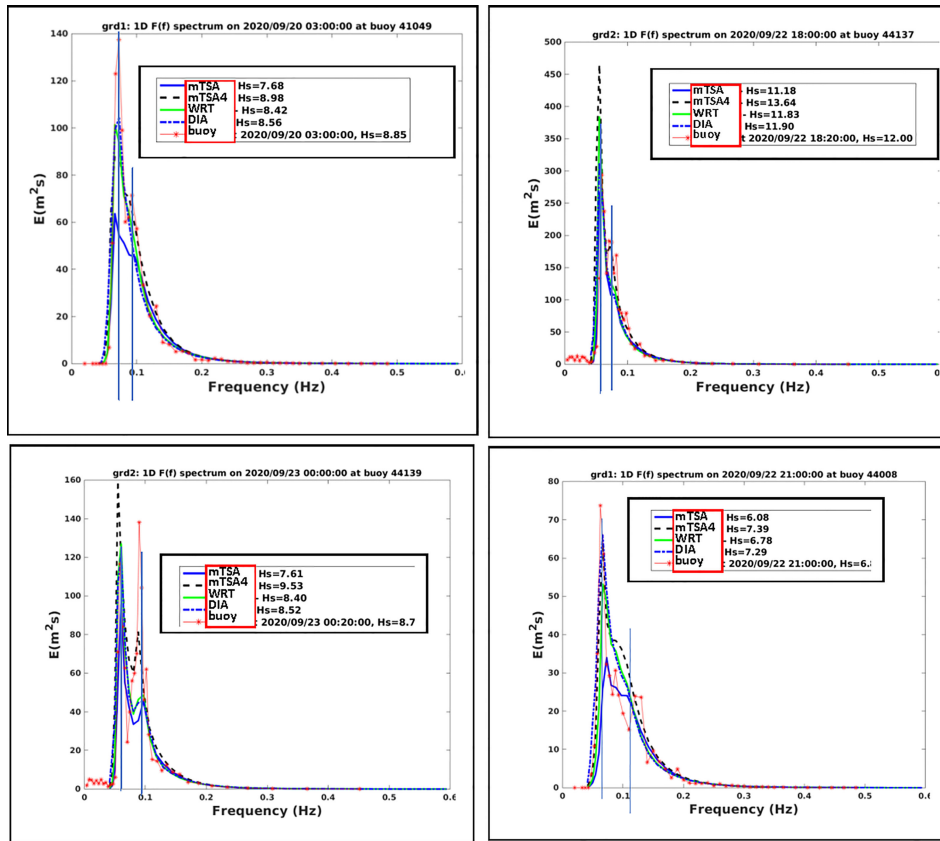


**FIGURE 8** | Hurricane Teddy at about the peak of the storm, showing 1D spectrum observed at buoys 41049, 44008, 44137, 44139 compared to simulated results from WW3 with ST4 source terms, DIA, WRT, and mTSA, where mTSA4 assumes the ST4 tuning used in Perrie et al. (2018).

of the occurrence of the secondary peak, e.g. a ‘wiggle’, but none simulate well the details suggested by the observed data. Also no simulation captures the primary peak, although mTSA4 and DIA appear to come close to so doing, whereas results from WRT and mTSA increasingly underestimate the observed peak data, respectively.

Results for buoy 44137 off Nova Scotia are similar to those of 41049, with a dominant peak around 0.06 Hz and a secondary peak at about 0.08 Hz. Different from the results at 41049, here the results from mTSA4 appear to capture the secondary peak, but notably overestimate results at the primary peak, as do results from WRT. By comparison, results from DIA and mTSA appear to provide a somewhat favorable simulation of the primary spectra peak.

Results for buoy 44139 on the Grand Banks are notable because of the double peak, a low frequency possible swell peak at about 0.06 Hz, and a higher wind-waves peak at about 0.09 Hz. In this case, all the simulations appear to provide some indication of the secondary wind-waves peak, although all present underestimates, with mTSA4 giving the best simulation. For the primary peak, mTSA4 provides an overestimate, whereas the other three manage to give somewhat reasonable simulations.

### (g) 2-D Wave Spectra

Comparisons between observed 2D wave spectra and model simulations for Hurricane Teddy at about its peak are shown in **Figure 9** for buoys 41049 and 44008. Results for the buoy measurements are calculated following the Longuet-Higgins approximation for the Fourier expansion method as recommended by the NDBC website ([www.ndbc.noaa.gov/measdes.shtml](http://www.ndbc.noaa.gov/measdes.shtml)). The observed data in **Figure 9** at both buoys show the response of the wave spectra to turning winds, as the hurricane passes by and as the primary peak modulates to the new direction of the developing wind-waves.

Model simulations suggest qualitatively similar results. Although the observed main directions of the low frequency primary peak and the developing secondary peak are approximately consistent with the simulations, the modelled maximum energy values are generally overestimated compared to the observed values,  $92.6 \text{ m}^2 \text{ Hz}^{-1} \text{ rad}^{-1}$  at buoy 41049 and  $38.3 \text{ m}^2 \text{ Hz}^{-1} \text{ rad}^{-1}$  at buoy 44008. The model simulations also appear to provide results with wider distributions of new wind-wave energy than is being generated in the new developing wind direction, compared to more restricted directional spreading

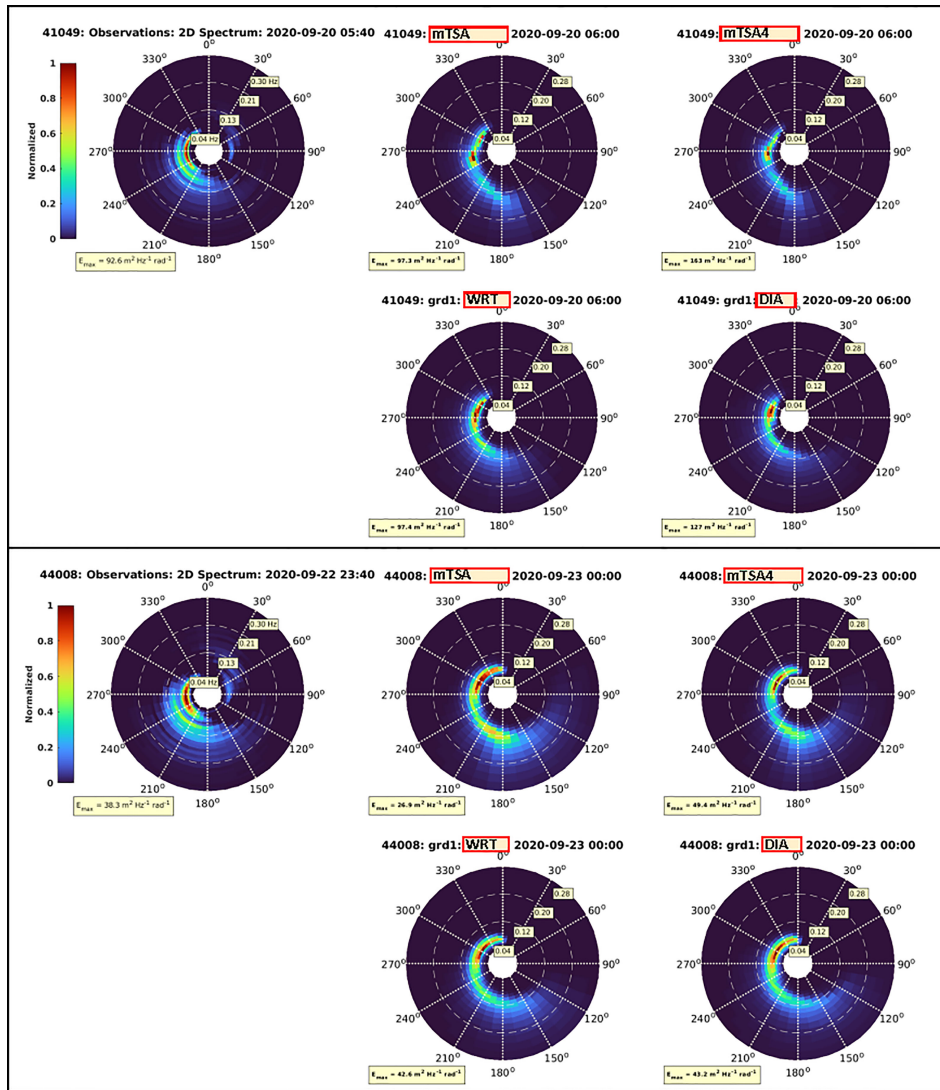


**FIGURE 9** | As in **Figure 7** for 2D spectrum for Hurricane Teddy at about the peak of the storm, 20 Sept 2020 at 5:40 UTC at buoy 41049, and 22 Sept 2020 at 23:49 UTS at buoy 44008, showing the observed spectrum compared to simulated results from WW3 with ST4 source terms, and DIA, WRT, mTSA4 for nonlinear wave-wave interactions  $S_{nl}(f, \theta)$ . Here, mTSA4 assumes the ST4 tuning from Perrie et al. (2018).

suggested by the observed spectra. Often it is the other way around, with rather wide directional distributions reported for buoy wave data compared to narrow distributions estimated by wave models. An example of the latter can be found in the comparisons of 2-D modelled and measured spectra by Perrie et al. (2018), which may be attributed to the Longuet-Higgins approximation for the Fourier expansion method.

Overall, the directional distributions resulting for the three  $S_{nl}$  formulations do not differ significantly, except in terms of the magnitude of the simulated 2D spectral peaks compared to the observed data. At buoy 41049, magnitudes of peak 2D spectral values are approximately the same as observed, and mTSA4 is too high. See **Table 3**. At buoy 44008, magnitudes of peak 2D

spectral values are approximately the same as observed for results from DIA and WRT, whereas mTSA is too low and mTSA4 is too high. Therefore, as mentioned before, although the ST4 tuning of the two parameters, BETAMAX, the wind-wave growth parameter, and ZALP, the wave age shift of the long waves to account for gustiness, may improve simulations of  $H_s$  in **Tables 1** and **2**, and the 1D spectra in **Figure 7**, that is not always the case for the 2D spectra.

Another possible constraint on the models is numerics, in terms of the shifting of direction of the spectral peak, and spectral direction distributions. WW3 uses third-order upwind propagation. This is the mechanism that can contribute to the model’s ability to shift the dominant wave directions in response to changing wind directions.



**TABLE 3** | Observed maximum 2-D wave spectra for Hurricane Teddy, compared to simulations.

Buoy	Observed	DIA	mTSA	mTSA4	WRT
41049	92.6	127.0	97.3	163.0	97.4
44008	38.3	43.2	26.9	49.4	42.6

Units are  $m^2 \text{ Hz}^{-1} \text{ rad}^{-1}$ .

**TABLE 4** | Computational efficiency for the simulation of nonlinear interactions  $S_{nl}$ . In this comparison, FBI is the full Boltzmann integration representation of nonlinear interactions as used in earlier studies like Resio and Perrie (2008).

Numerical model	Ratio/DIA-time
DIA	1.0
TSA-4	26.5
FBI-4	30.2
FBI	~110
mTSA	~100
WRT	110.7

FBI-4 and TSA-4 represent previous older formulations that incorporate alternating computational loops to improve efficiency.

## (h) Computational Efficiency

The presentation of results is not complete without mention of computational efficiency. However, the focus of this study has been computational accuracy, rather than computational efficiency. The new mTSA code has not been optimized with MPI (Message Passing Interface) or other methodologies, whereas WRT has had such optimizations. Therefore, in its present formulation, mTSA does not run efficiently. For example, whereas mTSA allows a very large reduction in the number of computations needed to approximate the full integration for the Boltzmann integral for the wave-wave interactions, the separation within the spectrum is presently quite demanding and has not been optimized.

A summary of computational efficiency of mTSA relative to DIA and other formulations for  $S_{nl}$  is given in **Table 4**. In this comparison, FBI is the full Boltzmann integration representation of these quadruplet interactions, which is similar to WRT, and has been used extensively in earlier comparison studies of TSA, such as in Resio and Perrie (2008), with similar run times,  $\sim 110 \times$  DIA. By comparison, the present mTSA methodology is about  $\sim 100 \times$  DIA, whereas previous older parameterizations of these formulations, FBI-4 and TSA-4, which incorporate alternating frequency and angle computational loops to accelerate the efficiency, and additional parameterizations to attempt improved accuracy, have a computational efficiency in the range of about  $\sim 26$  to  $30 \times$  DIA. Future work will focus on optimizing mTSA and the need to enhance computational efficiency.

## 5 DISCUSSION AND CONCLUSIONS

We have considered formulations for the nonlinear wave-wave interactions  $S_{nl}$  for application in operational wave forecast models like WAVEWATCHIII<sup>TM</sup>, also denoted WW3. These formulations are DIA formulation from Hasselmann and Hasselmann (1985) and the WAMDI Group (1988), the WRT full integration for the Boltzmann integral based on Webb (1978);

Tracy and Resio (1982); Resio and Perrie (1991), and Van Vledder (2006), and the original two-scale approximation, denoted TSA by Resio and Perrie (2008) and Perrie et al. (2013). All of these have been implemented into WW3 in previous studies. Here, in this study, we have proposed a slight generalization of the original TSA, denoted 'multiple TSA' or mTSA, to allow better simulation of complicated wave spectra, as may occur in critical situations such as rapidly changing storm situations, shearing spectra, and interactions of swell with wind-waves etc.

To test mTSA, we conduct a variety of test cases, involving hypothetical and real wave spectra. The hypothetical cases are based on a single-point model integration, for complicated wave spectra in interactions between sheared spectra, swell and opposing wind-sea, swell and wind-sea and orthogonal generating wind-waves, etc. which might occur in rapidly changing storm conditions. With respect to the best simulations by WRT, these suggest that the new proposed mTSA is accurate and reliable compared to both DIA, and the previously proposed original version of TSA by Resio and Perrie (2008), which is denoted sTSA in this study. The other source terms used in these tests cases are provided from the ST4 source term formulation of Ardhuin et al. (2010), for example, for wind input  $S_{in}$  and wave dissipation  $S_{ds}$ .

We also conducted real test cases, comparing observations from field data with results from simulations with WW3 using these  $S_{nl}$  formulations. These test cases are the observations from NDBC and Canadian buoys as collected during Hurricane Teddy in 2020. This storm had its genesis as a strong tropical wave off the west coast of Africa; from there it moved further westward, intensified and then began heading northward from around Bermuda, eventually making landfall in Nova Scotia. Comparisons show that simulations with mTSA, and also mTSA4 with tuned ST4 source terms, are competitive with simulations using DIA or WRT.

## DATA AVAILABILITY STATEMENT

Publicly available datasets were analyzed in this study. This data can be found here: Forecast wind products are posted daily to ECCO's website (<https://dd.weather.gc.ca/>). NDBC buoy data are available at <https://www.ndbc.noaa.gov/>.

## AUTHOR CONTRIBUTIONS

WP planned the paper, contributed to the theory design of the TSA model, the test cases and real Hurricane Teddy case, and wrote the paper. BT developed the basic computer codes and ran all the simulations tests. MC performed the pre- and post-processing of data from model simulations, and the

visualization of the results. All authors contributed to the article and approved the submitted version.

## ACKNOWLEDGMENTS

We received funding from the Northeastern Regional Association of Coastal Ocean Observing Systems (NERACOS), Canada's

Ocean Frontier Institute (OFI), Competitive Science Research Fund (CSRF) and Marine Environmental Observation, Prediction and Response (MEOPAR) to support this development work. Earlier forms of this work were supported by Canada's Panel on Energy Research and Development (PERD) and US Office of Naval Research. Special thanks to Don Resio for discussion of basic concepts for this work.

## REFERENCES

- Ardhuin, F., Rogers, E., Babanin, A. V., Filipot, J. F., Magne, R., Roland, A., et al. (2010). Semi-Empirical Dissipation Source Functions for Ocean Waves. Part I: Definition, Calibration, and Validation. *J. Phys. Oceanogr.* 40 (9), 1917–1941. doi: 10.1175/2010JPO4324.1
- Blake, E. (2021). Hurricane Teddy. National Hurricane Center Tropical Cyclone Report 25.
- Booij, N., Ris, R. C., and Holthuijsen, L. H. (1999). A Third-Generation Wave Model for Coastal Regions, Part 1: Model Description and Validation. *J. Geophys. Res.* 104 (C4), 7649–7666. doi: 10.1029/98JC02622
- Donelan, M. A., Hamilton, J., and Hui, W. H. (1985). Directional Spectra of Wind-Generated Waves. *Phil. Trans. R. Soc. London A* 315, 509–562. doi: 10.1098/rsta.1985.0054
- Hasselmann, K., Barnett, T. P., Bouws, E., Carlson, H., Cartwright, D. E., Enke, K., et al. (1973). Measurements of Wind-Wave Growth and Swell Decay During the Joint North Sea Wave Project (JONSWAP). *Ergänzungsheft zur Deutschen Hydrographischen Zeits.* 8 (12), 1–95.
- Hasselmann, S., and Hasselmann, K. (1985). Computations and Parametrizations of the Nonlinear Energy Transfer in a Gravity Wave Spectrum, Part I, A New Method for Efficient Computations of the Exact Nonlinear Transfer Integral. *J. Phys. Oceanogr.* 15, 1369–1377. doi: 10.1175/1520-0485(1985)015<1369:CAPOTN>2.0.CO;2
- Holthuijsen, L. H. (2007). *Waves in Oceanic and Coastal Waters* (New York: Cambridge Univ. Press), 387.
- Hsiao, S.-C., Hongey, C., Han-Lun, W., Wei-Bo, C., Chih-Hsin, C., Wen-Dar, G., et al. (2020). Numerical Simulation of Large Wave Heights From Super Typhoon Nepartak, (2016) in the Eastern Waters of Taiwan. *J. Mar. Sci. Eng.* 8 (3), 217. doi: 10.3390/jmse8030217
- Komen, G. J., Cavaleri, L., Donelan, M., Hasselmann, K., Hasselmann, S., and Janssen, P. A. E. M. (1994). *Dynamics and Modelling of Ocean Waves* (England, UK: Cambridge University Press), 532 + xxi pages.
- Perrie, W., and Resio, D. (2009). A Two-Scale Approximation for Efficient Representation of Nonlinear Energy Transfers in a Wind Wave Spectrum. Part II: Application. To Observed Wave Spectra. *J. Phys. Oceanography.* 39, 2451–2476. doi: 10.1175/2009JPO3947.1
- Perrie, W., Toulany, B., Resio, D. T., Roland, A., and Auclair, J. P. (2013). A Two-Scale Approximation for Wave-Wave Interactions in an Operational Wave Model. *Ocean Model* 70, 38–51. doi: 10.1016/j.ocemod.2013.06.008
- Perrie, W., Toulany, B., Roland, A., Dutour-Sikiric, J. M., Chen, C., Beardsley, R. C., et al. (2018). Modeling North Atlantic Nor'easters With Modern Wave Forecast Models. *J. Geophys. Res.* 123 (1), 533–557. doi: 10.1002/2017JC012868
- Resio, D. T., Long, C. E., and Vincent, C. L. (2004). Equilibrium-Range Constant in Wind-Generated Wave Spectra. *J. Geophys. Res.* 109, C01018. doi: 10.1029/2003JC001788
- Resio, D. T., and Perrie, W. (1991). A Numerical Study of Nonlinear Energy Fluxes Due to Wave-Wave Interactions. Part 1. Methodology and Basic Results. *J. Fluid Mech.* 223, 609–629. doi: 10.1017/S002211209100157X
- Resio, D. T., and Perrie, W. (2008). A Two-Scale Approximation for Efficient Representation of Nonlinear Energy Transfers in a Wind Wave Spectrum, Part 1: Theoretical Development. *J. Phys. Oceanogr.* 38, 2801–2816. doi: 10.1175/2008JPO3713.1
- Swail, V., Alves, JH., Brown, J., Greenslade, D., and Jensen, R. (2021). The 2nd International Workshop on Waves, Storm Surges and Coastal Hazards Incorporating the 16th International Workshop on Wave Hindcasting and Forecasting. *Ocean Dyn.* 71, 957–961. doi: 10.1007/s10236-021-01476-7
- SWAMP Group (1985). *Ocean Wave Modeling* (New York: Plenum Press), 256.
- Tolman, H. (2009) *User Manual and System Documentation of WAVEWATCH III™ Version 3.14*. Available at: [http://polar.ncep.noaa.gov/mmab/papers/t276/MMAB\\_276.pdf](http://polar.ncep.noaa.gov/mmab/papers/t276/MMAB_276.pdf).
- Tolman, H. L. (2013). A Generalized Multiple Discrete Interaction Approximation for Resonant Four-Wave Interactions in Wind Wave Models. *Ocean Model.* 70, 11–24. doi: 10.1016/j.ocemod.2013.02.005
- Tolman, H. L., and Grumbine, R. W. (2013). Holistic Genetic Optimization of a Generalized Multiple Discrete Interaction Approximation for Wind Waves. *Ocean Model* 70, 25–37. doi: 10.1016/j.ocemod.2012.12.008
- Tracy, B. A., and Resio, D. T. (1982). Theory and Calculation of the Nonlinear Energy Transfer Between Sea Waves in Deep Water. WES rep. 11, US Army Engineer Waterways Exp. Sta., Vicksburg, MS.
- Van Vledder, G. P. (2006). The WRT Method for the Computation of Nonlinear Four Wave Interactions in Discrete Spectral Wave Models. *Coastal Eng.* 53, 223–242. doi: 10.1016/j.coastaleng.2005.10.011
- WAMDI Group (1988). The WAM Model – a Third Generation Oceans Wave Prediction Model. *J. Phys. Oceanogr.* 18, 1775–1810. doi: 10.1175/1520-0485(1988)018<1775:TWMGTGO>2.0.CO;2
- Webb, D. J. (1978). Non-Linear Transfers Between Sea Waves. *Deep-Sea Res.* 25, 279–298. doi: 10.1016/0146-6291(78)90593-3
- WW3DG (WAVEWATCHIII™) Development Group (2016) *User Manual and System Documentation of WAVEWATCH III R Version 5.16*. Available at: <https://polar.ncep.noaa.gov/waves/wavewatch/manual.v5.16.pdf>.

**Conflict of Interest:** The authors declare that the research was conducted in the absence of any commercial or financial relationships that could be construed as a potential conflict of interest.

**Publisher's Note:** All claims expressed in this article are solely those of the authors and do not necessarily represent those of their affiliated organizations, or those of the publisher, the editors and the reviewers. Any product that may be evaluated in this article, or claim that may be made by its manufacturer, is not guaranteed or endorsed by the publisher.

Copyright © 2022 Perrie, Toulany and Casey. This is an open-access article distributed under the terms of the Creative Commons Attribution License (CC BY). The use, distribution or reproduction in other forums is permitted, provided the original author(s) and the copyright owner(s) are credited and that the original publication in this journal is cited, in accordance with accepted academic practice. No use, distribution or reproduction is permitted which does not comply with these terms.

## APPENDIX

Given a double-peaked spectrum obtained from observational data such as a buoy, this section provides the procedure for getting the JONSWAP parameters of the two broad-scale terms, the final broad-scale term for the entire spectrum, and the associated local-scale term.

- i. The first step is to examine the entire spectrum and find the spectral peak. This is the absolute largest peak. This is the energy maximum. Secondly, this process is repeated and the second spectral peak is determined. This is a local peak, which means it is a local maximum and has at least one frequency bin with lower energy on the left side in a lower frequency bin, and at least one frequency bin with lower energy on the right side, in a higher frequency bin.
- ii. Subsequently, just for bookkeeping, the two peaks are labelled so that the lower one on the frequency range is called " $f_{p1}$ " and the other one is " $f_{p2}$ ". Therefore,  $f_{p1}$  is the peak with lower frequency and  $f_{p2}$  is the peak with higher frequency.
- iii. The total frequency range is from the lowest frequency in the spectrum, at frequency bin "= one", or  $f_1$ , to the highest frequency in the spectrum, which for observed data corresponds to the Nyquist frequency,  $f_{Nyquist}$ . We divide the frequency range into 2 regions; one for  $f_{p1}$  and one for  $f_{p2}$ . The division point is defined by the separation frequency, which is approximated as sitting halfway between the 2 peaks,  $f_{p1}$  and  $f_{p2}$ . We do not use optimal fitting to try to somehow refine the splitting of the frequency range between  $f_{p1}$  and  $f_{p2}$ , because that reduces the computational efficiency and has not been found to be beneficial. Therefore, the separation frequency is halfway between  $f_{p1}$  and  $f_{p2}$ .
- iv. The "first region" is from the lowest frequency in the spectrum,  $f_1$ , to the separation frequency, and the "second region" is from the separation frequency to the highest frequency,  $f_{Nyquist}$ . For each region, we have one spectrum with one peak. Therefore, we do JONSWAP fitting on each separate region. This is performed by a subroutine (previously developed in the original TSA formulation) that does an optimal five-parameter JONSWAP fitting. Therefore, in the first region for  $f_{p1}$ , the five-parameter JONSWAP fitting is done for the frequency sub-range from  $f_1$  to the separation frequency. And in the second region for  $f_{p2}$ , the five-parameter JONSWAP fitting is also done for the frequency sub-range extending from the separation frequency to the highest frequency,  $f_{Nyquist}$ . Therefore, we handle the  $f_{p1}$  region and the  $f_{p2}$  region independently.
- v. Until now, the JONSWAP fitting is always done in 1-D. To go to 2-D, we apply a directional distribution like  $\sim \cos^m(\theta - \theta_p)$  to the 1-D parameterizations, at each step, in order to get the two 2-D broad-scale terms for the two regions, for the  $f_{p1}$  region and for the  $f_{p2}$  region, independently.
- vi. To get the broad-scale term for the total frequency range, we add together the broad-scale term for the  $f_{p1}$  region, to the broad-scale term for the  $f_{p2}$  region. This completes the fitting for the broad-scale term for the entire frequency range. There is the possibility of a "discontinuity or jump" in the two broad-scale terms at the separation frequency between  $f_{p1}$  and  $f_{p2}$ . This is resolved by smoothing, over three frequency bins.
- vii.

The local-scale spectrum, or residual spectrum is then determined as the difference between the given input spectrum *minus* the broad-scale term.



# Long-Term Variability of the East Sea Intermediate Water Thickness: Regime Shift of Intermediate Layer in the Mid-1990s

JongJin Park \*

School of Earth System Sciences/Kyungpook Institute of Oceanography, Kyungpook National University, Daegu, South Korea

The shipboard measurements over approximately 55 years in the southwestern part of the East Sea (Sea of Japan) demonstrate a remarkable basin-wide, interannual-interdecadal variability in the temperature-based thickness of the East Sea Intermediate Water (ESIW) whose temporal variability shows strong correlation with the density-based thickness ( $r = 0.97$ ). Relevant to the long-term variability of the ESIW thickness, clear changes in horizontal and vertical features have been observed at the intermediate layer in the mid-1990s, such as 1) increases in vertical temperature gradient in the thermocline by shoaling of 2°C–5°C isotherms, 2) relatively high correlations among isotherms in the interdecadal timescale, 3) appearance of zonal phase difference in the ESIW thickness variability after the mid-1990s, and 4) correlation phase change between the Arctic Oscillation Index and the ESIW thickness. The ESIW thickness could be smaller when its formation is weaker and when the formation of deep-water mass below it becomes stronger. Based on the features observed, we hypothesized on the regime shift concerning the East Sea meridional overturning circulation; before the mid-1990s, active deep-water formation mainly controlled the ESIW layer variability, but after the mid-1990s, the ESIW formation rate predominantly affected its own thickness variability.

## OPEN ACCESS

### Edited by:

Giovanni Besio,  
University of Genoa, Italy

### Reviewed by:

Sebastian Solari,  
Universidad de la República, Uruguay  
Wenli Zhong,  
Ocean University of China, China

### \*Correspondence:

JongJin Park  
jjpark@knu.ac.kr

**Keywords:** East Sea Intermediate Water, regime shift, thermocline water, thickness variability, Arctic Oscillation, long-term variation, ship-board measurements, Argo float

### Specialty section:

This article was submitted to  
Physical Oceanography,  
a section of the journal  
Frontiers in Marine Science

**Received:** 18 April 2022

**Accepted:** 01 June 2022

**Published:** 12 July 2022

### Citation:

Park JJ (2022) Long-Term Variability  
of the East Sea Intermediate  
Water Thickness: Regime Shift of  
Intermediate Layer in the Mid-1990s.  
*Front. Mar. Sci.* 9:923093.  
doi: 10.3389/fmars.2022.923093

## 1 INTRODUCTION

The East Sea (Japan Sea, hereafter ES) is a marginal sea connected to the North Pacific through four straits shallower than 200 m, i.e., the Korea Strait, Tsugaru Strait, Soya Strait, and Tatar Strait, the water masses of which are independent of the intermediate and deep waters in the North Pacific. The water masses of the ES below the thermocline are formed inside the ES and classified as intermediate, central, and bottom water according to their formation processes and sites (Kim et al., 2004; Talley et al., 2006). The formation process of each water mass is very similar to that of the open ocean.

Above the thermocline, three different types of water masses are mostly found in the southern part of the ES (c.f. Park et al., 2016): the low-salinity Tsushima Warm Water (TWW) and the high-salinity TWW flow in through the Korea Strait. The former one is near the sea surface in summertime, which is the diluted water of Changjiang River in China, and the latter is right below the former one, persistent throughout the year and originated from the Kuroshio water. Lastly, the Ten Degree Water with thermostat is located below the high-salinity TWW and formed in the

southern part of the ES in winter, which is also comparable to the subtropical mode waters in the open ocean.

There is also a subpolar front near 38°N in the ES created by the TWW flowing in through the Korea Strait. Therefore, the southern and northern parts of the ES have the thermal characteristics of the subtropical and subpolar regions of the open ocean, respectively. Due to these characteristics, the ES is also called the “miniature ocean.”

However, because the water masses of the ES are formed in relatively similar regions (northwestern part of the ES), the variation in their physical properties is still not as substantial as that in the open ocean. The small deviation in the properties makes it difficult to properly distinguish the differences between water masses before introducing conductivity-temperature-depth instruments with high precision and high resolution. In the past, the deep layer below the permanent thermocline was recognized as a single water mass called the Japan Sea Proper Water (Uda, 1934). However, the properties and dissolved oxygen (DO) profiles, which were precisely measured by the Circulation Research Experiment in East Asian Marginal Seas program since the mid-1990s, have demonstrated that there were several different water masses below the thermocline. These water masses are formed in slightly different waters in the Western Japan Basin through different processes (Kim and Kim, 1999; Talley et al., 2004).

Although the East Sea is a small sea, there are two types of intermediate water, i.e., the East Sea Intermediate Water (ESIW) with salinity minimum layer and the High Salinity Intermediate Water with salinity maximum layer. The ESIW predominates the ES, except in the eastern part of the Japan Basin. The High Salinity Intermediate Water is present within the near-barotropic cyclonic gyre in the central and eastern Japan Basin where the ESIW is not found and barely spreads to the southern part of the ES (Kim and Kim, 1999; Watanabe et al., 2003; Kang et al., 2016). Alternatively, the ESIW is subducted to the south under the subpolar front, contributing to the East Sea meridional overturning circulation (EMOC), unlike the High-Salinity Intermediate Water (Park et al., 2016).

The ESIW exists just below the permanent thermocline, similar to that in the open ocean, and is characterized by the extreme (low salinity minimum) salinity values. The Intermediate Water has a high DO concentration, and it was observed to be formed by subducting surface water in contact with the atmosphere in the northern part of the ES. The DO of the ESIW is  $>250 \mu\text{mol kg}^{-1}$  and the salinity is  $<34.06 \text{ g kg}^{-1}$ , the water temperature range of this layer is  $1^{\circ}\text{C}–5^{\circ}\text{C}$ , and its potential density ranges from 26.9 to  $27.3 \sigma_{\theta}$  (Kim and Chung, 1984; Cho and Kim, 1994; Kim and Kim, 1999; Senjyu, 1999; Kim et al., 2004; Yun et al., 2004). As noted by Kim and Kim (1999), the characteristics of the ESIW may vary depending on the observed time and region because researchers have not conclusively defined the ESIW layer.

**Abbreviations:** ESIW, East Sea Intermediate Water; ES, East Sea or Japan Sea; TWW, Tsushima Warm Water; EMOC, East Sea meridional overturning circulation; NFK, North Korean Front; DO, dissolved oxygen; AO, Arctic Oscillation; NKCW, North Korean Cold Water; NIFS, National Institute of Fisheries Science; SSH, sea surface height; PC, principal component; JSPW, Japan Sea Proper Water.

During winter in the ES, the northwesterly wind from the Siberian continent becomes jet-shaped due to the orographic effect near Vladivostok, which forms a wind stress curl of a dipole structure, and the curl in the west becomes negative, causing the Ekman downwelling. At the center where this dipole wind stress curl appears, the North Korean Front (NKF) is formed. This happens only in winter and is easily found in the satellite sea surface temperature data; a southward or southeastward ocean current is created along the front. The eastern side of the NKF has a low water temperature of  $1^{\circ}\text{C}$  or less, similar to the temperature of the central Japan Basin, but the western side has a relatively high temperature of  $3^{\circ}\text{C}–7^{\circ}\text{C}$ , and anticyclonic eddies also are found (Park et al., 2005; Talley et al., 2006).

The ESIW has been known to form in the western side of the NKF or in the Western Japan Basin (Yoon and Kawamura, 2002; Park and Lim, 2018). The winter surface salinity in the area is lower than that in other regions of the ES, except near the Russian coast, and aids the formation of the salinity minimum layer. Park and Lim (2018) showed the possibility that the fresher surface water in the ESIW formation area mostly originated from the low-salinity TWW, flowing in through the Korea Strait. This implies that the salinity properties of the ESIW can be greatly controlled by ocean advection, even though they are under the influence of seasonal atmospheric forces. Therefore, the salinity itself can hardly serve as a suitable proxy for the ESIW response to the long-term climate change. In addition, it is noted that the sea water density in the ES is mainly determined by the water temperature especially below the main thermocline, while the salinity does not significantly affect the density change. Indeed, the salinity variation at the surface of the ESIW formation site is from 33.95 to  $34.00 \text{ g/kg}$ , but the temperature ranges from 2 to  $6^{\circ}\text{C}$  (Park and Lim, 2018). Thus,  $\alpha \delta T$  is about 10 times larger than  $\beta \delta S$  in the formation area. It means that the salinity variability may not greatly affect the ESIW volume change defined by density range.

Studies on the long-term variability of the East Sea water masses have been conducted in response to climate change. Since 1969, a clear warming has been observed in the deep sea below 500 m (c.f. Kwon et al., 2004). Together with the warming trend, reports until the late 1990s showed that the DO concentration has been continuously decreasing in the deep and bottom oceans but increased in the central layer between intermediate and deep layers (c.f. Gamo, 1999; Kim et al., 2004). These results are interpreted as a decrease in water masses delivered to the deep and bottom layer, as the East Sea continues to warm, combined with an increase in central water, resulting from the shallowing of the ventilation system (Kim et al., 2004). Kang et al. (2004) reported the possibility that the East Sea Bottom Water would disappear in 2050, when the volume of each water mass was linearly reduced using a simple box model. Alternatively, Yoon et al. (2018) suggested that the rates of decrease in DO concentration observed in the deep layers (below 1,500 m) slowed down. They also showed the rapid decrease in DO even in the central layer from 1996 to 2015. Because DO in the water mass reservoir is determined

by a time integration of influx by water mass formation and outflux mainly due to biodegradation, this result cannot be simply interpreted as reinforcing of deep-water or bottom-water formation, although occasional bottom-water formation was temporarily observed in the winter of 2000/2001 (Kim et al., 2002; Tsunogai et al., 2003). However, due to global warming, a continuous decrease in deep and bottom waters in the ES is expected in the long-term (Talley et al., 2006).

The long-term change in water mass in the East Sea includes interannual and decadal variability and trend-like changes related to global warming. Minami et al. (1999) and Watanabe et al. (2003) pointed out that oxygen, phosphate, and water properties fluctuate over a cycle of approximately 18 years under a water depth of 2,000 m in the eastern Japan Basin and Yamato Basin. Cui and Senjyu (2010) also showed that DO in the Japan Sea Proper Water varies over a cycle of approximately 20 years, showing a rough positive correlation with the Arctic Oscillation (AO). However, the positive AO phase is not a favorable condition for deep-water formation because the winter water temperature is relatively high, they suggested that atmospheric disturbances would occur more violently during the positive AO phase, resulting in more active occasional cold air outbreak and stronger deep-water formation (Isobe and Beardsley, 2007).

However, not many studies have been conducted on the long-term variability of the ESIW corresponding to thermocline water. Nam et al. (2016) utilized the coastal observation data from 1994 to 2011 to show a clear positive relationship between the ESIW and AO on the interannual timescale. However, the observation site, which was approximately 9 km away from the coast, might not sufficiently represent the interior ESIW variability, considering the first baroclinic Rossby deformation radius of approximately 11 km (Park, 2019). Yun et al. (2004) examined the fluctuations in the perspective of isopycnal fluctuations of the ESIW through careful data observation, but they only focused on the cold water of the Korean Strait. Yun et al. (2016) utilized observation data obtained during 1929–1941 and 1985–1996 to argue that the ESIW tends to be strongly formed during the strong *El Nino* period, which creates shoaling of the isopycnal surface of  $27.0 \sigma_\theta$  in the Ulleung Basin. However, any comprehensive understanding of long-term variability of the ESIW in the ES interior was not mainly viewed from the perspective of long-term continuous datasets.

Lastly, it should be noted that the previous studies on the ESIW variability were based on the unclear separation between the North Korean Cold Water (NKCW), mainly found near the eastern coast of Korean peninsula, and the ESIW in the ES. The NKCW has similar property ranges as the ESIW, yet their core properties at a shipboard measurement are often found to differ substantially (Kim et al., 1991; Min and Kim, 2006; Kim and Min, 2008). Such discrepancy of the NKCW and the ESIW properties was reported by Cho and Kim (1994), but it was well-known even in the early 1980s (Kim and Chung, 1984). Two hypotheses have been proposed to explain this discrepancy. While Cho and Kim (1994) proposed that the NKCW and the ESIW are different water masses formed in

different areas, other studies suggested that they are the same water masses but with different routes extending to the southern part of the ES (Kim et al., 2006; Kim et al., 2008). Because a study on the long-term variability of the ESIW should inevitably address the long overdue issue, spatial distributions of the ESIW variability in this study will demonstrate which hypothesis would be more reasonable to understand the discrepancy of the intermediate water property between the coastal and offshore areas.

Generally, when linking the property variability of water mass and climate variability, we assume that the properties of the corresponding water mass outcropped to the sea surface in winter during its formation should be mainly controlled by the atmospheric buoyancy forcing. Then, climatic conditions in winter can be imprinted onto the subducted water mass properties. However, because the salinity of the ESIW is significantly affected by the presence of low-salinity TWW, which are advected from the southern waters into the formation area (Park and Lim, 2018), the ESIW salinity variability does likely not show a simple correlation with the variability of winter atmospheric conditions. Therefore, in this study, the ESIW variability was analyzed in terms of its thickness, not salinity, using the regular shipboard measurement data obtained from the southwestern part of the ES over approximately 55 years, from 1965 to 2020. The data used in this study are described in the next section, the definition of the ESIW and its thickness are shown in the *Methods*, the analysis of its long-term variability is presented in the *Results*, and pertinent conclusions have been drawn in the *Conclusion*.

## 2 DATA AND METHODS

### 2.1 Data

#### 2.1.1 National Institute of Fisheries Science Hydrographic Data

The National Institute of Fisheries Science (NIFS) has conducted hydrographic measurements every year on a bimonthly basis at eight zonal lines covering the Ulleung Basin of the ES (**Figure 1A**). Most data are provided at 14 standard depths (0, 10, 20, 30, 50, 75, 100, 125, 150, 200, 250, 300, 400, and 500 m) and were collected over approximately 55 years, from February 1965 to December 2019. For all data, spike test was performed through Ocean Data View (<https://odv.awi.de>), and linear interpolation was performed at intervals of 1 m for thickness calculation. In general, water mass has a strong tendency to spread along isopycnal surfaces; therefore, usually, the vertical thickness of a water mass is determined based on potential density. However, as demonstrated quantitatively by Park (2021), the salinity values of the NIFS hydrographic data contain a serious time-dependent bias error. The one-standard errors were estimated to be 0.05–0.25 g kg<sup>-1</sup> in the 1960s and 1970s and about 0.05 g kg<sup>-1</sup> in the 1980s and early 1990s (**Supplementary Figure S1A**). With salinity bias errors of 0.1 and 0.15 g kg<sup>-1</sup>, the thickness errors can reach approximately 60 and 120 m, respectively, based on the mean temperature and salinity profile (**Supplementary Figure S1B**). Because of the uncertainty of

the salinity data, the ESIW thickness cannot be estimated with sufficient accuracy based on potential density ranges using NIFS data. Therefore, in this study, only temperature data were used in calculating the thickness of the ESIW, and the correlation between temperature-based thickness and density-based thickness must be evaluated first. Therefore, quality-controlled Argo float data were used as an evaluation standard. (**Supplementary Figure S1B**)

### 2.1.2 Argo Float Data

Temperature and salinity profile data obtained from the Argo floats between 1999 and 2015 were used to compare the temperature-based and density-based ESIW thickness. The hydrographic data obtained from Argo floats were neither uniform in space and time, nor was their observation period long enough to observe long-term variability; however, they can be a good countermeasure to support the analysis of shipboard data. The 36 profiling floats in the ES were deployed by the University of Washington, USA, in 1999 for the Office of Naval Research program. The remaining floats were deployed annually by the Korea Institute of Ocean Science and Technology and the Korea Meteorological Administration & Korean National Institute of Meteorological Sciences as part of the Korean Argo program. In total, about 22,000 temperature and salinity profile data were produced from January 1999 to December 2015 from more than 150 floats (**Figure 1B**). Basically, all the float data were processed by following the delayed mode quality control procedure from the Argo data management team (Wong et al., 2019), but because the natural property variability in the ES is 10 times smaller than that in the open ocean, the data quality was improved by the method optimized for the ES, and the estimated one-standard salinity error was reported to be  $0.004 \text{ g kg}^{-1}$  (Park and Kim, 2007).

### 2.1.3 Satellite Altimetry Data

The satellite-derived sea surface height (SSH) data were also utilized to analyze whether spatial distribution and temporal variability of the ESIW thickness depend on the upper ocean circulation patterns. The spatial structures of the upper ocean circulation in the southern part of the ES are clearly shown in the SSH maps (Choi et al., 2004; Park and Nam, 2018). The SSH data are a merged product of multiple altimeter missions, daily gridded onto  $0.25^\circ \times 0.25^\circ$  over the time period January 1993 to December 2020 (<https://resources.marine.copernicus.eu/>). After removing the seasonal variability using the 1-year box-car filter method, the monthly mean SSH was obtained to compare SSH with the ESIW thickness and isotherm depths.

### 2.1.4 Arctic Oscillation Index

The daily AO Index was provided by the Climate Prediction Center, National Oceanic and Atmospheric Administration (NOAA), USA (<https://www.cpc.ncep.noaa.gov/>), which is constructed by projecting the daily 1,000 mb height anomalies poleward of  $20^\circ\text{N}$  onto the leading EOF mode. The time series are normalized by the standard deviation of the base period, 1979–2000. The leading Empirical Orthogonal Function (EOF)

pattern of AO is obtained using the monthly mean height anomaly dataset.

The AO is a representative phenomenon that greatly affects the atmospheric environment, especially during winter in the ES. There have been several studies to show the correlation between the AO and the water mass properties of the ES and the great influence on the surface water temperature and wind patterns of the ES (Isobe and Beardsley, 2007; Cui and Senjyu, 2010; Nam et al., 2016). In addition, a positive winter AO strongly correlates with warmer winters over East Asia by enhancing the Polar westerly jet (c.f. Park et al., 2011; Wu et al., 2015). The AO Index has been filtered with box-car windows of 3 years, whose raw data are shown in **Supplementary Figure S2**.

## 2.2 Methods

### 2.2.1 Density-Based East Sea Intermediate Water Thickness

When a large amount of water mass volume is formed, the vertical layer of the corresponding water mass defined by the range of isopycnal surfaces must be thicker while looking at the area that is not far from the formation site, and the volume change of the water below and above it can be ignored. Even though the thickness of the water mass can be changed under the influence of mixing after being subducted, it is assumed that mixing-induced thickness change will not produce interannual-decadal variability. However, the ESIW thickness can change by not only the amount of formation but also the expansion and contraction of water volume above and below it; therefore, the analysis must be cautiously performed.

Usually, since water masses easily expand along isopycnal surfaces, vertical range occupied by the water masses is often defined by density ranges. Kim et al. (1999) exhibit that the ESIW has a density range between  $26.9$  and  $27.3 \sigma_\theta$ . In this study, the density-based ESIW thickness is defined as the depth difference of those two isopycnal surfaces suggested by Kim et al. (1999). However, as described above, the thickness of the ESIW based on density could not be accurately calculated because of the low quality of NIFS salinity data. Thus, the density-based ESIW thickness is computed only using Argo float data to compare with the temperature-based thickness obtained from the NIFS data.

### 2.2.2 Evaluation of the Temperature-Based East Sea Intermediate Water Thickness

Before the ESIW thickness is calculated based on temperature only, the existence of a potential correlation between thickness and density must be examined. The red dot in **Figure 2A** is a comparison of potential density-based ( $26.9$ – $27.3 \sigma_\theta$ ) and potential temperature-based ( $1^\circ\text{C}$ – $5^\circ\text{C}$ ) thickness using Argo float data within the NIFS observation area shown in **Figure 1B**. There is a clear linear relationship with each other ( $R^2 \sim 0.78$ ), but the temperature-based thickness is statistically underestimated.

This is because the temperatures and densities at the ESIW top and bottom suggested by the previous studies do not match. **Figure 2B** shows the histograms of the temperatures on the isopycnals of  $26.9$  and  $27.3 \sigma_\theta$ . The temperature-based range of

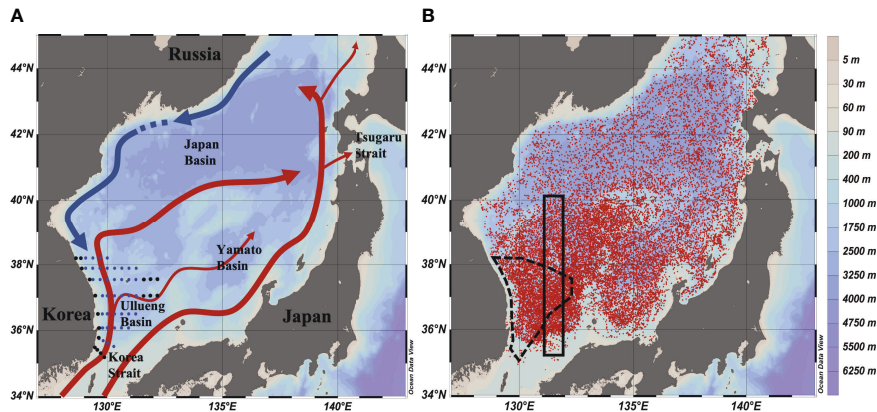


**FIGURE 1 |** Map of the East Sea and stations for **(A)** National Institute of Fisheries Science (NIFS) hydrographic data and **(B)** Argo float (1999–2015). Red and blue arrows in panel **(A)** denote warm and cold surface currents. All NIFS station data are for thickness comparison with Argo data and the only blue stations are for studying long-term variability of the East Sea Intermediate Water (ESIW). The black solid-line rectangular box shows the area for which Argo data were taken for **Figure 2**. The area with dashed lines is for **Figure 3**.

the ESIW ( $1^{\circ}\text{C}$ – $5^{\circ}\text{C}$ ) is found to be quite conservative compared to the density-based one. The temperature range corresponding to the density range may be  $0.8^{\circ}\text{C}$ – $5.6^{\circ}\text{C}$  in terms of median values. The width of the temperature histogram for  $26.9 \sigma_{\theta}$  is wider than  $27.3 \sigma_{\theta}$ . However, it is simply because of the difference in vertical gradient of temperature. In fact, the mismatch of the ESIW bottom boundary based on temperature and density is mainly responsible for the underestimation of the temperature-based thickness. Unfortunately, the temperature at the ESIW bottom cannot be set to  $0.8^{\circ}\text{C}$  instead of  $1.0^{\circ}\text{C}$  because the ESIW bottom is often deeper than 500 m, which is the maximum NIFS observation depth.

**Figure 3** shows the density- and temperature-based ESIW thicknesses calculated from Argo float data within the NIFS

observation area in time series. The 5-month moving averaged lines demonstrate that the temperature-based thickness (green) is underestimated by about 30% compared to the density-based thickness (black). However, in terms of variabilities, they fluctuate almost identically with the high correlation of 0.97. The green dotted line, which represents 1.3 times the temperature-based thickness, is comparable to the density-based one, confirming that the temperature-based thickness can be used as a substitute variable indicative of the thickness variability of the ESIW.

The ESIW thickness was first calculated from the NIFS profile data, and stations that were not in the temperature range of  $1^{\circ}\text{C}$ – $5^{\circ}\text{C}$  were excluded from the calculation. From 1978 to 1981, the northernmost Line 107 ( $38.21^{\circ}\text{N}$ ) observation was not made at a depth of 500 m, so it was not counted. The NIFS

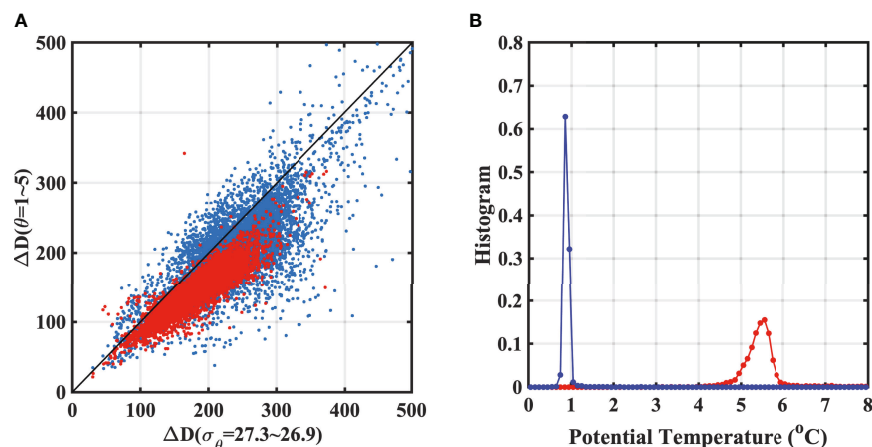


**FIGURE 2 | (A)** Scatter plot between the density-based ( $26.9$ – $27.3 \sigma_{\theta}$ ) and temperature-based ( $1^{\circ}\text{C}$ – $5^{\circ}\text{C}$ ) thickness obtained from Argo data. Red dots represent the data within the area denoted using dashed line in **Figure 1B**, and blue dots represent data from the whole East Sea. **(B)** Histograms of temperatures on the isopycnal surfaces of  $26.9$  and  $27.3 \sigma_{\theta}$  shown in red and blue lines, respectively, which are computed from the Argo data obtained from the area of dashed line in **Figure 1B**.



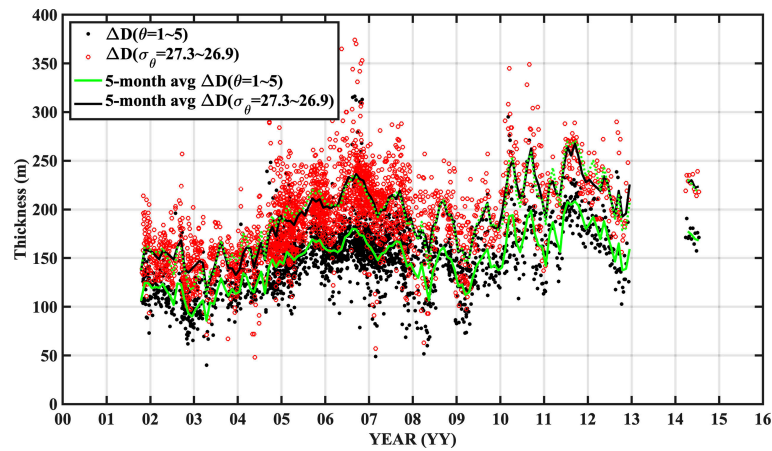


**FIGURE 3** | Time series of temperature-based thickness and density-based thickness in the area denoted by the dashed line (**Figure 1B**). Black and open red dots denote temperature- and density-based thickness, respectively. Green and black lines show the 5-month moving averages of the temperature-based and density-based thickness, respectively. The green dotted line represents 1.3 times the temperature-based thickness.

shipboard measurements are usually scheduled to be carried out in February, April, June, August, October, and December every year, but the observations were not conducted on the same day every year due to weather conditions. Therefore, due to missing data or temporal irregularities, a linear interpolation was performed at intervals of 2 months and  $0.1^\circ$  for spatial analysis, and seasonal variations were eliminated by applying a 14-month box-car filter.

### 2.2.3 Mean Temperature Reconstruction by Basin-Wide Average of Isothermal Layer Depth

To analyze and understand temporal variability of the ESIW thickness and to examine how the vertical structure of basin-wide averaged temperature changes with time, a basin-wide average of temperature profiles was performed in terms of isothermal layer depth rather than a simple depth coordinate. The horizontal circulation structure of the observation area and the presence of mesoscale eddies play an important role in determining the thermocline depth. In such an environment, when basin-wide averaged temperature was calculated on pressure or depth coordinates, fictitious vertical diffusion occurred, creating a vertically smoothed temperature structure (Lozier et al., 1994; Nurser and Lee, 2004) and affecting the thickness in the thermocline water. Therefore, to prevent such an error, thicknesses of the isotherm layers by  $0.5^\circ\text{C}$  bins were spatially averaged and then vertically integrated to calculate the depth value of each temperature as follows.

$$Z_g(T) = \int_{T_{\text{bottom}}}^{T_{\text{top}}} \frac{1}{A} \int_A \frac{dD}{dT} dA dT$$

where  $T$  denotes potential temperature;  $D$ , the isotherm depths; and  $A$ , the domain area.  $T_{\text{top}}$  and  $T_{\text{bottom}}$  are  $15^\circ\text{C}$  and  $1^\circ\text{C}$ , respectively.

However, the basin-wide averaged temperature estimated in this manner has a limitation, especially near the surface and the bottom in that predetermined isotherm layers were not found. Therefore, it is suitable only for the middle or deep layers where the isotherm layers are mostly found. In this study, the problem is minimized because the observation area is far enough away from the formation area and mostly below the thermocline. In this calculation,  $T_{\text{top}}$  was set to  $15^\circ\text{C}$  and the temperature of  $9^\circ\text{C}$ – $15^\circ\text{C}$  can outcrop in the limited area of the observation domain only in winter. In this case, the depth of the corresponding isotherm surface was taken as 0.

To estimate the basin-wide averaged temperature, the isotherm layers were obtained at  $0.5^\circ\text{C}$  intervals from all the NIFS temperature profile data, and seasonal variations were removed using 14-month moving averages. The filtered data were reconstructed in the form of an equal grid using three-dimensional (3D) linear interpolation to obtain a spatial grid of  $0.1^\circ \times 0.1^\circ$  and a time grid of 2 months. By averaging the gridded isothermal layer data over the observation area, the depth of each isothermal layer was calculated temporally and converted into temperature profiles.

## 3 RESULTS

### 3.1 Variability of the East Sea Intermediate Water Thickness and Property Based on Argo Float Data

Considering the Argo float data obtained between  $131^\circ\text{E}$  and  $132^\circ\text{E}$  as cross-sectional data in a meridional direction ( $35.5^\circ\text{N}$ – $40.0^\circ\text{N}$ ), **Figure 4A** shows the variation in the layer thickness of isopycnal surfaces between  $26.9$  and  $27.3 \sigma_\theta$  where the ESIW resides, and **Figure 4B** presents the salinity variation on the  $3^\circ\text{C}$  isotherm surface. Because the Argo data have a spatiotemporal irregular distribution, it is interpolated by the

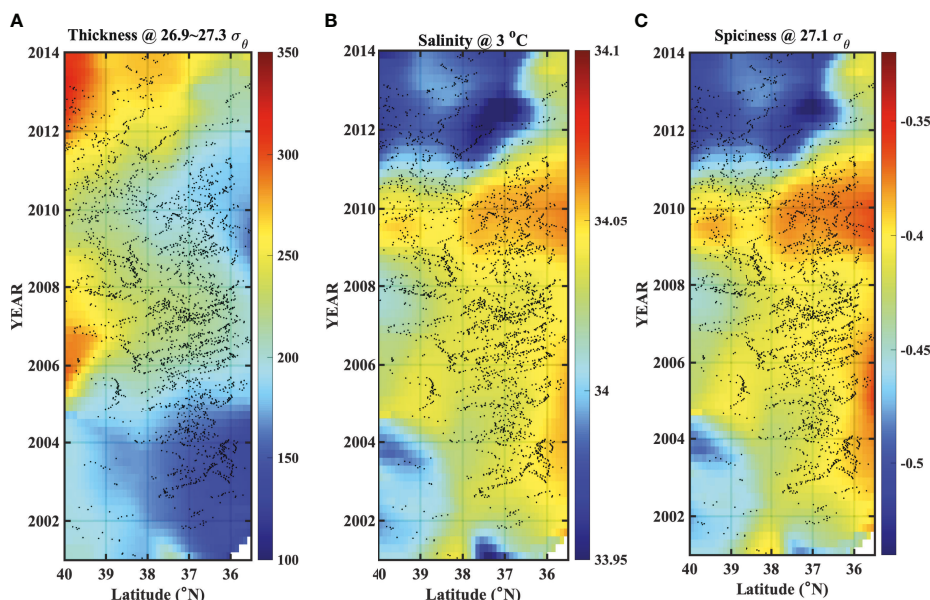


**FIGURE 4 | (A)** Hovmöller diagram for the ESIW thickness (meter) from Argo float data within the solid-line rectangular box ( $35^{\circ}\text{N}$ – $40^{\circ}\text{N}$ ,  $131^{\circ}\text{E}$ – $132^{\circ}\text{E}$ ) in **Figure 1B**. **(B)** The same as panel **(A)** but for salinity (g/kg) at  $3^{\circ}\text{C}$  and **(C)** for spiciness at  $27.1 \sigma_{\theta}$ . Black dots denote where the Argo data are.

Gaussian weighted average method with a temporal (1.5-year) and spatial ( $0.25^{\circ}$ ) decorrelation scale.

The thickness is higher in the north close to the formation site and becomes thinner further south (the potential vorticity is not conserved). In terms of temporal variability, the layer is thick in 2005–2008 and in 2011–2014, and it expands to the south over time. The rate of expansion could not be accurately determined because of the greatly smoothed sparse data, but it appears to take about 0.5 to 1.5 years at latitudes  $40^{\circ}\text{N}$  to  $38^{\circ}\text{N}$ . Importantly, the spatiotemporal variation of thickness is quite similar to the pattern of the salinity on the  $3^{\circ}\text{C}$  isotherm surface that corresponds to the central part of the ESIW. Relatively low-salinity properties appear in the years of large thickness, and high-salinity properties appear when the thickness is thin. However, the temporal variability of salinity does not have a linear relationship with the thickness (not sensitive on isotherm surfaces). For example, at latitude  $39^{\circ}\text{N}$ , even though there is no significant difference in thickness between 2007 and 2013, there is a noticeable difference in salinity.

A similar trend was observed for spiciness on the isopycnal surface of  $27.1 \sigma_{\theta}$ . Spiciness shows whether a water mass is spicy (warmer and saltier) or minty (colder and fresher) in a specific density aspect, which is the orthogonal quantity to isopycnals on the  $\theta$ - $S$  diagram (McDougall and Krzysik, 2015). Because the ESIW density is predominantly controlled by water temperature, there is little difference in the spatiotemporal structure of spiciness on the isopycnal surface or salinity on the corresponding isothermal surface (refer to **Supplementary Figure S3** for thickness of  $1^{\circ}\text{C}$ – $5^{\circ}\text{C}$  and salinity at  $27.1 \sigma_{\theta}$ ). Although the salinity in 2011–2014 was  $0.05$ – $0.06 \text{ g kg}^{-1}$  lower than that in 2005–2008, the effect of this salinity change on

density is approximately  $0.04 \text{ kg m}^{-3}$ , which is one-tenth smaller than the total density range of the ESIW ( $0.4 \text{ kg m}^{-3}$ ).

Therefore, the thickness variability close to the formation site is strongly linked with that in the southern area. As Park and Lim (2018) pointed out, the ESIW salinity is influenced by the characteristics of the fresher surface water advected into the formation site. However, the amount of fresher surface water entering the formation site does alter the ESIW salinity yet does not significantly affect the amount of formation because its effect on density is small.

### 3.2 Long-Term Variability of the East Sea Intermediate Water Thickness

**Figure 5** presents the temperature-based ESIW thickness variability (hereafter referred to as the ESIW thickness) for which the seasonal variability is removed at each station (Raw data can be found in **Supplementary Figure S4**). The color indicates the latitude of each NIFS measurement station, as shown in **Figure 1**. Interannual-interdecadal variability clearly exists, and the variabilities tend to appear similarly over entire stations. Compared with the ESIW thickness fluctuations obtained from the Argo float data in 2002–2013 (**Figures 2, 4**), the patterns of thickness variability are comparable between Argo and NIFS data; for example, the larger thickness observed in the years 2005–2008 and 2010–2013.

**Figure 6** shows the spatial distribution and principal component (PC) time series of the first and second EOF modes of the ESIW thickness, respectively. The first mode accounts for 75.7% of the total variance, and the second mode accounts for only 6.4%. Most of the ESIW thickness variations can be explained in the first mode. The spatial distribution

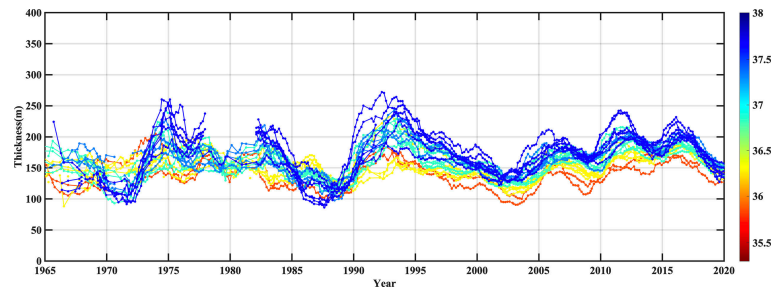


**FIGURE 5** | Fourteen-month moving averaged time series of the ESIW temperature-based thickness obtained from the NIFS data (1965–2020). Each color denotes latitudes of the corresponding NIFS stations. Raw data are shown in **Supplementary Figure S4**.

of the EOF first mode has positive values over the observation area, so it fluctuates stronger in the north and weaker in the south according to the pattern shown in the PC first spatial mode. The first mode PC time series sufficiently captures the temporal fluctuations shown in **Figure 5**. The periodic fluctuations of 3–6 years and long-term fluctuations of 15–18 years were predominant, rather than the year-to-year variations suggested by Kim et al. (1999). It is noted that the fluctuation pattern before the 2000s tended to increase rapidly and then decrease slowly in interdecadal timescales, while the fluctuation pattern seems to have changed in the 2000s and 2010s, although there is the limitation of observation period.

From the spatial distribution of the ESIW thickness when the negative and positive peaks appear in the PC time series, it can be confirmed that the thickness varies over the entire domain (**Figure 7**). The northwestern part of the domain is thicker and the southeastern part is relatively thin in the years with

positive peaks (1974, 1993, and 2011). The spatial structure of the EOF first mode sufficiently captures the characteristics of the observation data.

The temporal change of spatial pattern of the thickness is not likely affected by the upper ocean circulation patterns (**Figures 8A**). The East Korea Warm Current and the Ulleung Warm Eddy are dominant features that control the surface circulation in the southwestern part of the ES, manifested in the spatial map of SSH that mostly represents the first baroclinic structure (Choi et al., 2004; Park and Nam, 2018). The SSH map shows that the East Korea Warm Current moves northward along the east coast, and then separates from the coast at a latitude of 37°N–38°N and flows southward at around 131°E. These features vary over the years. Additionally, the warm eddy structures with locations and strengths differently over the years. However, those upper circulation structures do not appear in the ESIW thickness shown in **Figures 7D–F**.

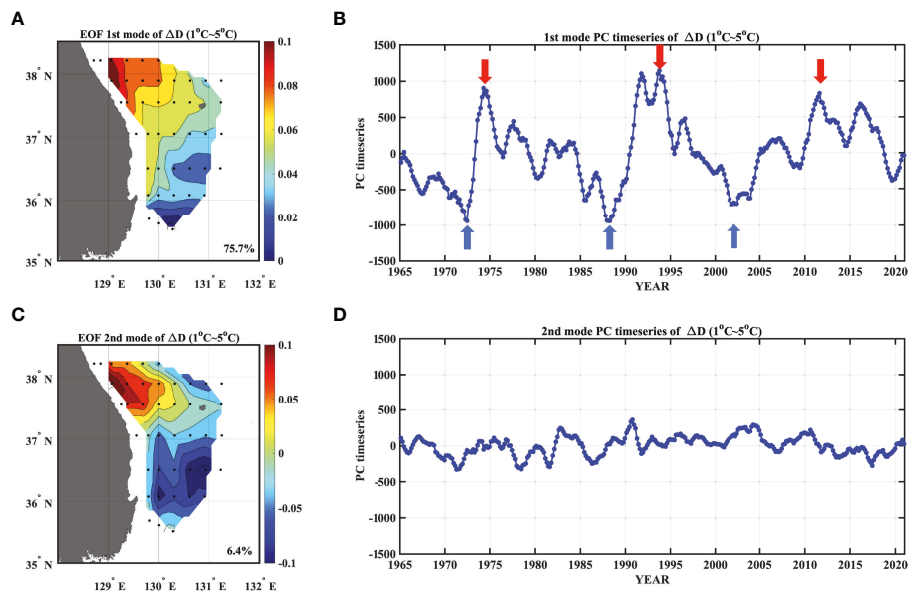


**FIGURE 6** | **(A)** EOF first mode loading vector for the ESIW thickness, **(B)** EOF first mode PC time series for the ESIW thickness, **(C)** EOF second mode loading vector, and **(D)** EOF second mode PC time series.

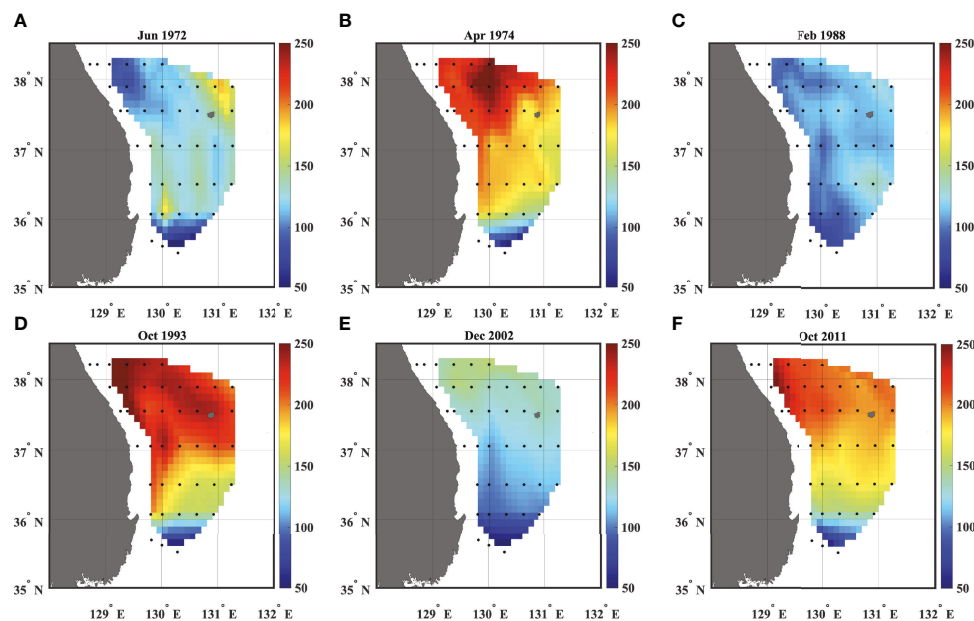


**FIGURE 7** | Spatial distribution of the ESIW thickness at the peak years of the EOF first mode PC time series shown in **Figure 6B** such as **(A)** June 1972, **(B)** April 1974, **(C)** February 1988, **(D)** October 1993, **(E)** December 2002, and **(F)** October 2011.

Alternatively, the isotherm depth spatial structures of 1°C and 5°C are clearly influenced by the upper circulation structure. We interpret that the upper ocean circulation pattern produces shoaling and deepening of the isotherm surface but does not significantly affect the isothermal layer thickness corresponding to the ESIW. It can be also confirmed with Argo data that the spatiotemporal distribution of the ESIW thickness is not directly related to the local upper circulation pattern (**Supplementary Figure S5**).

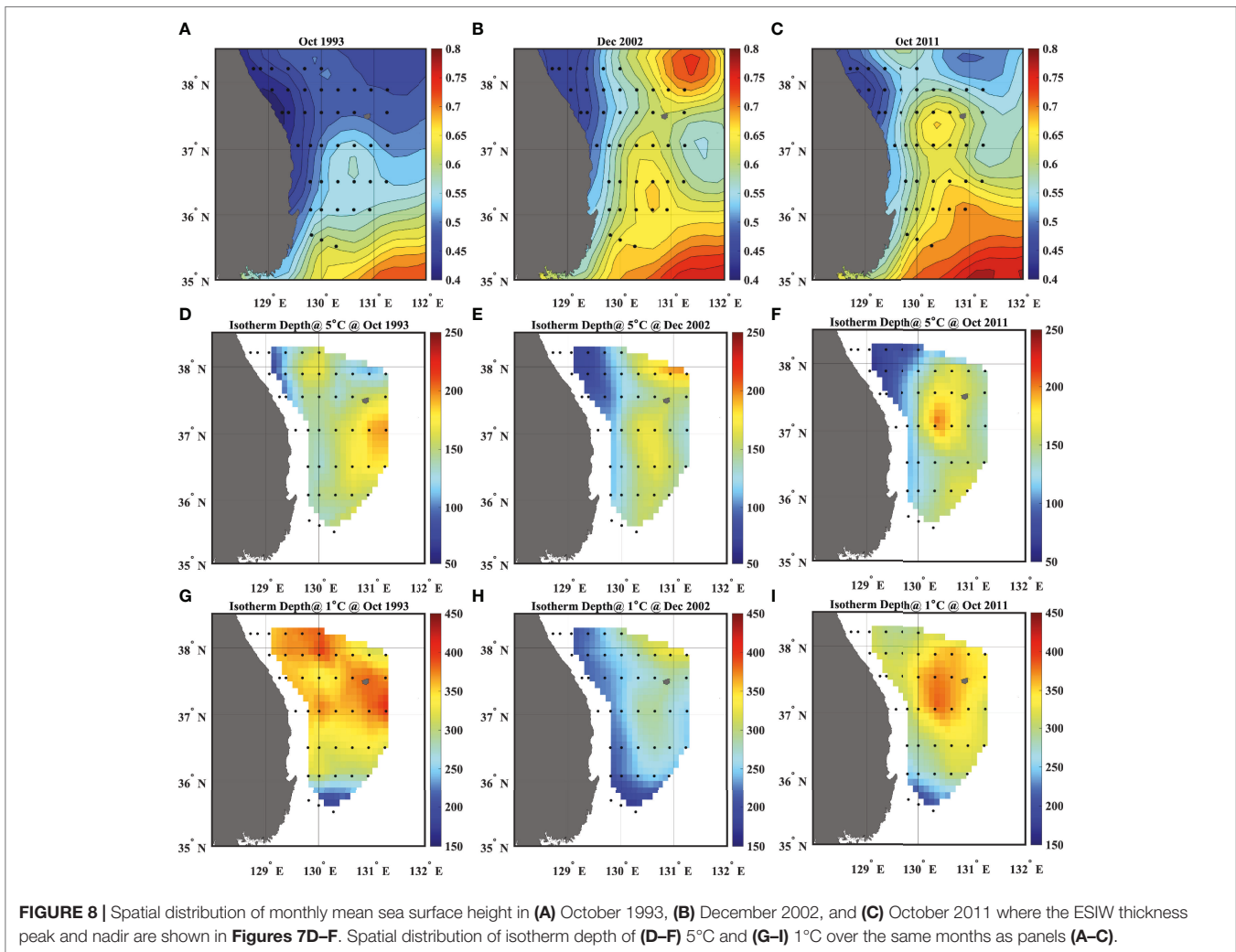
We demonstrated that the first mode temporal variability of the ESIW thickness mostly has basin-wide fluctuations rather than mesoscale structures. Therefore, to investigate the variability of the vertical structure of temperature associated with the ESIW thickness variability, the basin-averaged temperature will be examined in the next section.

### 3.3 Basin-Wide Averaged Temperature

**Figures 9A, B** show the basin-averaged temperature on z-coordinate and isotherm layer averaged temperature, respectively. Due to the fictitious diffusion, the thicknesses of the isotherm layers in the thermocline are thicker overall in **Figure 9A** than those in **Figure 9B**. In particular, the structure of the thermocline is greatly smoothed out, for example, resulting in the thickness of 1°C–5°C in **Figure 9A** being thicker by 25% or more. Also, the interannual variabilities of the isotherms of 1°C and 2°C have unrealistically large amplitudes in the z-coordinate averages. This is more likely a result of contamination by spatial variability of isotherms rather than the actual basin-wide temporal variability. Thus, in this study, **Figure 9B** was used to see the basin-averaged temperature structure to understand the ESIW thickness fluctuations.

The ESIW corresponds to the area between the red line and the black dotted line in **Figure 9B**. The decadal variability of the 1°C isotherm appears to correlate with isotherms of higher temperatures in the upper layer, especially before the mid-1990s. Furthermore, the dominant decadal-scale variabilities with relatively large amplitudes below 5°C decreased after the mid-1990s and the interannual scale variabilities are more pronounced. However, because isotherms with temperatures higher than 10°C show no predominance on decadal-scale variability before or after the mid-1990s, the decadal scale variability possibly originates from the deeper ocean.

One striking feature is that the thickness between 5°C and 10°C isotherms has remarkably decreased since the mid-1990s. **Figure 9C** is the vertical temperature gradient estimated from **Figure 9B** and demonstrates that the temperature gradient in the thermocline layer has significantly increased since 1995. This increase occurs because the isotherm depth at 10°C does not change significantly around 100 m, yet the isotherm depth at 5°C becomes shallow. As shown in **Figure 10A**, the linear trends of the 2°C and 5°C isotherm depths are  $-5.9 \pm 1.7$  m/10 years and  $-2.3 \pm 1.4$  m/10 years, showing a strong shallowing trend within 95% confidence level. Alternatively, the 1°C isotherm depth did not show a significant trend at  $+1.0 \pm 2.0$  m/10 years, while the 15°C isotherm depth showed a clear deepening trend at  $+2.4 \pm 0.5$  m/10 years, implying the warming trend. The deepening trend of the upper isotherms weakens as it goes deeper, and the trend sign changes around the 8°C isotherm. The clear shallowing trends below 10°C are responsible for the decrease of the thickness between 5°C and 10°C isotherms. It is noted that, in the z-coordinate averages, the trends of the isotherm depths are difficult to be identified



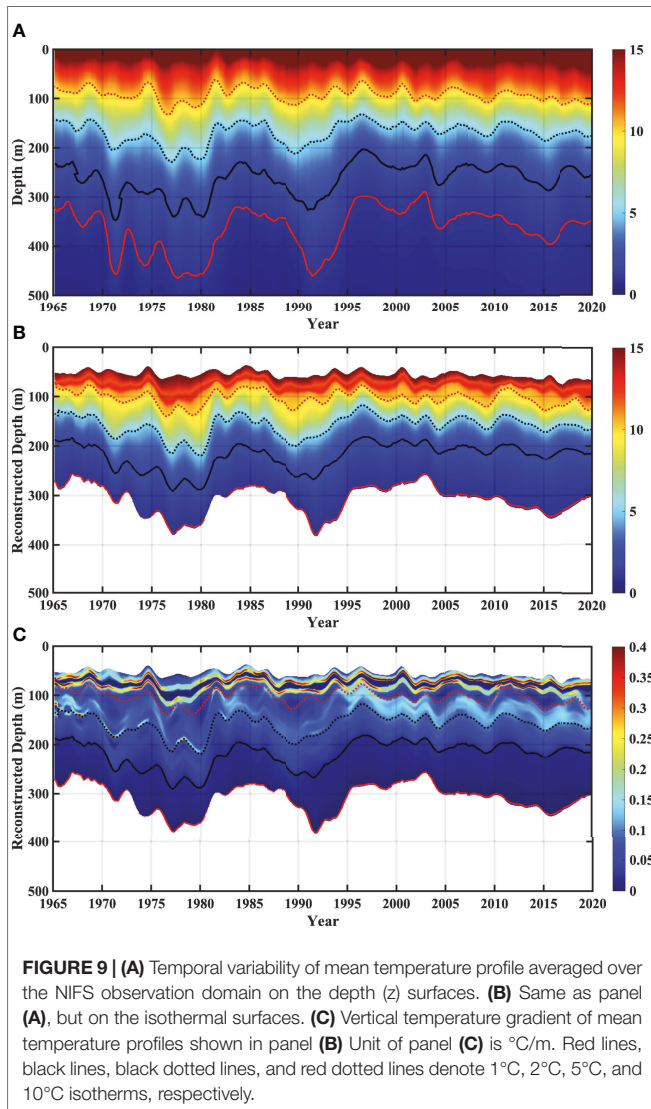
and also the increase of vertical temperature gradient in the upper thermocline is not clearly seen (not shown).

To analyze the relationship between the ESIW thickness and isotherm depths, the thickness of the isotherms between 1°C and 5°C in **Figure 9B** is shown as a red dotted line in **Figure 10A**. The variability of the thickness computed from the basin-averaged temperature (**Figure 10A**) is comparable to the first mode PC time series in **Figure 6B**. The correlations between the variation of the ESIW thickness and the corresponding isotherm are presented in **Figure 10B**. With the data before the year 1995, the ESIW thickness has a significant positive correlation only with the 1°C isotherm, but after 1995, it has negative correlations with the isotherms between 4°C and 11°C, implying that when the ESIW thickness is thick, those isotherms appear shoaling.

The correlations between the 1°C isotherm and other isotherms have significant positive correlations before 1995, but after 1995, the correlation almost disappears, as shown in **Figure 10C**. It should be noted that any linear trend was removed for estimating each correlation. Before 1995, the 1°C isotherm variability dominates that of the other upper isotherms in the

thermocline layer. However, after 1995, the 1°C isotherm does not vary with the upper isotherms anymore.

Based on the above results, one scenario can be considered within the framework of the 1D advection–diffusion model of Munk (1966) in terms of the thermocline formation and maintenance. If the thickness variation of the ESIW before the mid-1990s is predominantly determined by the change in upwelling of the deep water below the intermediate water in the ES, it should be primarily expressed as a variability at the 1°C isotherm depth, and this effect would also be projected onto the upper isotherms. Because there is vertical diffusion that is stronger in the upper thermocline layer with a higher vertical temperature gradient, and the upper ocean temperature is constrained by the atmospheric condition and oceanic inflow, the effect of deep-water upwelling should be weakened while going up. In that case, the correlation between the ESIW thickness of 1°C–5°C and the isotherm depth of 1°C can be positive. Conversely, if the upwelling effect of the deep layer was significantly decreased since the mid-1990s, the ESIW variability itself must primarily control the upper isotherm variabilities, producing shoaling of 5°C isotherm as



the ESIW layer thickens. Therefore, this process could explain the results showing a positive correlation between the ESIW thickness and  $1^{\circ}\text{C}$  isotherm and a negative correlation with  $5^{\circ}\text{C}$  isotherm.

### 3.4 Spatial Basin-Wide Averaged Temperature

If the temporal variabilities of isotherms in the thermocline were mainly due to upwelling of the deep layer before the mid-1990s and the volume change of the ESIW itself after the mid-1990s, there should be some difference manifested in the spatial distribution of the ESIW thickness for the two periods. Firstly, the spatial correlation maps of the ESIW thickness with time lags are presented in **Figure 11**. **Figures 11A, B** show the maximum correlations of the ESIW thickness at  $37.5^{\circ}\text{N}$  and  $130.5^{\circ}\text{E}$  (shown in blue diamonds) as a reference point and in the rest of the observation area. **Figures 11C, D** show the time lags where the

maximum correlation coefficients appear. Except for south of  $36^{\circ}\text{N}$ , the results are not sensitive to the point of reference.

The maximum correlation has a high positive correlation of 0.6 or more in most regions, except for the southern edge before and after 1995. This is consistent with the basin-wide feature of the interannual-interdecadal variability of the ESIW thickness in **Figure 6**. Interestingly, most regions, except for the southern waters, have time lags of less than 3 months before 1995 (**Figure 11C**), but a spatially distinct lag difference appears after 1995 (**Figure 11D**), although the ESIW thickness appears to be basin wide. From **Figure 11D**, these lags appear more clearly in the zonal direction than in the meridional direction, and the zonal difference of the lags is approximately 12–14 months. A positive lag implies that the thickness variability in the corresponding area leads that at the reference location. The results indicate that the ESIW thickness change emerges quicker along the continental shelf slope, followed by the change in the offshore area or the Ullueng Basin approximately a year later.

**Figure 12** presents the meridional and zonal sections of the ESIW thickness based on  $37.5^{\circ}\text{N}$  and  $130.5^{\circ}\text{E}$ . As for the temporal variability of the meridional distribution, the thickness tends to be higher in the north and lower toward the south. However, as shown in **Figure 11**, the time lag of the variability between  $38^{\circ}\text{N}$  and  $36^{\circ}\text{N}$  is indistinguishably small in the bimonthly dataset. These characteristics, at least for the south of  $38^{\circ}\text{N}$ , are not significantly different from the Argo float data in **Figure 2** (direct comparisons in **Supplementary Figure S6A** and **S6C**). Notably, the thickness is larger in the north than the south where it is thinner, but the tendency is not always applicable when it is thinner. After 1995, such a meridional tendency still holds even with the thinner ESIW, but it was not clear before 1995.

The temporal change of the zonal section (**Figure 12B**) remarkably demonstrates the phase difference of the thickness fluctuations in the western and eastern areas, especially after the mid-1990s, while hardly any zonal phase change appears before the mid-1990s. Such leading appearance of the thickness in the coastal area is also evident in the Argo float data (**Supplementary Figure S6F**, also see the comparable figure from the NIFS data shown in **Supplementary Figure S6F**). The solid line and dotted line in **Figure 12B** are the lines connecting crests and troughs in the ESIW thickness variability at  $129.4^{\circ}\text{E}$  and  $131.2^{\circ}\text{E}$ , respectively. The phase difference ranges from 10 to 14 months, which is comparable to the lag correlation, converting into the slopes of 14–20 km/month ( $0.4\text{--}0.6\text{ cm s}^{-1}$ ). In spite of the zonal lags, the thickness variabilities in the western and eastern sides are clearly correlated, at least after the mid-1990s. One might think that the ESIW signal in the offshore could be the one expanded from the coast (c.f. Shin et al., 1998). However, the amplitude of the thickness variability increased in both the western and eastern edges of the observation domain, as was clearly observed in **Figure 12B** from 2005 to 2015. If the ESIW thickness signal solely comes from the coast, its variability would simply become smaller as it goes to the offshore along the solid and broken lines in **Figure 12B**. Yet, as it goes from  $130.5^{\circ}\text{E}$  to  $131.2^{\circ}\text{E}$ , the peak thicknesses increase (decrease) along the solid lines (the broken lines). This behavior implies that the ESIW

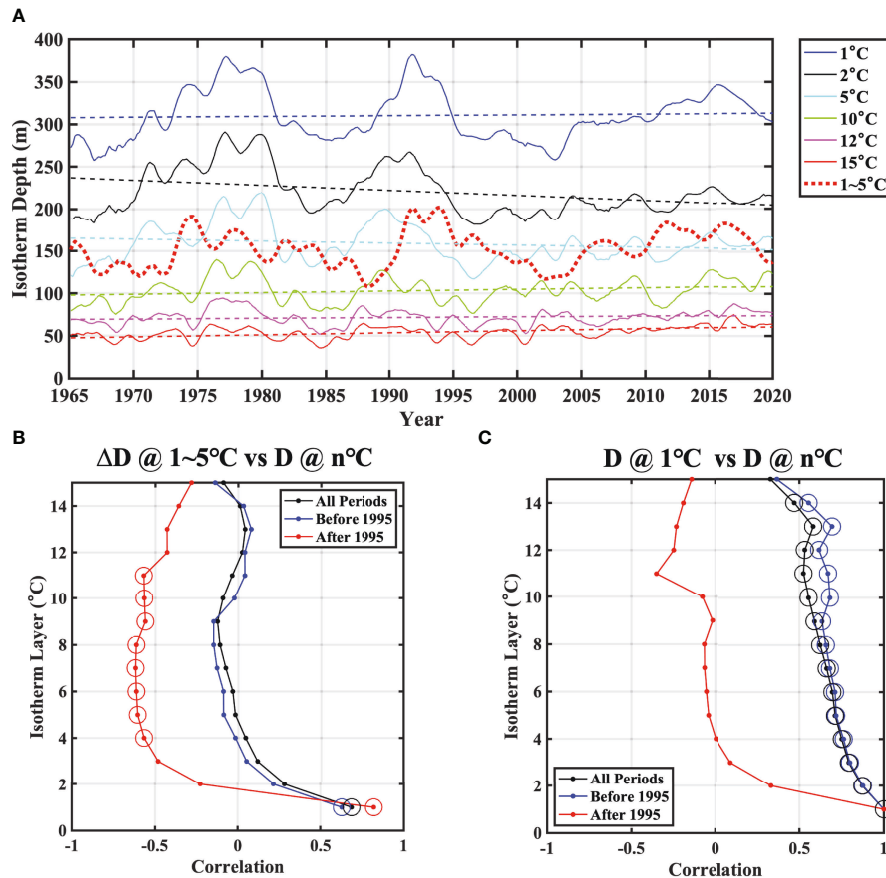


**FIGURE 10 | (A)** Temporal variability of isotherm depths of 1°C, 2°C, 5°C, 10°C, 12°C, and 15°C and the ESIW thickness computed from the mean temperature profile data shown in **Figure 8B**. Dotted lines are linear fits of each isotherm depth. **(B)** Correlation between the isotherm thickness shown in panel **(A)** and other isotherms (in °C). **(C)** Correlation between the isotherm depth of 1°C and other isotherms. In panels **(B, C)**, black line is by using the data for the whole time period. Blue line is from 1965 to 1994 (30 years), and red line is from 1995 to 2020 (25 years). Open circles denote where the significances are above 95%.

thickness in the eastern area does not depend solely on the thickness of the coastal area, despite the offshore signal being followed by the coastal one. Note that the thickness trough in the coastal region becomes thicker as it goes offshore and then becomes thinner as it reaches 131°E.

The physical reason of the two-mode structure of the ESIW often found in the zonal hydrographic section (Cho and Kim, 1994) can be explained by the temporal variability of zonal structure of the ESIW thickness. If the NKCW and the ESIW were completely different water masses and were formed under different conditions or processes, their thicknesses should have no or low correlation between the coastal and offshore areas. However, according to the results of this study, the ESIW thickness variabilities near the coast and offshore are linked to each other with a year lag, implying that they are the same water mass but have different arrival times. Only with a snapshot observation data obtained at a specific time would it appear to be different water masses due to this time lag. Furthermore, as shown in **Figure 4**, the spatiotemporal variability of the ESIW thickness is closely related to that of its salinity property (also see **Supplementary**

**Figure S6**). Therefore, the results shown in this study indicate that the two-mode structure of the ESIW shown in zonal hydrographic sections should result from the difference of the ESIW propagation path between near the coast and offshore, as previous researchers have suggested (Cho and Kim, 1994; Kim et al., 2006; Shin et al., 2007). It is important to note that even though the two-mode feature in the ESIW property was observed in the early 1980s, the zonal phase difference in the ESIW thickness was clearly visible only after the mid-1990s.

### 3.5 Correlation With the Arctic Oscillation Index

The AO Index and the ESIW thickness time series (**Figure 13A**) were observed to fluctuate together with a phase shift of a few years, especially before the 1990s. Therefore, the AO Index delayed by 2 years is redrawn in **Figure 13B**. Before the mid-1990s, the 2-year shifted AO Index and the ESIW thickness time series appear almost in phase; interestingly, they appear out of phase thereafter. The lag correlations between the AO Index and the ESIW thickness demonstrate a clear positive

correlation of 0.8, with a lag of about 2.5 years before 1995 and a statistically significant negative correlation of 0.6 with a lag of about 1.5 years after 1995 (Figure 13C). This result shows that there has been a major change in the relationship with the AO Index since the mid-1990s.

The spatial correlation between the AO and the ESIW thickness also exhibits consistent features from the above results. Figure 14 shows the maximum absolute correlation and lag between the AO and the ESIW thickness before and after 1995 (Figures 14A, B) and the corresponding time lag (Figures 14C, D). Positive correlations with AO are dominant over the domain before 1995, while negative correlations prevail in a basin-wide manner after 1995.

The lag time where the maximum absolute correlation appears is important. The overall lags before 1995 are larger than those after 1995 in the corresponding area. Before 1995, the AO fluctuations lead the ESIW thickness with a lag of larger than 20 months near the coastal region and a lag of about 28 months in the offshore area, the Ulleung Basin. However, after 1995, the ESIW thickness responded noticeably quicker to the AO in the vicinity of the ES coast with a lag of about 12 months and slowly in the Ulleung Basin with a lag of about

26 months. The zonal lag difference for the post-1995 period is much more pronounced than the pre-1995 period, reaching 14 months. In addition, these results are also consistent with the spatial correlation map of the ESIW thickness shown in Figure 11.

## 4 DISCUSSION

To analyze the 55-year-long hydrographic data, the correlation was assumed to hold in the past as well. The main reason that the isotherm-based thickness has a strong correlation in time with the isopycnal-based one is that the effect of salinity on the ESIW density range in the southwestern ES is significantly smaller than that of temperature. In the hydrographic observation in 1969 (Senjyu, 1999), the salinity range of the ESIW salinity minimum layer in the southwestern ES was 34.00–34.02 g kg<sup>-1</sup>. Additionally, Kim and Chung (1984) showed a range of 34.00–34.05 g kg<sup>-1</sup> from the observations in 1981, and Cho and Kim (1994) showed a range of 33.95–34.05 g kg<sup>-1</sup> in the 1991 observations. All the salinity ranges of the ESIW in the past years are commonly found in the ESIWs

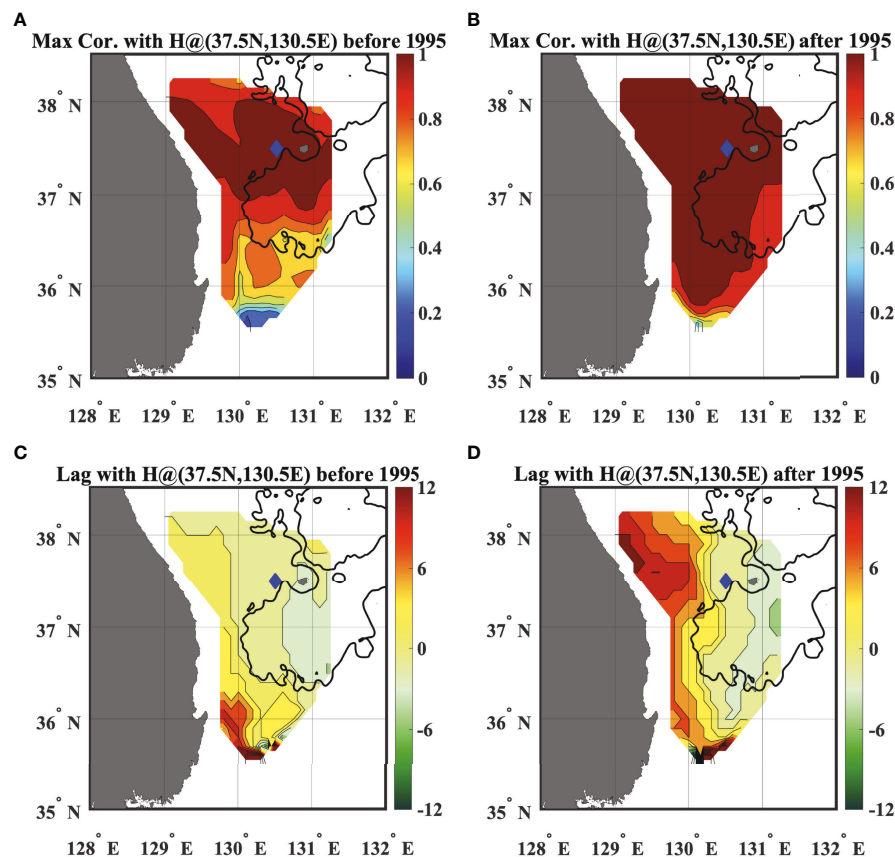


**FIGURE 11** | Spatial maximum correlation map of the ESIW thickness with the reference point at 37.5°N 130.5°E (A) from 1965 to 1994 and (B) from 1995 to 2020. Panels (C, D) show the monthly lag where the maximum correlations in (A, B) are, respectively. Blue diamonds denote the reference point. Contour intervals are 0.1 in (A, B) and 2 months in (C, D).



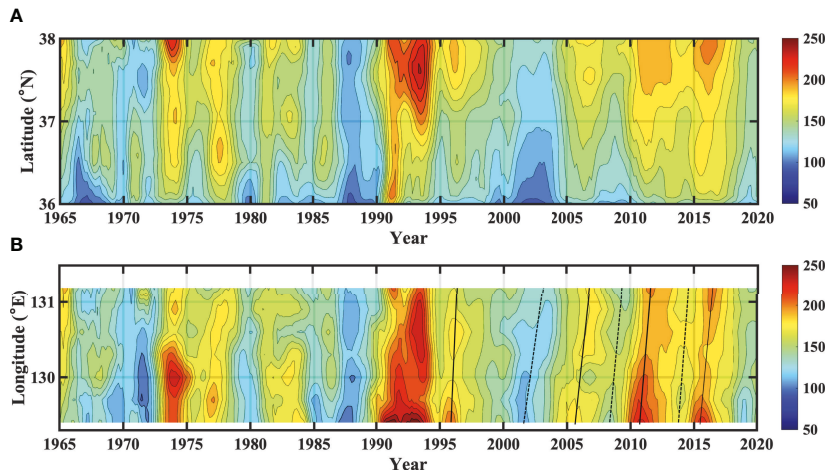


**FIGURE 12** | Spatiotemporal variability of the ESIW thickness on (A) latitude-time domain at 130.5°E and (B) longitude-time domain at 37.5°N. Black solid lines connect crests in the ESIW thickness at 129.4°E and 131.2°E. Black dotted lines are the same as the solid line but for troughs

of the 2000s. Therefore, it can be assumed that there was no dramatic salinity change in the past that could have affected the ESIW density.

It was also assumed that the error of temperature data after the quality control should be small enough, and that even if an error existed, it would not have spatiotemporal correlations. The first mode PC time series extracted through the EOF analysis and isothermal surface averaged ESIW thickness fluctuations appear almost similar, which could supposedly minimize the non-correlated error. Also, the spatial patterns of the thickness are consistent with the EOF and the basin-averaged analysis results. Thus, the long-term variability of the ESIW thickness in this study was confirmed to be robust.

The spatiotemporal variability of the ESIW thickness was also found to have a relationship with the ESIW salinity from the Argo data (2001–2014) in **Figure 2** (also see **Supplementary Figure S6**). Based on the non-correlated features of the thickness with the local SSH or local wind stress curl (**Supplementary Figure 5**), and the thicker ESIW in the northern region close to the formation area, the variability information of the thickness seems relevant to the amount of formation volume, at least, for the Argo observation period. However, the ESIW salinity itself is not a strong factor in determining the formation rate because the salinity has little effect on the density range in the ESIW. Therefore, the ESIW salinity variability alone is not sufficient to explain the ESIW variation directly responding to climate

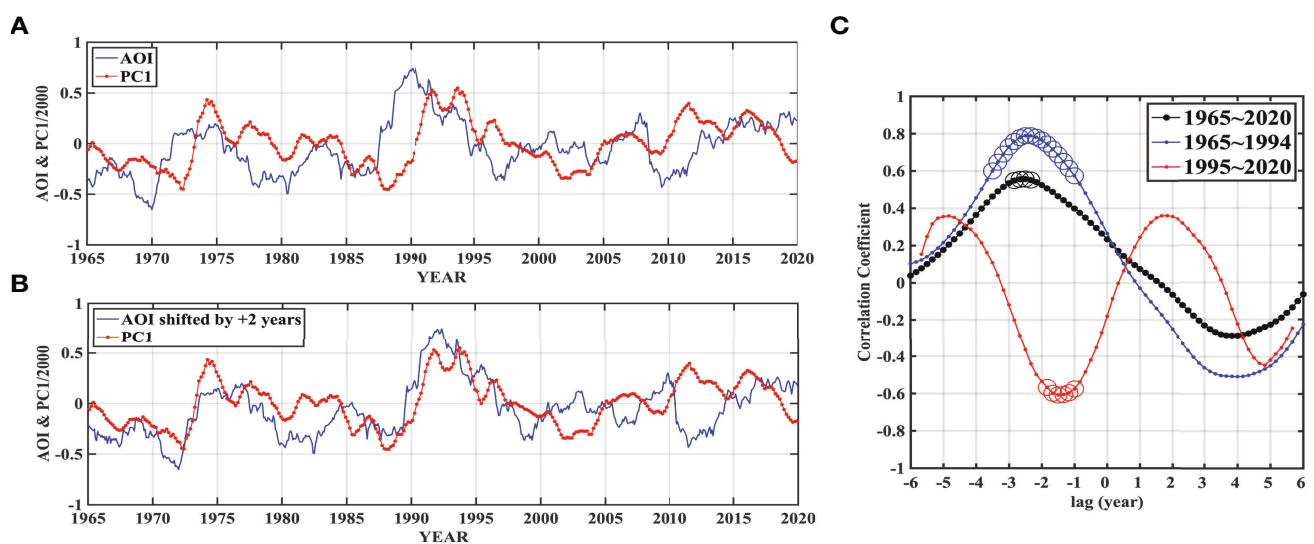


**FIGURE 13** | (A) Time series of 3-year moving-averaged AOI (blue) and the EOF first mode PC of the ESIW thickness scaled by 1/2,000 (red). (B) Same as panel (A) but AOI shifted by 2 years and (C) lagged-correlation diagram between AOI and first mode PC of the ESIW thickness. The black line is from the whole data. The blue line is from the data of 1965–1994 and the red one is of 1995–2020. The open circles denote where the correlations are above 95% significance levels.

variability. Indeed, as pointed out by Park and Lim (2018), it is consistent with the fact that the ESIW salinity is mainly determined by the amount of inflow of surface low-salinity water into the ESIW formation site by ocean advection rather than air-sea freshwater exchange.

The AO and the ESIW thickness since 1995 have almost the same lag along the ES coast as shown in **Figure 14**, whereas such alongshore tendency is not clear prior to 1995. The nearly uniform lag along the vicinity of the coast from 36°N to 38°N indicates that the advection or propagation timescale is shorter than 2 months of the hydrographic data intervals. Alternatively, the thickness signal travels along the coast faster than about  $2 \text{ cm s}^{-1}$ . Also, if the same signal propagation process works for the northern area as the observation area, it can be inferred that it would not take as long as 12 months for the signal to propagate from the 40°N–41°N region where the ESIW is formed (Park and Lim, 2018) to the observation site. However, the time lag between the AO and ESIW thickness in **Figure 14D** is about 12 months. Similarly, the time lag of 26 months in the Ullung Basin is too long to be considered as just the advection timescale of the offshore propagation path of the ESIW, suggested to be 6–12 months in previous studies

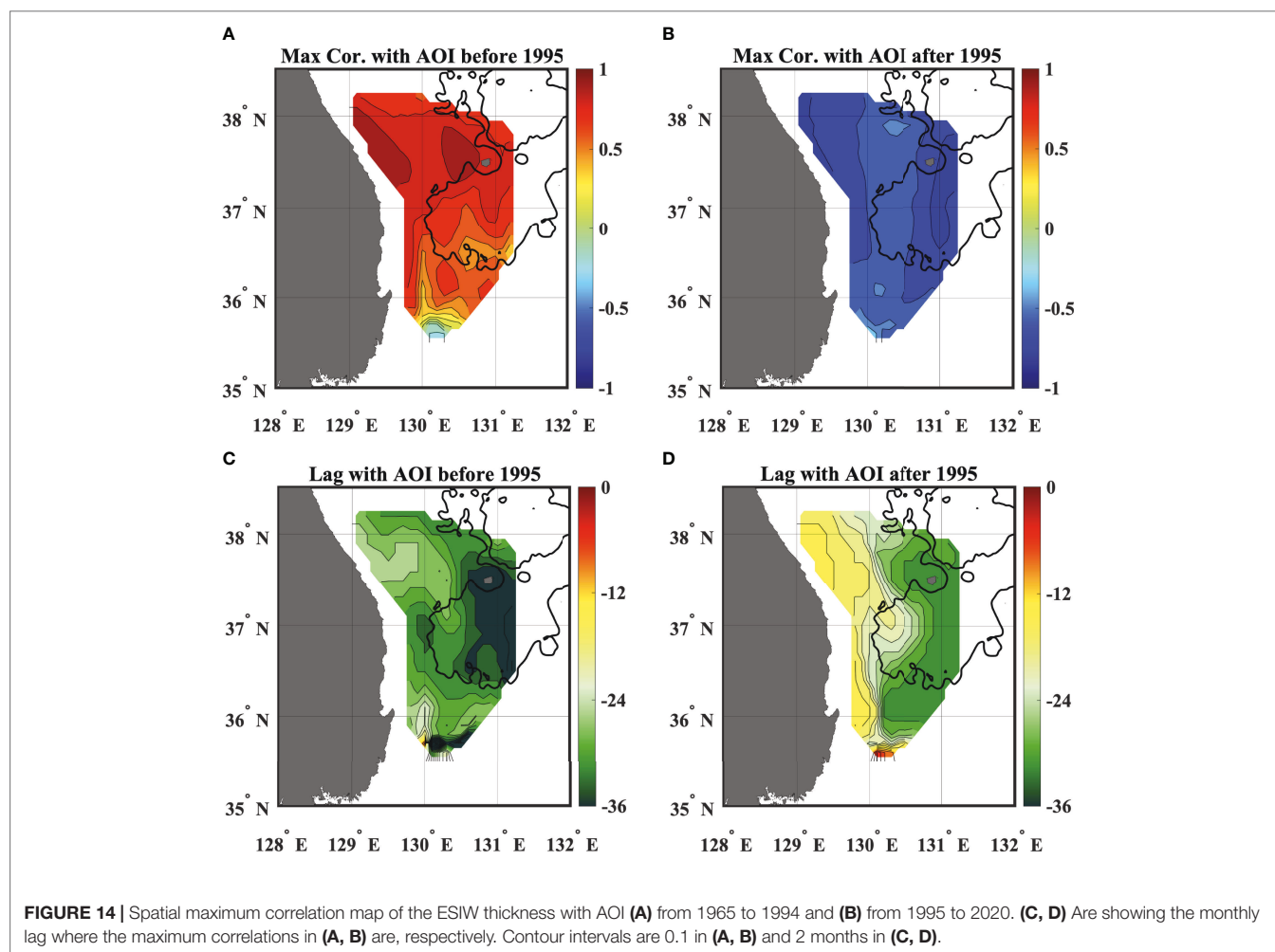
(Yanagimoto and Taira, 2003; Yun et al., 2004; Park and Kim, 2013). Therefore, additional studies are required to explain the time lag between the AO and the water mass variability downstream.

More importantly, even though it has been confirmed that there is a persistent southward flow at the intermediate level along the eastern coast of the Korean Peninsula since the 1960s (Kim and Kim, 1983; Kim et al., 2006), the alongshore uniform lag is only prominent after 1995 and not before. This is a similar argument as the two-mode ESIW property addressed in the section *Spatial Basin-Wide Averaged Temperature*.

## 5 CONCLUSION

### 5.1 Long-Term Variability of the East Sea Intermediate Water Thickness

This study demonstrated that the long-term ESIW thickness variability has basin-wide features and clear interannual-interdecadal timescales, such as 15–18 years and 3–5 years as shown in the NIFS hydrographic data. The thickness variability increased toward the northern part of the observation area and



decreased toward the south. This temporal thickness variation is not closely related to the SSH features, showing that the ESIW thickness variability is not dependent on the upper ocean circulation patterns.

The ESIW thickness variability is mostly determined by the 1°C isotherm fluctuation and is somewhat interacted with the upper layers above it. As for the horizontal structure, within the NIFS observation domain, the ESIW thickness fluctuates almost simultaneously in the meridional direction, while it has a clear zonal phase difference. However, the vertical and horizontal characteristics of the thickness variability are dramatically changed in the mid-1990s. The details are in the following section.

## 5.2 Regime Shift in the Mid-1990s

The following four distinct changes were observed concerning the long-term variability of the ESIW thickness beginning in the mid-1990s.

Changes in the vertical temperature structure of the upper ESIW layer: The vertical temperature gradient has been shown to increase, as the layer between 5°C and 10°C is significantly reduced since 1995. This appears to be because the 2°C–5°C isotherms are clearly shoaling, despite the deepening of the isotherms for 9°C and higher.

Changes in the correlation between the thermocline isotherms: There are nearly zero correlations between the ESIW thickness and the isotherms in the thermocline layer before 1995 with the exception of the 1°C isotherms but negative correlations with the 4°C–11°C isotherms after 1995. This implies that after 1995, as the ESIW becomes thicker, the upper layer is pushed up and shoaled. However, before 1995, all isotherms vibrated similarly with a slight phase difference, though with different amplitudes (smaller as it goes up). The ESIW thickness for this time period was mainly produced by the phase and amplitude difference between isotherms.

Changes in the spatial distribution of the ESIW thickness: Long-term variability of the ESIW thickness has time lags of several months depending on the locations. The fluctuations tend to occur first in the vicinity of the ES coast and appear later in the offshore, the Ulleung Basin. This zonal lag has become remarkable since 1995 and is related to the unique characteristics of the ESIW property suggested in a previous study where it appears as two modes in the zonal hydrographic section (Cho and Kim, 1994). Consistently, it has been reported that the ESIW flowing southward along the coast extends to the offshore to the Ullung Basin in the zonal direction (Shin et al., 1998; Shin et al., 2007). Due to these lags, the ESIWs found near the coast and in the basin could be misinterpreted as different water masses because their properties look different from the hydrographic data obtained in a specific year.

Changes in the relationship with the AO representing atmospheric conditions associated with water mass formation: The AO and the ESIW thickness clearly have a positive and negative correlation before and after the mid-1990s, respectively. The lag with the AO is also different, where the lag is longer before the mid-1990s than after. Cui and Senjyu (2010) showed that the

AO and Sea Surface Temperature (SST) at the formation site of Japan Sea Proper Water (JSPW) had out-of-phase fluctuations and also pointed out that the DO concentration at 1,000 m had a higher correlation with cold air outbreak (Isobe and Beardsley, 2007). Because the AO Index is closely related to the winter atmospheric condition in the ES, it is relevant to the water mass formation rate and is a type of volume flux. However, the DO concentration in the downstream area is a kind of reservoir property that is basically integrated by fluxes. Considering the advection timescale or ventilation timescale of the water mass, there should be still some lag between the formation rate (relevant to AO) and the reservoir characteristics (relevant to the thickness) depending on the variation timescale. Therefore, a further study will be conducted on why the AOI index and the ESIW thickness have such a high correlation with some time lags.

Based on the observational results, a working hypothesis is suggested to explain the changes of the ESIW thickness variabilities and the discrepancies from the previous studies discussed in the *Discussion*.

## 6 SUGGESTION OF WORKING HYPOTHESIS

### 6.1 Response of Intermediate Water on Changes of Meridional Overturning Circulation

Intermediate waters are generally found over the world's oceans and located between the upper ocean water, which is strongly influenced by atmospheric conditions or upper circulation, and the deep water, which is formed in the limited cold region by atmospheric conditions in winter due to local convection or subduction in the MOC perspective. The MOC becomes closed as the deep water mixes with the upper ocean water, with the intermediate water acting as a conduit between the upper and deep water.

Assume that the deep ES consists of a single water mass like JSPW. From the perspective of the Stommel–Arons model (Stommel and Arons, 1960), JSPW will make nearly uniform upwellings as it fills the ES seabed, causing the isotherms to shoal, which will also shoal the ESIW layer. However, above the ESIW, because there is the TWW coming through the Korea Strait, the upper ocean in the southern part of the ES is continuously refreshed by the advected TWW. As a result, the ESIW will be eroded by the TWW in the upper ocean, and one can expect that the ESIW volume would decrease as the deep waters are expanded. Therefore, the ESIW thickness variation basically includes the amount of its own formation and the volume change of deep waters.

Because the ES is a marginal sea with a small area, atmospheric conditions in winter of a certain year will be simultaneously applied on various water masses with different formation processes. The deep-water formation area is known to be in the east of the NKF (Park et al., 2005) off the Peter the Great Bay, Russia, and the ESIW is formed in the west of the NKF (Park and Lim, 2018). The formation regions of the ESIW and deep water

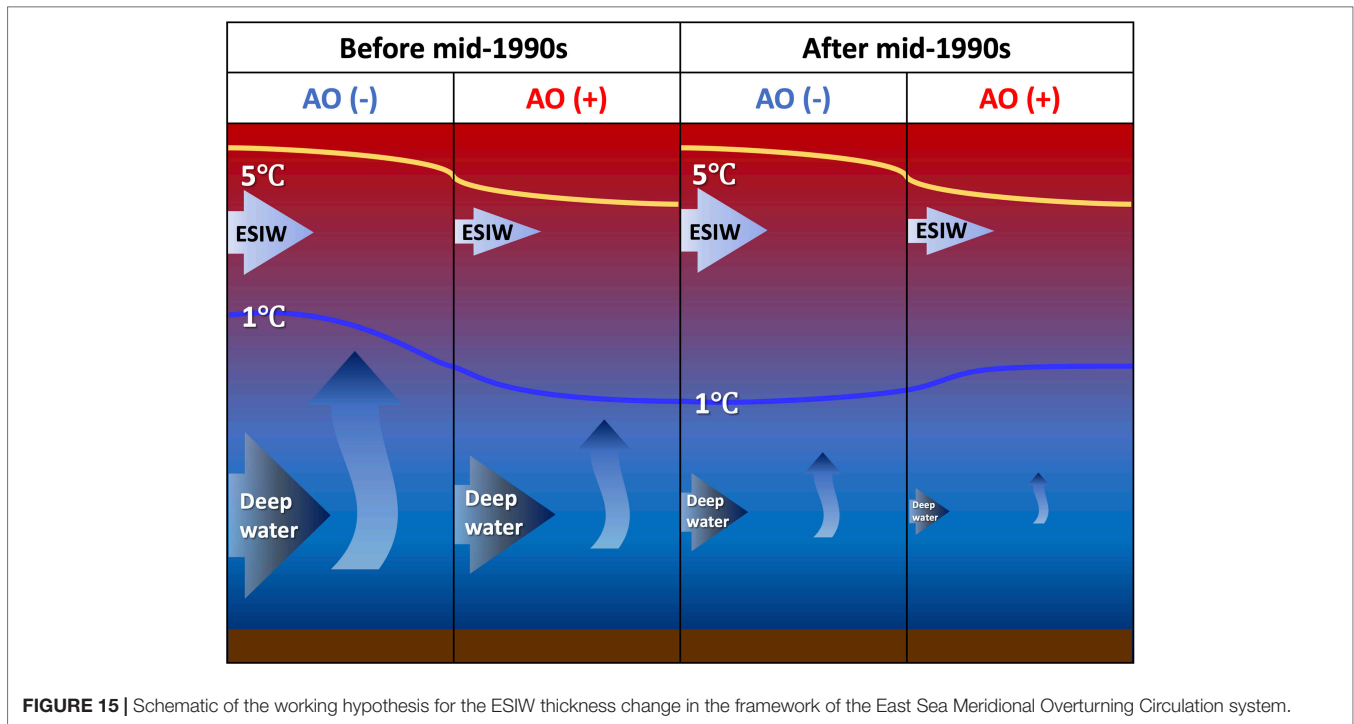


**FIGURE 15 |** Schematic of the working hypothesis for the ESIW thickness change in the framework of the East Sea Meridional Overturning Circulation system.

are close enough compared to the atmospheric mesoscale, so they seem to be under similar atmospheric conditions in wintertime when formed. Alternatively, if the winters in the ES were colder than normal, it would favor the formation of all water masses: intermediate, deep, or bottom waters. That might be a reason why the ESIW thickness is positively correlated with AO before 1995. This point will be discussed in the next section.

In the past, DO concentration in the deep sea of the ES has been reported to be rapidly decreasing (Gamo, 1999; Kim et al., 2001; Yoon et al., 2018). The DO concentrations at the water depth of 2,000–3,000 m decreased steadily from 1954 to 2015, and at 500–1,500 m, it increased briefly in the mid-1990s, then decreased again in the 2000s. As of 2015, the vertical DO structure below the intermediate layer is almost constant. If the formation of water mass below the intermediate was limited and became insensitive to AO conditions, the ESIW thickness would be inferred to vary purely with the amount of its formation.

## 6.2 A Possible Scenario of the East Sea Intermediate Water Thickness Change Under Global Warming

The following scenario is proposed to explain the distinct difference in characteristics related to the ESIW thickness variability in the southwestern part of the ES in the mid-1990s (Figure 15). Typically, the water mass formation rate should be determined according to the AO, and there is a time lag of 1–2 years until the effect appears in the observation domain.

As shown in Figure 15, before the mid-1990s, in the AO negative (positive) phase, cold (warm) winter conditions prevailed, and the formation of the ESIW and deep water (JSPW

or CW+BW) was strengthened (weakened). Because the volume variability of deep water was much larger than that of the ESIW, it created shoaling (deepening) of overall isotherm surfaces under the thermocline in the southern seas of the ES. Therefore, the ESIW thickness variability can be primarily controlled by the change in the volume of deep water, and it shows in-phase behavior with AO.

However, since the mid-1990s, as the deep-water formation rapidly decreased under the influence of global warming and the AO-associated response was weakened, the overall isotherm surfaces were less affected by the volume change of the deep-water layer. As a result, the ESIW thickness was mainly determined by the ESIW formation itself, so it may be that the isotherm surfaces below and above the ESIW fluctuate in opposite directions.

The lag difference from the mid-1990s shown in the time series of the AO and the ESIW thickness in Figure 13 can also be interpreted consistently with the above scenario, such as the lag of 2.5 years before the mid-1990s and 1.5 years after. After the mid-1990s, the AO signal could be projected directly onto the much shallower and faster-circulating ESIW layer, resulting in the shorter lag, while before the mid-1990s, the ESIW thickness might respond more slowly to the AO because the signal came through the deep water.

Previously, several researchers have reported that the variability of deep-water properties (nitrate, DO,  $PO_4$ , etc.) within the timescales of about 18 years exists in the ES (Watanabe et al., 2003; Cui and Senjyu, 2010), similar to the 15–18-year timescales shown in the ESIW thickness. Even though the deep-water properties and volumes may not have the variability with the same phase, the existence of such decadal variability in deep-water properties indicates that there should be also a variability

in the volume of deep-water formation with a comparable timescale, producing the undulation of the upper isotherms.

The two-mode state of the ESIW salinity structure in the zonal conductivity-temperature-depth section is a distinct feature of ESIW that is not seen in other water masses. The zonal difference in the ESIW salinity has been reported in many previous studies since the 1980s (Kim et al., 1991; Cho and Kim, 1994). However, the zonal phase difference in the ESIW thickness has been shown only since the mid-1990s, which can also be explained by the above scenario. Because the ESIW thickness was mainly controlled by the deep-water volume change before the mid-1990s, such zonal phase difference of the thickness that could emerge due to deep-water layers is faded after the mid-1990s. In other words, the two-mode ESIW property existed before the regime shift appeared, but the fact that the two-mode thickness was seen since the mid-1990s proves that the thickness variation before the mid-1990s does not reflect the volume change of the ESIW itself.

## 7 REMAINING STUDIES AND IMPLICATIONS

To understand how the AO controls the water mass formation, accurate observational data at the formation site are required, but unfortunately, such data are not available. Satellite sea surface temperature data exist only since 1987, and reanalysis data are not suitable for such analysis because their resolution and accuracy are low in the ES. However, model-based studies can reveal a physical process to understand such a clear correlation between the ESIW thickness and AO in the future.

This study demonstrates that the sudden regime shift in the thermocline layer of the ES occurred in the mid-1990s. Clearly, a control process responsible for such rapid change must be understood. Additionally, the process should be reconciled with the ventilation timescale of the ESIW. The ventilation timescale, which is the time taken by the water mass to leave the formation site and arrive at the target area, might be about a few years or less based on the time-lag correlation between the AO and the ESIW thickness. However, the ESIW ventilation ages, estimated using chemical tracers like apparent oxygen utilization and partial pressure of chlorofluorocarbons, have varied over 10–23 years (Min and Warner, 2005; Kim et al., 2010). The large discrepancy in the ventilation timescale from the results in this study may be due to the strong vertical mixing of the ESIW with the TWW above it, which has low DO and chlorofluorocarbon concentration, because diapycnal mixing can greatly bias the chemical tracer-based age (Fine et al., 2017).

Modeling studies also estimated the ventilation time of the ESIW to be 6–10 years from the point of view of particle dispersion (Seung and Kim, 1997; Yoshikawa et al., 1999), and this may be related to the problem in which the low-resolution numerical models of the past underestimated the mean and eddy circulation at mid and deep layers (Park and Kim, 2013). The latest model results suggested that the ESIW arrived at the

Ulleung Basin in a relatively short time of 1–2 years (Kim et al., 2021), which is comparable to the results of this study, although there is still a significant difference from the observed results in terms of the ESIW formation area. Because the ESIW ventilation timescale is important information, a study reconciling the chemical tracer-based, numerical model-based, and physical observation-based timescales is required.

Additionally, Yoshikawa et al. (1999) estimated the turnover time of the ESIW to be approximately 26 years by utilizing the ESIW formation rate and reservoir volume estimated by the numerical model. In perspectives of the long-term variability in the ESIW thickness shown in the NIFS data and the salinity variability shown in the Argo float data, the ESIW signal in the western part of the ES seems quickly refreshed within the order of years rather than lasting more than 20 years. Although it can propagate away to other basins in the ES, such as the Yamato Basin, the actual turnover time of the ESIW might be much faster than the previously simulated one. Indeed, Kim et al. (1999) showed that the ESIW property over the ES basins changed in a year-to-year manner, but additional research is required on this topic.

The scenarios discussed above explain the variation in the intermediate layer in terms of EMOC changes in response to AO under global warming. If the ES has been changing according to the scenario, the ESIW has the potential to serve as a good proxy for showing EMOC changes. Because the ES has a small domain size and ventilation timescales significantly shorter than that of the open ocean, the response to interannual-interdecadal atmospheric variability can appear quickly enough to be identified with the modern observations of less than 100 years. In addition, the ES is a unique marginal sea in that while the various water masses were formed under the influence of the same atmospheric conditions, they responded differently to global warming.

Although it is obvious that the water mass formation in winter is limited by global warming, it can be assumed easily that not all water mass formation rates are limited to the same extent. In the case of deep-water formation area in the ES, the mixed layer can be developed up to 1,000–2,000 m, which is favorable to the open ocean deep convection. However, because the vertical temperature gradient below the permanent thermocline in the ES is much smaller than the open ocean, even slight warming in the mixed layer can significantly reduce the mixing depth in winter, resulting in the slow formation rate. Alternatively, the ESIW is mainly formed above the thermocline by subduction due to the flow convergence in the mixed layer. Because the ESIW formation area is strongly stratified even in winter compared to the deep-water formation area, the mixed layer (Lim et al., 2012). depth could be less sensitive to a slight increase in surface temperature due to global warming.

## DATA AVAILABILITY STATEMENT

Argo float data were collected and made freely available by the International Argo Program and the National programs that contribute to it (<http://www.Argo.ucsd.edu>, <http://Argo.jcommops.org>). Satellite SSH data were processed by SSALTO/

DUACS and distributed by AVISO+ (<https://www.aviso.altimetry.fr>) with support from CNES.

Korea (NRF) grant funded by the Korea government (MSIT) (NRF-2022R1A2C1004059).

## AUTHOR CONTRIBUTIONS

JP conceptualized the study, performed all data analyses, and entirely contributed to writing the draft.

## FUNDING

This research was a part of the project titled “Development of the core technology and establishment of the operation center for underwater gliders” funded by the Ministry of Oceans and Fisheries, Korea (1525012198). This work was also supported by the National Research Foundation of

## ACKNOWLEDGMENTS

I would like to thank my students, Bong-Joon Kim, In-Ha Seo, and Joo-Hee Park, who helped complete this article. In addition, I want to thank Dr. Y.-G. Kim, Prof. Y.-H. Kim, and Prof. S.-T. Yoon for their invaluable discussion on the earlier draft.

## SUPPLEMENTARY MATERIAL

The Supplementary Material for this article can be found online at: <https://www.frontiersin.org/articles/10.3389/fmars.2022.923093/full#supplementary-material>

## REFERENCES

- Choi, B.-J., Haidvogel, D. B. and Cho, Y.-K. (2004). Nonseasonal Sea Level Variations in the Japan/East Sea From Satellite Altimeter Data. *J. Geophys. Res.* 109, C12028. doi: 10.1029/2004JC002387
- Cho, Y.-K. and Kim, K. (1994). Two Modes of the Salinity-Minimum Layer Water in the Ulleung Basin. *La Mer.* 32, 271–278.
- Cui, Y. and Senjyu, T. (2010). Interdecadal Oscillations in the Japan Sea Proper Water Related to the Arctic Oscillation. *J. Oceanogr.* 66, 337–348. doi: 10.1007/s10872-010-0030-z
- Fine, R. A., Peacock, S., Maltrud, M. E. and Bryan, F. O. (2017). A New Look at Ocean Ventilation Time Scales and Their Uncertainties. *J. Geophys. Res. Oceans* 122, 3771–3798. doi: 10.1002/2016JC012529
- Gamo, T. (1999). Global Warming May Have Slowed Down the Deep Conveyor Belt of a Marginal Sea of the Northwestern Pacific: Japan Sea. *Geophys. Res. Lett.* 26, 3137–3140. doi: 10.1029/1999GL002341
- Isobe, A. and Beardsley, R. C. (2007). Atmosphere and Marginal-Sea Interaction Leading to an Interannual Variation in Cold-Air Outbreak Activity Over the Japan Sea. *J. Clim.* 20, 5707–5714. doi: 10.1175/2007JCLI1779.1
- Kang, D.-J., Kim, J.-Y., Lee, T. and Kim, K. R. (2004). Will the East/Japan Sea Become an Anoxic Sea in the Next Century? *Mar. Chem.* 91, 77–84. doi: 10.1016/j.marchem.2004.03.020
- Kang, S. K., Seung, Y. H., Park, J. J., Park, J.-H., Lee, J. H., Kim, E. J., et al. (2016). Seasonal Variability in Mid-Depth Gyral Circulation Patterns in the Central East/Japan Sea as Revealed by Long-Term Argo Data. *J. Phys. Oceanogr.* 46, 937–946. doi: 10.1175/JPO-D-15-0157.1
- Kim, K., Chang, K.-I., Kang, D.-J., Kim, Y. H. and Lee, J.-H. (2008). Review of Recent Findings on the Water Masses and Circulation in the East Sea (Sea of Japan). *J. Oceanogr.* 64, 721–735. doi: 10.1007/s10872-008-0061-x
- Kim, K. and Chung, J. Y. (1984). On the Salinity Minimum and Dissolved Oxygen Maximum Layer in the East Sea (Sea of Japan). *Elsevier Oceanogr. Ser.* 39, 55–65. doi: 10.1016/S0422-9894(08)70290-3
- Kim, C. H. and Kim, K. (1983). Characteristics and Origin of the Cold Water Mass Along in the East Coast of Korea. *J. Oceanolog. Soc Kor* 18, 73–83.
- Kim, Y.-G. and Kim, K. (1999). Intermediate Waters in the East/Japan Sea. *J. Oceanogr.* 55, 123–132. doi: 10.1023/A:1007877610531
- Kim, K., Kim, Y.-G., Cho, Y.-K., Takematsu, M. and Volkov, Y. (1999). Basin-To-Basin and Year-to-Year Variation of Temperature and Salinity Characteristics in the East Sea (Sea of Japan). *J. Oceanogr.* 55, 103–109. doi: 10.1023/A:1007873525552
- Kim, Y. H., Kim, Y.-B., Kim, K., Chang, K.-I., Lyu, S. J., Cho, Y.-K., et al. (2006). Seasonal Variation of the Korea Strait Bottom Cold Water and Its Relation to the Bottom Current. *Geophys. Res. Lett.* 33, L24604. doi: 10.1029/2006GL027625
- Kim, K., Kim, K.-R., Kim, Y. G., Cho, Y. K., Kang, D.-J., Takematsu, M., et al. (2004). Water Mass and Decadal Variability in the East Sea (Sea of Japan). *Prog. Oceanogr.* 61, 157–174. doi: 10.1016/j.pocean.2004.06.003
- Kim, K.-R., Kim, G., Kim, K., Lobanov, V., Ponomarev, V. and Salyuk, A. (2002). A Sudden Bottom-Water Formation During the Severe Winter 2000–2001: The Case of the East/Japan Sea. *Geophys. Res. Lett.* 29, 75–71. doi: 10.1029/2001GL014498
- Kim, K., Kim, K.-R., Min, D.-H., Volkov, Y., Yoon, J.-H. and Takematsu, M. (2001). Warming and Structural Changes in the East Sea (Japan Sea): A Clue to Future Changes in Global Oceans? *Geophys. Res. Lett.* 28, 3293–3296. doi: 10.1029/2001GL013078
- Kim, C. H., Lie, H.-J. and Chu, K. S. (1991). On the Intermediate Water in the Southwestern East Sea (Sea of Japan). *Elsevier Oceanogr. Ser.* 54, 129–141. doi: 10.1016/S0422-9894(08)70091-6
- Kim, Y.-H. and Min, H.-S. (2008). Seasonal and Interannual Variability of the North Korean Cold Current in the East Sea Reanalysis Data. *Ocean. Polar. Res.* 30, 21–31. doi: 10.4217/OPR.2008.30.1.021
- Kim, I.-N., Min, D.-H., Kim, D. H. and Lee, T. (2010). Investigation of the Physicochemical Features and Mixing of East/Japan Sea Intermediate Water: An Isopycnic Analysis Approach. *J. Mar. Res.* 68, 799–818. doi: 10.1357/002224010796673849
- Kim, S.-Y., Park, Y.-G., Kim, Y. H., Seo, S., Jin, H., Pak, G., et al. (2021). Origin, Variability, and Pathways of East Sea Intermediate Water in a High-Resolution Ocean Reanalysis. *J. Geophys. Res. Oceans* 126, e2020. doi: 10.1029/2020JC017158
- Kwon, Y. O., Kim, K., Kim, Y. G. and Kim, K. R. (2004). Diagnosing Long-Term Trends of the Water Mass Properties in the East Sea (Sea of Japan). *Geophys. Res. Lett.* 31, L20306. doi: 10.1029/2004GL020881
- Lim, S. H., Jang, C. J., Oh, I. S. and Park, J. J. (2012). Climatology of the Mixed Layer Depth in the East/Japan Sea. *J. Mar. Syst.* 96–97, 1–14. doi: 10.1016/j.jmarsys.2012.01.003
- Lozier, M. S., McCartney, M. S. and Owens, W. B. (1994). Anomalous Anomalies in Averaged Hydrographic Data. *J. Phys. Oceanogr.* 24, 2624–2638. doi: 10.1175/1520-0485(1994)024<2624:AAIAHD>2.0.CO;2
- McDougall, T. J. and Krzysik, O. A. (2015). Spiciness. *J. Mar. Res.* 73, 141–152. doi: 10.1357/002224015816665589
- Minami, H., Kano, Y. and Ogawa, K. (1999). Long-Term Variations of Potential Temperature and Dissolved Oxygen of the Japan Sea Proper Water. *J. Oceanogr.* 55, 197–205. doi: 10.1023/A:1007889929187
- Min, H. S. and Kim, C.-H. (2006). Water Mass Formation Variability in the Intermediate Layer of the East Sea. *Ocean Sci. J.* 41, 255–260. doi: 10.1007/BF03020629
- Min, D.-H. and Warner, M. J. (2005). Basin-Wide Circulation and Ventilation Study in the East Sea (Sea of Japan) Using Chlorofluorocarbon Tracers. *Deep-Sea Res. II: Top. Stud. Oceanogr.* 52, 1580–1616. doi: 10.1016/j.dsr2.2003.11.003

- Munk, W. H. (1966). Abyssal Recipes. *Deep Sea Res. Part I Oceanogr. Res. Pap.* 13, 707–730. doi: 10.1016/0011-7471(66)90602-4
- Nam, S. H., Yoon, S.-T., Park, J.-H., Kim, Y. H. and Chang, K.-I. (2016). Distinct Characteristics of the Intermediate Water Observed Off the East Coast of Korea During Two Contrasting Years. *J. Geophys. Res. Oceans* 121, 5050–5068. doi: 10.1002/2015JC011593
- Nurser, A. J. and Lee, M.-M. (2004). Isopycnal Averaging at Constant Height. Part I: The Formulation and a Cast Study. *J. Phys. Oceanogr.* 34, 2721–2739. doi: 10.1175/JPO2649.1
- Park, J. J. (2019). First Observational Finding of Submesoscale Intrathermocline Eddy in the East Sea Using Underwater Glider. *J. Kor. Soc. Oceanogr.* 24 (2), 332–350. doi: 10.7850/jkso.2019.24.2.332
- Park, J. J. (2021). Quality Evaluation of Long-Term Shipboard Salinity Data Obtained by NIFS. *J. Kor. Soc. Oceanogr.* 26 (1), 49–61. doi: 10.7850/jkso.2021.26.1.049
- Park, K.-A., Chung, J. Y., Kim, K. and Cornillon, P. C. (2005). Wind and Bathymetric Forcing of the Annual Sea Surface Temperature Signal in the East (Japan) Sea. *Geophys. Res. Lett.* 32, L05610. doi: 10.1029/2004GL022197
- Park, T.-W., Ho, C.-H. and Yang, S. (2011). Relationship Between the Arctic Oscillation and Cold Surges Over East Asia. *J. Clim.* 24, 68–83. doi: 10.1175/2010JCLI3529.1
- Park, J. J. and Kim, K. (2007). Evaluation of Calibrated Salinity From Profiling Floats With High Resolution Conductivity-Temperature-Depth Data in the East/Japan Sea. *J. Geophys. Res.* 112, 1–9. doi: 10.1029/2006JC003869
- Park, J. J. and Kim, K. (2013). Deep Currents Obtained From Argo Float Trajectories in the Japan/East Sea. *Deep-Sea Res. II: Top. Stud. Oceanogr.* 85, 169–181. doi: 10.1016/j.dsr2.2012.07.032
- Park, J. J. and Lim, B. (2018). A New Perspective on Origin of the East Sea Intermediate Water: Observations of Argo Floats. *Prog. Oceanogr.* 160, 213–224. doi: 10.1016/j.pocean.2017.10.015
- Park, J. J. and Nam, S. H. (2018). Interannual Variability of Winter Precipitation Linked to Upper Ocean Heat Content Off the East Coast of Korea. *Int. J. Climatol.* 38, e1266–e1273. doi: 10.1002/joc.5354
- Park, J. J., Park, K.-A., Kim, Y.-G. and Yun, J.-Y. (2016). “Water Masses and Their Long-Term Variability,” in *Oceanography of the East Sea (Japan Sea)*. Ed. Chang, K.-I. (Germany: Springer International Publishing), 460.
- Senjyu, T. (1999). The Japan Sea Intermediate Water; Its Characteristics and Circulation. *J. Oceanogr.* 55, 111–122. doi: 10.1023/A:1007825609622
- Seung, Y. H. and Kim, K.-J. (1997). Estimation of the Residence Time for Renewal of the East Sea Intermediate Water Using MICOM. *J. Kor. Soc. Oceanogr.* 32, 17–27.
- Shin, C.-W., Byun, S.-K., Kim, C., Lee, J. H., Kim, B.-C., Hwang, S.-C., et al. (2007). General Characteristics of the East Sea Intermediate Water. *Ocean Polar Res.* 29, 33–42. doi: 10.4217/OPR.2007.29.1.033
- Shin, C.-W., Byun, S.-K., Kim, C. and Seung, Y.-H. (1998). Southward Intrusion of the East Sea Intermediate Water Into the Ulleung Basin: Observations in 1992 and 1993. *J. Kor. Soc. Oceanogr.* 33, 146–156.
- Stommel, H. and Arons, A. (1960). On the Abyssal Circulation of the World Ocean. I. Stationary Planetary Flow Patterns on a Sphere and II. An Idealized Model of the Circulation Pattern and Amplitude in Ocean Basins. *Deep-Sea Res.* 6, 140–154. doi: 10.1016/0146-6313(59)90065-6
- Talley, L. D., Min, D.-H., Lobanov, V. B., Luchin, V. A., Ponomarev, V. I., Salyuk, A. N., et al. (2006). Japan/East Sea Water Masses and Their Relation to the Sea's Circulation. *Oceanography* 19, 32–49. doi: 10.5670/oceanog.2006.42
- Talley, L. D., Tishchenko, P., Luchin, V., Nedashkovskiy, A., Sagalae, S., Kang, D. J., et al. (2004). Atlas of Japan (East) Sea Hydrographic Properties in Summer 1999. *Prog. Oceanogr.* 61, 277–348. doi: 10.1016/j.pocean.2004.06.011
- Tsunogai, S., Kawada, K., Watanabe, S. and Aramaki, T. (2003). CFC Indicating Renewal of the Japan Sea Deep Water in Winter 2000–2001. *J. Oceanogr.* 59, 685–693. doi: 10.1023/B:JOCE.0000009597.33460.d7
- Uda, M. (1934). The Results of Simultaneous Oceanographical Investigations in the Japan Sea and Its Adjacent Waters in May and June 1932. *J. Imp. Fish. Exp. Sta.* 5, 57–190.
- Watanabe, Y. W., Wakita, M., Maeda, N., Ono, T. and Gamo, T. (2003). Synchronous Bidecadal Periodic Changes of Oxy-Gen, Phosphate and Temperature Between the Japan Sea Deep Water and the North Pacific Intermediate Water. *Geophys. Res. Lett.* 30, 2273. doi: 10.1029/2003GL018338
- Wong, A., Keeley, R. and Carval, T. (2014). Argo Quality Control Manual for CTD and Trajectory Data Version 3.2 2019J. doi: 10.13155/33951
- Wu, B., Su, J. and D'Arrigo, R. (2015). Patterns of Asian Winter Climate Variability and Links to Arctic Sea Ice. *J. Clim.* 28, 6841–6858. doi: 10.1175/JCLI-D-14-00274.1
- Yanagimoto, D. and Taira, K. (2003). Current Measurements of the Japan Sea Proper Water and the Intermediate Water by ALACE Floats. *J. Oceanogr.* 59, 359–368. doi: 10.1023/A:1025572112019
- Yoon, S. T., Chang, K. I., Nam, S., Rho, T., Kang, D. J., Lee, T., et al. (2018). Re-Initiation of Bottom Water Formation in the East Sea (Japan Sea) in a Warming World. *Sci. Rep.* 8, 1576. doi: 10.1038/s41598-018-19952-4
- Yoon, J.-H. and Kawamura, H. (2002). The Formation and Circulation of the Intermediate Water in the Japan Sea. *J. Oceanogr.* 58, 197–211. doi: 10.1023/A:1015893104998
- Yoshikawa, Y., Awaji, T. and Akitomo, K. (1999). Formation and Circulation Processes of Intermediate Water in the Japan Sea. *J. Phys. Oceanogr.* 29, 1701–1722. doi: 10.1175/1520-0485(1999)029<1701:FACPOI>2.0.CO;2
- Yun, J. Y., Chang, K. I., Kim, K. Y., Cho, Y. K., Park, K. A. and Maggaard, L. (2016). ENSO Teleconnection to the Isopycnal Depth Fluctuations of the East/Japan Sea Intermediate Water in the Ulleung Basin During 1968–2002. *J. Phys. Oceanogr.* 46, 2675–2694. doi: 10.1175/JPO-D-15-0225.1
- Yun, J.-Y., Maggaard, L., Kim, K., Shin, C.-W., Kim, C. and Byun, S.-K. (2004). Spatial and Temporal Variability of the North Korean Cold Water Leading to the Near-Bottom Cold Water Intrusion in Korea Strait. *Prog. Oceanogr.* 60, 99–131. doi: 10.1016/j.pocean.2003.11.004

**Conflict of Interest:** The author declares that the research was conducted in the absence of any commercial or financial relationships that could be construed as a potential conflict of interest.

**Publisher's Note:** All claims expressed in this article are solely those of the authors and do not necessarily represent those of their affiliated organizations, or those of the publisher, the editors and the reviewers. Any product that may be evaluated in this article, or claim that may be made by its manufacturer, is not guaranteed or endorsed by the publisher.

Copyright © 2022 Park. This is an open-access article distributed under the terms of the Creative Commons Attribution License (CC BY). The use, distribution or reproduction in other forums is permitted, provided the original author(s) and the copyright owner(s) are credited and that the original publication in this journal is cited, in accordance with accepted academic practice. No use, distribution or reproduction is permitted which does not comply with these terms.



# Effects of Internal Climate Variability on Historical Ocean Wave Height Trend Assessment

Mercè Casas-Prat<sup>1\*</sup>, Xiaolan L. Wang<sup>1</sup>, Nobuhito Mori<sup>2</sup>, Yang Feng<sup>1</sup>, Rodney Chan<sup>1</sup> and Tomoya Shimura<sup>2</sup>

<sup>1</sup>Climate Research Division, Science and Technology Branch, Environment and Climate Change Canada, Toronto, ON, Canada, <sup>2</sup>Disaster Prevention Research Institute, Kyoto University, Kyoto, Japan

## OPEN ACCESS

### Edited by:

Giovanni Besio,  
University of Genoa, Italy

### Reviewed by:

Andrea Lira Loarca,  
University of Genoa, Italy  
José Pinho,  
University of Minho, Portugal  
Sebastian Solari,  
Universidad de la República, Uruguay

### \*Correspondence:

Mercè Casas-Prat  
merce.casasprat@ec.gc.ca

### Specialty section:

This article was submitted to  
Global Change and  
the Future Ocean,  
a section of the journal  
Frontiers in Marine Science

**Received:** 31 December 2021

**Accepted:** 30 May 2022

**Published:** 14 July 2022

### Citation:

Casas-Prat M, Wang XL, Mori N,  
Feng Y, Chan R and Shimura T  
(2022) Effects of Internal Climate  
Variability on Historical Ocean  
Wave Height Trend Assessment.  
*Front. Mar. Sci.* 9:847017.  
doi: 10.3389/fmars.2022.847017

This study assesses the effects of internal climate variability on wave height trend assessment using the d4PDF-WaveHs, the first single model initial-condition large ensemble (100-member) of significant wave height ( $H_s$ ) simulations for the 1951–2010 period, which was produced using sea level pressure taken from Japan's d4PDF ensemble of historical climate simulations. Here, the focus is on assessing trends in annual mean and maximum  $H_s$ . The result is compared with other model simulations that account for other sources of uncertainty, and with modern wave reanalyses. It is shown that the trend variability arising from internal climate variability is comparable to the variability caused by other factors, such as climate model uncertainty. This study also assesses the likelihood to mis-estimate trends when using only one ensemble member and therefore one possible realization of the climate system. Using single member failed to detect the statistically significant notable positive trend shown in the ensemble in some areas of the Southern Ocean. The North Atlantic Ocean is found to have large internal climate variability, where different ensemble-members can show trends of the opposite signs for the same area. The minimum ensemble size necessary to effectively reduce the risk of mis-assessing  $H_s$  trends is estimated to be 10; but this largely depends on the specific wave statistic and the region of interest, with larger ensembles being required to assess extremes. The results also show that wave reanalyses are not suitable for analyzing  $H_s$  trends due to temporal inhomogeneities therein, in agreement with recent studies.

**Keywords:** global wave climate, internal climate variability, ocean wave height, trend assessment, wave reanalysis

## 1 INTRODUCTION

Waves are an important element of the climate system, modulating interactions between oceans and atmosphere (Cavaleri et al., 2012). They are also a key environmental variable for coastal and offshore engineering (International Organization for Standardization, 2007; Gudmestad, 2020), navigation planning (Grifoll et al., 2018), and are a potential source of renewable energy (Reguero et al., 2019). Furthermore, waves are important drivers of coastal dynamics processes, such as coastal erosion (Stive et al., 2002; Huppert et al., 2020), and contribute to sea-level extremes at multiple time scales (Melet et al., 2018; Melet et al., 2020). This is critical as over 300 million people live on low-lying coastal areas (Griggs and Reguero, 2021).



Detailed knowledge of wave climate is essential to address the aforementioned environmental and societal impacts. However, our current understanding is affected by several sources of uncertainty, as highlighted by Morim et al. (2019), who presented the latest comprehensive large ensemble of global wave projections. They found a large uncertainty in the historical annual mean significant wave height ( $H_s$ ) climatology with discrepancies exceeding 20% in some areas. The climate model and the method to simulate ocean waves were found to be dominant uncertainty factors. However, the wave method uncertainty, as defined in Morim et al. (2019), included uncertainty factors beyond the mere relationship between atmospheric forcing and wave parameters, as some of the wave methods bias-corrected the forcing drivers (using different wave reanalysis as reference) while others used atmospheric forcing as directly output by climate models. Therefore, this wave method uncertainty implicitly included factors related to different atmospheric model parameterizations and data assimilation associated to the corresponding reference datasets used for calibration.

Despite the recent coordinating efforts to better characterize waves, the role of internal climate variability, and particularly its effects on trend assessment, is still poorly known. Morim et al. (2019) only accounted for one realization per model and scenario combination. Wang et al. (2015) considered multi-run  $H_s$  simulations but these had 10 runs per model/scenario at most, and the study focused on signal uncertainty rather than trend assessment. Recently, Song et al. (2021) developed centuries of global ocean wave data, including 165-year (1850–2014) of historical data. Despite being a unique database for ocean wave climate research, it only simulates one realization given the same climatological forcing. In terms of the driving wind fields, Morim et al. (2020) found that the underlying physics of the atmospheric component of climate models is the dominant source of bias in simulated wind fields, and that inter-model uncertainty is typically 2–4 times larger than the uncertainty associated with internal variability. However, they used a relatively small sample (3–10 model realizations).

Historical simulations are one possible realization of the climate system within its boundaries of internal variability. Studies based on single model realizations might underestimate extreme events or confound trends with internal (climate) variability. For example, internal variability can mask or enhance human-induced sea-ice loss on timescales ranging from years to decades (Swart et al., 2015). Also, differences between models or a model and observations can easily be misinterpreted as significant differences, while they could be simply caused by an insufficient sample size (Milinski et al., 2020). For instance, at least thirty ensemble members are required for a robust estimate of El Niño–Southern Oscillation (ENSO) variability, which plays a primarily positive role in intensifying anomalous wave climate (Yang and Oh, 2020). In terms of annual hurricane frequency, Mei et al. (2019) concluded that twenty ensemble was sufficient to detect year-to-year variations. The number of ensemble members required for robust estimates depends on targets or on temporal and spatial averaging scale (Ishii and Mori, 2020).

Despite the increasing amount and type of observations (mostly thanks to satellite records since 1979) and the continuous

development of climate models, there are still many challenges in the characterization of the historical wave climate and the trends therein. State-of-the-art wave reanalysis and hindcasts present notable discrepancies and even exhibit opposite trends at global and regional scales (Sharmar et al., 2020). For example, modern reanalyses simulate contrasting positive and negative statistically significant trends in the annual mean  $H_s$  of the South Atlantic (of up to 0.05 m/decade in absolute value). The inconsistencies of reanalysis data sets are due to the changing quantity and quality of the satellite data incorporated into the products (Stopa et al., 2019). Discrepancies were also obtained by Dodet et al. (2020) when comparing the trends derived from satellite records after considering two different post-processing data approaches. To date, wave climate studies have focused on uncertainties related to model resolution and parameterization, downscaling methods, observations errors and data assimilation but there is little knowledge about the role of internal wave climate variability.

A Single Model Initial-condition Large Ensemble (SMILE) is a set of simulations conducted using a single model with identical external forcing and a large ensemble of different initial conditions (Maher et al., 2021). SMILEs are valuable data to investigate the climate system as they can help separate internal climate variability of the forced system from the forced response to changes in external forcing, and to sample extreme events with large return periods (Maher et al., 2021). For example, they are beneficial for robust attribution of climate changes to anthropogenic forcing (Kirchmeier-Young et al., 2021), and to investigate the uncertainty associated to compound events (Santos et al., 2021).

Here we present and analyze the first SMILE-based ensemble of global ocean significant wave height ( $H_s$ ) simulations, which was produced using the 100-member ensemble of mean sea level pressure (SLP) taken from Japan's d4PDF ensemble of historical climate simulations (Mizuta et al., 2017). After a slight modification in two of the 11 modelling regions (the tropical Pacific regions were split into two, see Section 2.1), the statistical model developed by Wang et al. (2012, 2014) was used to obtain the wave heights driven by d4PDF SLP fields. This study investigates for the first time the role of internal climate variability in trend assessment of ocean wave heights at global scale. This helps to gain insight in the understanding of historical wave conditions and changes therein, bringing additional perspective in the context of the aforementioned discrepancies in modern reanalysis/hindcast products.

## 2 MATERIALS AND METHODS

### 2.1 d4PDF-WaveHs

The d4PDF-WaveHs ensemble analyzed in this study is a SMILE-based ensemble of global historical  $H_s$ . This ensemble consists of 100 members of 6-hourly  $H_s$  for the period 1951–2010 on a  $1^\circ \times 1^\circ$  lat.-long. grid over the global oceans. It was produced using an advanced statistical model with SLP-based predictors derived from the SLP historical simulations taken from the d4PDF large ensemble, which includes historical climate and future projections (Mizuta et al., 2017). The 60 km resolution atmospheric global

circulation model (AGCM) MRI-AGCM developed by the Japan Meteorological Research Institute was used to generate d4PDF (Mizuta et al., 2012). The 100 historical simulations constitute a SMILE-type ensemble as they were generated by perturbations of the historical sea surface temperature (SST), sea ice concentration (SIC) and sea ice thickness (SIT) in relation to the observed errors (while using the same forcing, and global mean concentration of greenhouse gases (GHG) based on observations). More than 70 papers related to d4PDF have been published to date, including impact assessment and social implementation studies (Ishii and Mori, 2020). d4PDF satisfactorily simulates the past climate in terms of climatology, natural variations, and extreme events such as tropical cyclones (Ishii and Mori, 2020).

To be able to generate 6,000 years ( $100 \times 60$  years) of  $H_s$  data with a reasonable computational cost, the statistical model developed by Wang et al. (2012, 2014) was used to produce the d4PDF-WaveHs. This method consists of a multivariate regression model with lagged-dependent variable to represent the relationship between  $H_s$  and SLP-derived predictors (anomalies of SLP and squared SLP gradients), including leading principal components of large areas to account for swell waves. In particular, the 6-hourly  $H_s$  at a target wave grid point (of the  $1^\circ \times 1^\circ$  lat.-long grid) is simulated with a multivariate regression model of the form:

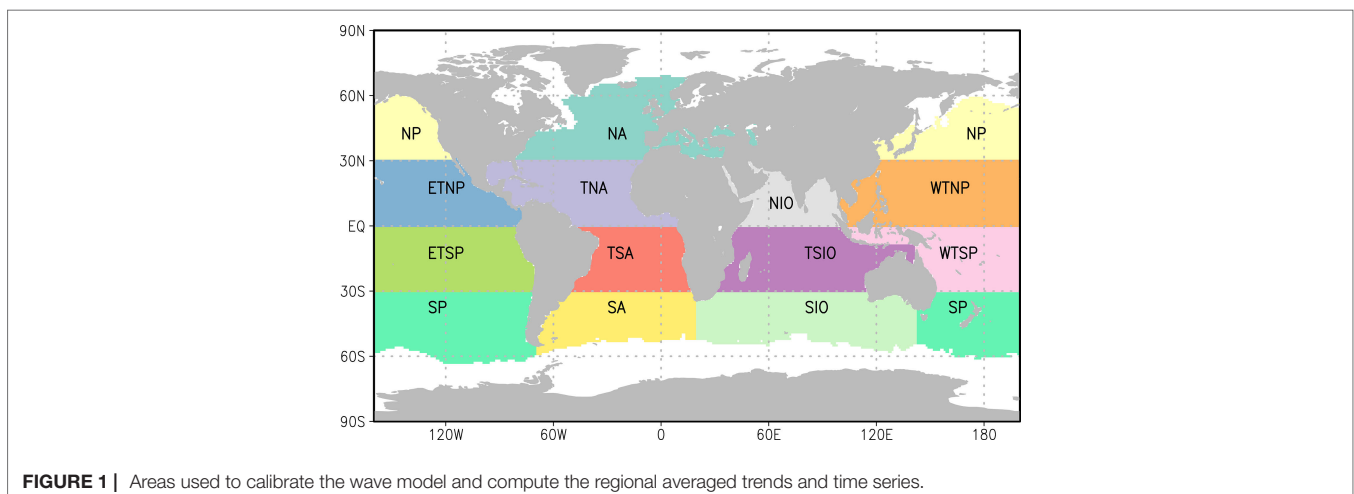
$$H_t = a + \sum_{k=1}^K b_k X_{k,t} + \sum_{p=1}^P c_p H_{t-p} + u_t \quad (1)$$

where  $H_t$  is the Box-Cox transformed  $H_s$  (Box and Cox, 1964),  $X_{k,t}$  are the  $K$  selected SLP-based predictors,  $P$  is the order of lags of the dependent variable (the predictand) and the residuals  $u_t$  are modelled as an  $M$ -order autoregressive process. The Box-Cox transformation is applied to bring the residuals close to a normal distribution, as assumed in the regression analysis. The SLP-based predictors consist of a pool of 62 potential predictors: the anomalies (relative to the 1981–2000 mean) of, respectively, SLP and the squared SLP gradient (which represents the geostrophic wind

energy) and their respective 30 leading principal components over a selected area to represent the large scale patterns of atmospheric circulation affecting the wave climate of a target grid point. A forward model-selection procedure with  $F$  test with equivalent sample size (vonStorch and Zwiers, 1999) was used to determine the  $K$  selected SLP-derived predictors [see Eq. (1)] for a target wave grid point. The  $P$  and  $M$  values were also determined using the  $F$  test with the equivalent sample size. To account for seasonality of atmospheric circulation regimes,  $H_s$  is modelled in each of the four seasons separately. More details of this statistical modelling approach can be found in Wang et al. (2012, 2014). Note that the two tropical Pacific regions, TNP and TSP (the two largest regions) in Wang et al. (2012, 2014) were each split into two regions (ETNP, WTNP, ETSP, WTSP); so that the model was calibrated for 13 regions over the globe in this study (rather than 11 regions; see **Figure 1**). The smaller regions slightly improved the model skill for those regions.

As in Wang et al. (2014), Eq. (1) was calibrated and evaluated using the European Center for Medium-Range Weather Forecasts (ECMWF) Reanalysis Interim (ERAint) (Dee et al., 2011). Before calculating the  $X_{k,t}$  predictors to produce the  $H_s$  simulations, the d4PDF-WaveHs SLP fields were adjusted to have the same climatological mean and standard deviation as the ERAint SLP data. As explained in Wang et al. (2014), this is needed in order to apply the Box-Cox transformations which were optimized for the ERAint data. Additionally, we excluded (set to missing) any simulated  $H_s$  values that exceed twice the largest  $H_s$  from ERAint for a given season. This cap is needed as, very rarely, the Box-Cox transformation of the SLP gradients leads to an overgrowth of the sharp SLP gradients of rapidly forming low pressure centers which, in turn, leads to unrealistic  $H_s$  values. This is arguably caused by the higher spatial resolution of the d4PDF SLP fields, as compared to ERAint, which might be able to simulate stronger SLP gradients than those generated by ERAint. However, note that this overgrowth is extremely rare and occurs with a frequency of less 0.05% in all simulated  $H_s$  data.

This statistical wave modelling approach to simulate  $H_s$  has been used and validated in many studies to derive regional and global



historical/future  $H_s$  datasets and to assess trends, projected changes and variability (Wang et al., 2012; Wang et al., 2014; Wang et al., 2015). For example, it was used to derive one of the contributing datasets of the latest coherent, community-driven, multi-method ensemble of global wave climate projections (Morim et al., 2019). In this study, we further assessed the reliability of the statistical modelling method by comparing the resulting trends of the annual mean and maximum  $H_s$  as obtained from one member of the d4PDF-WaveHs with those derived from the traditional dynamical modelling approach for the same d4PDF member. The single-member dynamical wave simulations were conducted using WAVEWATCH III (WW3) driven by the surface wind fields of the d4PDF member in question. We used the same WW3 version (5) and model configuration as in Shimura and Nobuhito (2019) which has a spatial resolution of  $\sim 0.5^\circ$ . For both datasets, the annual mean  $H_s$  trend is remarkably positive in the Southern Ocean but the statistical approach simulates a less intensive tendency to increase over a smaller area (Figure S1). This can be arguably explained by the lower spatial resolution of the simulations obtained with the statistical modelling approach ( $1^\circ$ ) in comparison to the WW3 simulations ( $\sim 0.5^\circ$ ). Indeed, there is a better agreement in terms of the trends relative to the 1951–2010 climatological mean, as they are less affected by spatial resolution (see Figure S2). For the annual maximum  $H_s$ , both approaches simulate a noisier spatial pattern of trends than for the annual mean  $H_s$ , as expected for this extreme statistic. For both datasets, positive increases in the annual maximum  $H_s$  are seen in the Southern Ocean and in the Northern Pacific, Northern Atlantic and Indian Oceans. Overall, the results show that the statistical and dynamical methods are in reasonably good agreement with each other, showing similar spatial patterns of trends for both the annual mean  $H_s$  and maximum  $H_s$ .

## 2.2 Trend Analysis

This study focuses on the assessment of the annual mean and maximum  $H_s$  trends for the period 1951–2010 and the uncertainty derived from the internal climate variability. First, individual trends were computed for each ensemble member of d4PDF-WaveHs using the (non-parametric) Mann-Kendall method with lag-1 autocorrelation being accounted for (Wang and Swail, 2001). Second, the individual-member trends were averaged over the 100 ensemble members to obtain the ensemble averaged trend. Then, the regional average trends are calculated as the average over all gridpoints in each of the modelling areas shown in Figure 1.

At a given grid point, the ensemble averaged trend is considered statistically significant if >50% of the individual-member trends are significant at the 5% level, and >90% of these significant individual-member trends have the same trend sign. This method was used by Morim et al. (2019) as it was identified as a suitable method to identify regions of robustness (IPCC, 2013). As discussed later in the manuscript, this method is more restrictive than performing a t-test on the individual trend estimates, as the latter does not account for the inter-annual variability.

In addition, we investigate the impact of internal climate variability on the results of trend assessment, showing what we can gain from using a SMILE-based ensemble. In particular, we estimated the following three likelihoods:

1. the likelihood for an ensemble member to have the same trend conclusion as the ensemble averaged trend. Here trend conclusion is one of the following three outcomes: (a) statistically significant positive trend, (b) statistically significant negative trend, (c) statistically insignificant trend (regardless of the sign).
2. the likelihood for an ensemble member to have the same trend sign as the ensemble averaged trend, regardless of the significance level.
3. the likelihood for an ensemble member to give a trend conclusion that is opposite to that of the ensemble, showing a statistically significant trend of the opposite sign to the ensemble average trend (here both trend estimates are statistically significant).

We repeated the above analysis by considering  $x$ -size sub-ensembles (randomly sampled 100 times from d4PDF-WaveHs), where  $x$  goes from 2 to 50. This allows us to investigate the gain from using gradually larger ensembles, and to find the optimal ensemble size for estimating trend in the two  $H_s$  statistics analyzed.

## 2.3 Wave Datasets Used for Comparison

For comparison purposes, the trend assessment described in Section 2.2 is also performed for state-of-the-art wave reanalysis both at global and regional scales, as well as on a grid point basis. The goal is put the role of the internal climate variability for trend assessment (based on d4PDF-WaveHs) into perspective of the estimates and discrepancies among modern reanalysis datasets. In particular, we used the second version of the National Centers for Environmental Prediction (NCEP) Climate Forecast System Reanalysis (CFSR) (Saha et al., 2014), ERAint (Dee et al., 2011) and the more recent ECMWF 5<sup>th</sup> generation reanalysis (ERA5) (Herbach et al., 2020). Although ERA5 is available since 1950, we consider a common period of analysis from 1979 to 2009 for these three reanalysis datasets.

Additionally, we compared our trend estimates and uncertainty results with those obtained from historical wave simulations without data assimilation. First, we use the historical CMIP5-driven dataset developed by Wang et al. (2014), hereafter called CMIP5-HsWang, which used the same statistical modelling approach as this study. CMIP5-HsWang provides 6-hourly  $H_s$  produced using SLP simulations by 20 climate models (only one realization per model) for the period 1950–2005. With this comparison we investigate how internal climate variability compares to model variability in terms of trend estimates. Despite the forcing SLP data being adjusted to have the same climatological mean and variance as the ERAint SLP data, model variability was identified by Wang et al. (2014) as one major factor of uncertainty that is significantly different from zero globally.

Finally, we also performed the same trend analysis with the 1979–2004 COWCLIP historical ensemble (Morim et al., 2019), referred to as CMIP5-COWCLIP hereafter, which mainly accounts for climate model variability and wave method variability. Morim et al. (2019) identified both of these factors as key sources of uncertainty, with different contributions to total uncertainty depending on the region. Here we consider the 48 members that provide both annual mean and annual maximum  $H_s$ .

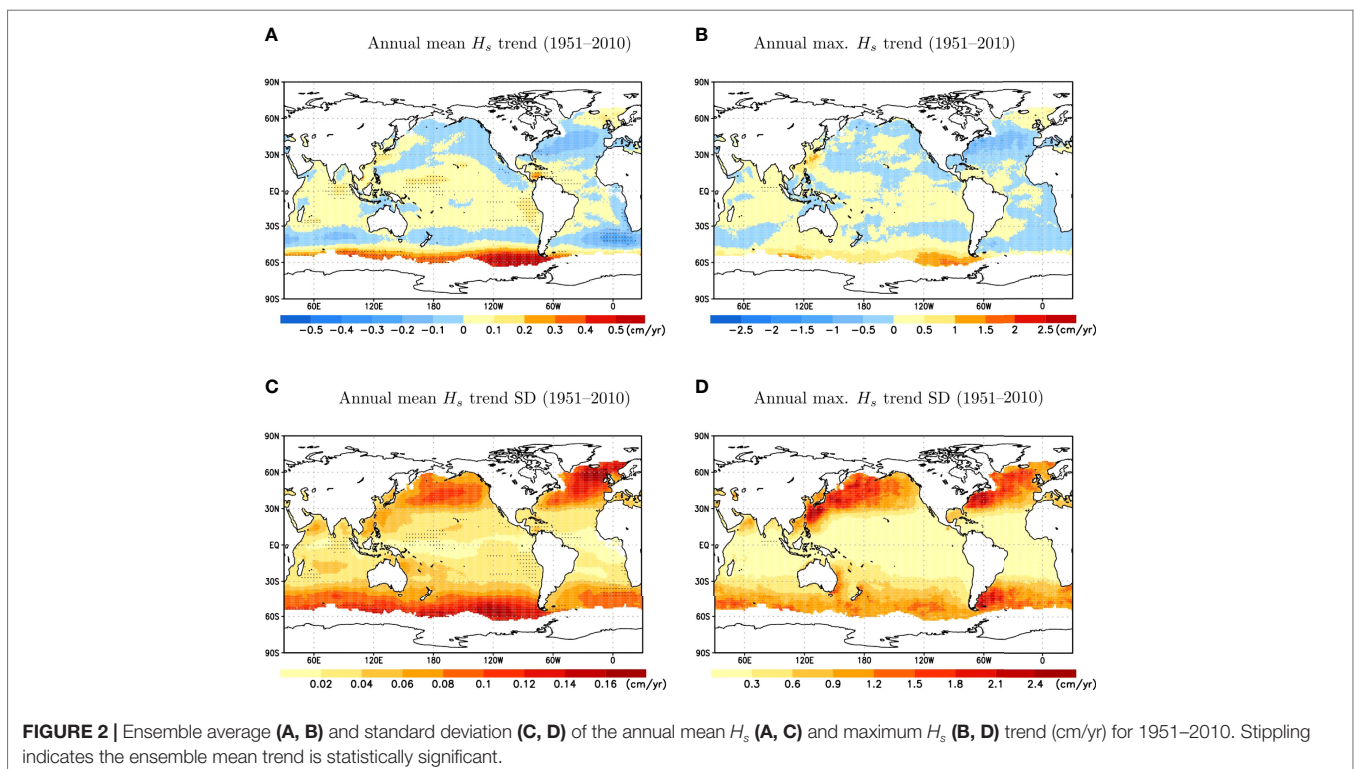
### 3 RESULTS

The ensemble average of trends in the annual mean  $H_s$  for the period 1951–2010, as simulated by d4PDF-WaveHs is positive and statistically significant (at 5% level) in the Southern Ocean with rates exceeding 0.5 cm/yr (Figure 2A), which represent an increase of up to 0.25%/yr relative to the 1951–2010 climatological mean (see Figure S3A). This rate of increase outstands from the rest of the oceans, which have positive/negative rates of up to 0.3 cm/yr in absolute value. This is reasonable given the more energetic wave climate of this unique continuous body of water encircling the Earth affected by continuous low pressure systems. Trends are also positive and statistically significant in areas of the tropical west Pacific, the southern East Pacific, the Southern Atlantic and the Indian Ocean. The only area with statistically significant negative trend is located south of Africa. A similar pattern is observed for the ensemble average of trends in the annual maximum  $H_s$  (Figures 2B and S3B) but in this case the

trends are statistically insignificant, and the latitudinal gradient between the Southern Ocean trends and the rest of the oceans is lower. Simulations of the annual maximum  $H_s$  trend show a noisier spatial pattern than for the annual mean  $H_s$  counterpart (see Figures S4–S7) due to the inherent additional uncertainty associated to extremes. This noise is implicitly reflected in the ensemble averaged trend with a lower statistical significance associated to the annual maximum  $H_s$  trends, as compared to those of the annual mean  $H_s$  (Figure 2A vs. Figure 2B).

Figures 2C, D illustrate the inter-member standard deviation (SD) of the annual mean and maximum  $H_s$  trends for the period 1951–2010. For the annual mean  $H_s$ , SD is larger in the extra-tropics of both the Northern and Southern Hemisphere, with the largest values being located in the North Atlantic Ocean. For the annual maximum  $H_s$ , we see a longitudinal gradient over the extra-tropics, with the larger SD being located in the Western parts of the North Pacific, North Atlantic, and South Atlantic basins. This is arguably related to these areas being more sheltered from swells and therefore more affected by local (more variable) extreme storms than the eastern side of the basin counterpart. Swells likely contribute to lower internal climate variability as they integrate different wave energy systems generated by different atmospheric systems across multiple locations.

It is important to note that the areas identified as statistically significant can differ notably depending on the statistical method used to assess uncertainty. As explained in Section 2.2, here we use a 2-step method that accounts for both inter-run and inter-annual variability, as recommended by the IPCC for assessing robustness. If we use a less conservative approach such as a t-test



to determine if the ensemble average trend is statistically different from zero, we obtain significantly larger areas of statistically significant trends that cover most of the domain (see **Figure 2** vs **Figure S8**). For example, in the North Atlantic Ocean, we obtain statistically significant positive trends in its north-east part while the central-west part exhibits a trend that is statistically significant and negative. Note that this t-test only accounts for the trend estimates associated to the individual ensemble members, without considering the inter-annual variability and the statistical significance associated to each individual member.

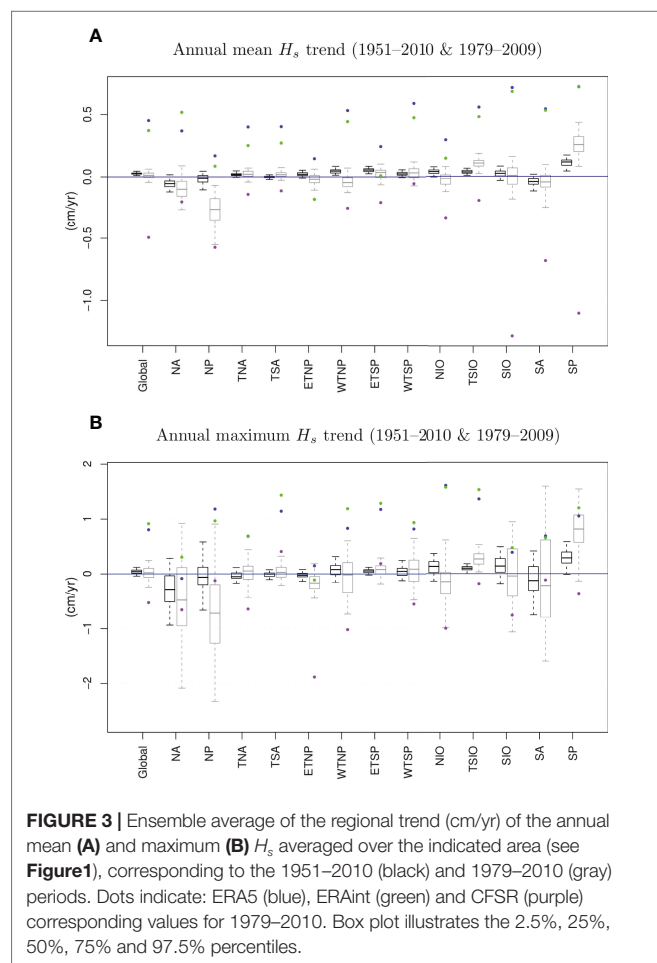
At regional scale, **Figure 3** shows the global and regional ensemble averages of the trends over the period 1951–2100 in the form of a boxplot, along with the 5%, 25%, 50%, 75%, and 95% percentiles of the trend estimates. The corresponding values relative to the 1951–2100 climatological mean are shown in **Figure S9**. One significant result is that at least 95% of the members exhibit a global positive trend for the annual mean  $H_s$ . At regional scale, the 5% percentile of the annual mean  $H_s$  trends also exceeds zero in some tropical areas, and in the Southern Hemisphere (WTNP, ETSP, TSIO and SP, see **Figure 1**). NA is the region with more members exhibiting a negative trend for the annual mean and maximum  $H_s$ . For the annual maximum  $H_s$ , the inter-member variability increases and a smaller number

of areas (TSIO and SP) have at least 95% members exhibiting positive trends. Overall, the areas where the trend estimate is more affected by internal climate variability are the extra-tropical areas, and particularly the Northern Hemisphere extra-tropics (NA and NP), which exhibit larger spread in both trend magnitude (cm/yr, see **Figure 3**) and percent relative to the 1951–2010 climatology (%/yr, **Figure S9**).

**Figure 3** also illustrates how the regional trends for the period 1979–2009 compare to the corresponding values of state-of-the-art reanalysis. As expected, the inter-member variability is larger due to considering a shorter period of time. We observe striking discrepancies between the analyzed NCEP and ECMWF products (CFSR vs. ERA5 and ERAint), which exceed the internal climate variability (as derived from d4PDF-WaveHs). While ERA5 and ERAint simulate positive trends for annual mean  $H_s$  over the majority of the regions, CFSR mostly depicts negative trends, which are particularly strong in the Southern Ocean. The corresponding regional average derived from d4PDF-WaveHs typically lies in between the values associated to these reanalyzes products. These discrepancies are also seen in the spatial patterns of the ensemble average trends for both the trend magnitude (cm/yr) and the trend relative to 1979–2009 (%/yr) of the annual mean  $H_s$  (**Figures S10, S11**). ERA5 and ERAint trends are mostly positive (and exceeding 0.5 cm/yr), while the corresponding values of CFSR are mostly negative with a similar amount.

For the regional annual maximum  $H_s$  trends, ERA5 and ERAint also simulate larger values than CFSR, often with opposite signs. However, such discrepancies are lower than what is in the annual mean  $H_s$  (relative to the d4PDF-WaveHs spread) and, for a few regions (NA, SIO and SA, see **Figure 1**), they even fall within the internal climate variability simulated by 4PDF-WaveHs. As for the annual mean  $H_s$  trend, the corresponding trend maps for the annual maximum  $H_s$  (**Figures S12, S13**) also illustrate disparities among the analyzed products but we find a larger agreement between 4PDF-WaveHs and CFSR, as better captured by the individual runs (**Figures S6, S7** vs **Figure S12B**).

As mentioned in the Introduction, recent studies also found significant discrepancies among modern wave reanalysis datasets. While differences in resolution and wave modelling method configurations can contribute to the differences in trends simulated by different wave climate products analyzed in this study, we argue that the major discrepancies are largely affected by temporal inhomogeneities introduced in assimilated data, in agreement with previous studies (e.g. Aarnes et al., 2015; Stopa et al., 2019; Wohlkand et al., 2019; Sharman et al., 2020). The comparison among reanalysis products alone seems to indicate that resolution is not a key factor explaining the discrepancies in the trends therein. ERAint (which has the same spatial resolution as 4dPDF-WaveHs) exhibits a trend pattern similar to ERA5 while the latter has significantly higher spatial resolution. Differently, ERA5 and CFSR have contrasting trends while having more similar spatial resolutions. Also, the discrepancies between ERAint/ERA5 and CFSR remain in terms of the relative trend (**Figures S12, S13**), which is a trend quantity less affected



by resolution. The difference between the statistical and the dynamical wave modelling approaches does not seem a key factor in explaining the discrepancies between the trends obtained from 4dPDF-WaveHs and the modern reanalysis either, as we showed how the annual mean and maximum  $H_s$  trends of the first run of 4dPDF-WaveHs exhibited similar patterns in comparison to the counterpart simulated by WW3 (Figures S1, S2).

The temporal inhomogeneities present in modern reanalysis can be illustrated with the abrupt changes in tendency and spread seen in the annual mean  $H_s$  time series of Figures 4 and 5 (see also Figures S14–S16 for other regions). For example, CFSR, ERAint and ERA5 simulate a global average of the annual mean  $H_s$  (Figure 4A) that goes from 2.23 m to 2.53 m in the first half of the reanalysis period, while the range is reduced to 2.28 m to 2.45 m for the second half. This is caused by an abrupt change in tendency starting in the 1990s, which coincides with the start of assimilated wave integrated parameters in the early 1990s, followed by an increase of overall satellite data in the 2000s (Herbach et al., 2020). The global annual maximum  $H_s$  (Figure 4B) does not exhibit such an abrupt breakpoint but the model spread also tends to decrease after the 1990s. Overall, we find a better agreement among the annual mean  $H_s$  trends simulated by 4dPDF-WaveHs and modern reanalysis datasets at global scale. For the global annual maximum  $H_s$ , the values simulated by 4dPDF-WaveHs (and also CMIP5-HsWang) are lower than those simulated by the reanalysis products. This is mostly caused by an underestimation of the annual maximum  $H_s$  in the tropics (see for example the WTNP, ETNP, TNA, WTSP, ETSP, TSA, TSIO regions in Figures S14–16) while

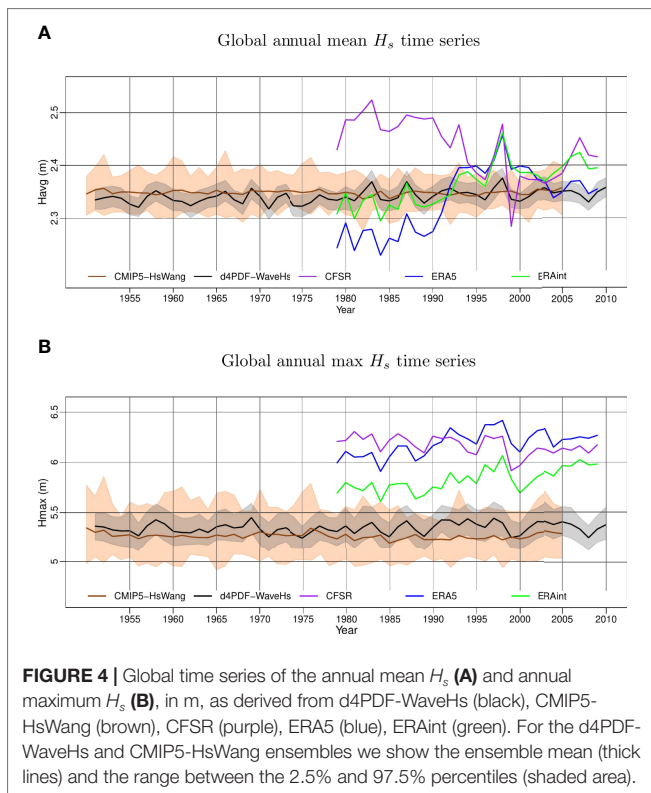


**FIGURE 4 |** Global time series of the annual mean  $H_s$  (A) and annual maximum  $H_s$  (B), in m, as derived from d4PDF-WaveHs (black), CMIP5-HsWang (brown), CFSR (purple), ERA5 (blue), ERAint (green). For the d4PDF-WaveHs and CMIP5-HsWang ensembles we show the ensemble mean (thick lines) and the range between the 2.5% and 97.5% percentiles (shaded area).

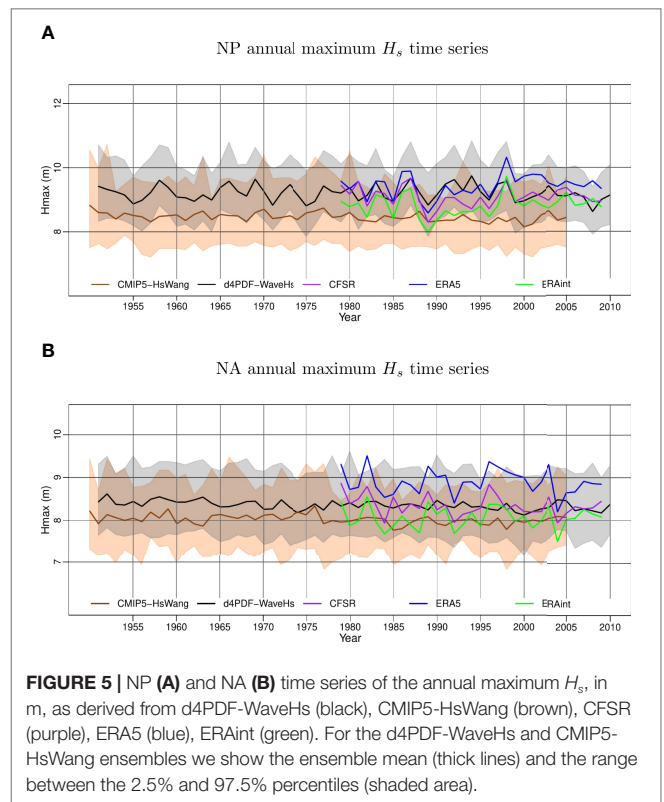
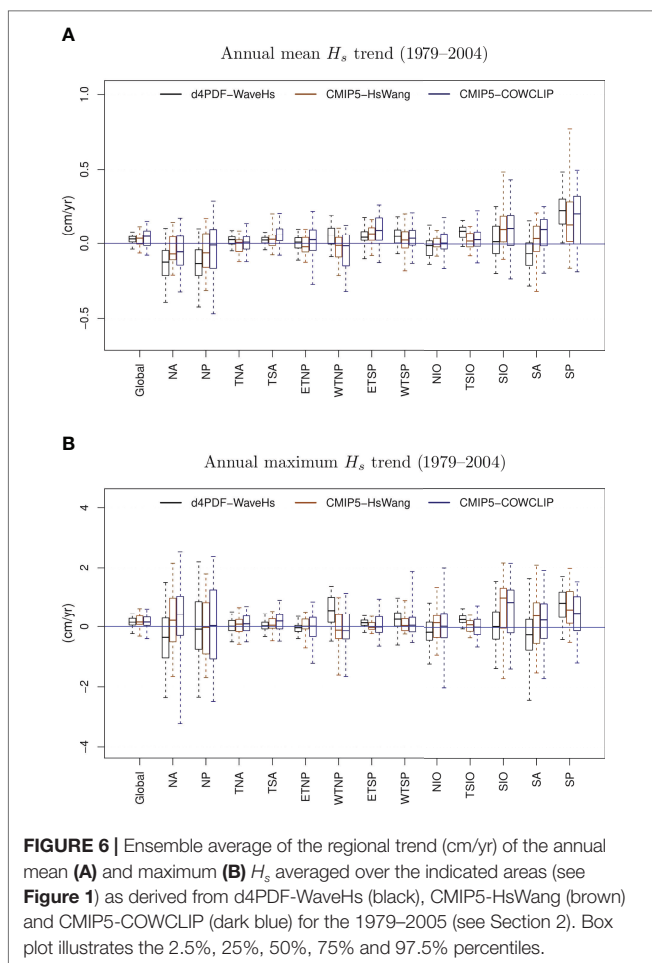


**FIGURE 5 |** NP (A) and NA (B) time series of the annual maximum  $H_s$ , in m, as derived from d4PDF-WaveHs (black), CMIP5-HsWang (brown), CFSR (purple), ERA5 (blue), ERAint (green). For the d4PDF-WaveHs and CMIP5-HsWang ensembles we show the ensemble mean (thick lines) and the range between the 2.5% and 97.5% percentiles (shaded area).

there is a good agreement for the annual maximum  $H_s$  over the mid to high latitudes (e.g. NP, NA, SP and SA regions, see Figure 5 and Figures S14–S16).

Since modern reanalysis datasets do not seem to be suitable observation proxies for trend analysis, we compare the trends derived from d4PDF-WaveHs with the corresponding values obtained from other model simulations without data assimilation: CMIP5-HsWang and CMIP5-COWCLIP (see Section 2.3). This also allows us to assess the role of the internal climate variability, as estimated from d4PDF-WaveHs, in the context of other sources of uncertainty. In terms of the global annual mean and maximum  $H_s$  time series, CMIP5-COWCLIP notably exhibits the largest variability, as expected since this ensemble considers a large variety of wave modelling approaches and configurations (see Figure S17). However, we find that the uncertainty of the global averaged trends (of both annual mean and maximum  $H_s$  trends) is fairly similar for the three data products, with significantly overlapping ranges of variability (see Figure 6 and Figure S18). d4PDF-WaveHs tends to have a lower spread, followed by CMIP5-HsWang and CMIP5-COWCLIP, respectively, which might indicate that the global variability induced by climate models is larger than the internal climate variability, and that adding another factor of uncertainty (wave method) further increases the variability, as expected. However, this is not the case for all regions. For example, the North Atlantic annual mean  $H_s$  trend variability derived from d4PDF-WaveHs equals the CMIP5-COWCLIP counterpart (while exceeding the CMIP5-HsWang value). In



any case, the differences in spread are mild and could be caused by the difference in sampling space (different ensemble sizes). For example, Figure S19 shows the spread of global trends that would be obtained from 20- and 48-size sub-ensembles randomly sampled from d4PDF-WaveHs, in comparison to the original 100-size ensemble.

Finally, we addressed the risk of using a single member to assess trends. In some areas of the Southern Ocean, there is a likelihood of up to 50% to miss the statistically significant strong positive trend that is clearly shown by the ensemble average for the annual mean  $H_s$  (Figure 7A). The chances to get the same trend sign (regardless of the significance) are however larger in those areas. In contrast, the likelihood to obtain the same trend sign decreases to about 50% in the North Atlantic (Figure 7B) as the wave climate in this region has larger internal climate variability, for which individual members can predict either positive or negative trends locally (Figures S4, S5). However, the results also show that, for the annual mean  $H_s$ , it is very unlikely for an individual member to have a statistically significant trend of the opposite sign to the ensemble average trend (Figure 7C). This only occurred in at most 5 out of the 100 members over a few scattered areas at the mid to high latitudes.

For the annual maximum  $H_s$ , the chances to get the same trend conclusion are very high, especially for the areas with positive trends (Figure 7A). This can be explained by the low statistical significance found in most of the members (using the more restrictive method to assess robustness, see Section 2.2), but there is a larger disagreement (>50% runs) in simulating the same trend sign (Figure 7B). Also, the areas where up to 5 individual ensemble members might simulate a statistically significant trend of the opposite sign to that of the ensemble average are more abundant and cover most of the mid and high latitudes (Figure 7C). The corresponding ensemble average of the annual mean and maximum  $H_s$  trends are shown in Figures S20 and S21.

The same analysis performed for sub-ensembles with varying ensemble size reveals that, as expected, the required ensemble size to replicate the results obtained from the whole 100-member ensemble depends on the  $H_s$  statistic and the region in question (see Figures S22–25). For example, for the annual mean  $H_s$ , the areas of trend conclusion disagreement (which considers both trend sign and significance) over the Southern Ocean, notably shrink when we consider sub-ensembles with size close to 20 members (Figure S22). Differently, if we want to simulate the same annual mean  $H_s$  trend sign over the North Atlantic, a 10-size ensemble seems to be sufficient (Figure S23). For the annual maximum  $H_s$ , we would generally require larger ensembles to obtain the same trend sign (for example close to 40 for the North Atlantic Ocean, see Figure S25), as expected due to the larger uncertainty associated with simulating extremes. Overall, at global scale we argue that a trend assessment using a SMILE-based ensemble with size from 10 to 20 would reduce significantly the likelihood for an erroneous trend assessment result.

## 4 DISCUSSION

We have used the d4PDF-WaveHs, the first SMILE-based large wave height ensemble to assess the effects of internal climate variability on trend assessment results. d4PDF-WaveHs consists of 100 ensembles of 60-year historical  $H_s$  simulations (1951–2010). In this study, we focused on the analysis of the annual mean and maximum  $H_s$  trends and the role that the internal variability plays in their assessment; but this dataset can be further exploited in future studies to investigate the role of internal climate variability on other target quantities, such as low-frequency  $H_s$  extremes.

The trends obtained from d4PDF-WaveHs are also compared to those derived from modern reanalysis datasets and from climate model simulations. This is of particular relevance given the notable discrepancies among reanalysis datasets in recent studies (Stopa et al., 2019; Sharmar et al., 2020). Moreover, this study also contributes to improve the current understanding of the internal wave climate variability, which is a key factor among other relevant sources of uncertainty affecting wave simulations (Morim et al., 2019).

We found a clear and statistically significant positive trend for the annual mean  $H_s$  over the Southern Ocean exceeding 0.5

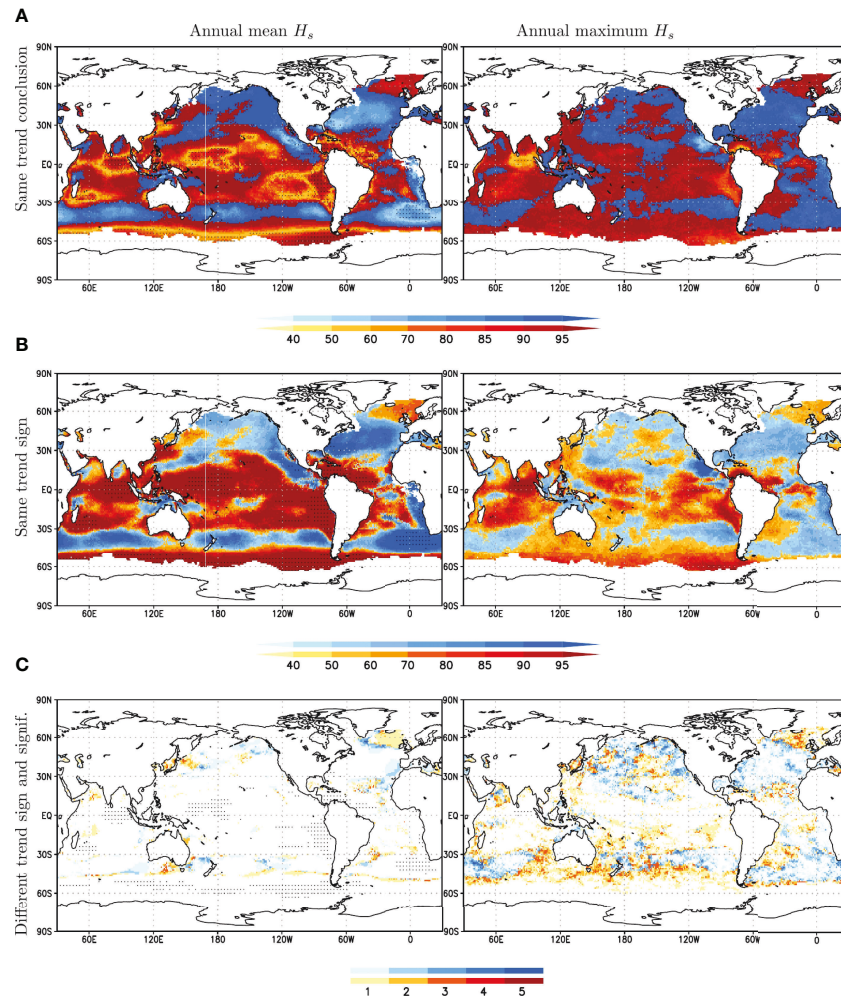


**FIGURE 7** | Fraction of ensemble members (%) with the same trend conclusion **(A)**, the same trend sign **(B)** and different trend sign that is statistically significant **(C)**, as compared to the ensemble average for the annual mean  $H_s$  (left) and the annual maximum  $H_s$  (right) (see Section 2.2 for more details). Warm(cold) shades indicate the ensemble mean trend is positive(negative). Stippling indicates the ensemble mean trend is statistically significant.

cm/yr in some areas. Statistically positive trends with a lower intensity (up to 0.3 cm/yr) were also seen for tropical areas. Over the North Pacific and Atlantic Oceans, the averaged trends are not statistically significant, which is caused by the large inter-annual variability in these areas, where individual ensemble-members might simulate opposite trends although most of the simulations show a negative regional trend. The annual maximum  $H_s$  trends show a similar spatial pattern but results are not statistically significant. Significance here is assessed with a two-step method that accounts for both the inter-annual variability in each individual member as well as the variability among members, as recommended by the IPCC to assess robustness.

The results here provide more evidence that modern reanalysis datasets are not suitable observation proxies to study historical wave height trends due to their temporal inhomogeneities. The main reason is arguably the increasing amount and type of available observations used in data assimilation, which

coincides with breakpoints that can be visually identified in the annual mean  $H$  time series. In most regions, ERA5 and ERAint simulate positive trends while CFSR simulate negative trends, and the results simulated by d4PDF-WaveHs fall in between these two family products. The discrepancies are more notable for the annual mean  $H_s$  than for the annual maximum  $H_s$ , which seems to be less affected by temporal inhomogeneities. While differences in resolution and wave modelling methodologies might contribute to add variability in the assessment of the wave climatology (particularly the extremes), the temporal inhomogeneity induced by data assimilation is arguably the main factor leading to the major discrepancies observed for the annual mean and maximum  $H_s$  trends.

Our results show that there is a non-negligible probability to miss-assess trends when using a single realization (member). Although we would likely detect the strong positive trend in the annual mean  $H_s$  over Southern Ocean with just one member, we could mis-estimate their spatial extension and therefore



mis-assess the trend locally (in up to 50% of the ensemble members). For the annual maximum  $H_s$ , there is a larger uncertainty; opposite trends are simulated by the individual members, particularly in the North Pacific and North Atlantic oceans. However, it is unlikely to obtain an individual trend that is fundamentally opposite of the corresponding ensemble average. To reduce the risk to miss-assess trends at global scale, it would be necessary to use at least 10 members. However, an optimal size depends on the statistic quantity and region analyzed.

This study also shows that, despite climate model variability leading to a large uncertainty for the assessment of the annual mean and maximum  $H_s$  time series, the role of the internal climate variability in the resulting trends is comparable to the uncertainty derived from climate models and wave methods. However, this comparison is challenging given the uneven sampling of the uncertainty factors in the available datasets. Typically, ensembles that consider different climate models have a limited amount of realizations and SMILEs are based on a single climate model by definition. Future studies with climate datasets that better represent the whole spectrum of uncertainty would likely help understand better the contribution of these uncertainty factors.

The dataset and analysis presented in this study bring significant insight into the role of internal variability in the context of the wave height trend assessment. However, results are based on a single-model ensemble and therefore rely on the ability of this particular climate model to replicate the internal climate variability. It would be ideal to perform a similar analysis with other SMILE-based large wave ensembles that consider other climate models in order to derive more robust conclusions that are not specific to a particular climate model. Additionally, results rely on the performance of the statistical wave modelling approach to obtain  $H_s$ . In this regard, we plan to re-calibrate the statistical wave modelling approach with a higher resolution product (e.g. ERA5) which might improve the underestimation seen in the tropics, and better capture the storms with sharp SLP gradients. Moreover, to fully address the main wave-driven impacts, we need to also consider and analyze other wave variables such as wave period and wave direction.

## REFERENCES

- Aarnes, O., Abdalla, S., Jean-Raymond, B. and Breivik, O. (2015). Marine Wind and Wave Height Trends at Different Era-Interim Forecast Ranges. *J. Climate* 28, 819–837. doi: 10.1175/JCLI-D-14-00470.1
- Box, G. and Cox, D. (1964). An Analysis of Transformation (With Discussion). *J. R. Stat. Soc.* 26, 211–246.
- Cavaleri, L., Fox-Kemper, B. and Hemer, M. (2012). Wind Waves in the Coupled Climate System. *Bullet. Am. Meteorolog. Soc.* 93, 1651–1661. doi: 10.1175/BAMS-D-11-00170.1
- Dee, D.P., Uppala, S.M., Simmons, A.J., Berrisford, P., Poli, P., Kobayashi, S. et al. (2011). The ERA-Interim Reanalysis: Configuration and Performance of the Data Assimilation System. *Quarterly. J. R. Meteorolog. Soc.* 137, 553–597. doi: 10.1002/qj.828
- Dodet, G., Piolle, J.-F., Quilfen, Y., Abdalla, S., Accensi, M., Arduin, F. et al. (2020). The Sea State CCI Dataset V1: Towards a Sea State Climate Data Record Based

## DATA AVAILABILITY STATEMENT

The raw data supporting the conclusions of this article will be made available by the authors, without undue reservation.

## AUTHOR CONTRIBUTIONS

MC-P wrote the manuscript. MC-P and XW co-designed/led the study. YF contributed to the statistical data analysis. XW conceived and produced the d4PDF-WaveHs dataset with the Disaster Prevention Research Institute (DPRI) of Kyoto University providing funding support for her two-month sabbatical at DPRI hosted by NM. YF, RC, NM and TS contributed to the production of the d4PDF-WaveHs dataset. NM and TS provided the d4PDF atmospheric data and WW3 wave simulations used for validation. All authors contributed to manuscript revision, and approved the submitted version.

## FUNDING

The Disaster Prevention Research Institute (DPRI) of Kyoto University provided funding support (including roundtrip airfare) for XW's two-month sabbatical at DPRI 29L01.

## ACKNOWLEDGMENTS

This study utilized the d4PDF, which was produced using the Earth Simulator as “Strategic Project with Special Support” of JAMSTEC in cooperation with the Program for Risk Information on Climate Change (SOUSEI), TOUGOU, the Social Implementation Program on Climate Change Adaptation Technology (SI-CAT), which all were sponsored by the Ministry of Education, Culture, Sports, Science and Technology of Japan (MEXT) Disaster Prevention Research Institute (DPRI) funding number is 29L01.

## SUPPLEMENTARY MATERIAL

The Supplementary Material for this article can be found online at: <https://www.frontiersin.org/articles/10.3389/fmars.2022.847017/full#supplementary-material>

on Satellite Observations. *Earth Syst. Sci. Data* 12, 1929–1951. doi: 10.5194/essd-12-1929-202

Grifoll, M., Martínez de Osés, F. and Castells, M. (2018). Potential Economic Benefits of Using a Weather Ship Routing System at Short Sea Shipping. *WMO. J. Maritime. Affairs.* 17, 195–211. doi: 10.1007/s13437-018-0143-6

Griggs, G. and Reguero, B. (2021). Coastal Adaptation to Climate Change and Sea-Level Rise. *Water* 13, 2151. doi: 10.3390/w13162151

Gudmestad, O. T. (2020). Modelling of Waves for the Design of Offshore Structures. *J. Mar. Sci. Eng.* 8, 293. doi: 10.3390/jmse8040293

Herbach, H., Bell, B., Berrisford, P., Hirahara, S., Horányi, A., Muñoz-Sabater, J. et al. (2020). The ERA5 Global Reanalysis. *Quarterly. J. R. Meteorolog. Soc.* 146, 1999–2049. doi: 10.1001/qj.3803

Huppert, K. L., Perron, J. T. and Ashton, A. D. (2020). The Influence of Wave Power on Bedrock Sea-Cliff Erosion in the Hawaiian Islands. *Geology* 48, 499–503. doi: 10.1130/G47113.1

- International Organization for Standardization (2007). *ISO 21650: Actions From Waves and Currents on Coastal Structures (ISO/TC 98/SC 3, ICS 91.080.01)*. Available at: <https://www.iso.org/standard/35955.html>
- IPCC (2013). "Climate Change 2013," in *The Physical Science Basis. Contribution of Working Group I to the Fifth Assessment Report of the Intergovernmental Panel on Climate Change*, vol. 1535. Eds. Stocker, T. F., Qin, D., Plattner, G.-K., Tignor, M., Allen, S. K., Boschung, J., Nauels, A., Xia, Y., Bex, V. and Midgley, P. M. (Cambridge, United Kingdom and New York, NY, USA: Cambridge University Press).
- Ishii, M. and Mori, N. (2020). d4PDF: Large-Ensemble and High-Resolution Climate Simulations for Global Warming Risk Assessment. *Prog. Earth Planet. Sci.* 7. doi: 10.1186/s40645-020-00367-7
- Kirchmeier-Young, M., Zhang, X., and Wan, H. (2021): Climate Change Attribution With Large Ensembles. *EGU General Assembly 2021*, EGU21-3404. doi: 10.5194/egusphere-egu21-3404
- Maher, N., Milinski, S. and Ludwig, R. (2021). Large Ensemble Climate Model Simulations: Introduction, Overview, and Future Prospects for Utilizing Multiple Types of Large Ensemble. *Earth System Dynamics*. 12, 401–418. doi: 10.5194/esd-12-401-2021
- Mei, W., Kamae, Y., Xie, S.-P. and Yoshida, K. (2019). Variability and Predictability of North Atlantic Hurricane Frequency in a Large Ensemble of High-Resolution Atmospheric Simulations. *J. Climate* 32, 3153–3167. doi: 10.1175/JCLI-D-18-0554.1
- Melet, A., Almar, R., Hemer, M., Le Cozannet, G. and Ruggiero, P. (2020). Contribution of Wave Setup to Projected Coastal Sea Level Changes. *J. Geophys. Res. Oceans*. 125, e2020JC016078. doi: 10.1029/2020JC016078
- Melet, A., Meyssignac, B., Almar, R. and Le Cozannet, G. (2018). Under-Estimated Wave Contribution to Coastal Sea-Level Rise. *Nat. Climate Change* 8, 234–139. doi: 10.1038/s41558-018-0088-y
- Milinski, S., Maher, N. and Olonscheck, D. (2020). How Large Does a Large Ensemble Need to be? *Earth Syst. Dynamics*. 11, 885–901. doi: 10.5194/esd-11-885-2020
- Mizuta, R., Murata, A., Ishii, M., Shiogama, H., Hibino, K., Mori, N., et al. (2017). Over 5,000 Years of Ensemble Future Climate Simulations by 60-Km Global and 20-Km Regional Atmospheric Models. *Bull. Am. Meteorolog. Soc.* 98, 1383–1398. doi: 10.1175/BAMS-D-16-0099.1
- Mizuta, R., Yoshimura, H., Murakami, H., Matsueda, M., Endo, H., Ose, T., et al. (2012). Climate Simulations Using Mri-Agcm3.2 With 20-Km Grid. *J. Meteorolog. Soc. Japan. Ser. II* 90, 233–258. doi: 10.2151/jmsj.2012-A12
- Morim, J., Hemer, M., Andutta, F., Shimura, T. and Cartwright, N. (2020). Skill and Uncertainty in Surface Wind Fields From General Circulation Models: Intercomparison of Bias Between AGCM, AOGCM and ESM Global Simulations. *Int. J. Climatol.* 40, 2659–2673. doi: 10.1002/joc.6357
- Morim, J., Hemer, M., Wang, X. L., Cartwright, N., Trenham, C., Semedo, A., et al. (2019). Robustness and Uncertainties in Global Multivariate Wind-Wave Climate Projections. *Nat. Climate Change* 9, 711–718. doi: 10.1038/s41558-019-0542-5
- Reguero, B. G., Nigo, L., Losada, I. and Méndez, F. J. (2019). A Recent Increase in Global Wave Power as a Consequence of Oceanic Warming. *Nat. Commun.* 10, 205. doi: 10.1038/s41467-018-08066-0
- Saha, S., Moorthi, S., Wu, X., Wang, J., Nadiga, S., Tripp, P., et al. (2014). The NCEP Climate Forecast System Version 2. *J. Climate* 146, 2185–2208. doi: 10.1175/JCLI-D-12-00823.1
- Santos, V. M., Casas-Prat, M., Poschod, B., Ragno, E., van den Hurk, B., Hao, Z., et al. (2021). Statistical Modelling and Climate Variability of Compound Surge and Precipitation Events in a Managed Water System: A Case Study in the Netherlands. *Hydrol. Earth System. Sci.* 25, 3595–3615. doi: 10.5194/hess-25-3595-2021
- Sharmar, V. D., Markina, M. Y. and Gulev, S. K. (2020). Global Ocean Wind-Wave Model Hindcasts Forced by Different Reanalyses: A Comparative Assessment. *J. Geophys. Res. Oceans*. 126, e2020JC016710. doi: 10.1029/2020JC016710
- Shimura, T. and Nobuhito, M. (2019). High-Resolution Wave Climate Hindcast Around Japan and its Spectral Representation. *Coast. Eng.* 151, 1–9. doi: 10.1016/j.coastaleng.2019.04.013
- Song, Z., Bao, Y., Zhang, D., Shu, Q., Song, Y. and Qiao, F. (2021). Centuries of Monthly and 3-Hourly Global Ocean Wave Data for Past, Present, and Future Climate Research. *Nat. Sci. Data* 7. doi: 10.1038/s41597-020-0566-8
- Stive, M. J., Aarninkhof, S. G., Hamm, L., Hanson, H., Larson, M., Wijnberg, K. M., et al. (2002). Variability of Shore and Shoreline Evolution. *Coast. Eng.* 47, 211–235. doi: 10.1016/S0378-3839(02)00126-6
- Stopa, J. E., Ardhuin, F., Stutzmann, E. and Lecocq, T. (2019). Sea State Trends and Variability: Consistency Between Models, Altimeters, Buoys and Sesimic Dat-2016). *J. Geophys. Res. Oceans* 124, 2923–3940. doi: 10.1029/2018JC014607
- Swart, N. C., Fyfe, J. C., Hawkins, E., Kay, J. E. and Jahn, A. (2015). Influence of Internal Variability on Arctic Sea-Ice Trends. *Nat. Climate Change* 5, 86–89. doi: 10.1038/nclimate2483
- vonStorch, H. and Zwiers, F. (1999). *Statistical Analysis in Climate Research* (Cambridge, United Kingdom: Cambridge University Press).
- Wang, X. L., Feng, Y. and Swail, V. R. (2012). North Atlantic Wave Height Trends as Reconstructed From the Twentieth Century Reanalysis. *Geophys. Res. Lett.* 39, L18705. doi: 10.1029/2012GL053381
- Wang, X. L., Feng, Y. and Swail, V. R. (2014). Changes in Global Ocean Wave Heights as Projected Using Multimodel Cmp5 Simulations. *Geophys. Res. Lett.* 41, 1026–1034. doi: 10.1002/2013GL058650
- Wang, X. L., Feng, Y. and Swail, V. R. (2015). Climate Change Signal and Uncertainty in CMIP5-Based Projections of Global Ocean Surface Wave Heights. *J. Geophys. Res. Oceans* 120, 3859–3871. doi: 10.1002/2015JC010699
- Wang, X. L. and Swail, V. R. (2001). Changes of Extreme Wave Heights in Northern Hemisphere Oceans and Related Atmospheric Circulation Regimes. *J. Climate* 14, 2204–2221. doi: 10.1175/1520-0442(2001)014<2204:COEWHI>2.0.CO;2
- Wohlkand, J., Omrani, N., Withaut, D. and Keenlyside, N. (2019). Inconsistent Wind Speed Trends in Current Twentieth Century Reanalyses. *J. Geophys. Res. Atmos.* 124, 1931–1940. doi: 10.1029/2018JD030083
- Yang, S. and Oh, J.-H. (2020). Effects of Modes of Climate Variability on Wave Power During Boreal Summer in the Western North Pacific. *Nat. Sci. Rep.* 10, 517. doi: 10.1038/s41598-020-62138-0

**Conflict of Interest:** The authors declare that the research was conducted in the absence of any commercial or financial relationships that could be construed as a potential conflict of interest.

**Publisher's Note:** All claims expressed in this article are solely those of the authors and do not necessarily represent those of their affiliated organizations, or those of the publisher, the editors and the reviewers. Any product that may be evaluated in this article, or claim that may be made by its manufacturer, is not guaranteed or endorsed by the publisher.

Copyright © 2022 Casas-Prat, Wang, Mori, Feng, Chan and Shimura. This is an open-access article distributed under the terms of the Creative Commons Attribution License (CC BY). The use, distribution or reproduction in other forums is permitted, provided the original author(s) and the copyright owner(s) are credited and that the original publication in this journal is cited, in accordance with accepted academic practice. No use, distribution or reproduction is permitted which does not comply with these terms.



## OPEN ACCESS

## EDITED BY

Youyu Lu,  
Bedford Institute of Oceanography  
(BIO), Canada

## REVIEWED BY

Vagner Ferreira,  
Hohai University, China  
Ozgur Kisi,  
Ilia State University, Georgia

## \*CORRESPONDENCE

Adem Akpınar  
ademakpinar@uludag.edu.tr

## SPECIALTY SECTION

This article was submitted to  
Physical Oceanography,  
a section of the journal  
Frontiers in Marine Science

RECEIVED 28 April 2022

ACCEPTED 19 July 2022

PUBLISHED 10 August 2022

## CITATION

Akçay F, Bingölbali B, Akpınar A and  
Kankal M (2022) Trend detection by  
Innovative polygon trend analysis  
for winds and waves.  
*Front. Mar. Sci.* 9:930911.  
doi: 10.3389/fmars.2022.930911

## COPYRIGHT

© 2022 Akçay, Bingölbali, Akpınar and  
Kankal. This is an open-access article  
distributed under the terms of the  
[Creative Commons Attribution License  
\(CC BY\)](https://creativecommons.org/licenses/by/4.0/). The use, distribution or  
reproduction in other forums is  
permitted, provided the original  
author(s) and the copyright owner(s)  
are credited and that the original  
publication in this journal is cited, in  
accordance with accepted academic  
practice. No use, distribution or  
reproduction is permitted which does  
not comply with these terms.

# Trend detection by innovative polygon trend analysis for winds and waves

Fatma Akçay<sup>1</sup>, Bilal Bingölbali<sup>2</sup>, Adem Akpınar<sup>1\*</sup>  
and Murat Kankal<sup>1</sup>

<sup>1</sup>Civil Engineering Department, Bursa Uludağ University, Bursa, Turkey, <sup>2</sup>İnegöl Vocation Schools Bursa Uludağ University, Bursa, Turkey

It is known that densely populated coastal areas may be adversely affected as a result of the climate change effects. In this respect, for coastal protection, utilization, and management it is critical to understand the changes in wind speed (WS) and significant wave height (SWH) in coastal areas. Innovative approaches, which are one of the trend analysis methods used as an effective way to examine these changes, have started to be used very frequently in many fields in recent years, although not in coastal and marine engineering. The Innovative Polygon Trend Analysis (IPTA) method provides to observe the one-year behavior of the time series by representing the changes between consecutive months as well as determining the trends in each individual month. It is not also affected by constraints such as data length, distribution type or serial correlation. Therefore, the main objective of this study is to investigate whether using innovative trend methods compared to the traditional methods makes a difference in trends of the climatological variables. For this goal, trends of mean and maximum WS and SWH series for each month at 33 coastal locations in Black Sea coasts were evaluated. Wind and wave parameters WS and SWH were obtained from 42-year long-term wave simulations using Simulating Waves Nearshore (SWAN) model forced by the Climate Forecast System Reanalysis (CFSR). Monthly mean and maximum WS and SWH were calculated at all locations and then trend analyses using both traditional and innovative methods were performed. Low occurrence of trends were detected for mean SWH, maximum SWH, mean WS, and maximum WS according to the Mann-Kendall test in the studied months. The IPTA method detected more trends, such as the decreasing trend of the mean SWH at most locations in May, July and November December. The lowest (highest) values were seen in summer (winter), according to a one-year cycle on the IPTA template for all variables. According to both methods, most of the months showed a decreasing trend for the mean WS at some locations in the inner continental shelf of the southwestern and southeastern Black Sea. The IPTA method can capture most of the trends detected by the Mann-Kendall method, and more missed by the latter method.

## KEYWORDS

monthly trend analysis, innovative polygon trend analysis, Mann-Kendall test, significant wave height, wind speed, Black Sea

## 1. Introduction

The coastal areas are generally densely populated. The attractiveness of the coasts leads to an increased number of buildings and assets close to the coastline. For example, in 2000, half of the major cities, counting more than 500,000 inhabitants, were located within 50 km of the coastline (UNEP, 2006). Variations in sea level caused by climate change, wave conditions, and storm surges are only a few significant environmental forces that have physical effects along the coast (Camus et al., 2017). Human activities thus stress coastal areas, and the impacts of climate change are expected to worsen the problems that coastal areas are already facing (IPCC, 2013).

The wind speed, the duration of the wind, wind direction, and fetch are the main factors influencing the wave climate in the open ocean. Therefore, the change in the wind pattern directly influences the wave height and period (Bhavithra and Sannasiraj, 2022). Waves combine local wind-sea and swell coming from distant storms (Young, 1999a). Despite being entirely forced by the wind field, the long-term trends of wave height may be affected by low-frequency variability, e.g., an increasing number of cyclones, in the form of a swell contribution (Young, 1999b; Gulev and Grigorieva, 2006). The need for long-term and reliable time series of marine near-surface winds and significant wave height (SWH) is increasing as climate projections require a baseline climatology against which to be compared, and even more so if dynamical models of the sea state are to be included in future coupled climate scenarios (Cavaleri et al., 2012; Dobrynin et al., 2012). There are also more immediate needs for reliable time series of historical wind and wave climates, such as estimates of return values in areas without observational records (Caires and Sterl, 2005; Aarnes et al., 2012; Breivik et al., 2013; Breivik et al., 2014) or decadal trends in wind and wave parameters.

Trend analysis examines whether the direction of increase or decrease in a time series changes over time. There are two types of trend analysis methods: parametric and nonparametric. The parametric approaches are dependent on the assumption that data fit the normal distribution. They are often preferable in trend analysis research since nonparametric methods do not make this assumption (Onyutha, 2016; Akçay et al., 2022). Mann-Kendall, Spearman's rho, and Sen's trend slope tests are some examples of nonparametric methods. The Mann-Kendall test is often preferred in trend analysis of hydro-meteorological data (Saphioğlu et al., 2014; Caloiero et al., 2018; Ali et al., 2019; Ay, 2020; Şen et al., 2021). It is also frequently used in trend analysis of wave and wind data (Shanas and Kumar, 2015; Akpınar and Bingölbali, 2016; Aydoğan and Ayat, 2018; Meucci et al., 2020; Amarouche et al., 2021). Innovative methods in trend analysis have attracted attention in recent years (Şen, 2012; Şen, 2014; Şen, 2017; Güçlü, 2018; Şen, 2018; Şen et al., 2019; Güçlü et al., 2020; Şen, 2021). The Innovative

Trend Analysis (ITA) proposed by Şen (2012) forms the basis of these innovative approaches. In this method, the data is divided into two equal parts. Both half series are sorted in ascending order, and the 45° line is added to the chart. If the scattering points fall above (below) the 45° line, it indicates an increasing (decreasing) trend. If the scattering points are lined up just above the 45° line, there is no change between the first and second half data. Besides, the data can be divided into low, medium, and high groups in this method. The Innovative Polygon Trend Analysis (IPTA) is one of the novel trend methods proposed by Şen et al. (2019). In this method, polygon patterns are obtained using the mean, minimum, maximum, standard deviation and skewness parameters of the data at different time scales (daily, monthly, etc.). In this way, the one-year behavior of the time series is symbolized. This method can obtain information when determining the trend and the magnitude and slope of trend transitions between successive segments (e.g., months). Innovative approaches are frequently used in investigating the trends of hydro-meteorological parameters (Haktanir and Çitakoğlu, 2014; Ay and Kisi, 2015; Dabanlı et al., 2016; Caloiero et al., 2018; Sanikhani et al., 2018; Kuriqi et al., 2020; Harkat and Kisi, 2021; Ahmed et al., 2022). However, the use of these methods in investigating the trend of wave parameters is quite limited (Caloiero et al., 2019; De Leo et al., 2020; De Leo et al., 2021). The ITA procedure recommended by Şen (2012) was applied in these studies. The IPTA method is applied to wave and wind parameters for the first time in this study.

There are various trend analysis studies conducted on the Black Sea (Valchev et al., 2012; Akpınar and Bingölbali, 2016; Divinsky and Kosyan, 2017; Aydoğan and Ayat, 2018; Onea and Rusu, 2019; Çarpar et al., 2020; Divinsky and Kosyan, 2020; Islek et al., 2020; Islek et al., 2021). Valchev et al. (2012) investigated the linear trends of storminess, mean wind speed (WS), mean and total wave energy in the western Black Sea between 1948 and 2010. Akpınar and Bingölbali (2016) determined the long-term changes of SWH and WS in 33 selected locations on the Black Sea based on 31-year (1979–2009) long-term wave simulations using Simulating Waves Nearshore (SWAN) model forced by the Climate Forecast System Re-analysis. Trends for annual mean and maximum WSs and significant wave heights (SWH) were investigated based on the Mann-Kendall test. Divinsky and Kosyan (2017) studied the spatiotemporal variability of the Black Sea wave climate using 37-year (1979–2015) ERA-Interim wind fields. Aydoğan and Ayat (2018) investigated the long-term trends of SWH in the Black Sea, both on a basin average and spatial basis, on an annual and monthly basis using Sen's slope method and least square linear regression. Divinsky and Kosyan (2020) investigated trends in the average and maximum power of wind seas, swell, and mixed waves using Mann-Kendall test based on the MIKE 21 SW model results for a 40-year (1979–2018) ERA-Interim dataset. Çarpar et al. (2020) spatially investigated the long-term trends of mean and 95%

percentile wind speeds in the Black Sea between 1979 and 2016 on a monthly basis with the help of the Mann-Kendall test. [Islek et al. \(2020\)](#) studied the long-term change of wind characteristics (the wind speed, direction, number and duration of storms, and wind power density) using linear regression on the Black Sea with two widely used data sources ERA-Interim and CFSR, spanning 40-year (1979–2018). [Islek et al. \(2021\)](#) determined the long-term trends of mean and maximum SWH, mean wave period, mean wave direction, storm duration, and wave steepness using linear regression for two separate data sets (SWAN simulations forced with the ERA-Interim and NCEP/NCAR) covering the years 1979–2018 on the Black Sea.

As seen from the literature review in the area of interest and the world, trends for winds and waves were not examined using the IPTA method. With the help of polygon graphics in the IPTA method, a new methodology, the annual behavior of the time series can be followed from January to December. This method questions the existence of a trend each month and allows the direction and size of the transitions between months to be determined. It provides the opportunity to make visual comments as well as numerical data. The following are the primary goals of this research:

\* To investigate monthly long-term trends of mean and maximum SWH and WS at 33 locations along the Black Sea coast.

\* To examine the one-year behavior of the mean and maximum SWH and WS at locations by examining the transitions between months with the IPTA method, which will assess the month-to-month trends and slopes. In this way, to observe seasonal variations through monitoring changes in successive months.

\* To compare traditional (Mann-Kendall) with innovative (IPTA) methods.

For the purposes mentioned above, the locations and data in the study carried out by [Akpınar and Bingölbali \(2016\)](#) were preferred and used. The dataset produced by [Akpınar and Bingölbali \(2016\)](#) was extended with SWAN simulations until 2020. After expanding the data, monthly mean and maximum SWH and WS were obtained for 33 locations. Traditional (Mann-Kendall) and the state of the art (IPTA) trend methods were applied for 42-year mean and max WS and SWH for each month, and trends were determined.

## 2. Materials and methods

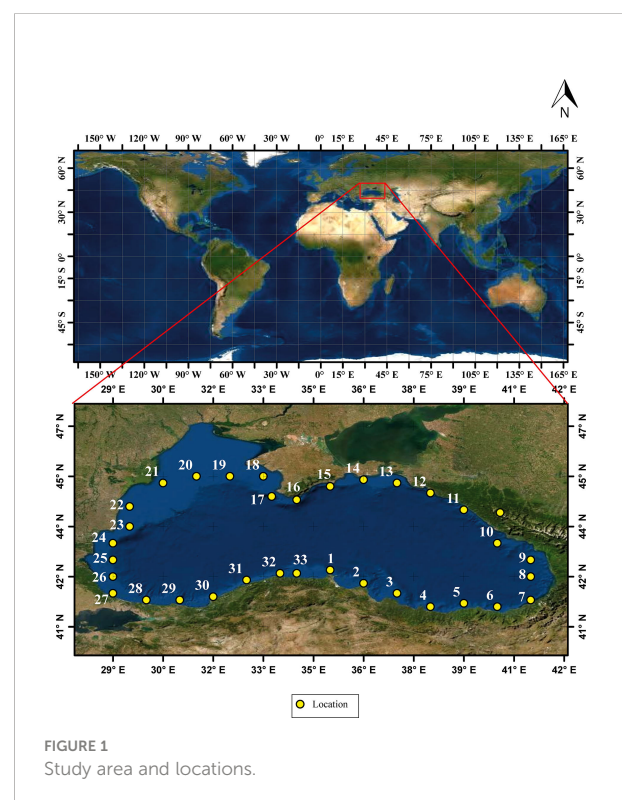
### 2.1. Study area and data used

The deep-water basin, which covers most of the sea, and the coastal shelf are two morphological aspects of the Black Sea. The shelf band in the northwestern section of the sea stretches up to 200 kilometers broad. A 20-kilometer-long continental slope and shelf differentiate the southern and eastern shores. With a

maximum depth of 2212 meters, the center part of the Black Sea basin is a relatively flat plain. The depths off the coasts of Crimea and the Caucasus are steadily rising, reaching 500 meters just a few kilometers from the shore ([Divinsky and Kosyan, 2020](#)). Thirty-three locations along these coastal regions of the Black Sea were determined within the scope of the study by taking a degree difference between longitudes. Of these 33 locations, nine are in the southeast (1–9), seven in the northeast (10–16), eight in the northwest (17–24), and nine in the southwest (25–33) of the Black Sea. The positions of these locations are shown in [Figure 1](#). Detailed information about the study area and locations can be found in [Akpınar and Bingölbali \(2016\)](#).

### 2.2. Wave model setup

Forced with CFSR wind fields, SWAN cycle III version 41.01, a third-generation wave model ([Booij et al., 1999](#); [Ris et al., 1999](#)), was used to generate and propagate wind waves between 1979 and 2009 by [Akpınar and Bingölbali \(2016\)](#) and extend the dataset until 2020 in the scope of the present study in the Black Sea. Thus, a 42-year long-term wind and wave dataset were formed. The SWAN model was in the third generation and operated in non stationary mode, with a time step of 15 min and one iteration per time step. [Akpınar et al. \(2012\)](#) found this setting to be adequately precise. As for the domain of the model, the entire Black Sea (27°E to 42°E and 40°N to 48°N) was taken



into consideration (shown [Figure 1](#)). In spherical coordinates, the Black Sea was within a 225×120 regular grid, including the Azov Sea. It has a consistent resolution of 0.067 degrees (1/15°) in both directions, translating into about 7.7 km of latitude and 5.43 km of longitude. Thus, there is 15 cells per latitude and longitude. Thirty-six directional bins and 35 frequency bins were used to discretize the spectrum function of the directional wave variance, which were geometrically positioned from 0.04 Hz to 1.0 Hz. The slightly dispersive BSBT (first-order upwind; backward space, backward time) scheme was used for the numerical scheme. Numerical settings of the SWAN model in the Black Sea were discussed in [Akpınar et al. \(2012\)](#), where the physical settings for the wave model calculations were done with a calibrated SWAN model by [Akpınar et al. \(2016\)](#). The formulation of [Komen et al. \(1994\)](#) was applied for wave growth by wind. [1991b](#); [Janssen's \(1991a\)](#) model's adaptations, where  $\delta=1$  according to [Rogers et al. \(2003\)](#), were used for wave energy dissipation by whitecapping. [2016](#); [Akpınar et al. \(2015\)](#) found that the  $C_{ds}=1.5$  coefficient for whitecapping dissipation was optimal for the SWAN model forced with the CFSR, so this study used the same. Nonlinear quadruplet interactions were calculated using the Discrete Interaction Approximation (DIA) by [Hasselmann et al. \(1985\)](#), in which  $\lambda$  is 0.25 and  $C_{nl4}$  is  $3 \times 10^7$ . A constant for the bottom-friction coefficient ( $C_{fjon}=0.038 \text{ m}^2 \text{ s}^{-3}$ ) based on JONSWAP was used to evaluate energy dissipation due to bottom friction as advised in [Zijlema et al. \(2012\)](#). The bore model of [Battjes and Janssen \(1978\)](#), in which  $\alpha$  is set to 1 and  $\gamma$  is 0.73, was used to model energy dissipation by depth-limited wave breaking. Triad Approximation (LTA) of [Eldeberky \(1996\)](#) was employed to calculate triad wave-wave interactions. The wave model was driven by NOAA, which includes two versions for CFSR winds. Version 1 of the CFS Re-analysis data set ([Saha et al., 2010](#)) is available from January 1, 1979, to March 31, 2011. Version 2 ([Saha et al., 2014](#)) of the data sets started in March 2011. CFSR wind data sets have a temporal resolution of 1 hour, and they possess a spatial resolution of  $0.3125^\circ \times 0.3125^\circ$  from 1979 to 2010 and  $0.2045^\circ \times 0.2045^\circ$  from 2011 to the present. With a resolution is 30 arcseconds in both latitude and longitude, the bathymetry shown in [Figure 1](#) was collected from the [GEBCO \(2014\)](#) database. Since currents and water level changes are insignificant to affect the model's results, they were simply not considered. Parameters like SWH and WS have been saved at a half-hour interval over the entire grid for 42 years. [2016](#); [Akpınar et al. \(2015\)](#) provide details on the calibration and validation of the SWAN model used.

## 2.3. Trend analysis

### 2.3.1. Mann-Kendall test

The Mann-Kendall test is a nonparametric trend analysis tool extensively used. The test statistic  $S$  of the method is

calculated as ([Mann, 1945](#); [Kendall, 1975](#)):

$$S = \sum_{i=1}^{n-1} \sum_{j=i+1}^n \text{sgn}(x_j - x_i) \quad (1)$$

where  $n$  is the data length,  $x_i$  and  $x_j$  indicates data values at times  $i$  and  $j$ , respectively.

$$\text{sgn}(x_j - x_i) = \begin{cases} 1 & ; & x_j > x_i \\ 0 & ; & x_j = x_i \\ -1 & ; & x_j < x_i \end{cases} \quad (2)$$

When  $n > 10$ , the variance of  $S$  is calculated as:

$$\text{Var}(S) = \left[ n(n-1)(2n+5) - \sum_{i=1}^p t_i(t_i-1)(2t_i+5) \right] / 18 \quad (3)$$

In Equation (3),  $p$  is the number of tied groups. It means there is equal data in the time series.  $t_i$  indicates how many times a data is repeated. Finally, the  $Z$  value is obtained from Equation (4):

$$Z = \begin{cases} \frac{S-1}{\sqrt{\text{Var}(S)}} & , & S > 0 \\ 0 & , & 0 \\ \frac{S+1}{\sqrt{\text{Var}(S)}} & , & S < 0 \end{cases} \quad (4)$$

The significance of this test is compared with the standard  $z$  value according to the confidence level (90%, 95%, 99%) determined in the standard normal distribution table. If the absolute calculated  $Z$  value is greater (less) than the standard  $z$  value, there is a significant trend (no trend). In the case of trend, if  $S$  is positive (negative), there is an increasing (decreasing) trend.

### 2.3.2. Innovative polygon trend analysis

Nonparametric tests have some limitations: Mann Kendall and Spearman's Rho tests are affected by the data length as a result of the simulation studies. As the data length increases, these tests become more powerful ([Yue and Wang, 2002](#); [Şen, 2012](#)). In addition, another disadvantage of the Mann-Kendall test is that it accepts serial independence. The presence of serial correlation in a time series showed that the Mann-Kendall test detects trends that do not actually exist ([Von Storch, 1995](#); [Şen, 2012](#)). However, [Douglas et al. \(2000\)](#) stated that the prewhitening method, which is used to reduce the serial correlation, will lose some of the existing trend. Contrary to these restrictions, Innovative Trend Analysis (ITA) method proposed by [Şen \(2012\)](#) does not contain any restrictions such as data length, normal distribution fit, and serial correlation removal. The validity of the method was tested by Monte Carlo simulations ([Şen, 2012](#)). The IPTA is one of the novel trend methods proposed by [Şen et al. \(2019\)](#). The method has no limitations as it is based on the ITA method. In this method,

polygon templates are obtained using the mean, minimum, maximum, standard deviation, and skewness parameters of the data at different time scales (daily, monthly, etc.). If the monthly time scale is preferred, the method is applied as: The monthly values (mean or maximum) of the relevant parameters were divided into two equal groups. In this way, the first half of 42 years of monthly data ( $21 \times 12 = 252$  months of data) represent the first group, while 252 months of data for the recent period represent the second group. After that, for each month, the averages (or optionally minimum, maximum, standard deviation, skewness, etc.) of the first half data group (monthly means of the past 21 years) and the second half data group (monthly means of the recent 21 years) were taken and the averages of the first group data were marked on the x-axis and the averages of the second group data were marked on the y-axis, and the 12 points obtained were connected and a polygon was obtained. Finally, the slope and length between two points are obtained by standard formulas. The difference between two months is measured by the line length (transition). The line slope concerning the horizontal axis is known as the trend slope. In the Cartesian coordinate system 1:1 ( $45^\circ$ ), a straight line divides the diagram into two parts. If scatter points are above (below) the 1:1 line, there is an increasing (decreasing) trend (Şen, 2012). In this method, the measure of significance can be obtained by the relative error percentage ( $\alpha$ ) between the two half-series (Şen, 2020):

$$\alpha = 100 \frac{|\bar{x}_1 - \bar{x}_2|}{\bar{x}_2} \quad (5)$$

When  $\alpha < \pm 5\%$ , it is considered that there is no significant trend in the given time series (Şen, 2020).

This approach is a nonparametric method with no assumption. The polygon symbolizes the one-year behavior of the time series. The straight lines connecting the months give information about the changes between months. If the slopes of the straight lines between the months are close, the contribution of the changes between months to the average change in the time series is not significant. The more dynamic and complex a hydro-meteorological event is, the more complex polygons tend to arise.

## 3. Results

### 3.1. Mann-Kendall test results

The Mann-Kendall Test results at 95% confidence level for mean and maximum SWH and WS are shown in Figures 2–5, respectively. A significant trend was not observed in approximately 89% of all time series (33 locations  $\times$  12 months) of mean SWH (Figure 2). No trends were detected in April, June, July, and October. Increasing trends in March (six locations), August (sixteen locations) and September (ten

locations) and decreasing trends in May (five locations) are noteworthy. Trends detected in other months are limited to a few locations. Increasing trends were concentrated in the southeast for March and in the northwest for August and September. Decreasing trends were generally observed at locations in the southwestern part. For the maximum SWH (Figure 3), no trend was observed in any location in February, June, July, and October. There is no trend in approximately 94% of the all time series, but an increasing trend is detected in 5%. Increasing trends were observed in January, August, and September and mostly in locations in the western region.

Figure 4 presents the monthly Mann-Kendall test results of mean WS. Similar to the mean SWH, increasing trends in the western and northern regions were observed in August and September. A decreasing trend was observed in all months at location 30, located in the southwest. An increasing (decreasing) trend was detected in the winter months (other months) in the some locations belonging to the southeast part where the trend was determined. No significant trends were found in 340 of the 396 (33 locations  $\times$  12 months) months (33 locations  $\times$  12 months) for maximum WS (Figure 5). In the southeast (west) region, the decreasing (increasing) trends in July and December (January) are noteworthy.

### 3.2. Innovative polygon trend analysis results

The graphs of the IPTA were obtained for 33 selected locations. A single plot for locations with similar characteristics was presented to provide a summary presentation and ease of review. Results were given for eight locations, two in each of the four identified regions (Figures 6–9). Eight different locations were preferred to evaluate different wind and wave parameters. Trends for the months are seen in the IPTA charts visually. However, when querying the trend assets of the months the relative error percentage ( $\alpha$ ) between two half series is required to be greater than 5%, as mentioned in the method section 2.3.2. Tables 1–4 are considered a significant trend only in the months that meet this condition. The IPTA graphs for the monthly mean SWH are shown in Figure 6. Significant trends detected in mean SWH are shown in Table 1. While a narrowing polygon structure was observed in the summer months at the locations in the southeast (locations 1–9) region, a wider polygon was encountered in the spring and winter months (Figure 6). The lowest (highest) SWH values are observed in the summer (winter) months when the one-year behavior is examined. Especially the increasing (decreasing) trends in March (November) are stronger in terms of distance to the  $45^\circ$  line. The transitions between February–March–April and October–November–December are large compared to the others. In October, November, and December, the transitions were increasing. They still remained in the decreasing trend region

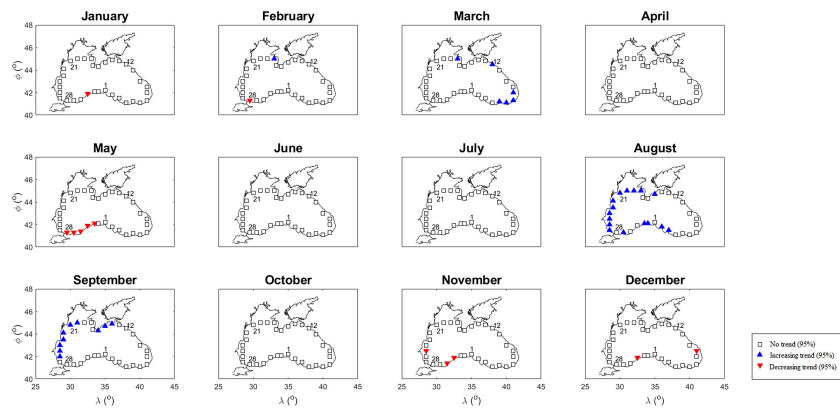


FIGURE 2  
Mann-Kendall results for monthly mean SWHs during 42 years between 1979 and 2020.

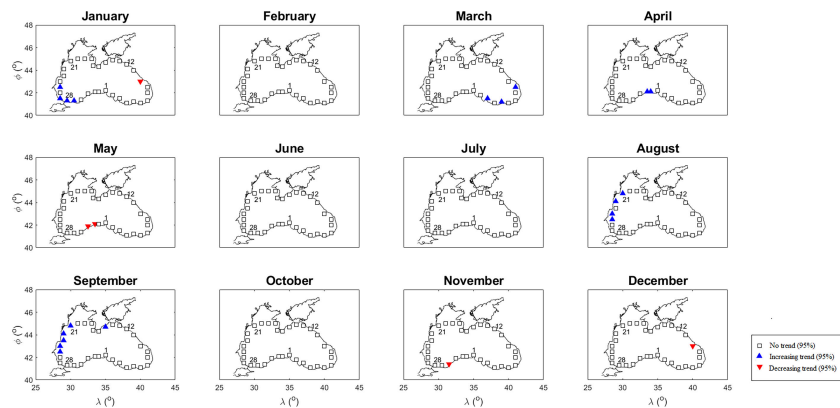


FIGURE 3  
Mann-Kendall results for monthly maximum SWHs during 42 years between 1979 and 2020.

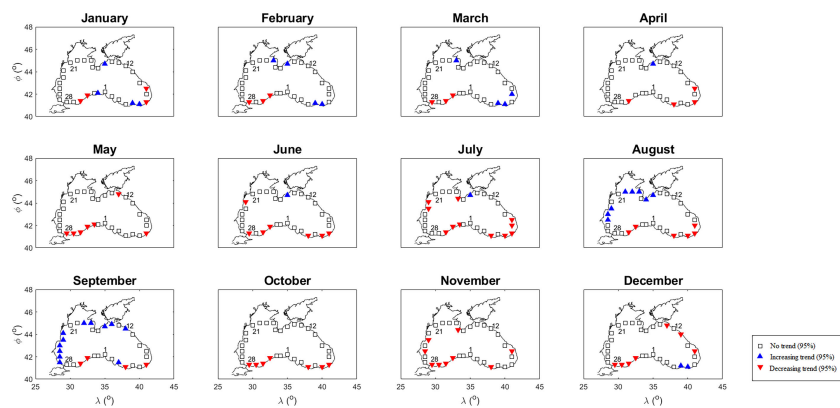
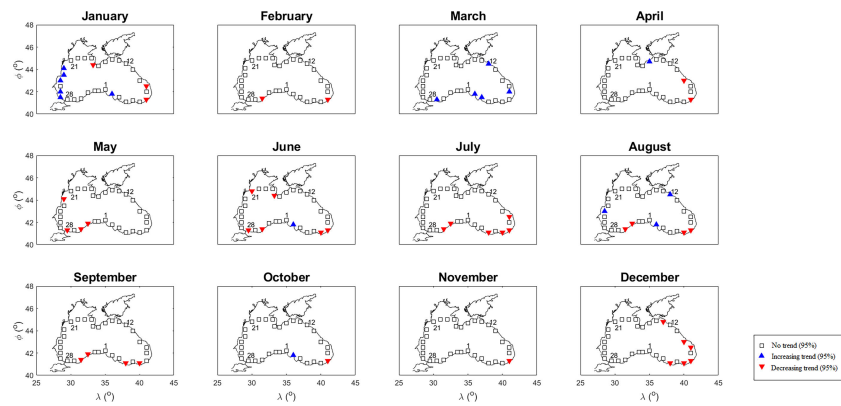
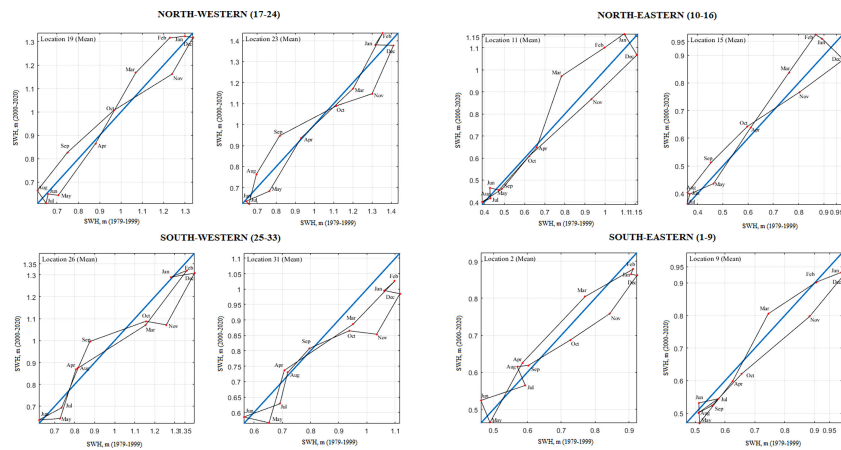


FIGURE 4  
Mann-Kendall results for monthly mean WSs during 42 years between 1979 and 2020.





**FIGURE 5**  
Mann-Kendall results for monthly maximum WSs during 42 years between 1979 and 2020.



**FIGURE 6**  
IPTA results for monthly mean SWHs during 42 years between 1979 and 2020.

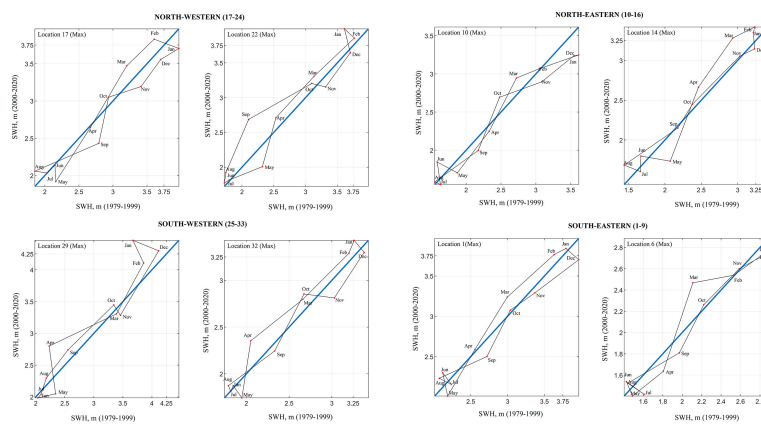


**FIGURE 7**  
IPTA results for monthly maximum SWHs during 42 years between 1979 and 2020.

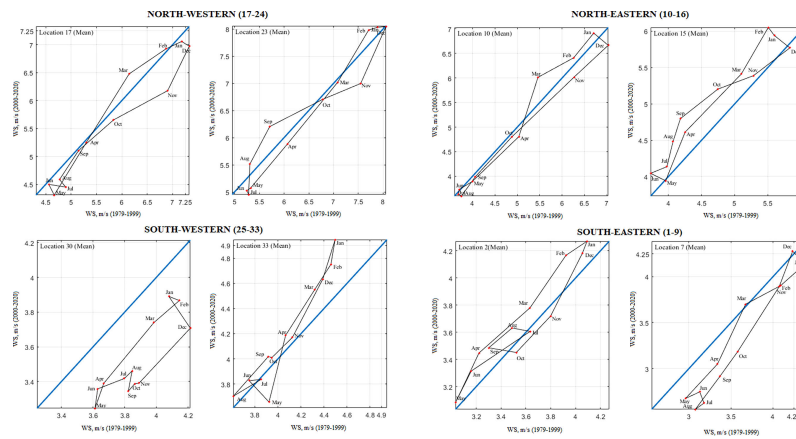


FIGURE 8  
IPTA results for monthly mean WSs during 42 years between 1979 and 2020.

because mean SWH values in the second half were lower than in the first half. Transitions between February–May period show a decrease. At locations 11 and 15 in the northeast region (locations 10-16), a significant increase (decrease) was observed for the mean SWH values in the January-March period (December). In the northwest (locations 17-24) locations, two separate loops were formed for low and high values. Transitions from July to August were from decreasing area to increasing area. A significant decreasing trend was observed for May and July and the October-December period (locations 25-33). The significant decreases in value in the second half of May, July, November, and December caused a complex structure in the transition between the months, with five different polygons. The IPTA graphs between successive months for the monthly maximum SWH were presented in Figure 7. Table 2 shows significant detected

trends in maximum SWH. Similar to the mean SWH, the highest (lowest) values were observed in the winter (summer) months for all locations. A wide loop starting from October and ending in March-April was formed at the upper values. Strong increasing (decreasing) trends were observed in March (May) in most locations. For maximum SWH, a complex structure was observed in which more than two loops were formed.

IPTA graphs for monthly mean WS were presented in Figure 8. It was observed that the data of the waves in the two locations representing the regions were generally compatible with

each other; this was not the case for the wind data. For example, increases (insignificant) occurred for almost all months in location 2 in the southeast, but a decreasing trend occurred in location 7 in the same region for almost all months. This

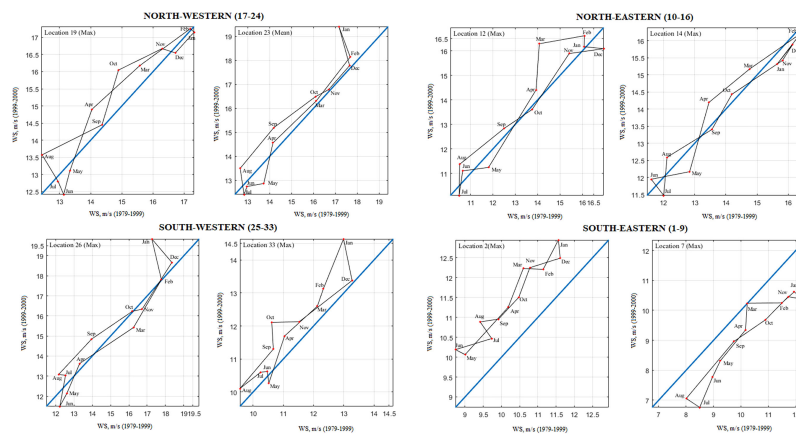


FIGURE 9  
IPTA results for monthly maximum WSs during 42 years between 1979 and 2020.









although there is no study in which the IPTA was applied to wave and wind data. Aydoğan and Ayat (2018) investigated the long-term trends of SWH in the Black Sea, both on a basin average and spatial basis, on an annual and monthly basis. Aydoğan and Ayat (2018) detected decreasing trends in the southeast (western) of the Black Sea in July (November) similar to the results of the IPTA method in this study. In May and December, Aydoğan and Ayat (2018) detected significant trends at less than the 90% confidence level in the Black Sea region. In this study, while the Mann-Kendall test detected a trend in very few locations for May and December (95%), the IPTA detected a decreasing trend in most locations. Aydoğan and Ayat (2018) analyzed the MIKE 21 SW model simulations between 1979 and 2016 using the ERA-Interim winds. The present study used SWAN wave model simulations between 1979 and 2020 using CFSR winds. It is therefore estimated that the reason for the inconsistency between the present study and the study performed by Aydoğan and Ayat (2018) for Mann Kendall trend test results may be due to the use of different reanalysis datasets, different physical parameterizations, and numerical settings usage in third-generation models and the difference in data lengths of the wave model used. Çarpar et al. (2020) spatially investigated the long-term trends of monthly mean and 95% percentile WSs in the Black Sea between 1979 and 2016. Results of ERA-Interim and CFSR winds were compared. According to the CFSR, increasing trends were seen in the southeast in March, June, and September. According to Mann-Kendall and IPTA in this study, trends were detected in very few locations for the southeast of the Black Sea in January, February, and March. In September (Çarpar et al., 2020), an increasing trend was determined, especially in the northern and eastern regions, according to the CFSR. This study detected increasing trends, especially in locations 18-27 in September, according to both methods. The reason why this study does not fully agree with Çarpar et al. (2020) may be the different data intervals.

The IPTA approach, according to the findings of this study, can broadly match the trends observed by the Mann-Kendall test. On top of it, the IPTA detected trends in more locations and months; this shows that this new approach to trend analysis is more sensitive. The past studies showed that the IPTA can successfully detect the trends detected by the Mann-Kendall test and give more sensitive results (Şan et al., 2021; Akçay et al., 2022). Innovative graphical ways can provide both visual numerical and verbal comments in addition to trendsetting success. IPTA is a new method in the literature that provides information about trend transitions between successive parts of a time series and determining the trend. No other study applies the IPTA to wave and wind data. By applying this method to mean and maximum wave and wind data, the one-year behavior of these data was observed with the help of polygons. Monthly transitions (January-February, February-March, etc.) were examined, and trends between consecutive months were also discovered. In this way, besides questioning the existence of the

trend in the examined months, its relationship with other months was obtained with the help of polygon. In the graphs of the mean SWHs, a polygon structure can be noticed, which narrows in the summer and widens in the spring and winter. The polygon graphs of the maximum SWHs had a more complex structure. The maximum WSs polygon graphs were narrower than the other variables, indicating that the behavior of the months was similar.

## 5. Conclusions

The results of this study have distinguished IPTA from the Mann-Kendall test, as IPTA detected more trends. The monthly mean and maximum SWH and WS did not show mostly a trend according to the Mann Kendall Test. Besides, the trends detected by the Mann-Kendall test were also caught by the IPTA at a very high rate. Considering the IPTA, in the analysis of mean SWH, the decreasing trends in the May, July, and November-December periods draw attention in most locations. In the analysis of maximum SWHs, most of the stations in the east showed an increasing trend in March, June and August, while all locations in the west showed a decreasing trend in May. Most of the months showed decreasing trends in the mean and maximum WS series at a few eastern locations. Based on a yearly cycle, the lowest (highest) mean SWH was seen in summer (winter); this is also valid for other variables: maximum SWH, average WS, and maximum WS. The transitions between months with the IPTA method showed that there are no temporal shifts, one of the effects of climate change in the meteorological and thus wave events. Wind or wave trends could be different for the same location and month due to distant storms. Significant wind trends in the same locations do not always coincide with SWH trends. This situation may be caused by the main wind direction and the waves that develop in reaction to the wind direction. It is thought that it will be useful to increase the number of locations and also analyze trends of the daily, annual and seasonal mean and maximum wave parameters.

## Data availability statement

The data generated during and/or analysed during the current study are available from the corresponding author on reasonable request.

## Author contributions

FA: Software, Formal analysis, Visualization, Writing - original draft. BB: Software, Resources, Formal analysis, Visualization, Writing - original draft. AA: Conceptualization, Methodology, Writing - review and editing, Supervision. MK:

Conceptualization, Methodology, Writing - review and editing, Supervision. All authors contributed to the article and approved the submitted version.

## Acknowledgments

We would like to thank The Scientific and Technological Research Council of Turkey (TUBITAK) for 2211-A Domestic Doctoral Scholarship Program and the Council of Higher Education for 100/2000 Doctoral Scholarship Project for the scholarship they provided to the first author. The authors would like to thank TUBITAK for their support of the previous project with grant number 214M436 because part of the wave data used in the present study was produced within that project.

## References

- Aarnes, O. J., Breivik, Ø., and Reistad, M. (2012). Wave extremes in the northeast Atlantic. *J. Climate* 25 (5), 1529–1543. doi: 10.1175/JCLI-D-11-00132.1
- Ahmed, N., Wang, G., Booi, M. J., Ceribasi, G., Bhat, M. S., Ceyhanlu, A. I., et al. (2022). Changes in monthly streamflow in the hindukush–Karakoram–Himalaya region of Pakistan using innovative polygon trend analysis. *Stochastic Environ. Res. Risk Assess.* 36 (3), 811–830. doi: 10.1007/s00477-021-02067-0
- Akçay, F., Kankal, M., and Şan, M. (2022). Innovative approaches to the trend assessment of streamflows in the eastern black Sea basin, Turkey. *Hydrolog. Sci. J.* 67 (2), 222–247. doi: 10.1080/02626667.2021.1998509
- Akpınar, A., Bekiroğlu, S., Van Vledder, G. P., Bingölbali, B., and Jafali, H. (2015). Temporal and spatial analysis of wave energy potential during south western coasts of the black Sea. *TUBITAK Project* 467.
- Akpınar, A., and Bingölbali, B. (2016). Long-term variations of wind and wave conditions in the coastal regions of the black Sea. *Nat. Hazards*. 84 (1), 69–92. doi: 10.1007/s11069-016-2407-9
- Akpınar, A., Bingölbali, B., and Van Vledder, G. P. (2016). Wind and wave characteristics in the black Sea based on the SWAN wave model forced with the CFSR winds. *Ocean. Eng.* 126, 276–298. doi: 10.1016/j.oceaneng.2016.09.026
- Akpınar, A., van Vledder, G. P., Kömürçü, M.İ., and Özger, M. (2012). Evaluation of the numerical wave model (SWAN) for wave simulation in the black Sea. *Continent. Shelf Res.* 50, 80–99. doi: 10.1016/j.csr.2012.09.012
- Ali, R., Kuriqi, A., Abubaker, S., and Kisi, O. (2019). Long-term trends and seasonality detection of the observed flow in Yangtze river using Mann-Kendall and sen's innovative trend method. *Water* 11 (9), 1855.
- Amarouche, K., Bingölbali, B., and Akpınar, A. (2021). New wind-wave climate records in the Western Mediterranean Sea. *Clim. Dyn.* 1-24, 1899–1922.
- Ay, M. (2020). Trend and homogeneity analysis in temperature and rainfall series in western black Sea region, Turkey. *Theor. Appl. Climatol.* 139 (3), 837–848. doi: 10.1007/s00704-019-03066-6
- Aydoğan, B., and Ayat, B. (2018). Spatial variability of long-term trends of significant wave heights in the black Sea. *Appl. Ocean Res.* 79, 20–35. doi: 10.1016/j.apor.2018.07.001
- Ay, M., and Kisi, O. (2015). Investigation of trend analysis of monthly total precipitation by an innovative method. *Theor. Appl. Climatol.* 120 (3), 617–629. doi: 10.1007/s00704-014-1198-8
- Battjes, J., and Janssen, J. (1978). Energy loss and set-up due to breaking of random waves. *Coast. Eng. Proc.* 1 (16), 32. doi: 10.9753/icce.v16.32
- Bhavithra, R. S., and Sannasiraj, S. A. (2022). Climate change projection of wave climate due to vardah cyclone in the bay of Bengal. *Dyn. Atmos. Oceans* 97, 101279. doi: 10.1016/j.dynatmoce.2021.101279
- Booi, N., Ris, R. C., and Holthuijsen, L. H. (1999). A third-generation wave model for coastal regions: 1. model description and validation. *J. Geophys. Res.: Oceans*. 104 (C4), 7649–7666.
- Breivik, Ø., Aarnes, O. J., Abdalla, S., Bidlot, J. R., and Janssen, P. A. (2014). Wind and wave extremes over the world oceans from very large ensembles. *Geophys. Res. Lett.* 41 (14), 5122–5131. doi: 10.1002/2014GL060997
- Breivik, Ø., Aarnes, O. J., Bidlot, J. R., Carrasco, A., and Saetra, Ø. (2013). Wave extremes in the northeast Atlantic from ensemble forecasts. *J. Climate* 26 (19), 7525–7540. doi: 10.1175/JCLI-D-12-00738.1
- Caires, S., and Sterl, A. (2005). 100-year return value estimates for ocean wind speed and significant wave height from the ERA-40 data. *J. Climate* 18 (7), 1032–1048. doi: 10.1175/JCLI-3312.1
- Caloiero, T., Aristodemo, F., and Ferraro, D. A. (2019). Trend analysis of significant wave height and energy period in southern Italy. *Theor. Appl. Climatol.* 138 (1), 917–930. doi: 10.1007/s00704-019-02879-9
- Caloiero, T., Coscarelli, R., and Ferrari, E. (2018). Application of the innovative trend analysis method for the trend analysis of rainfall anomalies in southern Italy. *Water Resour. Manage* 32 (15), 4971–4983. doi: 10.1007/s11269-018-2117-z
- Camus, P., Losada, I. J., Izaguirre, C., Espejo, A., Menéndez, M., and Pérez, J. (2017). Statistical wave climate projections for coastal impact assessments. *Earth's Future* 5 (9), 918–933. doi: 10.1002/2017EF000609
- Çarpar, T., Ayat, B., and Aydoğan, B. (2020). Spatio-seasonal variations in long-term trends of offshore wind speeds over the black sea; an inter-comparison of two reanalysis data. *Pure Appl. Geophysics*. 177 (6), 3013–3037.
- Cavaleri, L., Fox-Kemper, B., and Hemer, M. (2012). Wind waves in the coupled climate system. *Bull. Am. Meteorol. Soc.* 93 (11), 1651–1661. doi: 10.1175/BAMS-D-11-00170.1
- Dabanlı, İ., Şen, Z., Yeleğen, M.Ö., Şişman, E., Selek, B., and Güçlü, Y. S. (2016). Trend assessment by the innovative-Şen method. *Water Resour. Manage* 30 (14), 5193–5203. doi: 10.1007/s11269-016-1478-4
- De Leo, F., Besio, G., and Mentaschi, L. (2021). Trends and variability of ocean waves under RCP8.5 emission scenario in the Mediterranean Sea. *Ocean. Dyn.* 71 (1), 97–117.
- De Leo, F., De Leo, A., Besio, G., and Briganti, R. (2020). Detection and quantification of trends in time series of significant wave heights: An application in the Mediterranean Sea. *Ocean. Eng.* 202, 107155. doi: 10.1016/j.oceaneng.2020.107155
- Divinsky, B. V., and Kosyan, R. D. (2017). Spatiotemporal variability of the black Sea wave climate in the last 37 years. *Continent. Shelf Res.* 136, 1–19. doi: 10.1016/j.csr.2017.01.008
- Divinsky, B. V., and Kosyan, R. D. (2020). Climatic trends in the fluctuations of wind waves power in the black Sea. *Estuarine. Coast. Shelf. Sci.* 235, 106577. doi: 10.1016/j.ecss.2019.106577
- Dobrynin, M., Murawsky, J., and Yang, S. (2012). Evolution of the global wind wave climate in CMIP5 experiments. *Geophys. Res. Lett.* 39 (18), L18606. doi: 10.1029/2012GL052843

## Conflict of interest

The authors declare that the research was conducted in the absence of any commercial or financial relationships that could be construed as a potential conflict of interest.

## Publisher's note

All claims expressed in this article are solely those of the authors and do not necessarily represent those of their affiliated organizations, or those of the publisher, the editors and the reviewers. Any product that may be evaluated in this article, or claim that may be made by its manufacturer, is not guaranteed or endorsed by the publisher.



- Douglas, E. M., Vogel, R. M., and Kroll, C. N. (2000). Trends in floods and low flows in the united states: impact of spatial correlation. *J. hydrology*. 240 (1-2), 90–105. doi: 10.1016/S0022-1694(00)00336-X
- Eldeberky, Y. (1996). *Nonlinear transformation of wave spectra in the nearshore zone (Ph.D. thesis)* (The Netherlands: Delft University of Technology).
- GEBCO (2014). *British Oceanographic data centre, centenary edition of the GEBCO digital atlas [CDROM]*. (Liverpool: Published on behalf of the Intergovernmental Oceanographic Commission and the International Hydrographic Organization).
- Güçlü, Y. S. (2018). Alternative trend analysis: half time series methodology. *Water Resour. Manage.* 32 (7), 2489–2504.
- Güçlü, Y. S., Şişman, E., and Dabanlı, İ. (2020). Innovative triangular trend analysis. *Arabian. J. Geosci.* 13 (1), 1–8.
- Gulev, S. K., and Grigorjeva, V. (2006). Variability of the winter wind waves and swell in the north Atlantic and north Pacific as revealed by the voluntary observing ship data. *J. Climate* 19 (21), 5667–5685. doi: 10.1175/JCLI3936.1
- Haktanir, T., and Citakoglu, H. (2014). Trend, independence, stationarity, and homogeneity tests on maximum rainfall series of standard durations recorded in Turkey. *J. Hydrolog. Eng.* 19 (9), 05014009. doi: 10.1061/(ASCE)HE.1943-5584.0000973
- Harkat, S., and Kisi, O. (2021). Trend analysis of precipitation records using an innovative trend methodology in a semi-arid Mediterranean environment: Chelif watershed case (Northern Algeria). *Theor. Appl. Climatol.* 144 (3), 1001–1015. doi: 10.1007/s00704-021-03520-4
- Hasselmann, S., Hasselmann, K., Allender, J. H., and Barnett, T. P. (1985). Computations and parameterizations of the nonlinear energy transfer in a gravity-wave spectrum. part II: Parameterizations of the nonlinear energy transfer for application in wave models. *J. Phys. Oceanogr.* 15, 1378–1391. doi: 10.1175/1520-0485(1985)015<1378:CAPOTN>2.0.CO;2
- IPCC (2013). “Summary for policymakers. in: Climate change 2013: The physical science basis. contribution of working group I to the fifth assessment report of the intergovernmental panel on climate change, *Climate change 2013: The physical science basis*”. Eds. T. F. Stocker, D. Qin, G.-K. Plattner, M. Tignor, S. K. Allen, J. Boschung, A. Nauels, Y. Xia, V. Bex and P. M. Midgley (Cambridge, United Kingdom and New York, NY, USA: Cambridge University Press), 1–30. doi: 10.1017/CBO9781107415324.004
- Islek, F., Yuksel, Y., and Sahin, C. (2020). Spatiotemporal long-term trends of extreme wind characteristics over the black Sea. *Dyn. Atmospheres. Oceans*. 90, 101132. doi: 10.1016/j.dynatmoce.2020.101132
- Islek, F., Yuksel, Y., Sahin, C., and Guner, H. A. A. (2021). Long-term analysis of extreme wave characteristics based on the SWAN hindcasts over the black Sea using two different wind fields. *Dyn. Atmospheres. Oceans*. 94, 101165. doi: 10.1016/j.dynatmoce.2020.101165
- Janssen, P. A. (1991a). “Consequences of the effect of surface gravity waves on the mean air flow,” in *Breaking waves* (Berlin, Heidelberg: Springer), 193–198.
- Janssen, P. A. (1991b). Quasi-linear theory of wind-wave generation applied to wave forecasting. *J. Phys. Oceanogr.* 21 (11), 1631–1642. doi: 10.1175/1520-0485(1991)021<1631:QLTOWW>2.0.CO;2
- Kendall, M. G. (1975). *Rank correlation methods*. (London: Charles Griffin).
- Komen, G. J., Cavaleri, L., Donelan, M., Hasselmann, K., Hasselmann, S., and Janssen, P. A. E. M. (1994). *Dyn. and modelling of ocean waves* (Cambridge: Cambridge University Press), 554.
- Kuriqi, A., Ali, R., Pham, Q. B., Gambini, J. M., Gupta, V., Malik, A., et al. (2020). Seasonality shift and streamflow flow variability trends in central India. *Acta Geophysica*. 68 (5), 1461–1475. doi: 10.1007/s11600-020-00475-4
- Mann, H. B. (1945). Nonparametric tests against trend. *Econometrica: J. Econometric. Soc.* 13, 245–259. doi: 10.2307/1907187
- Meucci, A., Young, I. R., Aarnes, O. J., and Breivik, Ø. (2020). Comparison of wind speed and wave height trends from twentieth-century models and satellite altimeters. *J. Climate* 33 (2), 611–624. doi: 10.1175/JCLI-D-19-0540.1
- Onea, F., and Rusu, L. (2019). Long-term analysis of the black sea weather windows. *J. Mar. Sci. Eng.* 7 (9), 303. doi: 10.3390/jmse7090303
- Onyutha, C. (2016). Identification of sub-trends from hydro-meteorological series. *Stochastic. Environ. Res. Risk Assess.* 30 (1), 189–205. doi: 10.1007/s00477-015-1070-0
- Ris, R. C., Holthuijsen, L. H., and Booij, N. (1999). A third-generation wave model for coastal regions: 2. verification. *J. Geophys. Res.: Oceans*. 104 (C4), 7667–7681.
- Rogers, W. E., Hwang, P. A., and Wang, D. W. (2003). Investigation of wave growth and decay in the SWAN model: three regional-scale applications. *J. Phys. Oceanogr.* 33 (2), 366–389. doi: 10.1175/1520-0485(2003)033<0366: IOWGAD>2.0.CO;2
- Şan, M., Akçay, F., Linh, N. T. T., Kankal, M., and Pham, Q. B. (2021). Innovative and polygonal trend analyses applications for rainfall data in Vietnam. *Theor. Appl. Climatol.* 144 (3), 809–822.
- Şen, Z. (2012). Innovative trend analysis methodology. *J. Hydrologic. Eng.* 17 (9), 1042–1046.
- Şen, Z. (2014). Trend identification simulation and application. *J. Hydrologic. Eng.* 19 (3), 635–642.
- Şen, Z. (2017). Innovative trend significance test and applications. *Theor. Appl. Climatol.* 127 (3-4), 939–947.
- Şen, Z. (2018). Crossing trend analysis methodology and application for Turkish rainfall records. *Theor. Appl. Climatol.* 131 (1), 285–293.
- Şen, Z. (2020). Up-to-date statistical essentials in climate change and hydrology: a review. *Int. J. Global Warming* 22 (4), 392–431.
- Şen, Z. (2021). Conceptual monthly trend polygon methodology and climate change assessments. *Hydrolog. Sci. J.* 66 (3), 503–512.
- Şen, Z., Şişman, E., and Dabanlı, İ. (2019). Innovative polygon trend analysis (IPTA) and applications. *J. Hydrology*. 575, 202–210. doi: 10.1016/j.jhydrol.2019.05.028
- Saha, S., Moorthi, S., Pan, H. L., Wu, X., Wang, J., Nadiga, S., et al. (2010). The NCEP climate forecast system reanalysis. *Bull. Am. Meteorol. Soc.* 91 (8), 1015–1058. doi: 10.1175/2010BAMS3001.1
- Saha, S., Moorthi, S., Wu, X., Wang, J., Nadiga, S., Tripp, P., et al. (2014). The NCEP climate forecast system version 2. *J. Clim.* 27 (6), 2185–2208. doi: 10.1175/JCLI-D-12-00823.1
- Sanikhani, H., Kisi, O., Mirabbasi, R., and Meshram, S. G. (2018). Trend analysis of rainfall pattern over the central India during 1901–2010. *Arabian. J. Geosci.* 11 (15), 1–14. doi: 10.1007/s12517-018-3800-3
- Saphoğlu, K., Kilit, M., and Yavuz, B. K. (2014). Trend analysis of streams in the western mediterranean basin of Turkey. *Fresenius Environ. Bull.* 23 (1), 313–327.
- Shanas, P. R., and Kumar, V. S. (2015). Trends in surface wind speed and significant wave height as revealed by ERA-interim wind wave hindcast in the central bay of Bengal. *Int. J. Climatol.* 35 (9), 2654–2663. doi: 10.1002/joc.4164
- UNEP (2006). *Marine and coastal ecosystems and human well-being: a synthesis report based on the findings of the millennium ecosystem assessment*. (Cambridge: UNEP-WCMC).
- Valchev, N. N., Trifonova, E. V., and Andreeva, N. K. (2012). Past and recent trends in the western black Sea storminess. *Natural Hazards. Earth System. Sci.* 12 (4), 961–977. doi: 10.5194/nhess-12-961-2012
- Von Storch, H. (1995). “Misuses of statistical analysis in climate research,” in *Analysis of climate variability: Applications of statistical techniques*. Eds. H. von Storch and A. Navarra (New York: Springer-Verlag), 11–26.
- Young, I. R. (1999a). *Wind generated ocean waves*. Vol. 2 (Amsterdam: Elsevier), 284.
- Young, I. R. (1999b). Seasonal variability of the global ocean wind and wave climate. *Int. J. Climatol: A. J. R. Meteorol. Soc.* 19 (9), 931–950. doi: 10.1002/(SICI)1097-0088(199907)19:9<931::AID-JOC412>3.0.CO;2-O
- Yue, S., and Wang, C. Y. (2002). Applicability of prewhitening to eliminate the influence of serial correlation on the Mann-Kendall test. *Water Resour. Res.* 38 (6), 4–1. doi: 10.1029/2001WR000861
- Zijlema, M., Van Vledder, G. P., and Holthuijsen, L. H. (2012). Bottom friction and wind drag for wave models. *Coast. Eng.* 65, 19–26. doi: 10.1016/j.coastaleng.2012.03.002



## OPEN ACCESS

## EDITED BY

Bahareh Kamranzad,  
Kyoto University, Japan

## REVIEWED BY

Francisco Taveira-Pinto,  
University of Porto, Portugal  
Talea L. Mayo,  
Emory University, United States  
Ian Young,  
The University of Melbourne, Australia

## \*CORRESPONDENCE

Chengcheng Qian  
q.chengcheng@163.com

## SPECIALTY SECTION

This article was submitted to  
Physical Oceanography,  
a section of the journal  
Frontiers in Marine Science

RECEIVED 21 March 2022

ACCEPTED 22 August 2022

PUBLISHED 09 September 2022

## CITATION

Cao C, Chen G, Qian C and Shang J  
(2022) Spatiotemporal variability  
and climate teleconnections  
of global ocean wave power.  
*Front. Mar. Sci.* 9:900950.  
doi: 10.3389/fmars.2022.900950

## COPYRIGHT

© 2022 Cao, Chen, Qian and Shang.  
This is an open-access article  
distributed under the terms of the  
[Creative Commons Attribution License  
\(CC BY\)](https://creativecommons.org/licenses/by/4.0/). The use, distribution or  
reproduction in other forums is  
permitted, provided the original  
author(s) and the copyright owner(s)  
are credited and that the original  
publication in this journal is cited, in  
accordance with accepted academic  
practice. No use, distribution or  
reproduction is permitted which does  
not comply with these terms.

# Spatiotemporal variability and climate teleconnections of global ocean wave power

Chuanchuan Cao<sup>1,2</sup>, Ge Chen<sup>1,2</sup>,  
Chengcheng Qian<sup>3\*</sup> and Jie Shang<sup>3</sup>

<sup>1</sup>Frontiers Science Center for Deep Ocean Multispheres and Earth System, School of Marine Technology, Ocean University of China, Qingdao, China, <sup>2</sup>Laboratory for Regional Oceanography and Numerical Modeling, Qingdao National Laboratory for Marine Science and Technology, Qingdao, China, <sup>3</sup>Department of Information and Files, North China Sea Marine Forecasting Center of State Oceanic Administration, Qingdao, China

Climate change impacts have driven a transformation of the global energy system. The utilization of renewable energies is required to meet energy demands while protecting the environment. Wind-generated waves, carrying energy from the atmosphere, are a possible energy supply. However, global and long-term variability in wave resources due to the effects of climate change remain uncertain. This study quantified the spatiotemporal patterns and availability of global wave power (GWP) based on the ERA5 hourly and monthly reanalysis products, spanning from 1979 to 2020. The most promising wave resources appeared centralized in the westerlies of both hemispheres, and the wave power exhibited a “rich-get-richer” trend in the Southern Ocean, dominating the overall distribution and variability of GWP. Significant seasonal and interannual oscillation trends in GWP were observed, but with little variations on daily and hourly time scales. We found the average GWP in ERA5 products increased by 12.89% suddenly in 1991, mainly caused by the beginning of altimeter assimilation. This also implies the potential underestimation of wave fields in the modeling results before the advent of altimeter. In the altimeter era, annual GWP exhibits (quasi-) decadal oscillation (variation near  $\pm 4\%$ ), which differed from the monotonous increases previously reported. An analysis and source tracing based on the climate teleconnections indexes revealed that the primary climate driver of the variability was the Southern Annual Mode ( $r = 0.84$ ). This study provides scientific guidance for wave power utilization and helps deepen our understanding of air-sea interactions.

## KEYWORDS

renewable energy, ocean wave power, spatiotemporal variability, decadal oscillation, climate teleconnections

# 1 Introduction

Global warming is one of the most significant manifestations of climate change and poses the most immediately foreseeable threat to human existence today. The emissions from fossil fuels consumption are regarded as the soundest indicator for defining climate policies (Rosa and Ribeiro, 2001). Most recently, China has committed to peak carbon dioxide emissions by 2030 and become carbon neutral before 2060 (Mallapaty, 2020). However, reducing the energy-consumption presents the most significant challenge in achieving this commitment because coal is the principal fuel providing more than half (60%) of China's electricity generation in 2019 (Outlook, 2020). Given that dependencies like this exist worldwide (Moriarty and Honnery, 2012), transitioning away from the dominance of fossil fuels becomes a desperate challenge that all countries must solve. The development and utilization of green energies, to a great extent, is an effective strategy to maintain development while ensuring environmental sustainability.

Renewable energy sources are naturally replenishing, but are generally flow-limited (i.e., an almost infinite duration but a finite amount of energy available per unit of time). In the face of lower cost and often more convenient alternatives, the potentially large scale of renewables only contributes a very small share of world primary energy, with major portions being hydropower and traditional biomass fuels in developing countries (Gross et al., 2003). According to the International Energy Statistics (IEA, 2018), the global renewable generation capacity (non-combustible) amounted to 6,254,184 GWh (23.40% of the total electricity), of which hydropower accounted for 69.15%, wind power for 20.36%, solar power for 9.05%, geothermal energy for 1.42%, and marine energy for just less than 0.02% (e.g., tide, wave, and ocean current generation). The strikingly tiny proportion from marine energy sources reveals the severe lack of marine energy utilization. There are many dynamic phenomena that occur at different spatial-temporal scales within the ocean, each of which represent an enormous energy resource. The aggregate potential of global ocean energy sources is significantly greater than our global electricity consumption (Gross et al., 2003; Melikoglu, 2018). As the two most developed ocean energies, the potential global tidal energy dissipation is estimated at nearly 3.5 TW (Egbert and Ray, 2000), and that of wave energy dissipation is around 3.0 TW (Gregg, 1973), while the world electricity demand is less than 3.0 TW (Sleiti, 2017). However, the progress in exploiting these resources is much slower than conventional energy because the technologies are still mostly under development.

Wind-generated surface gravity waves (hereafter called waves) dominate the ocean wave spectrum in terms of energy and are generally the focus of oceanography studies. Wave energy converters can harvest energy from the potential and

kinetic energy of ocean waves. Systems for harvesting utility-scale electrical power from ocean waves were proposed more than 40 years ago (e.g., Salter, 1974). The potential of wave energy resource is promising, especially on the west-facing coasts of westerly zones (latitudes between 35° and 65°) in both hemispheres, but the potential costs of grid integration have limited its application (Scruggs and Jacob, 2009). Limited by the investment costs and technological development, only a small amount of wave power is efficiently extracted near ocean coastlines, islands, or in semi-enclosed basins (Rusu, 2014). However, energy transition goals have increased the demand for renewable energy and helped address the underdeveloped status of these technologies. Indeed, the study and harvest of ocean wave power have become hot topics in oceanography once again. The worldwide wave power potential is estimated at around 29,500 TWh/a (Rusu and Onea, 2018), roughly equivalent to the current global electricity consumption. Besides, previous estimations of global wave power (GWP) have varied widely, ranging from 16,025 to 32,000 TWh/a (e.g., Mørk et al., 2010; Gunn and Stock-Williams, 2012; Reguero et al., 2015). With improvements in ocean modeling and assimilation technology, the spatial distribution and the long-term variability of wave energy can be further clarified. Moreover, these ubiquitous surface waves can be classified into two main types: wind waves (or wind sea, which refers to young waves with short wavelengths that are undergrowth or inequilibrium with the forcing of local wind) and swell (generally formed remotely by storms and propagated thousands of kilometers across the ocean, without momentum input from wind) (e.g., Chen et al., 2002; Hanley et al., 2010). Their role in understanding the redistribution and spatiotemporal variability of GWP need to be further explored.

Surface waves are the most intuitive response of the ocean to the influence of the atmosphere, and they can be seen as a potential climate change indicator (e.g., Young et al., 2011; Jiang and Mu, 2019; Young and Ribal, 2019). The relationship between waves and climate variability has been widely studied, but most studies have focused on historical trends using mean and extreme wave height values. This is evidenced by Patra et al. (2020), who presented a detailed summary on the topic (see details in their Table 1). However, wave heights are not the only parameter influenced by atmospheric forcing, and the wave period and direction should be considered (e.g., Dodet et al., 2010; Hemer et al., 2010). Wave power increases nonlinearly with significant wave height and linearly with peak wave period, so considering both will provide a more comprehensive picture of the response of ocean waves to climate change. Bromirski and Cayan (2015) indicated that wave power exhibited a decreasing trend across the North Atlantic from 2000 to 2008, and was strongly influenced by the North Atlantic Oscillation. Recently, Reguero et al. (2019) found that upper-ocean warming changed

the global wave climate and made waves stronger, and observed slow increases in GWP of 0.41% per year from 1948 to 2008. The wave energy estimates for given regions have significant variations in monthly, seasonal, and annual patterns and therefore should not be ignored (e.g., Kamranzad et al., 2013; Bingölbali et al., 2020; Vieira et al., 2020). Wave powers show both regional diversity and long-term uncertainty. Therefore, the spatio-temporal variability of global ocean wave power is reinvestigated based on the new ERA5 data, with the goal of providing scientific guidance for the upcoming renewable energy harvesting boom. The remainder of this paper is organized as follows: A brief description of the data and the methodology of wave power evaluation is provided in section 2. The spatial distribution, temporal variability, and the optimal harvesting zones for ocean wave sources are analyzed and described in section 3. Discussions on the variational mechanism of wave power and conclusions are given in section 4 and 5.

## 2 Data and method

### 2.1 ERA5 dataset

The European Center for Medium-Range Weather Forecasts (ECMWF) has a long history of reanalysis in climate monitoring applications. The state-of-the-art product of ERA5 was released in April 2019, replacing the widely used ERA-Interim reanalysis. ERA5 is the fifth generation reanalysis product from the ECMWF for global climate and weather over the past 4 to 7 decades. Besides, ERA5 is highly regarded in the Copernicus Climate Change Service (C3S), which provides a precise and consistent record for a large number of basic climate variations for the C3S Climate Data Store (CDS). See the detail descriptions in Hersbach et al. (2020).

In this study, the hourly and monthly ocean-wave products are used from 1979 to 2020 from CDS, interpolated to a regular grid with a  $0.5^\circ \times 0.5^\circ$  spatial resolution. The key parameters include the significant wave height, mean wave period, and mean wave direction, as derived from the wave spectrum. These parameters were classified into three types: wind-sea wave components, swell components, and ensemble waves of both.

### 2.2 Evaluation of wave power

Wave power  $P_w$  (W/m) is defined as the wave energy flux per unit of wave-crest length (Dean and Dalrymple, 1991) and wave energy transport at wave group velocity ( $c_g$ ). Thus, wave power in the wave propagation direction can be written as  $P_w = \rho g \int_0^\infty \int_0^{2\pi} S(f, \theta) c_g(f, d) df d\theta$ , where  $S(f, \theta)$  is the directional

spectrum corresponding to the wave frequency ( $f$ ) and direction ( $\theta$ ). It is simplified as  $P_w = E_w \cdot c_g$ , with  $E_w = \frac{1}{8} \rho g H_s^2$  (J/m<sup>2</sup>) being the averaged wave energy density per unit horizontal area (including the kinetic and potential energy), where  $H_s$  is the significant wave height;  $g=9.80$  (m/s<sup>2</sup>) is the acceleration of gravity; and the  $\rho=1025$  (kg/m<sup>3</sup>) is the averaged density of the seawater. Furthermore, the wave power ( $P_w$ ) can be determined from  $T_e$  and  $H_s$  in deep waters as follows:

$$P_w = \frac{\rho g^2}{64\pi} H_s^2 \cdot T_e \quad (1)$$

where  $T_e$  is the wave energy period. The determination of this parameter was controversial in previous studies. Reguero et al. (2015); Reguero et al. (2019) assumed that  $T_e = \alpha \cdot T_{01} = 0.538 T_{01}$  (s) for the JONSWAP spectrum. While Fairley et al. (2017) and Rusu and Rusu (2021) used the mean wave periods for wave power assessment. As introduced in ECMWF documentation, the mean period ( $T_{m-1}$ ) is also known as the energy period (ECMWF, 2020) and can be used in Eq.(1) directly.

Due to the “shoaling” effects, as waves move from the open ocean into shallow water, their crests become steeper, increase in height, and shorten in wavelength. The difference in averaged wave power between deep and shallow water is caused by their group velocities (Izadparast and Niedzwecki, 2011). According to the dispersion relationship in shallow water ( $\omega^2 = gk^2 d$ , where  $\omega$  is the angular frequency;  $k$  is wave number; and the  $d$  is the water depth), the group and phase velocities are both determined solely from water depth ( $c_g = \sqrt{gd}$ ), and wave power in shallow waters can be expressed as:

$$P_{ws} = \frac{\rho g^{3/2}}{8} H_s^2 \cdot d^{1/2} \quad (2)$$

Thus, wave power varies with the square root of water depth and is independent of wave period. Generally, average wavelengths near shore are less than 100 m, and Eq. (2) should be applied when water depths are less than 5 m based on the shallow-water limit ( $d < \frac{1}{20} \lambda$ ) of linear wave theory. Since the grid resolution of ERA5 data is  $0.5^\circ$  (about 55 km in ground distance) and a minimum water depth is 5 m, the impacts of shallow water conditions on wave power estimation are trivial and can be neglected in this study. Additionally, a parametrization scheme of subgrid bathymetry was implemented in ERA5 data to correct the wave propagation and wave energy flux (ECMWF, 2020). Ozkan and Mayo (2019) indicated that the simplified equation potentially underestimates available wave power in coastal Florida compared with the spectral wave power equation. However, only three wave parameters mentioned above were selected in the ERA5 hourly product, but bring a huge amount of data. The computational burdens limit the application of

spectral methods in wave power assessment. Altimeter measurements can only provide  $H_s$  in the assimilation process of wave modeling (Hersbach et al., 2020), potentially supporting more reliable wave height products. Therefore, Eq. (1) was used to estimate the wave power in this study.

Furthermore, the mean wave direction (oceanographical convention) for wave power analysis is introduced. The mean wave direction was decomposed into zonal and meridional components based on significant wave height ( $\theta_{H_s}=[H_s \cdot \sin\theta_0, H_s \cdot \cos\theta_0]$ ) and wave power ( $\theta_{WP}=[P_w \cdot \sin\theta_0, P_w \cdot \cos\theta_0]$ ). Then the climate direction of  $H_s$  and  $P_w$  could be estimated.

## 2.3 Related climate teleconnection indexes

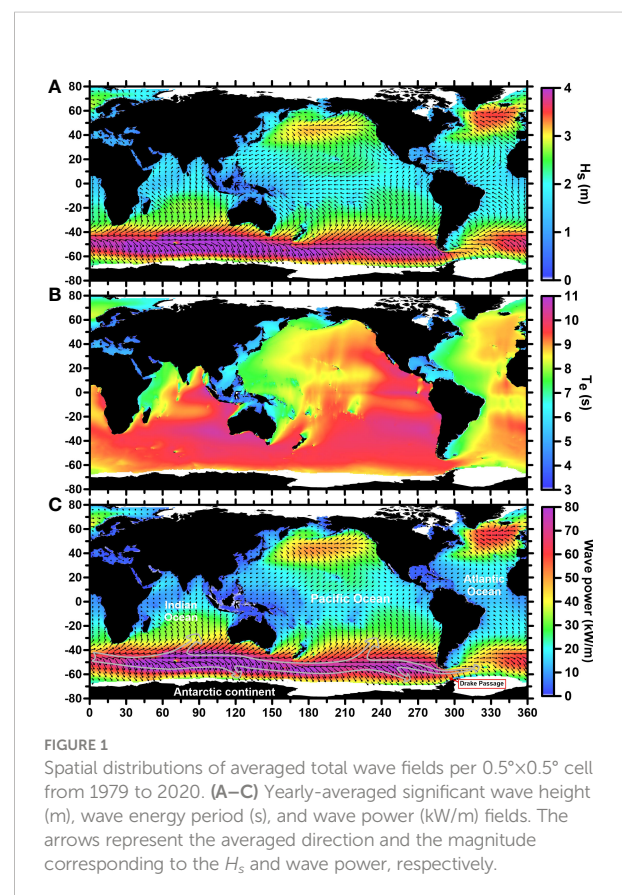
Various factors that affect wave power can be used, for example, since surface waves are extensions of past wind forcing, predicted changes in wind patterns can inform future predictions of surface waves. Particularly, the interannual or decadal variations in GWP reflect the long-term climate variability (e.g., Vieira et al., 2020; Reguero et al., 2019), which can be spontaneously connected with the climate teleconnection patterns.

According to geostrophic relationships, pressure gradients determine wind fields (Pedlosky, 1987). Therefore, the climate indexes related to pressure (or wind) are good candidates for analyzing potential relationships with wave power. Chen (2014) has made systematic works on characterizing the spatiotemporal patterns of significant atmospheric oscillations over global oceans. Thus, the following indexes were selected for analysis: The Pacific Decadal Oscillation (PDO; index for Pacific climate variability based on SST anomalies with time scales usually greater than 10 years), the North Atlantic Oscillation (NAO; index based on surface sea-level pressure difference between the subtropical (Azores) high and the subpolar low pressure), the Southern Oscillation (SOI; a bimodal variation index based on sea-level barometric pressure differences between observation stations at Darwin, Australia and Tahiti), the Arctic Oscillation (AO; a climate pattern index characterized by winds circulating counterclockwise around the Arctic at a latitude around 55°N, with a positive phase when colder air masses are confined in polar regions, and a negative phase when southward penetration occurs), and the Southern Annual Mode (SAM; i.e., the Antarctic Oscillation; dependent on atmospheric pressures at the Antarctic and at about 40°S–50°S). Each of these indexes is related to the variability in atmospheric circulation and, therefore, is linked to surface waves *via* wind forcing. The SAM index was acquired from National Center for Atmospheric Research (NCAR; Marshall, 2003), while all other climate index data were downloaded from the National Oceanic and Atmospheric Administration (NOAA).

## 3 Spatial-temporal characteristics of ocean wave power

### 3.1 Spatial distribution

In this section the wave power from total wave, swell, and wind-sea are presented and computed at the global level based on monthly ERA5 data. Figure 1 shows the averaged  $H_s$ ,  $T_e$ , and  $P_w$  fields, calculated from the total wave fields over the 42-year time interval (1979–2020). The  $H_s$  and  $P_w$  fields exhibited similar patterns, with higher values concentrated in the latitude bands from 40° to 60° (interior of the prevailing westerlies zones) in both hemispheres, and smaller values mainly appearing in tropical and nearshore areas. The distributions and magnitudes were similar to those obtained by Rusu and Rusu (2021).  $T_e$  exhibited a pattern that was different from  $H_s$  and  $P_w$ , with values in the Southern Hemisphere being significantly larger than those in the Northern Hemisphere, and the Pacific and Indian Oceans having larger values than the Atlantic Ocean. The eastern portions of ocean basins generally had larger values than their respective western portions, and some jet-shaped patterns can be seen in Figure 1B, with values exceeding 11 s. Secondly, the



maximum value of  $P_w$  beyond 100 kW/m was located in the Southern Ocean, and  $P_w$  transport occurred in three main directions, as indicated by the arrows in Figure 1C. The pattern in wave power showed deflection southward (northward) upon approaching the Antarctic continent (the lower latitude ocean), and along the path eastward there was a sharp decrease to the east of the Drake Passage (See the schematic arrows in the figure). The tracks leading to the Atlantic Ocean exhibited a lower  $P_w$  field than the Indian and Pacific Oceans in the southern hemisphere. As a result, the strongest wave power field (approximately 60 kW/m) of the Atlantic Ocean was in the westerly zone of the Northern Hemisphere. Additionally, there were dominant trends showing ocean waves traveling and transporting energy from high latitude to equatorial regions and towards shores. Meanwhile,  $P_w$  values were reduced sharply during the propagating processes, and were only one-third of their original magnitudes after leaving the westerlies (see Figure 1C).

Studies on global wave power (GWP) have rarely compared swell and wind-sea waves. However, wave parameters integrated from the entire wave spectrum might only provide a limited description of the wavefield (Qian et al., 2019). The swell fields (Figures 2A–C) exhibited the same patterns as the total wave fields (Figures 1A–C), but had slightly larger wave periods and lower significant wave heights ( $H_s$ ) and wave power ( $P_w$ ). Wind-sea wave fields exhibit the weakest magnitude of wave parameters (see Figures 2D–F). There was a region with remarkably low  $P_w$  values along the equator in the wind-sea field (the white belt zone in Figure 2F), which corresponded to a calm belt near the equator. Furthermore, the transport directions of  $P_w$  in the wind-sea field were different from those in the swell field. In particular, all the  $H_s$  and  $P_w$  in the Southern Ocean

moved poleward across the westerlies and approached Antarctica. By comparing the averaged fields of the total waves, swell, and wind-sea, it was found that significant wave energy potential existed in the two zones with prevailing westerlies, and the swell components contributed most of the total wave power.

### 3.2 Temporal variability

The period of surface waves was generally less than twenty seconds. However, they were forced by the seasonal or long-term winds (or wind stress curl) and, as such, carry the atmosphere's imprint. Analyzing temporal variability is helpful for evaluating  $P_w$  and accurately predicting its trends. Thus, the time-series of averaged global wave power (GWP) were calculated at yearly and monthly resolutions using the ERA5 monthly products and at daily and hourly resolutions using the ERA5 hourly products. Note that valid data are used for GWP statistics (e.g., some locations at certain times of the year may experience ice coverage, and only grid with ice-free periods longer than half a year are valid). The results over the 42-year period are shown in Figure 3, and the GWPs of the total wave, swell, and wind-sea are marked by the black, red, and blue lines, respectively.

These results also support that swell components dominate the total GWP, including the trends in magnitudes and variation. One unanticipated finding was that annual GWP (Figure 3A) did not exhibit a steady increase, instead there was a sharp increase after 1991 accompanied by a (quasi) decadal fluctuation. As suggested by Hersbach et al. (2020), the altimeter assimilation of wave information began in 1991, and validation of matched buoy results has also shown much

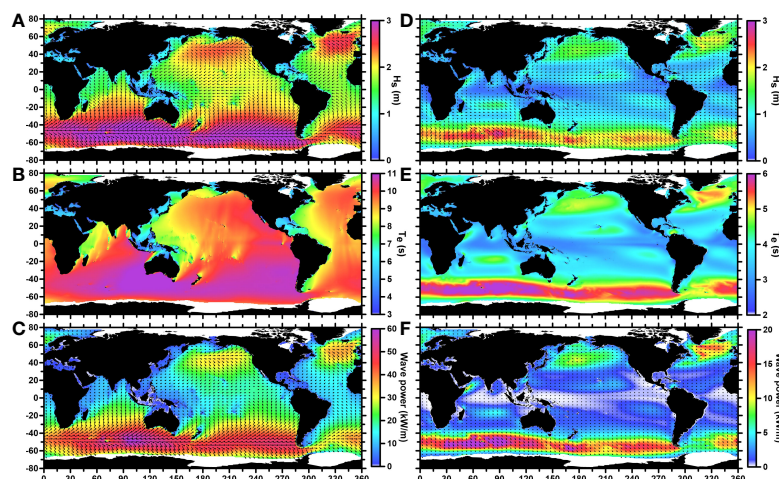


FIGURE 2

Swell and wind-sea wave components, as in Figure 1. Panels show  $H_s$ ,  $T_e$ , and  $P_w$  for the (A–C) swell and (D–F) wind-sea wave fields, respectively. Averaged wave powers of less than 1 kW/m are shown as approaching white.

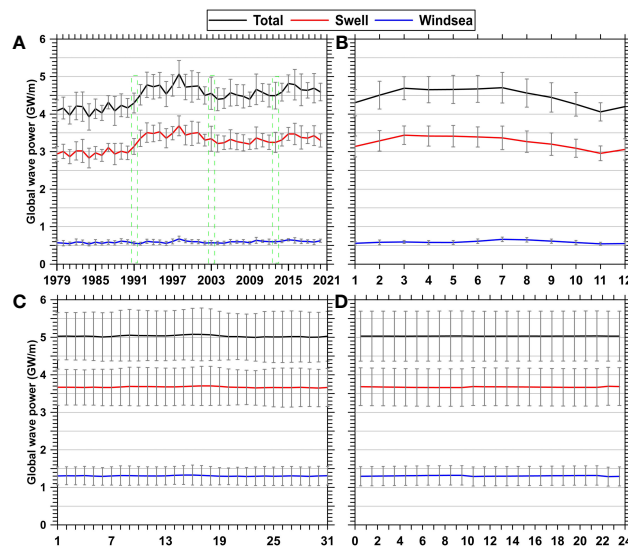


FIGURE 3

Temporal changes in the averaged wave power calculated globally from 1979 to 2020. (A) Yearly and (B) monthly global wave power based on the monthly product, and (C) daily and (D) hourly global wave power based on the hourly product. The error bars represent the standard deviations.

smaller errors (scatter index less than 16%) in the ERA5 products since then. Similar “jump” phenomenon can be found in the results of Reguero et al. (2019); and Muhammed Naseef and Sanil Kumar (2019); which may indicate the intrinsic dependence of contemporary wave models on altimeter assimilation, and potential underestimate wave power or wave fields prior to the appearance of altimeter observations. Validation results with *in-situ* observations (e.g., Muhammed Naseef and Sanil Kumar, 2019; Wang and Wang, 2021) give us more confidence in the wave model products in the altimeter era. The grey error bars represent the standard deviations, and the longer-term averaged GWPs tended to have lower standard deviations. Interestingly, the variabilities in the total GWP at the inter-annual (Figure 3A) and seasonal (Figure 3B) scales were remarkable, while there was barely any variability at daily and hourly scales (Figures 3C, D). Moreover, the values of the averaged GWP from the monthly product were slightly smaller than from the hourly product. The former fluctuated over the range from 4 to 5 GW/m, while the latter was steady at 5 GW/m. This may have been because the short-term variability in winds resulted in short-term high  $P_w$  values in the hourly product, while the process of merging monthly products smoothed out these short-term anomalies.

By focusing on the fluctuating trends in total GWP (Figure 3A), the decadal oscillation phases in the series appear to be separated by years 1991, 2003, and 2014 (marked by the green dotted lines in Figure 3A). Because long-term variability was our primary concern, the distribution of averaged  $P_w$  was further compared within the four phases to understand the cause

of GWP variation, and their time-averaged fields were shown in Figures 4A–D. There were significant differences in the intensities of  $P_w$  among the Southern Ocean (SO), Northern Pacific, and Atlantic oceans (NP and NA), but the mean directions of wave powers were generally similar. Furthermore, Figure 4E shows the positive discrepancy between the averages of years 1992–2003 (Figure 4B) and 1979–1991 (Figure 4A), with a maximum difference that was more than 10 (5) kW/m in the SO (NP and NA). In contrast, a negative discrepancy field (Figure 4F) was obtained when Figure 4C was subtracted from Figure 4B. The wave power reduction in Figure 4F was significantly lower than the increases in wave power in Figure 4E. In short, there was a net increment of GWP during 1979 ~ 2013. Notably, the reduction in wave power in the SO was smaller than those in the Northern Hemisphere basins, which may imply that SO had a larger role in the overall enhancement of total GWP (in Figure 3A) after 1991. Meanwhile, another major positive difference field was produced (not shown) by comparing Figures 4D, C. Furthermore, when looking differences between the four phases, the averaged rates of change in GWP were 12.89%, -3.97%, and 4.05%, respectively. Therefore, the sudden increases, general fluctuations, and decadal oscillations in GWP were quantified in our results. Particularly, accurate simulation of wave fields in the Southern Ocean is the core to improving wave models in the future.

Additionally, Figure 3B shows evidence of seasonal variation. The maximum GWP values were near 4.7 GW/m in March and July (which likely corresponded to times of high intensity wave action in both hemispheres), while the minimum

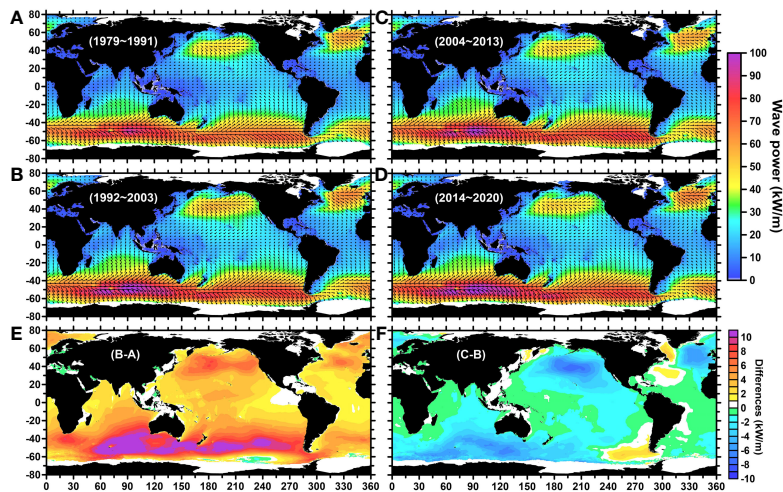


FIGURE 4

Year-averaged global wave power fields and decadal variability. (A) Averaged wave power from 1979 to 1991, (B) from 1992 to 2003, (C) from 2004 to 2013, and (D) from 2014 to 2020. (E) The averaged differences in wave power between (A) and (B); and (F) the averaged differences in wave power between (C, B).

value was slightly less than 4.1 GW/m in November. Moreover, a slight GWP peak in the wind-sea appeared from June to October. Therefore, the seasonal wave power fields (seasons here correspond to seasons in the Northern Hemisphere) are calculated, as shown in Figure 5. The strongest wave power field occurred in winter (DJF), with extreme values of more than 100 kW/m in the NP and NA (Figure 5A), while this season (i.e., summer in the Southern Hemisphere) had the weakest wave power field in the SO with extreme values remaining below 60 kW/m. In contrast, the weakest wave power field in the Northern Hemisphere (almost below 10 kW/m) occurred in summer (Figure 5C). Notably, the Northern Indian Ocean had the

highest  $P_w$  field (exceeding 50 kW/m) in the year due to the incoming wave power from the Southern Ocean Swell. The  $P_w$  distributions exhibited similar patterns in spring and autumn (i.e., two transition seasons between winter and summer), and there were only slight differences in  $P_w$  between the two westerlies.

The stability of wave resources is an essential factor for reliable energy harvesting. Thus, the coefficient of variation (standard deviation divided by the mean,  $CV = \frac{\sigma}{\bar{x}} \times 100$ ) is calculated within the four seasonal fields. The lowest variabilities in  $P_w$  were observed in winter (Figure 6A) and summer (Figure 6C), with CVs lower than 25%, while the highest CV

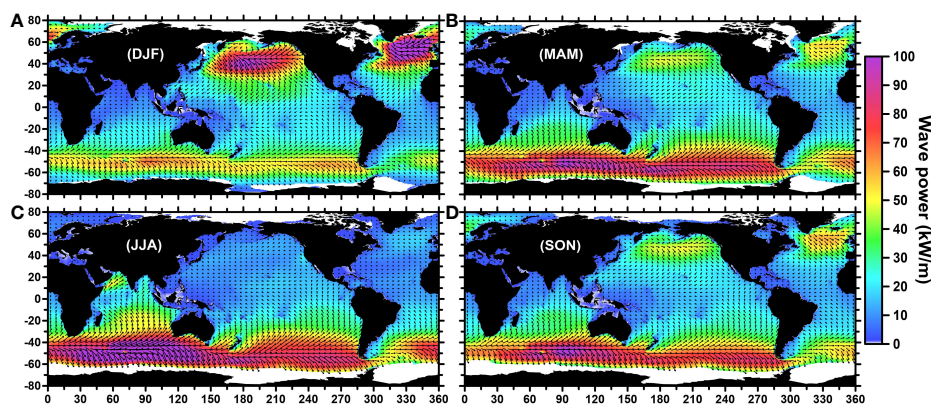


FIGURE 5

Seasonal distribution of the averaged wave power (seasons correspond to the Northern Hemisphere). (A) Winter (DJF: December, January, February), (B) spring (MAM: March, April, May), (C) summer (JJA: June, July, August), and (D) autumn (SON: September, October, November).



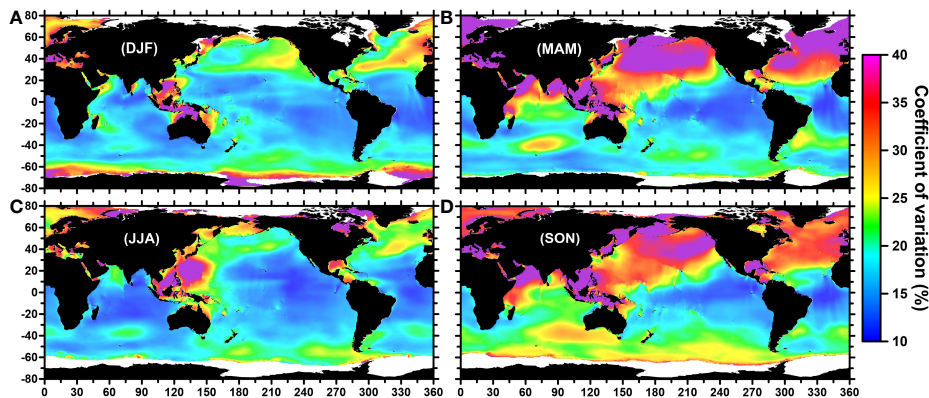


FIGURE 6

Coefficient of variation of seasonal wave power (seasons correspond to the Northern Hemisphere). (A) Winter (DJF: December, January, February), (B) spring (MAM: March, April, May), (C) summer (JJA: June, July, August), and (D) autumn (SON: September, October, November).

values were mainly concentrated in nearshore areas. However, there was significant variability in  $P_w$  in spring (Figure 6B) and autumn (Figure 6D). Specifically, their CVs were higher than 35% in the Northern Hemisphere, while a small variability (lower than 10%) was exhibited in the tropical oceans but the magnitudes of  $P_w$  in these oceans were also lower than 10 kW/m (see Figures 5B, D). These results show that the Southern Hemisphere contains more stable wave resources which make it an ideal energy harvesting field.

The hourly variation in GWP was rarely trivial, as suggested by Figure 3D. However, it is well understood that the air-temperature differences between day and night can significantly change the wind field which will influence ocean waves. Therefore, to examine the difference between day and night periods, the distributions of wave power during the day (i.e., the local time between 6 am to 6 pm) and night were calculated separately. Figures 7A, B show the day and night wave power distributions. As expected, their patterns were very similar (i.e., the energetic wave power was mainly concentrated in the westerly zones). However, the difference between the day and night distribution produced a novel result, revealing some large-scale “bubble” or wave-like patterns, as shown in Figure 7C, and significant differences were mainly concentrated in higher latitudes. Since this result was obtained by averaging hourly climate data, these spatial scales were too large to be attributed to local noise. Their morphological features were intuitively reminiscent of the widespread eddies or Rossby waves which form in the ocean and atmosphere. These striped patterns also revealed a significant trend of westward intensification or propagation from latitudes  $\sim \pm 40^\circ$  equatorward, with more divergence patterns in higher latitudes. These patterns may be related to wind stress, and exhibited similar patterns in previous studies (e.g., Chelton et al., 2004). Due to the lack of further evidence and because its dynamic mechanisms were outside of our scope of this study, we

supposed this may be a mirror effect imposed on the ocean by atmospheric forcing in the sea-air coupled model of ERA5 products.

### 3.3 Optimal wave power resources

The ultimate goal of studying the spatiotemporal distribution and variability of GWP is to scientifically identify

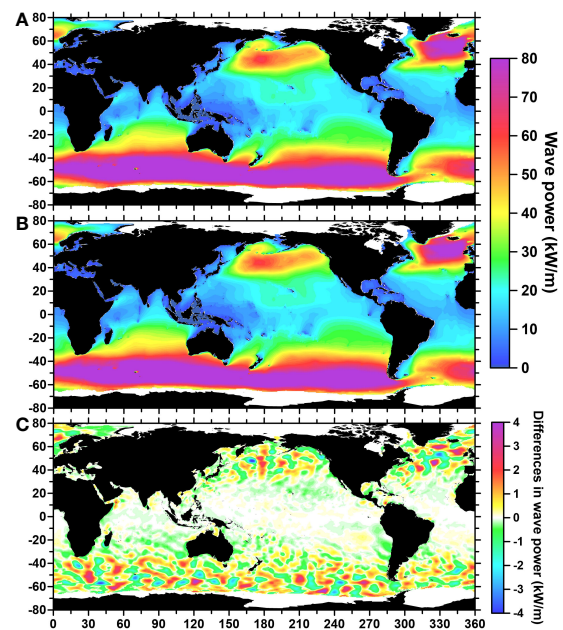


FIGURE 7

Wave power distribution in the day and night. (A) Day, (B) night, and (C) the differences in wave power between the two.

the best strategy for the development and harvesting of ocean wave resources. Therefore, the probability distribution of  $P_w$  per  $0.5^\circ$  cell over the 42-year data series with a high temporal resolution is calculated in Figure 8. The probability is also considered as the evaluation of the potential working time of the wave energy converters during which a specific  $P_w$  threshold would be met. The low-efficiency region where the probability was less than 0.3 (i.e., the effective working time would be less than 2600 hours in a year) is defined. In contrast, the high-efficiency regions had probabilities greater than 0.8 (i.e., the effective working time is higher than 7,000 hours in a year). Moreover, to identify optimal locations for power generation, water depth must be considered. In nearshore areas, wave energy is dissipated as waves interact with the seabed. However, deploying wave power plants and connecting it to a shore-based power station is often impractical and uneconomical in deeper water conditions. Generally, optimal depths are between 40 and 1000 m, which had large wave periods and amplitudes (Scruggs and Jacob, 2009). Therefore, the 1000 m water depth is marked on the maps with red contours.

As is shown in Figure 8A, the high-efficiency regions covered almost the entire the ocean basins when the criterion of  $P_w \geq 5$  kW/m was used, except in nearshore areas and oceanic western boundary zones. In particular, China's most promising wave resources were apparent in the South China Sea where the probability was near 0.55, indicating that the working time would be approximately 4800 hours/year. Furthermore, the highly-effective regions were significantly reduced in the Northern Hemisphere when a threshold of 10 kW/m was used (Figure 8B), while there were only a few differences in the Southern Hemisphere. Notably, only the westerlies of the Southern Hemisphere were identified as high-efficiency regions

when the criterion was increased to 20 kW/m (Figure 8C). The nearshore areas close to the Southern Ocean are geographically predisposed to obtaining more wave energy. According to the optimized criteria for water depth, effective working times, and wave power, regions with high potential for wave energy harvesting are identified (white rectangles in Figure 8C). These included the southern coast of Africa, the western and southern coasts of Australia, the nearshore area of New Zealand, and the southern coast of South America. These regions were all close to the westerlies of the Southern Ocean, benefitting from their proximity to the significant wind fields therein (Figure 8D). Therefore, these regions are optimal for the efficient harvest of wave and wind energies simultaneously.

## 4 Variational mechanism of global wave power

When identifying regions to invest in for wave energy harvesting, anticipating how climate variability will affect the prospects or predictability of GWP is critical. In addition to altimeter assimilation, the widely mentioned climate change is also highly expected to explain part of variation trends of GWP, and should be the dominate factor in the altimeter era. Figure 3A provides insight into the potentially interannual or decadal variability factors affecting the wave power.

The correlation coefficients between the climate pattern indexes and the global wave power anomaly (GWPA; yearly GWP minus climate average GWP) were calculated over the entire 42-year time series. A 5-year running mean was adopted for removing small-scale variability (Figure 9), and the decadal-oscillation trends were apparent in the GWPA time series.

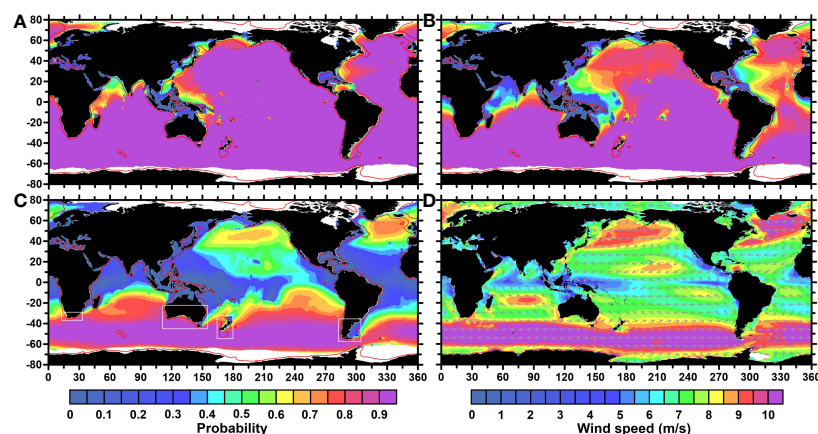


**FIGURE 8**  
Distributions of the daily wave power and wind speed per  $0.5^\circ \times 0.5^\circ$  cell. Probabilities for wave power values great than (A) 5, (B) 10, and (C) 20 kW/m. (D) Averaged wind speeds. The red lines denote water depths contours of 1000 m, while the white rectangles mark regions with high wave power harvesting potential.

According to the statistical analyses, the SAM (PDO) Index and GWPA had the largest positive (negative) correlation coefficient at 0.84 (-0.57), as shown in Figure 9A. Furthermore, to evaluate the different roles of the climate patterns in modulating local ocean basins, the coefficients were independently estimated from the wave power anomalies (WPA) of the Southern Ocean (40°S~80°S), North Pacific Ocean (130°E~250°E), and Northern Atlantic Ocean (310°E~360°E), and the results are shown in Figure 9B. The correlation coefficients ( $r$ ) between the SAM index and WPA were the largest in all three basins, with values of 0.86, 0.72, and 0.61, respectively. The PDO index had the strongest negative correlation ( $r = -0.51$ ) with WPA in the SO, which was consistent with the strong negative correlation between PDO and GWPA (Figure 9A). However,  $r$  is only equal to -0.25 in the northern Pacific Ocean, which indicated that the role of PDO was weaker in the wave climates of the northern Pacific Ocean. The AO index and WPA had the strongest correlation ( $r = 0.56$ ) in the Northern Atlantic Ocean, but it was irrelevant to the WPA in the Northern Pacific Ocean ( $r = 0.06$ ). Therefore, the SAM index was most closely related to the variability in wave power in all three oceans, while the AO index was vital for  $P_w$  in the

Northern Atlantic Ocean. The PDO index was negatively correlated with wave power and better correlated with WPA in the Southern Ocean ( $r = -0.51$ ). Therefore, wave power seemed to bridge SAM and other climate indexes. Clearly, local climate variability can drive the wave power variability throughout the oceans, which means that the GWP can also be seen as an effective indicator of climate change.

Since the station-based SAM index is derived by the analyzing the zonal pressure differences between twelve stations at around 65°S and 40°S (Marshall, 2003), it is an actual indicator independent from model products and altimeter observations. These data supported that the transformation of the SAM index from negative to positive was another reason for the sharp increase in GWP after 1991. In the subsequent time series, the SAM index maintained a positive (quasi-) decadal oscillating trend, forming the variation patterns of GWP. Meanwhile, the weak influences of other climate indexes may also modulate the oscillating trends (see in Figure 8A). Furthermore, the GWPA is predicted to maintain its downward trend after 2020, and the SAM index appears close to the trough of an oscillation, as suggested by Figure 9, which means that the GWP may soon reach the lowest level of almost two decades.

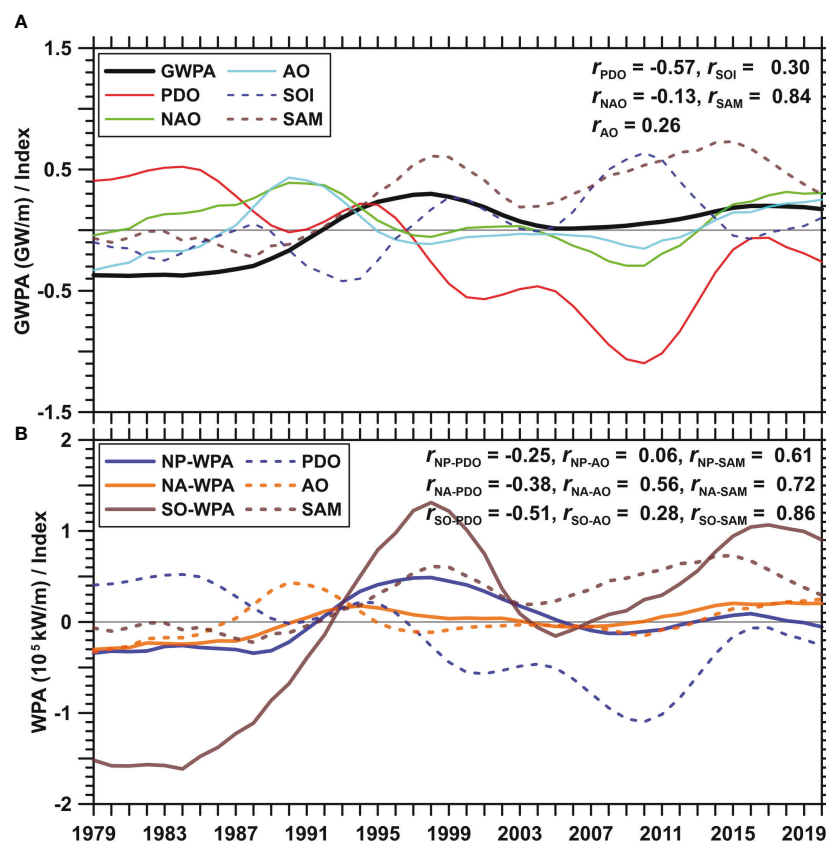


FIGURE 9

Time series of the wave power anomaly and the climate variability indexes (PDO, Pacific Decadal Oscillation; NAO, North Atlantic Oscillation; AO, Arctic Oscillation; SOI, Southern Oscillation Index; SAM, Southern Annular Mode). (A) For annual global wave power anomaly, (B) for wave power anomaly in the North Pacific (NP, 130°E~250°E), North Atlantic (NA, 310°E~360°E), and Southern Oceans (SO, 40°S~80°S). Their correlation coefficients are shown in the panels.

## 5 Conclusions

The urgent need to reduce carbon emissions has recently promoted an upsurge of research into renewable energies. Oceanic resources are abundant and diversified in composition, but the investment and utilization rates are remarkably low. As the most ubiquitous dynamic ocean phenomenon, wave energy has been identified as a good energy harvesting resource. The GWP distribution and variability are systematically analyzed based on recent ERA5 reanalysis data with hourly and monthly temporal resolutions. The main conclusions were as follows:

1) Global wave power is mainly centralized in two westerly zones (latitude bands of 40°~60° in both hemispheres), and swell dominates the magnitude (approximately to 70%) and distribution characteristics of total wave energy. With global warming, potential wave power in the Southern Ocean is growing (like the economic term “rich-get-richer”), and the composited information on the direction of wave power confirms its importance to the GWP distribution.

2) Wave power exhibits seasonal characteristics. The strongest wave power (greater than 100 kW/m) occur during the local winter, while the weakest (less than 10 kW/m in the Northern Hemisphere and less than 60 kW/m in the Southern Hemisphere) occur in the local summer. These two seasons also correspond to the lowest variabilities in wave power, generally less than 25%. Besides, the differences in wave power between day and night revealed novel wave-like patterns, implicating a mirroring effect in the oceanic response to atmospheric forcing.

3) A decadal oscillation was apparent in the GWP, rather than a monotonously increasing trend as observed in previous studies. The start of altimeter assimilation is an intrinsic cause of the abrupt increase of GWP values in ERA5 products by 12.89% in 1991. Then, a quasi-decadal period variation of wave power (variation near  $\pm 4\%$ ) can be revealed by more reliable model products in the altimeter era. Furthermore, the potentially relevant climate teleconnection indexes (PDO, NAO, AO, SOI, and SAM) are introduced to explain the variability rule of GWP. It is found that SAM had the strongest positive correlation (0.84) with GWP, and the transformation in the SAM index from negative to positive value was the main climate driver behind the sharp increase of GWP after 1991. Also, SAM was highly correlated with wave power in other local basins, implicating ocean waves as a potential mediator between the climate teleconnection patterns. Accurate simulation of the wave field in the Southern Ocean is central to the improvement of the wave model.

A better understanding of the spatiotemporal variability in GWP can help inform wave energy system design and large-scale deployment. Presently, the potential of global wave energy resources remains high but underdeveloped. In addition to paying more attention to the untapped energy reserve of ocean waves, improving funding for wave energy extraction technology is fundamental to its advancement. Besides, achieving high-

accuracy simulations, independent of concurrent observational data, is still highly expected in the future ocean wave modelling.

## Data availability statement

The original contributions presented in the study are included in the article/supplementary material. Further inquiries can be directed to the corresponding author. The data used to support the findings of this study are available as follows. The ERA5 data for this study can be found in the Copernicus Climate Change Service (C3S, <https://cds.climate.copernicus.eu/>). The wind fields can be obtained from the Remote Sensing System (<https://www.remss.com>). The climate teleconnection indexes can be downloaded from the National Oceanic and Atmospheric Administration (NOAA, <https://www.ncdc.noaa.gov/teleconnections/>) and National Center for Atmospheric Research (NCAR, <https://climatedataguide.ucar.edu/climate-data>).

## Author contributions

CC performed methodology, software, validation, data curation, visualization, and writing of the original draft. GC contributed to conceptualization, and supervision. CQ performed methodology, validation, and investigation. JS performed validation and review. All authors contributed to the article and approved the submitted version.

## Funding

This research was jointly supported by the Marine S & T Fund of Shandong Province for National Laboratory for Marine Science and Technology (Qingdao) (No. 2022QNL050301-1), the National Natural Science Foundation of China (Grant No. 41906182), and Open Funding Project of Shandong Provincial Key Laboratory of Marine Ecology and Environment and Disaster Prevention and Mitigation (No. 201901).

## Conflict of interest

The authors declare that the research was conducted in the absence of any commercial or financial relationships that could be construed as a potential conflict of interest.

## Publisher's note

All claims expressed in this article are solely those of the authors and do not necessarily represent those of their affiliated organizations, or those of the publisher, the editors and the reviewers. Any product that may be evaluated in this article, or claim that may be made by its manufacturer, is not guaranteed or endorsed by the publisher.

## References

- Bingölbalı, B., Jafari, H., Akpınar, A., and Bekiroğlu, S. (2020). Wave energy potential and variability for the south west coasts of the black Sea: The WEB-based wave energy atlas. *Renew. Energy* 154, 136–150. doi: 10.1016/j.renene.2020.03.014
- Bromirski, P. D., and Cayan, D. R. (2015). Wave power variability and trends across the north Atlantic influenced by decadal climate patterns. *J. Geophys. Res.: Oceans* 120, 3419–3443. doi: 10.1002/2014jc010440
- Chelton, D. B., Schlax, M. G., Freilich, M. H., and Milliff, R. F. (2004). Satellite measurements reveal persistent small-scale features in ocean winds. *Science* 303, 978–983. doi: 10.1126/science.1091901
- Chen, G. (2014). Revisit to atmospheric oscillations over global oceans: a combined climatology/modality approach. *Int. J. Climatol.* 34, 2715–2729. doi: 10.1002/joc.3870
- Chen, G., Chapron, B., Ezraty, R., and Vandemark, D. (2002). A global view of swell and wind sea climate in the ocean by satellite altimeter and scatterometer. *J. Atmospheric Oceanic Technol.* 19, 1849–1859. doi: 10.1175/1520-0426(2002)019<1849:Agvosa>2.0.Co;2
- Dean, R. G., and Dalrymple, R. A. (1991). *Water wave mechanics for engineers and scientists* Vol. 2 (Singapore: World Scientific Publishing Co. Pte.).
- Dotet, G., Bertin, X., and Taborda, R. (2010). Wave climate variability in the north-East Atlantic ocean over the last six decades. *Ocean Model.* 31, 120–131. doi: 10.1016/j.ocemod.2009.10.010
- ECMWF (2020) *IFS documentation-Cy47r1 "Part VII: ECMWF WAVE MODEL". e. coli.* Available at: <https://www.ecmwf.int/node/19751> (Accessed June 30, 2020).
- Egbert, G. D., and Ray, R. D. (2000). Significant dissipation of tidal energy in the deep ocean inferred from satellite altimeter data. *Nature* 405, 775–778. doi: 10.1038/35015531
- Fairley, I., Smith, H. C. M., Robertson, B., Abusara, M., and Masters, I. (2017). Spatio-temporal variation in wave power and implications for electricity supply. *Renew. Energy* 114, 154–165. doi: 10.1016/j.renene.2017.03.075
- Gregg, M. C. (1973). The microstructure of the ocean. *Sci. Am.* 228 (2), 64–67.
- Gross, R., Leach, M., and Bauen, A. (2003). Progress in Renew. energy. *Environ. Int.* 29, 105–122. doi: 10.1016/s0160-4120(02)00130-7
- Gunn, K., and Stock-Williams, C. (2012). Quantifying the global wave power resource. *Renew. Energy* 44, 296–304. doi: 10.1016/j.renene.2012.01.101
- Hanley, K. E., Belcher, S. E., and Sullivan, P. P. (2010). A global climatology of wind-wave interaction. *J. Phys. Oceanogr.* 40, 1263–1282. doi: 10.1175/2010jpo4377.1
- Hemer, M. A., Church, J. A., and Hunter, J. R. (2010). Variability and trends in the directional wave climate of the southern hemisphere. *Int. J. Climatol.* 30, 475–491. doi: 10.1002/joc.1900
- Hersbach, H., Bell, B., Berrisford, P., Hirahara, S., Horányi, A., Muñoz-Sabater, J., et al. (2020). The ERA5 global reanalysis. *Q. J. R. Meteorol. Soc.* 146, 1999–2049. doi: 10.1002/qj.3803
- IEA (2018) *International energy agency. data and statistics.* Available at: <https://www.iea.org/data-and-statistics/>.
- Izadparast, A. H., and Niedzwecki, J. M. (2011). Estimating the potential of ocean wave power resources. *Ocean Eng.* 38, 177–185. doi: 10.1016/j.oceaneng.2010.10.010
- Jiang, H., and Mu, L. (2019). Wave climate from spectra and its connections with local and remote wind climate. *J. Phys. Oceanogr.* 49, 543–559. doi: 10.1175/jpo-d-18-0149.1
- Kamranzad, B., Etemad-shahidi, A., and Chegini, V. (2013). Assessment of wave energy variation in the Persian gulf. *Ocean Eng.* 70, 72–80. doi: 10.1016/j.oceaneng.2013.05.027
- Mallapaty, S. (2020). How China could be carbon neutral by mid-century. *Nature* 586, 482–483. doi: 10.1038/d41586-020-02927-9
- Marshall, G. J. (2003). Trends in the southern annular mode from observations and reanalyses. *J. Climate* 16, 4134–4143. doi: 10.1175/1520-0442(2003)016<4134:Titsam>2.0.Co;2
- Melikoglu, M. (2018). Current status and future of ocean energy sources: A global review. *Ocean Eng.* 148, 563–573. doi: 10.1016/j.oceaneng.2017.11.045
- Mørk, G., Barstow, S., Kabuth, A., and Pontes, M. T. (2010). “Assessing the global wave energy potential,” *29th International Conference on Ocean, Offshore and Arctic Engineering*, Vol. 3. doi: 10.1115/OMAE2010-20473
- Moriarty, P., and Honnery, D. (2012). What is the global potential for Renewable energy? *Renew. Sustain. Energy Rev.* 16, 244–252. doi: 10.1016/j.rser.2011.07.151
- Muhammed Naseef, T., and Sanil Kumar, V. (2019). Climatology and trends of the Indian ocean surface waves based on 39-year long ERA5 reanalysis data. *Int. J. Climatol.* 40, 979–1006. doi: 10.1002/joc.6251
- Outlook, E. (2020) *International energy outlook 2020. e. coli.* Available at: [https://www.eia.gov/outlooks/ieo/section\\_issue\\_Asia.php](https://www.eia.gov/outlooks/ieo/section_issue_Asia.php) (Accessed October 14, 2020).
- Ozkan, C., and Mayo, T. (2019). The Renewable wave energy resource in coastal regions of the Florida peninsula. *Renew. Energy* 139, 530–537. doi: 10.1016/j.renene.2019.02.090
- Patra, A., Min, S. K., and Seong, M. G. (2020). Climate variability impacts on global extreme wave heights: Seasonal assessment using satellite data and ERA5 reanalysis. *J. Geophys. Res.: Oceans* 125(12), e2020JC016754. doi: 10.1029/2020jc016754
- Pedlosky, J. (1987). *Geophys. fluid dynamics* Vol. Vol. 710 (New York: Springer), 10–1007.
- Qian, C., Jiang, H., Wang, X., and Chen, G. (2019). Climatology of wind-seas and swells in the China seas from wave hindcast. *J. Ocean Univ. China* 19, 90–100. doi: 10.1007/s11802-020-3924-4
- Reguero, B. G., Losada, I. J., and Méndez, F. J. (2015). A global wave power resource and its seasonal, interannual and long-term variability. *Appl. Energy* 148, 366–380. doi: 10.1016/j.apenergy.2015.03.114
- Reguero, B. G., Losada, I. J., and Mendez, F. J. (2019). A recent increase in global wave power as a consequence of oceanic warming. *Nat. Commun.* 10, 205. doi: 10.1038/s41467-018-08066-0
- Rosa, L. P., and Ribeiro, S. K. (2001). The present, past, and future contributions to global warming of CO2 emissions from fuels. *Climatic Change* 48, 289–308. doi: 10.1023/A:1010720931557
- Rusu, E. (2014). Evaluation of the wave energy conversion efficiency in various coastal environments. *Energies* 7, 4002–4018. doi: 10.3390/en7064002
- Rusu, E., and Onea, F. (2018). A review of the technologies for wave energy extraction. *Clean Energy* 2, 10–19. doi: 10.1093/ce/zky003
- Rusu, L., and Rusu, E. (2021). Evaluation of the worldwide wave energy distribution based on ERA5 data and altimeter measurements. *Energies* 14 (2), 394. doi: 10.3390/en14020394
- Salter, S. H. (1974). Wave power. *Nature* 249, 720–724. doi: 10.1038/249720a0
- Scruggs, J., and Jacob, P. (2009). Engineering. harvesting ocean wave energy. *Science* 323, 1176–1178. doi: 10.1126/science.1168245
- Sleiti, A. K. (2017). Tidal power technology review with potential applications in gulf stream. *Renew. Sustain. Energy Rev.* 69, 435–441. doi: 10.1016/j.rser.2016.11.150
- Vieira, F., Calvacante, G., Campos, E., and Taveira-Pinto, F. (2020). Wave energy flux variability and trend along the United Arab Emirates coastline based on a 40-year hindcast. *Renew. Energy* 160, 1194–1205. doi: 10.1016/j.renene.2020.07.072
- Wang, J., and Wang, Y. (2021). Evaluation of the ERA5 significant wave height against NDBC buoy data from 1979 to 2019. *Mar. Geodesy* 45, 151–165. doi: 10.1080/01490419.2021.2011502
- Young, I. R., and Ribal, A. (2019). Multiplatform evaluation of global trends in wind speed and wave height. *Science* 364, 548–552. doi: 10.1126/science.aav9527
- Young, I. R., Zieger, S., and Babanin, A. V. (2011). Global trends in wind speed and wave height. *Science* 332, 451–455. doi: 10.1126/science.1197219



## OPEN ACCESS

## EDITED BY

Giovanni Besio,  
University of Genoa, Italy

## REVIEWED BY

Han Soo Lee,  
Hiroshima University, Japan  
Dominique Mouazé,  
Université de Caen Normandie,  
France

## \*CORRESPONDENCE

Jian Su  
jis@dmu.dk

## SPECIALTY SECTION

This article was submitted to  
Coastal Ocean Processes,  
a section of the journal  
Frontiers in Marine Science

RECEIVED 31 March 2022

ACCEPTED 21 September 2022

PUBLISHED 18 October 2022

## CITATION

Su J, Murawski J, Nielsen JW and  
Madsen KS (2022) Regional wave  
model climate projections for coastal  
impact assessments under a high  
greenhouse gas emission scenario.  
*Front. Mar. Sci.* 9:910088.  
doi: 10.3389/fmars.2022.910088

## COPYRIGHT

© 2022 Su, Murawski, Nielsen and  
Madsen. This is an open-access article  
distributed under the terms of the  
[Creative Commons Attribution License  
\(CC BY\)](https://creativecommons.org/licenses/by/4.0/). The use, distribution or  
reproduction in other forums is  
permitted, provided the original  
author(s) and the copyright owner(s)  
are credited and that the original  
publication in this journal is cited, in  
accordance with accepted academic  
practice. No use, distribution or  
reproduction is permitted which does  
not comply with these terms.

# Regional wave model climate projections for coastal impact assessments under a high greenhouse gas emission scenario

Jian Su\*, Jens Murawski, Jacob W. Nielsen  
and Kristine S. Madsen

Danish Meteorological Institute, Copenhagen, Denmark

In the future, shifts in wind storms across the North and Baltic Seas are highly unpredictable, challenging the projection of wave conditions for managing coastal hazards. Moreover, regional sea level rise (SLR), with very large uncertainty, complicates the situation for stakeholders seeking recommendations for climate adaptation plans. The purpose of this study is to examine the change of the storm surge and wind wave components of the water level due to climate change in a low tidal range Køge Bay near the entrance of the Baltic Sea. Under a high greenhouse gas emission scenario RCP8.5, we employed a regional climate model (HIRHAM) forced wave model (WAM) and focused on the wave model results during the “storm surge conditions” (exceeding 20 years storm surge events) and “stormy conditions” (exceeding 90th percentile of wave heights). We find that the change in both wave height and period in the future is negligible under “stormy conditions”. Nevertheless, under “storm surge conditions” when considering SLR, the simulated wave height is projected to double in the near future (mid-century) under RCP 8.5, and the wave period may also increase by about 1.5 seconds. This is because some high significant wave height events in the future are associated with the storm surge events when considering SLR. The findings suggest that the combined effects of mean sea level rise, storm surge and waves are likely to increase the risk to a bay with geography and exposure comparable to Køge Bay. As a result, the future plan for climate engineering protection should place a premium on the additional wave energy protection associated with storm surges.

## KEYWORDS

climate change, Wave projection, Significant wave height, wave period, Sea state modelling, Risk management

## Introduction

As the mean sea level rises, high water level events along the coasts will become more frequent and intense, causing more damage. Water levels contain components that operate on a variety of temporal and spatial scales, such as the effects of sea level rise (SLR), tides, oceanic currents, storm surge, and locally generated wind waves (Woodworth et al., 2019). However, these components of sea level are highly variable on a regional and interannual basis. Thus, the earlier global evaluations of the dominant components are inapplicable to regional and local issues, as they are often based on global climate models (GCMs) with a relatively coarse spatial resolution (Muis et al., 2016; Morim et al., 2019; Lobeto et al., 2021). Multiple components frequently have a dominating role in a region, although this role changes depending on the coastline morphology and sea state features. As a result, projections of future coastal water levels and flooding should identify which processes are of leading order, and, where appropriate, local impact modeling is required to aid in the development of local climate adaptation strategies (see review of those processes in Idier et al. (2019) and references therein). Our study area, the southern regions of the Copenhagen metropolitan area in Denmark, is vulnerable to future climate change, particularly sea level rise, because relatively small changes in the mean sea level would result in large changes in the return time of storm surge flooding at a

given level (Ditlevsen et al., 2019; Su et al., 2021). According to a specialized research in the region (Hallegatte et al., 2011a; Hallegatte et al., 2011b; Jebens et al., 2016), sea level rise will dramatically increase flood risks in Copenhagen in the absence of adaptation (Figure 1), and the city has been designated as flood prone under the EU flood regulation (European Commission [EC], 2019). Furthermore, a number of studies provide evidence for positive projected trends in extreme wave events along the western European coast (Debernard and Røed, 2008; Grabemann and Weisse, 2008).

With respect to the future changes in wave climate and extreme ocean wave events, it is often derived from wave climate projections (Meucci et al., 2020; Lobeto et al., 2021; Morim et al., 2021). Regional wave projections can be downscaled using physical and atmospheric variable outputs from GCMs dynamically (Dobrynin et al., 2012; Hemer et al., 2013; Casas-Prat et al., 2018) or statistically (Perez et al., 2015; Cannaby et al., 2016; Camus et al., 2017; Leach et al., 2021). The Coordinated Ocean Wave Climate Project (COWCLIP) contributes to integrating and assessing the robustness of wave climate studies (Morim et al., 2018; Morim et al., 2019). Our research location, Køge Bay, is situated in an area that is characterized as a low wave energy environment due to the coastline's orientation with regard to dominant westerly winds and limited fetches. Due to the bay's shape, the shoreline is largely shielded from large waves. The predominant direction of wave energy is southeast

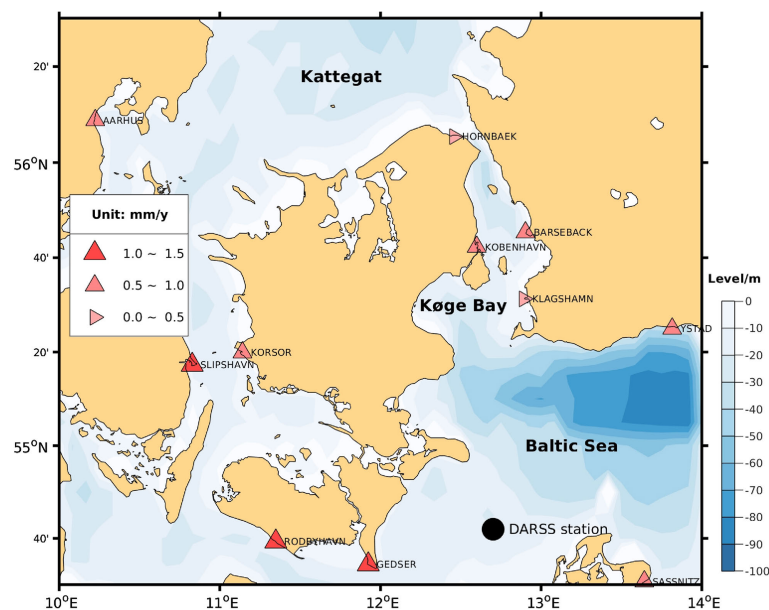


FIGURE 1

Background shaded color: bathymetry (m) of the Inner Danish Waters. The study area is Køge Bay, located at the south of Copenhagen. The closest PSMSL tide gauge station (Permanent Service for Mean Sea Level (PSMSL), 2020) is København (Copenhagen) station. Top symbols: relative sea level rise trends (by change rate,  $\text{mm y}^{-1}$ ) of the PSMSL data set (Permanent Service for Mean Sea Level (PSMSL), 2020). For the methods to calculate the relative sea level rise trends, please refer to <https://www.psmsl.org/products/trends/methods.php>; black dot is the position of the wave buoy station DARSS.

(Sisternans and Nieuwenhuis, 2004). Over the last century, a barrier island system has formed (Figure 2, low-right panel). The first barriers appeared in 1909, and they have gradually grown since then. The beach park at Køge Bay (Køge Beach) was built in 1977 as an extension of the natural barrier islands, and has an 8 km beach today. It is an environmentally friendly land reclamation project (Figure 2), demonstrating how it is feasible to cooperate with natural processes (sand deposition) to construct a sturdy structure with minimum maintenance requirements. Not only is the beach park a recreational zone, but it also acts as a buffer zone against floods in the hinterland. Based on prior well-designed interviews conducted as part of the Copernicus Climatic Change Service (C3S) project, it is obvious that climate projections for sea level rise, storm surge, and waves are needed for local municipalities to design climate adaptation plans (Madsen et al., 2019). Sea level rise and storm surge climate projections were developed as part of the Danish Climate Atlas project (Su et al., 2021). The purpose of this work is to demonstrate the feasibility of using a reasonably efficient and low-cost approach for regional wave model climate projections. Therefore, we employ a dynamical projection approach of regional wave climate using a regional wave model-WAM in this study. This study also serves as the first

step towards insight into a more pressing problem that must be investigated, namely whether wind-driven wave disasters are a concern in the study area. In the context of climate change impact, the concept of risk is a key aspect of concern (IPCC, 2012).

Extreme wave events have severe consequences, such as endangering the safety of coastal residents, causing damage to coastal infrastructure, reshaping a coastline, and elevating coastal sea levels through wave run-up. Nevertheless, the intensity of the impact of extreme weather events is highly dependent on the degree of vulnerability and exposure to these events (IPCC, 2012). Climate-related hazards, exposure, and vulnerability combine interactively to produce the risks associated with climate change consequences (Ara Begum et al., 2022). In the climate community, “vulnerability” is defined as the propensity of an individual or group to be harmed by various risks, hazards, or stressors, whereas “exposure” is the “external side of vulnerability” and refers to the negative impacts of a hazard that have the potential to change the social conditions of a system (Cardona et al., 2012). A study based on social vulnerability models for Denmark showed that the municipalities around Køge Bay expose moderate levels of vulnerability (Pappa, 2019), but extreme wave events are not taken into account. Traditionally, in order to quantify the risk assessment, an

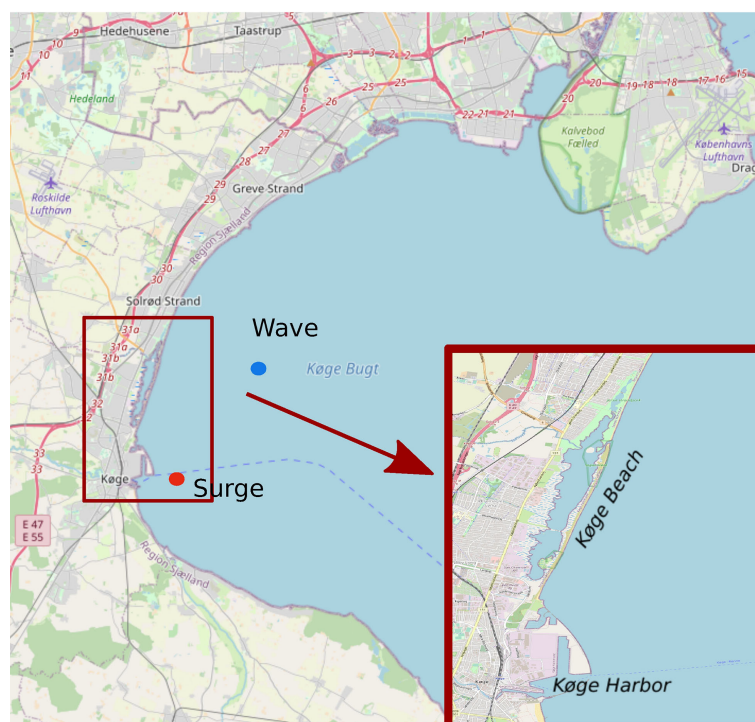


FIGURE 2

Map of the Køge Bay with a red rectangle box indicating the location of the Køge Bay Beach Park. The Beach Park in the bottom right panel shows the barrier islands and the location of Køge harbor. The blue dot represents the grid point from which we extracted the wave model results, and the red dot represents the grid point from which we retrieved the surge level data, since it is the closest grid point to the Køge Harbor tidal gauge station. Base map and data from OpenStreetMap and OpenStreetMap Foundation under the [Open Database License](https://openstreetmap.org/).



analytical framework linking climate information to impact models would be established, followed by the application of damage models and decision-making tools (Hallegatte et al., 2011a; Halsnæs and Kaspersen, 2018). Our study serves as a first step toward risk assessment, i.e. developing a paradigm for wave climate information using impact models. We focus on the extreme conditions in Køge Bay, i.e. storm surge and wind wave components of the water level, as well as their interactions with mean sea level rise. The bay is located in the transition zone between the North and Baltic Seas and has a small tidal range. The Baltic Sea is a semi-closed basin with a tidal range of less than twenty centimeters (Medvedev et al., 2016). Thus, sea level research is simplified compared to that in a hypertidal estuary (Lyddon et al., 2018). Local wind waves often play a significant part in rising sea levels and inundating the shore during a catastrophic high sea level event. During a storm surge event, the coupling impact of surge and wave would increase the threat to coastal zones (Staneva et al., 2016; Marcos et al., 2019). Additionally, the storm surge and wave contributions to a disaster depend on the geography and coastline morphology (Wolf, 2009).

## Methods

### Atmospheric forcing from regional climate model and weather forecast

The meteorological forcing was derived from a single regional climate model, DMI-HIRHAM, developed at the Danish Meteorological Institute (DMI, Christensen et al., 1998), which is a part of CORDEX (Coordinated Regional Climate Downscaling Experiment) ensemble in Europe (EURO-CORDEX, Jacob et al., 2014). The regional model was downscaled from an EC-EARTH r3i1p1 global climate model simulation. The spatial resolution of this EURO-CORDEX ensemble member is 0.11 degree (EUR-11, 12.5 km). The ensemble approach aims at presenting a data set from a multi-model multi-scenario ensemble of regional climate simulations for impact research (Kotlarski et al., 2014). However, a clear definition of the ensemble statistical method for extreme wind speed has not reached a consensus. We show an example of the ensemble annual maximum wind speed time series (16 members) at the Køge Bay (Figure 3). The ensemble annual maximum wind speed (thick black line) is the median of the multi-model results, which shows a very small variability (standard deviation < 2 m/s). Such a small variable time-series is not suitable for this study, which focuses on extreme winds. As a result, we are employing a single member as a driving forcing in our investigation. The variables of DMI-HIRHAM used to force the WAM model are hourly 10 m wind (m/s) and mean sea level pressure (hPa).

In Køge Bay, annual maximum wind speed in DMI-HIRHAM was larger than in other RCMs (Figure 3). The coastal wind is rather dynamic, since it is a result of a variety of factors such as differential heating between land and sea, topography and morphology of the

coastline, and so on. Generally, the shoreline displays a sharp discontinuity in surface roughness. Therefore, we preprocess the forcing data to exclude wind over land.

Apart from the regional climate model, we use the operational forecast suite DMI-HIRLAM (Sass et al., 2002) to get an accurate portrayal of a severe weather event in 2017 (Table 1). HIRLAM (High Resolution Limited Area Model) forecasting is a numerical weather prediction model created by the worldwide HIRLAM consortium (Undén et al., 2002). Throughout the research period, the DMI-HIRLAM model system generated the atmospheric forcing employed in practical storm surge and wave modeling at DMI.

### Regional ocean circulation model

The climate ocean circulation simulations were conducted using the operational model HBM (the HIROMB-BOOS Model) at DMI. The use of operational models in climate research enables the same degree of detail in climate predictions as is possible with the operational setup used for ocean forecasts, ensuring a well-tested and verified approach. DMI runs the regional three-dimensional ocean model HBM for the North and Baltic Seas in order to forecast the physical state of the Danish and adjacent seas in the near future (Berg and Poulsen, 2012; Fu et al., 2012). The model code version was HBM-2.8, and the set-up used in the present study is the DKSS2013 operational version launched at DMI in October 2013 (details on <http://ocean.dmi.dk/models/hbm.uk.php>). The spatial resolution in Køge Bay is 0.5 nautical miles, and the model grid point for validation is close to Køge Harbor (Figure 2, red dot). The validation of HBM to the storm surge events can be found in Andrée et al. (2021). The validation for the storm surge forecast includes online validation and case studies, and details can be found on <http://ocean.dmi.dk/validations/surges/index.uk.php>.

Apart from meteorological forcing, hydrodynamic model simulations need initial conditions, boundary conditions, and runoff data. We used the operational forecasted state vector valid on 1st July 2014 00z as the initial condition, and applied a two-and-a-half-year spin-up period for each time slice. We used boundary conditions derived from the EC-EARTH global climate model findings. We utilized E-HYPE3 run-off for the historical period and added trends from the literature for the scenario simulations.

### Regional ocean wave simulations and wave buoy data

The DMI operational wave forecasting service DMI-WAM makes use of the third generation spectral wave model WAM Cycle version 4.5.4 (Günther et al., 1992; Komen et al., 1996)

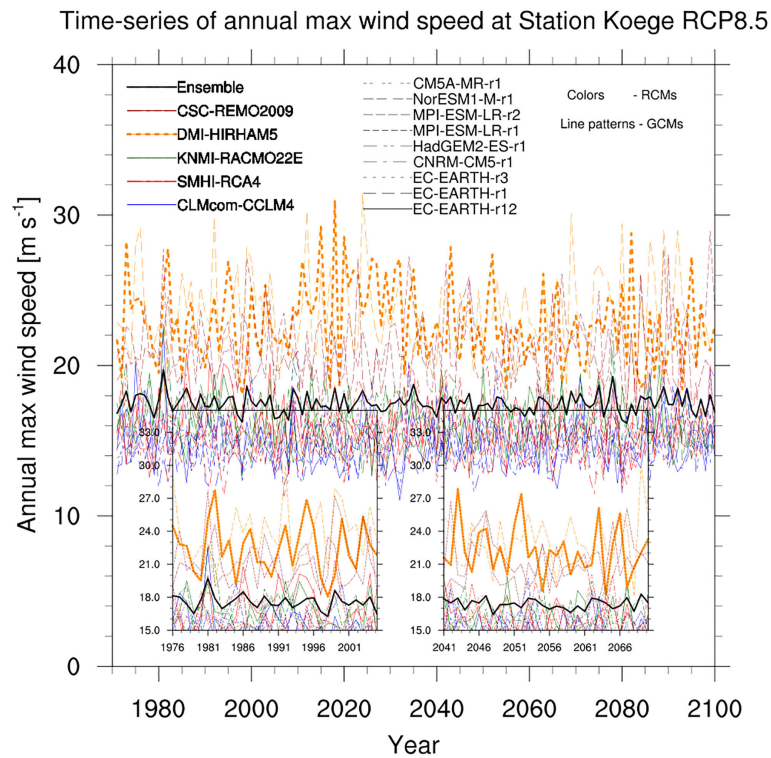


**FIGURE 3**

Time series of annual maximum wind speed at the Køge station for 130 years of simulations from multi-RCMs (16 members, including 5 RCMs, REMO2009: 2; HIRHAM5: 2; RACMO22E: 3; RCA4: 5; CCLM4: 4 members) under RCP 8.5 scenario. The line colours indicate different RCMs, while different line patterns refer to GCMs (downscale to RCMs). DMI-HIRHAM5 downscaled from EC-EARTH (used in this project) is the single dashed thick yellow line. The two panels depict the same time series during two time slices of the projection simulations, i.e. 1976 - 2005 and 2041 - 2070.

which is forced by DMI’s numerical weather prediction model referred to in the above section. The details of the setup are listed in Table 1, and also on <http://ocean.dmi.dk/models/wam.uk.php>. Køge Bay is in the Inner Danish Waters nested model domain (Table 1), and the spatial resolution is 1 km. We

extracted the wave model results at a model grid point close to Køge Beach (Figure 2, blue dot). The closest wave buoy data used for validating the wave model hindcast simulation is from a permanent buoy station DARSS sill station, located outside the Køge Bay at 54.7 °N, 12.7 °E (Figure 1, black dot). There is

**TABLE 1** Regional wave model DMI-WAM setup and meteorological forcing used in this study.

Model domain	North Atlantic	North & Baltic Seas	Inner Danish Water
Spatial resolution	~25 km	~5 km	~1 km
Number of directions	36	36	36
Number of frequencies	35	35	35
Longitude range	69W-30E	13W-30E	7E-16E
Latitude range	30N-78N	47N-66N	53N-60N
Met-forcing in hindcast simulation (spatial resolution)	ECMWF (9 km)	HIRLAM (2.5 km)	HIRLAM (2.5 km)
Met-forcing in projection simulations (spatial resolution)	HIRHAM (12.5 km)	HIRHAM (12.5 km)	HIRHAM (12.5 km)
Open boundary	JONSWAP	nested	nested

The wave energy is discretized into 36 directions (10° resolution), and 35 frequencies ranging from 0.04177 Hz to 1.06417 Hz. That corresponds to wave periods of 0.94-23.94 seconds, and wave lengths of 1.37-895 meters. The North Atlantic model uses the JONSWAP wind-sea spectrum as open boundary data. DMI-WAM is cold started at the beginning of the model simulation periods, and the spin-up time is 10 days. The variables used to force the WAM model are hourly 10 m wind (m/s) and mean sea level pressure (hPa).

also online validation for the forecast periods between the simulated wave height results and buoy measurements. Besides the validation, a monthly report for a global comparative wave model verification and a simple comparison between the model and satellite wave data are shown on <http://ocean.dmi.dk/validations/waves/index.uk.php>.

Regarding the time frame and IPCC scenarios of the wave-related climate issues, we conducted interviews of the municipalities, outlined in Madsen et al. (2019). We found that time scales are determined by how the data is used for climate preparation, i.e., risk assessments (ten to fifty years), or long-term strategic planning (50-to-200 years). Clients are interested in near-future data for wind wave disasters for risk management. Therefore, the study of the near-future weather extremes under the high greenhouse gas emission scenario (RCP8.5 scenario) is more relevant than the examination of low emission scenarios. For these reasons, we decided to perform both HBM and WAM simulations for the historical period and near-future periods under RCP8.5, respectively, from 1976 to 2005 and 2041 to 2070.

## Wave projections under “stormy conditions” and “storm surge conditions”

“Stormy conditions” are defined as the significant wave height (SWH) exceeding the 90th percentile of the distribution (Figure 4). This “stormy condition” may be used to reflect the winter wind conditions in Køge Bay. Wave heights below the 90th percentile are referred to as “normal conditions”.

“Storm surge conditions” are defined in this research as a water surge level that exceeds the 20-year-return storm surge level. The classification of high sea level events as a 20-year return value is in accordance with the Danish Storm Council’s standard. The storm surge statistics were calculated using the peak over threshold (POT) and generalized Pareto distribution (GPD) methods, following the suggestion of Arns et al. (2013). The POT threshold for storm surge statistics is based on the statistics from the Danish Coastal Authority (111 cm for Køge Bay, Ditlevsen et al., 2019). We calculated the 20-year return values for two simulated time periods. The median value of the mean sea level increase for the period 2041-2070 under RCP8.5

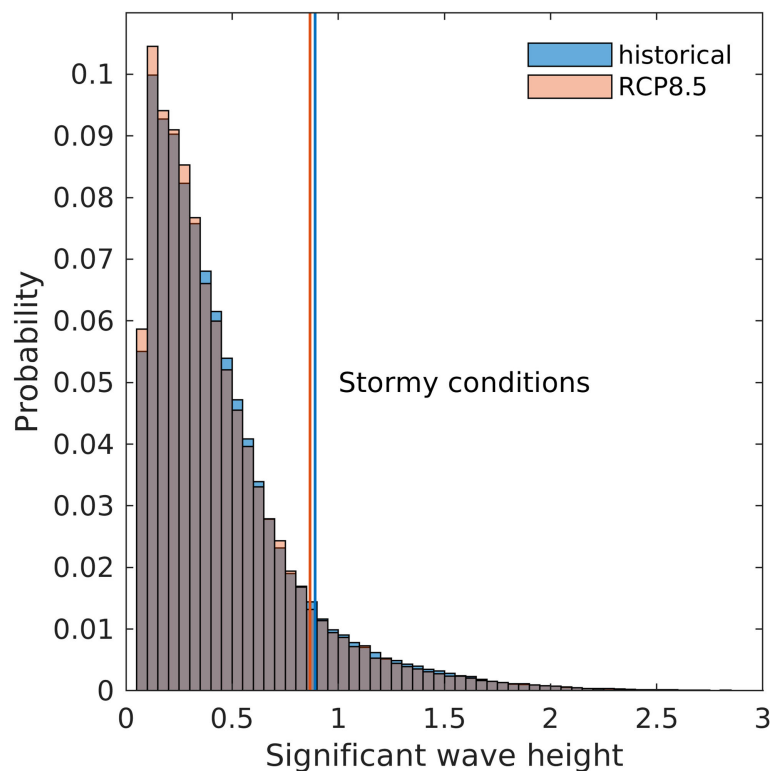


FIGURE 4

Significant wave height (SWH) histograms for historical (blue) and mid-century (orange) periods under RCP8.5. The model output has a temporal resolution of ten minutes. The lines denote the 90th percentile of the distribution. “Stormy conditions” are defined as those in which SWH exceeds the 90th percentile.

is 22 cm, which was simply added to the return values [see the sea level rise calculation in Su et al. (2021)]. The wave climate indicators show the changes in SWH and wave period in 2041 - 2070 compared to the reference period (1976 - 2005), taking into consideration future sea level rise and wind pattern changes.

## Results

### The surge and wave model results and validation of WAM

In practice, model outputs are commonly extracted or interpolated to a particular location in order to validate them against observed data. Consequently, model results should be evaluated cautiously for various purposes. We chose the closest model grid point to Køge Harbor, where the tidal gauge station is located, for the surge model results (Figure 2). This is also common practice for forecasting and warnings of storm surges. The time series of the results from the storm surge forecast model in Køge Bay revealed that storm surge events exceeding 1 m had occurred around 10 times in the last decade (Figure 5, blue line). The highest recorded level was 1.57 m during the January 2017 storm surge event, which we will discuss in depth in the next section.

It is common to calculate an area mean of wave parameters for a bay area when analyzing wave model results. However, we extracted the results at one model grid point offshore Køge Beach (see Figure 2 for the location). As noted in the introduction, the region offshore Køge Beach is the most exposed to waves in Køge Bay, and it is here that we should make recommendations for a climate adaptation plan. The time series of wave heights depicted in Figure 5 (yellow line) demonstrates that high wave events (>2 m) are not always associated with a large storm surge event. For example, the

highest SWH from a wave forecast in recent decades was close to 3 m, which is during the Bodil windstorm in 2013 (Clemmensen et al., 2016). Luckily, the Bodil windstorm did not result in a storm surge event in Køge Bay.

The validation of SWH in DMI-WAM hindcast simulation is shown in Table 2. We extracted the WAM results at the DARSS wave buoy station (54.7 °N 12.7 °E, Figure 1), which is the closed observation station to our study area. We provided annual based error statistics for recent 10 years (2008-2017) in the hindcast simulation period. The mean error statistics for 10 years are: mean error/bias (observation - model) is 0.03 m, root mean square error (RMSE) is 0.26 m, scatter index (RMSE divided by mean of the values) is 0.32, correlation coefficient is 0.9, annual peak event error (observation - model) is 0.47 m, mean error of annual 10 maximum wave events is 0.19 m (Table 2). In cases of peak values, the WAM underestimates SWH, although it is acceptable in long simulations (Cherneva et al., 2008). In general, model outputs and buoy-measured data are in good agreement, which ensures the quality of simulations by giving a good scatter index and correlation coefficients.

### The sea state under normal and storm surge conditions

On January 4-5, 2017, a storm surge hit the southern Baltic Sea and Køge Bay. A period of persistent westerlies increased the mean sea level of the semi-enclosed Baltic Sea by approximately half a meter. This was followed by the passage of an extratropical storm from west to east. A strong easterly wind has developed across the central Baltic Sea, moving the Baltic water mass into the west Baltic Sea, where Køge Bay is located. A number of harbors experienced a storm surge that was classified as a 100-year storm surge event, despite the fact that local wind conditions were not extreme (She and Nielsen, 2019). At the

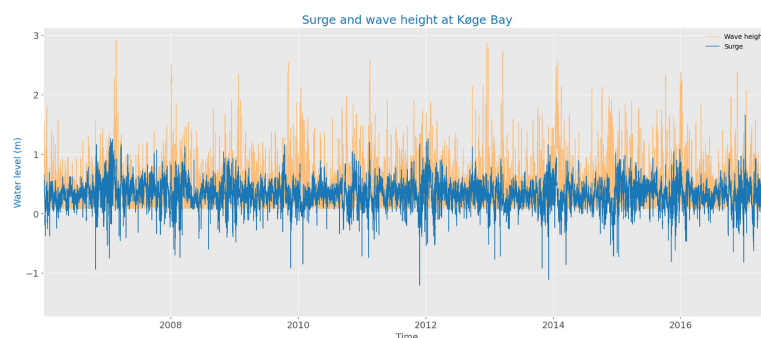


FIGURE 5

The time series of water level (blue) and significant wave height (yellow) from HBM and WAM model results forced by the weather forecast model from 2006 to 2017. The model grid points to extract the water level are shown in Figure 2. The validation of the WAM model with the wave buoy data refers to Table 2.

**TABLE 2** The validation of significant wave height (SWH) in DMI-WAM hindcast simulation against the wave buoy observation at DARSS position (54.7° N 12.7° E).

### Standard error

Year	2008	2009	2010	2011	2012	2013	2014	2015	2016	2017	Total mean
Mean error (m)	-0.01	-0.02	-0.01	0.09	-0.03	-0.12	0.11	0.12	0.08	0.08	0.03
R.M.S error (m)	0.24	0.22	0.3	0.26	0.24	0.34	0.25	0.28	0.25	0.26	0.26
Scatter index	0.31	0.29	0.28	0.35	0.29	0.36	0.35	0.36	0.35	0.3	0.32
Corr. coefficient	0.92	0.9	0.92	0.92	0.89	0.84	0.9	0.91	0.9	0.92	0.9
<b>Peak error</b>											
Date (DD/MM)	22/03	09/11	10/01	09/12	09/10	28/10	27/05	14/11	26/12	13/09	
SWH (m)	3.68	2.9	4.03	2.83	2.67	3.52	3.2	2.66	3.25	3.3	
Error (m)	-0.14	-0.44	0.14	1.25	-0.24	1.47	0.05	0.46	0.75	1.36	0.47
10 peaks mean error (m)	0.05	0.09	0.24	0.62	-0.04	-0.5	0.3	0.58	0.29	0.27	0.19

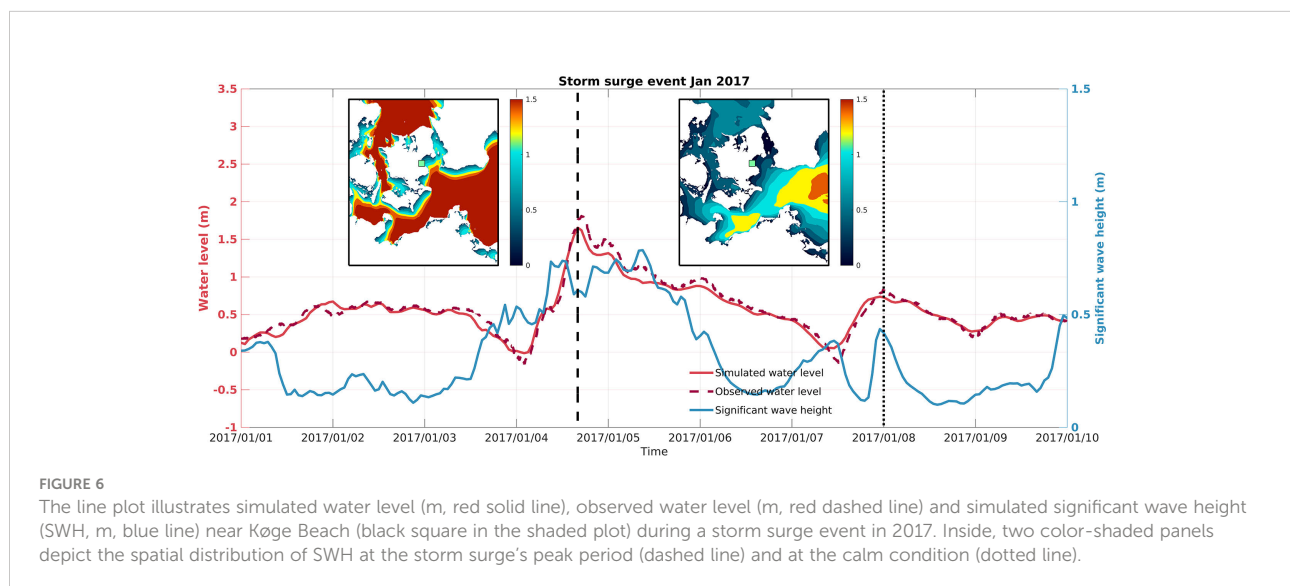
We provided annual based error statistics for recent 10 years (2008–2017) in the hindcast simulation period. The error statistics include mean error/bias (observation - model), root mean square error, scatter index, correlation coefficient, annual peak event error, and mean error of 10 maximum events.

Køge tide gauge station, the maximum water level was registered at 1.57 m (Figure 6, red line), which is the highest level recorded since the tidal gauge station was established in 1955. It was estimated to be a 100-year event (Ditlevsen et al., 2019) that occurred during relatively calm circumstances, and has therefore been named “the silent storm surge” (She and Nielsen, 2019). The surge was well predicted in advance, and the coastal defense was implemented to avert casualties and significant material damage. Nonetheless, the event served as a wake-up call, as large sections of the Køge Bay were on the verge of flooding, and it could have been much worse if the wind had been stronger, resulting in a larger local wind wave, or the average sea level had been higher due to climate change. This has accelerated Denmark’s climate adaption efforts.

Køge Bay is very well sheltered from large waves due to limited fetches. Even though the wind was not as strong as it is during the stormy days, the SWH remained over 0.6 m, with a

maximum of 0.8 m, for nearly a day (Figure 6, blue line). The decreasing of the surge level, in particular, is relatively gradual, which is characteristic of a storm surge in general. Throughout the decreasing surge phase, the SWH is somewhat larger than the average wind wave level during the flooding period. The surge-wave coupling characteristics exacerbated the situation at Køge Bay, and the authorities reported that they were approaching their protection capacity.

The spatial distributions of the maximum and low surge levels during the “silent storm surge” are shown on inside panels of Figure 6. This depicts the “storm surge situation” and “normal condition” described in *Wave projections under “stormy conditions” and “storm surge conditions”*. First, wave heights in Køge Bay and nearby bays remain much lower than in waters outside the bays. Second, the offshore wave height in the western Baltic Seas approaches more than 2 m at the peak of the surge level (Figure 6, inside panel). As a consequence, the coastline



morphology of a bay is more vulnerable to surge flooding than to waves. Third, the wave height in the bay is very modest under normal conditions, suggesting that it will not be an extreme event even with future mean sea level rise.

## The projected future change of the sea state

The time series of the wave model results at Køge Bay (location in Figure 2) over the 2041–2070 period (near-future) under RCP8.5 scenario is depicted in Figure 7. During both historical and near-future 30-year time slices, the number of storm surge events (exceeding 20-year event) is two. When SLR (22 cm) under RCP8.5 is taken into account, the number of storm surge events increases to seven. Intuitively, some high SWH events are associated with storm surge events when considering SLR. This indicates that some of the high wave events in the present climate may reach a critical level and become a problem in the future, when more of these events might be associated with storm surges. In other words, storm events with high SWH, and a similar magnitude of wind speed as during the Bodil Storm, might become a concern in the future. As a result, the wave height during “storm surge conditions” increases from 0.75 m during the historical period to 1.63 m during the near-future period (Figure 8).

The wave climate indicators measure the change in mean SWH and in wave periods during stormy and storm surge conditions and are shown in Figure 8. It was computed as changes in wave height and wave periods from one single ensemble forced model result (see *Wave projections under “stormy conditions” and “storm surge conditions”*). During stormy conditions, the change in wave height in the future is negligible (Figure 8, second column). Nevertheless, during storm surge conditions (exceeding 20 years return value), the simulated

wave height is projected to double in the near future (Figure 8, third column), and the wave period may also increase by about 1.5 second (Figure 8). The results indicate a possible increased coastal risk from the combined effects of storm surge and waves. For municipalities, it is quite relevant to coastal planning.

## Discussion

### Uncertainty and spatial resolution

Uncertainty of the wave projection has numerous ways to assess, including multi-models, multi-scenarios, and uncertainty of SLR, etc. A multi-model ensemble is frequently necessary in order to conduct a comprehensive risk assessment for a wave model climate projection study. However, prior to the estimation of the level of uncertainty, our study presents first insight into a more pressing problem that must be investigated, namely, whether or not increasing disastrous wind waves may be a concern in our study region. From our model results, it is evident that mean SLR and the associated uncertainty are the most important threats to the coasts under RCP8.5 scenario (Figure 8). Therefore, we contend that uncertainty of wind wave height and period, based on a multi-model ensemble, is of secondary importance in this region. The arguments listed below also support our conclusions.

Firstly, the existing multi-model ensemble based on GCMs is insufficient to systematically sample the uncertainty associated with wave-climate projections (Hemer et al., 2013). While the comparison of high wind events among EURO-CORDEX members is essential in this work, the effects of extreme wind on climate scenario simulations have not been thoroughly addressed in prior ensemble studies (Kunz et al., 2010). Other relevant parameters, such as the time averaged wind field and mean sea level pressure, have been carefully investigated in a

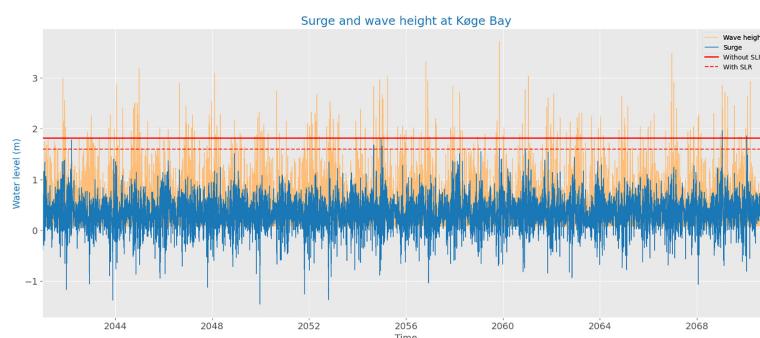
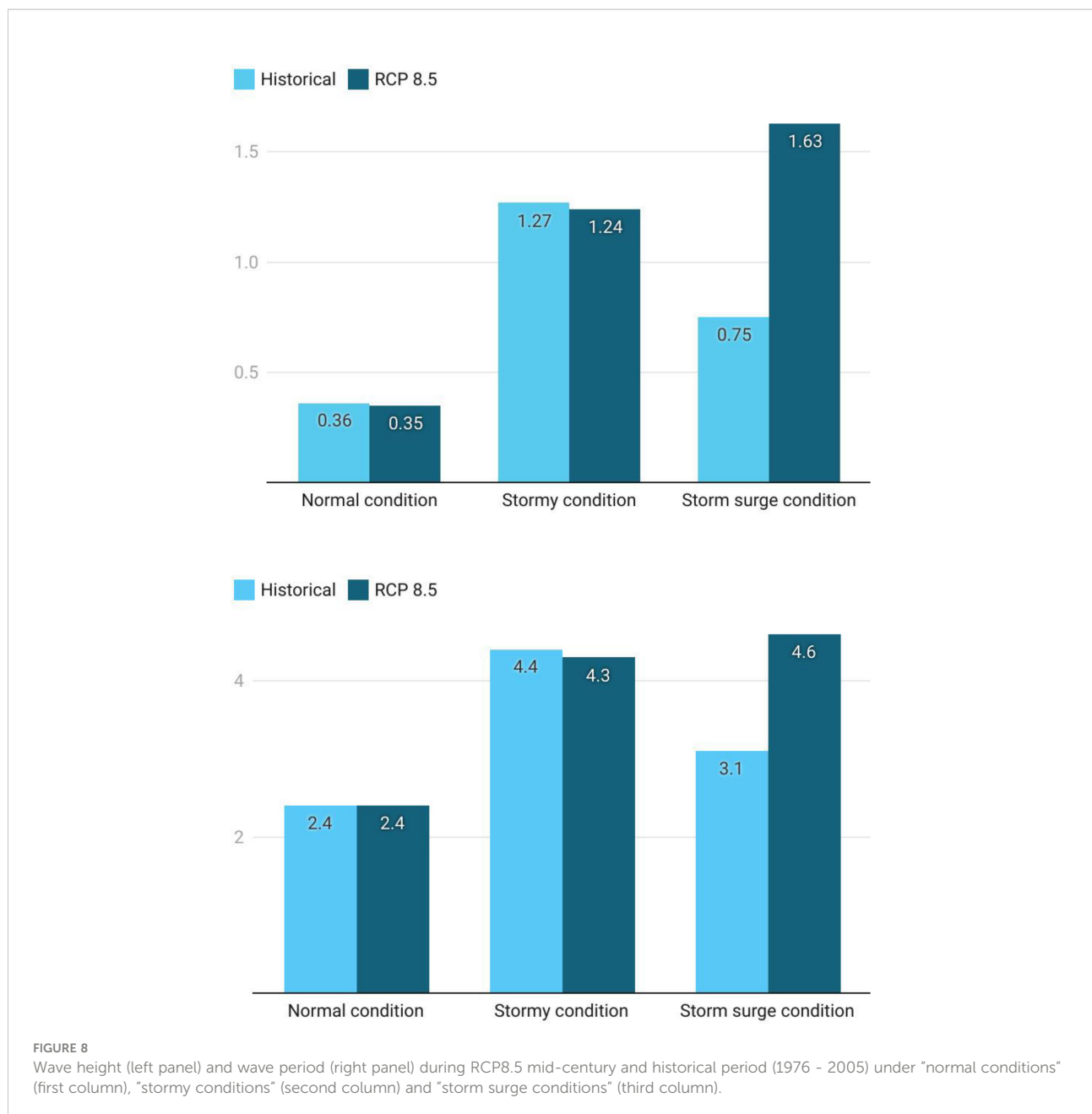


FIGURE 7

During the future period under RCP8.5 scenario (2041–2070), the time series of the surge (blue) and wave height (yellow) are shown. The red line represents the 20-year-event without consideration for sea level rise (SLR, 1.82 m), whereas the red dashed line represents the 20-year-event with regard to SLR (1.6 m). Note that to keep the same line as present day, we need to lower the threshold under SLR conditions. Two events are considered “storm surge conditions” in the absence of SLR, whereas seven events are included with SLR.



number of papers (Kotlarski et al., 2014; Jacob et al., 2014; Tobin et al., 2016; Moemken et al., 2018). We illustrate, using a time series of annual maximum wind speed from Køge Bay, why ensemble averages of the highest wind fields are inappropriate for our investigation (Figure 3). It is worth noting that among all RCMs, in Køge Bay HIRHAM annual maximum coastal winds are the strongest, but this result cannot be generalized. We analyzed several locations (not shown) and found HIRHAM results lower than other RCMs. Following the analysis from Kotlarski et al. (2014), we conclude that the wind results of DMI-HIRHAM are within the ensemble spread. However, extreme winds across Europe should be investigated further, particularly

in comparison to observed winds during catastrophic events. Without a systematic assessment of the uncertainty of extreme winds, the quantification of the uncertainty of the wave projections remains unreliable.

Secondly, the uncertainty associated with multi-scenarios is impractical for coastal risk management. The main use of various climate scenarios is for mitigation measures, which is not very relevant for wave climate projections. In particular, sea state conditions in scenarios with low greenhouse gas emissions are similar to present day values. In this paper, we focus on the high greenhouse gas emission scenario, which offers a foundation for risk management to be well-prepared for the

intensifying future weather extremes. Furthermore, the regional wave model climate simulation is costly. It is reasonable to question whether the benefits of uncertainty quantification based on model ensembles outweigh the costs.

Another relevant concern of the wave disaster is the wave run-up. Wave run-up is an important component of coastal flooding and erosion processes, particularly under extreme conditions when it is paired with high tides and storm surges (Senechal et al., 2011). For the climate projection study, an empirical formula for wave run-up may be utilized based on probabilistic models for surge, wave and morphological conditions. However, the complexity of wave run-up on realistic cross-shore profiles precludes analytical solutions; hence, simplified wave run-up formulae should rely on field observations and laboratory experimentation (Didier et al., 2015; Park and Cox, 2016). The complexity of the Køge Bay shoreline is also the reason the municipalities near the Køge Bay stressed that they require spatially high-resolution wave data sets that cover the local coasts of their urban and sub-urban municipalities at a spatial resolution of 100 meters to resolve wave run-ups (Madsen et al., 2019). We argue that the risk management for the disaster of the wave run-up is associated with storm surge conditions, which is in line with our suggestions in this paper, i.e. storm surges under SLR are the most important threat to concern. Moreover, a very high resolution wave model is beyond the capability of our operational wave model in its present configuration. In other words, warnings related to wave run-up and storm surges are merged in the present day. Consequently, we believe that the wave run-up study is more pertinent to understanding wave-surge coupling processes using a high resolution coupled wave-circulation model, such as the study in Staneva et al. (2016); Ding et al. (2020). Then, the spatial resolution of the meteorological forcing of RCMs, (12.5,km) is not suitable for this study; hence, it falls beyond the scope of the wave projection work.

## Implications to climate risk management

Model results of extreme sea level and wave events aid decision-making in the domain of coastal zone management, planning, and defense. In Denmark, these choices are determined at the municipal level, with cooperation from the Danish Coastal Authority. Our research region, Køge Bay, serves as a recreational area and port sector for the Copenhagen metropolitan area, and has experienced tremendous expansion in services, trade, transport, and logistics, among other industries. Consequently, the vulnerability to extreme flooding event has increased with the urbanization in recent years (Sørensen, 2016). To quantify the risk assessment, a damage model and decision-making tools would be required (Halsnæs and Kaspersen, 2018), which is outside the scope of this study.

Consequently, we only present the qualitative implications of our model results for climate risk management.

Due to the fact that coastal climate change significantly increases the danger of flooding from storm surges, adaptation offers obvious advantages for municipalities, particularly when long-term planning is considered (Zougmore et al., 2012). The targeted coastal climate information derived from our data and methods will assist municipalities in making future business decisions by establishing a credible foundation for decision making and prioritizing resources for coastal climate adaptation. Our model experiment revealed that mean SLR is the most important threat to the coasts under a high emission scenario. In the future, the coastal hazards under SLR scenarios should be considered for future spatial planning and urban recreational development. We propose that the risk caused by wind-generated waves is of secondary significance for long-term coastal zone planning. The combined effects of mean SLR, storm surge, and waves are anticipated to enhance the threat to Køge Bay, and should thus be considered first.

The connection between climate data and decision-making should be strengthened so that society can manage the risks and possibilities associated with climate change. Effective engagement between users and providers of climate services is a crucial component of any climate service, according to Hewitt et al. (2012); the added value of the Danish Climate Atlas initiatives (Su et al., 2021) is precisely this. The research from the Danish Climate Atlas reveals that a rise in mean sea level will significantly increase the risk of flooding from storm surges in the study region, with significant economic consequences. Our wave model results were communicated during the subsequent workshop on designing climate indicators for the wave catastrophe. The municipalities recognized that this study is a first step in the development of a paradigm for wave projections.

## Conclusion

The aim of this research is to analyze the change in storm surge and wind wave (surge-wave) components of the water level caused by climate change in the low tidal range Køge Bay, located near the Baltic Sea entrance. We utilized a regional climate model driven wave model to study the wave climate projections in the near future under RCP8.5 scenario. Under “stormy” conditions, we find that wave height and period will not change significantly in the future. It is possible that under “storm surge conditions” when taking into account SLR, the wave height may double and the wave period increase by around 1.5 seconds under RCP8.5. This is due to future storm surge events being linked to high-significance wave height events when sea level is rising. The results indicate that the flooding and erosive threats to a bay with a similar coastline and exposure as Køge Bay are expected to grow due to the combined effects of mean SLR, storm surge, and wind waves. Storm surges are the



major threats, but additional wave run-up protection should be prioritized in the near future.

Additionally, our studies advocate that long-term urban planning should include adaptation as a component of initiatives to mitigate the consequences of climate change. For example, one of Denmark's greatest climate adaptation projects is located south of Copenhagen, and involves the elevation and expansion of dikes, as well as the development of additional flood gates (Danish Nature Agency [DNA], 2013). This work gives a first step toward developing a paradigm for climate wave projections in the study region, i.e. wave information should be considered only when combining storm surge and SLR.

## Data availability statement

The datasets for this study can be found in the Climate Data Store (CDS) from Copernicus Climate Change Service, at <https://climate.copernicus.eu/climate-change-koge-bay-region-baltic-sea>.

## Author contributions

JS: Drafting of manuscript, analysis and interpretation of data. JM: Acquisition of data, analysis and interpretation of data. JN: Performed the model simulation required for derivation of indicators. KM: Study conception and design, project coordinator. All authors contributed to manuscript revision, read, and approved the submitted version.

## References

- Danish Nature Agency [DNA]. (2013). *Klimatilpasningsplaner og klimalokalplaner - guidelines*. Available at: [http://www.klimatilpasning.dk/media/598918/klimatilpasningsvejledning\\_web.pdf](http://www.klimatilpasning.dk/media/598918/klimatilpasningsvejledning_web.pdf) (Accessed Jan 21, 2021).
- Andrée, E., Su, J., Larsen, M. A. D., Madsen, K. S., and Drews, M. (2021). Simulating major storm surge events in a complex coastal region. *Ocean Model.* 162, 101802. doi: 10.1016/j.ocemod.2021.101802
- Ara Begum, R., Lempert, R., Ali, E., Benjaminsen, T., Bernauer, T., Cramer, W., et al. (2022). "Point of departure and key concepts," in *The intergovernmental panel on climate change* (Cambridge, United Kingdom and New York, NY, USA: Cambridge University Press). Available at: [https://www.ipcc.ch/report/ar6/wg2/downloads/report/IPCC\\_AR6\\_WGII\\_Chapter01.pdf](https://www.ipcc.ch/report/ar6/wg2/downloads/report/IPCC_AR6_WGII_Chapter01.pdf).
- Arns, A., Wahl, T., Haigh, I., Jensen, J., and Pattiaratchi, C. (2013). Estimating extreme water level probabilities: A comparison of the direct methods and recommendations for best practise. *Coast. Eng.* 81, 51–66. doi: 10.1016/j.coastaleng.2013.07.003
- Berg, P., and Poulsen, J. W. (2012). Implementation details for HBM. *Tech. Rep.*, 12–11. Danish Meteorological Institute.
- Camus, P., Losada, I. J., Izaguirre, C., Espejo, A., Menéndez, M., and Pérez, J. (2017). Statistical wave climate projections for coastal impact assessments. *Earth's Future* 5, 918–933. doi: 10.1002/2017EF000609
- Cannaby, H., Palmer, M. D., Howard, T., Brichenno, L., Calvert, D., Krijnen, J., et al. (2016). Projected sea level rise and changes in extreme storm surge and wave events during the 21st century in the region of Singapore. *Ocean Sci.* 12, 613–632. doi: 10.5194/os-12-613-2016
- Cardona, O.-D., van Aalst, M. K., Birkmann, J., Fordham, M., McGregor, G., Perez, R., et al. (2012). *Determinants of risk: Exposure and vulnerability* (Cambridge, United Kingdom and New York, NY, USA: Cambridge University Press, 65–108. doi: 10.1017/CBO9781139177245.005
- Casas-Prat, M., Wang, X., and Swart, N. (2018). CMIP5-based global wave climate projections including the entire Arctic ocean. *Ocean Model.* 123, 66–85. doi: 10.1016/j.ocemod.2017.12.003
- Cherueva, Z., Andreeva, N., Pilar, P., Valchev, N., Petrova, P., and Guedes Soares, C. (2008). Validation of the WAMC4 wave model for the black Sea. *Coast. Eng.* 55, 881–893. doi: 10.1016/j.coastaleng.2008.02.028
- Christensen, O. B., Christensen, J. H., Machenhauer, B., and Botzet, M. (1998). Very high-resolution regional climate simulations over Scandinavia—present climate. *J. Climate* 11, 3204–3229. doi: 10.1175/1520-0442(1998)011<3204:VHRRCS>2.0.CO
- Clemmensen, L. B., Glad, A. C., and Kroon, A. (2016). Storm flood impacts along the shores of micro-tidal inland seas: A morphological and sedimentological study of the vesterlyng beach, the belt Sea, Denmark. *Geomorphology* 253, 251–261. doi: 10.1016/j.geomorph.2015.10.020
- European Commission [EC]. (2019). *Flood risk management - water - environment - European commission*. Available at: [https://ec.europa.eu/environment/water/flood\\_risk/](https://ec.europa.eu/environment/water/flood_risk/) (Accessed Jan 21, 2021).
- Debernard, J. B., and Roed, L. P. (2008). Future wind, wave and storm surge climate in the northern seas: a revisit. *Tellus A: Dynamic Meteorology Oceanography* 60, 427–438. doi: 10.1111/j.1600-0870.2007.00312.x

## Funding

This work is co-funded by CoDEC and Danish Climate Atlas projects. CODEC is funded by the Copernicus Climate Change Service the C3S\_422\_Lot2\_Deltares contract on coastal climate change. Danish Climate Atlas is funded by the Danish State.

## Acknowledgments

We would like to thank Dr. Ole Bøssing Christensen for his advice and assistance with the regional climate model analyses.

## Conflict of interest

The authors declare that the research was conducted in the absence of any commercial or financial relationships that could be construed as a potential conflict of interest.

## Publisher's note

All claims expressed in this article are solely those of the authors and do not necessarily represent those of their affiliated organizations, or those of the publisher, the editors and the reviewers. Any product that may be evaluated in this article, or claim that may be made by its manufacturer, is not guaranteed or endorsed by the publisher.

- Didier, D., Bernatchez, P., Boucher-Brossard, G., Lambert, A., Fraser, C., Barnett, R. L., et al. (2015). Coastal flood assessment based on field debris measurements and wave runup empirical model. *J. Mar. Sci. Eng.* 3, 560–590. doi: 10.3390/jmse3030560
- Ding, Y., Ding, T., Rusdin, A., Zhang, Y., and Jia, Y. (2020). Simulation and prediction of storm surges and waves using a fully integrated process model and a parametric cyclonic wind model. *J. Geophysical Research: Oceans* 125, e2019JC015793. doi: 10.1029/2019JC015793
- Ditlevsen, C., Ramos, M., Sørensen, C., Ciocan, U., and Piontkowitz, T. (2019). Højvandsstatistikker 2017. *Tech. Rep.* Kystdirektoratet.
- Dobrynin, M., Murawsky, J., and Yang, S. (2012). Evolution of the global wind wave climate in CMIP5 experiments. *Geophysical Res. Lett.* 39:L18606 doi: 10.1029/2012GL052843
- Fu, W., She, J., and Dobrynin, M. (2012). A 20-year reanalysis experiment in the Baltic Sea using three-dimensional variational (3DVAR) method. *Ocean Sci.* 8, 827–844. doi: 10.5194/os-8-827-2012
- Grabemann, I., and Weisse, R. (2008). Climate change impact on extreme wave conditions in the north Sea: an ensemble study. *Ocean Dynamics* 58, 199–212. doi: 10.1007/s10236-008-0141-x
- Günther, H., Hasselmann, S., and Janssen, P. A. (1992). The WAM model cycle 4. *Tech. Rep.*
- Hallegatte, S., Henriot, F., and Corfee-Morlot, J. (2011a). The economics of climate change impacts and policy benefits at city scale: a conceptual framework. *Climatic Change* 104, 51–87. doi: 10.1007/s10584-010-9976-5
- Hallegatte, S., Ranger, N., Mestre, O., Dumas, P., Corfee-Morlot, J., Herweijer, C., et al. (2011b). Assessing climate change impacts, sea level rise and storm surge risk in port cities: a case study on Copenhagen. *Climatic Change* 104, 113–137. doi: 10.1007/s10584-010-9978-3hallegatte2011assessing
- Halsnæs, K., and Kaspersen, P. S. (2018). Decomposing the cascade of uncertainty in risk assessments for urban flooding reflecting critical decision-making issues. *Climatic Change* 151, 491–506. doi: 10.1007/s10584-018-2323-y
- Hemer, M. A., Fan, Y., Mori, N., Semedo, A., and Wang, X. L. (2013). Projected changes in wave climate from a multi-model ensemble. *Nat. Climate Change* 3, 471–476. doi: 10.1038/nclimate1791
- Hewitt, C., Mason, S., and Walland, D. (2012). The global framework for climate services. *Nat. Climate Change* 2, 831–832. doi: 10.1038/nclimate1745
- Ilder, D., Bertin, X., Thompson, P., and Pickering, M. D. (2019). Interactions between mean Sea level, tide, surge, waves and flooding: Mechanisms and contributions to Sea level variations at the coast. *Surveys Geophysics* 40, 1603–1630. doi: 10.1007/s10712-019-09549-5
- IPCC (2012). *Managing the risks of extreme events and disasters to advance climate change adaptation* (Cambridge, England: Cambridge University Press).
- Jacob, D., Petersen, J., Eggert, B., Alias, A., Christensen, O. B., Bouwer, L. M., et al. (2014). EURO-CORDEX: New high-resolution climate change projections for European impact research. *Regional Environ. Change* 14, 563–578. doi: 10.1007/s10113-013-0499-2
- Jebens, M., Sorensen, C., and Piontkowitz, T. (2016). Dynamics and modelling of ocean waves,” in *E3S Web of Conferences*, (Cambridge, United Kingdom: Cambridge University Press) 7, 23005. doi: 10.1051/e3sconf/20160723005
- Komen, G. J., Cavaleri, L., Donelan, M., Hasselmann, K., Hasselmann, S., and Janssen, P. A. E. M. (1996). Dynamics and modelling of ocean waves.
- Kotlarski, S., Keuler, K., Christensen, O. B., Colette, A., Déqué, M., Gobiet, A., et al. (2014). Regional climate modeling on European scales: a joint standard evaluation of the EURO-CORDEX RCM ensemble. *Geoscientific Model. Dev.* 7, 1297–1333. doi: 10.5194/gmd-7-1297-2014
- Kunz, M., Mohr, S., Rauthe, M., Lux, R., and Kottmeier, C. (2010). Assessment of extreme wind speeds from regional climate models – part 1: Estimation of return values and their evaluation. *Natural Hazards Earth System Sci.* 10, 907–922. doi: 10.5194/nhess-10-907-2010
- Leach, C., Hague, B. S., Kennedy, D. M., Carvalho, R. C., and Ierodiaconou, D. (2021). Identifying oceanographic conditions conducive to coastal impacts on temperate open coastal beaches. *Natural Hazards* 109, 499–521. doi: 10.1007/s11069-021-04845-z
- Lobeto, H., Menendez, M., and Losada, I. J. (2021). Future behavior of wind wave extremes due to climate change. *Sci. Rep.* 11, 7869. doi: 10.1038/s41598-021-86524-4
- Lyddon, C., Brown, J. M., Leonardi, N., and Plater, A. J. (2018). Flood hazard assessment for a hyper-tidal estuary as a function of tide-surge-morphology interaction. *Estuaries Coasts* 41, 1565–1586. doi: 10.1007/s12237-018-0384-9
- Madsen, K. S., Murawski, J., Blokhina, M., and Su, J. (2019). Sea Level change: Mapping Danish municipality needs for climate information. *Front. Earth Sci.* 7. doi: 10.3389/feart.2019.00081
- Marcos, M., Rohmer, J., Vousedoukas, M. I., Mentaschi, L., Le Cozannet, G., and Amores, A. (2019). Increased extreme coastal water levels due to the combined action of storm surges and wind waves. *Geophysical Res. Lett.* 46, 4356–4364. doi: 10.1029/2019GL082599
- Medvedev, I. P., Rabinovich, A. B., and Kulikov, E. A. (2016). Tides in three enclosed basins: The Baltic, black, and Caspian seas. *Front. Mar. Sci.* 3. doi: 10.3389/fmars.2016.00046
- Meucci, A., Young, I. R., Hemer, M., Kirezci, E., and Ranasinghe, R. (2020). Projected 21st century changes in extreme wind-wave events. *Sci. Adv.* 6, eaaz7295. doi: 10.1126/sciadv.aaz7295
- Moemken, J., Meyers, M., Feldmann, H., and Pinto, J. G. (2018). Future changes of wind speed and wind energy potentials in EURO-CORDEX ensemble simulations. *J. Geophysical Research: Atmospheres* 123, 6373–6389. doi: 10.1029/2018JD028473
- Morim, J., Hemer, M., Cartwright, N., Strauss, D., and Andutta, F. (2018). On the concordance of 21st century wind-wave climate projections. *Global Planetary Change* 167, 160–171. doi: 10.1016/j.gloplacha.2018.05.005
- Morim, J., Hemer, M., Wang, X. L., Cartwright, N., Trenham, C., Semedo, A., et al. (2019). Robustness and uncertainties in global multivariate wind-wave climate projections. *Nat. Climate Change* 9, 711–718. doi: 10.1038/s41558-019-0542-5
- Morim, J., Vitousek, S., Hemer, M., Reguero, B., Erikson, L., Casas-Prat, M., et al. (2021). Global-scale changes to extreme ocean wave events due to anthropogenic warming. *Environ. Res. Lett.* 16, 074056. doi: 10.1088/1748-9326/ac1013
- Muis, S., Verlaan, M., Winsemius, H. C., Aerts, J. C., and Ward, P. J. (2016). A global reanalysis of storm surges and extreme sea levels. *Nat. Commun.* 7, 11969. doi: 10.1038/ncomms11969
- Pappa, M. (2019). *Social vulnerability to coastal floods in Denmark: Investigating the spatial patterns among the Danish*. Available at: <https://projekter.aau.dk/projekter/files/307155336/PappaMariathesis.pdf> (Accessed May 31, 2022).
- Park, H., and Cox, D. T. (2016). Empirical wave run-up formula for wave, storm surge and berm width. *Coast. Eng.* 115, 67–78. doi: 10.1016/j.coastaleng.2015.10.006
- Perez, J., Menendez, M., Camus, P., Mendez, F. J., and Losada, I. J. (2015). Statistical multi-model climate projections of surface ocean waves in Europe. *Ocean Model.* 96, 161–170. doi: 10.1016/j.ocemod.2015.06.001
- Permanent Service for Mean Sea Level (PSMSL) (2020). Available at: <http://www.psmsl.org/data/obtaining/>. [Dataset]
- Sorensen, C. S. (2016). “Water NOT wanted-coastal floods and flooding protection in Denmark,” in *Sicherung von dämmen, deichen und stauanlagen: Handbuch für theorie und praxis*. Eds. R. A. Herrmann and J. Jensen (Siegen: Universität Siegen), 3–21.
- Sass, B. H., Nielsen, N. W., Jørgensen, J. U., Amstrup, B., Kmit, M., and Mogensen, K. S. (2002). “The operational DMI-HIRLAM system 2002-version,” in *Technical report 02-05* (Copenhagen, Denmark: Danish Meteorological Institute).
- Senechal, N., Coco, G., Bryan, K. R., and Holman, R. A. (2011). Wave runup during extreme storm conditions. *J. Geophysical Research: Oceans* 116, C07032. doi: 10.1029/2010JC006819
- She, J., and Nielsen, J. W. (2019). Silent’ storm surge extremes in the western Baltic Sea on 4 January 2017. *J. Operational Oceanography* 12, S111–S11+. doi: 10.1080/1755876X.2019.1633075
- Sistermanns, P., and Nieuwenhuis, O. (2004) EUROSION case study - Koge Bay. Available at: [http://copranet.projects.eucc-d.de/files/000110\\_EUROSION\\_koge\\_bay.pdf](http://copranet.projects.eucc-d.de/files/000110_EUROSION_koge_bay.pdf) (Accessed March 1, 2022).
- Staneva, J., Wahle, K., Koch, W., Behrens, A., Fenoglio-Marc, L., and Stanev, E. V. (2016). Coastal flooding: impact of waves on storm surge during extremes – a case study for the German bight. *Natural Hazards Earth System Sci.* 16, 2373–2389. doi: 10.5194/nhess-16-2373-2016
- Su, J., Andrée, E., Nielsen, J. W., Olsen, S. M., and Madsen, K. S. (2021). Sea Level projections from IPCC special report on the ocean and cryosphere call for a new climate adaptation strategy in the skagerrak-kattegat seas. *Front. Mar. Sci.* 8. doi: 10.3389/fmars.2021.629470
- Tobin, I., Jerez, S., Vautard, R., Thais, F., van Meijgaard, E., Prein, A., et al. (2016). Climate change impacts on the power generation potential of a European mid-century wind farms scenario. *Environ. Res. Lett.* 11, 34013. doi: 10.1088/1748-9326/11/3/034013
- Undén, P., Rontu, L., Jarvinen, H., Lynch, P., Calvo Sánchez, F. J., Cats, G., et al. (2002). HIRLAM-5 scientific documentation. *Tech. Rep.* Swedish Meteorological and Hydrological.
- Wolf, J. (2009). Coastal flooding: impacts of coupled wave–surge–tide models. *Natural Hazards* 49, 241–260. doi: 10.1007/s11069-008-9316-5Wolf2009
- Woodworth, P. L., Melet, A., Marcos, M., Ray, R. D., Wöppelmann, G., Sasaki, Y. N., et al. (2019). Forcing factors affecting sea level changes at the coast. *Surveys Geophysics* 40, 1351–1397. doi: 10.1007/s10712-019-09531-1
- Zougmore, R., Kadi, M., McGregor, G. R., Rao, P., Pulwarty, R., Ndiaye, O., et al. (2012). “Improving climate risk management at local level - techniques, case studies, good practices and guidelines for world meteorological organization members,” in *Risk management - current issues and challenges*. Ed. N. Banatiene (London, United Kingdom: IntechOpen).



## OPEN ACCESS

EDITED BY  
Bahareh Kamranzad,  
Kyoto University, Japan

REVIEWED BY  
Riccardo Farneti,  
The Abdus Salam International Centre  
for Theoretical Physics (ICTP), Italy  
Yonggang Liu,  
University of South Florida,  
United States

\*CORRESPONDENCE  
Youyu Lu  
Youyu.Lu@dfo-mpo.gc.ca


SPECIALTY SECTION  
This article was submitted to  
Physical Oceanography,  
a section of the journal  
Frontiers in Marine Science

RECEIVED 30 March 2022  
ACCEPTED 19 October 2022  
PUBLISHED 15 November 2022

CITATION  
Ma Y, Lu Y, Hu X, Gilbert D,  
Socolofsky SA and Boufadel M (2022)  
Model simulated freshwater transport  
along the Labrador current east of the  
Grand Banks of Newfoundland.  
*Front. Mar. Sci.* 9:908306.  
doi: 10.3389/fmars.2022.908306

COPYRIGHT  
© 2022 Ma, Lu, Hu, Gilbert, Socolofsky  
and Boufadel. This is an open-access  
article distributed under the terms of  
the [Creative Commons Attribution  
License \(CC BY\)](https://creativecommons.org/licenses/by/4.0/). The use, distribution  
or reproduction in other forums is  
permitted, provided the original  
author(s) and the copyright owner(s)  
are credited and that the original  
publication in this journal is cited, in  
accordance with accepted academic  
practice. No use, distribution or  
reproduction is permitted which does  
not comply with these terms.

# Model simulated freshwater transport along the Labrador current east of the Grand Banks of Newfoundland

Yongxing Ma<sup>1</sup>, Youyu Lu<sup>1\*</sup>, Xianmin Hu<sup>2</sup>, Denis Gilbert <sup>3</sup>,  
Scott A. Socolofsky<sup>4</sup> and Michel Boufadel<sup>5</sup>

<sup>1</sup>Ocean and Ecosystem Sciences Division, Bedford Institute of Oceanography, Fisheries and Oceans Canada, Dartmouth, NS, Canada, <sup>2</sup>Department of Oceanography, Dalhousie University, Halifax, NS, Canada, <sup>3</sup>Maurice Lamontagne Institute, Fisheries and Oceans Canada, Mont-Joli, QC, Canada, <sup>4</sup>Zachry Department of Civil and Environmental Engineering, Texas A&M University, College Station, TX, United States, <sup>5</sup>Center for Natural Resources, The New Jersey Institute of Technology, Newark, NJ, United States

The freshwater transport (FWT) by the Labrador Current (LC) around the Grand Banks of Newfoundland (GBN) is diagnosed with the 26-year Global Ocean Physical Reanalysis 1/12° data (GLORYS12v1) during 1993 - 2018. The time-mean FWT of the LC above the 1027.25 kg/m<sup>3</sup> isopycnal surface is 83.6 mSv (1 mSv = 10<sup>3</sup> m<sup>3</sup>/s) southward through the Flemish Pass. Among this 83.6 mSv, 42% (35.2 mSv) is exported into the interior of the North Atlantic along the whole pathway of the LC from the Flemish Pass to the Tail of the GBN, with 25.5 mSv by the mean advection and 7.2 mSv by the mesoscale eddy transport. The seasonal and inter-annual variations of the FWT in the east of the GBN are mainly caused by the variation of the horizontal velocity of the LC, and the variation of salinity makes a nontrivial contribution to the variation of the FWT to the north of 45°N. Around the Tail of the GBN, the mesoscale eddies make significant contributions to the time-mean FWT and the seasonal and inter-annual variations of the FWT.

## KEYWORDS

Grand Banks of Newfoundland, Labrador Current, freshwater transport, retroflection, multi-scale variations

## 1 Introduction

The Labrador Current (LC) flows southward offshore of Labrador and Newfoundland, carrying cold and fresh water to meet the warm and salty water of the North Atlantic Current (NAC) in the east and south of the Grand Banks of Newfoundland (GBN), as shown schematically in [Figure 1](#). The freshwater within the

LC enters the interior of the North Atlantic through different processes, such as the wind-driven Ekman transport, eddy exchange (Howatt et al., 2018) and advection by the time-mean flow (Fratantoni and McCartney (2010), hereinafter referred to as F&M2010). This freshwater, entering the interior of the North Atlantic, modifies the upper layer stratification. Eventually, the strength of upper layer stratification in the subpolar North Atlantic affects the amount of deep water formation through vertical convection in winter and hence tunes the Atlantic Meridional Overturning Circulation (AMOC) that has a strong impact on climate (e.g., Zhang, 2015). Studies have suggested a linkage between freshwater discharge into the North Atlantic and the climate variability (Renssen et al., 2002).

As a confluence of the West Greenland Current, the Baffin Island Current and the outflow from the Hudson Strait, the LC has multiple freshwater sources: the Arctic seawater, river discharge and ice sheet melting from continents. The Arctic Ocean exports its freshwater into the LC through two main pathways: one through the Fram Strait and continuing along the east and then west coasts of Greenland (Aagaard and Carmack, 1989); the other through the Canadian Arctic Archipelago (CAA) to the Baffin Bay and the Davis Strait (Cuny et al., 2005). Additionally, a small portion of the Arctic water flows through the Fury and Hecla Straits into the Hudson Bay and outflows through the Hudson Strait (Straneo and Saucier, 2008). The discharge of continental rivers into the Hudson Bay and CAA is another freshwater source for the LC (Déry et al., 2009). Moreover, the ice sheets over Greenland are an additional freshwater source for the LC in the form of melting water and sea ice (Mernild et al., 2009).

Receiving freshwater from those sources with significant seasonal variations, the salinity of the LC has an evident seasonal cycle. Using historical hydrographic observation data, F&M2010 studied the seasonal variation of the salinity of the LC within the shelf water layer between the isopycnal surface of  $1026.8 \text{ kg/m}^3$  and the ocean surface. Overall, they found that the LC south of  $51^\circ\text{N}$  is fresher in summer and saltier in winter because of more river discharge and ice melting in summer (Petrie et al., 1991; Schmidt and Send, 2007; Straneo and Saucier, 2008). At the downstream of the LC on the eastern shelf break of the GBN, the salinity anomaly signal can be mainly attributed to advection from upstream rather than being caused locally by the freshwater flux across the air-sea interface (F&M2010).

The LC transports the low salinity water from the upstream, and along its pathway, this freshwater is gradually lost into the interior of the North Atlantic. Previous observations and numerical model simulations (Lazier and Wright, 1993; Han et al., 2008; Ma et al., 2016) have shown that the LC has an inshore branch flowing along the coast of Newfoundland and an offshore branch near the shelf break. A part of the inshore branch of the LC passes through the Avalon Channel, and the other part joins the offshore branch of the LC around  $49^\circ\text{N}$ . The

offshore branch bifurcates around  $48^\circ\text{N} \sim 49^\circ\text{N}$  north of the Flemish Pass, with a small portion of freshwater exported eastward but the major part exported southward through the Flemish Pass. The offshore branch of the LC can exchange the freshwater with the interior of the North Atlantic along its pathway. Based on the observations with the gliders, Howatt et al. (2018) revealed that the freshwater can be exported from the Labrador Shelf into the interior of the Labrador Sea by the Ekman transport and mesoscale eddies. They concluded that only a small proportion (approximately 3%) of freshwater originating from the Hudson and Davis Straits is exported across the shelf break into the interior of the Labrador Sea. Observations by Loder et al. (1998) suggested that a large portion of freshwater, carried by the branch of the LC on the shelf break, is lost in the region between Flemish Pass and the Tail of the GBN. F&M2010 suggested that, in the east of the GBN, the retroflexion of the LC above the main pycnocline is the primary process of the freshwater transport (FWT) into the interior of the North Atlantic. They described the retroflexion of the LC as the “Southwest Corner” of the subpolar gyre overshooting, analogous to the “Northwest Corner” that is the overshooting of the subtropical gyre.

Depending on where the freshwater enters the interior of the North Atlantic, the impacts of freshwater on the upper layer stratification can be different. As the major process of transporting freshwater from the LC to the interior of the North Atlantic, the LC retroflexion was previously believed to only occur at the Tail of the GBN. F&M2010 constructed a map to show the depth of the  $1027.25 \text{ kg/m}^3$  isopycnal surface with the time-mean hydrographic data. They interpreted the contours of the isopycnal surface depth as the streamlines of the geostrophic flows, and suggested that the LC retroflected along the entire pathway of the LC from the Flemish Cap to the Tail of the GBN. While F&M2010 depicted the picture of the FWT with the time-mean retroflexion of the LC, they were unable to describe the temporal variations of the FWT or quantify the contribution of the mesoscale eddies due to the temporal-spatial sparseness of the hydrographic surveys and the lack of velocity observations.

In this contribution, a high-resolution, data assimilative global ocean reanalysis product is analyzed to diagnose the spatial and temporal variations of the FWT of the LC near the GBN. This product, referred to as GLORYS12v1, is obtained from the Copernicus Marine Service (CMS, <https://marine.copernicus.eu>; <https://doi.org/10.48670/moi-00021>). It has a horizontal resolution of  $1/12^\circ$  in longitude/latitude and 50 levels in the vertical direction and spans from January 1993 to December 2018. The ocean model is based on the Nucleus for European Modelling of the Ocean (NEMO). The assimilated observational data include the sea surface heights (SSH), sea surface temperature and sea ice concentration retrieved from satellite remote sensing, and vertical profiles of salinity and temperature from multiple versions of CORA (Coriolis Ocean database for Re-Analysis) database containing ship-board

surveys and Argo floats, etc. Comprehensive evaluations of GLORYS12v1 are described in details in a “Quality Information Document” at the CMS website, and also in Lellouche et al. (2018) and Lellouche et al. (2021). These evaluations suggest that GLORYS12v1 possesses good skills in reproducing the observed mean state and mesoscale variations of ocean circulation and salinity, as well as other ocean and sea-ice parameters. We use the monthly-mean GLORYS12v1 output of the salinity and the horizontal velocities to compute the volume flux and FWT.

In section 2, we introduce the method of decomposing the variations of the FWT into different components based on time scales. The results of the time-mean FWT are presented in section 3. Section 4 presents the analysis of the temporal variations of the FWT. Finally, section 5 presents the conclusions and discussion of the results.

## 2 FWT calculation

### 2.1 Regional ocean climatology

With the monthly salinity and temperature from GLORYS12v1, the monthly potential density is calculated

during 1993 - 2018 for all the 50 levels in the region around the GBN. Following F&M2010, the FWT is calculated for the upper layer with a potential density less than  $1027.25 \text{ kg/m}^3$ . Figure 1 presents the depth of the  $1027.25 \text{ kg/m}^3$  isopycnal surface, interpolated from the potential density averaged over 1993 - 2018. Along two sections at  $45^\circ\text{N}$  and  $50^\circ\text{W}$ , Figure 2 shows that this isopycnal surface only varies slightly in different seasons. In Figure 1, the GBN shelf is shaded grey because the maximum density on the seafloor is smaller than  $1027.25 \text{ kg/m}^3$ . The  $1027.25 \text{ kg/m}^3$  isopycnal surface is shallower than 150 m in the region of the LC and deeper in the NAC region, exceeding 400 m to the south of  $42^\circ\text{N}$ . To the east of the shelf break of the GBN, the  $1027.25 \text{ kg/m}^3$  isopycnal surface shows a ridge shape whose minimum depth is about 150 m at  $45^\circ\text{N}$ , and this ridge disappears close to the Tail of the GBN. As described by F&M2010, the contours of this isopycnal depth represent the streamlines of the time-mean geostrophic flow. Thus the map of Figure 1 reveals a retroflexion of the LC: the LC flowing southward along the eastern shelf break of the GBN, turning offshore near the Tail of the GBN and continuing flowing northeastward. The map of the depth of the  $1027.25 \text{ kg/m}^3$  isopycnal surface also indicates a flow meander around ( $47^\circ\text{W}$ ,  $44^\circ\text{N}$ ), corresponding to a similar meander of the 4000 m isobath. Figure 2 shows the time-mean (a) meridional and (b) zonal

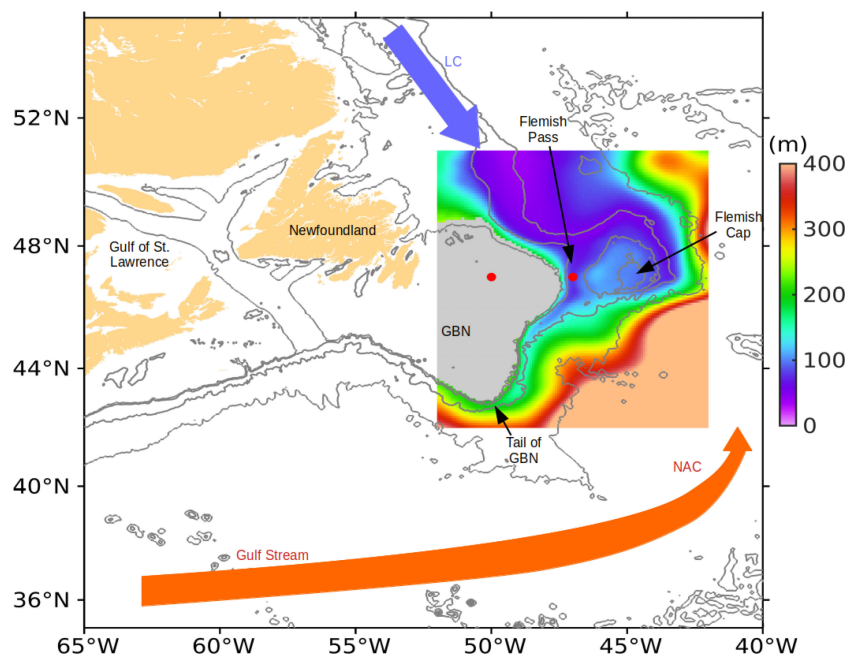
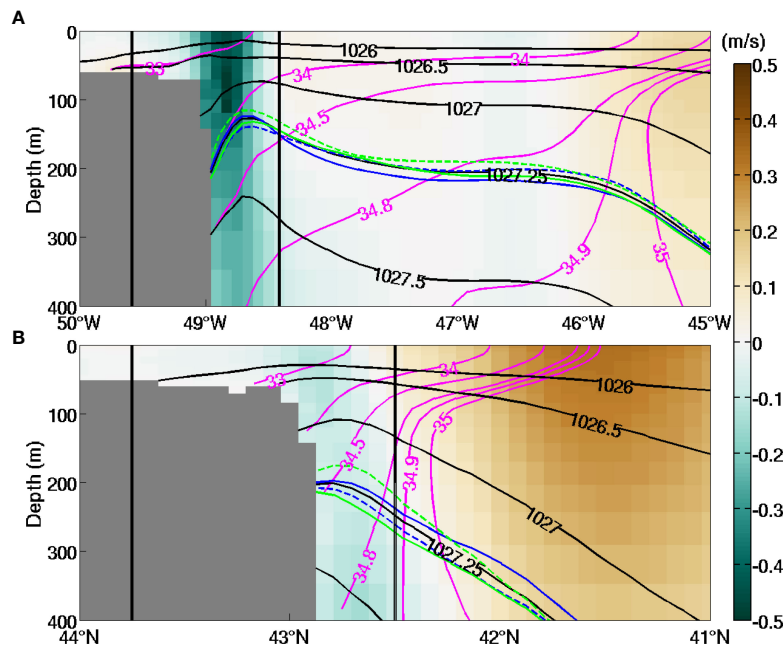


FIGURE 1

The western North Atlantic with the red and blue vectors denoting the direction of the North Atlantic Current (NAC) and Labrador Current (LC). The box outlines the Grand Banks of Newfoundland (GBN) and adjacent oceans. The color shading shows the depth of the isopycnal surface of  $1027.25 \text{ kg/m}^3$  determined from the potential density averaged over 1993 - 2018. In grey shaded area, the maximum potential density is less than  $1027.25 \text{ kg/m}^3$ . Black contours are isobaths of 200 m, 500 m, 2000 m and 4000 m. The two red dots at ( $50^\circ\text{W}$ ,  $47^\circ\text{N}$ ) and ( $47^\circ\text{W}$ ,  $47^\circ\text{N}$ ) are the positions for calculating the sea surface height differences shown in Figure 9.



**FIGURE 2** Velocity, salinity and potential density averaged over 1993–2018 on sections at (A) 45°N, and (B) 50°W. Colors present the meridional velocity (northward as positive) in (A) and zonal velocity (eastward as positive) in (B). The magenta and black contours are the isohalines and isopycnals averaged for all the seasons. The seasonal variations of the 1027.25 kg/m<sup>3</sup> isopycnals are presented using the solid blue (Winter: January to March), dashed blue (Spring: April to June), solid green (Summer: July to September), and dashed green (Fall: October to December) curves. The two vertical black lines show the locations of sections B and D.

velocities across the sections at 45°N and 50°W. On the 45°N section, a steep ridge of the 1027.25 kg/m<sup>3</sup> contour appears in the core of the LC around 48.6°W, where the maximum southward velocity reaches 0.5 m/s. On the 50°W section, the same isopycnal does not show a ridge, but the 1027 kg/m<sup>3</sup> contour at shallower depth contains a gradual ridge associated with a much weaker time-mean zonal flow. On both sections at 45°N and 50°W, the 34.8 isohaline mainly lies below the 1027.25 kg/m<sup>3</sup> isopycnal surface within and adjacent to the LC and shoals rapidly in the region where the NAC is present.

## 2.2 Freshwater flux

The freshwater flux vector (FWV),  $\vec{U}_{FW}(x, y, z, t)$ , is defined as

$$\vec{U}_{FW}(x, y, z, t) = S_R(x, y, z, t) \vec{U}(x, y, z, t). \quad (1)$$

Here  $x, y, z$  are the coordinates in the zonal, meridional and vertical directions with the positive directions as eastward, northward and upward;  $t$  is time;  $\vec{U}(x, y, z, t)$  is the horizontal velocity. The non-dimensional variable  $S_R(x, y, z, t)$  is the relative salinity, defined as

$$S_R(x, y, z, t) = \frac{S_{ref} - S(x, y, z, t)}{S_{ref}}, \quad (2)$$

where  $S(x, y, z, t)$  is the salinity of the seawater, and  $S_{ref}$  is a reference salinity. The value of  $S_{ref}$  is set to be 34.8, consistent with the previous studies of the FWT of the LC (Mertz et al., 1993; Petrie and Buckley, 1996).

The salinity and horizontal velocity vary on different time scales, i.e., seasonal, inter-annual and intra-seasonal. In order to investigate the contributions of the variations on different time scales to the variations of the FWT,  $S_R(x, y, z, t)$  and  $\vec{U}(x, y, z, t)$  are decomposed according to

$$S_R(x, y, z, t) = \bar{S}_R(x, y, z) + \tilde{S}_R(x, y, z, t) + S_R^*(x, y, z, t) + S_R'(x, y, z, t), \quad (3)$$

$$\vec{U}(x, y, z, t) = \bar{\vec{U}}(x, y, z) + \tilde{\vec{U}}(x, y, z, t) + \vec{U}^*(x, y, z, t) + \vec{U}'(x, y, z, t).$$

The symbol “ $\bar{\quad}$ ” denotes the time-mean quantity, obtained by averaging the monthly data over 1993–2018. The symbol “ $\tilde{\quad}$ ” stands for the seasonal cycle, obtained by taking the average of the data of the same calendar month over the 26 years and with the above time-mean value subtracted. The symbol “ $\ast$ ” denotes the inter-annual anomaly, calculated as averaging the data of each year, again with the time-mean value subtracted. Finally, the symbol “ $\prime$ ” denotes the residual that mainly represents the intra-seasonal anomaly mostly due to the mesoscale eddies.

Substituting (3) into (1), the various components of  $\vec{U}_{FW}$  are defined as

$$\begin{aligned} \vec{U}_{FW} &= (\bar{S}_R + \tilde{S}_R + S_R^* + S_R') \left( \vec{U} + \vec{U} + \vec{U}^* + \vec{U}' \right) \\ &= \vec{U}_{FW} + \vec{U}_{FW} + \vec{U}_{FW}^* + \vec{U}_{FW}'. \end{aligned} \tag{4}$$

The first term on the right-hand-side (r.h.s) of (4) is the time-mean FWV, expressed as

$$\vec{U}_{FW} = \bar{S}_R \vec{U} + \tilde{S}_R \vec{U} + S_R^* \vec{U}^* + S_R' \vec{U}'. \tag{5}$$

It is obtained by taking the time average of all products of different components of  $S_R$  and  $\vec{U}$ , but only keeping those terms that have a non-zero mean. For example,  $S_R$  and  $\vec{U}$  at different time scales are not correlated hence their products have zero mean values, while  $S_R$  and  $\vec{U}$  at the same time scales can have non-zero mean values.

The second term on the r.h.s of (4) is the seasonal variation, practically obtained by averaging the monthly anomalies of  $\vec{U}_{FW}$  in the same calendar month over different years. Mathematically it can be expressed as

$$\vec{U}_{FW} = \bar{S}_R \vec{U} + \tilde{S}_R \vec{U} + \tilde{S}_R \vec{U} + S_R' \vec{U}'. \tag{6}$$

That is, this term represents the sum of the seasonal components that may be contained in the products of various components of  $S_R$  and  $\vec{U}$ . For example, the third term at r.h.s. of (6) comes from the product of the seasonal variations of  $S_R$  and  $\vec{U}$ , which can include a non-zero mean component [second term at r.h.s. of (5)] and a semi-annual variation accounted here as the seasonal component. In practice, all terms at r.h.s. of (6)

can be obtained by averaging the monthly anomalies of each product term in the same calendar month over different years. The seasonal components in the products of  $\tilde{S}_R$  with  $\vec{U}^*$  and  $\vec{U}'$  should be very small because the anomalies at different time scales are not correlated, and similarly for products of  $S_R^* \vec{U}$ ,  $S_R^* \vec{U}'$ ,  $S_R' \vec{U}$  and  $S_R' \vec{U}^*$ .

The third term on the r.h.s. of (4) is the inter-annual variations, practically obtained by taking the annual average of the monthly anomalies of  $\vec{U}_{FW}$ . Following the similar argument as deriving equation (6) this term can be approximately expressed as

$$\vec{U}_{FW}^* = \bar{S}_R \vec{U}^* + S_R^* \vec{U} + (S_R^* \vec{U}^*)^* + (S_R' \vec{U}')^*. \tag{7}$$

And finally, the fourth term is the intra-seasonal variation of the FWV, defined as

$$\vec{U}_{FW}' = \vec{U}_{FW} - \vec{U}_{FW} - \vec{U}_{FW} - \vec{U}_{FW}^*. \tag{8}$$

Figure 3 shows the meridional component of  $\vec{U}_{FW}$  on the section at 45°N. The southward FWV within the LC mostly occurs above the depth of the 1027.25 kg/m<sup>3</sup> isopycnal surface. Thus, the layer between the ocean surface and the 1027.25 kg/m<sup>3</sup> isopycnal surface is selected for studying the FWT of the LC. In the following, the FWT per unit length (hereinafter referred to as unit FWT),  $\vec{F}(x, y, t)$ , is obtained by vertically integrating  $\vec{U}_{FW}$  for this layer as

$$\vec{F}(x, y, t) = \int_{-H(x,y)}^0 \vec{U}_{FW}(x, y, z, t) dz. \tag{9}$$

Here,  $H(x,y)$  is the depth of the 1027.25 kg/m<sup>3</sup> isopycnal surface determined from the time-mean density field (see Figure 1). Replacing  $\vec{U}_{FW}(x, y, z, t)$  in (9) with its components of

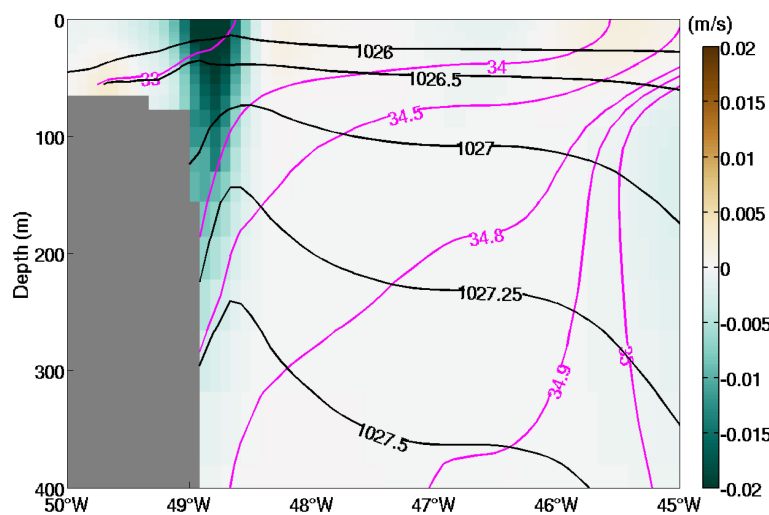


FIGURE 3 Same as in Figure 2A except that the colors show the meridional component of  $\vec{U}_{FW}$ .

$\vec{U}_{FW}$ ,  $\vec{U}_{FW}^*$ ,  $\vec{U}_{FW}'$  and  $\vec{U}_{FW}^*$  as given in (5), (6), (7) and (8), we can obtain the time-mean value, and the seasonal, inter-annual and intra-seasonal variations of the FWT per unit length, denoted as  $\vec{F}$ ,  $\vec{F}^*$ ,  $\vec{F}'$  and  $\vec{F}'^*$ , respectively. Additionally, the vertically integrated volume flux per unit length,  $\vec{V}(x, y, t)$ , is defined as

$$\vec{V}(x, y, t) = \int_{-H(x,y)}^0 \vec{U}(x, y, z, t) dz. \quad (10)$$

### 3 Time-mean FWT

#### 3.1 Horizontal view of the FWT

Figures 4A, B show the horizontal view of  $\vec{V}(x, y)$  and  $\vec{F}(x, y)$  during 1993 - 2018. Because we focus on the transport of seawater with low salinity, the region with the depth-mean salinity greater than  $S_{ref}$  is shaded grey. High amplitudes of both  $\vec{V}$  and  $\vec{F}$  appear on the shelf break of the GBN, indicating the main pathway of the LC. In Figure 4A, the center-line of the LC (magenta curve) is identified as the locations where the amplitude of  $\vec{V}$  are the largest across the LC. Figure 4B shows that the main source of freshwater of the LC on the eastern shelf break of the GBN is the inshore branch of the LC that directs eastward at 49°N. A small portion of  $\vec{F}$  splits from the main branch and directs eastward to the north of the Flemish Cap. To the south of 47°N,  $\vec{F}$  directs southward, and its amplitude decreases dramatically before reaching the Tail of the GBN. Further offshore,  $\vec{V}$  and  $\vec{F}$  have opposite directions from those on the shelf break.

A control volume is closed by four horizontal sections (marked with A, B, C and D in Figure 4), the mean 1027.25 kg/m<sup>3</sup> isopycnal surface (see Figure 1) and the ocean surface. Section D is set at the location where the meridional component of  $\vec{V}$  vanishes between 43°N and 47°N. Similarly, at 50°W, the endpoint of section D is located at the position where the zonal component of  $\vec{V}$  is equal to zero. Moreover, the point at 43°N and the endpoint at 50°W, obtained from the above steps, are smoothly connected with a cubic polynomial curve. In this way, section D separates the flows with opposite directions, the south- or westward LC and the north- or eastward retroflexion of the LC and the NAC. Section B is set to have a fixed distance of 60 km from the center-line of the LC, but its locations do not extend westward of 50°W. Sections A and C are set at the fixed latitude of 47°N and longitude of 50°W, respectively, with the same endpoints as sections B and D. Moreover, a short section E is set to characterize the retroflexion of the LC after its westward passing across section C. Section E is along the meridian of 50°W starting from the southern endpoint of section C till the location where the salinity, averaged over time and depth within the layer above the 1027.25 kg/m<sup>3</sup> isopycnal surface, equals 34.8. At each boundary of the control volume, a flux/transport is defined as positive (negative) if it is out of (into) the control volume. As for section E, the eastward flux/transport is defined as positive.

The time-mean volume flux and FWT ( $\pm$  standard deviation) across the five sections, defined above in unit of milli-Sverdrup (mSv, 1 mSv = 10<sup>3</sup> m<sup>3</sup>/s), are shown in Figure 4. The freshwater is transported into the control volume through sections A and B with the time-mean FWT of 83.6 mSv and 1.5 mSv. The main part of their sum, about 42%, directs out of the control volume across the

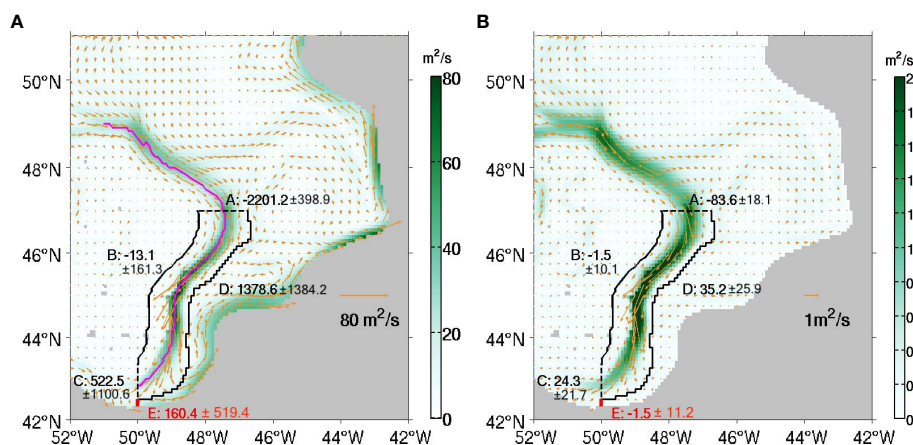


FIGURE 4

Vectors and color shading: (A)  $\vec{V}$  and (B)  $\vec{F}$  and their amplitudes. The grey-shaded area represents the region where the salinity, averaged temporally over 1993 - 2018 and vertically above the 1027.25 kg/m<sup>3</sup> isopycnal surface, is greater than  $S_{ref} = 34.8$ . The magenta curve in (A) marks the centre line of the LC, which is obtained as the locations where the amplitudes of  $\vec{V}$  reach the maximum values across the LC.

Numbers beside sections A, B, C, D (boundaries of the control volume) and E are the integrals of  $\vec{V}$  and  $\vec{F}$  along these sections with the units of mSv. Negative (positive) values denote that the fluxes/transports are into (out of) the control volume, or westward (eastward) across section E. The values following the  $\pm$  sign are the standard deviations of the monthly time series.



offshore section D. The outflow of low salinity water across section D mixes with the northeastward NAC, then passes the east of the Flemish Cap to the Northwest Corner. About 29% of the FWT of the LC directs westward across section C. Across section E, the FWT is only 1.5 mSv and directs westward, while the volume flux is eastward with a value of 160.4 mSv that is about 31% of the westward volume flux through section C. The opposite directions between the volume flux and FWT through section E are related to the contributions to FWT by the mesoscale eddies. The FWT and volume flux through these sections have significant amplitude of standard deviations related to seasonal, inter-annual and intra-seasonal variations. The time variations of FWT will be discussed in section 4.

In order to examine the locations where the LC water is exported out of the control volume through section D, the cumulative volume flux and FWT across section D are computed by integrating  $\bar{V}$  and  $\bar{F}$  starting from the northern endpoint of section D at 47°N till the southern endpoint at 50°W, as shown in Figure 5. The outward volume flux and FWT occur at almost all locations along section D, consistent with the findings of F&M2010 that the retroflection occurs along the whole pathway of the LC in the east of the GBN. Moreover, the outward transports are more intense south of 43.5°N, indicating that a larger proportion of the retroflection takes place there.

### 3.2 Decomposition of time-mean FWT

Figure 6 shows the spatial distributions of the vector norms of the four components of  $\bar{F}$ , which represent contributions of the mean advection and the seasonal, inter-annual and intra-seasonal

variations of the horizontal velocity and salinity, respectively, calculated by vertically integrating the r.h.s. of (5). Across section A, the dominant component of 84.4 mSv of the southward FWT is due to the mean advection, which is slightly greater than the total time-mean FWT of 83.6 mSv southward through this section. The seasonal variations of the velocity and salinity induce a northward FWT of 0.6 mSv, and the components of the FWT caused by the inter-annual and intra-seasonal variations are both 0.1 mSv northward. The mean advection contributes 1.2 mSv FWT through section B into the control volume, which accounts for 80% of the total FWT across this section. The remaining contributions to the FWT are from the inter-annual variation (13%) and intra-seasonal variation (7%).

Through section C, the time-mean velocity causes 15.4 mSv FWT out of the control volume, which accounts for 63% of the total FWT across this section. Seasonal and inter-annual variations also contribute to the westward FWT with the values of 1.3 mSv and 2.6 mSv, respectively. The intra-seasonal variation makes a 5 mSv contribution to the westward FWT, which is 21% of the total FWT through section C. Across section D, the mean advection contributes 25.5 mSv to the FWT, which accounts for 72% of the total eastward FWT through this section. The seasonal, inter-annual, and intra-seasonal variations contribute the remaining 28% with the values of 0.4 mSv, 2.2 mSv and 7.2 mSv, respectively.

Across section E, the mean advection contributes an eastward 2.0 mSv to the total FWT. However, the contributions to the time-mean FWT by the seasonal, inter-annual and intra-seasonal variations are 0.1 mSv, 1.1 mSv and 2.3 mSv, respectively, and direct westward. Thus the net FWT through section E is 1.5 mSv westward.

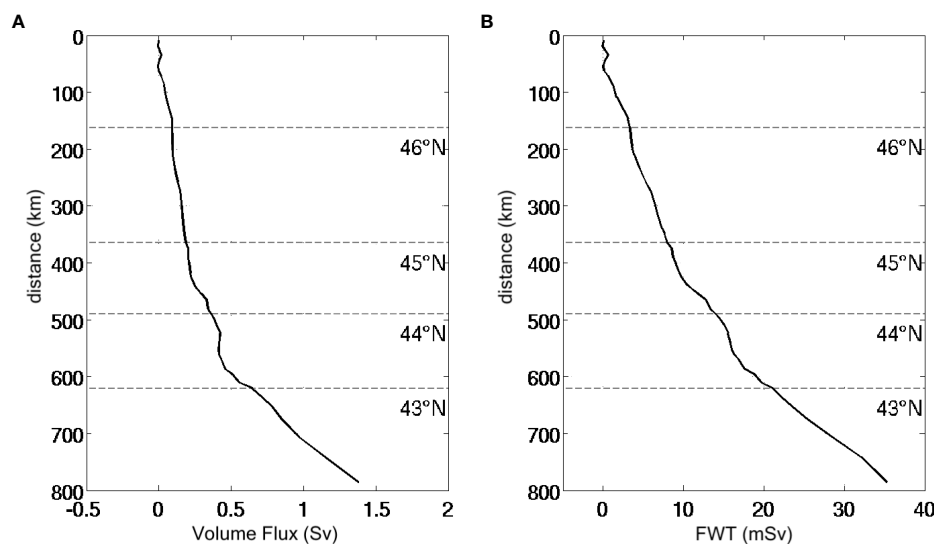


FIGURE 5 The cumulative time-mean (A) volume flux and (B) FWT, along section D starting from its northern endpoint at 47°N. The vertical axis is the distance from a location on section D to the northern endpoint, with the corresponding latitudes marked with the horizontal dashed lines.

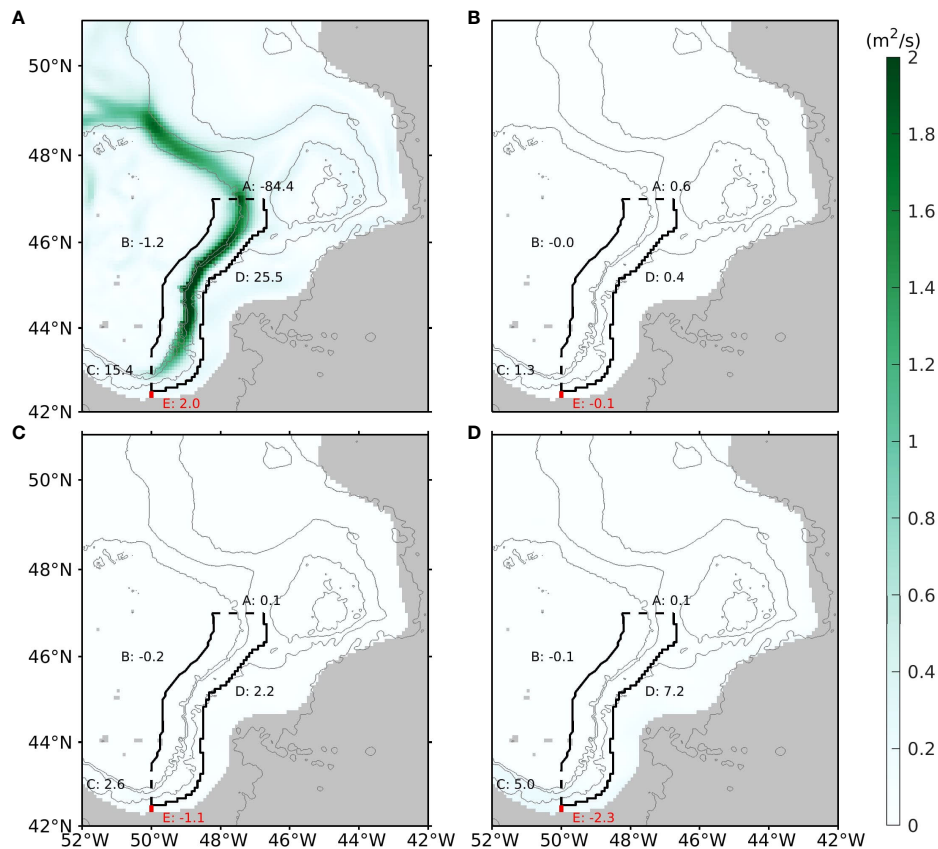


FIGURE 6

Same as Figure 4B, except for the contributions to  $\bar{F}$  by the (A) mean advection, (B) seasonal variation, (C) inter-annual variation, and (D) intra-seasonal variation, calculated by vertically integrating (5).

## 4 Time variations OF FWT

Figure 7 shows the monthly time series of the FWT through the A, B, C and D boundaries of the control volume and section E, superimposed with the low-pass filtered time series with a cut off frequency of 0.67 cpy (18-month period). A wavelet analysis is performed for each time series of above, and the results are shown in Figure 8. For this analysis, we adopt the method proposed by Liu et al. (2007), which rectifies the bias towards the low frequencies in traditional wavelet analysis method. Statistical significance testing is performed for a red-noise process with a lag-1 coefficient of 0.72 (Torrence and Compo, 1998), and the 90% confidence level is shown as the black contour lines in the left column of Figure 8. According to the time-averaged wavelet power spectra (right column of Figure 8), the variations of the FWT through sections A, C and D exhibit an evident seasonal cycle. At sections A and C, the seasonal cycle dominates the FWT variations over other (inter-annual and intra-seasonal) time scales (right panels of Figures 8A, C). This feature of seasonal cycle dominance at these two sections

presents in most the years during 1993 - 2018 (left panels of Figures 8A, C).

Section B shows no seasonal cycle but an evident semi-annual cycle. Moderate inter-annual variations of the FWT are present at sections B, C and D. Intra-seasonal variations make significant contributions to the variances of the FWT across sections B, C, D and E. At section E, the variation of the FWT covers the broad time scales from intra-seasonal to inter-annual without an evident seasonal cycle, while the time evolution of the wavelet spectrum (left panel of Figure 8E) and the time series of the FWT (Figure 7E) suggest extremely strong eddy variations during 2009 and 2015. These strong meso-scale eddy events near the Tail of GBN are evident in an animation of the SSH anomalies (not shown).

### 4.1 Seasonal variation

The seasonal variation of the FWT of the LC can be attributed to the variation of the major sources of freshwater,

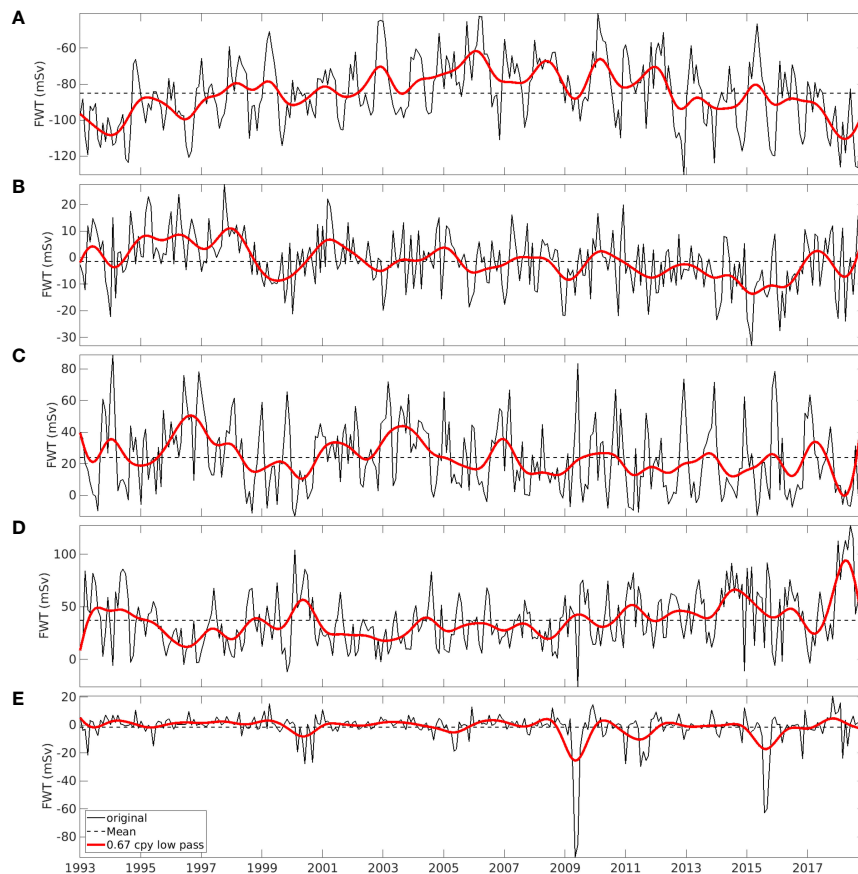
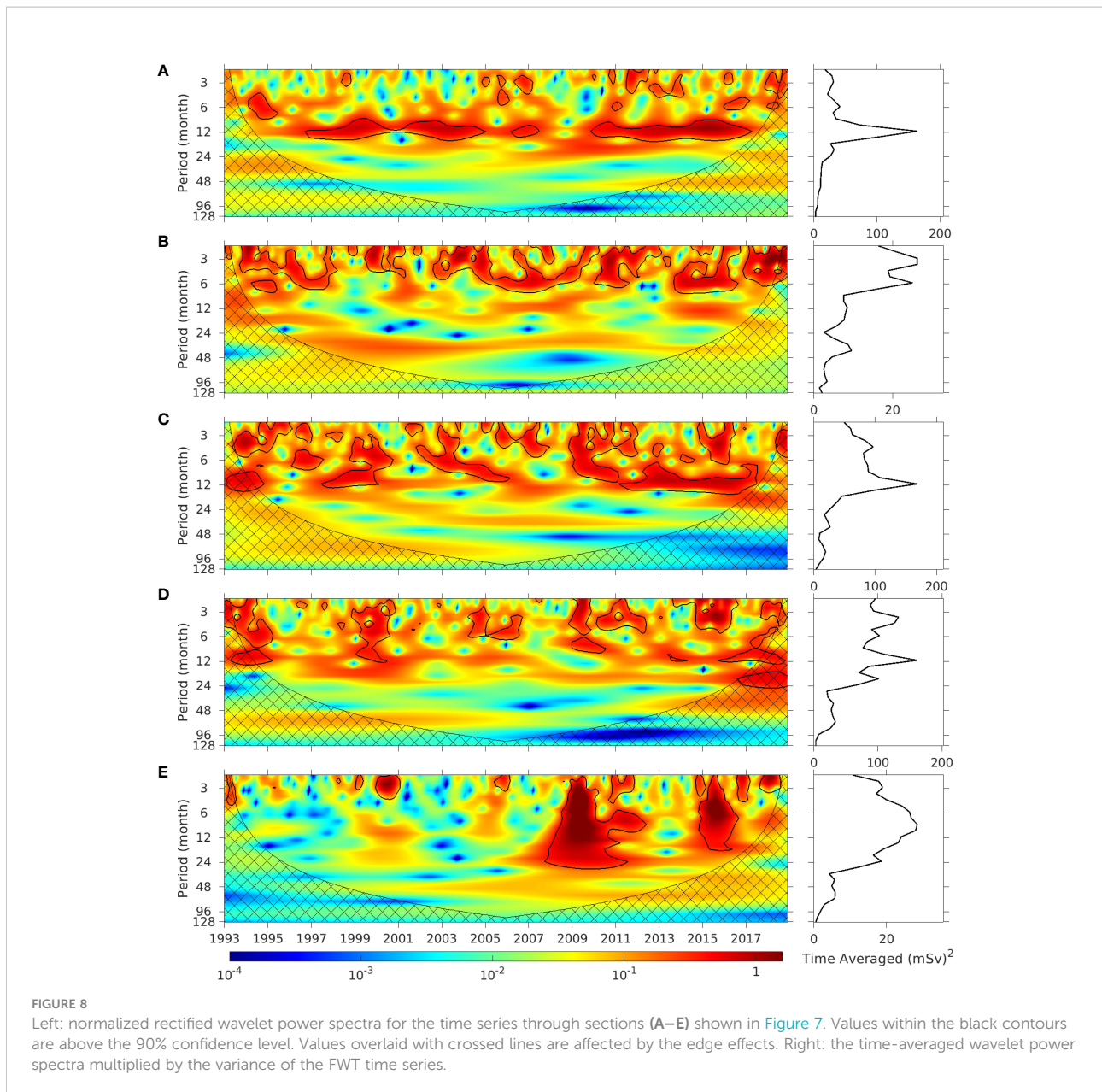


FIGURE 7

Monthly time series (black curve) of FWT through the boundaries (A–D) of the control volume and section (E), superimposed with the low pass filtered time series (red curve) with a cut-off period of 1.5 years. The dashed lines indicate the time-mean values of the corresponding monthly time series.

e.g., outflows through the Hudson Strait and the Davis Strait. The southward FWT through the Davis Strait, calculated using the one-year-long observational data, has a mean value of 116 mSv and peaks in December-January (Curry et al., 2011). The FWT through the Hudson Strait into the LC was estimated to be 42 mSv (Dickson et al., 2007) with a peak in October-December (Straneo and Saucier, 2008). At the downstream of the LC on the Labrador Shelf, the minimum salinity at 200 m appears in December (Lazier, 1982), consistent with the peaks of FWT from both upstream straits. However, Lazier (1982) showed that the minimum salinity occurred in July-August at the surface and progressively later with increasing depth. F&M2010 found that the minimum values of the salinity appeared in July-September for both the inshore and offshore branches of the LC above the isopycnal surface of  $1026.8 \text{ kg m}^{-3}$  (less than 100 m on the Labrador Shelf). F&M2010 suggested that the seasonal pulses of the low salinity along the shelf break and close to the coast were more dominated by the advection process rather than the local atmosphere forcing.

With the observational data, the above studies (Lazier, 1982; F&M2010) were able to characterize the seasonal variation of the salinity. However, the seasonal variation of the FWT consists of different components as in (6). Figure 9 shows the seasonal variations of the volume flux and FWT across the four boundaries of the control volume and section E, obtained by averaging the monthly anomalies in the same calendar month during 1993–2018. Through section A, the seasonal variation of the volume flux reaches the positive (northward) maximum value of 0.34 Sv in June and negative (southward) maximum value of -0.25 Sv in January, and the seasonal variation of the FWT reaches the positive (northward) maximum value of 9.8 mSv in February and the negative (southward) maximum value of -14.1 mSv in September. Note that a positive (northward) maximum value of the variation of the volume flux or FWT across section A means that the southward LC is seasonally the weakest across this section and vice versa for the minimum value. The difference in seasonal phases between the volume flux and FWT across section A is caused by the phase difference



between the salinity and velocity. Across this section, the first two terms at r.h.s. of (6) make similar contribution to the seasonal FWT (Figure 10), with their phases determined by the seasonal velocity and salinity, respectively.

The seasonal phases of the horizontal velocity and salinity in the vicinity of section A are discussed below. As reviewed in the introduction, in summer the salinity within this part of LC is low as a result of the southward advection of low salinity water from upstream. The low salinity in combination with high water temperature leads to higher SSH within the LC. Further to the west on the GBN the increase of SSH is smaller, thus the SSH gradient from west to east is reduced. This is confirmed by the magenta curve in Figure 9, which is the mean seasonal cycle of

the SSH at (50°W, 47°N) minus that at (47°W, 47°N) (the two locations marked in Figure 1). Again the mean seasonal cycle is calculated by taking the average of the SSH difference in the same calendar month during 1993 - 2018. This mean seasonal SSH difference has a minimum value in June. It corresponds to the minimum southward LC velocity (or the maximum northward anomaly), because the LC velocity has a weak vertical shear (Figure 2A) hence closely follows the variation of the SSH difference. While the southward FWT across section A increases due to the lower salinity, the southward volume flux decreases because of the reduced velocity.

Across section B, the volume flux and FWT show weak semi-annual variation with two troughs in January and July and two

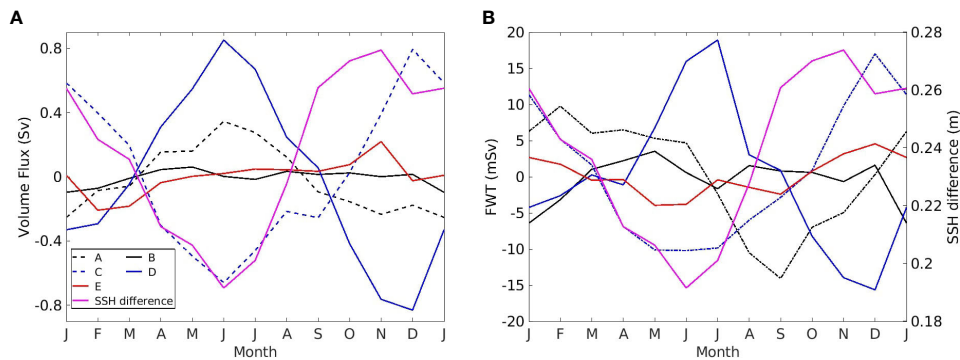


FIGURE 9

Seasonal variations of the (A) volume flux and (B) FWT through the 5 sections, and the result by subtracting the SSH value at (47°W, 47°N) from that at (50°W, 47°N), then taking the average for the same calendar month over 1993- 2018. The positive directions of the seasonal variations of the volume flux and FWT for each section are (A): northward; (B): westward; (C): westward; (D): eastward, and (E): eastward. The two locations for calculating the SSH difference are shown in Figure 1.

peaks in May and December in Figure 9. Across section D, the volume flux and FWT out of the control volume both reach maximum (minimum) in June/July (December). At section C, the seasonal variations of the volume flux and FWT have the

opposite phases from those at section D. Hence, the stronger outflow through section D corresponds to the weaker outflow through section C. With a weaker inflow from section A in summer, there is more LC water passing through section D, and

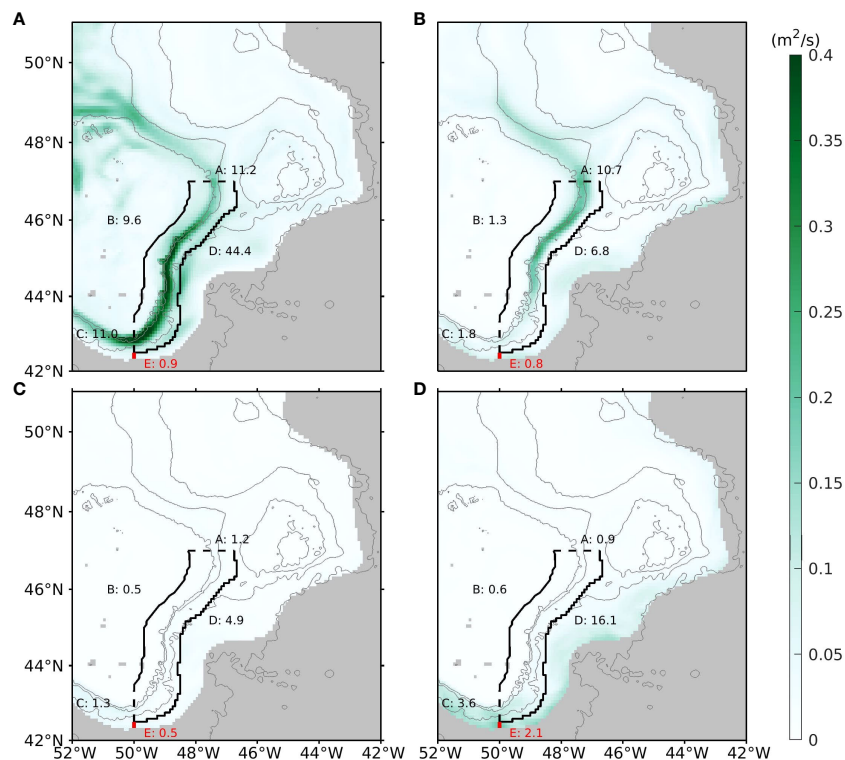


FIGURE 10

The RMS of the vector norms of the four components of  $\vec{F}$ : (A)  $\int_{-H(x,y)}^0 \bar{s}_R \vec{U} dz$ , (B)  $\int_{-H(x,y)}^0 \bar{s}_R \bar{U} dz$ , (C)  $\int_{-H(x,y)}^0 \bar{s}_R \vec{U}' dz$  and (D)  $\int_{-H(x,y)}^0 \bar{s}_R \bar{U}' dz$ , which are the vertical integrals of the four terms on the right hand side of (6). Numbers having the unit of mSv are the RMS of the four components of the seasonal variation of the FWT across different sections.

vice versa in winter. In the study of the Agulhas Current retroflection with an idealized model, [Dijkstra and De Ruijter \(2001\)](#) stated that the inertia plays a more important role in controlling the retroflection than the side-wall friction if the Agulhas Current is strong. Apply this to the LC, the stronger flow in winter could overshoot the Tail of the GBN, westward pass across section C and retroflect eastward across section E, resulting in a larger westward volume flux or FWT across section C. On the other hand, with the weaker incoming flow in summer, the LC may detach from the shelf break of the GBN, analogous to the phenomenon of the western boundary currents separating from their coasts as investigated by many others ([Dengo, 1993](#); [Pichevin et al., 2009](#); [Pierini et al., 2011](#); [Ezer, 2016](#)). Thus in summer, the LC may retroflect at higher latitudes rather than after overshooting the Tail of the GBN, resulting in more LC water exported across section D. Through section E, the volume flux and FWT show weak seasonal variations with different phases. The eastward FWT through section E roughly corresponds to the westward FWT through section C.

[Figure 10](#) shows the Root Mean Square (RMS) of the vector norm of each component of  $\vec{F}$  (seasonal unit FWT). Along the LC pathway,  $\vec{F}$  can be mainly attributed to the seasonal variation of the horizontal velocity ([Figure 10A](#)). The contribution due to the seasonal variation of the salinity is significant to the north of 44°N. By integrating the four components of  $\vec{F}$  along each section, the values of the RMS of each component at different sections are indicated with numbers in [Figure 10](#). The variation of the horizontal velocity results in 11.2 mSv of the RMS of the seasonal variation of the FWT across section A, while the seasonal variation of the salinity causes 10.7 mSv. Through section B, the seasonal variation of the FWT is mainly caused by the variation of the horizontal velocity with an RMS value of 9.6 mSv, much greater than the other three components. Through section C, the seasonal variation of the horizontal velocity makes the most contribution to the FWT seasonal variation, and the seasonal variation of the salinity is not important, while the seasonal variation of mesoscale eddies makes a sizable contribution of 3.6 mSv to the RMS. Section D is similar to section C, where the seasonal variations of the horizontal velocity and mesoscale eddies both make major contributions. Finally, through section E, intra-seasonal variations (mesoscale eddies) make the largest contribution to the seasonal variation of FWT.

## 4.2 Inter-annual variation

[Figure 11](#) shows the inter-annual variations of the volume flux and FWT through boundaries A, B, C and D of the control volume and section E. The inter-annual variation of the southward volume flux through section A has a magnitude of 0.4 Sv. The variations of the volume fluxes through sections C and D have larger magnitudes of 1.8 Sv and 2.2 Sv, respectively,

and their correlation coefficient is -0.92. The increase of volume flux westward through section C corresponds to the decrease of the volume flux eastward through section D. The fact that the magnitude of the variation of the volume flux across either section C or D is much greater than that across section A can be caused by multiple mechanisms, including the inter-annual variation of the location of the LC retroflection position and the impact of the NAC. Although the magnitude of the inter-annual variation of the volume flux through section C or D is greater than that through section A, the inter-annual variations of the FWT through sections A, C and D have the similar magnitudes of 40 mSv. Thus is related to the combined contributions of the inter-annual variations of velocity and salinity, to be discussed below.

[Figure 12](#) shows the RMS of the vector norms of the four components of  $\vec{F}^*$  (inter-annual unit FWT). Similar to the seasonal variation ( $\vec{F}$ ),  $\vec{F}^*$  is mainly caused by the inter-annual variation of horizontal velocity in most regions. The inter-annual variation of the salinity makes a significant contribution to the RMS of vector norm of  $\vec{F}^*$  in the north of 44°N. The variation of the salinity makes a significant contribution to the RMS of the inter-annual variation of the FWT across section A. The contribution due to the interaction between the inter-annual anomalies of the velocity and salinity is smaller than the first two components in most regions but is nontrivial at section D. Finally, the fourth component, mainly representing the inter-annual variation of mesoscale eddies, makes significant contributions at sections C, D and E.

## 5 Conclusion and discussion

The global ocean reanalysis product, GLORYS12v1, is analyzed for quantifying the spatial-temporal variations of the FWT above the 1027.25 kg/m<sup>3</sup> isopycnal surface in the region east of the GBN. Firstly, the results for the time-mean FWT are presented in [Figures 4–6](#) and [Table 1](#). The GLORYS12v1 product enables the quantification of the spatial variation of the time-mean FWT and the magnitudes of the standard deviations, as well as the contributions to the time-mean by the mean advection and the interactions between the time variations of velocity and salinity on seasonal, inter-annual and intra-seasonal time scales [equation (5)]. Through section A at the Flemish Pass, the southward LC is the dominant FWT into the defined control volume due mainly to the mean advection. A major proportion of the freshwater carried by the LC enters into the interior of the North Atlantic along the offshore boundary of the LC between the Flemish Pass and the Tail of the GBN. Across section D, the eastward FWT amounts to 42% of the southward FWT across section A. The FWT through section D can be further decomposed to 72% due to the mean advection and 27% due to the combined contributions of the inter-annual and intra-seasonal variations of the circulation and salinity. At the Tail of the GBN,

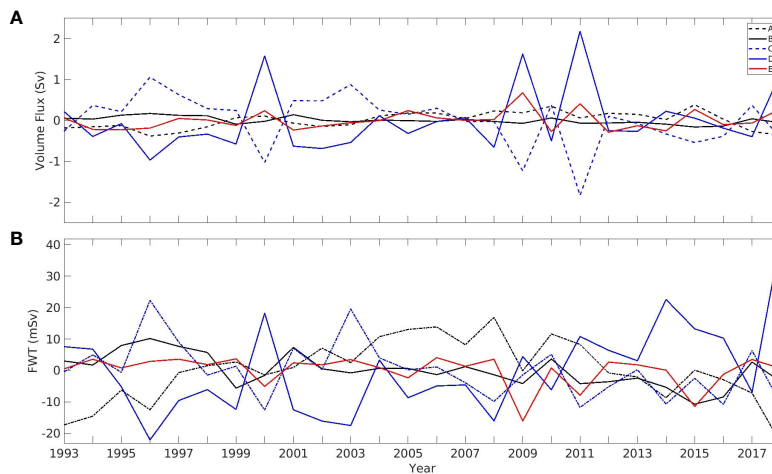


FIGURE 11  
As in Figure 9, except for the inter-annual variations of the (A) volume flux and (B) FWT.

the westward FWT through section C accounts to 29% of the southward FWT through section A, and 63% of this westward FWT is due to mean advection while 37% is due to the other three components. After the LC passes across section C, a part of this cold and fresh water continues flowing westward to the Scotian Slope (Loder et al., 1998; Brickman et al., 2018), and another part mixes with the NAC and retroflects eastward to the interior of the North Atlantic (F&M2010). The retroflexion of the LC is diagnosed through a short section E to the south of the Tail of the GBN. Through section E, the time-mean FWT is westward, amounting to 6% of the westward FWT through section C. We note that the FWT due to the mean advection is eastward, consistent with the direction of the LC retroflexion. However, the eastward mean advection is overtaken by the westward FWT due to the inter-annual and intra-seasonal variations of the circulation and salinity.

The monthly FWTs across the five sections, based on 26 years of data from GLORYS12v1, show significant magnitudes of standard deviations. The time series and power density spectra further show the FWT variations at the seasonal, inter-annual and intra-seasonal time scales. The seasonal and inter-annual variations are further decomposed into contributions due to the variations of velocity and salinity, including their correlations (equations (6) and (7), Figures 10, 12). For FWT variations at both time scales, the variations of velocity (advecting the time-mean salinity) cause the largest FWT RMS values across sections A, B, C and D. Only across section A, the variations of salinity (advected by the time-mean velocity) cause the RMS values comparable to that caused by the variations of velocity. The correlations between variations of velocity and salinity, at both seasonal and inter-annual scales, cause relatively smaller RMS values across each section. Finally, the correlation between the intra-seasonal variations the velocity and salinity causes

significant RMS values across sections C and E, and specifically the largest across section E, for both seasonal and inter-annual FWT variations.

The inter-annual variations of the volume fluxes across sections C and E are negatively correlated, as shown in Figure 11A, with the correlation coefficient of -0.69. On the other hand, the inter-annual variations of the FWT across these two sections are positively correlated, as shown in Figure 11B. The above behavior can be explained by the variation of the positions of the LC or NAC in the meridional direction, and the contribution of the mesoscale eddies. Because the two sections are separated at  $\bar{V} = 0$ , a northward shift of NAC (LC) will decrease the westward volume transport across section C while increase the eastward transport across E. In the meanwhile, as the high salinity water shifts northward, the westward FWT across section C decreases. Across section E, the increases of both eastward velocity and salinity favor the decrease of the eastward FWT. The opposite occurs when the NAC (LC) shifts southward. Note that the inter-annual variations of the FWT across section E are mostly caused by the correlation between intra-seasonal variations of the velocity and salinity, representing the contributions due to the mesoscale eddies. A cyclonic cold-core (low salinity) eddy, near the separation position between sections C and E, will cause  $u' > 0$  and  $S'_R > 0$  (smaller  $S$ ) across E, hence the increase of the eastward FWT, while  $u' < 0$  (increased westward velocity) and  $S'_R < 0$  (larger  $S$ ) across C cause the increase of the westward FWT. The opposite occurs when an anti-cyclonic warm-core (high salinity) eddy is present. Thus, the mesoscale eddies cause evident inter-annual variations of the westward FWT across section C, which is positively correlated with the eastward FWT across section E.

Overall, the main results of the present study are consistent with the conclusions of previous studies. However, the continuous time

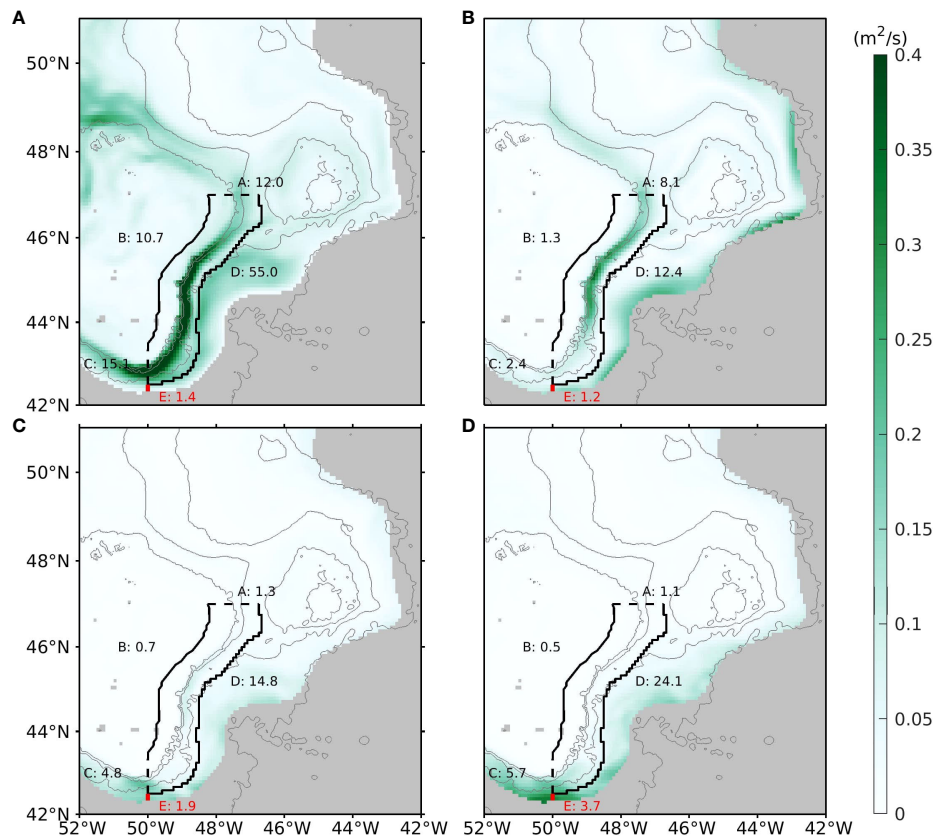


FIGURE 12

As in Figure 10, except for the four components of  $\vec{F}^*$ : (A)  $\int_{-H(x,y)}^0 \bar{S}_R \bar{U}^* dz$ , (B)  $\int_{-H(x,y)}^0 S_R^* \bar{U} dz$ , (C)  $\int_{-H(x,y)}^0 (S_R^* \bar{U}^*)' dz$  and (D)  $\int_{-H(x,y)}^0 (S_R^* \bar{U}')^* dz$ .

series of a multi-decade eddy-resolving ocean product (GLORYS12v1) enables a more comprehensive quantification of the multi-scale variations of the FWT carried by the Labrador Current, and the different contribution components to the time-mean, and seasonal and inter-annual variations of the FWT. Such quantification is difficult to achieved using sparse observation data and coarse resolution or short-term model simulation results. The model results may help to assess the accuracy of the FWT estimates derived from observations and guide the design of observations. For

example, for the time-mean FTW, through sections A and B they are mainly caused by the mean advection, hence the accuracy of their estimations depends on that of the measured time-mean velocity and salinity; for sections C, D and E, simultaneous measurements of the time variations of and salinity are needed because their correlations make significant contributions to the time-mean FWT.

The present study focuses on the LC east of the GBN till reaching its southern tail. In future work it would be interesting

TABLE 1 A summary of time-mean FWT ( $\pm$  standard deviation) through the 5 sections as shown in Figure 4B and the four components that contribute to the time-mean FWT as shown in Figure 6.

Section	Time-mean (mSv)	Mean advection (mSv)	Seasonal (mSv)	Inter-annual (mSv)	Intra-seasonal (mSv)
A	-83.6 $\pm$ 18.1	-84.4	0.6	0.1	0.1
B	-1.5 $\pm$ 10.1	-1.2	0.0	-0.2	-0.1
C	24.3 $\pm$ 21.7	15.4	1.3	2.6	5.0
D	35.2 $\pm$ 25.9	25.5	0.4	2.2	7.2
E	-1.5 $\pm$ 11.2	2.0	-0.1	-1.1	-2.3



to analyze how the fresh (and cold) water carried by the LC impacts the variations of hydrography from the west of the tail to the Scotian Slope. Furthermore, because of the significant influences of intra-seasonal (mesoscale) variations, exploring the predictability of hydrography (and circulation) in this region is challenging, and we hope that advancements in this aspect can be achieved using more advanced analysis methods (e.g., machine learning). Finally, GLORYS12v1 is one of the eddy-resolving global analysis products created with intensive assimilation of ocean observational data in recent years. Its  $1/12^\circ$  horizontal resolution, and also the use of monthly data in this study, may cause underestimation of the contribution of the mesoscale eddies. It would be valuable to compare the present analysis results with that based on daily output of GLORYS12v1 and the simulation/reanalysis results of other models with similar and higher spatial resolutions.

## Data availability statement

Publicly available datasets were analyzed in this study. This data can be found here: <https://marine.copernicus.eu/>.

## Author contributions

YL and DG initiated the analysis topic. YM analyzed the data. YM and YL wrote the manuscript. XH provided data analysis software and analysis. All authors contributed to the refinement of the manuscript writing and approved the submitted version.

## References

- Aagaard, K., and Carmack, E. C. (1989). The role of sea ice and other fresh water in the arctic circulation. *J. Geophys. Res.: Oceans*, 94, 14485–14498. doi: 10.1029/JC094iC10p14485
- Brickman, D., Hebert, D., and Wang, Z. (2018). Mechanism for the recent ocean warming events on the scotian shelf of eastern canada. *Cont. Shelf. Res.* 156, 11–22. doi: 10.1016/j.csr.2018.01.001
- Cuny, J., Rhines, P. B., and Kwok, R. (2005). Davis Strait volume, freshwater and heat fluxes. *Deep. Sea. Res. Part I*, 52, 519–542. doi: 10.1016/j.dsr.2004.10.006
- Curry, B., Lee, C. M., and Petrie, B. (2011). Volume, freshwater, and heat fluxes through davis strait 2004–05. *J. Phys. Oceanogr.* 41, 429–436. doi: 10.1175/2010JPO4536.1
- Dengo, J. (1993). The problem of gulf stream separation: A barotropic approach. *J. Phys. Oceanogr.* 23, 2182–2200. doi: 10.1175/1520-0485(1993)023<2182:TPOGSS>2.0.CO;2
- Déry, S. J., Hernández-Henríquez, M. A., Burford, J. E., and Wood, E. F. (2009). Observational evidence of an intensifying hydrological cycle in northern canada. *Geophys. Res. Lett.* 36, L13402. doi: 10.1029/2009GL038852
- Dickson, R., Rudels, B., Dye, S., Karcher, M., Meincke, J., and Yashayaev, I. (2007). Current estimates of freshwater flux through arctic and subarctic seas. *Prog. Oceanogr.* 73, 210–230. doi: 10.1016/j.pocean.2006.12.003
- Dijkstra, H. A., and De Ruijter, W. P. M. (2001). On the physics of the agulhas current: Steady retroreflection regimes. *J. Phys. Oceanogr.* 31, 2971–2985. doi: 10.1175/1520-0485(2001)031<2971:OTPOTA>2.0.CO;2
- Ezer, T. (2016). Revisiting the problem of the gulf stream separation: on the representation of topography in ocean models with different types of vertical grids. *Ocean. Modell.* 104, 15–27. doi: 10.1016/j.ocemod.2016.05.008
- Fratantoni, P. S., and McCartney, M. S. (2010). Freshwater export from the labrador current to the north atlantic current at the tail of the grand banks of newfoundland. *Deep. Sea. Res. Part I*, 57, 258–283. doi: 10.1016/j.dsr.2009.11.006
- Han, G., Lu, Z., Wang, Z., Helbig, J., Chen, N., and de Young, B. (2008). Seasonal variability of the labrador current and shelf circulation off newfoundland. *J. Geophys. Res.: Oceans*, 113, C10013. doi: 10.1029/2007JC004376
- Howatt, T., Palter, J., Matthews, R., Deyoung, B., Bachmayer, R., and Claus, B. (2018). Ekman and eddy exchange of freshwater and oxygen across the labrador shelf break. *J. Phys. Oceanogr.* 48, 1015–1031. doi: 10.1175/JPO-D-17-0148.1
- Lazier, J. R. N. (1982). Seasonal variability of temperature and salinity in the Labrador current. *J. Mar. Res.* 40(suppl.), 341–356.
- Lazier, J. R. N., and Wright, D. G. (1993). Annual velocity variations in the labrador current. *J. Phys. Oceanogr.* 23, 659–678. doi: 10.1175/1520-0485(1993)023<0659:AVVITL>2.0.CO;2
- Lellouche, J.-M., Greiner, E., Bourdallé-Badie, R., Garric, G., Melet, A., Marie, D., et al. (2021). The Copernicus global  $1/12^\circ$  oceanic and Sea ice GLORYS12 reanalysis. *Front. Earth Sci.* 9, 698876. doi: 10.3389/feart.2021.698876
- Lellouche, J.-M., Greiner, E., Galloudec, O. L., Garric, G., Regnier, C., Drevillon, M., et al. (2018). Recent updates to the Copernicus marine service global ocean

## Funding

We acknowledge the funding support to this study by the Marine Environmental Observation, Prediction and Response, the International Governance Strategy and the Multi-Partner Research Initiative on marine oil spill research by Fisheries and Oceans Canada.

## Acknowledgments

The GLORYS12v1 product is obtained from the Copernicus Marine Service. We thank our colleagues Drs. Zeliang Wang and Igor Yashayaev and three reviewers for providing constructive reviews.

## Conflict of interest

The authors declare that the research was conducted in the absence of any commercial or financial relationships that could be construed as a potential conflict of interest.

## Publisher's note

All claims expressed in this article are solely those of the authors and do not necessarily represent those of their affiliated organizations, or those of the publisher, the editors and the reviewers. Any product that may be evaluated in this article, or claim that may be made by its manufacturer, is not guaranteed or endorsed by the publisher.

- monitoring and forecasting real-time 1/12° high-resolution system. *Ocean. Sci.* 14, 1093–1126. doi: 10.5194/os-14-1093-2018
- Liu, Y., Liang, X. S., and Weisberg, R.H. (2007). Rectification of the bias in the wavelet power spectrum. *J. Atmos. Ocean. Technol.* 24, 2093–2102. doi: 10.1175/2007jtecho511.1
- Loder, J., Petrie, B., and Gawarkiewicz, G. (1998). The coastal ocean off northeastern north America: A large-scale view," in *The Sea, volume 11: The global coastal ocean: Regional studies and syntheses*, vol. 5. Eds. A. R. Robinson and K. H. Brink (Hoboken, NJ, USA: John Wiley & Sons, Inc), 105–133.
- Ma, Z., Han, G., and Chassé, J. (2016). Simulation of circulation and ice over the newfoundland and labrador shelves: The mean and seasonal cycle. *Atmos. Ocean.* 54, 248–263. doi: 10.1080/07055900.2015.1077325
- Mernild, S. H., Liston, G. E., Hiemstra, C. A., Steffen, K., Hanna, E., and Christensen, J.H. (2009). Greenland Ice sheet surface mass-balance modelling and freshwater flux for 2007, and in a 1995–2007 perspective. *Hydrol. Processes.* 23, 2470–2484. doi: 10.1002/hyp.7354
- Mertz, G., Narayanan, S., and Helbig, J. (1993). The freshwater transport of the labrador current. *Atmos. Ocean.* 31, 281–295. doi: 10.1080/07055900.1993.9649472
- Petrie, B., and Buckley, J. (1996). Volume and freshwater transport of the labrador current in flemish pass. *J. Geophys. Res.: Oceans.* 101, 28335–28342. doi: 10.1029/96JC02779
- Petrie, B., Loder, J., Akenhead, S., and Lazier, J. (1991). Temperature and salinity variability on the eastern newfoundland shelf: The annual harmonic. *Atmos. Ocean.* 29, 14–36. doi: 10.1080/07055900.1991.9649390
- Pichevin, T., Herbette, S., and Floch, F. (2009). Eddy formation and shedding in a separating boundary current. *J. Phys. Oceanogr.* 39, 1921–1934. doi: 10.1175/2009JPO4151.1
- Pierini, S., Falco, P., Zambardino, G., McClimans, T. A., and Ellingsen, I. (2011). A laboratory study of nonlinear western boundary currents, with application to the gulf stream separation due to inertial overshooting. *J. Phys. Oceanogr.* 41, 2063–2079. doi: 10.1175/2011JPO4514.1
- Renssen, H., Goosse, H., and Fichefet, T. (2002). Modeling the effect of freshwater pulses on the early holocene climate: The influence of high-frequency climate variability. *Paleoceanography* 17, 10–1–10–16. doi: 10.1029/2001PA000649
- Schmidt, S., and Send, U. (2007). Origin and composition of seasonal labrador sea freshwater. *J. Phys. Oceanogr.* 37, 1445–1454. doi: 10.1175/JPO3065.1
- Straneo, F., and Saucier, F. (2008). The outflow from hudson strait and its contribution to the labrador current. *Deep. Sea. Res. Part I.* 55, 926–946. doi: 10.1016/j.dsr.2008.03.012
- Torrence, C., and Compo, G. P. (1998). A practical guide to wavelet analysis. *Bull. Am. Meteorol. Soc.* 79, 61–78. doi: 10.1175/1520-0477(1998)079<0061:apgtwa>2.0.co;2
- Zhang, R. (2015). "Atlantic Meridional overturning circulation and climate," in *Climate change: Multidecadal and beyond*, vol. 8. Eds. C.-P. Chang, M. Ghil, M. Latif and J. M. Wallace (Singapore: World Scientific), 125–139. doi: 10.1142/9789814579933\_0008

# Frontiers in Marine Science

Explores ocean-based solutions for emerging global challenges

The third most-cited marine and freshwater biology journal, advancing our understanding of marine systems and addressing global challenges including overfishing, pollution, and climate change.

## Discover the latest Research Topics

[See more →](#)

### Frontiers

Avenue du Tribunal-Fédéral 34  
1005 Lausanne, Switzerland  
[frontiersin.org](https://frontiersin.org)

### Contact us

+41 (0)21 510 17 00  
[frontiersin.org/about/contact](https://frontiersin.org/about/contact)

